Preliminary Analysis of PEN Experiment: A Precision Measurement of the Pion Electronic Decay Branching Ratio

Charles Joseph Glaser III

Bloomington, Minnesota

Bachelor of Science in Mathematics, University of Minnesota 2010

Bachelor of Science in Chemistry, University of Minnesota 2010

Bachelor of Science in Physics, University of Minnesota 2011

Bachelor of Science in Astrophysics, University of Minnesota 2011

Master of Arts in Physics, University of Virginia 2017

A Dissertation presented to the Graduate Faculty of the University of Virginia in Candidacy for the Degree of Doctor of Philosophy

Department of Physics

University of Virgina

Abstract

Lepton universality is a key hypothesis of the Standard Model of particle physics which predicts that the charged leptons couple equally in electroweak interactions. All electroweak interactions with the charged leptons are therefore identical under the umbrella of lepton universality. This hypothesis may be confirmed through either high energy collisions, or low energy precision experiments. The PEN experiment, performed at the Paul Scherrer Institute, sought to obtain the pion electronic decay branching ratio $\Gamma(\pi \to e\nu(\gamma)/\Gamma(\pi \to \mu\nu(\gamma))$ to a relative precision of 5×10^{-4}. This ratio provides the best test for electron-muon universality. Deviations from Standard Model expectation would be indicative of physics beyond the Standard Model, or "new physics". Confirmation of the Standard Model expectations put limits on new physics. This dissertation describes a blinded cut-based preliminary blinded analysis for the period comprising the 2009 and 2010 data taken by the PEN collaboration. This dissertation includes the reconstruction of key observables from detector response, the construction and implementation of an ultra-realistic Monte Carlo simulation, and the necessary event selection criteria in order to obtain the branching ratio. Emphasis is placed on the construction of the Monte Carlo simulation needed for the characterization of the low energy tail of the CsI electromagnetic calorimeter as well as determination of the acceptances and cut efficiencies used in the analysis. Characterization of various quantities and uncertainties needed to obtain the branching ratio is also discussed. The partial unblinding of the analysis when including key cut efficiencies is $(1.2534 \pm 0.0013) \times 10^{-4}$ with a relative statistical uncertainty of 8.3×10^{-4} for the 2009 run period. Full unblinding is expected to lower the branching ratio value on the order of 2% . The blinded branching ratio for the 2010 run period results in a $(1.1751 \pm 0.0010) \times 10^{-4}$ result with a relative statistical uncertainty of 6.7×10^{-4}. Combining the two years of the data results in 5.3×10^{-4} relative statistical uncertainty and an overall relative uncertainty of 7.6×10^{-4}. With further study on acceptances, event rejection criteria, and inclusion of the 2008 data, the statistical uncertainty will be diminished to produce a more competitive result with the inclusion of higher statistics.

Contents

List of Figures

List of Tables

1 Introduction

> Before I refuse to take your questions, I'd like to make an opening statement
>
> Ronald Reagan

1.1 Standard Model

Developed in the 1960's, the Standard Model is a theory that accounts for the types of fundamental particles that are expected in nature and for the ways in which they interact. This theory makes definite predictions for almost all measurable quantities, including ones not yet studied. The Standard Model sorts all elementary particles in our universe into two groups: those that experience the strong interactions such as gluons and quarks and those that do not such as electrons and muons. Since its inception, this beautiful theory has been experimentally verified over and over again. However, despite its successes, the Standard Model is known not to be complete. For example, the theory does not address the nature of dark matter or why there are three generations of quarks and leptons. It is the task of physicists to test the Standard Model and to see if there is physics beyond the Standard Model. In order to understand Beyond Standard Model (BSM) physics, a review of the Standard Model is needed. Here a qualitative description will suffice; however, note that a more rigorous mathematical review is available in Appendix A.

The Standard Model is a quantum theory of elementary particles and gauge fields. In this theory, fields become space and time dependent operators. Expectation values of these operators are classical fields in the environment of quantum states. Since the Standard Model is a physical model, it must be governed by Einstein's principle of relativity, i.e., that is that the laws of physics are the same in every inertial frame of reference. So the equations of motion that govern the Standard Model Lagrangian must be Lorentz invariant. This constrains the type of interactions that are allowed in the theory. Further, the Standard Model is required to adhere to global and local gauge invariance. That is to say that the choice to represent the physical state is arbitrary up to a relative phase and that by performing transformations, the physical states themselves remain unchanged. The requirement of global gauge invariance results in charge conservation, while local gauge invariance results in minimal coupling of the current to a gauge field. In addition, renormalizability

is expected. In a renormalizable theory, there exists a systematic procedure for eliminating divergences encountered in calculations of higher order corrections to a given process. That is to say, infinities appear in a finite number of parameters. When quantization finally occurs, this is done using Feynman path integral approach for non-abelian gauge fields because gauge fields are not uniquely defined in a given physical situation but can be defined up to a gauge. With these requirements one can form a Standard Model Lagrangian. The full Lagrangian specifies the types of particles and interactions that should be expected or allowed, and the manner in which these interactions are mediated. The physical and mathematical requirements give rise to a Lagrangian which describes a universe consisting of quarks and leptons whose interactions are mediated by gauge bosons. Mathematically, this is represented by the Standard Model Lagrangian:

$$
\begin{aligned}
\mathcal{L} = & \underbrace{-\frac{1}{4}B_{\mu\nu}B^{\mu\nu} - \frac{1}{8}tr(\mathbf{W}_{\mu\nu}\mathbf{W}^{\mu\nu}) - \frac{1}{2}tr(\mathbf{G}_{\mu\nu}\mathbf{G}^{\mu\nu})}_{\text{U(1), SU(2) and SU(3) gauge terms}} \underbrace{+(\bar{\nu}_L, \bar{e}_L)\widetilde{\sigma}^{\mu}i\mathcal{D}_{\mu}\begin{pmatrix}\nu_L\\ e_L\end{pmatrix} + \bar{e}_R\sigma^{\mu}i\mathcal{D}_{\mu}e_R + \bar{\nu}_R\sigma^{\mu}i\mathcal{D}_{\mu}\nu_R + (h.c)}_{\text{lepton dynamical term}} \\
& \underbrace{-\frac{\sqrt{2}}{v}\left[(\bar{\nu}_L, \bar{e}_L)\phi M^e e_R + \bar{e}_R\bar{M}^e\bar{\phi}\begin{pmatrix}\nu_L\\ e_L\end{pmatrix}\right]}_{\text{electron, muon, tau mass term}} \underbrace{-\frac{\sqrt{2}}{v}\left[(-\bar{e}_L, \bar{e}_L)\phi^* M^{\nu}\nu_R + \bar{\nu}_R\bar{M}^{\nu}\phi^T\begin{pmatrix}-e_L\\ \nu_L\end{pmatrix}\right]}_{\text{neutrino mass term}} \\
& \underbrace{+(\bar{u}_L, \bar{d}_L)\widetilde{\sigma}^{\mu}i\mathcal{D}_{\mu}\begin{pmatrix}u_L\\ d_L\end{pmatrix} + \bar{u}_R\sigma^{\mu}i\mathcal{D}_{\mu}u_R + \bar{d}_R\sigma^{\mu}i\mathcal{D}_{\mu}d_R + (h.c)}_{\text{quark dynamical term}} \underbrace{-\frac{\sqrt{2}}{v}\left[(\bar{u}_L, \bar{d}_L)\phi M^d d_R + \bar{d}_R\bar{M}^d\bar{\phi}\begin{pmatrix}u_L\\ d_L\end{pmatrix}\right]}_{\text{down, strange, bottom quark mass term}} \\
& \underbrace{-\frac{\sqrt{2}}{v}\left[(-\bar{d}_L, \bar{u}_L)\phi^* M^u u_R + \bar{u}_R\bar{M}^u\phi^T\begin{pmatrix}-d_L\\ u_L\end{pmatrix}\right]}_{\text{up, charmed, top quark mass term}} \underbrace{+(\bar{\mathcal{D}_{\mu}}\phi)\mathcal{D}^{\mu}\phi - m_h^2[\bar{\phi}\phi - v^2/2]^2/2v^2}_{\text{Higgs dynamical and mass term}}
\end{aligned}
\tag{1}
$$

Equation 1 and table 1 shows the type of particles expected in the Standard Model and how they interact with each other. These particles are quarks, leptons, force mediators (gauge bosons), and the Higgs boson. At this point, it should be noted that the constants in the Lagrangian, whether it be the mass of particles such as the electron or Higgs, or the coupling terms of the electromagnetic, weak, or strong force, must be determined experimentally. Succinctly speaking, there are no numbers in the above equation. One key observation is to note that according to the Standard Model Lagrangian, leptons differ only in the coupling to the Higgs boson. This becomes important for the main motivation behind the PEN experiment.

Table 1: *Particles of the Standard Model*

Flavor/Generation

Charge	I	II	III
Quarks $+\frac{2}{3}$ C	u(up)	c (charm)	t (top)
Quarks $-\frac{1}{3}$ C	d(down)	s(strange)	b (bottom)
Leptons -1 C	e (electron)	μ muon	τ (tau)
Leptons 0 C	ν_e (electron neutrino)	ν_μ (muon neutrino)	ν_τ (tau neutrino)

Force	Mediator
Strong	G gluon
Electromagnetic	γ photon
Weak	$W^{\pm}$ charged, Z^0 neutral boson

Mass Generator
ϕ Higgs boson

1.2 The Pion

The pion is the lightest meson and a spin 0 boson with valence quarks consisting of first generation quark anti-quark pair. The three different species of the isospin triplet are defined by the type of valence quarks characterizing the particle. A π^+ is characterized by $u\bar{d}$ valence quarks, A π^- is characterized by $\bar{u}d$ valence quarks, and π^0 is characterized by $(u\bar{u} - d\bar{d})/\sqrt{2}$ valence quarks. The pion is a versatile particle in that it has a number of different decay channels. These channels and associated Feynman diagrams are shown in Table 2 and Fig 1.1 respectively.

Table 2: *Decay Channels for Pions*

	Mode	Fraction (Γ_i/Γ)
Γ_1	$\mu(\gamma)\nu_\mu$	$(99.98770 \pm 0.00004)\%$
Γ_2	$\mu\gamma\nu_\mu$ $(E_\gamma > 1$ MeV$)$	$(2.00 \pm 0.25) \times 10^{-4}$
Γ_3	$e(\gamma)\nu_\mu$	$(1.230 \pm 0.004) \times 10^{-4}$
Γ_4	$e\gamma\nu_e$ $(E_\gamma > 10$ MeV$, \theta_{e,\gamma} > 40^\circ)$	$(7.39 \pm 0.05) \times 10^{-7}$
Γ_5	$\pi^0 e\nu_e$	$(1.036 \pm 0.006) \times 10^{-8}$
Γ_6	$ee^-e^+\nu_e$	$(3.2 \pm 0.5) \times 10^{-9}$

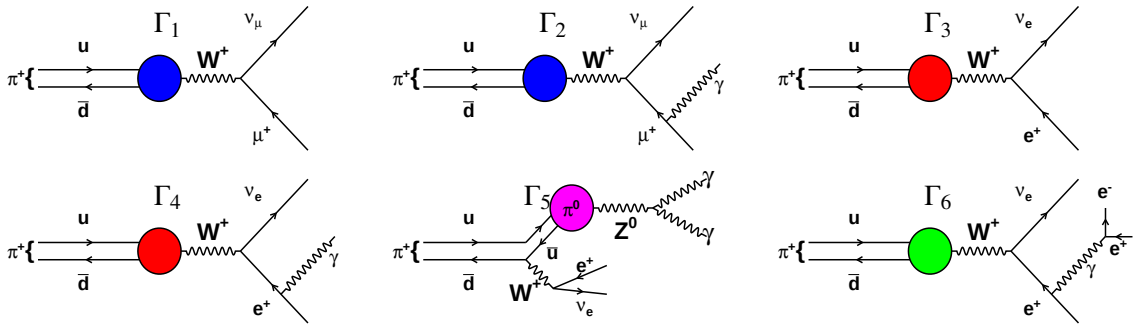

Figure 1.1: *Different decay channels for π^+ .Photons are not shown in decays with soft photons.*

Note the difference between Γ_1 and Γ_2, or Γ_3 and Γ_4, is simply the parenthesis. The parenthesis is used to indicate that the photon emitted is a soft (low energy) photon. Strictly speaking, there is no such process as a non-radiative pion electronic decay. However, most of the decays emit photons that are just too low in energy to be detected. Thus, the distinction between the non-detected radiative decay channels and the detected radiative decay channels is subject to concrete specifications. Ultimately detecting the low energy photons depends on the detector efficiency and resolution, resulting in some flexibility in defining where the soft photon spectrum ends and hard photon spectrum begins. However, as the photon energy increases, the probability of having such an event becomes smaller and therefore higher energy photons emitted in radiative decay are suppressed.

Since the pion more often than not (in fact 99.99% of the time) decays into a muon, muon physics must be understood in order to differentiate between the two main decay channels of the pion as the ultimate product results in a positron for both channels. Muon decay channels and their Feynman diagrams are tabulated and written.

Table 3: *Decay Channels for Muons*

	Mode	Fraction (Γ_i/Γ)
Γ_1	$e\bar{\nu}_e\nu_\mu$	$\approx 100\%$
Γ_2	$e\bar{\nu}_e\nu_\mu\gamma$ $(E_\gamma > 10$ MeV)	$(1.4 \pm 0.4)\%$
Γ_3	$e\bar{\nu}_e\nu_\mu e^+e^-$	$(3.4 \pm 0.4) \times 10^{-5}$

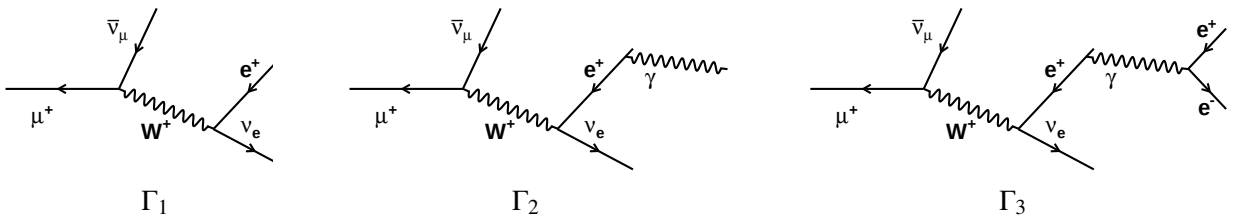

Γ_1 Γ_2 Γ_3

Figure 1.2: *Muon decay Feynman diagrams.*

1.3 Lepton Universality and Rare π Decays

Historically, the pion decay has provided key information regarding Standard Model physics for both weak interactions and radiative corrections. The pion plays a key role in the hadronic sector of the long range particle exchange in effective nucleon-nucleon Lagrangians. One of the most important roles of the pion for particle physics is that it provides the most sensitive test for violation of lepton universality. This is manifested by studying the ratio of the decay rates of $\pi \rightarrow e\nu(\gamma)$ and $\pi \rightarrow \mu\nu(\gamma)$. The theoretical ratio of decay rates, otherwise known as the branching ratio, according to Standard Model calculations is governed by the following equation:

$$R_{e/\mu}^{\pi\ \mathrm{SM}} = \frac{\Gamma(\pi \rightarrow e\nu)}{\Gamma(\pi \rightarrow \mu\nu)} = \left(\frac{g_e}{g_\mu}\right)^2 \left(\frac{m_e}{m_\mu}\right)^2 \frac{\left(1 - m_e^2/m_\mu^2\right)^2}{\left(1 - m_e^2/m_\pi^2\right)^2}(1 + \delta_R) \tag{2}$$

The term δ_R, in Eqn 2 represents the combination of the radiative and loop corrections from the tree level theory and g_e and g_μ represent the strength of the coupling of the W boson to the respective lepton. The m's in the equation represent the masses of the respective particles. The factor $(m_e/m_\mu)^2$ term is manifestation of the $V - A$ nature of these particular interactions.

In the introduction to the Standard Model, it was pointed out that the only difference between the leptons is their coupling to the Higgs, i.e., the mass. In other words, the coupling between the W boson and the leptons is taken to be the same across lepton flavors at least according to the Standard Model hypothesis known as lepton universality. In the context of the branching ratio, Standard Model expectations predict $g_e/g_\mu = 1$. The violation of lepton universality may be studied by reparameterizing the coupling constants as

$$g_l \rightarrow g_l(1 - \epsilon_l/2) \tag{3}$$

where ϵ_l represents deviation from Standard Model expectations for a particular lepton ℓ. This allows us to view the ratio of the couplings in a new light. In particular,

$$\frac{g_{l1}}{g_{l2}} = 1 + \frac{\epsilon_{l1} - \epsilon_{l2}}{2} \tag{4}$$

These parameterizations will have experimental constraints on $\Delta_{l1l2} = \epsilon_{l1} - \epsilon_{l2}$. Even though there are three couplings (or alternatively, three different Δ's) corresponding to the three leptons, only two are independent parameters, because one ratio is the product of the other two. Deviations from Standard Model physics would indicate that there are terms missing in the Standard Model Lagrangian. Consequently, this would signify new types of particles and interactions that have not yet been discovered. A more detailed discussion of lepton universality is given in the theory and motivation chapters.

1.4 Review of pion discovery and decay experiments

In 1935, H. Yukawa predicted that the neutron and proton were attracted to each other by some sort of field characterized by an exchange particle with a predicted mass ~ 300 times mass of the electron (or one-sixth the mass of a proton)[82] . This virtual particle would come to be known as a meson. No particle at this point in scientific history, up to 1935 that is, had been seen that would fit this description. In 1937, Neddermeyer and Anderson [68] identified what was believed to be Yukawa's particle, until discrepancies were discovered. The lifetime was wrong and the mass was seen to be lighter than the predicted particle. The particle discovered by Anderson and Neddermeyer would in time come to be known as the muon. However, in 1946 cosmic rays were observed to interact weakly with atomic nuclei and, low and behold, Cecil Powell and collaborators from the University of Bristol observed two distinct particle tracks for each decay recorded in the photographic emulsion. To achieve this, they had to climb high into the Andes mountains in Bolivia. The true Yukawa particle, the π meson, and the lighter μ which resulted when the pion decays.[54][70]. This discovery eventually won Powell the Nobel Prize in 1950.

Before long it was believed that in addition to decaying into a muon, the pion could decay via the channel $\pi \to e\nu$. Friedman and Rainwater [83] were the first to suspect this decay exists when they had seen 1 or 0 events out of 1419 $\pi \to \mu\nu$ backgrounds. This experiment was followed by other primitive measurements

for the rate of pion decay. Steinberger [85] used a counter to look at short decay times and high energy signatures, and determined the branching ratio to be $R^{\pi\ \mathrm{exp}}_{\mathrm{e}/\mu} = (-3 \pm 9) \times 10^{-5}$. Later, Anderson [6] used a magnetic spectrometer to single out the positron but ultimately failed by stating $R^{\pi\ \mathrm{exp}}_{\mathrm{e}/\mu} = (.4 \pm 9) \times 10^{-6}$. By that time Feynman and Gell Mann had already predicted the branching ratio to be 1.2×10^{-4} from a simple $V - A$ theory.[42]

It wasn't until a CERN group with a telescope detector [41] and Columbia group using a hydrogen bubble chamber [51] that the $\pi^+ \rightarrow \mathrm{e}^+\nu_e$ decays were first detected. However, only later a precise value for the branching ratio obtained. Anderson [7] measured $R^{\pi\ \mathrm{exp}}_{\mathrm{e}/\mu} = (1.03 \pm 0.2) \times 10^{-4}$ and updated it to $(1.21 \pm 0.07) \times 10^{-4}$ using an improved beam profile and higher duty cycle. In this experiment, the researchers were able to observe 10 $\pi \rightarrow \mathrm{e}\nu$ events per hour and ultimately record 1346 such events using stopped pions in plastic scintillator.

In 1963, Di Capua [36] observed 10800 signal events using a NaI(Tl) detector. In this experiment they looked at a 33 ns gate for the presence of a positron. However, only a fraction of the solid sphere (7.25×10^{-3}) was available from the stopping counter. This experiment was the first to use an inorganic crystal scintillator. Upon observing the response of the signal and background in this experiment, the experimenters noted the difficulty in separating the signals because of the long low energy tail of the signal events. They noted that however, small changes in the width of peak response function due to symmetric broadening such as that from the energy spread from the target, had little effect on the low energy tail. The branching ratio obtained in their experiment was $R^{\pi\ \mathrm{exp}}_{\mathrm{e}/\mu} = (1.247 \pm 0.028) \times 10^{-4}$

In 1986, [22] Bryman et al, attempted to measure the pion electronic decay branching ratio with their own NaI(Tl) crystal. They used stopped pions with a beam rate of $20 \times 10^3 \mathrm{s}^{-1}$. A solid angle acceptance of their detector was $\sim$ 0.7%. A method similar to Di Capua was used, the so called "two-bin" method, in which counts were made at two different time intervals. The first t_1 after the pion stops and the second after $t_1 + t_\mathrm{s}$ after the pion stopped where $t_\mathrm{s} >> t_1$. Since this second time is long compared to the pion lifetime, these events would mostly be associated with the background. A cut was made above a certain energy and a tail correction was determined using Monte Carlo simulation. Correction was also made for multiple Coulomb scattering (an energy dependent process where positrons may be scattered into or out of

acceptance), pileup, positron annihilation and false vetos. In this type of method, the branching ratio is

$$R_{e/\mu}^{\pi\ \mathrm{exp}} = \left(\frac{\lambda_\mu}{\lambda_\pi - \lambda_\mu}\right) \frac{N_{\pi e}\left[1 - e^{-(\lambda_\pi - \lambda_\mu)t_s}\right]}{N(2)_{\pi\mu e} e^{\lambda_\mu t_s} - N(1)_{\pi\mu e}} \tag{5}$$

Here, $\lambda_\pi = 1/\tau_\pi$ and $\lambda_\mu = 1/\tau_\mu$ and N(1) and N(2) are the number of background events observed in the first and second time window. Using the two bin method they obtained a branching ratio $R_{e/\mu}^{\pi\mathrm{exp}} = (1.218 \pm 0.014) \times 10^{-4}$. In addition to using this method, they did a simple extraction of branching ratio from measuring the decay time distribution amplitudes. This method resulted in a branching ratio of $R_{e/\mu}^{\pi\ \mathrm{exp}} = (1.219 \pm 0.014) \times 10^{-4}$, consistent with the first method.

Bryman et al, once again measured the pion electronic decay branching ratio in 1992 [23] using a beam momentum of 83 MeV/c, stopping pions in a plastic scintillator, using vetos for μ decay and observing positrons perpendicular to the incoming pion beam. They used Na(Tl) "TINA" which had a 2.9% solid angle acceptance and resulted in observing 1.2×10^5 $\pi^+ \to e^+\nu$ events. $\pi \to \mu\nu$ events were prescaled by 1:16 in $-120 - 300$ ns within the pion stopping. Events which occurred in the the first 30 ns or less for energy greater than 50 MeV were recorded. This experiment included the measurement of target energy or energy loss of all particles in the target. If the total target wave energy was deemed too high, most probably due to the 4 MeV deposited by the intermediate muon, this event would be classified as background. However, this biased against long pathlengths taken by the positron in good signal events and a tail fraction correction was made for these events. The tail response due to TINA was $\sim 0.4\%$, again attributed to energy leakage through the electromagnetic calorimeter. Monte Carlo corrections were made for annihilation and multiple scattering, but this contributed to $\sim 0.1\%$ of the tail. The results of their work determined a branching ratio of $R_{e/\mu}^{\pi\ \mathrm{exp}} = (1.2265 \pm 0.0034(\mathrm{stat}) \pm 0.0044(\mathrm{syst})) \times 10^{-4}$.

In 1992 Czapek et al, [33] performed a rare pion decay experiment at the Paul Scherrer Institute (PSI). They used stopped pions with an electrostatic separator to separate out beam positrons, and time-of-flight discrimination to separate out beam muons. Accepted events occurred between $7.5 - 200$ ns after the pion stopped. The target scintillator light was collected by 2 Bismuth Germanium Oxide (BGO) crystals which also served as light guides and elements of the electromagnetic calorimeter. The BGO calorimeter provided a solid angle of nearly 4π steradians, with only 0.2% acceptance loss originating from the entrance of the calorimeter. The crystals comprising the calorimeter were tested for output light uniformity as a function of

position of the crystals and was found to be uniform with a deviation of 1.5%. The analysis was performed by observing events in three energy regions. The regions were defined by total energy, that is, the kinetic energy of the decaying pion and the energy of the outgoing positron, as well as any deposited energy by an intermediate muon. The region of interest in energy was 83.5–101 MeV, which comprised the main signal. The region above 101 MeV mostly consisted of hadronic interactions of the pion. Energy regions below 83.5 MeV were mostly background events, but consisted of some signal events caused by energy leakage of the electromagnetic shower out of the calorimeter. The low energy tail from event signals required a correction for photonuclear absorption. Monte Carlo software was used to account for photonuclear absorption with neutron emission. The main contribution was absorption on bismuth with a cross section σ ~500 mb because of a giant resonance energy of ~ 13 MeV. The only significant contributions were (n,γ) and (n,α). Their result was a branching ratio of $R^{\pi\ \mathrm{exp}}_{\mathrm{e}/\mu} = (1.235 \pm 0.005) \times 10^{-4}$ with a statistical error of 0.28% and systematic error of 0.29% .

One of the two more recent experiments on rare pion decays was once again performed by Bryman et al, [25] at Triumf in the PiENu experiment. The experiment used a 75 MeV/c beam and stopped pions in the target. Wire chambers were used to track decay particles and a NaI(Tl) (19 radiation lengths) electromagnetic array was used as the positron detector. The main positron detector was further surrounded by a pure CsI detector. Events were recorded in a time window of $-300 - 540$ ns with regard to the incoming pion. Events were selected based on energy regimes. The raw branching ratio was constructed from a simultaneous fit for both the low and high energy regions where the two regions were determined by above or below 52 MeV. The lower energy regime was mostly the $\pi \rightarrow \mu \rightarrow$e background, as well as π decays in flight to muons, π_{DIF}, and muons from previous pions, i.e., pileup, in the target. The high energy region consisted of the signal events, high energy pileup, muon decays in flight, μ_{DIF}, and radiative muon events. The biggest uncertainty came from the low energy tail of the electromagnetic calorimeter. Simulation for this experiment was not able to reproduce the hadronic interactions accurately in the NaI(Tl) calorimeter so corrections were made based off experimental data and theoretical knowledge. Using time spectra that satisfied both the high and low energy events simultaneously with processes that existed in both regimes, a branching ratio was determined to be $R^{\pi\ \mathrm{exp}}_{\mathrm{e}/\mu} = (1.2344 \pm .0023 \pm .0019) \times 10^{-4}$.

The importance of looking at historical experiments similar to the PEN experiment is obvious. One can learn from past experience. In the modern experiments, studying pion decays requires an electromagnetic

calorimeter instead of a magnetic spectrometer. Corrections to the low energy tail of the electromagnetic calorimeter's response are needed. In addition, a precise understanding of photonuclear processes in the inorganic crystals is required in order to properly correct the low energy tail due to these processes. Naturally, discrimination between background and signal is of high importance and different experiments have used different methods in order to achieve this. A longer discussion of how previous experiments influence the setup of the PEN experiment and analysis is presented in the experimental section and analysis section.

1.5 Looking ahead

Previous experiments have demonstrated that the branching ratio analysis is one that must be done with care and planning. The analysis that the PEN experiment is undertaking requires many different components. The reader can obtain some insight when understanding the simple kinematics and timing involved in the two decay processes observed in the leptonic decay of the pion. In the measurement, the two decay chains are that of the $\pi \to e\nu$ and the $\pi \to \mu\nu$. However, the muon itself decays and produces a positron with two neutrinos. In the previous experiments the $\pi \to \mu\nu$ decays were counted by counting the number of positrons emerging from the muon decay. Because the muon and pion have vastly different lifetimes, $\tau_\mu = 2.2\ \mu$s and $\tau_\pi = 26.03$ ns respectively, this can be used to understand some of the choices that were made by previous experiments and this one. In particular when these decays are most prominent and what time window should be used in which to choose study each of these decays. The probability distribution of the positron birth in the two decay chains are shown in Fig 1.3.

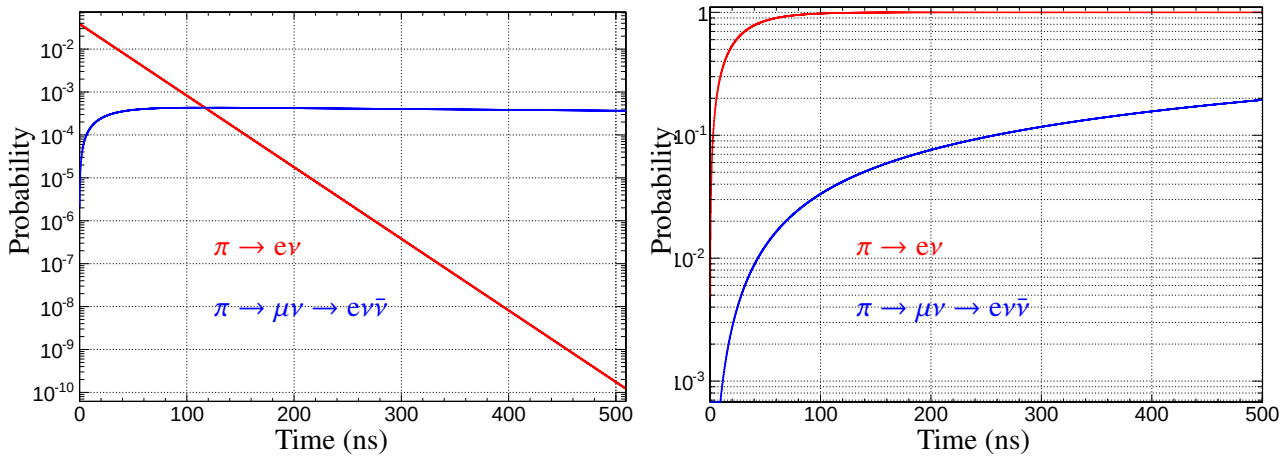

Figure 1.3: *Decay time probabilities for positronic pion decay (red) and the positron from the muon decaying following the pion decay (blue) as a function of time after the pion stops. Left: Probability distribution function. Right: Cumulative distribution function.*

Fig 1.3 shows that in order to count the number of positron pion decays, it is best to use an early time window following the pion stop time to minimize the number of $\pi \to \mu\nu$ background and to ensure that a sufficiently large number positronic decays are counted so as to maintain a reasonable statistical uncertainty. In addition, it is best to use a later decay time window for the $\pi \to \mu\nu$ chain so that the number of positronic pion decays becomes negligible but ensuring that the window is sufficiently large so as ensure that the statistical uncertainty of the normalization background does not become an issue. While the timing in the two decay chains is one of the two main observables that distinguishes the two decay chains, the other is energy.

From simple kinematics and approximating the positron and neutrino to be massless, the emerging positron must have equal and opposite momentum and their energies are both one-half the pion mass, or approximately 70 MeV. In the case of a positron emerging from the muon decay, the electron can have a range of energies up to half the muon mass. It is therefore the energy of the positron that is used to deduce which of the two decay channels the positrons belongs. This is seen mostly easily in Fig 1.4 where the energy deposited for the two main channels is shown.

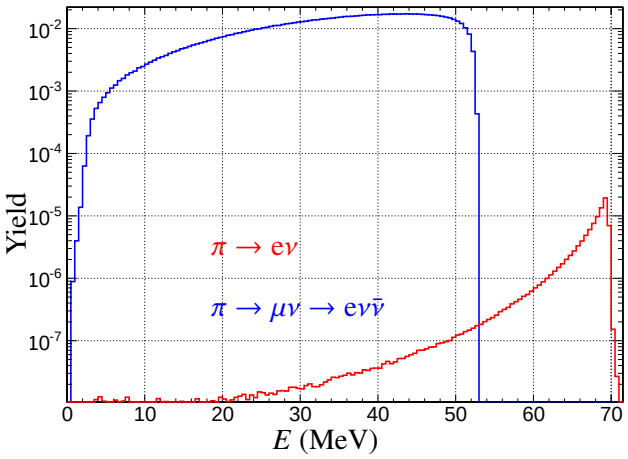

Figure 1.4: *Positron energy deposition for the two main decay channels.*

While the majority of events of the positronic decay occur near the peak region near the aforementioned 70 MeV, there is a non-negligible contribution due to the low energy tail which forms due to energy leakage in the calorimeter and goes all the way to zero energy. The difficulty becomes apparent in that the tail is underneath an enormous normalization background. This indicates that counting the number of events in the positronic decay is a matter of understanding the low energy tail at the desired level of precision in addition to counting the number of events which occur in the peak region. It is also clear that the counts from the muon decay are performed by counting the number of events below a particular energy threshold and ensuring that the number of overlapping pion decay events from the tail are either statistically insignificant or subtracted out. Fig 1.4 and Fig 1.3 therefore provides some insight into how to proceed with the analysis.

After the acquisition of raw data from the experiment, calibrations are of course made in order to take signals into observables. The calibrated data are then purged of unavoidable unwanted background all while constructing observables that can discriminate between the two main channels of interest. As discussed, total target energy was used in previous experiments, where due to the extra muon present in the target, the $\pi \to \mu\nu$ decay possess more energy deposition in the target than the $\pi \to e\nu$ decay channel. Higher order observables can be constructed to aid in the separation between the two decay channels. Simultaneously, a Monte Carlo simulation is constructed in order to obtain the acceptances of the experiment as well as the low energy tail. As the previous experiments have noted, the low energy tail is indeed a very difficult quantity to obtain, but one that is necessary to obtain the branching ratio. For the PEN experiment, the branching analysis is broken into small pieces, each of which is necessary to obtain the branching ratio. By writing the

number of $\pi \to e\nu$ decays as $N_{\pi\to e\nu} = N^{\text{peak}}_{\pi\to e\nu} + N^{\text{tail}}_{\pi\to e\nu}$, the number of $\pi \to e\nu$ decays is then rearranged to be

$$N_{\pi\to e\nu} = N^{\text{peak}}_{\pi\to e\nu}(1 + \epsilon_{\text{tail}}) \tag{6}$$

The number of $\pi \to e\nu$ is akin to counting the number of events above some energy threshold and then characterizing the tail fraction of the energy spectrum. The branching ratio is more than just counting the number of events of a particular decay chain but also entails making systematic corrections. Accounting for the number of events not counted due to finite data sampling time, r_f, the efficiencies of reconstructing the event due to tracking, $\epsilon_{\text{MWPC}}(E)$, and accounting for decays in flight, cut, and geometric acceptances, r_A, produces a branching ratio expression in Eqn 7.

$$B = \underbrace{\frac{N^{\text{peak}}_{\pi\to e\nu}}{N_{\pi\to\mu\nu}}}_{\text{Experiment}} \cdot \underbrace{(1 + \epsilon_{\text{tail}})}_{\text{Monte Carlo}} \cdot \underbrace{r_f}_{\text{Theory}} \cdot \underbrace{\epsilon_{\text{MWPC}}(E)}_{\text{Experiment}} \cdot \underbrace{r_A}_{\text{Monte Carlo}} \tag{7}$$

The branching ratio therefore requires an understanding of the data, the theory, and the Monte Carlo simulation at the level 10^{-4} level. The analysis of the branching ratio then follows the flow chart outlined in Fig 1.5. It should also be noted that somewhere in the analysis portion, a method by which radiative decays be included in Eqn 7 as the hard radiative decays contribute to the overall decay rate of the two main channels. In addition, it is expected that these quantities are not completely unrelated. The number of peak events in the pion decay count depends on where the dividing line between tail and peak events occur. A higher dividing line produces a lower peak count and lower dividing line produces a higher peak count. The uncertainties play a role in where to choose the optimal dividing line. For the pion decay count, the number of peak events, tail fraction, and decay time window is chosen so as to minimize the total relative uncertainty.

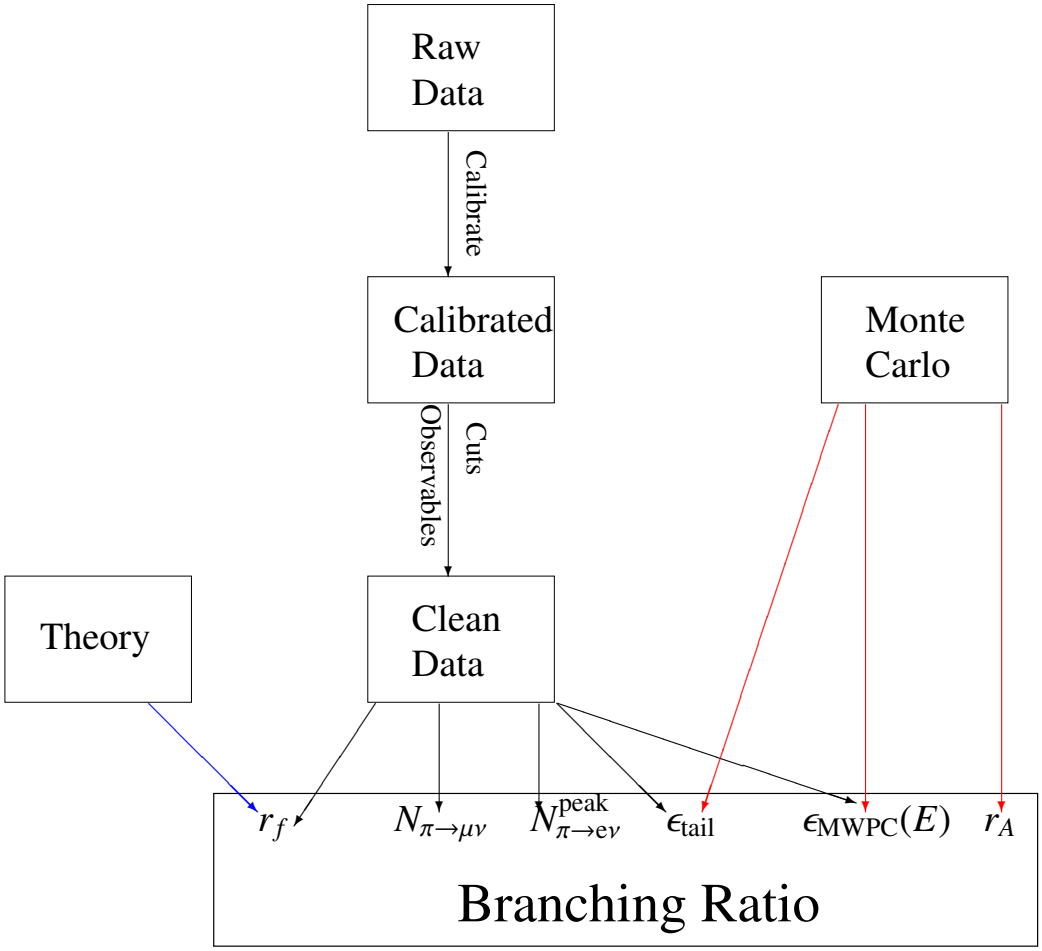

Figure 1.5: *Flow chart of analysis strategy.*

The various quantities necessary to obtain the branching ratio outlined in Fig 1.5 show the overlap between the different components in the analysis moving forward. This hopefully provides the reader with some insight into the structure and organization in this work.

2 Theory of Pion Decays

> There could be no fairer destiny for any physical theory than that it should point the way to a more comprehensive theory in which it lives on as a limiting case
>
> Albert Einstein

This section reviews the underlying theory and implications of the different pion decay channels, in particular discussing those that are relevant in the PEN experiment. Although this work is mostly focused on the $\pi \to l\nu_l(\gamma)$ decays, it is incomplete without a short discussion of muon decays as they are the biggest background in the PEN experiment. Muon decays alone can and have been used to search for Physics Beyond the Standard Model. A discussion of hard radiative decays will also be appropriate for two specific reasons. The first is that radiative decays have implications regarding the pion structure itself. The second reason, which is most important to this analysis, is that there really is no such thing as non-radiative decays. All real decays are radiative and this phenomenon will be explained in greater detail and will ultimately be accounted for in the final analysis. Lastly, it would be an injustice if the pion beta decay was not briefly mentioned since the PEN experiment is the successor to the PiBeta experiment which looked at this particular channel in great detail.

2.1 Leptonic Decay: $\pi^+ \to l^+(\gamma)\nu_l$

The decay process that is most interesting to this work is the $\pi \to l\nu_l$ decay. The underlying physics of this process may be understood by starting with Fermi's golden rule. Fermi's golden rules states that the probability of a process to transition from initial state, $\langle i|$, to a final state, $|f\rangle$, is proportional to $|\langle f|H_{\text{int}}|i\rangle|^2\rho$ and is denoted Γ_{fi}. In this expression, ρ represents the density of final states, a kinematics factor that imposes energy and momentum conservation, and $|\langle f|H_{\text{int}}|i\rangle|^2$ is related to the interaction itself. This term can be used to obtain Lorentz invariant observable quantities such as decay rates and lifetimes provided proper normalization of the initial and final state wavefunctions. The differential decay rate for $\pi \to \ell\nu$ is given by

$$d\Gamma = \frac{1}{2m_\pi}|M|^2 \frac{1}{2E_l 2E_\nu} \frac{d^3p_l}{(2\pi)^3} \frac{d^3p_\nu}{(2\pi)^3} \delta^4(q - p_l - p_\nu), \tag{8}$$

where m_π is the pion mass, q, p_l, and p_ν are the four momenta of the pion, lepton, and neutrino, and M is the matrix element of the interaction. This matrix element originates from the Lagrangian. The type of interaction which the particle undergoes determines the decay rate of a particular process, and the types of interactions which may occur are indicated in the interaction terms in the Lagrangian. For instance, during the Fermi era when β^- decays were being studied in great detail, the interaction term for the Lagrangian would be written as

$$\mathcal{L}_{\text{int}} = \frac{-G_F}{\sqrt{2}} \left[\bar{\psi}_p \gamma_\lambda \psi_n \bar{\psi}_e \gamma^\lambda \psi_{\nu_e} + \bar{\psi}_n \gamma_\lambda \psi_p \bar{\psi}_{\nu_e} \gamma^\lambda \psi_e \right]. \tag{9}$$

In these expressions, the final and initial particle states are written around the term that represents the interaction itself. The expression on the right inside the brackets represent the process $n \rightarrow pe\bar{\nu}_e$, neutron beta decay. Notice there are two γ terms, one of which is contravariant, the other covariant, producing a Lorentz invariant quantity. The second expression is electron capture. This Lagrangian was constructed analogous to quantum electrodynamics. Thus any physical process may be understood and constructed in this type of formalism. One important thing to note is that the two gamma terms are not the only way in which a Lorentz invariant quantity can be constructed. Fermi, Gammow, and Teller [46] argued that a general method to construct the Lagrangian is to have a linear combination of all different types of Lorentz invariant terms, and therefore a matrix element in general, would have the following form

$$\mathcal{M} = \frac{G_F}{\sqrt{2}} \Sigma_i \int C_i \bar{\psi}_p O_i \psi_n \bar{\psi}_l O_i \psi_{\bar{\nu}_e}, \tag{10}$$

where i is summed over all types of operators. The different operators are scalar (a number), pseudoscalar (γ_5), vector(γ_ν), axial-vector (or pseudo-vector $\gamma_5\gamma_\nu$) and tensor($\sigma_{\mu\nu}$). The Lagrangian terms must conform to conservation (or non-violation) of laws of nature. For example, momentum and energy conservation arise from invariance of spacetime translation in the Lagrangian. Parity, that is the laws of physics appear the same in mirror processes, was once considered as something conserved. Meaning if a process would occur, then so would its mirror process. Lee and Yang [58] were the first to propose that parity is not a conserved quantity which was confirmed by a Wu et al. [81]. Since parity conservation was no longer

considered to be conserved, the Lagrangian doesn't need to be invariant under parity transformation. Studies of β^- decays revealed that ν_e are left handed and $\bar{\nu}_e$ are right handed. This ultimately meant that the scalar, pseudoscalar and tensor term had to be very small (or zero). So a matrix element with vector and axial vector interaction would be expected and generalized as

$$\frac{1}{2}\gamma_\lambda(C_V + C_A\gamma_5) \tag{11}$$

From Møller scattering, results showed [87] that β decays are longitudinally polarized with helicity $(-v)/c$ for electrons and $(+v)/c$ for positrons, which lead to the conclusion that $C_V = -C_A$, which leads to the now expected interaction for weak decays as

$$\frac{1}{2}\gamma_\lambda(1 - \gamma_5). \tag{12}$$

While this interaction characterizes the electroweak interaction, a caveat exists. There has been no mention as to whether the decaying particle is a lepton, or a composite particle hadron such as the π. The manner in which this is handled was proposed by Feynman and Gell-Mann and independently Sudarshan and Marshak [78]. They proposed that all charged weak processes are described by an effective Lagrangian that has a weak current, J_μ that coupled to itself, giving a Lagrangian of

$$\mathcal{L} = -\frac{1}{2}\frac{G_F}{\sqrt{2}}(J_\mu J^{\dagger\mu} + J^{\dagger\mu} J_\mu) \tag{13}$$

The weak current itself is a sum of two portions, $J_\mu = j_{l\mu} + j_{h\mu}$, a leptonic portion, $j_{l\mu}$, which is the $V - A$ interaction that has been mentioned, and the hadronic portion, $j_{h\mu}$ which is similar to the $V - A$ interaction, but acting on quarks. For the pion decay, the hadronic portions takes the form

$$j_{h\mu} = \bar{D}_C\gamma_\mu(1 - \gamma_5)U. \tag{14}$$

Where $\bar{D}_C$ is the Cabbibo rotated $\bar{D}\cos\theta_C$ because the weak interactions couple to the weak eigenstates of the down and strange quarks instead of the mass eigenstates. Once Feynman rules are applied, a small problem arises with this theory in that unitarity is not respected. A contradiction of experiment and this theory arises for electron-neutrino scattering cross section for this process at sufficiently high energies. Meaning the theory is not complete. This was remedied by an intermediate vector boson acting as a force

carrier of the weak force . With this last piece, the full interaction was realized and the matrix element takes the form

$$\mathcal{M} = i\frac{1}{M_W^2 - q^2}\left(g^{\mu\nu} - \frac{q^\mu q^\nu}{M_W^2}\right) j_{\pi\mu} j_{l\nu}. \tag{15}$$

Here the pion is the acting hadron and the lepton will either be the muon or positron, and M_W is the mass of the intermediating W boson. For the case of low momentum transfer, that is energies much less than mass of the W boson (80 GeV), the Fermi theory, where unitarity is not maintained, can be recovered and the matrix element becomes

$$\mathcal{M} = \frac{iG}{\sqrt{2}} \langle 0|V^\mu - A^\mu|\pi\rangle \, \bar{u}_l \gamma_\mu (1 - \gamma_5) v_{\nu_l}. \tag{16}$$

Since the first part of the matrix element involves the pseudoscalar pion to the vacuum using a vector term, this term should vanish, describing a matrix element

$$\mathcal{M} = \frac{-iG}{\sqrt{2}} \langle 0|A^\mu|\pi\rangle \, \bar{u}_l \gamma_\mu (1 - \gamma_5) v_{\nu_l}. \tag{17}$$

The first term is a quantity that should be a Lorentz four-vector to maintain invariance, and since the only four-vector available is the momentum transfer q^μ, one may write

$$\langle 0|A^\mu|\pi\rangle = f_\pi q^\mu. \tag{18}$$

The term f_π is the pion decay constant which is determined experimentally in leptonic pion decays. The matrix element then becomes

$$\mathcal{M} = \frac{-iG}{\sqrt{2}} f_\pi q^\mu \bar{u}_l \gamma_\mu (1 - \gamma_5) v_{\nu_l}. \tag{19}$$

After accounting for spin polarizations, the square of the matrix element is

$$|\mathcal{M}|^2 = 4G^2 f_\pi^2 m_l^2 p_l p_\nu. \tag{20}$$

The matrix element is proportional to the mass. This is not unexpected as the longitudinal part, which couples to the pion, is part of the Higgs scalar so the interaction is proportional to the mass.

When all is said and done and the phase space factor (density of states) is accounted for (see Appendix

B), the rate of the decay for a particular channel is

$$\Gamma(\pi \to l\nu_l) = \frac{G_F^2 f_\pi^2 m_l^2}{8\pi m_\pi^3}(m_\pi^2 - m_l^2)^2 \tag{21}$$

By taking the ratio between the $\pi \to e\nu$ and that of $\pi \to \mu\nu$, it is seen that the the ratio of the decay rates depends on the ratio of square of the lepton masses. In particular, the branching ratio is given as

$$\frac{\Gamma(\pi \to e\nu)}{\Gamma(\pi \to \mu\nu)} = \frac{m_e^2}{m_\mu^2}\frac{(m_\pi^2 - m_e^2)^2}{(m_\pi^2 - m_\mu^2)^2} \approx 1.283 \times 10^{-4}. \tag{22}$$

An important thing to note is the that pion decay constant no longer appears. By studying the ratio of the two decay rates, the hadronic terms and accompanying loops associated with Quantum Chromodynamics (QCD) will cancel, eliminating uncertainty associated with QCD. Of further note is that the ratio of the masses squared appears in the branching ratio. This term is extremely small, $\approx 2.5 \times 10^{-5}$, and is a manifestation of the $V - A$ nature of the electroweak interaction. It is this term that so highly suppresses the $\pi \to e\nu$ decay channel and makes the branching ratio so susceptible to non $V - A$ interactions. The nature of the weak interaction reveals that electroweak decays prefer to pick out left-handed chiral states for massless fermions and right-handed chiral states for massless anti-fermions. This is apparent in a term that appears in the Feynman rules (matrix element calculation) as $1 - \gamma_5$, which is the left-handed chirality projection operator for massless leptons. Since the positron and muon are not massless, their chiralities are mixed according their masses. This wouldn't seem like such a problem since both the positron and neutrino are particles with small mass. However, when a pion decays at rest, the essentially massless neutrino will decay as a left-handed particle. The problem arises due to another conserved quantity, angular momentum. The pion is a spin 0 particle, and its two daughter particles are spin-1/2 particles. Since the neutrino is left handed, the emerging positron must also emerge in the opposite direction of the neutrino with a left-handed chiral state as well. This conflicts with the weak interaction which prefers the positron to be right-handed. The $V - A$ interaction, specifically the $1 - \gamma_5$ term, picks out left handed chiral states massless fermions and right handed chiral states massless antifermions. Since the positron is not massless, the spinor can be decomposed into right handed and left handed chiral components which shows this description is true with a correction on the order of m_e/E. It can then be shown that the probability of picking out a left handed state

from this type of interaction is $\sim (1 - v_l/c)$, yielding

$$\frac{\Gamma(\pi \to \mathrm{e}\nu)}{\Gamma(\pi \to \mu\nu)} \sim \frac{1 - v_e/c}{1 - v_\mu/c} \sim \frac{m_e^2}{m_\mu^2}. \tag{23}$$

Also note that if the positron were a massless particle, then the velocity emerging from the interaction would be c, and thus the branching ratio would be 0, that is to say that the $\pi \to \mathrm{e}\nu$ decay would never occur. Thus far, only tree level calculations have been discussed. The branching ratio is not complete unless radiative and loop corrections are accounted for. These corrections for a pion decay process will depend on the mass of the resulting lepton and they originate from the emission of a photon via Inner Bremsstrahlung, and the virtual emission and reabsorption of photons. Classically, Bremstrahulung radiation is emitted whenever a charged particle is accelerated or decelerated (bremsstrahulung is German for breaking radiation). Whenever a charged particle scatters in a medium, its velocity changes. This means that acceleration has occurred and therefore a photon must be emitted. A positron can not radiate a photon unless it exchanges a soft photon with the nucleus that is near. Once the corrections are put into the branching ratio, the branching ratio becomes

$$\frac{\Gamma(\pi \to \mathrm{e}\nu)}{\Gamma(\pi \to \mu\nu)} = \frac{m_e^2}{m_\mu^2}\frac{(m_\pi^2 - m_e^2)^2}{(m_\pi^2 - m_\mu^2)^2}(1 + \delta)(1 + \epsilon) = 1.233 \times 10^{-4} \tag{24}$$

where $\delta = -3\alpha/\pi \ln\left(m_\mu/m_e\right)$ and $\epsilon = -.92\alpha/\pi$. In leading up to this ratio, the assumption of lepton universality was made. Lepton universality assumes that the W boson couples with equal strength to e, μ, τ. Thus the hypothesis proposes that the only difference between these three leptons in the Standard Model is their coupling to the Higgs.

To include the possibility of violation of lepton universality and combining the radiative corrections, we obtain

$$R_{\pi_{\mathrm{e}2}}^{\mathrm{SM}} = \frac{\Gamma(\pi \to \mathrm{e}\nu)}{\Gamma(\pi \to \mu\nu)} = \left(\frac{g_e}{g_\mu}\right)^2 \left(\frac{m_e}{m_\mu}\right)^2 \frac{\left(1 - m_e^2/m_\mu^2\right)^2}{\left(1 - m_e^2/m_\pi^2\right)^2}(1 + \delta_R) \tag{25}$$

where the radiative corrections and loop corrections have been combined into δ_R, and lepton universality holds if the ratio of the coupling between the W boson and the two leptons are the same, i.e., $g_{\mathrm{e}} = g_\mu$. Ac-

cording to the recent Standard Model calculations of the branching ratio, which assumes lepton universality

$$R^{\mathrm{SM}}_{\pi_{e2}} = \begin{cases} (1.2352 \pm 0.0005) \times 10^{-4} & [61] \\ (1.2354 \pm 0.0002) \times 10^{-4} & [44] \\ (1.2352 \pm 0.0001) \times 10^{-4} & [30] \end{cases}$$

Now as mentioned, there is no distinction between the radiative and "non-radiative" events. The decay in question has a photon but the photon is mostly infrared (very low energy) and therefore usually undetectable in these experiments. This is because individual photon can be emitted with arbitrarily small energies that can always escape detection. However, the radiative decay does allow some interesting physics to be probed which will be reviewed later on.

2.2 Muon Decay and Radiative Muon Decay: $\mu^+ \to e^+\nu_e\bar{\nu}_\mu(\gamma)$

Historically, muon decay, sometimes called Michel decay [64] has played an important role in verifying the $V - A$ relationship in the Standard Model. Understanding the muon decay will be important for this work because the main background of the experiment involves muon decays. For completeness, a brief description of the theoretical background and Standard Model implications are given in this section.

The muon decay is a pure leptonic weak decay; there is no structure of the parent or daughter particle that must be accounted for when calculating decay rates. Starting with the matrix element according to Langacker [53],

$$\mathcal{M} = \frac{G_F}{\sqrt{2}}\bar{\nu}_\nu\gamma_\lambda(1-\gamma_5)\bar{\nu}_e\gamma^\lambda(1-\gamma_5)u_\nu, \tag{26}$$

and following similar steps to the pion decay, the decay rate is determined to be

$$\Gamma = \frac{G_F^2 m_\mu^5}{192\pi^3}. \tag{27}$$

Once the decay rate, and therefore the lifetime $(1/\Gamma)$ is known, arguably that is all one would need to know for the main purpose of this experiment. However, a pion decay at rest is essentially a muon birth since this is the predominant decay channel for the pion. And muon decay physics may also be used to study processes beyond the Standard Model. Including all possible interactions that may occur due to Lorentz invariance, a

general matrix element for muon decay may be written as

$$\mathcal{M} = \frac{G_F}{\sqrt{2}}\Sigma\bar{u_e}O_i u_\mu \bar{u}_2 O_i(C_i + C_i'\gamma_5)\nu_1 \tag{28}$$

Using the general interaction, instead of a simple $V-A$, a more general decay rate is computed

$$\mathrm{d}\Gamma = \frac{G_F^2 m_\mu^5}{192\pi^3}\frac{D}{16}\epsilon^2\left(12(1-\epsilon) + \frac{4}{3}\rho(8\epsilon-6) \mp P_\mu\xi\cos\theta\left[4(1-\epsilon+\frac{4}{3}\delta(8\epsilon-6)\right]\right)\mathrm{d}\epsilon\mathrm{d}\cos\theta/2 \tag{29}$$

In this expression, $\cos\theta$ is the cosine of the angle between the electron momentum and the muon spin direction. The parameters ρ, η, ξ, and δ are defined as Michel parameters. They contain information with various couplings constants for the different possible interactions. Specifically,

$$\rho = (3g_A^2 + 3g_V^2 + 6g_T^2)/D \tag{30}$$

$$\eta = (g_S^2 - g_P^2 + 2g_A^2 - 2g_V^2)/D \tag{31}$$

$$\xi = (6g_S g_P\cos\phi_{SP} - 8g_A g_V\cos\phi_{AV} + 14g_T^2\cos\phi_{TT})/D \tag{32}$$

$$\delta = (-6g_A g_V\cos\phi_{AV} + 6g_T^2\cos\phi_{TT})/ \tag{33}$$

where

$$D = g_S^2 + g_P^2 + 4g_v^2 + 6g_T^2 j + 4g_A^2, \qquad \cos\phi_{ij} = Re(C_i^* C_j' + C_i' C_j^*), \qquad \text{and } g_i^2 = |C_i|^2 + |C_i'|^2 \tag{34}$$

For an amplitude with only V and A components that is $C_s = C_s' = C_T = C_T' = C_P = C_P' = 0$, and in particular a V$-$ A law, the Standard Model Michel parameters take the form:

$$D = 16|C_V|^2, \qquad \rho = \delta = \frac{3}{4}, \qquad \eta = 0, \qquad \xi = -1$$

These parameters may be tested experimentally. Specifically, η and ρ may be measured by the momentum spectrum of electrons in the decay of unpolarized muons. ξ and δ may be measured in the asymmetry in the decay of polarized muons, where a departure of ξ, for example, would signify the existence of a right-handed $(V+A)$ current.

In addition to "ordinary" muon decay, radiative muon decays can probe Standard Model expectations. For this type of decay, a new parameter, $\bar{\eta}$, emerges when the decay of a muon is accompanied by a hard photon. The definition of $\bar{\eta} = (2g_T + g_P + g_S)/A$, where A is a parameter that is measured in experiment. Measuring the value of $\bar{\eta}$ is equivalent to a measurement of the transverse polarization of the electron in the muon decay. Standard Model sets $\bar{\eta} = 0$. Deviations from $\bar{\eta} = 0$ would suggest the presence of non $V - A$ physics in weak interactions. A more detailed description and analysis on radiative muon decay is done in the PiBeta experiment by Emmanuel Munyangabe, Brent VanDevender, and Robin Smith [65][88][84].

2.3 Radiative Pion: $\pi^+ \to l^+\gamma\nu_l$

It was stated that the only difference between $\pi^+ \to l^+\gamma\nu_l$ and $\pi^+ \to l^+(\gamma)\nu_l$ is simply the parenthesis. The parenthesis is used to indicate that the photon emitted is a soft (low energy) photon. Once again, there is no such process as a non-radiative pion electronic decay and that most of the decays emit photons that are just too low of energy to be detected. This may be understood by considering Feynman diagrams. Virtual photons from loops contribute to the overall decay rate. Unfortunately, when calculating the rates of these processes/diagrams, an infrared divergence occurs. This infrared divergence is exactly canceled when considering the emission of a real photon from the decay process, from an inner bremsstrahlung process. This is the Bloch-Norsieck theorem [16]. So the overall real process includes the emission of a real photon because observable processes, like decay rates, must be finite. Moreover, the real photon that is emitted will typically have very low energy to the point where it may not easily (if at all) be detected. In these cases, the photons are typically colinear with the positron and the kinematics of such processes appear as if it were the two-body decay. Details of the descriptions and calculations may be referenced in [76], [90], [77]. However, for those photons that possess energies that are high enough to be detected, there is something new that can be learned. One of the caveats of studying the pion is that the Feynman diagrams which described this decay mode are too simplified. The pion is a charged particle, so treating it as a point particle will produce a pion bremsstrahulung process. However, the pion is in fact a composite particle composed of charged quarks, meaning that a photon can emanate from the structure of the pion, which brings about structure dependent terms in the decay amplitude. In particular it is governed by a vector and an axial vector form factor. The

photon is emitted from intermediate states that emerge from strong interactions, that is to say hadronic states. The matrix element contribution can therefore be broken into the structure dependent and inner bremsstrahlung contributions, where the inner bremsstrahlung differential decay rate is proportional to the the "non-radiative" decay rate. Hence this particular contribution is chirally suppressed, much like the "two-body decay", therefore the structure dependent term is accessible and may possibly provide information on the structure of the pion.

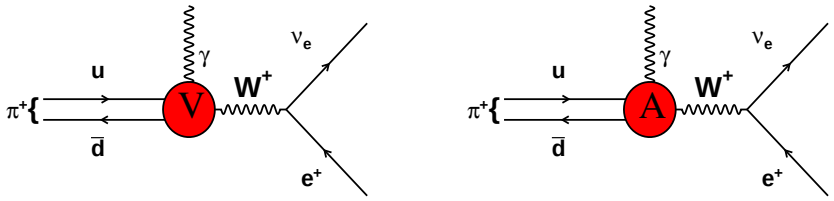

Figure 2.1: *Feynman diagrams for hard radiative pion decay.*

In writing the total differential decay rate of this process as a sum of the structure dependent and inner bremsstrahulung, it can be shown [21] that

$$\frac{d^2\Gamma}{dxdy} = \frac{\alpha}{2\pi}\Gamma_{\pi\to e\nu}\times$$
$$\left[IB(x,y) + \frac{1}{4}\frac{m_\pi^2}{m_e^2}\left(\frac{F^V}{f_\pi}\right)^2\left[(1+\gamma)^2 SD^+(x,y) + (1-\gamma)^2 SD^-(x,y)\right] + \frac{F^V}{f_\pi}\left[(1+\gamma)F(x,y) + (1-\gamma)G(x,y)\right]\right] \tag{35}$$

Here $F(x,y), G(x,y), SD^+(x,y)$, and $SD^-(x,y)$ are functions that depend on the kinematic terms x and y with $x = 2E_\gamma/m_\pi$ and $y = 2E_e/m_\pi$ and $\gamma = F^A/F^V$. The pion structure form factors may be probed with radiative pion decay in specific energy regimes. In particular, Fig 2.2 shows the energy regions where the individual terms in radiative branching fraction are most sensitive. Fig 2.2 also shows that for high energy photons and positrons, the $SD^{+/-}$ terms are most sensitive and susceptible to study in the PEN experiment.

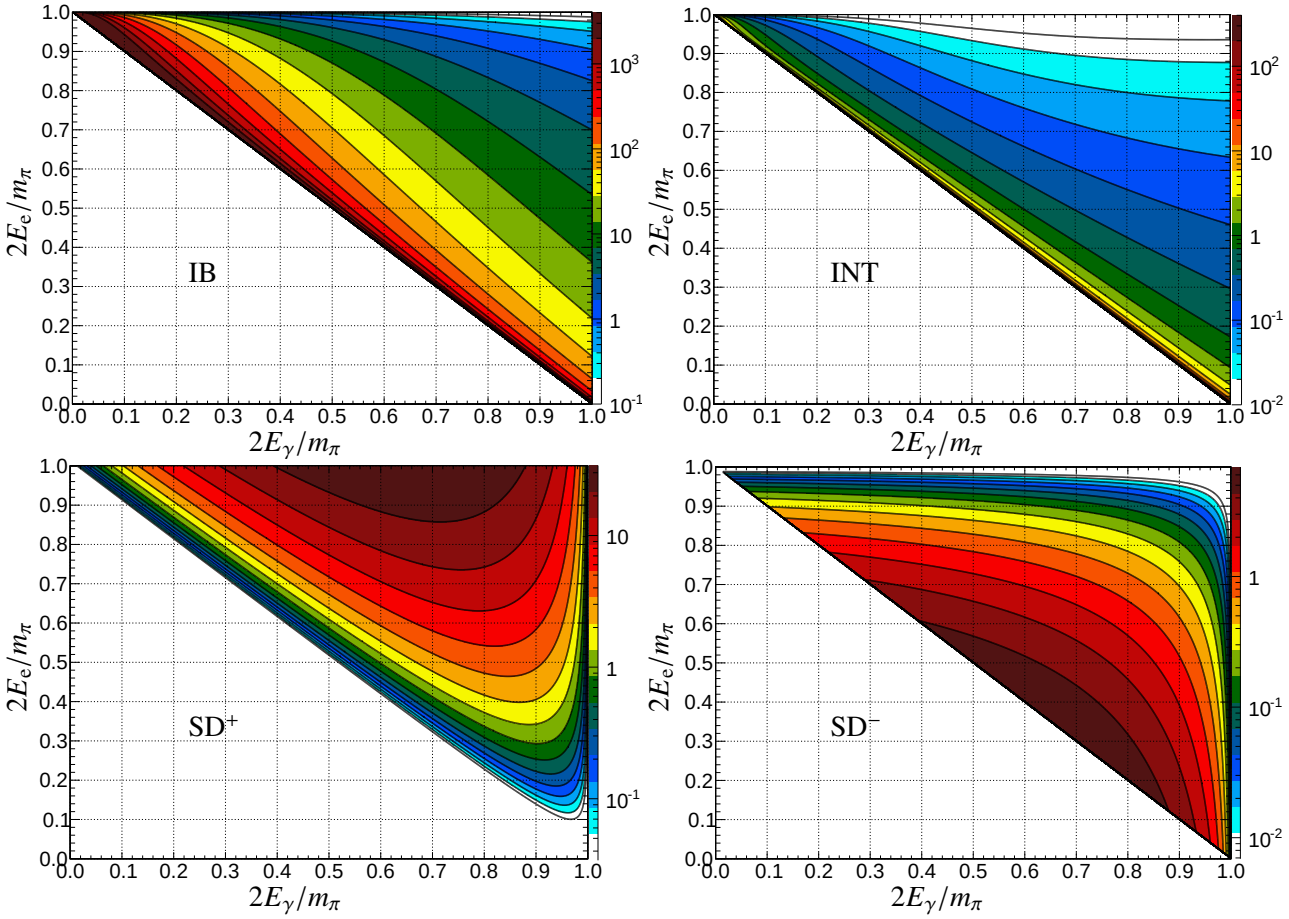

Figure 2.2: *Regions of phase space and their yields for different term contributions in the radiative pion decay. Upper Left: Inner Bremsstrahlung. Upper Right: Interference terms. Lower Left: SD^+ term. Lower Right: SD^-.*

It should be pointed out, that the opening angle between the photon and the positron depends on the two particles' energies and thus the ability to distinguish radiative to "non-radiative" decays also can depend on the opening angle used. The inner bremsstrahlung, IB, term occurs most often in the diagonal along and around $E_\gamma + E + \mathrm{e} = 70$ MeV energy regime. As seen in Fig 2.3, this corresponds to events in which the photon and positron possess a relatively small opening angle.

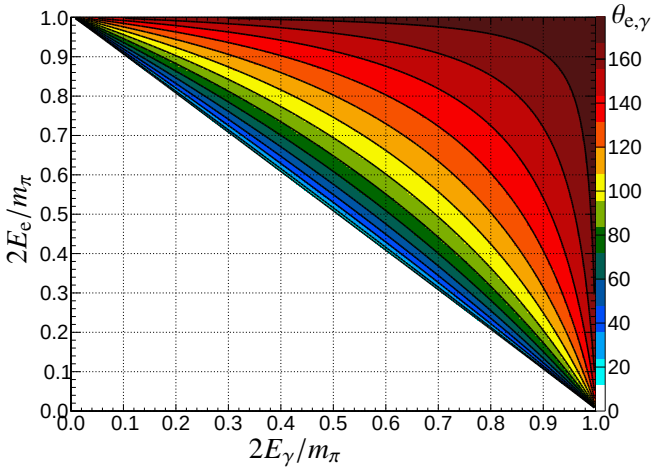

Figure 2.3: *Opening angle as a function of the energies of the positron and photon for the $\pi \to e\nu\gamma$ decay.*

For a more in depth treatment on radiative decays pertaining to PEN and PiBeta, see details in the works of Michael Vitz, Pete Alonzi, and Max Bychkov [89], [8],[26].

2.4 PiBeta: $\pi^+ \to \pi^0 + e^+\nu_e$

The PiBeta experiment is the preceding experiment to the PEN experiment and thus it seems appropriate to give a (brief) description of the theory that motivated these pion decay experiments. The pion beta decay is a vector transition between two spin 0 particles, the π^+ and the π^0, which of course belong to the same isospin triplet (π^+, π^0 ,π^-). A vector transition means is that the V component of the hadronic current will give a nonzero contribution to this decay. Axial vector contributions vanish here due to the intrinsic parity of the two particles and their spin. The matrix element for the transition is given by

$$\mathcal{M} = iG_F \cos\theta_c (p + p')_\mu \bar{u}_\nu \gamma^\mu (1 - \gamma^5) \nu_e, \tag{36}$$

where p is the 4-momentum of the π^+ and p' is the 4-momentum of the π^0. Since the π^0 is produced approximately at rest, the matrix element can be written as [53]

$$\mathcal{M} \sim 2iG_F \cos\theta_C m_\pi \bar{u}_\nu \gamma^0 (1 - \gamma^5) \nu_e \tag{37}$$

Using the chiral basis, the leptonic contributions amounts to $-4\sqrt{E_\nu E_\mathrm{e}}\cos(\theta_c/2)$ which ultimately leads to

$$|\mathcal{M}|^2 = 32G_F^2\cos^2\theta_c m_\pi^2 E_\nu E_\mathrm{e}(1+\cos\theta_{\mathrm{e}\nu}) \tag{38}$$

Once the phase space factors are included the decay rate is given by

$$\Gamma = \frac{G_F^2|V_{ud}|^2}{30\pi^3}\left(1-\frac{\Delta}{2m_{\pi^+}}\right)^3\Delta^5 f(\epsilon,\Delta)(1+\gamma), \tag{39}$$

where

$$\Delta = m_{\pi^+} - m_{\pi^0}, \epsilon = \left(\frac{m_\mathrm{e}}{\Delta}\right)^2 \tag{40}$$

and

$$f = \sqrt{1-\epsilon}\left[1-\frac{9}{2}\epsilon - 4\epsilon^2 + \frac{15}{2}\epsilon^2\ln\left(\frac{1+\sqrt{1-\epsilon}}{\sqrt{\epsilon}}\right) - \frac{3}{7}\frac{\Delta^2}{(m_{\pi^+}+m_{\pi^0})^2}\right] \tag{41}$$

This decay rate provides a test for CKM unitarity by measuring the value $|V_{\mathrm{ud}}|$, and thus provides a check on the conserved vector current hypothesis. For a more detailed discussion of the theory behind the pion beta decay, see Li et al. [56], for a discussion on the theory and the PiBeta paper for the experiment and analysis [75].

3 Motivation

> Motivation is the art of getting people to do what you want them to do because they want to do it
>
> Dwight Eisenhower

This chapter outlines some of physics that may be responsible for producing deviations from Standard Model expectations for the $\pi \rightarrow e\nu(\gamma)$ decay. The Standard Model is easily the most self-contained and self-consistent theory that has been developed in modern physics. With the announcement of the Higgs Boson discovery [10], yet another one of the many predictions of the Standard Model has come to fruition. However, the Standard Model is still not complete. There are questions that have yet to be answered which include: Why three generations of leptons? What is dark matter and what are candidates for dark matter? Will we find evidence Beyond Standard Model Physics such as supersymmetry? . Or are there other types of particles and interactions? The answers to these questions are essential in discovering the fundamental workings of the Universe in which we live. Currently there are many experiments on the horizon with the purpose of exploring extensions of the Standard Model. From the infamous three sigma deviation of the Muon $g-2$ experiment [48], to high energy experiments at CERN, nearly all sectors of physics are currently testing the boundaries and regions of the validity of the Standard Model. While a single experiment will not be able to probe all aspects or questions pertaining to physics beyond the Standard Model, it may be able to set limits on some of the possibilities that lie beyond the Standard Model. When approaching this type of a task, one should start (as one is taught to do in classical mechanics) by writing a Lagrangian. In this case, a Lagrangian of "new physics" that includes the type of terms and interactions expected normally in a Lorentz invariant theory may be written as:

$$\mathcal{L}_{\mathrm{NP}} = \left[\pm\frac{\rho_V}{2\Lambda_V^2}\bar{u}\gamma_\alpha d \pm \frac{\rho_A}{2\Lambda_A^2}\bar{u}\gamma_\alpha\gamma_5 d\right]\bar{e}\gamma^\alpha(1-\gamma_5)\nu + \left[\pm\frac{\rho_S}{2\Lambda_S^2}\bar{u}d \pm \frac{\rho_P}{2\Lambda_P^2}\bar{u}\gamma_5 d\right]\bar{e}(1-\gamma_5)\nu. \tag{42}$$

Here the Lagrangian of new physics shows a vector term, an axial-vector term, a scalar term, and a pseudo scalar term. These are the types of Lorentz invariant interactions that one would expect. The Λ values are the energy scales for which these new interactions would be measurable and the ρ terms are the

coupling constants. The PEN analysis, upon completion, may be able to set limits on these energy scales. The pion decay branching ratio, according to Standard Model, comes from Feynman rules of the Standard Model Lagrangian. If the "true" Lagrangian, that is the Lagrangian of the universe, was a combination of the Standard Model Lagrangian and the new physics Lagrangian, then this would require slightly different Feynman rules, which would imply a slightly different branching ratio, where the deviation from Standard Model calculations would depend on the value of the Λ's. Now since CKM unitarity and superallowed Fermi nuclear decays currently limit $\Lambda_V \geq 20$ TeV and $\Lambda_S \geq 10$ TeV, at $\Delta R^{\pi}_{e/\mu}/R^{\pi}_{e/\mu} = 10^{-3}$, the $\pi \rightarrow e\nu$ decay is sensitive to $\Lambda_P \leq 1000$ TeV, $\Lambda_A \leq 20$ TeV and through loop effects, $\Lambda_S \leq 60$ TeV [69]. Notice the pseudoscalar term seems to be the susceptible to see physics beyond the Standard Model. This is easily verified through Standard Model calculations. In particular, if the branching ratio were calculated assuming a pure pseudoscalar interaction in lieu of the $V - A$ interaction, then the ratio of rates would be on the order of 5 due to the absence of the chiral suppression imposed by the $V - A$ interaction. This substantially higher (orders of magnitude more so) value than the Standard Model suggests that even a small amount of pseudoscalar physics not included in the Standard Model would most likely show up as a deviation of Standard Model branching ratio and therefore detectable by a precision measurement. Note, one could add a tensor term in this Lagrangian. Greater than rank two however, the gauge requirements are so stringent that the theory would necessarily have to be non-interacting and therefore trivial [77][90].

In addition to putting limits on the "new physics," the PEN experiment can explore many different and specific issues regarding physics beyond the Standard Model. The precision measurement of pion decay can probe questions regarding lepton universality. This hypothesis of the Standard Model will fail if interactions and particles not in the Standard Model exist and couple to leptons differently. Examples of such particles include Higgs multiplets, lepto-quarks, massive neutrinos, and supersymmetric partners any one of which would make, the pion electronic branching ratio deviate from the Standard Model predictions. If for example, a massive neutrino exists, then the electronic decay of the pion will not be as helicity supressed as is predicted in the Standard Model which would give a branching ratio greater than predicted by the Standard Model. Further, since the decay of the pion into a massive neutrino and positron is still a 2-body decay, the daughter particles would still have monoenergetic spectra. Therefore, if a massive neutrino channel were to occur, one would expect an isolated positron signal peak under the michel decay spectrum background. The following section reviews the concept of lepton universality and explores some of the possibilities that

would result in a deviation of this hypothesis, namely, lepto-quarks, Higgs multiplets, massive neutrinos and supersymmetric particles among other possibilities.

3.1 Lepton Universality

In the introduction to the Standard Model, it was pointed out that the only difference according to Standard Model, between the leptons is their coupling to the Higgs, (i.e., their masses). In other words the coupling between the W boson and the leptons is taken to be the same across lepton flavors. This is the statement of lepton universality. For pion decay, this means that the ratio of the couplings, $g_e/g_\mu = 1$. The violation of lepton universality may be studied by reparameterizing the coupling constants as

$$g_l \rightarrow g_l(1 - \epsilon_l/2),$$

where ϵ_l represents deviation from Standard Model expectations. This allows us to view the ratio of the couplings in a new light in particular,

$$g_{l1}/g_{l2} = 1 + (\epsilon_{l1} - \epsilon_{l2})/2,$$

These parameterizations will have experimental constraints on $\Delta_{l1l2} = \epsilon_{l1} - \epsilon_{l2}$. Even though there are three couplings (or three different Δ's) only two are independent parameters. That is because the ratio of one is the product of the other two and Loinaz et al, [59] have indicated the possible phase space that may be explored through different types of decays measured by experiments. Fig 3.1 shows the region in which the PEN experiment can study deviations from lepton universality.

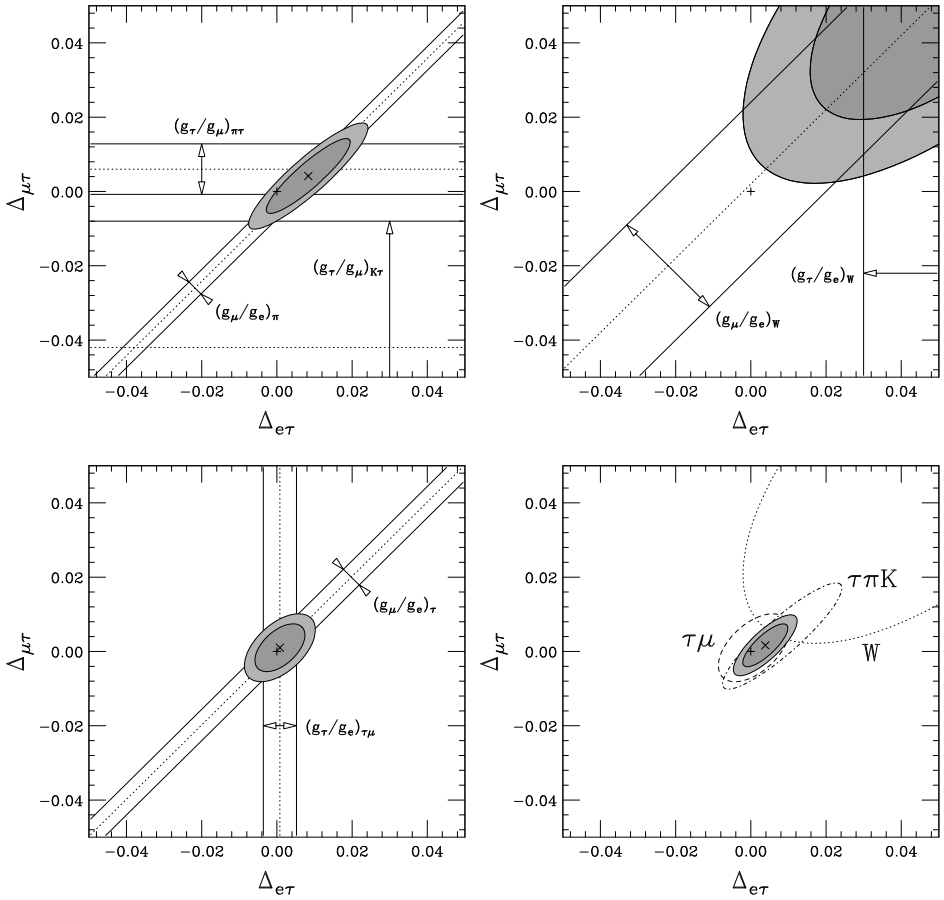

Figure 3.1: *Regions of susceptibility in violation of lepton Universality. Comparison of $\Delta_{\mu\tau}$ vs $\Delta_{e\tau}$. Upper Left: From pion and kaon decays. Upper Right: From high energy interactions. Lower Left: From tau decays. Lower Right: Different regions in phase space. Taken from [59].*

Fig 3.1 shows that while different decay modes of different particles allow the study of lepton universality, the pion decay provides the most precise value for lepton universality. Up until 2012, the values for the coupling ratios were

$$\left(\frac{g_e}{g_\mu}\right)_\pi = 0.9996 \pm 0.0012, \quad \left(\frac{g_\tau}{g_\mu}\right)_{\pi\tau} = 1.003 \pm 0.0034, \quad \left(\frac{g_e}{g_\mu}\right)_W = 0.999 \pm 0.011, \quad \left(\frac{g_\tau}{g_e}\right)_W = 1.029 \pm 0.014.$$

More recently [1][40][12], a renewed interest in lepton universality in regards to B meson decays have emerged. Experiments have shown deviations from Standard Model lepton universality of 2.1σ, 2.7σ and 2.0 σ in separate analyses indicating that there may be physics beyond the Standard Model that preferentially couple to the third generation of fermions, not unlike the Higgs scalar. Possible violations of lepton universality are leptoquarks particles, massive neutrinos, and suspersymmetric particles.

3.2 Pseudo-scalar interactions

In the derivation of the branching ratio, the interaction that was used for hadronic current was similar to $V-A$ interaction. As was explained, the V contribution was zero because of the nature of connecting the pion to the scalar vacuum. There are only two operators that would produce non-zero results. The axial vector, already discussed, and the pseudoscalar. This means that there could be another interaction which has the proper parity as axial vectors that could also be non-zero in this operation. This would be a pseudoscalar interaction that could contribute to the pion decay branching ratio. Following the arguments of Campbell [32], the matrix element associated with a pseudoscalar interaction would be

$$\mathcal{M}_P = \rho \frac{1}{\sqrt{2}\Lambda_P^2} \underbrace{\frac{f_\pi m_\pi^2}{m_u + m_d}}_{\tilde{f}_\pi} \left[\bar{l}(1-\gamma_5)\nu_l\right] \tag{43}$$

The matrix element of the entire interaction then would be a coherent sum of the this term and that of the Standard Model

$$\mathcal{M}_{SM} = G_F f_\pi \cos\theta_c \left[\bar{l}(1-\gamma_5)\nu_l\right] p_\mu. \tag{44}$$

Given a weak non-Standard Model pseudoscalar interaction, when summing over all final states the interference term between the Standard Model and the pseudoscalar term would be the main source of deviation from Standard Model expectations.

$$|\mathcal{M}_l|^2 = \underbrace{4G_f^2 f_\pi^2 \cos^2\theta_c m_l^2 \left(m_\pi^2 - m_l^2\right)}_{\text{SM term}} + \underbrace{8\frac{G_F \tilde{f}_\pi f_\pi \cos\theta_c \rho_P}{\sqrt{2}\Lambda^2} m_l \left(m_\pi^2 - m_l^2\right)}_{\text{Inteference}} + \underbrace{2\frac{\rho_P^2 \tilde{f}_\pi^{\,2}}{\Lambda^4}\left(m_\pi^2 - m_l^2\right)}_{\mathcal{M}_P^2} \tag{45}$$

The first term in the above equation is the Standard Model value contributing to the decay rate. The far right term is extremely small, because of the Λ^4 term that is present where Λ would be the presumably very high energy scale at which the interaction appears. Thus only the middle term would be possibly measurable in the pion decay branching ratio. In particular in the branching ratio R_π,

$$R_\pi \approx R_\pi(SM)\left(1 + \underbrace{\frac{\tilde{f}_\pi^{\,2}|\rho_e|^2}{2G_F^2\Lambda^4 f_\pi^2 m_e^2} - \frac{\tilde{f}_\pi^{\,2}|\rho_\mu|^2}{2G_F^2\Lambda^4 f_\pi^2 m_\mu^2}}_{\delta R_{\text{SM}}}\right) \tag{46}$$

Once QCD corrections are applied to these deviations,

$$-5.3 \times 10^{-3} < \delta R_{\mathrm{SM}} < 1.1 \times 10^{-3}$$

With these limits and the current experimental value of the pion branching ratio, we are on the outer edges of probing these limits. In particular,

$$1 - R_{\mathrm{exp}}/R_{\mathrm{SM}} \approx (1TeV/\Lambda)^2 \times 10^3$$

3.3 Leptoquarks

Leptoquarks are hypothetical particles that possess both lepton and baryon numbers. The concept first originated from Pati and Salam [73][74] who viewed the relationship between lepton number and baryon number as analogous to that of isospin and hypercharge. They proposed that both fermions and quarks belonged to some fermionic multiplet. The allure of such a prospect is that weak interactions would possess the same chirality projection operator and would act on both quarks and leptons equally. This is plausible because the electroweak interactions has a $V - A$ structure for both the hadronic and leptonic currents. The interactions governing the hypothetical particles would be present in some GUT models such as SU(5). Originally leptoquarks emerged in the Patti-Salam model where they supposed that lepton number is really a fourth color. The hypothetical particles have not been seen in the high energy colliders, however some phenomena in high energy colliders could be explained by leptoquark presence [39]. They may also be seen, if they exist, indirectly by precision measurements via deviations from Standard Model expectations as pointed out by Davidsen et al. [35]. If the leptoquark coupling does not depend on the lepton generation, that is the coupling of the positron and muon are the same to leptoquarks, then the pion branching ratio would not be affected. If they are unequal then denoting e_L^{ij} is the leptoquark coupling between lepton i and quark j, and m_{lq} is the mass of the leptoquark involved then,

$$e_L^{21} e_L^{n1}, e_L^{11} e_L^{n1} < 2 \times 10^{-3} \left(\frac{m_{lq}}{100GeV} \right)^2 .$$

3.4 Massive Neutrinos

Interacting and manifesting only in weak interactions, neutrinos are a very peculiar species of particles in the Standard Model. For the longest time there was speculation as to whether or not these particles possess mass and it was fairly recently [9][4][38] that neutrino oscillations were observed which led to the conclusion that these particles must indeed have mass. This discovery opened up new possibilities. The presence of a neutrino mass meant that the mass eigenstates of the neutrinos and the weak eigenstates of the neutrino were not one and the same, but rather related to each other by the PMNS matrix. Two natural questions arise. The first is by what mechanism do neutrinos obtain mass. The second question would be if there are more than three neutrinos. While precision measurements of the Z^0 width limit [86][63] the number of weak eigenstate neutrinos to three, or rather 3 ± 0.08, Shrock argues [57] the LEP results indicate that there are only three weak T=1/2, T_3=1/2 neutrino eigenstates with dominant mass eigenstates $m < m_z/2$. It does not specifically place a restriction on the number of mass eigenstates. In particular isosinglet neutrinos would produce a neutrino mixing matrix such that the Z^0 width would be unaffected. The eigenstates would be related to the mass eigenstates then by

$$\nu_l = \Sigma_{i=1}^{3+k} U_{li} \nu_i. \tag{47}$$

In the context of pion decays, the comparison of pion decays to leptons accompanied by a massive neutrino to that of the canonical neutrino could be shown as

$$\frac{\Gamma(\pi \to \mathrm{e}\nu_{X_1})}{\Gamma(\pi \to \mathrm{e}\nu_1)} = |U_{\mathrm{e}X_1}|^2 \rho_e, \qquad \frac{\Gamma(\pi \to \mu\nu_{X_2})}{\Gamma(\pi \to \mu\nu_2)} = |U_{\mu X_2}|^2 \rho_\mu \tag{48}$$

where ρ is a kinematics (phase space) factor, and ν_{X_1}, ν_{X_2} are the massive species that would emerge from the two decay modes. There have been searches for massive neutrinos emerging from decays into muon [2][34][19] as well as from emerging into positrons [11][71][50][18] performed. For the case of the pion decaying into a positron, the product $|U_{\mathrm{e}X_1}|^2 \rho_e$ increases as chirality suppression diminishes, but the term decreases at sufficiently high masses because of a diminished phase space available. More concretely, it was already stated that the probability of picking out the proper helicity was $\sim (1 - v/c)$. If in the two body decay, the mass of the neutrino were non-negligible, then the velocity of the emerging positron would be smaller than if the neutrino were less massive. With a smaller velocity, $(1 - v/c)$ then increases and therefore the ratio, $(1 - v_\mathrm{e}/c)/(1 - v_\mu/c)$ also increases. Thus the decay process would not be as chirally suppressed.

3.5 Higgs Multiplets

Standard Model descriptions with Higgs multiplets were discussed in [37]. A pair of Higgs doublets was discussed by Campbell [32]. The idea behind this description is that there are

$$\phi_i = \begin{pmatrix} \phi_i^+ \\ \\ \phi_i^0 \end{pmatrix} \tag{49}$$

for $i = 1, 2$. The off diagonal terms in the coupling matrices would then produce flavor changing neutral currents. In this case, the Lagrangian would have terms that contribute to the pion decay of the form

$$A^{11}\bar{u}_L H^+ d_R^1 + B^{11}\bar{d}_L^1 H^- u_R^1 + C^{11}\bar{\nu}_L^1 H^+ e_R^1 + C^{22}\bar{\nu}_L^2 H^+ e_R^2 + h.c \tag{50}$$

where deviations would be

$$\frac{\rho_e}{\Lambda^2} = \frac{Re\left((A^{11} - B^{11*})C^{11*}\right)}{m_H^2} \tag{51}$$

$$\frac{\rho_\mu}{\Lambda^2} = \frac{Re\left((A^{11} - B^{11*})C^{22*}\right)}{m_H^2}. \tag{52}$$

3.6 Supersymmetry

Among the the more exotic physics that can impact $R_{e/\mu}$ are supersymmetric weak scale effects. Relatively new compared to the Standard Model and more so compared to the notion of a V−A interaction, supersymmetry (SUSY) is a popular extensions of the Standard Model because of the unifying effect of new symmetries introduced in theory. While most searches occur in the high energy regime of particle physics, the effects or presence of SUSY may be studied at low energy scales provided the tests have a high enough level of precision. SUSY interactions can affect the pion leptonic decays and therefore change the theoretical Standard Model branching ratio from the experimental values. Such deviations would signal the presence of flavor-dependent physics. In Minimal Supersymmetric Standard Model (MSSM), a non-zero $\Delta R_{e/\mu}^{SUSY}$, would occur at tree level or loop level that would indicate physics beyond the standard model. In this section, a review of some of the types of interactions and impact of $R_{e/\mu}$ will be discussed by splitting the two types of SUSY extension into R-parity conserving and R-parity violating processes. R-parity is just

a different quantum number, $-1^{3B+L+2s}$ which is conserved in the Standard Model. B represents the baryon number, L the lepton number and s the spin

Following in the work of Musolf [66], at tree level the matrix element for $\pi^+ \to l^+\nu_l$ is

$$i\mathcal{M}_{AV}^{(0)} = -i\sqrt{2}G_\mu V_{ud}\langle 0|\bar{d}\gamma^\lambda P_L u|\pi^+\rangle \bar{u}_\nu \gamma_\lambda P_L \nu_l$$

$$= 2V_{ud}F_\pi G_\mu m_l \bar{u}_\nu P_R \nu_l \tag{53}$$

Now adding a pseudoscalar four-fermion term

$$\Delta\mathcal{L}_{PS} = -\frac{G_{PS}V_{ud}}{\sqrt{2}}\bar{\nu}(1+\gamma^5)l\bar{d}\gamma^5 u \tag{54}$$

to the matrix element, the total amplitude becomes

$$i\mathcal{M}_{AV}^{(0)} + i\mathcal{M}_{PS} = V_{ud}F_\pi G_\mu m_l \bar{u}_\nu(1+\gamma^5)\nu_l\left[1+\frac{G_{PS}}{G_\mu}\frac{m_\pi^2}{m_l(m_u+m_d)}\right], \tag{55}$$

where the term on the very right involving the ratios of masses is a factor that enhances the branching ratio due to the absence of helicity suppression. This is the same term as before, just written a different way. The contributions may originate through the mixing of both left and right handed superpartners that would contribute a non-negligible amount to the branching ratio provided some fine tuning. In addition to affecting the branching ratio through pseudoscalar interactions, axial vector contributions may also be present in some of the SUSY models. This may manifest in the one loop radiative corrections in the semi-leptonic decay. The amount of deviation from Standard Model expectations however is difficult to pin down due to the dependence on SUSY masses and parameters. These two contributions arise from R-parity conserving requirements. If R-parity is not conserved, the simple tree level diagrams involving the exchange of different sfermions will lead to a deviation from Standard Model expectations. The deviations will of course depend on the sfermion masses specifically the mass of the selectron and smuon, the supersymmetric partners of the electron and muon respectively. It will also depend on the couplings involved. Fig 3.2 shows the bounds set on different SUSY parameters based on the pion electronic decay branching ratio.

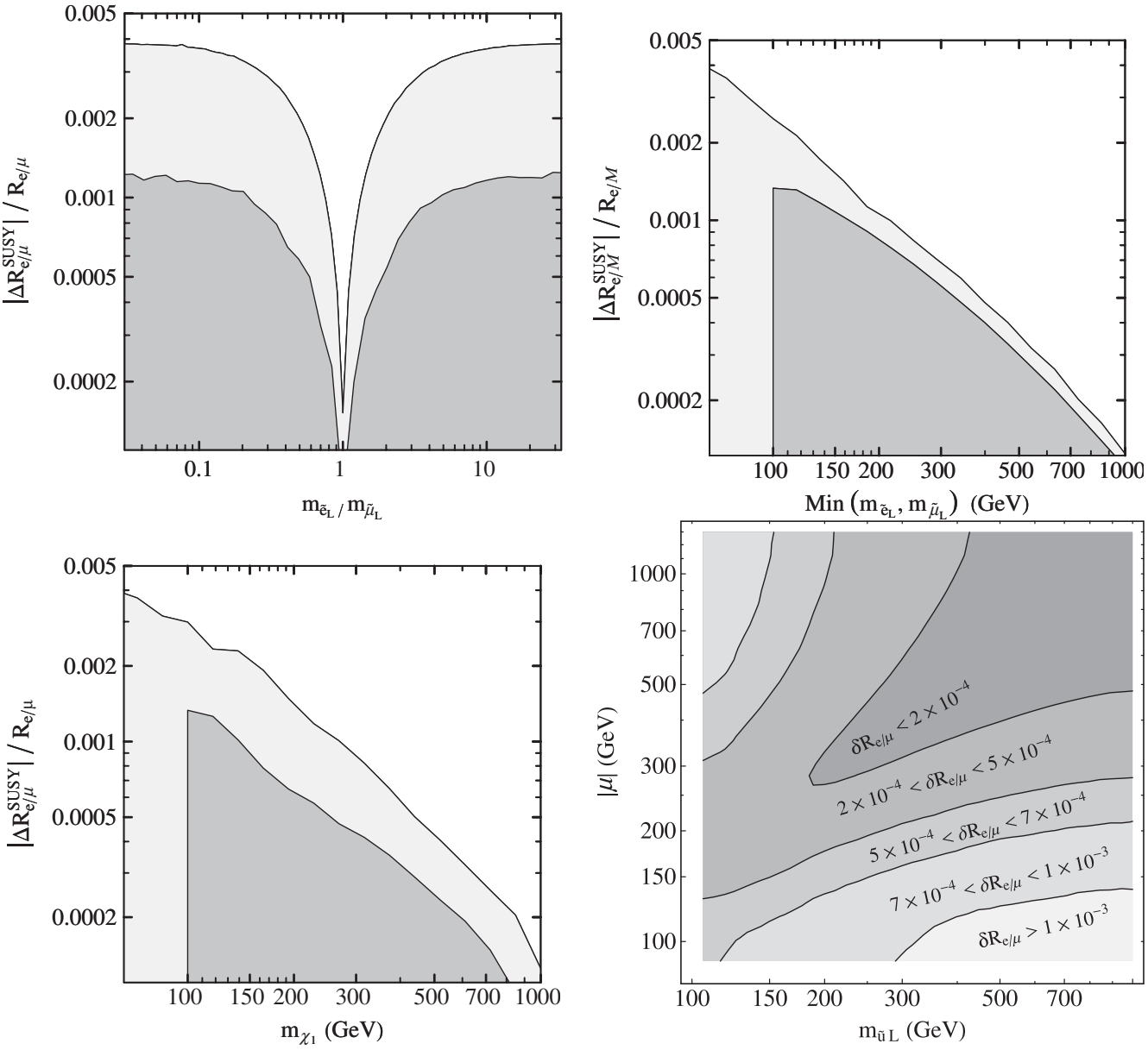

Figure 3.2: *Constraints on slepton masses from pion electronic decay branching ratio. Upper left: selectron and smuon mass ratio as a function of SUSY contribution to the branching ratio. Upper Right; minimal masses of the two sleptons as a function of SUSY contribution to branching ratio. Lower Left: Mass of lightest chargino as a function of SUSY contribution to branching ratio. Lower Right: Mass of supersymmetric partner of up quarks and Higgsino mass parameter constrained by the contours of pion branching ratio. Taken from [66].*

From Fig 3.2, an experiment at the order of 5×10^{-4} within Standard Model value puts the lower limit on the Higgsino mass at above 125 GeV.

4 Experiment

> It doesn't matter how beautiful your theory is, it doesn't matter how smart you are. If it doesn't agree with experiment, it's wrong
>
> Richard Feynman

The PEN experiment, named for the decay channel for which it is investigating, (**p**ion→ **e**lectron + **n**eutrino), was performed at the Paul Scherrer Institute (PSI) in three consecutive years of data taking occurring between 2008 and 2010 with the intended goal to measure the pion electronic decay branching ratio with a relative uncertainty of 5×10^{-4} or better. This chapter describes the experiment, the apparatus, and the physics underlying the decisions that were made about the experimental apparatus.

Figure 4.1: *PSI Facility*

4.1 Learning from History

Science progresses because scientists learn from the previous experiments and methods of the former generations of experiments. Techniques from the previous generation are sometimes abandoned or refined in favor of those that may be more effective with updated techniques and technology. In this experiment, the goal is to measure the pion electronic decay branching ratio to a high precision. That means one must decide

what kind of decays are going to be used (at rest or in-flight), and what kind of pions. If pion decays in flight were studied, one would need a high beam rate to ensure that the decay occurred in the fiducial volume of the apparatus. Further, since most of the time the pion decays into a muon, which has a long lifetime, a detector would be needed to detect these muons with a range of energies (due to the different Lorentz boosts from in-flight decays) and distinguish them from the positrons that would emerge from decays in flight. This daunting task therefore suggest that decaying pions at rest is a more manageable method to study the branching ratio. The pion best suited for decays at rest is the π^+. The π^- would undergo absorption and hadronic interaction with any material prior to decay due to its Coulomb attraction to positively charged nuclei. Most previous pion decay experiments similar to PEN used π^+ decaying at rest with a few exceptions. Most of these experiments used electromagnetic calorimeters for positron detection. In the earliest experiments, a magnetic spectrometer was used. The problem with the latter that there is the trajectory of the positron will highly depend on the momentum of the outgoing positron which in of itself is process dependent. This high dependence on the solid angle trajectory from momentum of the outgoing positron, can produce a significant systematic uncertainty. The position of the stopping target and positron detector would introduce uncertainties in position of the detector and acceptances that would not cancel in the branching ratio. Hence the magnetic spectrometer has been long since abandoned in favor of an electromagnetic calorimeter. This also permits the detection of neutral gammas accompanying the positron in pion decays. The experiment done at PSI in 1993, hadronic interactions were determined by the response of BGO calorimeter[33]. The problem with relying on the EM calorimeter alone to determine hadronic interactions should be obvious. Radiative decay events which would also be in the high energy region of the response would not be easily distinguished in the calorimeter from hadronic interactions in the target. This can be dangerous because as was pointed out earlier, radiative pion decays are not separable from "non-radiative" pion decays because in reality there is no such thing as a non-radiative decay. Therefore it is advantageous to determine whether or not a hadronic interaction occurred prior to the shower ignition in the EM calorimeter to separate genuine hadronic interactions from hard photon radiative events.

Discrimination of the main background, a $\pi \to \mu\nu_\mu$ decay is of utmost importance. Bryman et al [23] used the target energy to help determine if a muon was present in the target. As their analysis describes, this biased some of the events in which the pion decayed directly into a positron but traversed a longer distance out of the target. The effect could be curtailed by calculating or predicting the positron energy deposited in

the target using an independent method, and thus making the target energy discrimination more reliable.

Finally, the solid angle acceptance of the previous experiments should be mentioned. Only the previous experiment by Czapaek had a high, near 4π sr solid angle acceptance. This is of vital importance because if the solid angle acceptance is not high enough, the photon from a radiative decay may escape the calorimeter and the detected positron may have an energy spectrum more indicative of muon decay.

Thus a well designed experiment for the pion electronic decay branching ratio is one that contains a high solid angle acceptance to fully account for the hard radiative photons from the pion and muon decay. The experiment should use stopped positively charged pions. It should be designed in a way to determine whether or not hadronic interactions occurred without the use of the main calorimeter. The design should also include a method beyond simple target energy discrimination to determine the presence of a muon in the target.

4.2 PSI Facility

The PEN experiment measurements took place in the πE1 area of the Paul Scherrer (PSI) ring accelerator facility. The pions are produced in proton collisions with a carbon graphite target. Protons are obtained from an ion source and accelerated to 810 keV with a Cockroft-Walton accelerator. They are subsequently injected into a small injector cyclotron with 4 sector-magnets. This injector provides beams of 72 MeV protons which are injected into the main ring cyclotron where the protons are accelerated to 590 MeV with a proton beam current of 2.2 mA. The frequency of the accelerator is 50.63 MHz, which corresponds to a time between beam pulses of 19.75 ns. The protons are steered towards a 4 cm long cone of polycrystalline graphite where the collision produces, among other particles, pions. The accelerator, cyclotron, and target are shown in Fig 4.2. The pions are mostly emitted in the forward direction at an angle of 10°. Although lower mass targets do not provide a high yield of pions, they do result in a cleaner sample of particles, that is, a sample that possess fewer non pions in the production process. Whereas higher mass targets provide more yield of pions, but also produce many more unwanted particles. For these reasons graphite was chosen as the production target. The pions that emerge from the reactions are guided electromagnetically to the different beam lines. The layout of the PSI facility in which this occurs is shown in Fig 4.3.

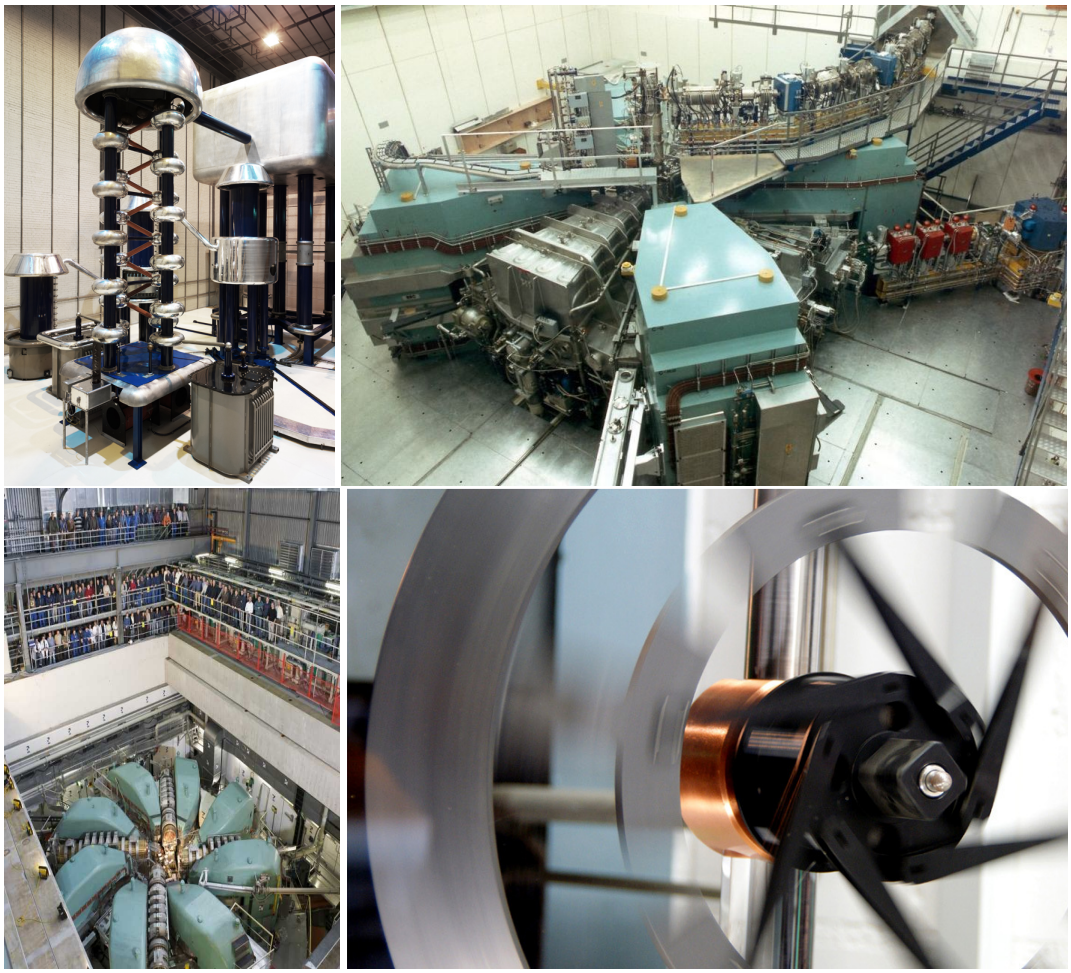

Figure 4.2: *Upper Left: Cockroft-Walton Accelerator. Upper Right: The injector cyclotron. Lower Left: 590 MeV proton accelerator. Lower Right: Carbon graphite pion production target.*

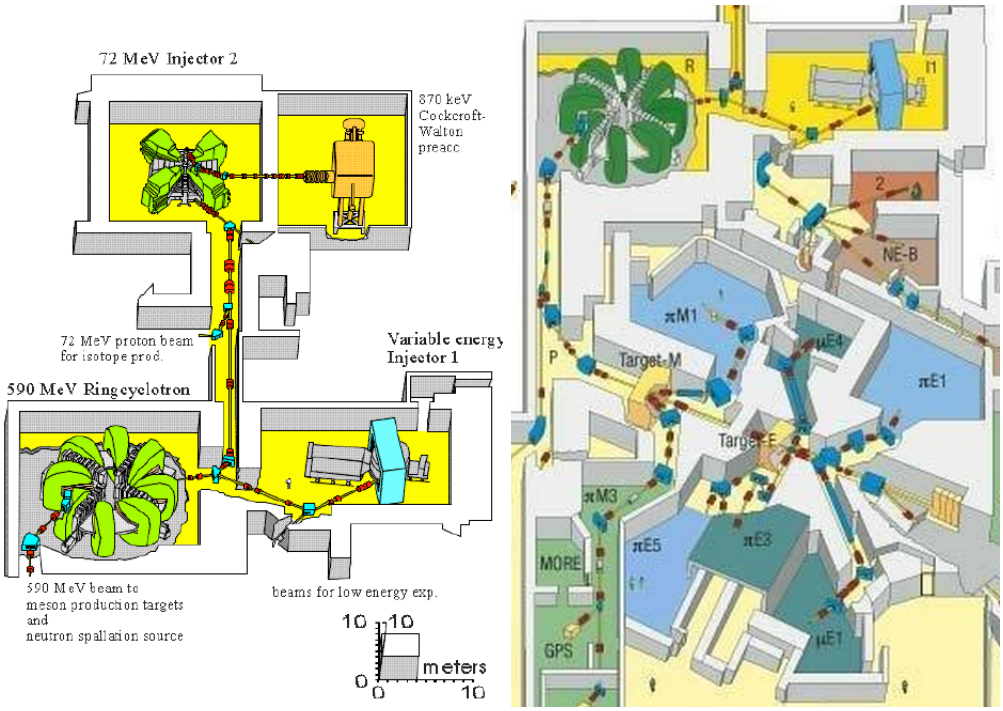

Figure 4.3: *Experimental Hall Layout.*

4.3 PEN Apparatus Overview

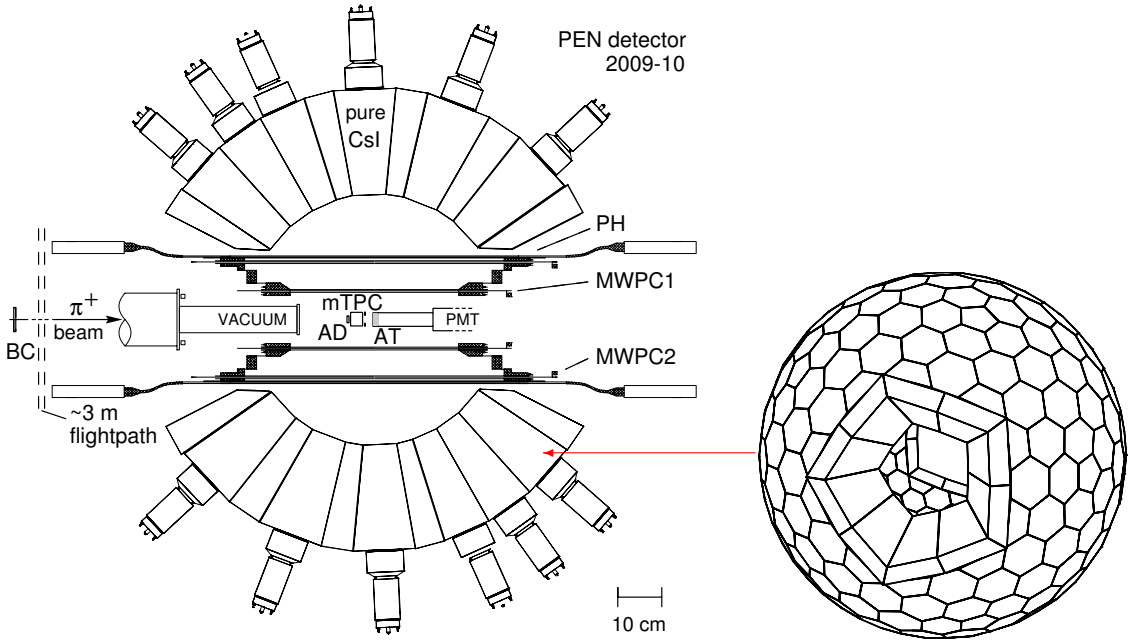

Figure 4.4: *Cross section of PEN apparatus*

The pions produced in PSI facility have a pion beam momentum between 70−83 MeV/c depending on the run period. The first PEN detector that the pion traverses through is the upstream beam counter (B0), a thin detector made of Bicron BC 408 plastic scintillator. The beam rate was intended to be 40,000 pion stops per second on average, but varied with run period. With 15 minutes per run, this is on the order of 10^7 pion stops per run. Fig 4.5 shows the number of pion stops as function of runnumber for the 2009 and 2010 run years.

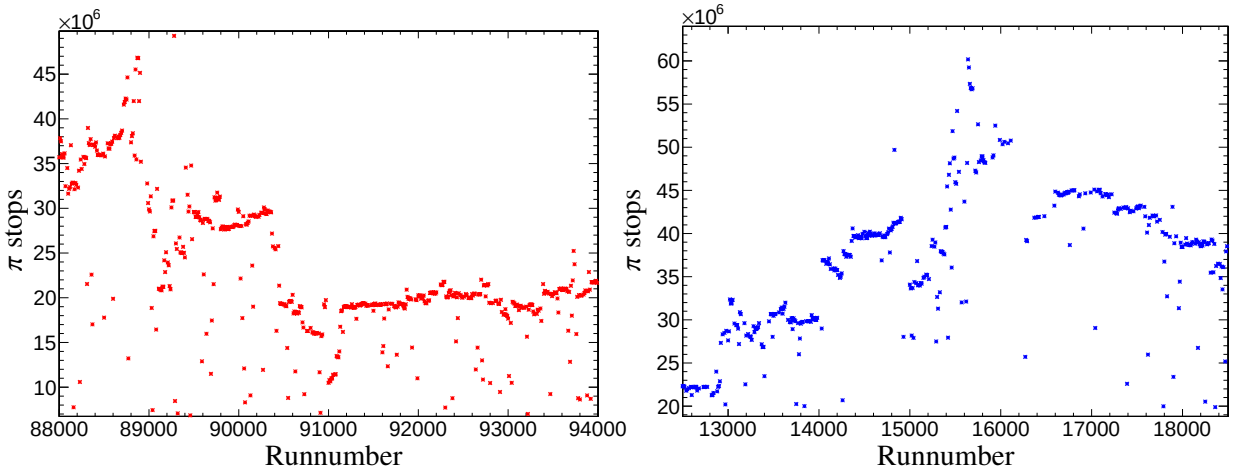

Figure 4.5: *Pion stops as measured by the scaler electronics. Left: 2009 run period. Right: 2010 run period.*

The thickness of the beam counter was 3 mm and it was located at the center of a beam collimator. After passing through a series of quadrupole magnets over three meters long, the pion would pass through the second detector, the active degrader, also composed of BC 408. In order to ensure that the pion would stop in the target, this plastic scintillator was placed after the beam counter but before the target. The active degrader had different specifications for the three run years. In 2008, the beam momentum was above 80 MeV so a thicker 4-wedged degrader was used. The purpose for this was two-fold. First, as mentioned, it would be used to slow down the pion before it entered the target by depositing some of the pion energy in this detector element. The second reason for a four wedged degrader was beam tracking. The degraders were placed such that the incoming pion position could be deduced and thus ultimately the stopping distribution deduced from the different energy spectra in the four wedges. The ratio of light collected in each of the scintillators would help determine how far from the beam axis the pion was. If the ratio ended up being one, then the pion flight was along the beam axis. During the 2009 run period, the momentum of the pion beam was 71.5 MeV/c so a smaller degrader, 5 mm thick, replaced the 4 wedged degrader. Further, to improve

the incoming pion beam tracking, a mini-Time Projection Chamber (mTPC) was used. 2010 had a slightly larger beam momentum around 76 MeV/c so a 9 mm thick degrader was used and in addition, a different mTPC was used as well.

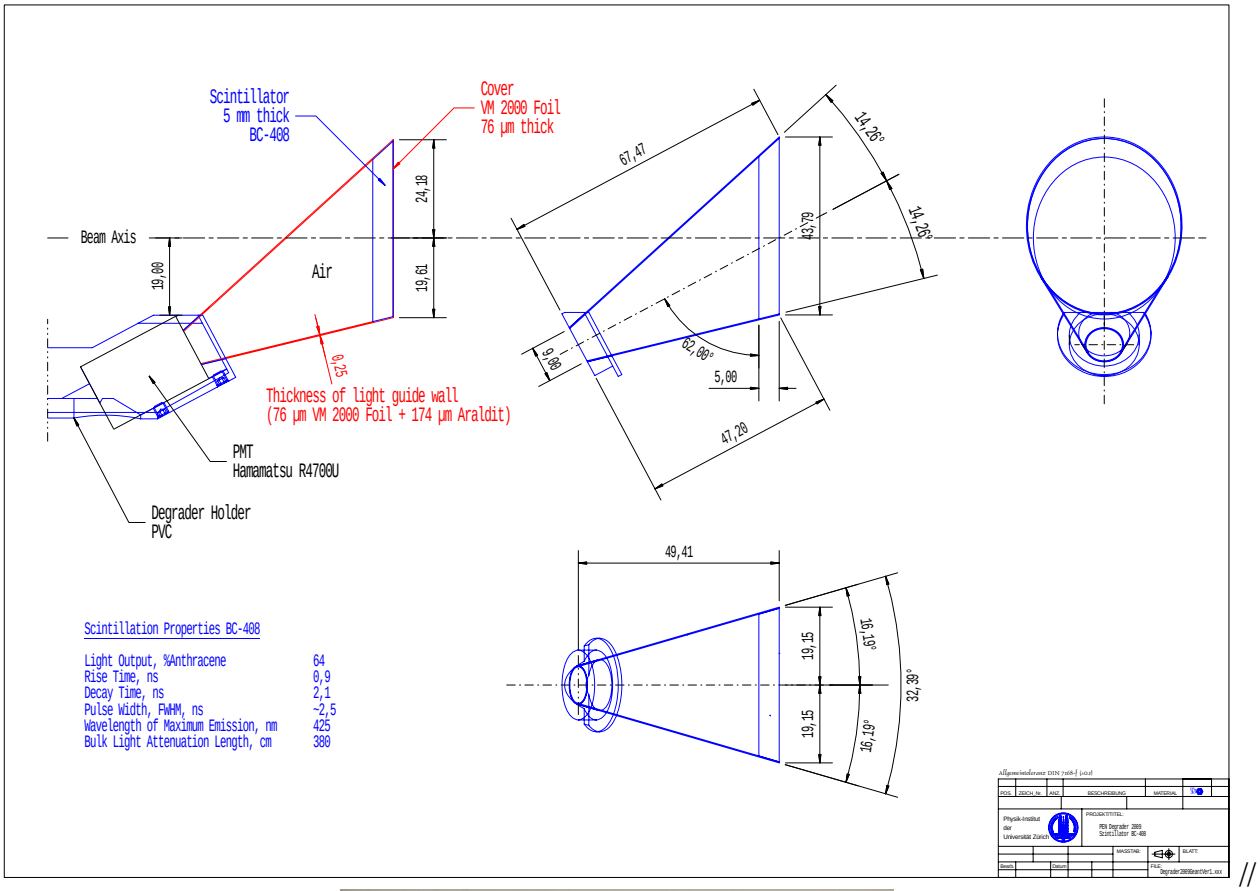

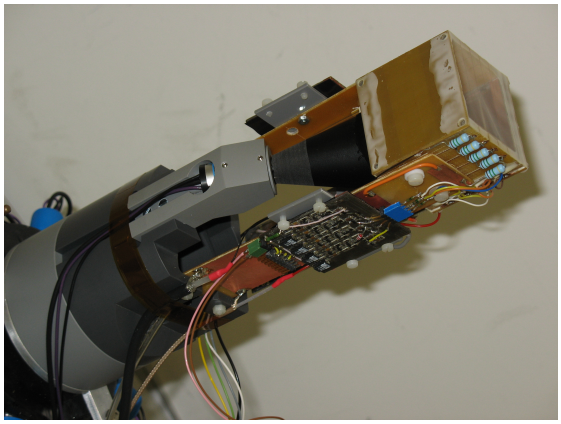

Figure 4.6: *Degrader and mini-TPC combination*

Signals from the beam counter and the degrader were directed for all years to a fast 2GS/s digitizer that recorded every event of interest, yielding signals with 0.9 ns rise, and 2.1 ns decay times. For the years

2009 and 2010, as stated, a mini-Time Projection Chamber (mTPC) was added for the determination of the beam profile and deduction of the stopping position in the xy plane for the incoming pions. The mini-TPC chamber was a cubic box with dimensions $50 \times 50 \times 50$ mm^3. Its geometry was optimized using the CERN GARFIELD drift chamber simulation package. The working region is subdivided into two volumes separated by a grid. The drift region had the dimensions of $50 \times 40 \times 40$ mm^3. The homogeneous electric field in the drift region is formed independently by the 10 electrodes on the side walls of the inner working volume. The thickness of the detector opening window is 20 μm and the thickness of the potential electrodes on the is 1 μm of aluminum. The grid is made of 50 μm wires separated by 10 mm. The four 10 μm thick and 40 mm long anode wires are perpendicular to the beam direction and are separated by 10 mm in z direction. The signal wire resistance is 30 Ohms. The working volume of the mTPC was filled with 90% Argon and 10% Methane. No connectors are placed directly on the mTPC. All necessary connections were fixed by soldering the signal, power, and HV cables. The HV dividers for the potential electrodes are placed outside the detector. The mTPC output waveforms were digitized using a 250 Ms/s digitizer. After passing through the mTPC, the pion would reach the target. The active target was a solid cylinder made of BC 418 plastic scintillator with length 15 mm and radius 15 mm. If the pion decays into a muon, the muon will travel 1.4 mm in the target on average, verified by Monte Carlo simulation in Fig 4.7

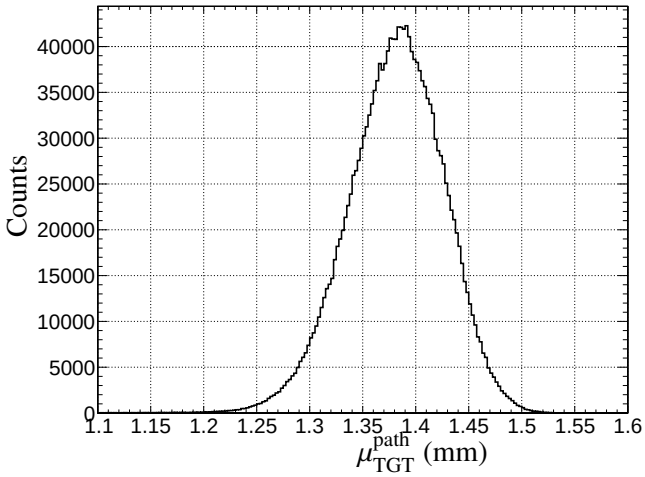

Figure 4.7: *Muon pathlength traveled in target according to Monte Carlo.*

The target was wrapped in an aluminum foil to ensure maximum light collection. The light collected by the photomultiplier tube viewing the target end via a light guide was digitized and recorded for every event. When the positron is born from either a pion or muon decay, it leaves the target and passes through

the cylindrical Multi-Wire Proportional Chambers (MWPCs).

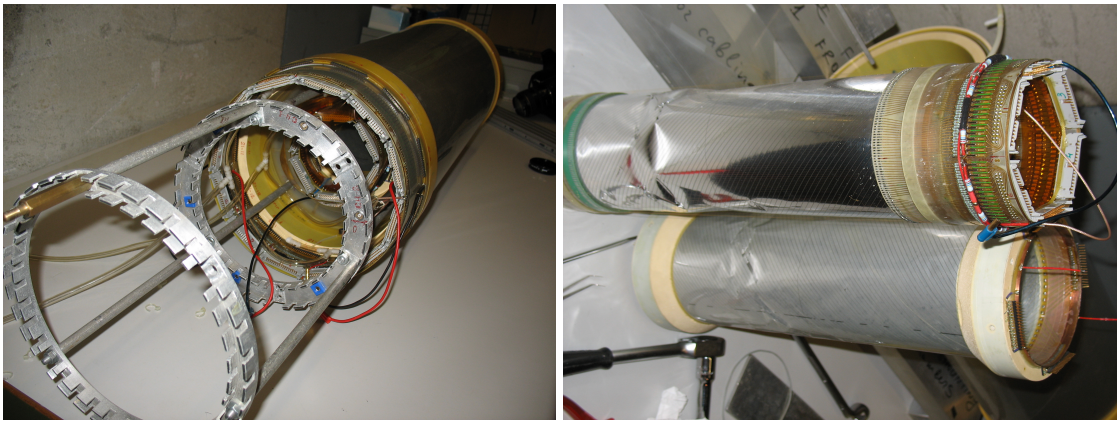

Figure 4.8: *Multiwire Proportional Chambers*

The inner chamber has a diameter of 12.5 cm and the outer chamber has a diameter of 25 cm. The inner chamber is comprised of 4 surfaces, inner and outer surfaces surrounding the anode plane for both upstream and downstream. The inner chamber comprised 192 anode wires and 256 cathode strips (64 on each surface). The outer chamber is comprised of 2 surfaces (inner and outer) and contains 384 wires with 384 cathode strips. As the positron passes through the MWPC, it ionizes the gas in the chambers, sometimes called magic gas, a combination of argon, isobutane, and freon, producing positive-negative ion pairs. Ion pairs drift towards the nearest anode wire which induces a positive signal on the nearest cathode strips. In the geometry of the PEN apparatus, the wire that produces a signal gives the x,y position of the positron as it passes through the chamber and the strip hit gives the z direction. The lengths of the chambers are 580 mm and 730 mm for the inner and outer chamber, respectively. The wire chambers diameters are 120 mm and 240 mm, respectively. Both chambers have anode to cathode gap of 2.5 mm. The Anode-wire resistance are 110 Ω and 155 Ω respectively. The strip slope on the inner surface are 36.96° and 44.60° for the inner and outer chambers respectivley. The strip slopes on the outer surface are −33.65° and −42.34°. The strips of the chambers are made of 6 μm aluminum foil and the terminal leads are welded to them. This and further information on the MWPC may be found in Karpukhin et al[52]. After passing through the MWPCs, the positron passes through the plastic scintillator hodoscopes shown in Fig 4.9. These are twenty plastic staves surrounding the wire chambers in a cylindrical pattern comprised of BC 408. Light guides and photomultiplier tubes are attached to each end of the 20 staves.

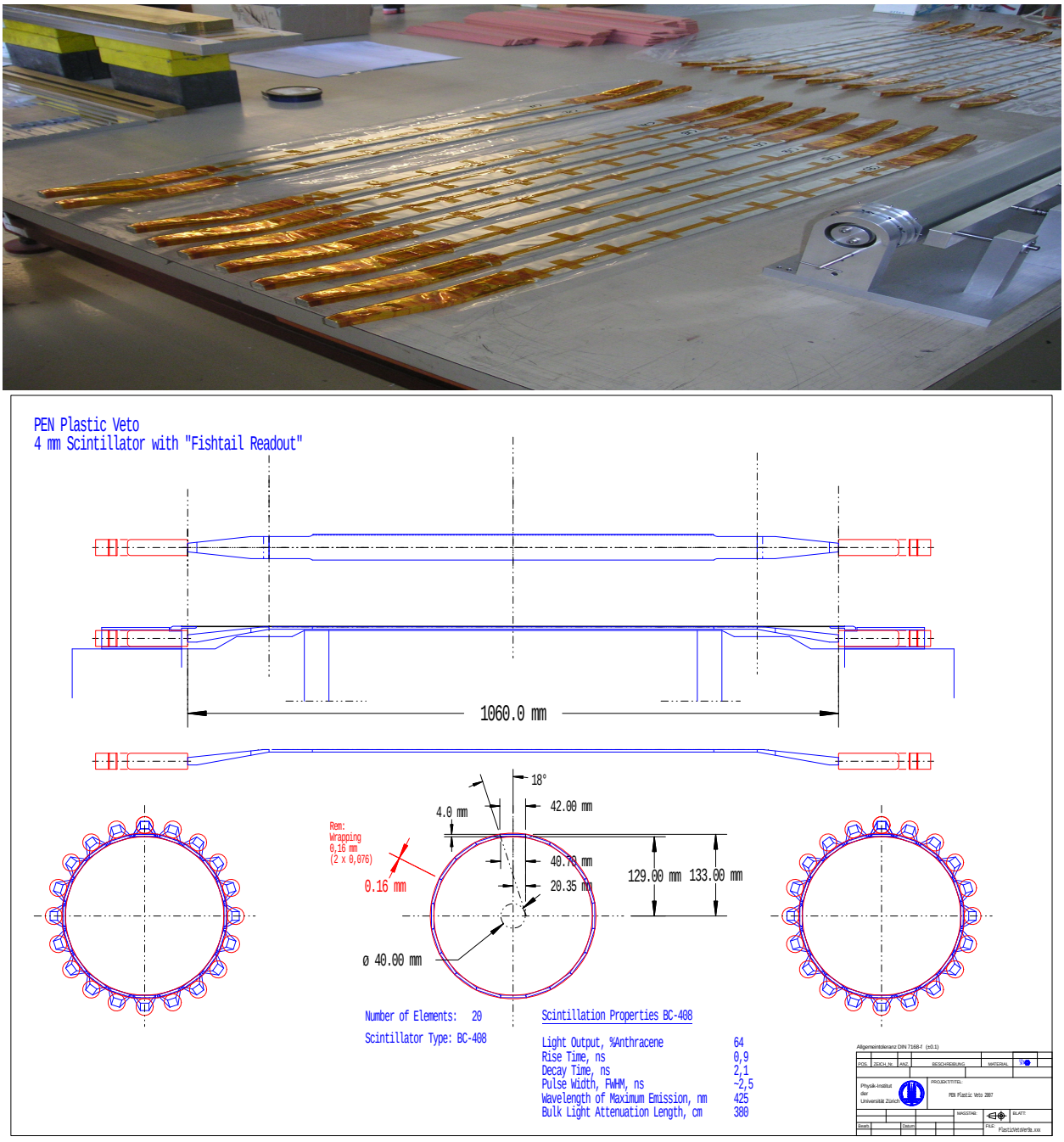

Figure 4.9: *Top: Plastic hodoscope staves. Bottom: Schematic drawing of signal hodoscope.*

The thickness of the staves are 4.0 mm. Once scintillation light is generated by a passing charged particle, the light travels along the staves into its ends where time to digital converters (TDCS) record the time and analogue to digital converters (ADCs) record the energy. The final element in the detector is arguably the most important. This is the pure CsI electromagnetic calorimeter. It comprises 240 pure CsI

crystals that covers 0.77 $\times 4\pi$ Sr. The crystals collect energy deposited by both charged particles and photons. The inner radius of the calorimeter is 26 cm, the outer radius is 48 cm, amounting to about twelve radiation lengths of CsI. Photomultiplier tubes and TDCs and ADCs are attached to each crystal individually.

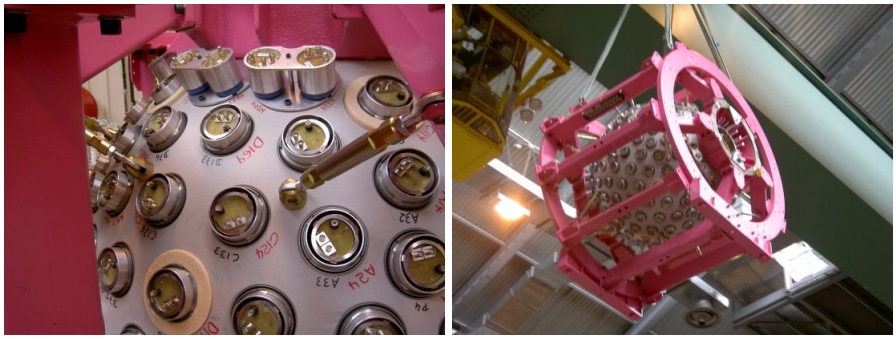

Figure 4.10: *240-Module Pure CsI calorimeter*

Since the thickness is 12 radiation lengths, there is expected to be some shower leakage through the back of the calorimeter by escaping photons. This leakage produces the infamous low energy tail in the main signal. Note that the apparatus is composed of pure CsI, not doped. The advantage of having a pure CsI detector is the response time (or decay time) of the crystals. This occurs on the order of ten nanoseconds, whereas a doped detector such as the traditional NaI(Tl) or CsI(Tl) will have a longer response time on the order of several hundred nanoseconds. This allows for more events to be recorded with a higher beam rate. The downside of pure CsI is that the energy resolution is not as good as a doped calorimeter. This is due to doping creating excitation sites that produce photons of higher wavelengths. The lack of doping ultimately leads to less output of light per MeV deposited which results in fewer photoelectrons per MeV deposited which finally results in lower energy resolution. A Mercator diagram of the calorimeter is shown in Fig 4.11. 220 crystals are truncated hexagonal and pentagonal pyramid crystals while the twenty veto crystals, the crystals nearest the openings, are tetragonal pyramids.

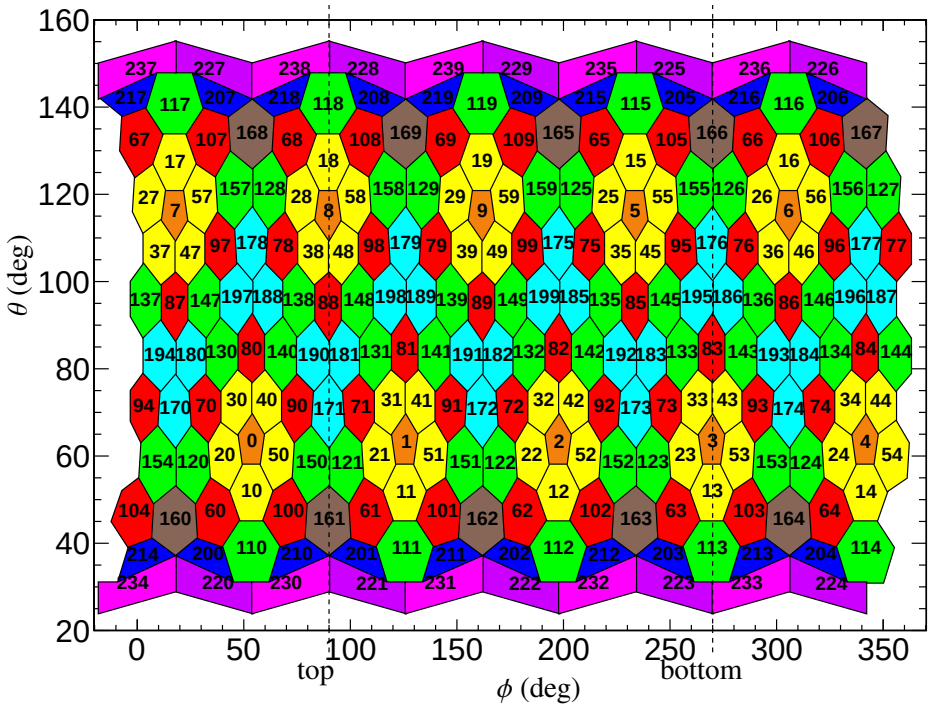

Figure 4.11: *Mercator Projection of CsI Calorimeter.*

4.4 Triggering and data acquisition

In order to record data, it must be determined what type of events will be recorded. If every event were recorded, the amount of dead time associated with recording the event could cost a large number of signal events. The amount of data recorded limited the number of events being recorded at about 150 events per second. On the other hand, sufficient background events are still required to keep statistical uncertainty in check. Further, if certain types of events are selected for both the signal channel, $\pi \rightarrow e\nu$, and the background channel, $\pi \rightarrow \mu\nu$, then systematic uncertainties may be eliminated or greatly reduced in determining the branching ratio. For example, choosing a particular time of flight between the B0 and degrader does not favor one process over the other. Therefore, by triggering on events for which the pion follows a particular behavior before the decay, we introduce no systematic uncertainties for one type of channel that is not shared by the other channel and since the pion hasn't decayed yet, it introduces no bias. Therefore, the first condition that an event should meet in order to be recorded is that the particle in the beam be a pion that ultimately stops. This is determined by the time of flight between the degrader and the beam counter. A pion will have a characteristic time of flight based on the momentum of the incoming particles, which is known to sufficiently high precision. The pion will also have a characteristic energy deposition in the beam

counters. The other main beam particles include muons and positrons which will deposit less energy in the upstream detectors. A further requirement is that a pion must have stopped in the target. This requires a certain amount of energy deposition in the target in addition to meeting the time of flight requirement. A pion that decays in the beam line will most likely not trigger these conditions and therefore these events will not be acquired. However, there is a probability that a pion will reach the target and decay while still in flight inside the target. These events will have a characteristic time spectrum which will be discussed later. Once it has been determined that a pion has stopped in the target, this opens up a time window called the pion gate. (πGATE). The width of the gate indicates how long the electronics will be open to recording data for that particular event. In PEN, the gate was open for approximately 220 ns after the pion stopped and approximately 50 ns before the pion stopped. The time before the pion stopping is included for a better understanding of background events. This time was chosen so that if the event were a signal event, i.e., $\pi \rightarrow e\nu$, then 99.99% of these events would be recorded. In addition, this would reduce the background $\pi \rightarrow \mu\nu$ events by about a factor of 10. This of course follows from the different timing spectra for the two processes in Fig 4.12.

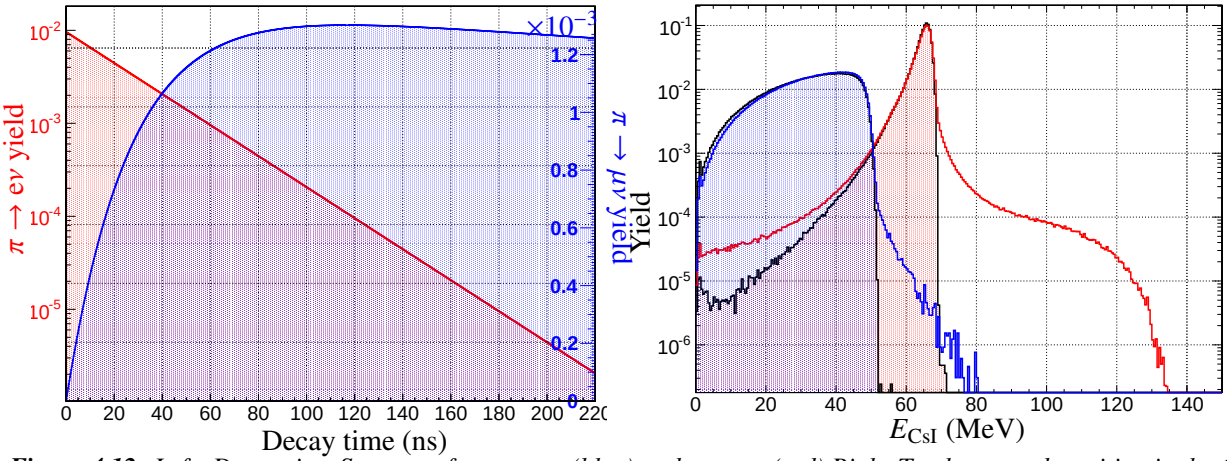

Figure 4.12: *Left: Decay time Spectrum for $\pi \rightarrow \mu\nu$ (blue) and $\pi \rightarrow e\nu$ (red) Right:Total energy deposition in the CsI for radiative and "non-radiative" (shaded) decays of μ and π.*

The difference in the decay time spectra of the two channels is because of the nature of the chains. The timing is determined as to when the positron is born. For a simple $\pi \rightarrow e\nu$ decay, this follows the probabilistic $\sim e^{-t/\tau_\pi}$ where, τ_π is the pion lifetime. The decay chain $\pi \rightarrow \mu\nu \rightarrow e\nu\bar{\nu}$ depicts the muon decaying into a positron, with probability, $\sim e^{-t/\tau_\mu}$, where τ_μ is the muon lifetime after the pion itself decays into a muon with a probability, $\sim e^{-t/\tau_\pi}$. This decay chain therefore follows a decay time distribution which

is a convolution of the two decay probabilities. Fig 4.12 shows clearly that beyond 220 ns the number of signal events, is statistically insignificant compared to the first 220 ns. While the decay time spectra of the two processes were studied in depth to determine optimal triggering conditions, timing differences alone do not distinguish the two processes. Fig 4.12 shows that there are also energy differences between the two processes despite the fact that positrons are the emerging particles in both processes. In the signal channel, ignoring the kinematics of the photon, the positron is a daughter particle of a two body decay at rest which has a well-defined energy and momentum. The positron and neutrino in the massless limit (since both of these particles are effectively massless) results in an energy of $E = m_\pi/2 = 69.8\,\text{MeV}$. On the other hand, a positron resulting from the background channel $\mu \rightarrow \text{e}\nu\bar{\nu}$ will have an energy spectrum that ends at half-the muon mass, $m_\mu/2 = 52.9\,\text{MeV}$. However, as already mentioned (and will be mentioned again) in reality the decays are radiative and a photon also emerges. In a vast majority of events, the emerging photon has low energy and is colinear with the positron, in which case the limits are still respected. In rare events, the photon is of higher energy and accounts for a substantial fraction of the event energy. The four different cases and the simulated energy spectra of the two decays are shown for the CsI calorimeter in Fig 4.12.

Given that the difference in energy spectra is also apparent, triggers for data acquisition were chosen so that anything above 48 MeV would be recorded and anything below 48 MeV would be prescaled by a factor of 64. This means that every 64th event that fulfills this requirement would ultimately be recorded. At 48 MeV, still a significant number of Michel events would be recorded. This, however, is useful for systematic, statistical, and calibration purposes. As photons can produce signals in the CsI calorimeter, one must be careful in selecting the events to be recorded. Since positrons of interest are those from the decaying pions, (and muons for background), care is taken to make sure that the electromagnetic shower originated from a charged particle and not a neutral particle (gamma). Thus a necessary requirement for the trigger was that there be energy deposited in the plastic hodoscope. Charged particles, such as a positron, deposit enough energy in these plastic scintillators to be efficiently detected, whereas neutral particles (photons) do not deposit any energy in these detectors. One could arguably include in the trigger signals in the MWPC, however, this would not be the best approach. It is known from the Bethe Bloch formula that the dE/dx in a gas is highly dependent on the energy of the incoming particle. For heavy particles, Bethe Bloche formula is used and $-dE/dx \sim 1/\beta^2$. The heavier the particle, the more energy deposited in a given pathlength. However, for positrons and electrons, the formula is modified because the assumption of small energy loss

and small deflection is no longer a safe assumption. In addition, there are bremsstrahlung considerations to be made. When all is said and done, for the chamber gas $-dE/dx \sim E$ for bremsstrahlung and $-dE/dx \ln E$ for ionization. So for positrons, the ability to produce a signal in the MWPC depends on the decay process. The $\pi \rightarrow e\nu(\gamma)$ signal process has, for the most part, a mono-energetic positron emerging from the decay with ~ 65 MeV (after accounting for energy deposited in the target). However, the positron emerging from the muon decay has a spectrum of energy ranging from 0 to 52.5 MeV minus the energy lost in the target. So if the MWPC were to be included in the triggering, the efficiencies of the triggering would depend on the process and accounting for this may be difficult especially post-measurement. To summarize, in order for the event to be recorded, the following requirements must have been met: The time difference between the degrader and B0 had to coincide with the time of flight of the pion. A minimum energy deposited in the target and degrader was required to ensure that the pion didn't decay between the degrader and target. An energy deposition in the plastic hodoscope and time coincidence between the hodoscope and target was also required. A minimal amount of energy deposited in the CsI was required. The energy amounted to a few MeV for 2009/2010 after the energy detected in all crystals was added. In 2008, the minimum energy requirement was imposed on appropriately defined clusters of crystals instead of the entire calorimeter.

It is also important to study the low energy tail of the electromagnetic calorimeter for signal events which is due to energy leakage in the electromagnetic calorimeter. Previous experiments have noted the difficulties in characterizing the low energy tail of the electromagnetic calorimeter that results from energy leakage. Therefore a separate tail trigger was introduced in 2009. This particular trigger records events in a small time window following pion stop time, specifically 80 ns for 2009 and 50 ns for 2010. The electronics for the tail trigger was configured such that a muon peak search was performed in real time and the tail trigger would only fire if no muon peak was observed in the target. This trigger was prescaled by a factor of 10. The number of tail triggers that were recorded throughout the runs are displayed in Fig 4.13.

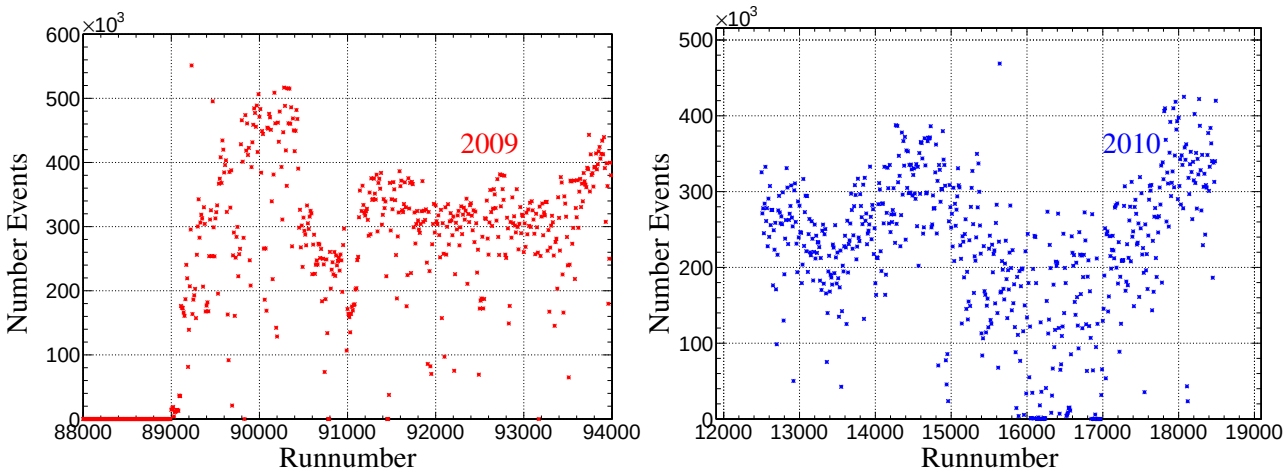

Figure 4.13: *Tail trigger events over run period.*

While this trigger is important in studying the low energy tail, it is also important to note that these events can not be used in the main analysis because of the complicated nature of the electronics and the inability to characterize the trigger efficiency to a precision of 10^{-4} or better. This is not a concern for the analysis as other trigger types normally trigger the event in addition to the low energy tail trigger. Hence these events are included in the main analysis. More details on the tail is discussed later on.

4.5 Data Storage and Software

The data acquisition system used the same system as was used for the predecessor of this experiment, that is the Maximum Integrated Data Acquisition System (MIDAS). This DAQ system has been widely used at PSI, TRIUMF, and other laboratories worldwide. This system has the capability of controlling hardware, higher order operations (run and stop, for example), and status updating. The MIDAS file system is also used in the Monte Carlo simulation, as the purpose of the simulation is to create synthetic data identical in format to that of the real measured data. The MIDAS files are divided into individual runs, with each run file containing full information written for each event. Here a “perfect” event is one in which the pion stops in the target and one of the resulting particles emerging from the target is a positron. Different pieces of information are written in different banks, which is nothing more than information pertaining to a piece of hardware. The different banks and uses are tabulated below

Table 4: *Banks for MIDAS Software*

Bank name	Information held
TRIG	trigger and prescaling information
BADC	Beam ADCs
LTDC/VTDC	TDC for plastic hodoscope and CsI (LTDC for 2008 only, VTDC for 2009/2010)
PCOS	MWPC wires hit
ZADC	ADC values for plastic hodoscope and CsI
RDGT	Raw waveform digitizer for B0, DEG, and TGT
ZCAT	MWPC cathode signals (from ADCs)
WTPC	mTPC waveform digitizer (2009 and 2010 only)

Table 5: *List of bank names for the MIDAS file systems.*

The data set is roughly 15 TB in size with 6 TB for each 2009 and 2010 and roughly 3 TB for 2008 run period.

5 Experimental Calibrations, Reconstructions, and Stabilities

Quality is not an act, it is a habit

Aristotle

This chapter focuses on how raw signals become observables and divided into two parts. The first part describes how raw signals are analyzed and calibrated in the different detector elements of the PEN apparatus. The second part introduces further calibration and analysis of the raw signals to construct useful observables used in the analysis. PEN collaborators will recognize this chapter mostly as a description of the PEN analyzer, the code used to decipher raw data and output processed data in the form of ROOT files or Ntuples [20]. Emphasis is placed on the ADCs and waveform digitizer as many of the observables that are used in the data analysis of data come from energy and timing information extracted by those means. Reconstruction of key observables from signals is only half the battle as this type of reconstruction must be optimized for each run period. This means that observables be used in the final analysis must be properly calibrated over the entire run period. Stability of the observables that are most often used and/or are critical will also be shown. Once calibration and stabilities have been assured, higher order observables may be constructed. A description of the most important observables is also given as these observables are used in the analysis of the low energy tail, MWPC efficiency, and/or the final branching ratio.

5.1 Plastic Hodoscopes

5.1.1 Analogue to digital converters (ADCs)

The interpretation of the ADCs in the plastic hodoscope helps identify the type of charged particle that traverses the detector. The task of the charge-integrating ADCs is to report the energy deposited in the detector using the information on the pulse amplitude in the form of ADC channels. However, there are a few caveats. The first is that for a given hodoscope, there are two ADCs, one on each end. The scintillation light in the plastic will travel in either direction along the length of the hodoscope. This means that PMTs on both ends of the plastic hodoscope will collect light attenuated based on the distance from the locus where the particle traversed the stave. The longer distance the light travels along the hodoscope, the more

the light is attenuated. Hence, proper evaluation of the deposited energy requires that the light attenuation in the detector is adequately understood. If the charged particle crosses the hodoscope and the light travels a distance, x, then the light attenuates by a factor $\sim e^{-x/\lambda}$, where λ is the attenuation length. In the case of the downstream ADC, the factor is $e^{(z-L/2)/\lambda}$ and for the upstream $e^{(-L/2-z)/\lambda}$, where z is the position where the charge particle travels and L is the length of the stave. Notice, by taking the geometric mean of these two values, one obtains a factor $\sim e^{-L/4\lambda}$= constant. By taking the geometric mean of the two ADC values in a given hodoscope, the result should be proportional to the energy deposited where attenuation is then accounted for. However, this is only true if the hodoscope is uniform throughout. If the hodoscope has some non-uniformities, then the above relationships no longer apply as in Fig 5.1 in which case a new method is needed.

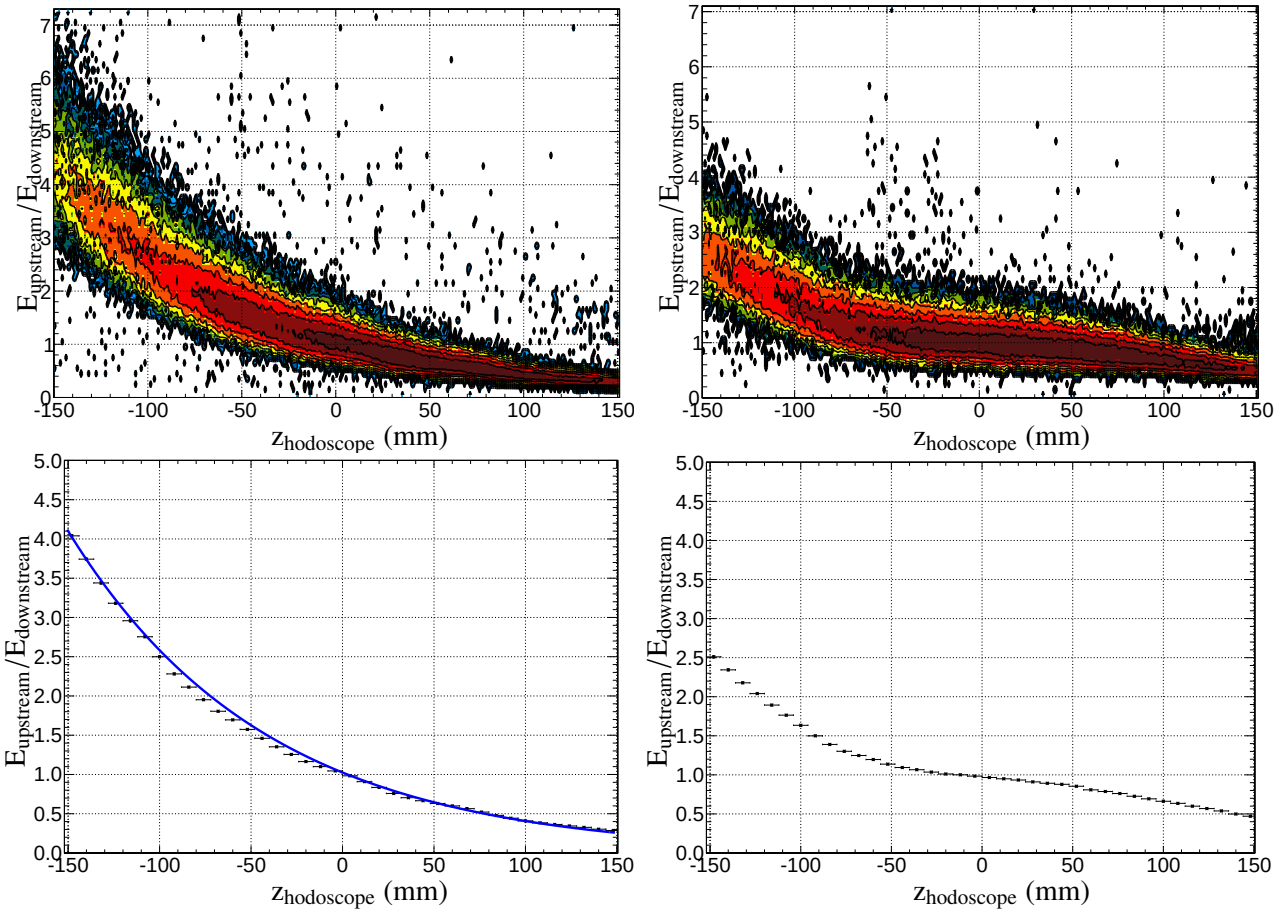

Figure 5.1: *Light attenuation in the hodoscope as a function of z. Upper Left: Hodoscope stave number 2. Upper Right: Hodoscope stave number 17. Lower Right 1-dimensional projection of plot above fitted with an exponential curve. Lower Right: 1-dimensional projection of plot above with no exponenetial fit. Hodoscope stave 2 shows no non-uniformities whereas hodoscope stave 17 does.*

Since the decay positron traversing the plastic is a minimum ionizing particle, its dE/dx is roughly constant regardless of the speed of the positron (in this case light speed). This in turn means that ADC corrections based on charged particles intersection with the hodoscope must be made. This position dependent correction accounts for non-uniformities and is implemented by requiring that the dE/dx through the hodoscope be the same regardless of where the positron crosses the hodoscope. By tracking the particle through the MWPCs for legitimate hits and using the thickness of the hodoscope 4 mm, corrections may be made by observing the ratio of the upstream and downstream signals and ensuring the they are calibrated so as to make sure dE/dx is the same. The comparisons of the two methods are shown below in Fig 5.2. Both are consistent with Monte Carlo expectations of energy deposition in the hodoscope. Since the positron is minimum-ionizing, the energy deposited should be roughly the same regardless of target position and pion beam momentum. Therefore the energy deposited in the hodoscope should peak at the same value for all runs for each of the twenty hodoscopes. Gain calibrations of the PMT readout were performed every twenty runs offline through software. A final gain was applied to all runs to ensure the peak of the hodoscope in the measured data peaks at the same location as that of the Monte Carlo (known) value. The energy as a function of run number is also shown.

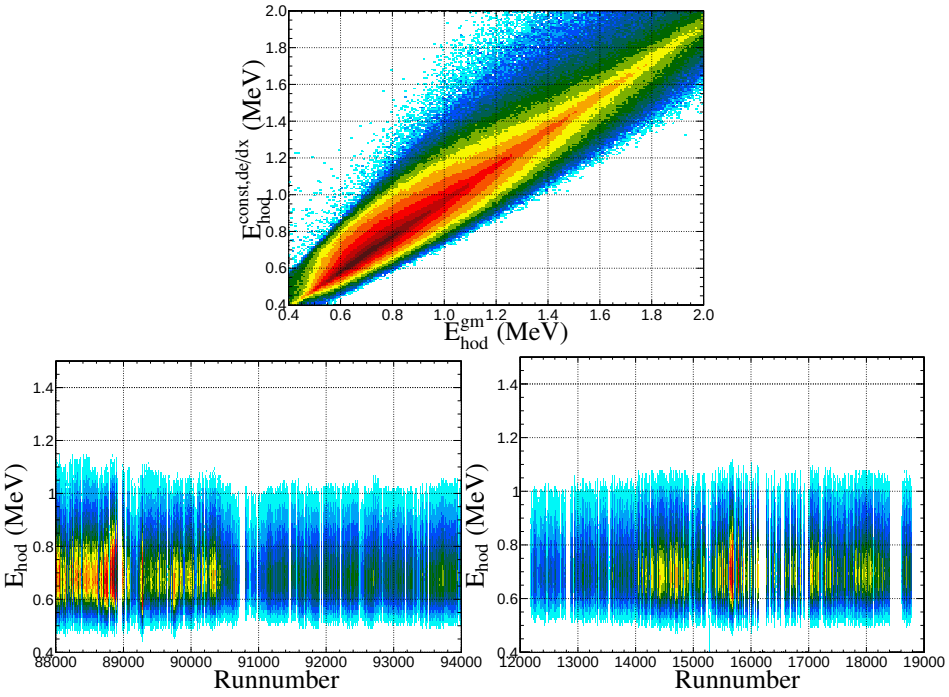

Figure 5.2: *Comparison of different methods of energy calibration in the plastic hodoscopes. Hodoscope energy as a function of runs. The two methods of calibration are consistent with each other.*

5.1.2 Time to digital converters (TDCs)

The hodoscope TDCs are one of the most important aspects of the experiment. The timing of the decay positron is determined from the plastic hodoscope. Naively, it may be better to use the positron time in the target waveform. However, a problem arises in that if a decay is fairly fast, then the target waveform may have to two or even three signals on top of each other and deciphering where the timing of the last waveform peak may not be feasible. One would like a consistent method to obtain positron timing that does not depend on the decay time. This is where the TDCs of the plastic hodoscope come in. Since a hit in the hodoscope was one of the requirements in order to trigger an event, all events that are recorded must have a TDC registered in the hodoscope (however, not necessarily in the CsI calorimeter). This means the best method is to use the hodoscope time for purposes of reconstructing the positron target time in all events while simultaneously calibrating the hodoscope time relying on well separated three peak waveforms in the target. These so-called "golden-Michels" permit the time extraction from the target waveform for the positron with great confidence for all events if done correctly. Using well separated signals in the target, the positron waveform time, along with the time of flight of the positron from the target to the hodoscope, it is straightforward to ensure that the hodoscope time is properly calibrated for the analysis. Timing calibration between two TDCs for a given hodoscope was done by ensuring the time difference between upstream and downstream hodoscope TDCs is zero for perpendicular tracks. The difference in the target waveform time for the positron and that of the time in the hodoscope after accounting for the time of flight of the positron is labeled `positronshift` by the PEN collaboration. The observable `positronshift` is plotted in Fig 5.3 for well separated Michel decays, the decays used for hodoscope calibration.

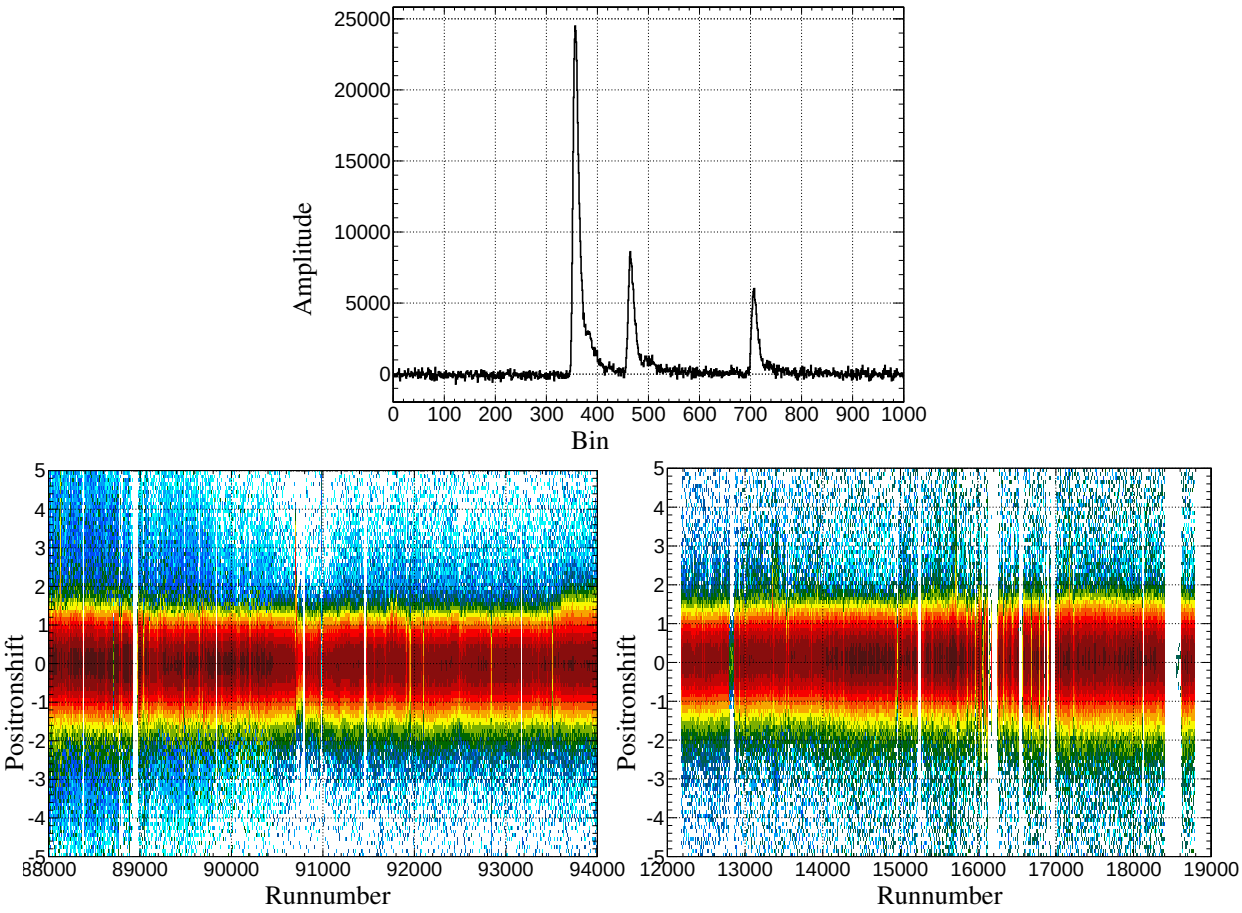

Figure 5.3: *Difference in hodoscope timing with waveform positron timing accounting for time of flight of positron from its birth to hodoscope hodoscope. Calibration is done for well separated (in time) Michel positrons (example waveform shown).*

5.2 The CsI Calorimeter

Arguably, the most important element in the detector system is the CsI calorimeter. It is the response of this detector that is ultimately required in order to obtain the necessary information to extract the branching ratio. There are 280 main ADCs which are used in the measurement. 240 of them are associated with each of the 240 crystals of the CsI calorimeter. The remaining 40 are on both sides of the 20 aforementioned plastic hodoscopes. For each of these ADCs, there is a corresponding TDC for the same detectors. Here we discuss how raw TDC and ADC values are transformed into values of energy and time, respectively, usable in the analysis.

5.2.1 ADC, TDC, and Clump Determination

Energy deposition in a given CsI calorimeter module is interpreted through light output of the detector, gathered by its photomultiplier tube which, in turn, produces a current pulse ultimately digitized via ADCs. Every channel or discrete increment of the ADC corresponds to a certain amount of energy, and it is the ADC which ultimately gets interpreted by the experimenter which then has to be re-interpreted as energy. Each ADC module has an internal current source that provides a non-zero charge during the interval of ADC integration with no signal present at the input. This is the so-called ADC "pedestal" value. Thus even when there is no energy deposition in a particular module, there is a non-zero ADC value attributed to this pedestal. A custom PMT/voltage divider, signal splitter system was used to ensure a high linearity presented to the ADCs outputs even near this pedestal value. Hence, in order to interpret the ADC channels as energy, a pedestal correction is done first. A second pedestal correction is then made to account for low frequency (50 Hz and harmonics) common noise by ADCs that are connected to the same block of electronics, i.e., ADCs that "breathe" together. Finally, a gain correction is made to re-interpret the signal as energy in MeV instead of raw ADC channels. The conversion between ADC channel and MeV varied by year. The conversions were 0.0381, 0.0465, and 0.0581 MeV/ADC channel for 2008, 2009, and 2010 respectively. Software gains were applied in increments of 20 runs in order to ensure that the crystal responses are as consistent as possible through the run periods. A final software gain was applied to put the energy peak at the correct location according to simulation (more on that later). The CsI TDCs were calibrated with reference to the corrected plastic hodoscope times. Since the time of flight between the hodoscope and CsI can be determined fairly easily using geometry, or Monte Carlo simulation, the CsI time was calibrated such that the difference between CsI times and the hodoscope was zero after accounting for the time of flight of the positron (a small correction). This was done for all 240 CsI crystal modules using good candidates for $\pi \rightarrow e\nu$ events with the main crystal being calibrated having sufficiently more energy than the rest of the crystals in the shower, thus ensuring that this is indeed the main or centrally hit crystal. First a crystal by crystal check was done for the full year, then run dependence was performed.

After the TDC and ADC calibrations are accomplished, the clump finding process begins. Loosely speaking a clump is the grouping of crystals within the electromagnetic shower that occurs due to an incident charged or neutral (gamma) particle. In particular, the main crystal hit and its nearest neighbors. The first step in clump finding is identifying the main crystal of the clump. This requires checking the energy of a

crystal against the energy in the nearest neighbors (and even next to nearest neighbors) and ensuring that it has the most energy. The crystal with the most energy in the clump is designated as the main crystal of that particular clump. After looping through all the crystals, the number of clumps is determined. The total energy of each clump is then determined, where if a common crystal is involved in two different clumps, then each clump gets a different portion of the energy of that particular crystal in proportion to the clump maxes. For example, suppose the maximum of one clump is 30 MeV and the second is 20 MeV. If the shared crystal in between the two clumps has 5 MeV, then the total energy associated with the first clump is 30/50 of the 5 MeV, and the second will is 20/50 of the 5 MeV. The times and the positions of the entire clumps are determined using a weighted average, the weights being the energy in each crystal. When the main crystal, the nearest neighbors and next to nearest neighbors are added together, this is referred to as a wide clump. Wide clump will contain the most (if not all) of the energy of the particle that induced the shower, provided little to no shower leakage. One of the caveats to remember, especially for the later chapters, is that the highest and most difficult systematic uncertainty of the experiment stems from the incomplete energy containment or detection in the CsI. The better the resolution of the detector, the easier it is to get the desired precision. Fig 5.4 shows roughly a 10% full width half max at 70 MeV for the CsI energy response from decay positron of the $\pi \to e\nu(\gamma)$ decays.

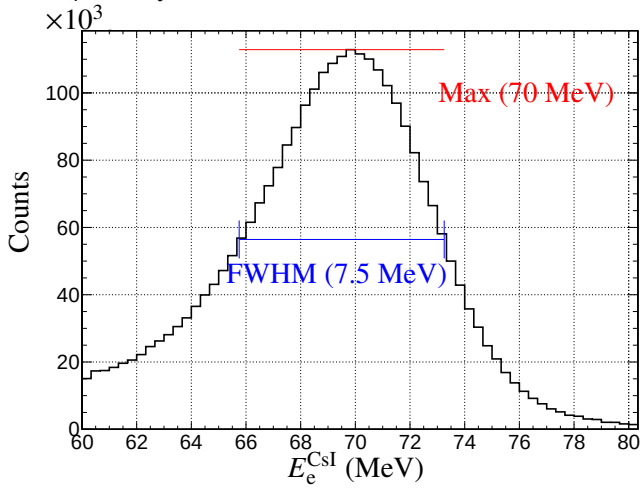

Figure 5.4: *Positron energy in the CsI with a peak at 70 MeV. Full width half max 7.5 MeV (or 10.7%). A smaller contribution to the relatively high FWHM is the various energies lost through different pathlengths taken through the target and plastic hodoscope staves.*

The relatively high full width half max provides complicates the clean separation of the Michel spectrum from pion decay spectrum without stringent event selections (cuts).

5.3 Mini time projection chamber (mTPC)

The mini-TPC was implemented in the 2009 and 2010 run periods in order to map the beam profile and stopping distribution for the incoming pions. The output to both left and right sides of all four mTPC wires was digitized with a CAEN V1720 waveform digitizer with a sampling rate of 250 Ms/s which ultimately produces eight separate signals[28]. The signals are multiplexed from the left and right side of each of the four wires, where the bins represented in increments of 512 describe which wire is being examined. The bins ranging from 0 to 512 represent the first wire, 513-1024 the second, etc. This is seen in Fig 5.5.

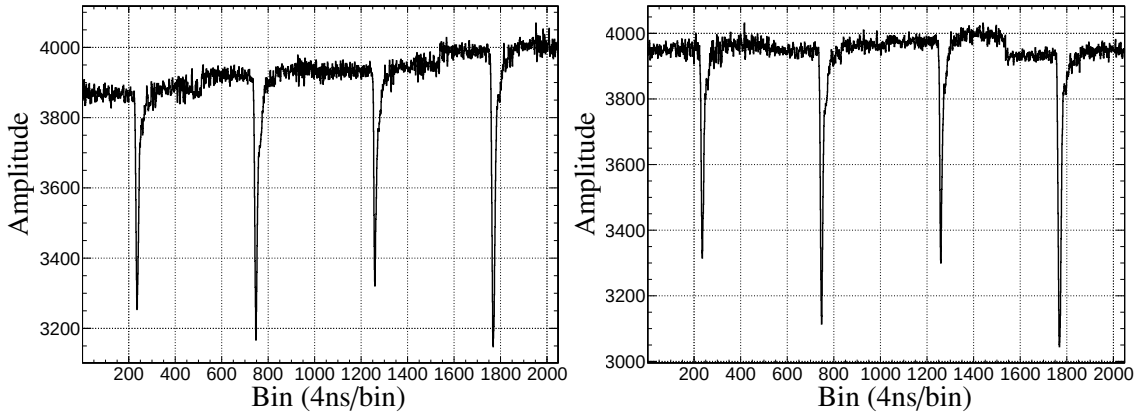

Figure 5.5: *Left: Raw mTPC waveforms left wire. Right: Raw mTPC waveforms right wire*

After baseline subtraction, the left and right waveforms are both analyzed. A search for peaks commences such that peaks are determined by requiring the sum of the left and right amplitudes to be greater than a prescribed threshold determined during test runs. Waveform analysis is needed in order to get information on the position of the pion passing through the mTPC. Time bins, that is the position of the signal, provide information on the y position, and the amplitudes provide information on the x position. The time bin of the pulse is determined by taking the geometric mean of the left and right waveform amplitudes and the derivative is taken to determine the highest slope. The maximum of the derivative (slope of highest rise time) is taken to be the value of the time bin only if this value is higher than that is expected based on any residual baseline or fluctuations in the signal. This can occur due to delta electrons, for example, when electrons obtain a sufficiently large enough energy such that the electron can cause secondary ionization.

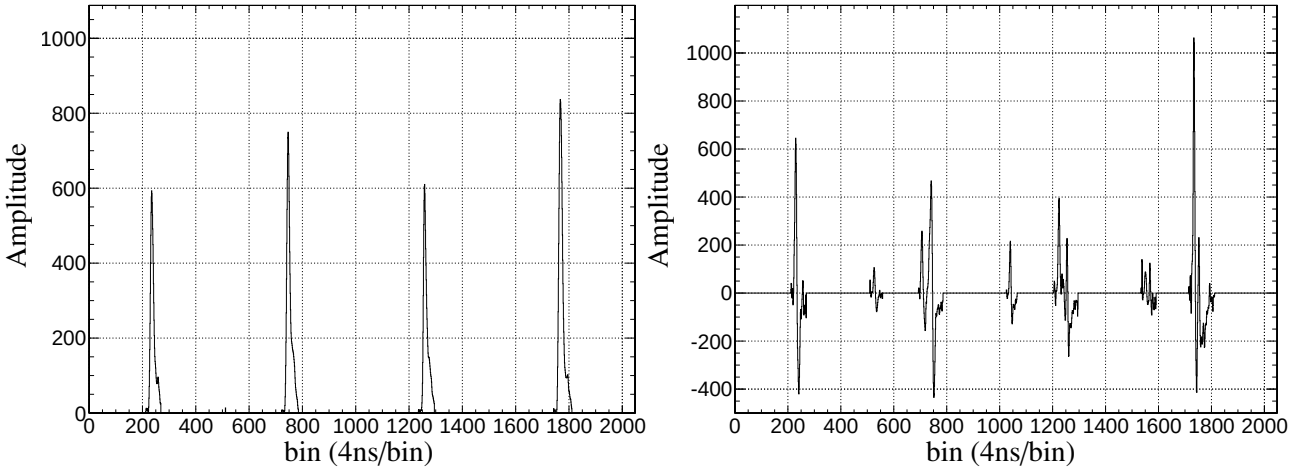

Figure 5.6: *Left: Geometric mean between left and right mTPC waveforms. Right: Derivative of geometric means.*

Knowledge of the time bin and the drift velocity provides the means to determine the *y* position that the pion crosses for each of the wires.

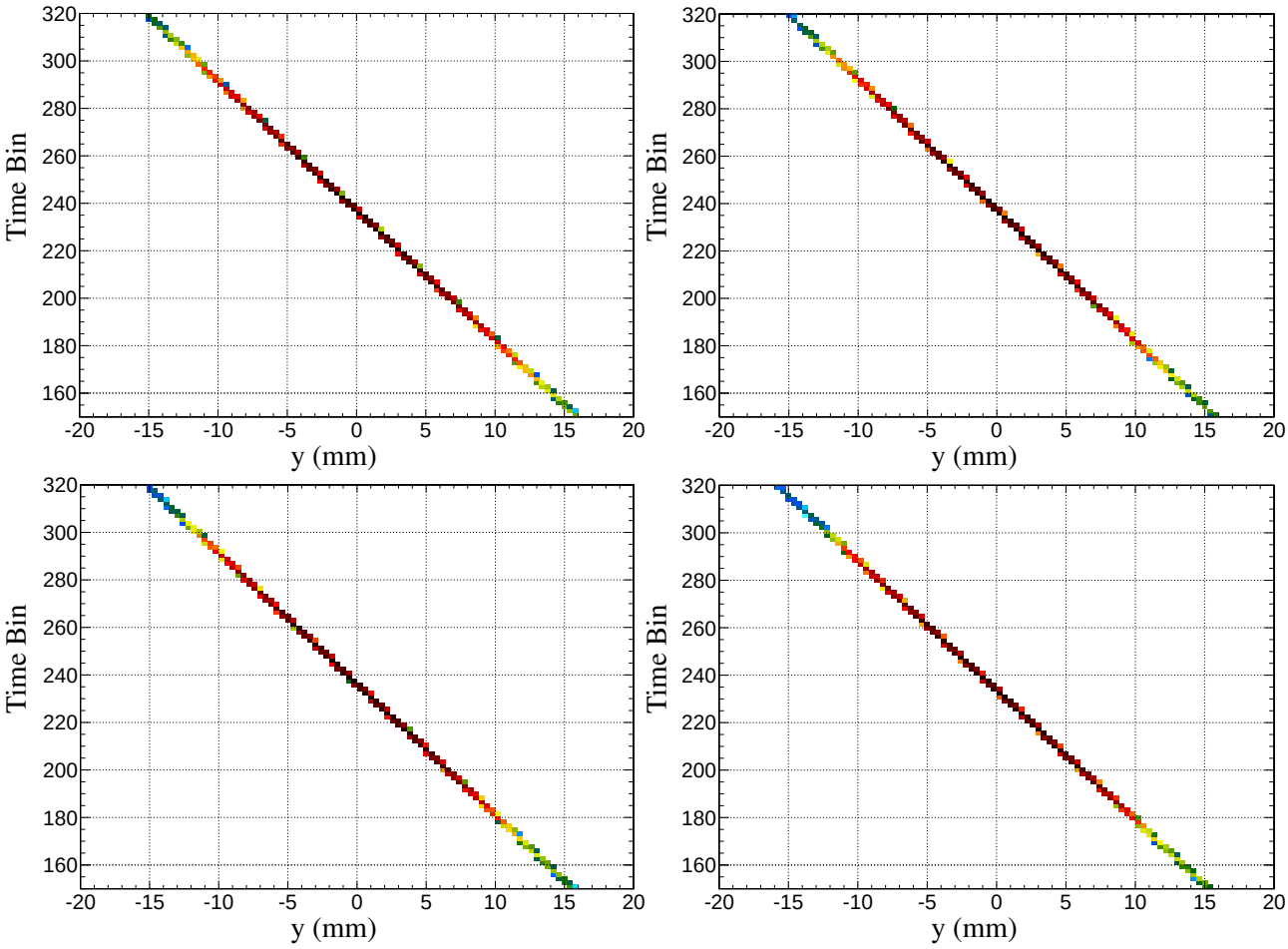

Figure 5.7: *y positions of each mTPC wire as a function of the time bin (position of mTPC peak) for wire1 (upper left), wire2 (upper right) wire3 (lower left), and wire4 (lower right)*

The difference in the integral of left and right wire waveforms provides the information on the x position of the particle. There is however, a small caveat. Not only does the charge deposited on the left and right sides of the wire depend on the x position where it crosses, it also depends on the amount of pion incoming energy. So simultaneously, the left and right sides of the wires will be correlated (more energy deposited, higher amplitude for both) and also anti-correlated (as the energy of one side goes up, the other goes down). When determining the positions of the particle, the waveforms are normalized to the sum of the left and right signals. Knowing this, a fairly simple charge division algorithm can be used to determine the x positions.

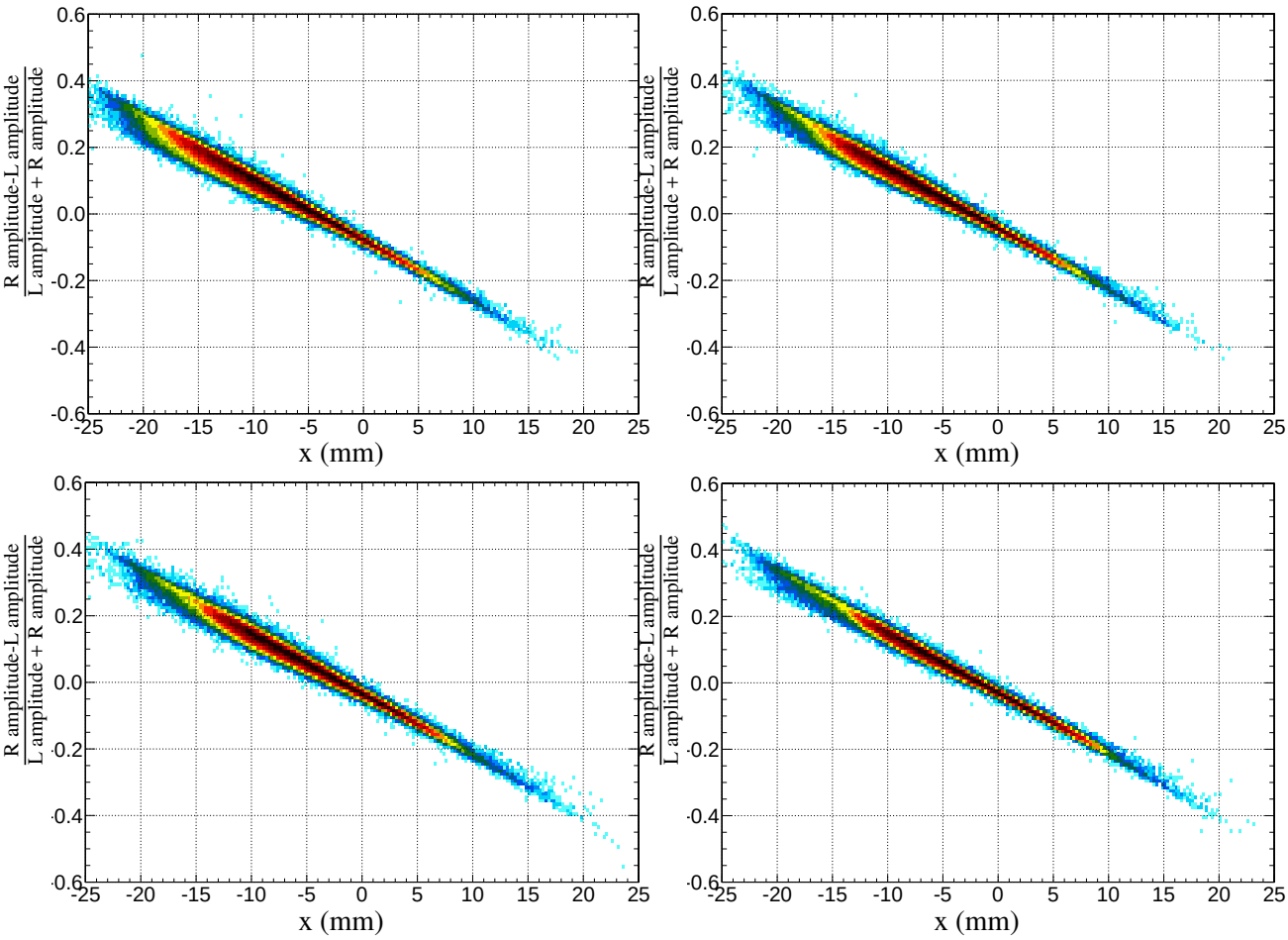

Figure 5.8: *Relative amplitude comparisons of left and right waveforms versus the x positions of the wires for wire0 (upper left), wire1 (upper right) wire2 (lower left), and wire3 (lower right)*

Once the x, y, and z positions are determined, it is desirable to find a way to check that these values make sense. The figure above shows that the sharing of charge on the left and right side of the wires is not equal at $x = 0$. This can be due to any type of offset, and or gain variations between left and right end of the wires. Given an ideal situation, there would be no scattering and the particle would travel in a straight

line. If this is the case, then a colinearity test can be constructed, which tests the linearity between different points of the four wire positions that the pion traverses. For this purpose, colinearity observables, col_{1x} and col_{2x}, are constructed to ensure that any offsets are properly accounted for. Here

$$\mathrm{col}_{1x} = x_1 + x_2 - x_0 - x_3 \quad \mathrm{col}_{2x} = x_1 - x_2 - (x_0 - x_3)/3 \tag{56}$$

Where x_0 is the x position of wire 1, x_1 is the x position of wire 2 etc. In a straight line, these two variables would be 0. This facilitates determining x and y positions for events in which there may be more than one beam particle.

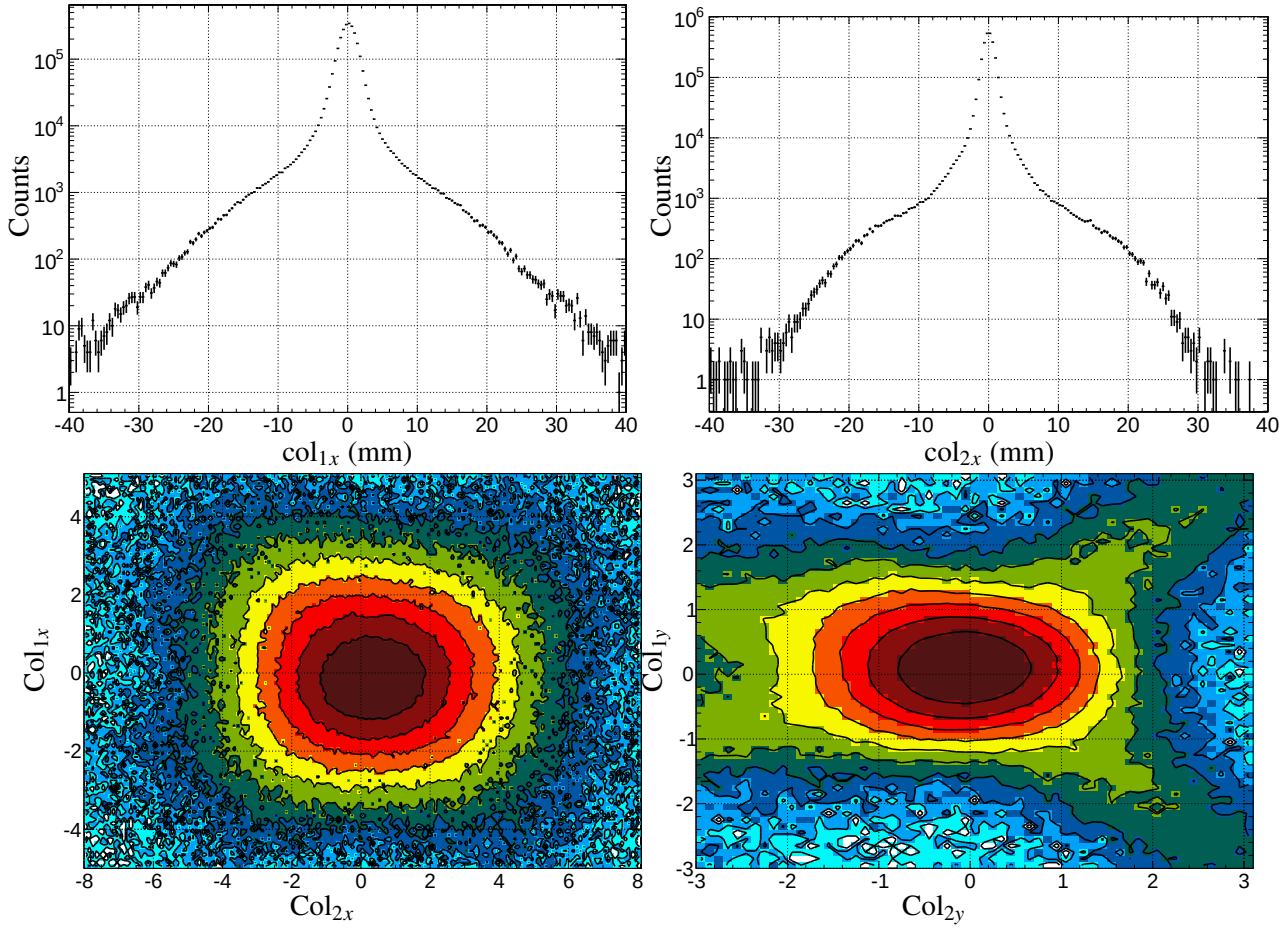

Figure 5.9: *Colinearity tests in the mTPC. Upper left, colinearity 1 for x. Upper Right: Colinearity 2 for x. Lower Left: Colinearity 1 vs Colinearity 2 for x. Lower Right: Same for y.*

Using the deduced x, y, and z positions of the wires hit aid in predicting the x and y stopping positions of the pion in the target. This is achieved by using the average dx/dz and dy/dz values for each of the

wire combinations so that x an y can be extrapolated at any z value. This allows the beam profile to be be reconstructed as well as the stopping distribution.

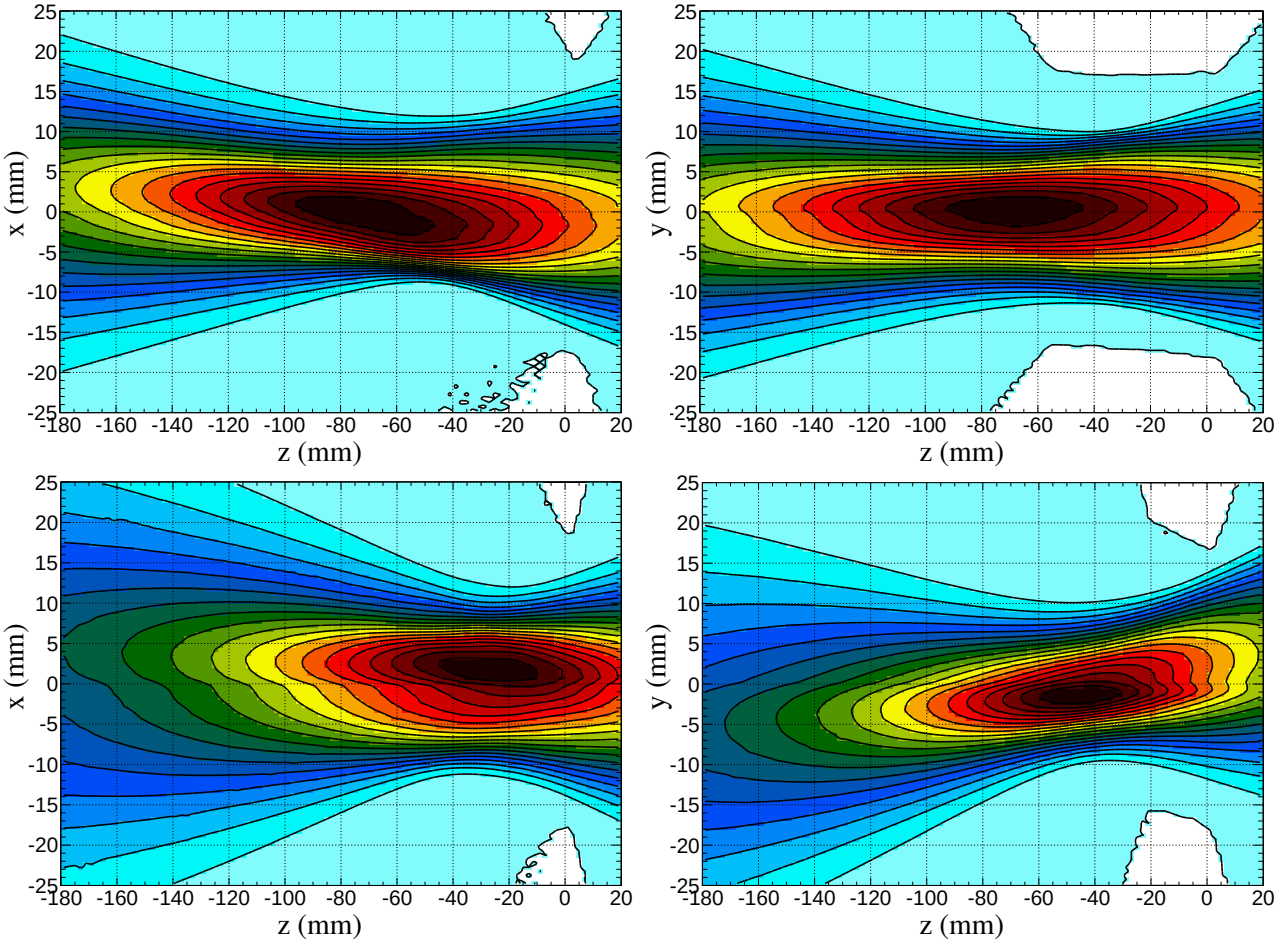

Figure 5.10: *Pion beam profile projections. Upper Row: 2009. Lower Row: 2010*

A crosscheck on these positions is made with the MWPC and its knowledge of the decay positron's trajectory. Using the MWPCs, and trajectories which are either horizontal or vertical, one can check to see if the stopping position as determined by the mTPC agree with the MWPCs. This agreement is seen in Fig 5.11.

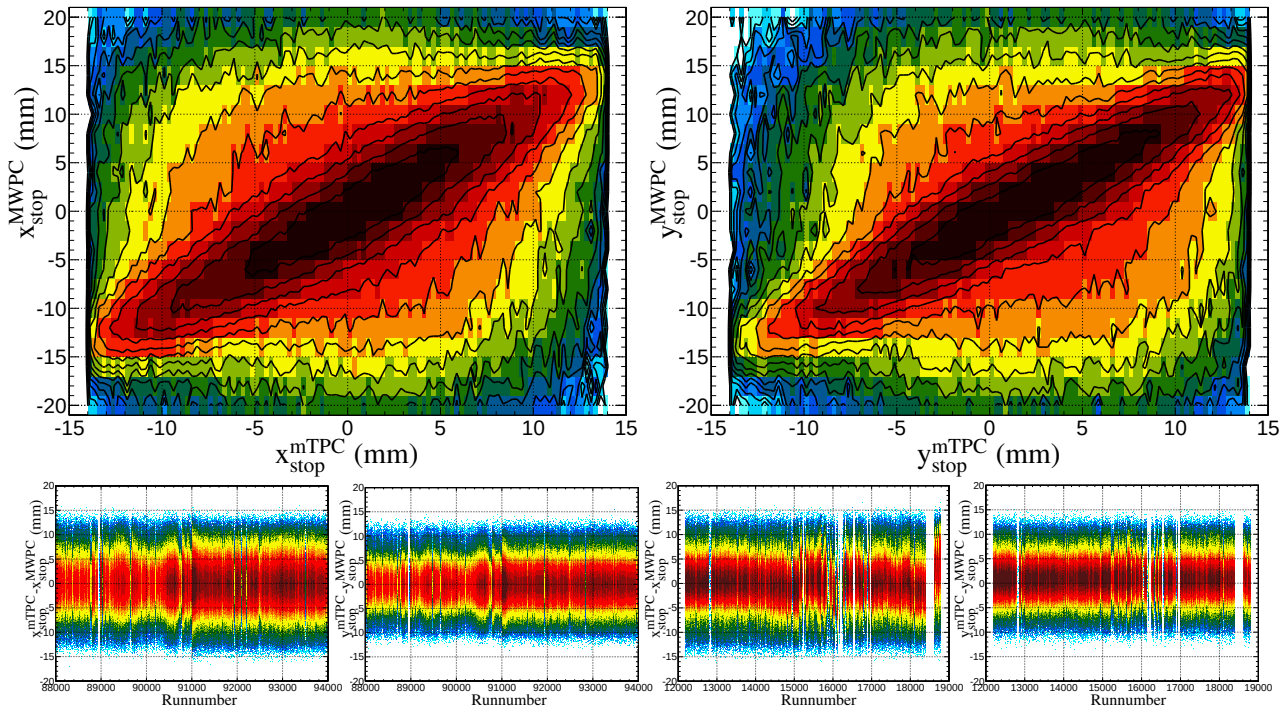

Figure 5.11: *Top Row: Stopping coordinates as determined by MWPC for vertical and horizontal trajectories of decay positron plotted against stopping position as determined by mTPC from beam pion. Bottom Row: Difference in stopping positions as determined by mwpc and mtpc vs run number.*

Further, a classification of the efficiencies of the mTPC as a function of wire number and run number was performed. This is simply done by observing the number of times a particular wire did not fire given that a legitimate pion stopped, i.e., the time of flight between the B0 and degrader coincides with the the time of flight of the pion and that there is an energy signature in the target indicative of a pion stopping. In addition, when one wire was under study, it was required that the other three wires fired to ensure false signals are ruled out. The efficiencies of the wires are plotted in Fig 5.12 below for the two years of operation.

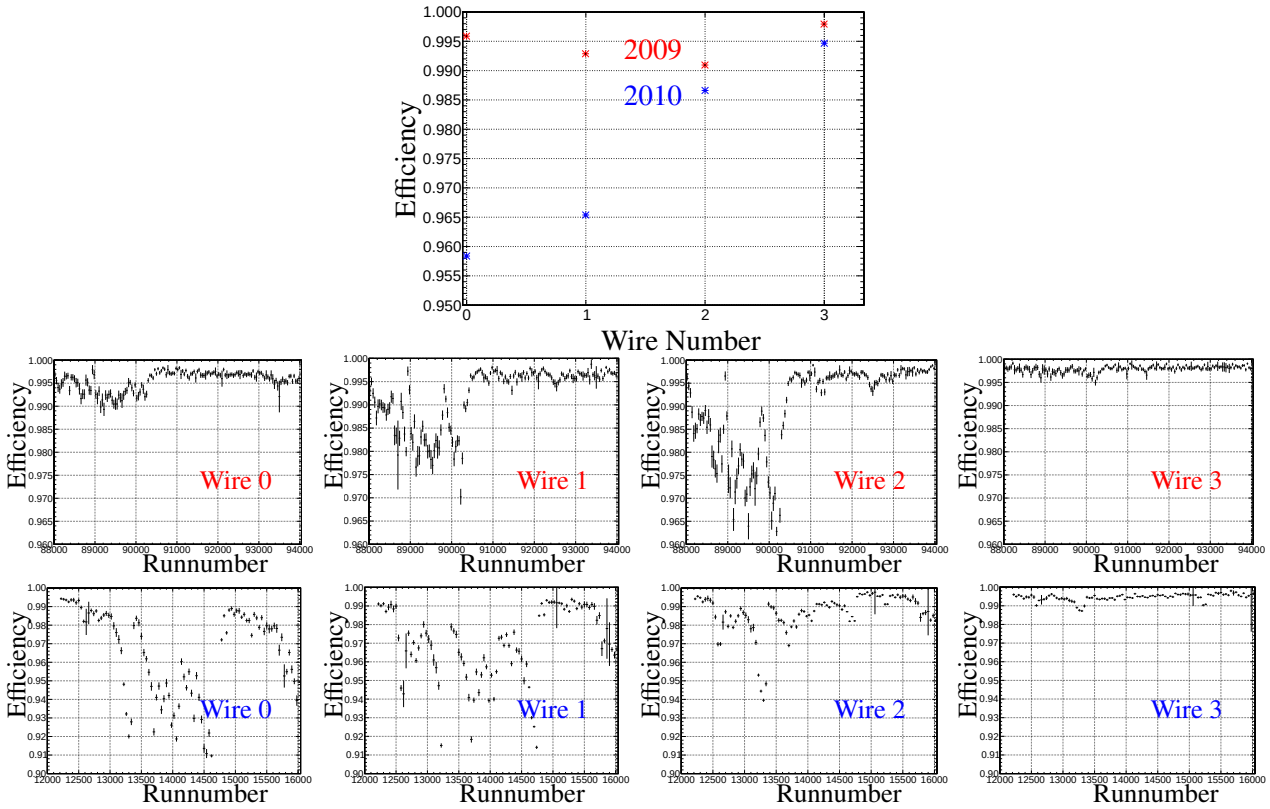

Figure 5.12: *mTPC efficiencies for 2009 and 2010 data set. Top Row: Efficiencies for each wire number. Middle Row: Efficiencies of each wire as a function of run number for 2009. Bottom Row: Efficiencies of each wire as a function of run number for 2010. Note efficiencies for 2010 are not well defined beyond 16000 because of failure of some wires of the detectors.*

The reader should be reminded that during the 2010 run, a different mTPC was used than the one used in 2009. The 2010 was a lower-mass mTPC with wire spacing 12.5 mm instead of 10 mm. The difference in the detectors is one of the factors which produces different efficiencies.

5.4 B0, Degrader, and Target Waveform Digitizers

This section shows how the raw detector waveforms are used to extract information on time and energy of charged particles in the beamline. As a particle traverses plastic scintillators, it deposits energy. This energy is lost due to collisions and interactions with the atoms and electrons in the scintillator material. When the energy is lost due to atomic excitations, the electrons can de-excite by emitting photons. These photons are collected, and produce a current signal in photomultiplier tubes which can then produce a signal to be analyzed to recover the amount of energy. The analysis begins by observing the maximal amplitude bin in

the raw waveform, calling this the temporary baseline level and then searching for a more precise baseline by taking a weighted average around this temporary baseline. A subtraction is then performed which centers the baseline at zero and flips the amplitude as seen in Fig 5.13.

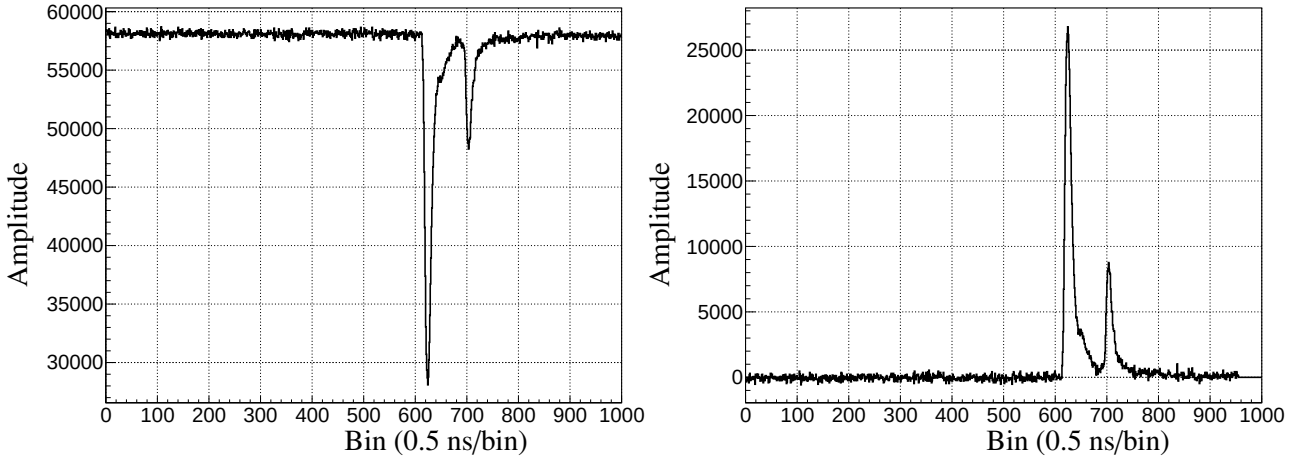

Figure 5.13: *Left: Raw waveform in the target. Right Waveform with average baseline subtracted.*

The next step is to find the presence of the waveform peak in the degrader. Starting with degrader is preferable because particles from the B0 may scatter out of the fiducial volume of the detector, in which case those signals would originate from particles that do not constitute a legitimate pion stop. Since either a pion or a proton deposits the most energy, the highest peak in the degrader is found. Whichever bin is to be the highest in the degrader, a search for the pion in the target is found around this bin in a range of ± 10 ns, and similarly in the B0. This algorithm is seen in Fig 5.14. Only events in which pions are identified in this time range for all three main detectors are considered for analysis. Once this is achieved, a check on the size of the signal is performed to veto out protons originating in the beam. The threshold was determined using both Monte Carlo simulation and solo runs with known particles. The threshold energy depended on the year, since the beam momentum changed during the three years.

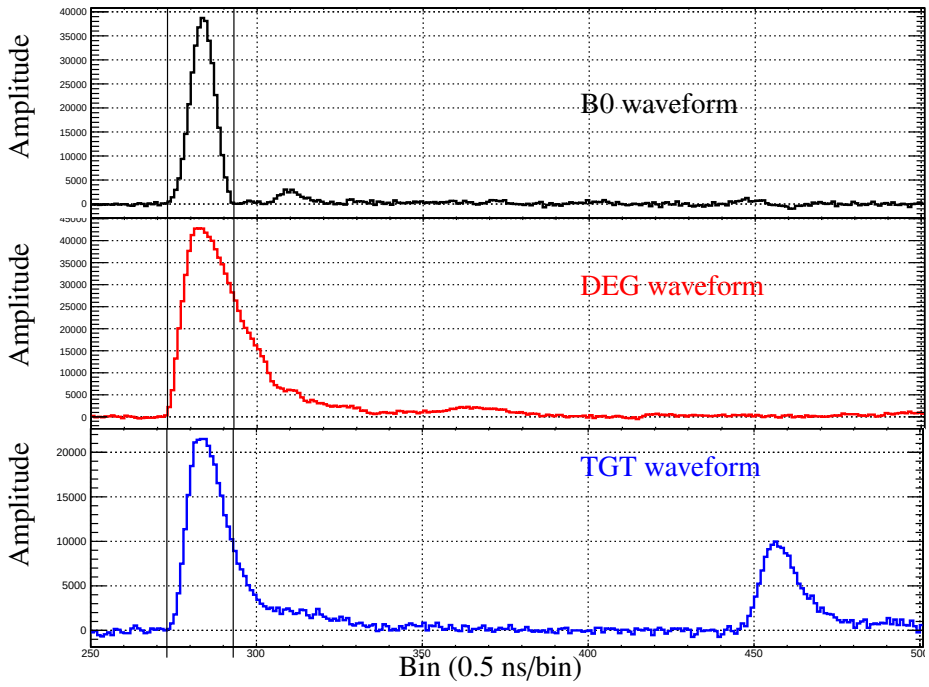

Figure 5.14: *Comparison of B0, DEG, and TGT waveforms with vertical lines at ± 10 bins from main bin in the degrader. B0 waveform is offset by time off flight.*

Next, signal searches from scattered beam particles are performed by looking for signals in the B0 digitizer which is required to have a sufficiently high amplitude in the bin while simultaneously fulfilling the requirement that the peak contains at least 40 percent of the entire signal, and is within 10 ns of the scatter bin. The scatter bin is the bin expected to find a signal in the B0 from a scattered beam positron. Since the decay positron is placed at a particular channel (2009 is around 705) and the time of flight of the beam positron is 12 ns (or 24 bins), the scatter bin is the the bin in the B0 that accounts for this difference (around 730). The presence of multiple beam particles is then examined by observing the degrader signal and searching for peaks with a nearby peak in the B0. The distance between the bins is computed to give a preliminary estimate of the time of flight between the two detectors, and the energy observed in these peaks evaluated by the integral determines which of the three particles, pion, muon, or positron produces the signal. The time of flight of the beam particle is then determined using the constant fraction time of the degrader and B0 waveforms, that is a time at which the leading edge of the pulse amplitude reaches a constant fraction of the amplitude. Any offsets are checked using the time of flight of beam positrons. Since the beam particles will have the same momentum, the positron beam emerge with momentum greater than 70 MeV, meaning their speed can be approximated to be that of light. Therefore, regardless of the beam momentum, the time of flight of the positron will be the same as shown in Fig 5.15.

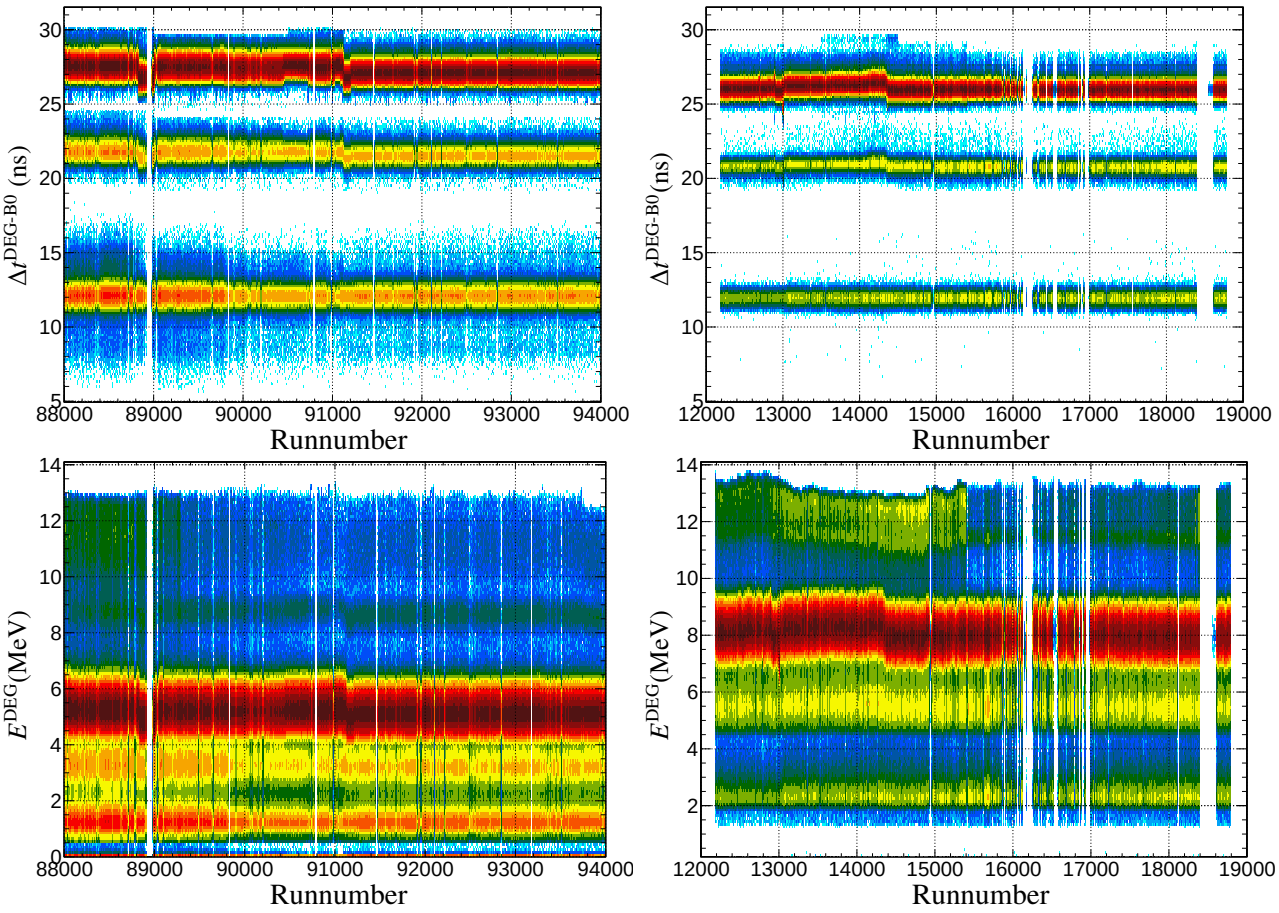

Figure 5.15: *Degrader energy and comparison of time of flight between B0 and degrader for 2009 and 2010. Upper Left: Time of flight for 2009. Upper Right: Time of flight for 2010. Lower Left: Degrader energy for 2009. Lower Right: Degrader energy for 2010.*

The energy deposited in the degrader and B0 are subsequently determined using appropriate calibrations and gains in the respective detectors determined by both simulation and during data acquisition. The target waveform analysis is slightly different than that for the upstream counters. For a good event, the beam counter and degrader contain only one signal from the incoming pion, whereas in the target waveform there will be two or three peaks depending on which decay chain occurred. The pion momentum varied throughout the run periods which means that the pion signal in the target will vary with run period. In addition, the change in beam momentum and profile translates to a different pathlength the positron traverses through the target which produces different energy spectra for different run periods. The best method to check the target gains over the different run periods is to use the muon signal. The muon always has a 4.11 MeV birth energy when the pion decays at rest due to kinematics requirements. So the electron equivalent energy should always be the same for any run during anytime for the muon signal. Target software gains are applied

in groups of 20 runs to the target waveform to preserve this constant of nature. This, in turn, then ensures that total target energy fluctuations are only due to varying pion energy in the beam and positrons that traverse different pathlengths through the target due to variation in stopping positions. A plot of the muon electron equivalent energy over run period is shown below in Fig 5.16.

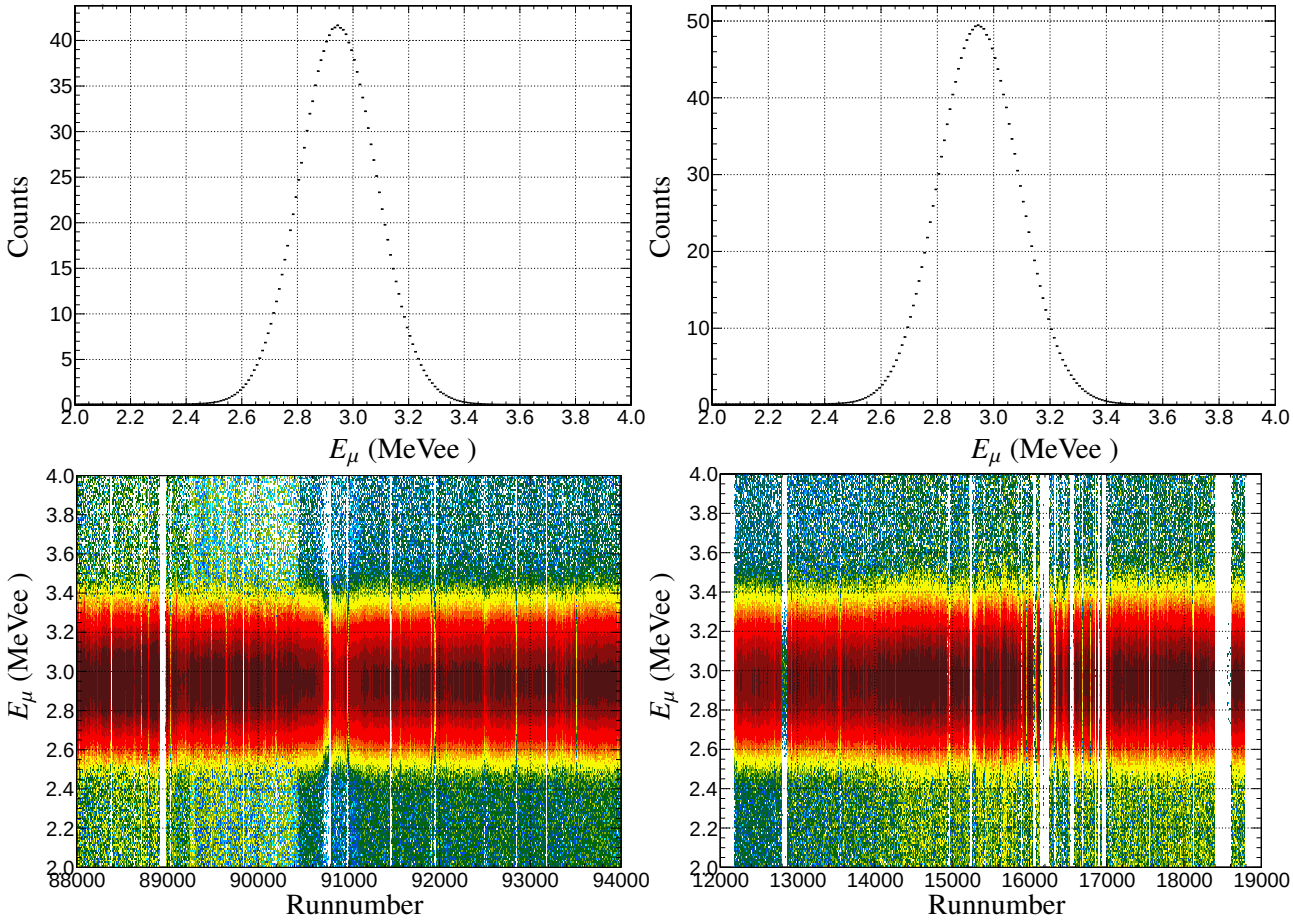

Figure 5.16: *Comparison of muon target energies for well separated decays. Upper Left: Muon peak for 2009. Upper Right: Muon peak for 2010. Lower Left: Muon peak as a function of runnumber for 2009. Lower Right: Muon peak as a function of runnumber for 2010.*

5.5 Multiwire proportional chambers (MWPCs)

An important feature of the PEN apparatus is the ability to track charged decay particles. This is accomplished using two concentric cylindrical multiwire proportional chambers. The inner chamber, consisting of 192 wires and 256 cathode strips, has a radius of 60 mm centered at the target scintillator. The outer chamber, consisting of 384 wires and 384 cathode strips with a radius of 120 mm is centered at the target scintillator. The wires lie parallel along the z-axis, i.e., parallel to the beam line. The wire that is hit

determines the azimuthal angle ϕ, or if you like (x, y), and the cathode strip with the highest signal will determine the z position, more specifically the sum of the cathode strips from the inner and outer surface. The correlations between wire and cathode responses as a function of the azimuthal position and z position is shown in 5.17

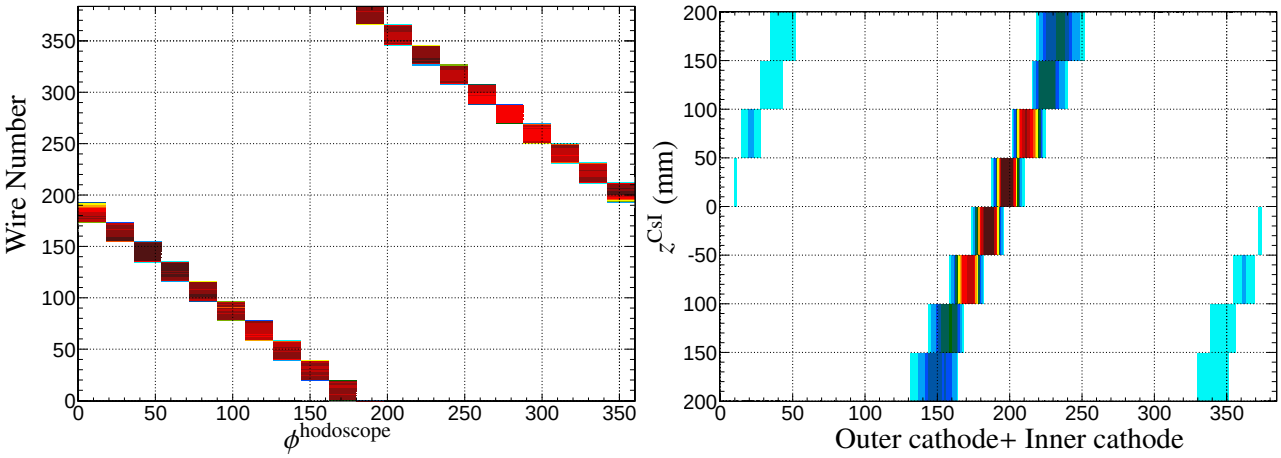

Figure 5.17: *Comparison of track knowledge obtained by MWPC and by other detector elements. Left: MWPC wire number vs phi determined by hodoscope number. Right: The z position of the main crystal hit compared to that of the sum of inner and outer cathode strip numbers.*

Additional PEN MWPC specifications may be found in Karpukhin et al [52]. A typical MWPC has a two cathode surfaces with an anode plane in between them. The two surfaces are needed to ensure that the there is no ambiguity in case of multiple charged tracks. In the PEN experiment, the surfaces are denoted as inner and outer surfaces. The inner surface is the one closest to the target (between the anode plane and the target) while the outer surface is on the other side of the anode plane. It must be noted, however, that the MWPCs of the PEN experiment actually consists of six surfaces. For the inner chamber there are four surfaces: inner and outer surfaces for both upstream ($z < 0$) and downstream ($z > 0$). This feature is an artifact of the previous incarnation of this detector, for the PiBeta experiment, where a higher beam rate required more surfaces to handle all the incoming information. For the outer chamber there is just the inner surface and outer surface. Aside from charged particle tracking, the MWPC is also used to identify protons that originate from the target or beam counters that occur when the incoming pion undergoes hadronic interaction in these detectors.

Analysis of the information of the MWPC begins with finding the cathodes strips and anode wires that were hit in a given event. The anode generates a simple bit of information which tells only whether a wire was fired or not. However, if two neighboring wires were hit, this suggests that the particle traversed in

between the two wires and the "half-wire" is taken. For example if wire 112 and 113 were hit, this would be interpreted as wire 112.5 being hit. Determining the hits on the cathode strips is not as easy however. The strip signals are interpreted from 640 separate ADC channels, each of which is characterized by its own pedestal noise. This is corrected by shifting the pedestal peak to zero by a subtraction. Sometimes common noise or cross-talk at the mV level is seen in the detectors due to common connections or close cables where the detectors "breathe" together. This type of electronic noise can be eliminated using a similar procedure performed in the PiBeta experiment [45]. In short, correlations were found between ADC channels which shared a common surface. These correlations were characterized by the correlation coefficients and sorted into a common groups. The relationship between these groups and individual detectors was quantified so that a proper subtraction would take place. The resultant effect is to reduce the correlation between common groups and decrease the pedestal width as seen in Fig 5.18.

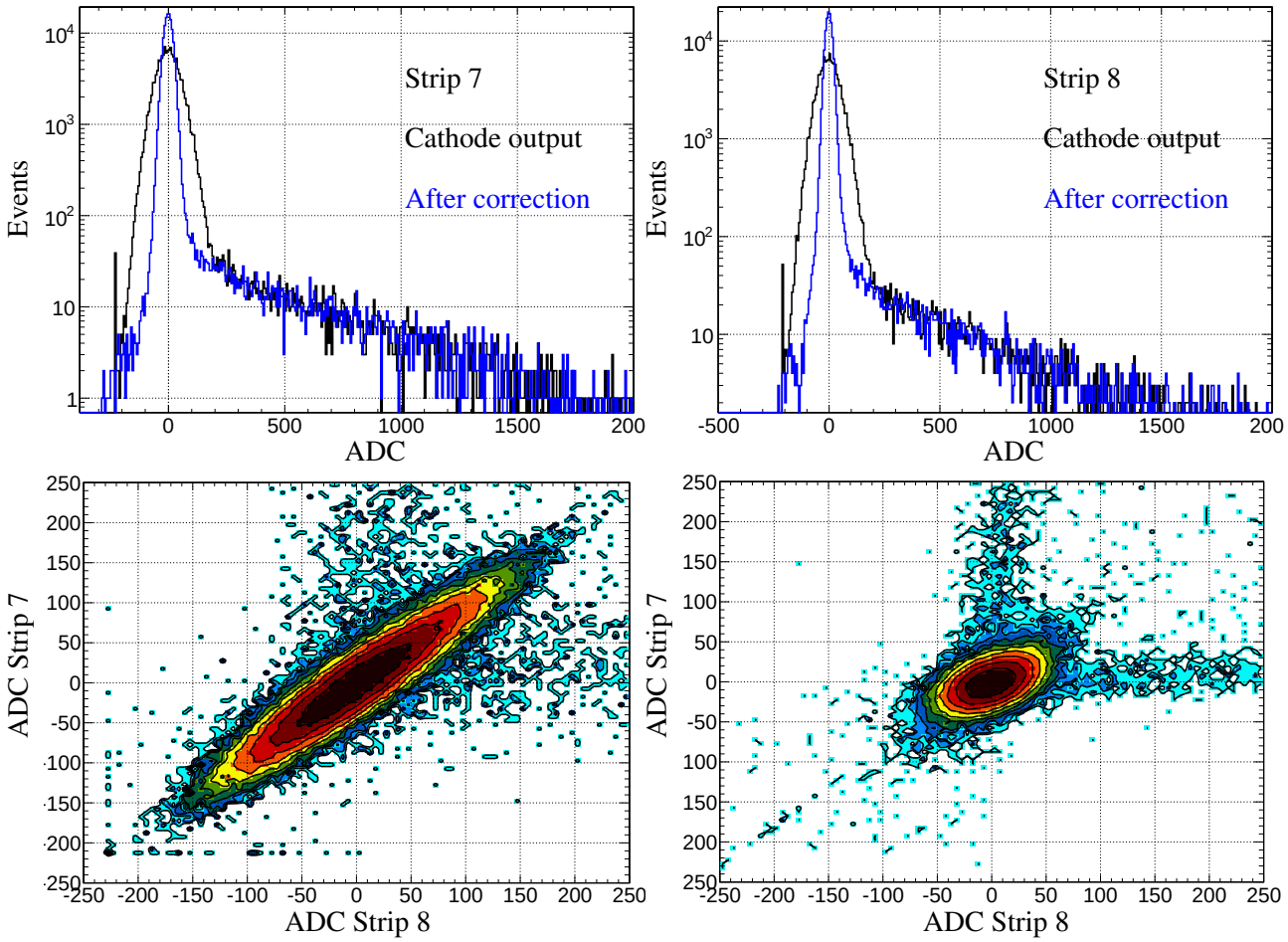

Figure 5.18: *Upper Left: Strip 7 output. Upper Right: Strip 8 output. Lower Left: Strip 8 vs Strip 7 output before common noise correction. Lower Right: Strip 8 vs Strip 7 output after common noise correction.*

Once the pedestals are properly corrected, the search for a signal in the cathode strips begins. First, a sum of nearest neighboring strips is done. This means that in the array of 640 cathode strip outputs, 640 new values are produced. These new values are simply the output of one cathode strip and its nearest neighbors. For instance, if strips 4, 5, and 6 have ADC values of 400, 1200, 300, then 1900 is the new value assigned to strip 5, the value the cathode strip plus the value of the strips to the left and right. This is done because in the cases where the decay positron traverses through the gas, it may easily travel near boundaries between two strips in which case finding a peak is less trivial. A maximum signal is then searched in this new array and is found by looking at the sum of the signal on a given strip and its neighbor to the left or right by three or six strips. The reason this range was chosen is because it was experimentally determined that the signal on strip groups typically includes a range of about six strips. The baseline was also determined in a similar manner where the smallest difference between signals 3 and 6 strips away in both the right and left directions were saved and subtracted. Once this is achieved, a threshold is set in order to find a signal in the surfaces. If no signal is found, the threshold is lowered. More than one peak may be found, but no more than four peaks in a surface are considered. Once the strip number of the strongest signal is determined, the z position is subsequently determined. This is accomplished by knowing the geometry (helix), the wire that was fired, and the slope of the helix. The advantage of the cylindrical structure is that only two of the three elements of the detector are needed to reconstruct the track using the MWPC information. The method of extracting the azimuthal and z coordinates leads to two possibilities. The first is if the all three elements, one anode wire, and two cathode surfaces, identify the signal. In that case, the inner and outer z coordinates are determined using the information of the wire and cathode strip number with the highest signals in the respective surfaces. The z value that is used is the arithmetic mean between the inner and outer surface z values determined for two surfaces. The second case is when only two of the three elements produce a signal. If one of the cathode signals is missing, the cathode surface that does produce a signal is still treated the same, and the z position of that decay positron is taken to be the z position of that surface. If the anode wire produces no signal, then the knowledge of the sum and difference of the strips is used. This is done by understanding the geometry of the helical MWPC, which outlines, one of the advantages of the PiBeta/PEN cylindrical wire chamber design is that the z and ϕ coordinates may be determined by either the firing of one strip and a wire, or two strips. The sum of the strip numbers provide information on z and the difference in strip numbers provides information in ϕ (or wire number).

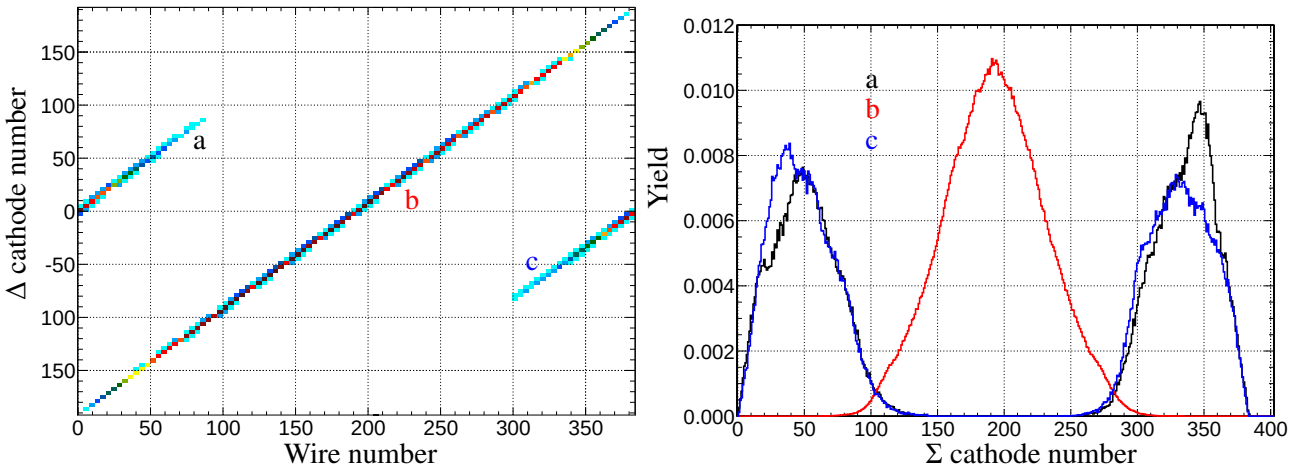

Figure 5.19: *Left: Relationship between difference in cathode numbers and wire number. Right: The sum of the cathode numbers for events a, b, c from the plot on the left.*

Notice the main diagonal in Fig 5.19 shows the correlation is offset by 192. By taking the cathode number difference, outer strip number − inner strip number, and adding 192, the hit wire number is determined and thus the angle deduced. For the left portion and right portion, notice when plotting the sum of the strip numbers in the the three regions, one can see that if the difference is greater than zero and the sum is either between 0 and 100 or 100 and 200, then the difference is the wire number. Finally if the difference is negative and the sum follows the same criteria then one would add 384 instead of 192, and once again one would retain the correct wire number. These criteria arise from the strip numbering relative to the wire numbering and the associated wrap-around. A similar, yet slightly more complicated relationship exists for the inner chamber. The inner chamber is more complicated because it has four surfaces instead of two. Even with this slight complication, the predicted and observed wire numbers coincide. If the anode wire fails to fire, the information on the azimuthal angle would be lost. However, the strip number that was supposed to fire may be recovered (and thus the azimuthal knowledge recovered) provided both the inner and outer cathode strips fire. In addition, if two charge tracks are present in the chamber, this check on the azimuthal angle, in the case of all three surfaces firing, aids in eliminating the tracking ambiguities caused by two (or more) charged particles. Similarly, if only one of the two cathode surfaces fires, the position in the z coordinate would normally be lost. However, if the anode wire fired in the case of only one of cathode surfaces, then the missing cathode surface may be recovered, which makes the z coordinate recoverable.

5.6 Key Observables

The detector calibrations and reconstructions having been presented for each of the individual detectors, we turn our attention to the construction of the some of the key physics observables. While there are a number of observables that can be constructed, this section will focus on those that were used in the analysis, either in the low energy tail analysis, chamber efficiency calculations, decay in flight corrections or the event selection/rejection.

5.6.1 Predicted time and energy for beam pion and decay positron

One of the most important aspects of the PEN analysis is that predicted and observed energies and times for both the pion and positron are constructed for each event. These observables will be seen to highly discriminate the main background and signal and are therefore very useful. The predicted pion energy is determined using the beam pion time of flight and the energy deposited in the degrader. The time of flight between the B0 and degrader determine the amount of energy the pion has in flight immediately before entering the degrader. Subtracting the energy the pion deposits in the degrader, the energy of pion before entering the target may be obtained. The predicted pion time comes from the timing in the degrader, and accounting for the time it takes to get from the degrader to the target plus the average stop time. The time it takes to get from the degrader to the target is easily calculated since the energy of pion leaving the degrader (predicted target energy) allows for the calculation of the pion speed, which is turned into time, based on the known distance between the degrader and the target. The additional time from reaching the target to stopping may be obtained from Monte Carlo simulation. The predicted energy deposited by the positron in the target comes from the knowledge of the pion stopping position and from the positron trajectory. While the x and y positions of the pion stop are determined by the the mTPC, the z position comes from knowing the energy of the pion before it enters target, and using a known momentum-range relation determined by Monte Carlo simulation, shown in Fig 5.20.

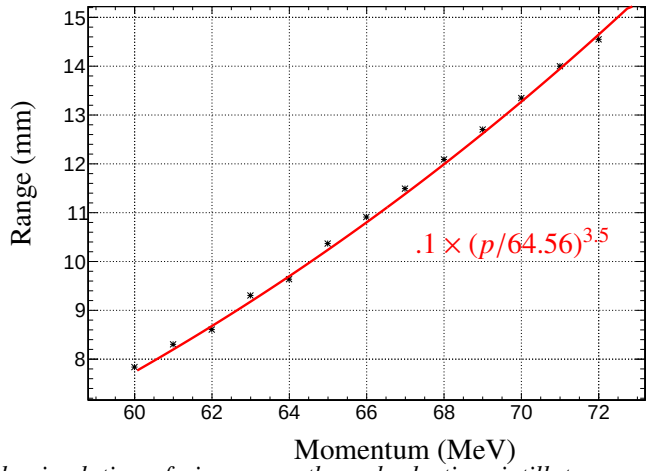

Figure 5.20: *Monte Carlo simulation of pion range through plastic scintillator as a function of the incoming pion momentum.*

The path traveled through the target can be calculated by tracing the trajectory of the decay positron back through the target and crossing the position where the pion stopped, or at least as close possible. Since the dE/dx of the target is known, 1.78 MeV/cm, a predicted energy is obtained via the calculated pathlength. The predicted positron time comes from the timing in the plastic hodoscope, accounting for the distance traveled in the target as well as the distance from the target surface to the plastic. The correlations between predicted and observed timings and energies are shown in Fig 5.21 for well separated Michel decays.

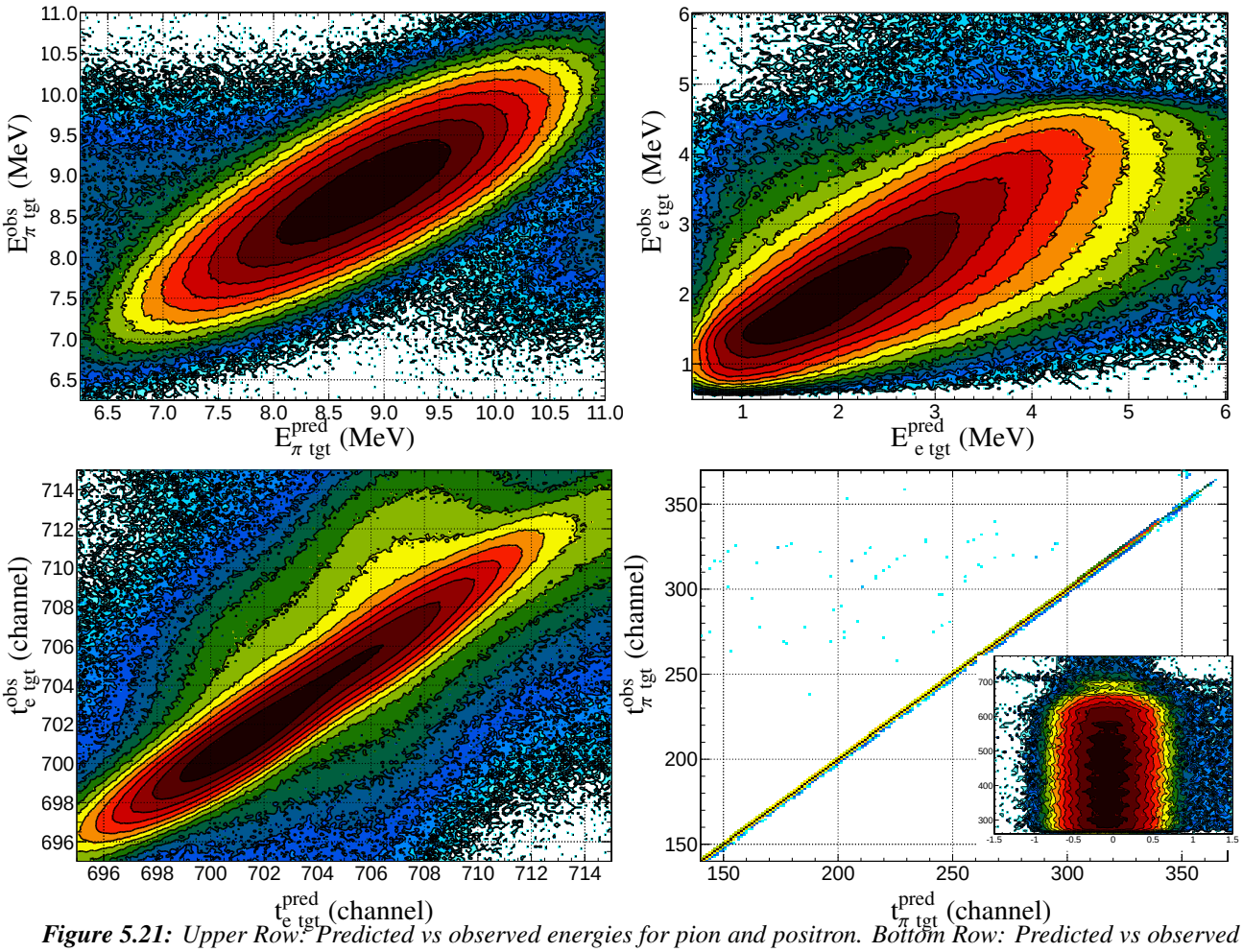

Figure 5.21: *Upper Row: Predicted vs observed energies for pion and positron. Bottom Row: Predicted vs observed times for pion and positron*

Predicted positron energy is arguably the most important of these observables as it is used in higher order variables such as ΔE_{2p} , $\Delta\chi^2$, and `restwave`, which will be discussed shortly. However, there are instances in which the observable predicted positron target energy is not reconstructed. By selecting events in which there is a clear positron in the target, the observed positron energy for the selection of selection is shown in Fig 5.22

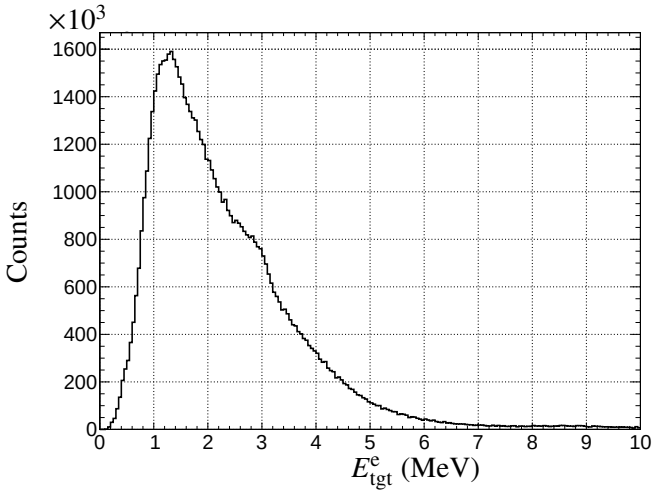

Figure 5.22: *Energy of the positron peak in the target for well separated Michel decays when predicted energies are not properly reconstructed.*

In the instances where the predicted positron target energy is not reconstructed, there is an energy deficit in the total reconstructed positron energy which entails adding up the target, hodoscope and CsI deposited energy. The lack of reconstructed energy can have undesirable effects on the analysis. Therefore, there are two different options to deal with the problem. The first is to understand and, if possible, fix or correct this lack of predicted energy. The second is to remove these events from the analysis, that is to cut out these events in which the predicted positron target energy is not reconstructed. The problem with the second option is that the failure of the reconstruction may be systematic or dependent on the particular decay process. In addition, events are lost. Therefore, the best course is to try and understand of why failure of a prediction occurs and determine whether the simulation can account for the failed reconstruction. Since the predicted positron energy relies on two hits in the MWPC and connects a line to where the predicted stopping position appears to be located, there are two ways in which the failure can occur. Either the stopping distribution is wrong, or the projection from the MWPC can't connect to stopping pion. If the stopping position of the pion is predicted to be outside the target, then there will be no target pathlength, which means that there is no predicted positron energy. Events that fail to produce a predicted positron energy are plotted in Fig 5.23.

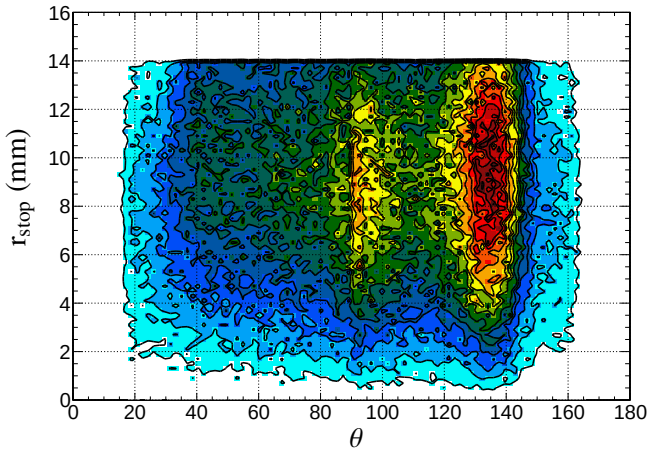

Figure 5.23: *Radial stopping distribution and θ trajectory for positron trajectories that are not properly reconstructed.*

For some of these events, the stopping radius could be greater then 15 mm, which is not possible since the radius of the target itself is 15 mm. In the analysis, a cut on the radial stopping distance must be applied in order to make sure that if a muon is present in the target, it will decay in the target after it traverses a short distance. Further, cuts on radial stopping distance should introduce no bias in either the signal or background because the pion hasn't decayed yet. There are two noticeable features in terms of θ, polar angle of the track. The first is the high θ, which is indicative of the scattering of the positron at some time during its travel from the target to the calorimeter. The second is the vertical band around 90 degrees. This is mostly due to failure of reconstruction of the MWPC around 90 degrees most likely due to the splitting of the inner chamber cathodes. The failure of predicted positron energy reconstruction for the the remainder of the events in which the radial stopping distance is valid is most likely due to positron scattering. Sometimes between the positron leaving the target and hitting the MWPC it is most likely scattered away, altering the "perfect" trajectory of stopping position to inner chamber and outer chamber. When all of the cuts are in place that require a legitimate hits in the MWPC and coincidence between other geometric elements of the apparatus, the number of failed events reconstructed is negligible.

5.6.2 Invariant Mass

The PEN detector indirectly measures the neutrino energy in pion or muon decays through momentum conservation. Since the pion decays at rest, the sum of the momenta of the outgoing particles follows

$\vec{p}_e + \vec{p}_\gamma + \vec{p}_\nu = 0$. The energy of the gamma and the positron are recorded and measured in the CsI. By reconstructing the momentum vectorially of the gamma and the positron, the magnitude of the vector sum of these two momenta is equal to the magnitude of the momentum vector of the neutrino, and thus the neutrino energy. Once the neutrino energy is determined, the full invariant mass may be reconstructed from $E_{obs} + p_\nu c = m_\pi c^2$. A more detailed discussion on the invariant mass with regards to-counting radiative decays is provided later on. It should be noted that when the muon decays, it produces two neutrinos. The invariant mass for these events represents deducing the the magnitude of the sum of the two neutrino momenta which is added to the energy of the photon and positron and summed such that the sum is less than the muon rest mass.

5.6.3 Variables: `vertex_quality`, `dz0`, `z0`, `totaldedxpv`, and `dEdxtotal`

In order for the analysis to proceed, the pion must have stopped in the target. The trajectory of the positron is deduced by the MWPCs. The variable *z0*, which is the z position of the positrons closest approach to the beam axis is determined by the formula $2z_1$-z_2 which is derived from geometry. In the 2009 data set, the presence of the collimator can be seen at $z = -37$ mm in Fig 5.24. The degrader presence in 2010 is seen around $z = -50$ mm as will be seen later on. Vertex quality is a measure of the distance of the closest approach from where the pion stops and that deduced positron trajectory. There are actually three methods of construction of vertex quality. They represent roughly the same variable, but are calculated in different ways. The two vertex quality observables used in the analysis are `vertex_quality2` and `vertex_quality3`. The value `dz0` is similar to vertex quality but only looks at the difference in z position from the deduced stopping position to that extrapolated from the MWPC. These observables are shown against the reconstructed invariant mass in Fig 5.24 to demonstrate what kind of background events are reconstructed at different positions and where they would end up in the analysis which relies on separating different decay channels by energy.

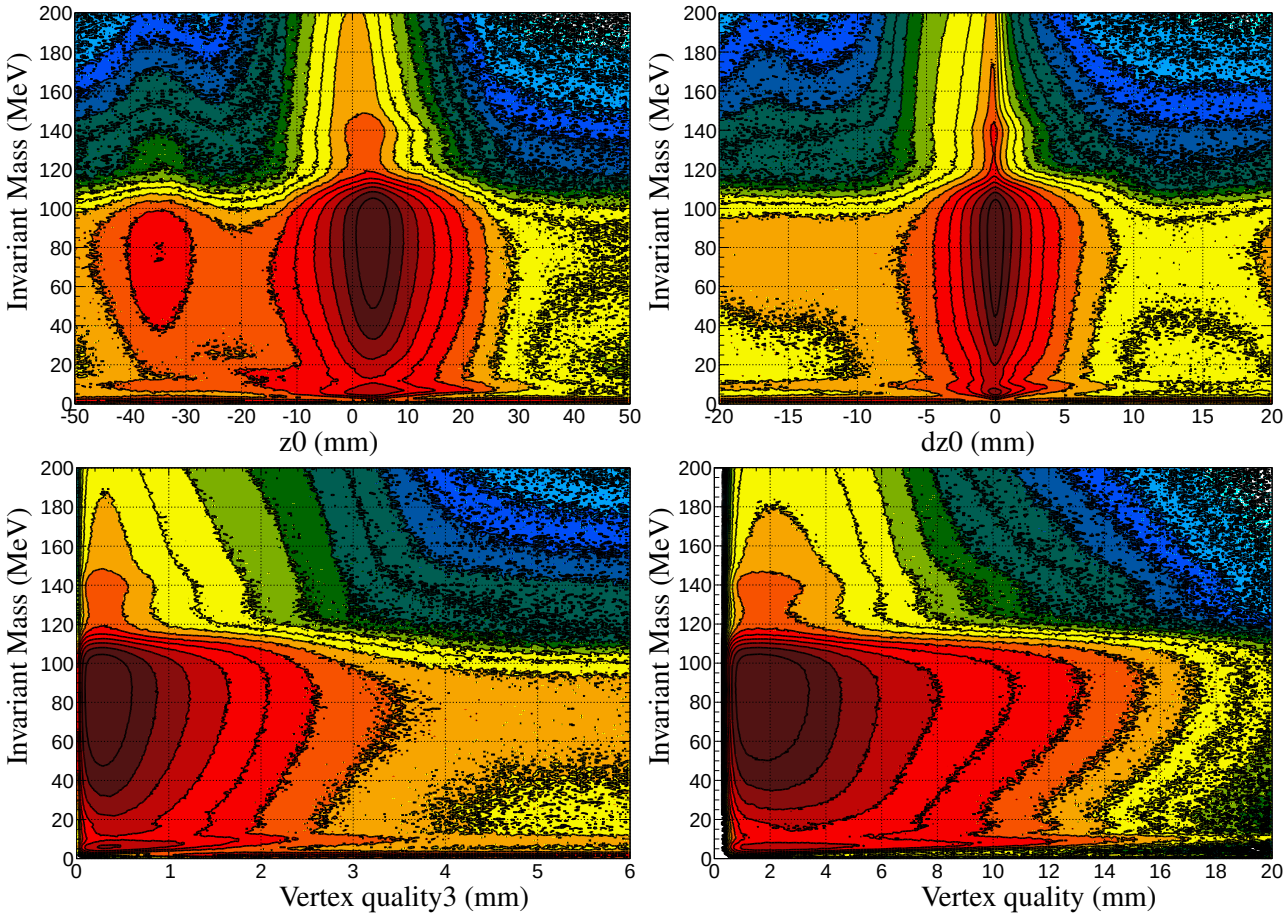

Figure 5.24: *Illustration of observables from tracking. Upper Left: z0 . Upper right. dz0. Lower Left: vertex quality 3, Lower Right: vertex quality.*

Fig 5.24 shows that events with `z0` and `dz0` around zero are where the main channels lie and that lower vertex quality is also desired. It is also highly desirable to eliminate bad events, events whose trajectories lie outside the acceptable region, without the use of the MWPCs. This is accomplished using the hodoscope. The energy in the hodoscope has already been discussed but another variable, dE/dx in the hodoscope may be constructed without the aid of the MWPC. First, we can use the MWPC to observe the up and down time difference as a function of z for legitimate events that cross the hodoscope. Once this characterization is achieved, the time difference between the up and down TDCs on a given hodoscope provides information on the z crossing as shown in Fig 5.25. Since the stopping position of the pion is known, then the path-length through the hodoscope can be determined and this information with the energy deposited can in turn determine the dE/dx. The `totaldedxpv` is determined then by adding the dE/dx of each hodoscope.

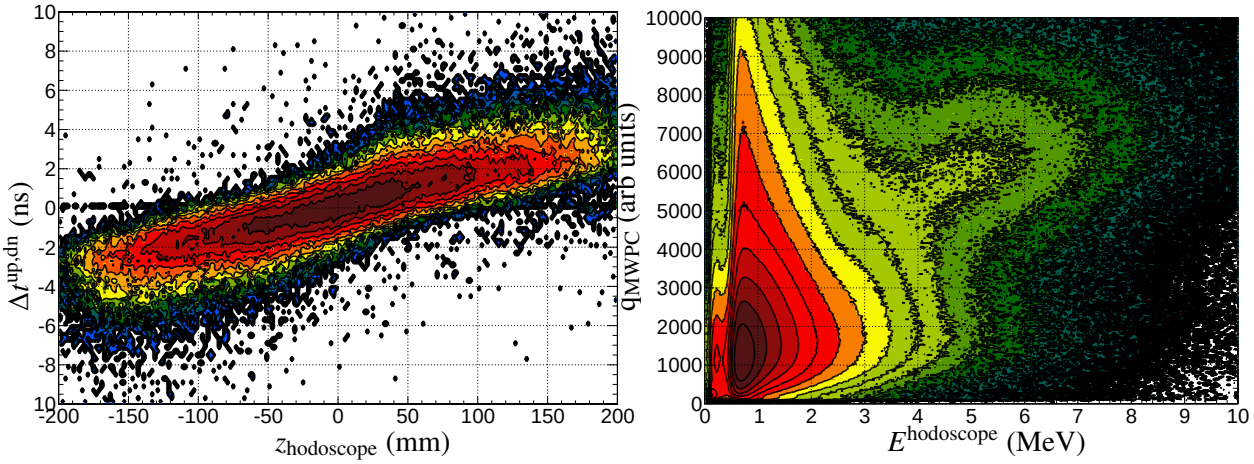

Figure 5.25: *Left: Time difference between upstream and downstream of the hodoscope as a function of the z at hodoscope. Right: Charge induced on the cathode strips as a function of energy in the hodoscope.*

Since the energy deposited in the MWPC gas depends on the type of particle, the knowledge of the dE/dx of the hodoscope, and the dE/dx in the gas, from the charge induced and trajectory, a dE/dx total which is a weighted average of the two detectors, can be constructed. The use of both the chamber and the hodoscope to identify the particle traversing gas is very useful, as will be seen. The different dE/dx values determined from both detectors are plotted against each other in Fig 5.26

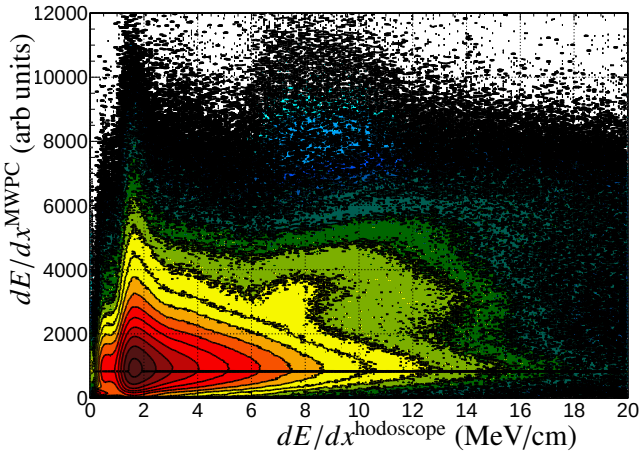

Figure 5.26: *dE/dx in the chamber versus dE/dx in the hodoscope. The lack of correlation in the low energy (positron) regime suggest that combining the two observables would produce a more discriminatory observable.*

5.6.4 Variables: `totalwave`, `restwave`, ΔE_{2p}, `target dE/dx`, χ_{2peak}, and $\Delta\chi^2$

Somewhere in the analysis it is desirable to find ways to discriminate between the two main channels that do not depend on energy in the CsI or decay time. The best option is to use the target information. Since

there is a three particle signal in the target for the Michel decay chain and there are only two particles in the target in the main signal decay chain, target energy may obviously be used. However, given that the PEN experiment utilizes detectors both upstream and downstream from the target to predict times and energies, the additional information may be used to distinguish the two decay chains more effectively. One observable that is formed from the predicted values is `restwave`. `Restwave` is simply the predicted target energy of the pion and positron being subtracted from the total target energy observed as determined by the target waveform. This is an important observable because it shows a good separation between the main background, positrons from Michel decays, and those from pion decays. Since both the pion and positron have predicted energies that are well correlated with their measured energy, when subtracting these predicted energies from the target waveform, one would expect only the muon energy in the target to remain. So for Michel decay, the `restwave` will center at the kinetic energy of the muon (4 MeV, or 3 electron equivalent) and for a positron originating from pion decay, one would expect the `restwave` to center at 0. In addition, an observable called ΔE_{2p}, is a modified version of `restwave`. Instead of just subtracting the predicted energies, the predicted target waveforms are subtracted from from the target waveform. Because the times and energies are both predicted, and because the shape of the response function of the target waveform is known, a predicted waveform can be constructed and compared to the actual target waveform as seen in Fig 5.27.

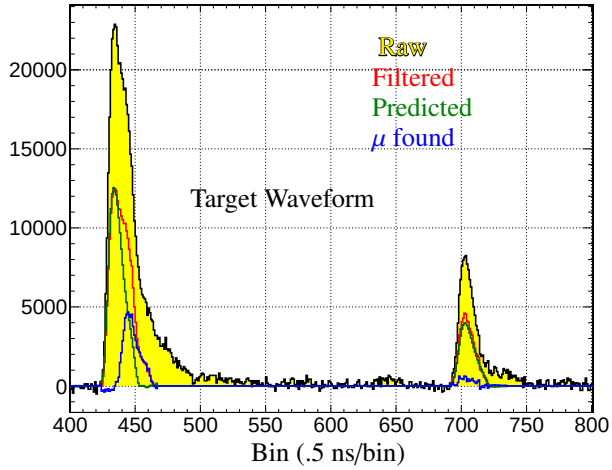

Figure 5.27: *Illustration of construction and comparison of predicted target waveforms with the observed target waveforms.*

Finding the difference between the predicted and observed waveforms provides additional information in the target. Similarly, an effective dE/dx can be constructed in the target. When taking the total target energy

and subtracting the predicted pion energy, the remaining energy will be that of the positron and possible muon. When dividing this remaining energy by the pathlength traveled by the positron in the target, an effective dE/dx for the positron is constructed. If a muon were present, then the effective dE/dx would be higher than that of a simple positron.

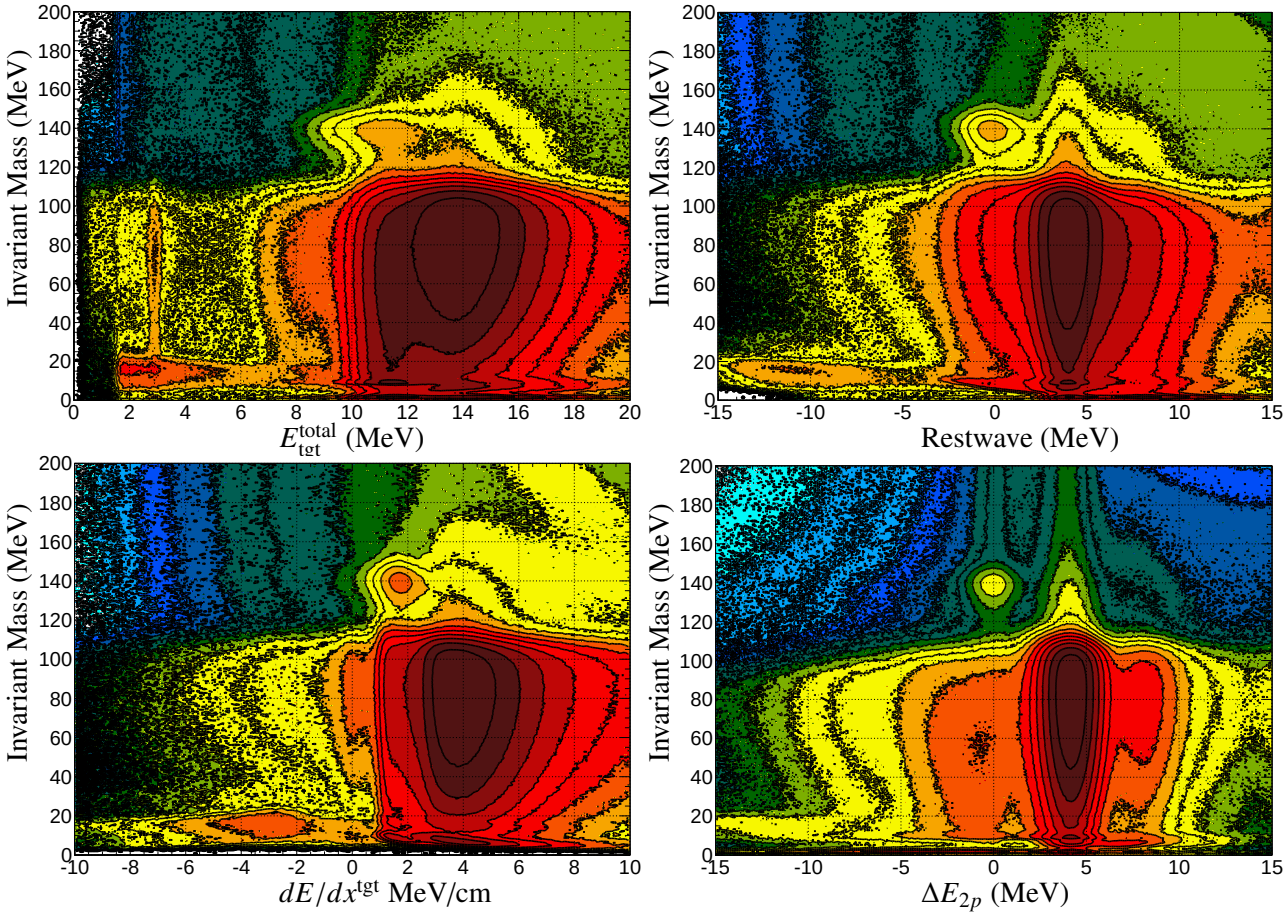

Figure 5.28: *Overview of waveform discriminatory variables plotted against the invariant mass. Upper Left: Total target energy. Upper Right: Restwave. Lower Left: Target effective dEdx. Lower Right: ΔE_{2p}.*

Fig 5.28 shows that the use of the predicted energies and times to construct predicted detectors waveforms is a very useful tool to discriminate between the two event types. `Restwave` and ΔE_{2p} cuts around zero favor the $\pi \rightarrow e\nu$ decay chain whereas energy values around four favor the Michel positron decay. But this can be made even better. Using the predicted and observed waveforms, a χ^2 fit can be performed by comparing the predicted and observed waveforms. This variable is called $\chi^2_{2\text{peak}}$. The most powerful tools used in the discrimination between Michel positrons and positrons originating from pion decays are χ^2_{2peak} and $\Delta\chi^2$. Because of the predicted and observed times of the pion and positron for the target wave form, a chi

square test can be constructed between the expected target waveform and the observed target waveform for a 2-peak fit as stated. When subtracting the predicted from the observed waveform, the resultant spectrum is either close to zero (in the case of $\pi \rightarrow e\nu(\gamma)$ decay) or a prominent muon peak in the case of the Michel chain. Since the resultant muon from the Michel chain is fixed by kinematics, then a chi squared comparison can be done with the net spectrum and with a muon waveform that is predicted. Since the muon can appear anywhere between the pion and positron signal in the target, the predicted muon peak search is performed in every bin between those two times and the minimum chi square comparison is used to determine where the muon is mostly likely to be present. The chi square fit of the 2-peak and the 3-peak is then subtracted from each other and normalized. This is the much used $\Delta\chi^2$ that is normalized so that the $\pi \rightarrow e\nu$ decay saturates at 1 and the Michel decay is most prominent at -1 as seen in Fig 5.29.

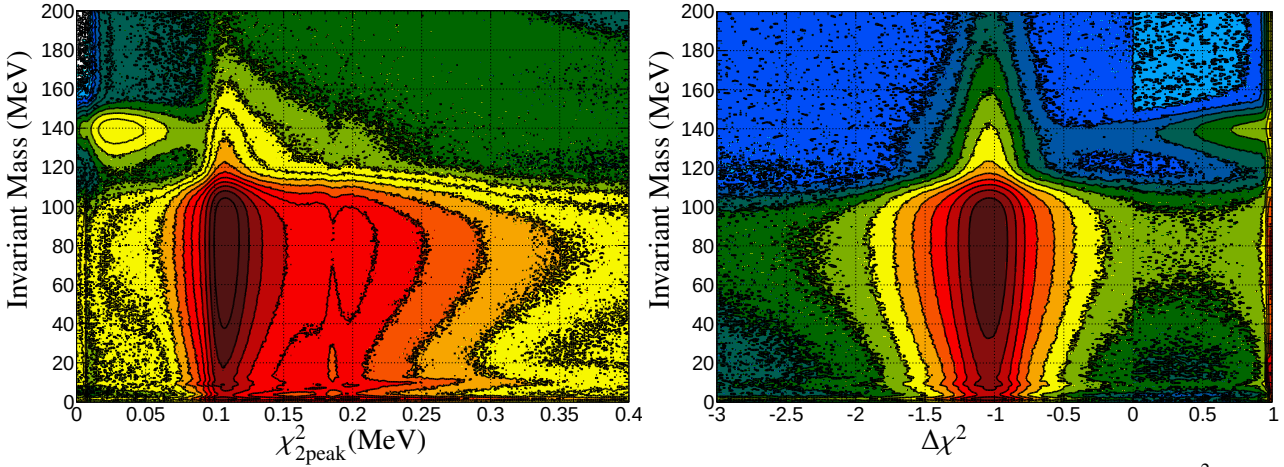

Figure 5.29: *Highly discriminatory waveform observables to select Michel decays or $\pi \rightarrow e\nu$ decays. Left: χ^2 of two peak fit in the target waveform. Right: $\Delta\chi^2$.*

5.6.5 The `decaytime` variable

One of the most important, if not the most important observable is the decay time. As stated before, the two different decay channels have different distributions based on the nature and lifetimes of the particles in the decay chain. The $\pi \rightarrow e\nu$ as a decay distribution of $\sim e^{-t/\tau_\pi}$. This means that the majority of the events in this decay are at early decay times whereas the Michel chain is a convolution of the muon and pion decay distributions producing more events in the later decay times and fewer in the earlier decay times. Experimentally, the decay time is the time between the pion stopping in the target and the decay which produces the positron. There are a number of methods by which the `decaytime` can be determined. The

detector elements that record time are the waveform digitizer in the degrader and target and the TDCs on the plastic hodoscope and CsI calorimeter. Somewhere in these detectors, the decay time must be determined. The ideal option would be to use the target waveform digitizer because this is the detector that detects particles in the target specifically the incoming pion, which stops in the target, and the emerging positron which is born then subsequently leaves the target. However, that becomes a problem when a decay occurs quickly. When the pion decays quickly into a muon/positron and/or a muon decays quickly in to a positron, even with advanced waveform filtering techniques it still may be difficult to obtain a proper decay time spectrum because signals overlap on each other because of these fast decay times. However, there is little to no ambiguity in the degrader waveform and TDCs of the plastic hodoscope. As stated before, predicted times for the pion and positron are constructed in order to aid in the analysis. Therefore, using predicted positron pion times enables us to construct a `decaytime` spectrum even for fast decays. One can check how well this `decaytime` is constructed by obtaining the decay time from the target waveform for well separated Michel decays and observing differences between this decay time and the one using predicted times. The difference between the decay times using predicted and observed times for well separated target signals is an observable called `decaytimecheck` and is shown in Fig 5.30.

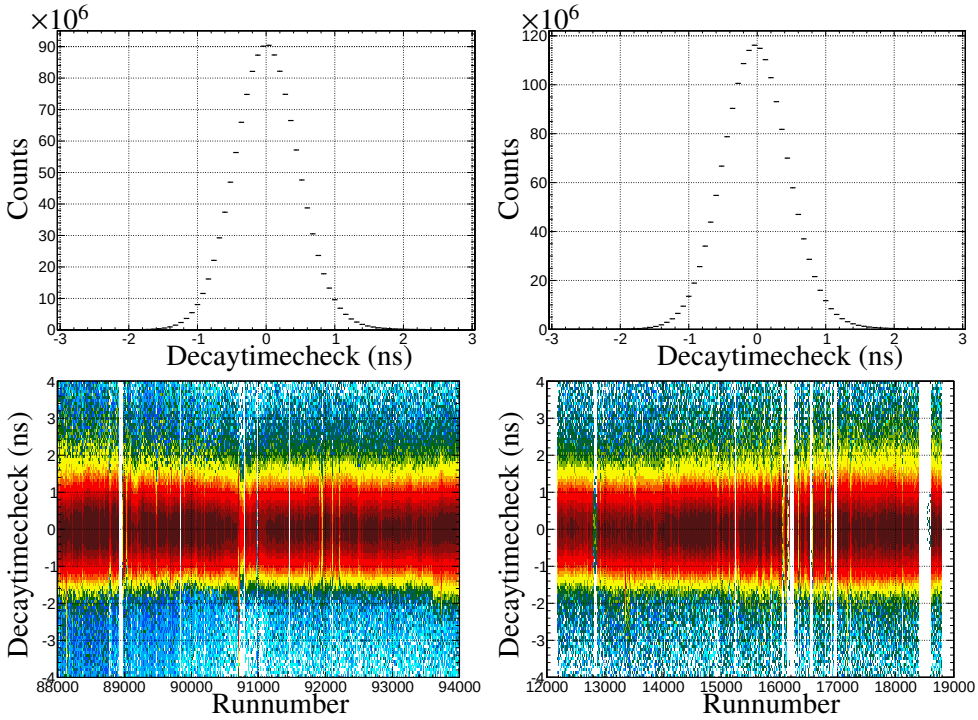

Figure 5.30: *Differences in the decay times as determined in well separated waveform Michel decays and that from the predicted times. Upper Left: 2009 difference. Upper Right: 2010 difference. Lower Left: Difference as a function of runnumber for 2009. Lower Right: Difference as a function of runnumber for 2010.*

Fig 5.30 shows that for well separated decays in time, the predicted and observed decay time of the positron agrees with each other indicating that the predicted decay time is sufficient in lieu of the observed decay time in the target preventing any systematic effect that would be introduced by searching for a pileup of target waveform signals due to fast decays.

5.6.6 The variable `ppileup`

As already pointed out, the majority of pion decays will be into muons. A small complication arises due to the fact that the muon has a lifetime of 2.2 μs. It is therefore conceivable that a muon could survive in the target long enough to witness a new incoming pion enter or approach the target. Since the data acquisition gate spans the 50 ns before the positron hits the hodoscope, we can study events in which the pion stops in the target (time 0) up to 50 ns after the positron hits the hodoscope, where the difference in time between the pion stopping and the positron hitting the hodoscope is perceived as negative time. This is a manifestation of pileup. For every event, hits in the beam TDCs are scrutinized to determine whether a pion was present sometime in the past. The time difference between the beam hit and the pion decay is put in terms of muon lifetimes, and this is `ppileup` (probability of pileup). The `ppileup` variable is shown in Fig 5.31 as a function of invariant mass and decay time.

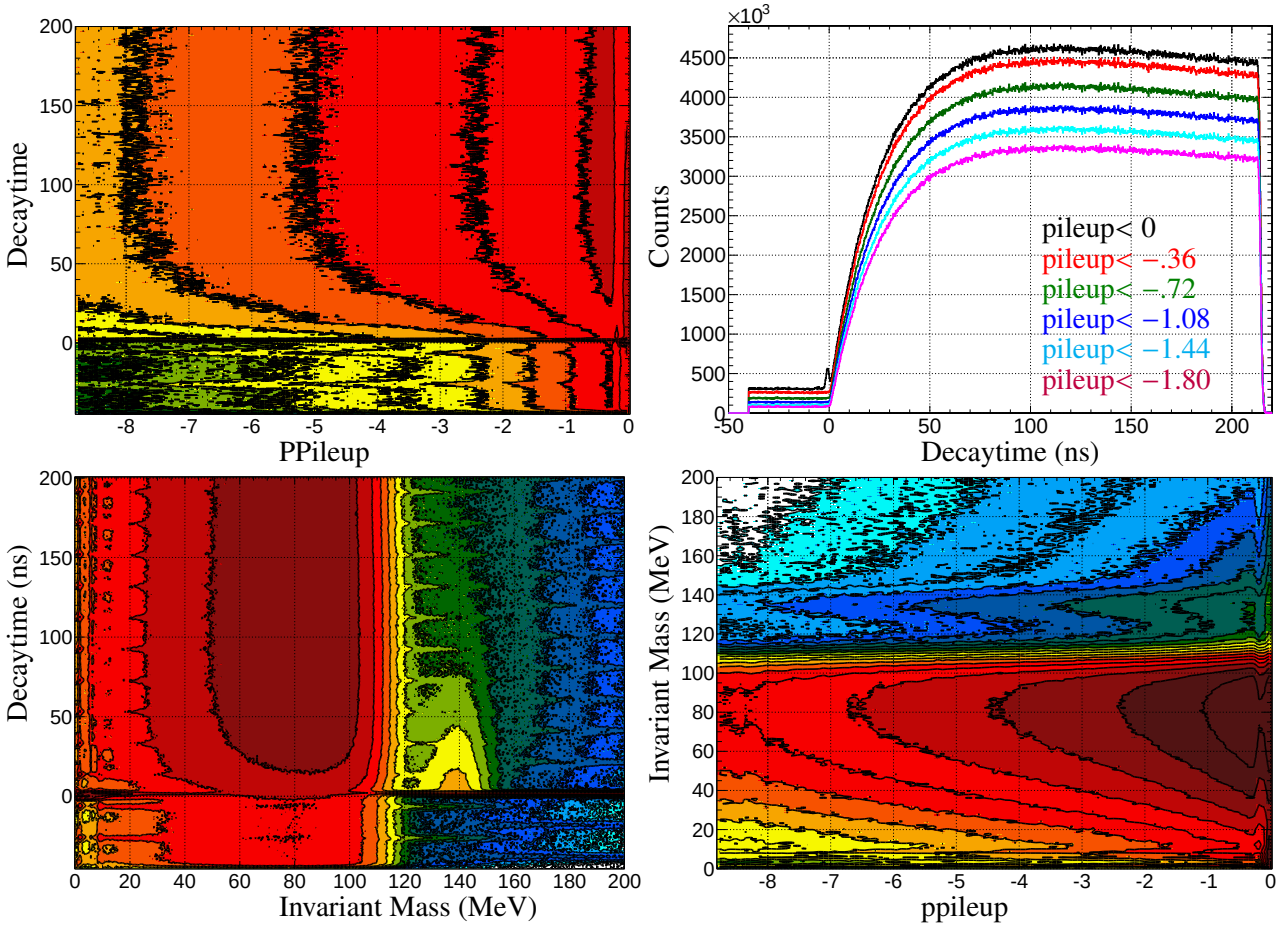

Figure 5.31: *Illustration of pileup. Upper Left: Decay time vs pileup. Upper Right: Decay time spectrum for Michel selection for different pileup values. Lower Left: Decay time vs invariant mass. Lower Right: Invariant mass vs pileup.*

One notes that high invariant mass values are not associated with many signals with negative `decaytime`. Aside from the periodic scattered beam, whose yield is comparable to those with positive `decaytime`, there are no events prior to zero time. Since a positron from pion decay will have high CsI energy, this event will be recorded immediately, and since the lifetime of the pion is fairly short compared to that of the muon, there should be little (if any) pileup for pion decays events. This is important in that it may be necessary to make a pileup cut for the Michel events but not for the pion decays.

5.6.7 Number of beam, `nbeam` and charged `ncharged` particles

One of the last, yet seemingly mundane observables that has to be constructed is the number of particles observed in a particular event. This can entail the number of particles in the beam but also the number of

particles observed in the decay or the number of particles that appear to be present due to the hits in the MWPC. In the case of the number of beam particles, a search for local maxima in the degrader waveform is performed. Once one is found, a search for signal in the B0 is performed around the same time. The total energy in the B0 and degrader identify the particle in question. This is done for all 1000 bins in the degrader/B0 digitized signal. Each time a local maximum passes the energy requirements for a beam particle and energy requirements are made, the number of beam particles is incremented and each identified based on the energy deposition and time of flight. The number of decay particles is determined using downstream detectors.

In the PEN experiment, there are two types of particles that will initiate an electromagnetic shower a shower in the CsI calorimenter. The first consists of a charged particle such as scattered beam positrons and pions, protons, deuterons, and decay positrons. The other is a photon. The analysis of the PEN data set determines the number of tracks and the number of these which are charged. The number of charged tracks is determined by observing how many detector planes have signals between the CsI calorimeter and the target. A search for a local maximum with a minimum signal is performed in each of the six cathode surfaces, knowing the slope of the helix and the cathode number. This is compared to the ϕ of the CsI clump. If the difference between them is less than fifteen, this is considered one coincident plane. If between fifteen and thirty, it is considered half a coincident plane. The ϕ value of the clump and anodes are also compared. If the difference in the ϕ angle is less 10 or 15 for chambers 1 and 2 respectively, these are also coincident planes. Finally if the ϕ angle is less than twenty degrees between the hodoscope and the calorimeter provided the time difference between the hodoscope and CsI is less than fifteen nanoseconds, this is another coincidence plane. If the number of coincidence planes is greater than or equal to four, this is considered a charged track provided the energy deposition in the hodoscope and MWPC are sufficient. Clumps that do not pass these coincidences are considered non-charged tracks, typically being photons.

6 Simulation

A mind is a simulation that
simulates itself

Erol Ozan

The GEANT4 [5] Monte Carlo simulation toolkit is an integral part of the PEN analysis. In order to determine the branching ratio, two quantities are required that may be obtained only from the simulation. The first is the $\pi \rightarrow e\nu(\gamma)$ low energy tail fraction in the CsI calorimeter. This low energy tail is due to the energy leakage in the CsI calorimeter and the correction needed can not be obtained from the measured data because there is too much background to eliminate in order to reach the desired precision, and even if a perfect background subtraction were to occur, there would be too few events to obtain the desired statistical precision. The low energy tail is seen in Fig 6.1.

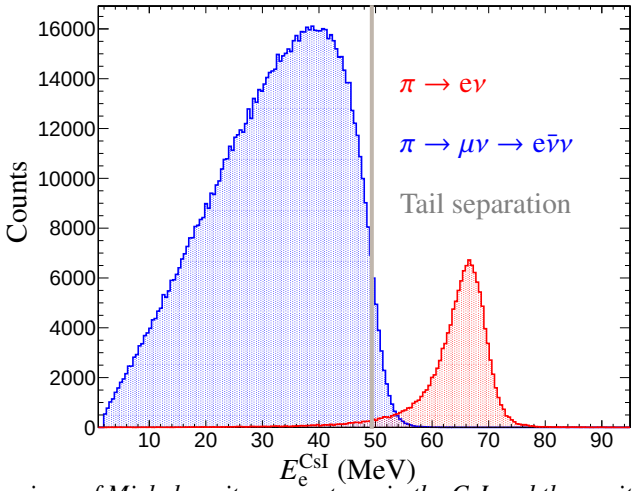

Figure 6.1: *Comparison of Michel positron spectrum in the CsI and the positrons from pion decay.*

The second factor are the acceptances. The acceptances represent the probability of detecting an event given that the event in question had happened. One might ask, how can we know whether or not an event occurred if it was not detected. The answer is we can not. Obtaining the acceptances is not possible in the experiment itself. The only way to get the experimental acceptances is if the experimenter were to have the ability to command the pions to decay in the target on demand and have daughter particles chosen by the experiment. Since the experimenter most likely does not have divine power, this is impossible. However, if the detector is properly simulated, that is to say the geometry, the physics, the intricate dependencies on

how each detector element relies on other detector elements, as well as triggering mechanisms, then the experimenter can play the role of a divine programmer, as it were. With the simulation, it then becomes a trivial matter for an individual to command numerous pions to stop in the target, decay through a particular channel and count the number of events that pass through the cuts. In addition, if the physics of the CsI response is properly simulated, then the response, the tail fraction, may be obtained. Further, practically every critical observable in the experiment is simulated in order to ensure understanding at the relevant level of detail. This is why the simulation is an integral part of the analysis.

Using the simulation might seem trivial. It is less trivial when the intricacies and shortcomings of GEANT4 are explained. GEANT4 is widely used by many physics collaborations in understanding detectors, determining energy depositions, timings, and particle positions. In the real experiment, however, these quantities are obtained by analyzing signals. GEANT does not take into account the full detector response of any of the detector elements. In the real experiment, energy is digitized i.e., discretized, the detector elements have noise and smearing from photoelectron statistics. For example, consider the energy deposited in a plastic hodoscope or a CsI crystal in Fig 6.2

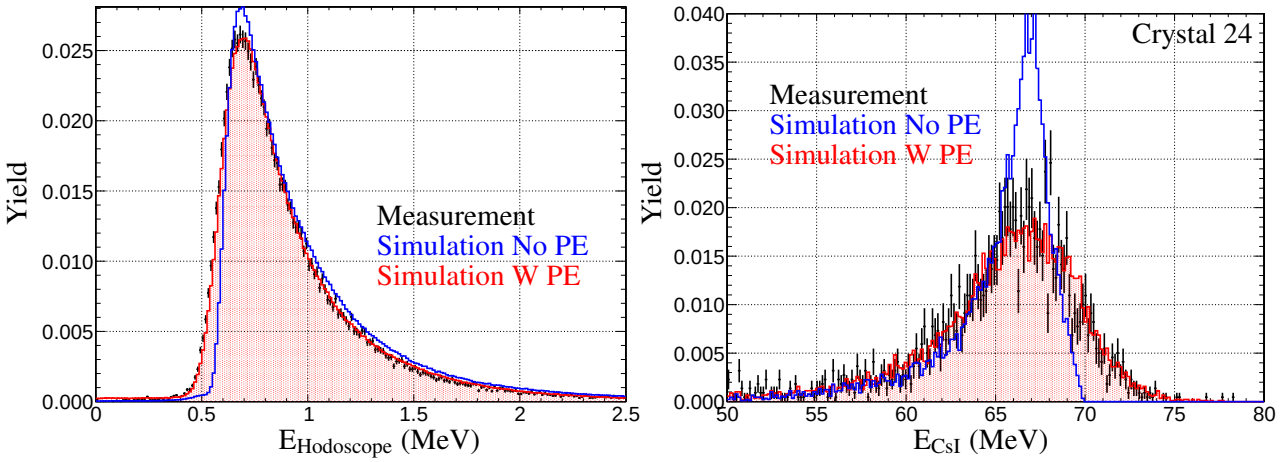

Figure 6.2: *Left: Hodoscope energy comparison with measurement, simulation intrinsic response (blue), simulation full response accounting for photoelectron statistics, non-uniformities, energy spreading in the target, and digitization (red). Right: Similar plot for energy in CsI crystal number 24 .*

On the right of Fig 6.2, the simulated energy in blue peaks around the same position as the measurement, but the spread is not consistent. Also note that the energy in blue curve cuts off at the physical energy of the positron from a $\pi \rightarrow e\nu$ decay. Kinematics restricts the positron energy to less than 70 MeV (barring any decays in flight). But of course there is no sharp cutoff in the measurement for two main reasons. The first is of course that the detector is no perfectly uniform, and the second is because the measured data also contains

radiative decays which can not be ignored as stated previously. In short, the blue curve does not account for the full detector response. Once the full detector response has been implemented, i.e., photoelectron statistics, noise, digitization of energy by ADC electronics, light attenuation lengths of detectors, etc., are taken into account, a more realistic response is achieved, as is seen in the red. It is easy to see, for example, that in the left plot there is a sharp edge around 0.5 MeV for the energy deposited in the plastic hodoscope, but with the full detector response, this threshold becomes more gradual. It should be clear that simulating a fully realistic detector is far more difficult then simple geometry placement and running many millions of simulated events and that the full detector response of the Monte Carlo is needed for the analysis to reach the level of desired precision.

Throughout this chapter the reader is guided on how the simulation is built in order to reproduce the full detector response. This chapter describes the process by which simulated events are obtained. The majority of this chapter will focus on the physics of the simulation, that is to show how the digitizer, mTPC, MWPC, hodoscope, and CsI are all constructed and calibrated to reproduce the realistic detector response. Finally this chapter will validate the physics behind the simulation. It should be noted that many of the calibrations in the simulation were performed using the dominating Michel background in the data. The reason for this is two-fold. The abundance of these events permits fine tuning of the simulation to be as accurate and precise as necessary. The second reason is that if the physics is fully represented with Michel background, then there is little to no chance that any accidental bias will be introduced to favor the more rare pion decays. A simple requirement of 3 peaks in the target with energy in the CsI with $20 - 50$ MeV in the CsI is used for most of the comparisons between simulation and measurement. This selection is also used for the fine tuning of the simulation so that it best agrees with the measured data. By using the Michel selection, the measured events are statistically large and are relatively clean which facilitates the comparison between between simulation (pure events) and approximately pure Michel events from the data set. Moreover, with the highly realistic simulation it is also possible to study the more rare decays such as $\pi^+ \rightarrow e^- e^+ e^+ \nu$, or even forbidden decays, those that are hypothesized in physics beyond Standard Model, including decays with massive neutrinos and even neutrinoless decays.

6.1 Structure of GEANT4 Simulation

The fundamental interactions of particles and matter is simulated using GEANT version 4.10.1p03. This version uses C++ and is therefore compatible with the ROOT and MIDAS software. The PEN Monte Carlo simulation occurs in three steps. The first is the running of the GEANT4 software. The second step adds the simulation of the full detector response using software developed in the PEN group, called the "frontend". This code takes GEANT4 values as its input and constructs the full detector response. Finally, after the frontend, the resulting files are put through the PEN MIDAS analyzer which creates ntuples of useful observables from the MIDAS files in the experiment and outputs a ROOT file. The analyzer is the exact same software that is used to take PEN experimental MIDAS data files from the data and creates ntuples for the measured data. In short, the simulation and data are analyzed identically.

The GEANT4 program, the first stage of the simulation contains the detector geometry for the PEN experiment for all different configurations. This includes differences in setups for the various apparatuses. For example, the 4 wedged degrader in 2008 was changed to a smaller degrader and mTPC for 2009 and 2010. Different positions of the target and other detector elements are also accounted for (the degrader and mTPC moved between the run periods of 2009 and 2010). In addition, the GEANT4 program contains the information related to beam development and tracking, energy depositions, timings, and decay tracking. A pion is created before the first detector, the beam counter (BC or B0 for beam origin). The momentum in the z-direction, is chosen so as to match the recorded beam momentum for the specific run period. The x and y components of the momentum are constructed so as to match the beam profile and stopping distributions with that of the measured data. When the pion crosses the BC, the degrader(s), the mTPC wires (there are 4 of them), and the target, the time, position, momentum direction, and kinetic energy of the particle are all recorded. Further, in all detectors any energy deposited in that particular detector is also recorded and added to the total energy deposited. For example, a pion that traverses the degrader will deposit energy in each step. In every step, the energy is added to the total energy value. The time at which the pion stops is recorded as well as the time that the pion decays. When the muon is present in the target (if applicable), the amount of energy that the muon deposits is recorded, along with the time and position where the muon decays. The time and position of the positron birth and when it leaves the target are recorded as well as the energy that the positron deposits. As the positron leaves outward it will go through the two multi-wire proportional chambers. When it does so, the position of the positron in the chambers is recorded as well

as the energy deposited. The amount of induced charge on the cathode strips is calculated and recorded as well. The time, position, and energy deposited are recorded in the hodoscope. Finally, the positron initiates an electromagnetic shower in the CsI calorimeter. Any energy deposited in a given crystal (recall there are 240 of them) is recorded for each crystal as well as the time in which energy is recorded in said crystal. All of these values are saved into a MIDAS file in a bank that is called GSIM. The GSIM bank contains the observables that are often referred to by the PEN group as "god's" knowledge. That is, they represent the time, energy and positions of anything interesting happening if a "perfect" detector were used. Of course, a perfect detector does not exist, so these godly values are used as inputs to the frontend to produce a more realistic response from the detector elements. The frontend is the most involved step in producing ultra-realistic responses in the Monte Carlo simulation.

6.2 Frontend

In the frontend software code, the full detector response is simulated using the aforementioned "god's" knowledge. Some experimental groups and researchers may call this "smearing" of god's knowledge. That is the known energy deposited is smeared or convolved in some way in order to be more faithful to the actual physical processes that occur during detection. The PEN simulation goes further than simple smearing in order to create ultra-realistic synthetic events. In order to recreate the measurement in every aspect, the first thing that must be considered is the structure of the file that will ultimately be passed on to analysis. Since the measured data are stored as MIDAS files and it is desired to treat the simulation and measurement in the same manner, the output of the frontend is saved as MIDAS files with banks that are identical to that of measured data with the exception that the simulated data has the extra GSIM bank, privied to "god's" knowledge. The banks will first be reviewed and construction of the full detector response will be explained. Before any of the banks are filled, the event is analyzed in a fill trigger bank module. This function determines whether or not the event in question would have been recorded according to the running conditions of the particular year being simulated. In 2008, there was an energy requirement for clusters of crystals. There were 60 combinations of 6 crystals which must have had a minimum amount of cluster energy in order to be a recorded event. For later years, the sum of all 240 crystals energies were considered. There must also have been a crystal hit within 220 ns of the pion stopping or the event would not be counted. Energy requirements for the hodoscope and target are also checked in this function. Provided all requirements are met, the event

would be a viable candidate in the measurement so this event is simulated so that the full detector response is recorded.

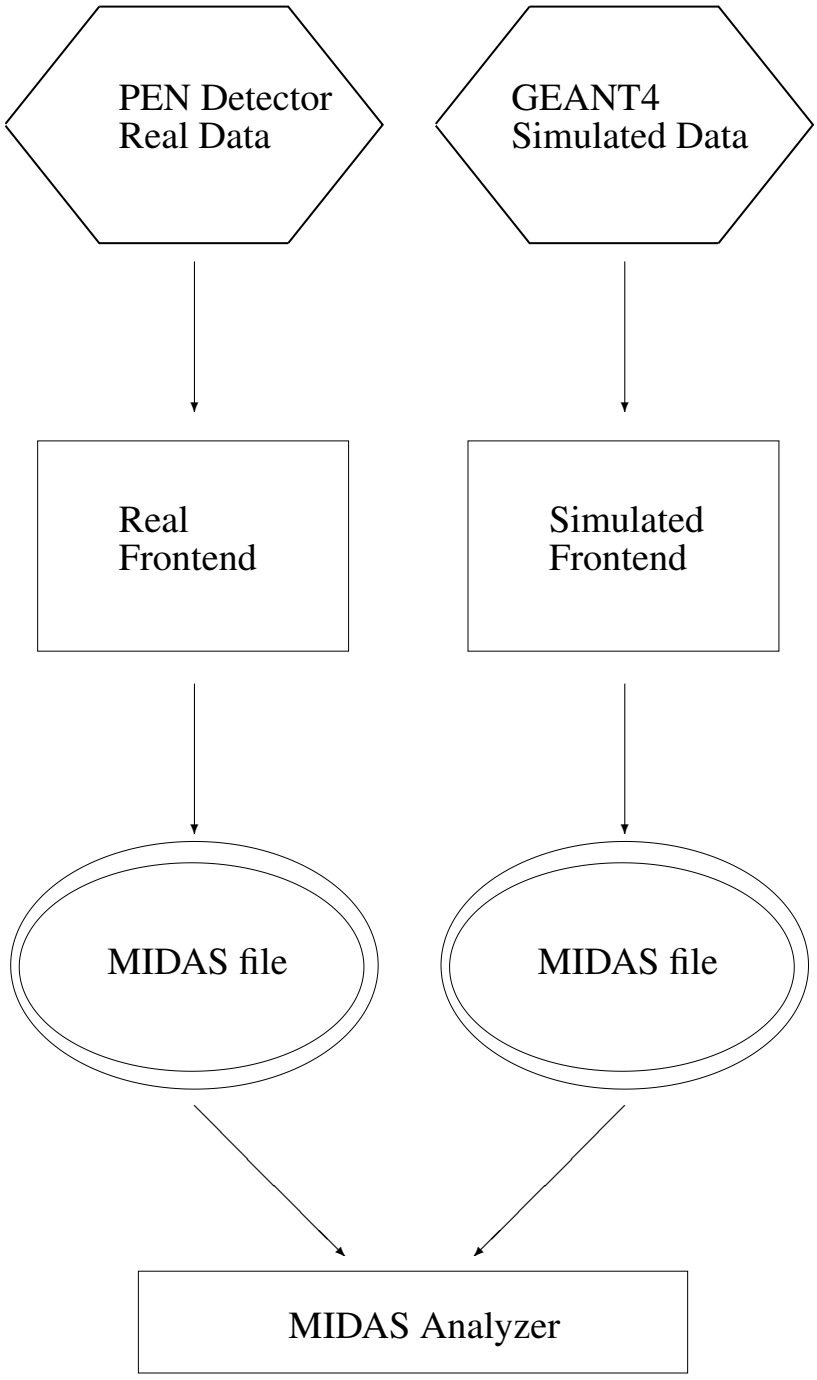

Figure 6.3: *Illustration of the simulation structure compared with that of the real data acquisition. The GEANT4 values consisting of energies, times, and positions are passed on to the PEN frontend simulation software which creates the same kinds of outputs that the experiment would see, i.e., waveforms, ADC, TDC values etc. These values are then stored in MIDAS files with the exact same structure as that of the measured data which are then analyzed identically.*

6.3 Number of Simulation Configurations

One of the important questions that should be asked is how many different simulation configurations are needed to accurately reproduce the experiment. Since certain parameters such as gains and offsets may vary from run to run, the outgoing individual might say as many runs as there are. Since the PEN collaboration has over 15000 runs in the data sample, this might seem too daunting a challenge. In order to accurately compare simulation and measurement, the measured data must have comparable statistics. Each run comprised of roughly 100,000 events, though some runs went as low as a few thousand, which means a very clean sample from the data will have far fewer than 100,000 events. Hence, run periods were grouped together to maximize statistics and minimize the number of simulations needed. The best method is to break the measured data into groups where the geometry changes. In order to obtain the correct acceptances, a different simulation must be created for each set of geometries that occurred. This means if there was a change in target position, or apparatus, then a new simulation must be created for this change. One could also argue that changes in the beam tune or momentum would also require a new simulation. It was decided that changes in momentum or beam tune, with a given geometry would be included in one single simulation where the thrown momentum, gains and offsets would be reconstructed so as to be representative of the multiple changes in the measured data. The changes in 2009 and 2010 are tabulated below along with simulated runs that represent these changes.

Table 6: *Simulations that account for changes in 2008. Note no geometry or beam changes were made during this run period. Thus only one simulation is needed to account for the year.*

Simulation Number	Run Numbers
2008	83580-84812

Table 7: *Configuration changes for 2009.*

Run Number	Change occurred
87979	Beam momentum 71 MeV/c → 72 MeV/c
88030	Beam tune
88833	Beam momentum 72 MeV/c →74 MeV/c
88850	Target center z +=.08 mm
89013	Beam momentum 74 MeV/c →72 MeV/c
89280	Energy requirement in target at trigger time
90700	Target center z -=.01 mm
90733	Beam momentum better tune
91000	Target center x: .2 mm→.7 mm
91122	Beam momentum 72 MeV/c →73 MeV/c
91128	Beam momentum 73 MeV/c →74 MeV/c
91206	Beam momentum 74 MeV/c →73 MeV/c
92080	Target center z -=.06 mm
93101	Target center x →.45 mm
93860	Target center z -=.07 mm

Table 8: *Simulations that account for changes in 2009.*

Simulation Number	Run Number
88000	87747-88849
89000	88850-89999
90000	90000-91000
91001	91001-92079
92000	92080-93100
93000	93101-93859
93900	93860-94000

Table 9: *2010 Configuration Changes.*

Run Number	Change occurred
12701	Beam Tune and momentum 76 MeV/c →75 MeV/c
12996-13016	Beam tune and momentum changed (multiple times)
13566	CsI 229 Died
14375	Beam Tune and momentum 75 MeV/c →76.2 MeV/c
14932-14977	CsI 170 fell below HI threshold
16179-16192	Wire 0 for mtpc shorted
16241	Target center x: 0.15 mm→ −0.13 mm
17594	MWPC cathode strips 192-255 lost a bit in the ADC
18398-18619	mtpc wire 1 broke and shorted

Table 10: *Simulations that account for changes in 2010.*

Simulation Number	Run Number
12000	12182-14977
15330	14978-16178
16241	16179-17593
18700	17594-18884

As an example of what this means in terms of simulations, consider the attempt at constructing a proper simulation for the run numbers 88850-89999. Even though these run periods represent one geometry setup, there is a substantial change in the momentum and pion time of fight as seen in the previous chapter in Fig 5.15 and therefore should be accounted for.

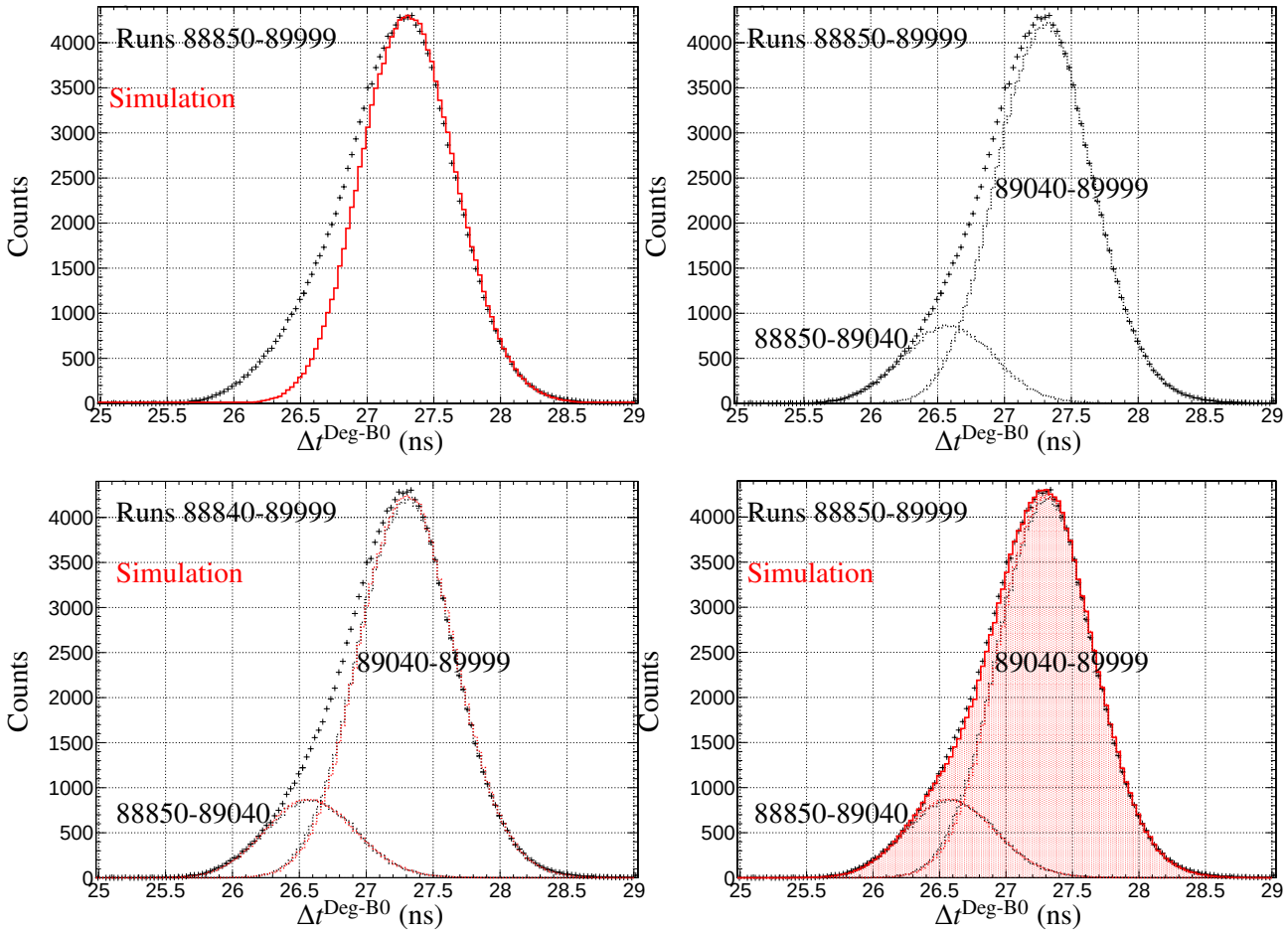

Figure 6.4: *Demonstration of different momentum in one simulation geometry. Top Left: One simulated momentum compared with simulated run period. Top Right: A break down of the time of flight in sub runs for the measurement. Bottom Left: A comparison of two momentum distributions being thrown in simulation for the run period beings simulated. Right: Throwing the two momentum according to how often it appears in the data.*

Therefore twelve different configurations of simulation geometries with multiple changes in the momentum distribution of the pion are incorporated in a particular geometry. If there was only a very small change in the momentum, then an average momentum distribution between the two were used with a slightly broader momentum distribution. Whereas in the 89000 run configuration, two distinct momenta are thrown according to the number events in each of the subsets of the included runs, the simulated configuration 12000 consists of five distinct and well separated momentum distributions, which can be seen in the 2010 data run in Fig 5.15.

6.4 Beam Profile

Before the simulation can get the full detector response, the simulated beam parameters must be the first thing that is determined. This means the pion momentum and the spread must be simulated and be representative of the actual experiment. Considering one 2009 run that is simulated, for example, the run according to documentation has a beam momentum that averages 73 MeV/c. However, this is an estimate and can be improved by analyzing measured data. One can get the proper momentum distribution by observing the time of flights of beam particles as well as the energy deposited in the target by decay positrons that go through the front face or back face of the target. These type of events are chosen because the dE/dx of a positron is well known and thus easily identified. Further, by observing events in which the positron leaves the front face or back face, we are able to deduce as to how far into the target (in z direction) the pion stops. If pion is simulated with too much momentum, the pion will go further into the target than in the experiment. When a decaying positron emerges through the back side of the target, the pathlength will be smaller and thus the energy deposited in the target will also be smaller. It will thus be greater when leaving the front face. If the pion has too low momentum when leaving the front face it will deposit energy which is too small and too much when leaving the back face. The energy deposition in these kinds of events are shown in Fig 6.5

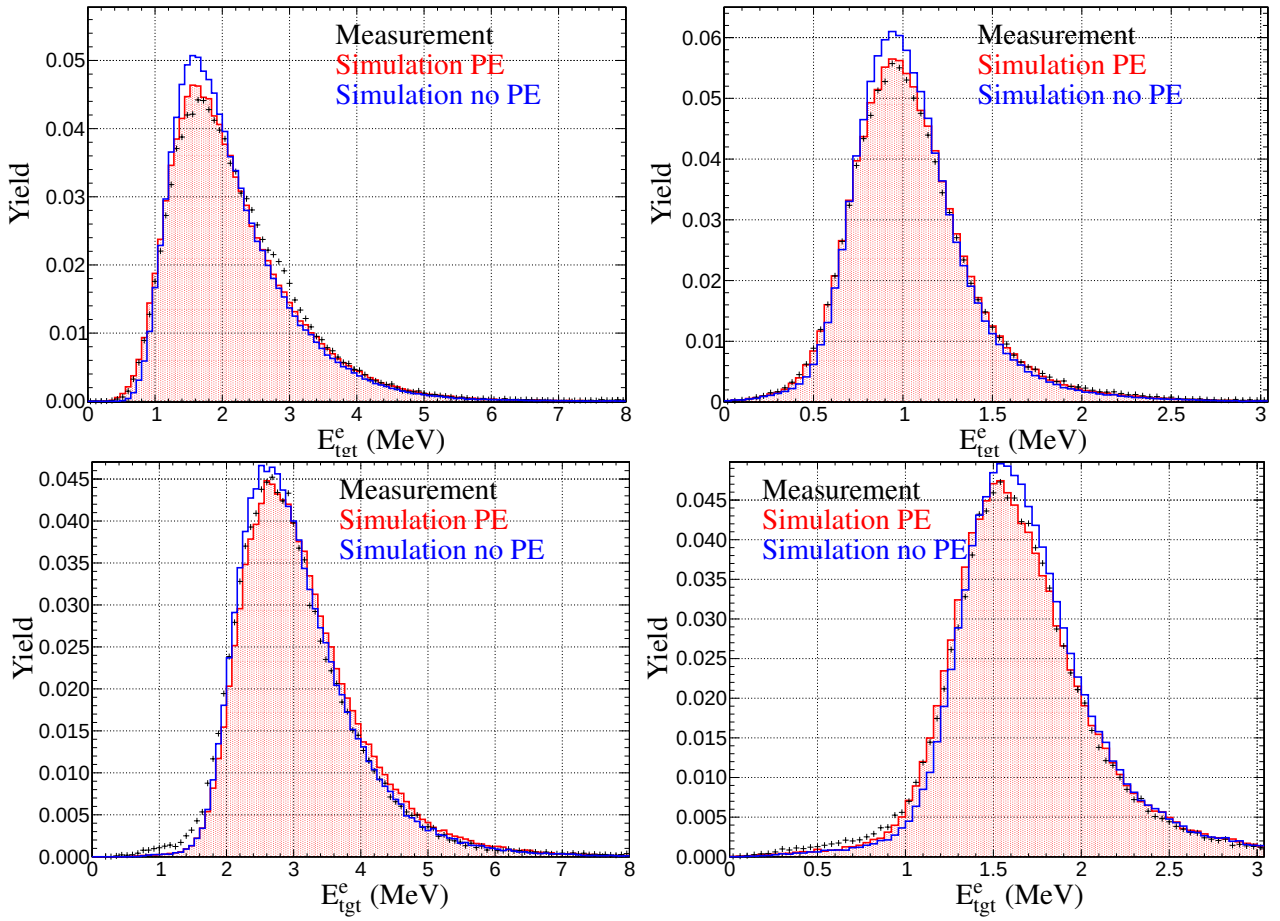

Figure 6.5: *Energy deposited in target by positron when leaving one of the faces. Upper left: Front face. Lower Left: Back face. Energy deposited in the target by positron multiplied by cosθ as it leaves (z component of momentum) Upper right: Front face. Lower Right: Back face.*

The momentum may also be cross-checked by observing the time of flight for the beam particles that are observed in measurement, that is pions, muons and positrons. Time of flight construction in the simulation is discussed in the next section as it uses analysis of the digitized waveforms from the beam detectors in order to deduce it. Here we just show the results of the time of flight of beam pions, positrons, and muons from the simulation and measurement in Fig 6.6.

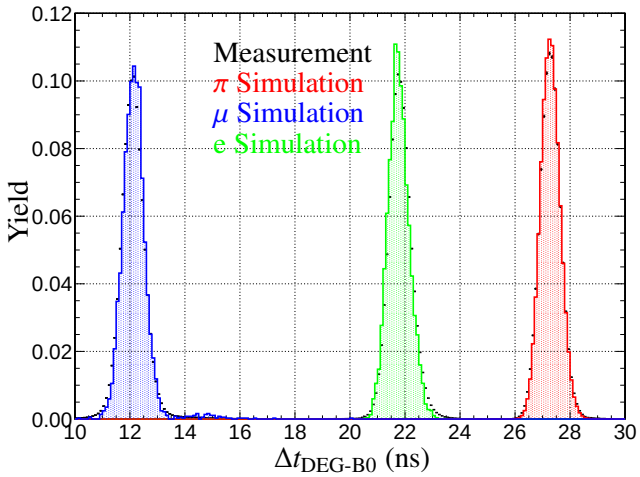

Figure 6.6: *Time of flight of beam particles from B0 to DEG. Measurement in black and simulation in color.*

In addition to the momentum, the beam profile, as deduced by the mini-time projection chamber, must also be simulated properly. A more detailed discussion of how mTPC is simulated will be given shortly. Here we just present the beam profiles of the 2009 beam which compared to the profile presented earlier in this work in Fig 5.10.

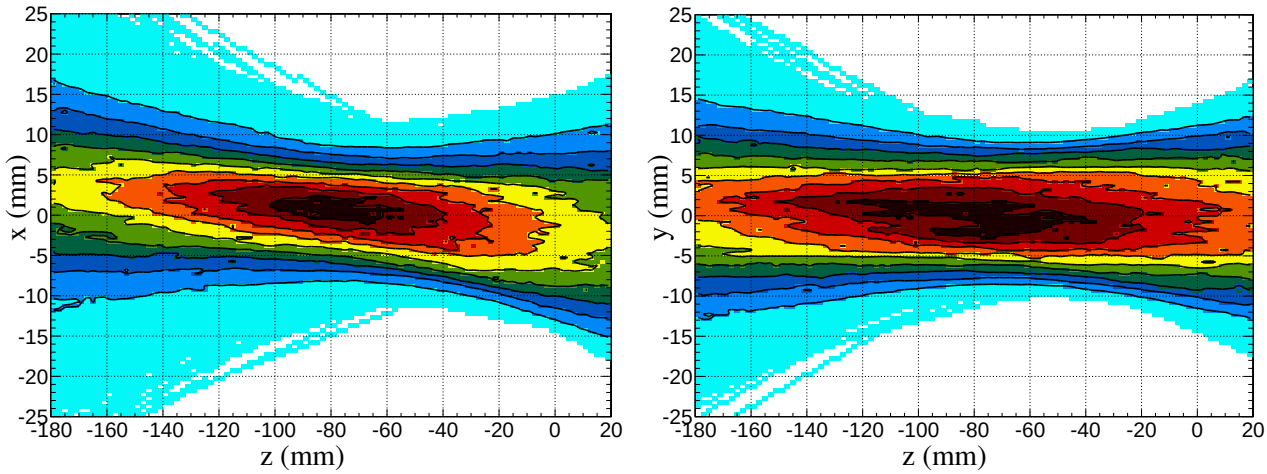

Figure 6.7: *Beam Profile. Upper Left: x vs z beam profile measurement. Upper Right: y vs z beam profile measurement. Lower Left: x vs z beam profile simulation. Lower Right: y vs z beam profile simulation.*

6.5 Simulation and Construction of RDGT Bank - Waveform Digitizer

This bank contains all the information from the Acqiris waveform digitizer at a sampling rate of 2GS/s [3]. The waveform digitizer produces digital signals, which, if properly constructed and calibrated, can determine timing and energy of beam particles and decay products. As stated before, the digitizer is used for

the beam counters (B0 and degrader) as well as the active target. Construction of synthetic waveforms in simulation is necessary because predicted energies and timings are obtained from the amplitude of the signals and the placement of the signals respectively. These observables are often used to discriminate between background and signal events. It is desired to treat measurement and simulation identically, so the simulation should produce synthetic waveforms because the measurement has them. Further, if cuts are made from predicted energies and timings on the measured data in order to eliminate background, then the efficiency or acceptance of the cut must be well understood. Thus it is necessary to properly construct the synthetic waveforms. Proper synthesis of waveforms requires a baseline and a response function of the detector. To properly form a synthetic baseline for the digitizer, one must look at the output of digitizer in its most raw form before any filtering or analysis. The digitizer output of the waveform in the baseline region (in fact everywhere) is discretized. This discretization presents an advantage for the simulation because it can be turned into a cumulative distribution function. Once simulation of the waveform occurs, the baseline can be formed by throwing a random number between 0 and 1 for each synthesized bin, and using the cumulative distribution of measured baseline to form a synthetic baseline. Experimental baselines shown in Fig 6.8

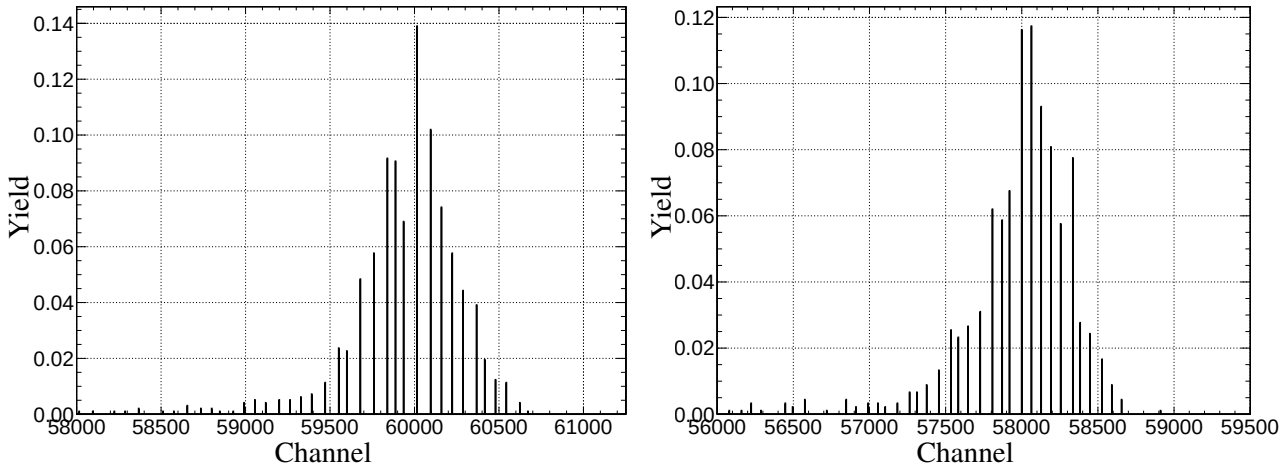

Figure 6.8: *Left: Baseline region for degrader waveform. Right: Baseline region for target waveform.*

The simulated baselines may be checked against the measurement by comparing sum and differences of nearest neighbors for both measured and simulated data as seen in Fig 6.8.

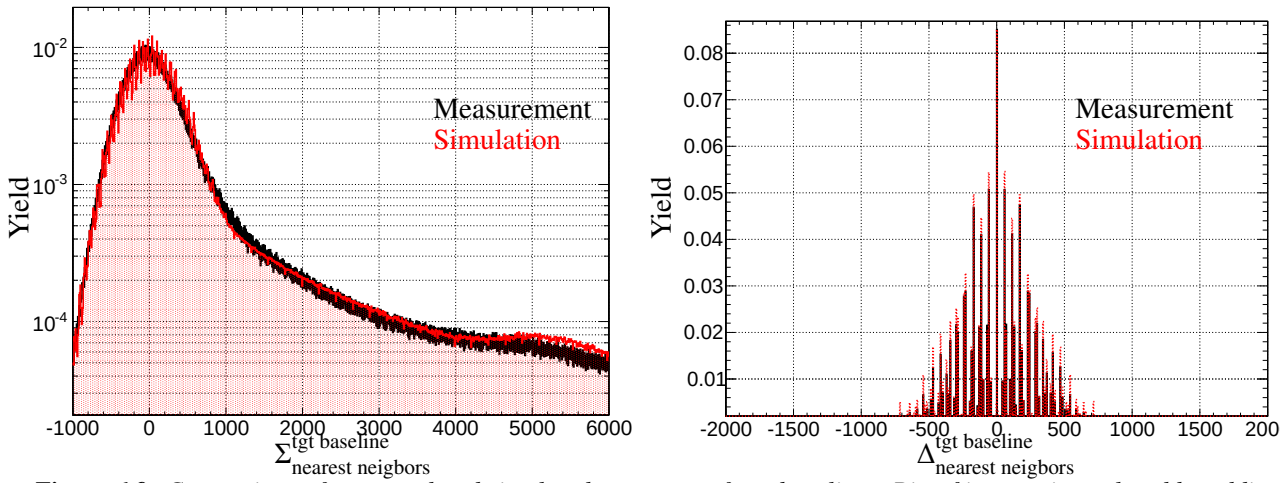

Figure 6.9: *Comparison of measured and simulated target waveform baselines. Bin of interest is analyzed by adding or subtracting the bin to the left and right.*

Once a realistic baseline has been created, the signal in the synthetic waveform under analysis must also be comparable to the measured data. In order to achieve this, a response function of the detector is required. This can be obtained by observing pure signals (responses with no overlapping due to multiple particles) in the data sample, taking multiple events from multiple runs, averaging them, and using a proper interpolation method to obtain a smooth function that can be used as a kernel to build the synthetic signals. Raw signals and interpolated kernels are shown in Fig 6.10

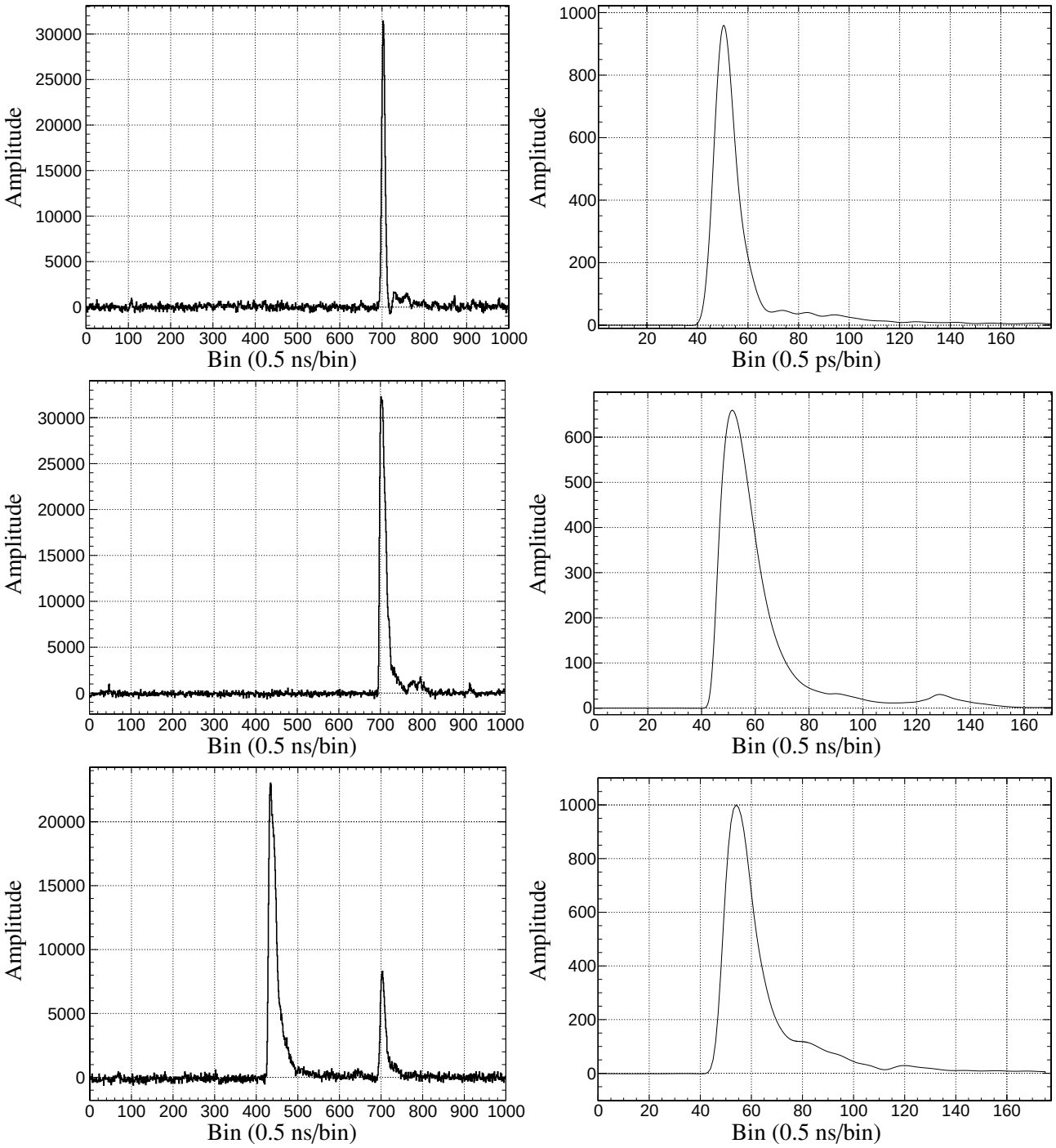

Figure 6.10: *Upper Left: Raw B0 waveform, Upper Right: Averaged and interpolated B0 Waveform. Middle Left: Raw DEG Waveform. Middle Right: Averaged and interpolated DEG Waveform. Lower Left: Raw TGT waveform, Lower Right: Averaged and interpolated TGT Waveform.*

The left columns show the response functions of the beam counter, degrader, and target respectively. The binning is such that 1 bin represents 0.5 ns. The interpolation was done such that a bin represents

0.5 ps. This binning was chosen because the systematic uncertainty in waveform timing is around 100 ps. The interpolation of 1 ps would ensure that no significant systematic uncertainties would be introduced. So every time a synthetic waveform is constructed, 1 bin of the constructed waveform corresponds to moving 2000 bins in the kernel. This is similarly done for the degrader and target as well. Proper interpolation is cross-checked by comparing the waveforms with respect to constant fraction time and placing the peaks at the same value, in this case zero is seen in Fig 6.11.

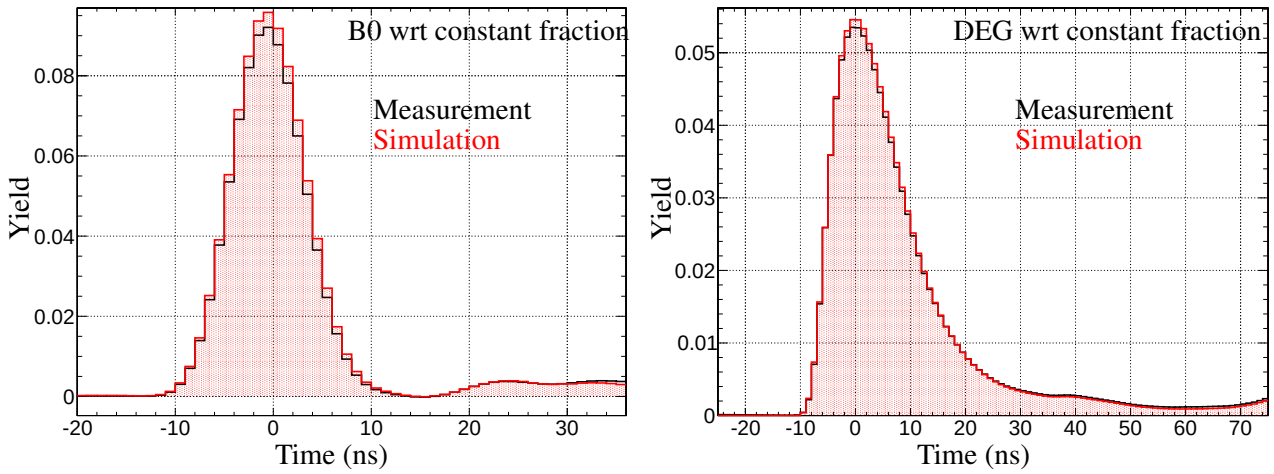

Figure 6.11: *Comparison of waveforms simulated (red) and measured with respect to constant fraction time. Right: B0 waveform. Left: Degrader waveform.*

With the response function constructed, the proper simulated amplitude is required for each event. Typically, the amplitude of waveform response is proportional to the energy deposited by the particle that produces the signal. But this is not the entire story. In a simple $\pi \rightarrow \mu\nu$ decay, the muon has 4.11 MeV of kinetic energy. If the muon is produced in a pion decay and subsequently decays in the target then one would naively expect that the peak or area of the waveform of the muon be mono-energetic and be centered at 4.11 MeV. Similarly if a positron deposits 4.11 MeV would also produce a signal which would naively seem these signals have the same amplitude. This is not correct and in order to understand this, an understanding of the scintillation process is required.

To first order, scintillation light intensity is proportional to the energy lost in the material, which corresponds to lost energy through ionization primarily. This is mostly true for minimum ionizing particles i.e., electrons and positrons, above a certain energy threshold, which is usually low. Particles with lower, non-relativistic velocity, mainly those heavier than electrons, dissipate a fraction of their energy in the form

of molecular or atomic recoil in addition to the ionization. The energy dissipated in molecular/atomic recoil does not produce light efficiently. Thus heavier particles will produce less light than electrons or positrons for the same energy deposited in matter. This effect is called light quenching. It has been demonstrated using a particular model that the light quenching depends mostly on the specific dE/dx, that is the the specific energy loss in the material and not on the species of the particle. In other words, particles with the same relativistic β will show similar specific energy loss. So parameterization of light quenching for a given material may be obtained. The Wright parameterization [91] is a formula that calculates the electron-equivalent energy for a particle traversing a total pathlength, L, in a detector volume. Where the electron-equivalent energy is the energy that an electron would deposit, given it has the same total energy of the particle of interest. The formula of interest is

$$E_{ee} = \frac{(dE/dx)_{min}}{\ln\left[1 + \alpha(dE/dx)_{min}\right]} \int_0^L \ln\left[1 + \alpha(dE/dx)_p\right] \mathrm{d}x \tag{57}$$

Here p is the particle of interest, *min* represents the dE/dx for a minimum ionizing particle (positron or electron) and α is the only free parameter which was found to be 0.025 ± 0.002 cmMeV^{-1} and $(dE/dx)_{min}$ is fixed in the GEANT4 to 1.78 MeV/cm. This is seen by plotting energy vs pathlength that the positron travels in the target and taking the slope as shown in Fig 6.12.

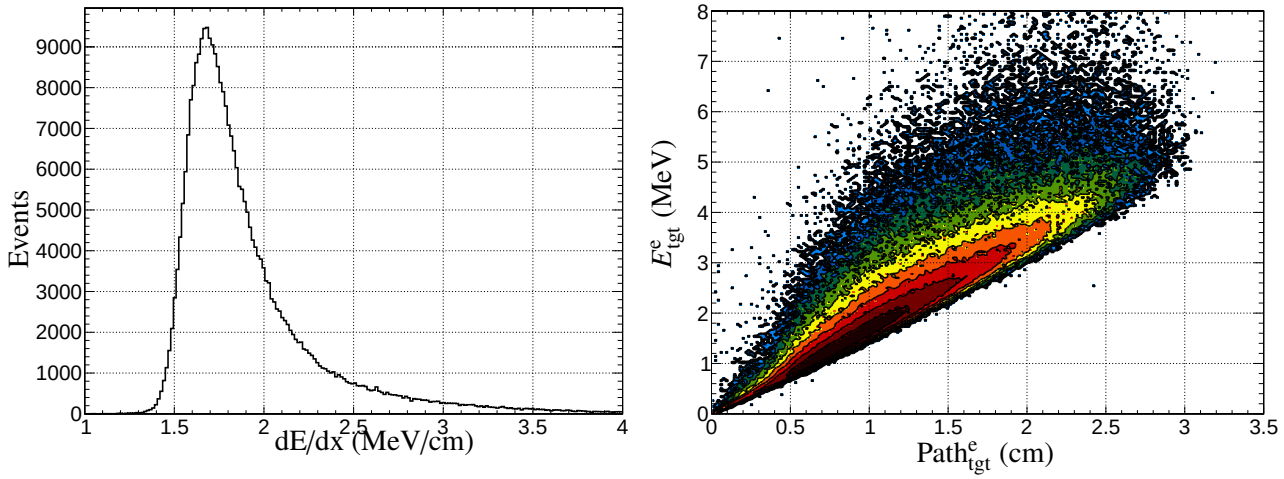

Figure 6.12: *Target dE/dx for a positron from simulation.*

With these known values, the term in front of the integral becomes 40.9±3.2 MeV/cm. So each and

every time the simulation is run and a heavier particle, i.e., a proton, pion, or muon takes a step, the energy deposited in that step is recorded as well as the step length, this dE/dx is multiplied by α, added to 1, and the result is natural log of this value times 40.9 times the step length. This result represents the electron equivalent energy of the particle deposited as it traverses the medium. In other words, this is the "electron equivalent" energy that detector will ultimately detect and record as scintillated light. One particular feature of this formula is that the species of the particle is not as relevant as the relativistic velocity as demonstrated in Fig 6.13.

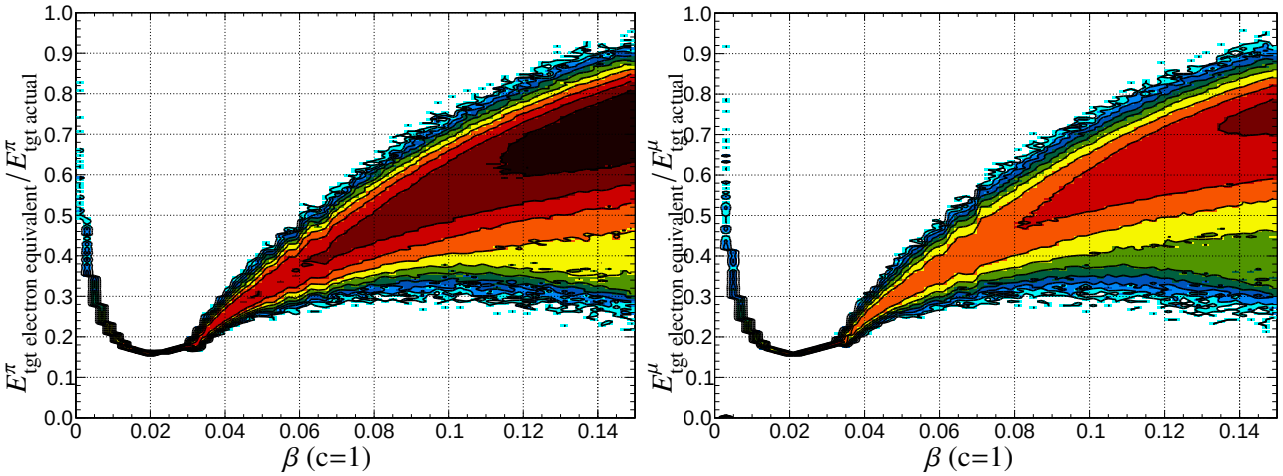

Figure 6.13: *The effects of quenching as a function of β. Left: pion quenching factor as a function of velocity. Right: muon quenching factor as a function of velocity.*

The effects, of the energy distributions from light quenching are seen in Fig 6.14 below. The average of the ratio between the quenched and unquenched energies are called the quench factor. This factor is only relevant for the pion in the degrader, the pion in the target, and the muon in the target. The quench factors are used in the PEN analysis to convert between real energy deposition (in the case of predicting energies) and the electron-equivalent deposited energies (those observed in plastic scintillator).

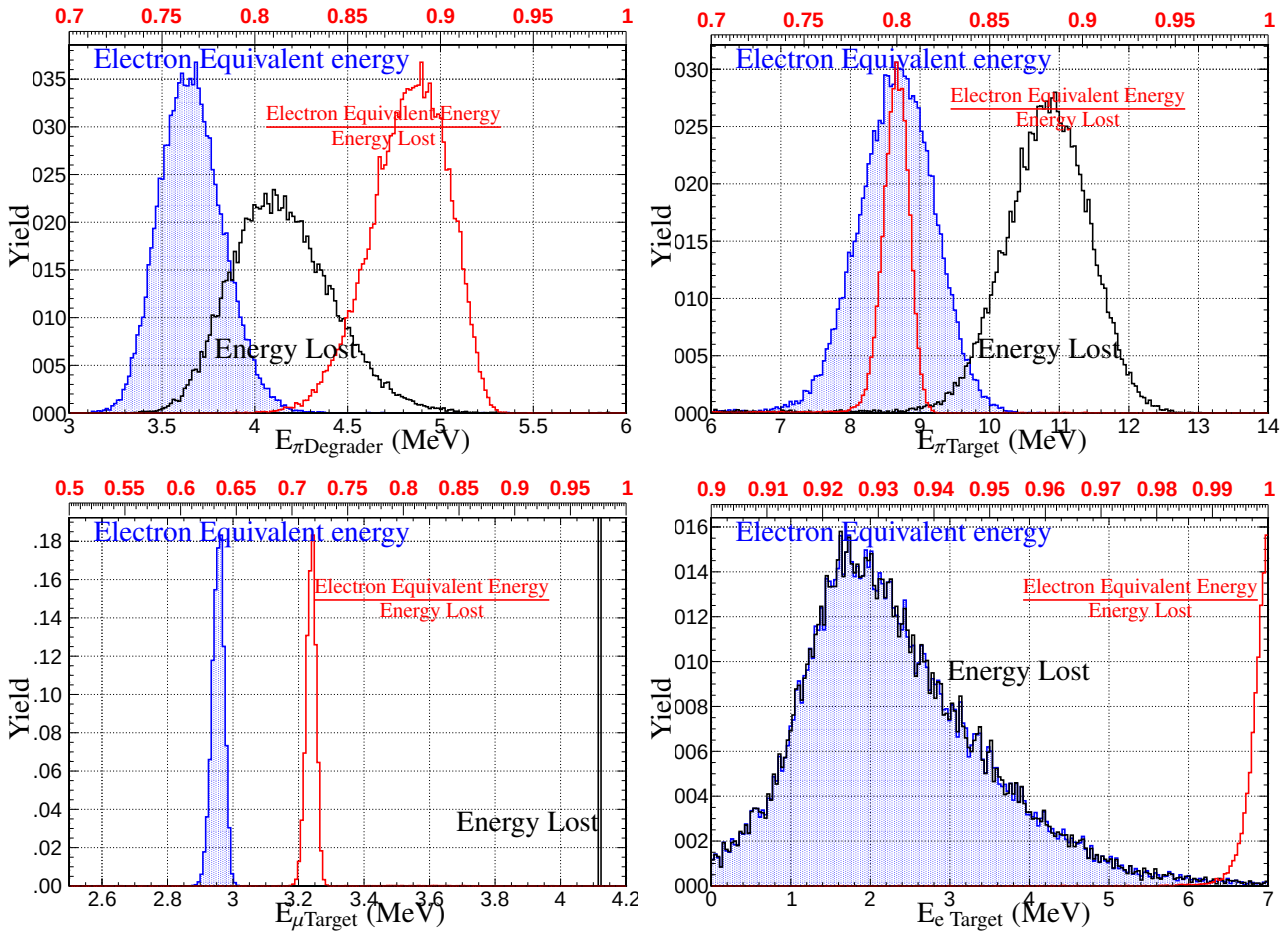

Figure 6.14: *Upper Left: Energy deposited in degrader. Upper Right: Energy deposited in target by π^+. Lower Left: Energy deposited in target by μ^+. Lower Right; Energy deposited in target by e^+. Black energy loss in the target. Blue is electron equivalent energy. Red is the ratio of the two.*

Notice that the energies in all but one plot are shifted to the left. This is expected since we expect to lose a fraction of the energy to molecular recoil. In addition, the muon energy deposition, which ideally is a delta function, is not a delta function, but rather a continuous distribution. This phenomenon can be ascribed to a few reasons one of which is the fact that in order to obtain the electron equivalent energy, one must use a numerical integration method, which of course has uncertainty. The second is because the function in Eqn 57 is nonlinear. There is also an additional caveat. The quench factor actually depends on step size that the particle takes in the simulation. The step size was chosen (0.005 mm) to minimize error, yet still allow the simulation to finish in a timely manner. The final noticeable feature is that the quenched energy is unchanged from the unquenched energy for the positron. This is expected since the empirical formula is to calculate the electron equivalent energy. Since the electron equivalent energy of an electron (or in this

case the positron) is the actual energy itself. Thus no change is expected for the positron. The ratios of the quenched to unquenched energies are also plotted in red in Fig 6.14.

Putting together these tools, the waveforms can now be constructed. In the measurement, the positron in the target is put at a particular bin for a specific run period and everything is relative with respect to the target positron. This is reproduced in the simulation as illustrated in Fig 6.15 for a 2009 run period.

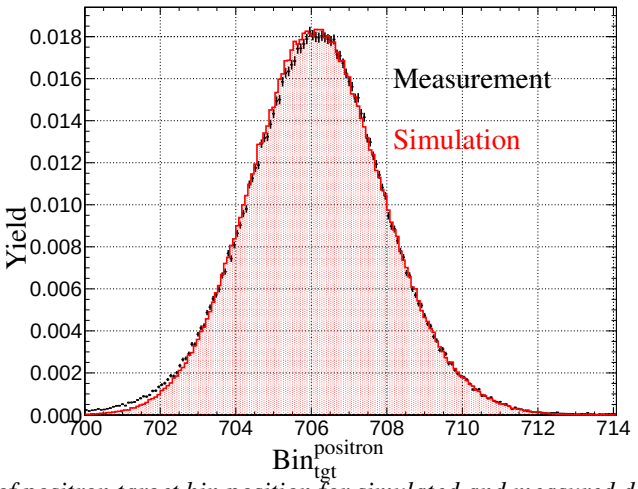

Figure 6.15: *Comparison of positron target bin position for simulated and measured data for run selection in 2009.*

However, it is not as simple as that (it never is). The position of the positron peak in the target waveform is determined using a coincidence with the plastic hodoscope. Each hodoscope, however, has a different delay. So it is not merely enough to put the positron signal at the particular bin in the target, but rather put the bin in the target given a particular hodoscope was fired as illustrated in Fig 6.16.

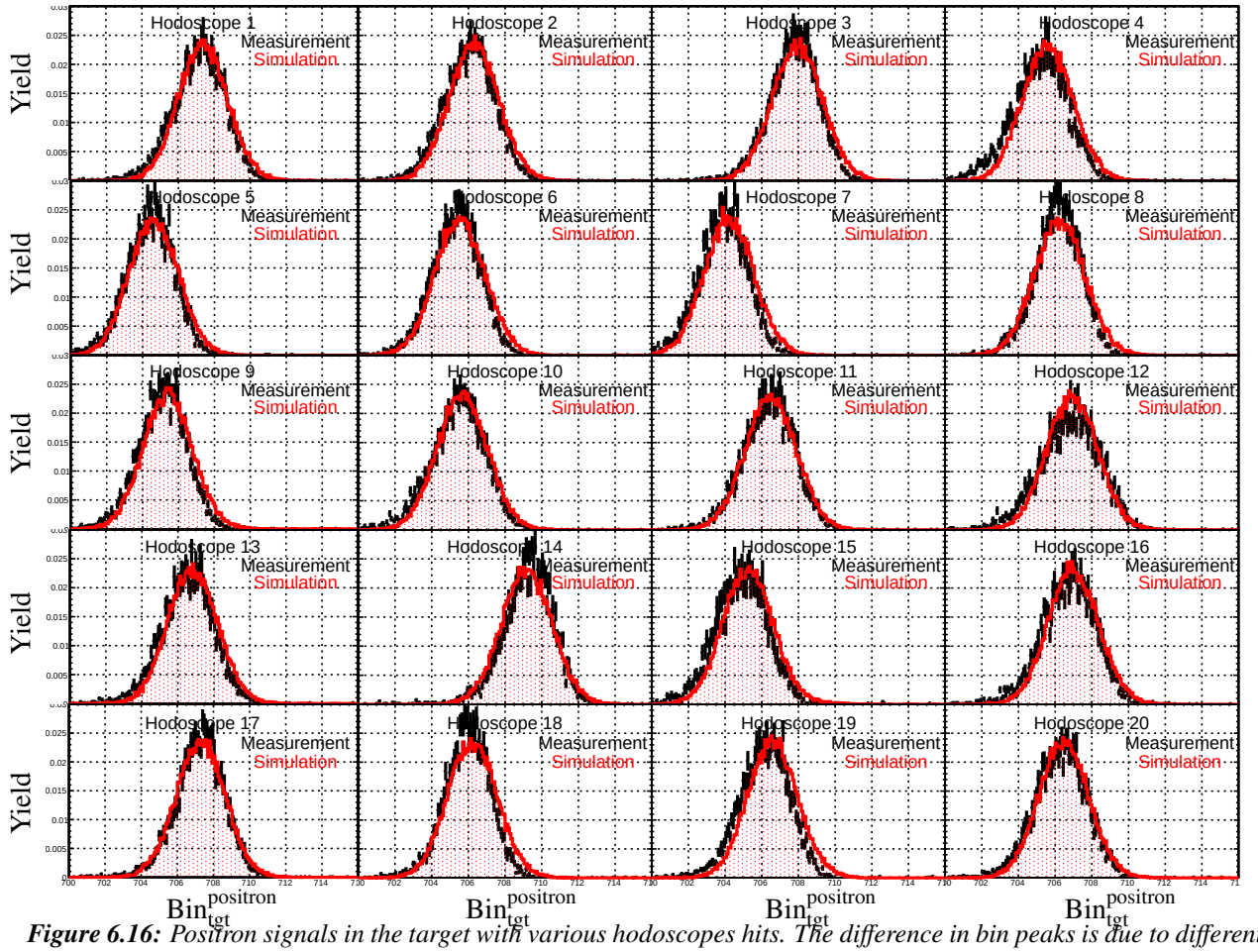

Figure 6.16: *Positron signals in the target with various hodoscopes hits. The difference in bin peaks is due to different delays (which are simulated) in the trigger offset dependent on which hodoscope is fired.*

Once the positron signal is put into the appropriate bin in the target waveform, all other signals in the target are placed relative to this bin according to their timings in GEANT4. Knowing the time difference between the pion or muon appearance in the target relative to the positron provides the information needed to synthesize target waveforms. Similarly, since the time when the pion traverses the upstream beam counters is known, the waveforms for these detectors can also be constructed.

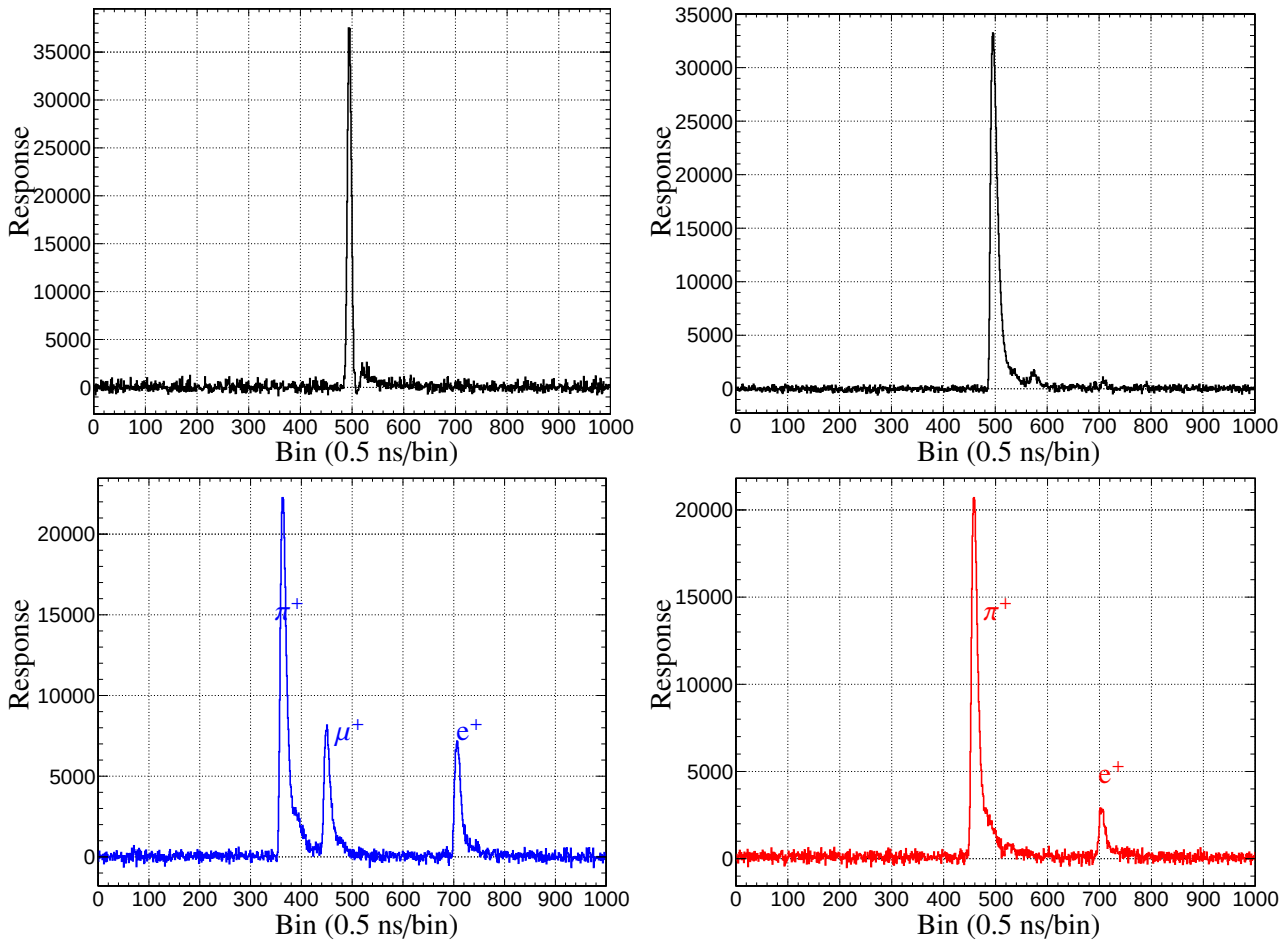

Figure 6.17: *Simulated Waveforms. Upper Left: B0. Upper Right: Degrader. Lower Left: Target for $\pi \rightarrow \mu\nu$ decay chain. Lower Right: Target for $\pi \rightarrow e\nu$*

After taking into account the quenching and proper interpolation of the response function and applying the appropriate gain proportional to quenched energy for the detector elements, the various observables constructed from these signals should be consistent with the measured data for the run period being simulated. Some simple ”upstream“ energies and times for measured data and simulated data are shown in Fig 6.18.

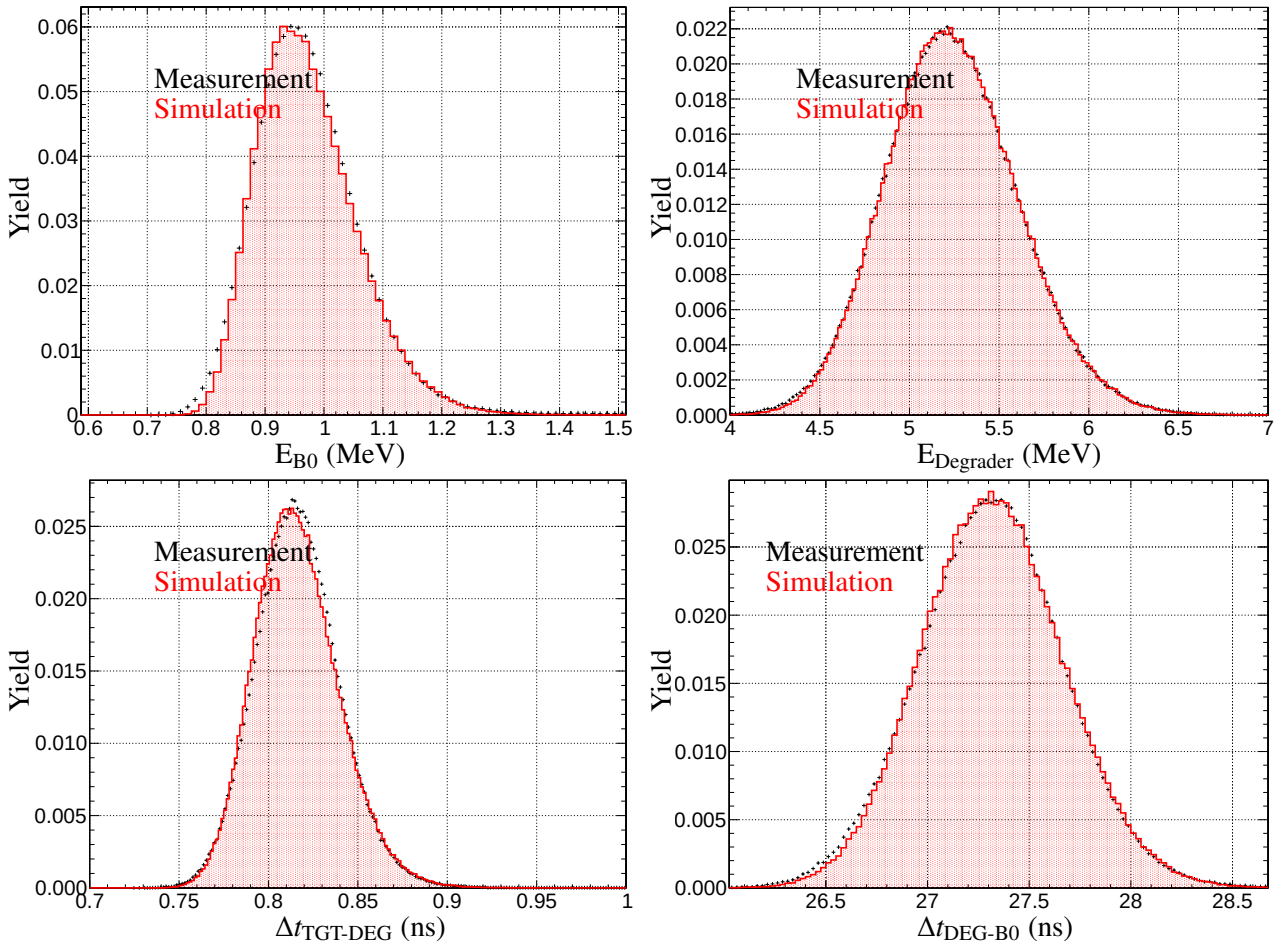

Figure 6.18: *Energy and Timing Spectra of beam counters. Upper Left: B0 energy. Upper Right: Degrader energy. Lower Left: Time between degrader and target. Lower Right: Time between B0 and degrader. Run Period and Simulation 90000.*

The target is the detector where (arguably) the light quenching effects are most important. For Michel events, frequently the muon signal is very close to the pion signal in the target waveform. When this happens, algorithms for finding the area of a peak might not be as effective as for well separated signals because the area of the first peak may be enhanced by a little of the area of the second peak, leading to deduce that there is more energy than what was really deposited, at least by the first particle. However, it is a great testament to the simulation if this phenomenon is correctly reproduced. Looking at the target waveform areas (and therefore energies) it is seen that indeed there is an overlap of areas that is close to the signal of interest, either the pion and muon or the muon and positron. Moreover, if a cut is made such that there is sufficient time between muon and pion signal, then individual areas of the muon and pion peaks should reflect only the one peak corresponding to the energy of that particular particle with no overlap. This is illustrated in

Fig 6.19.

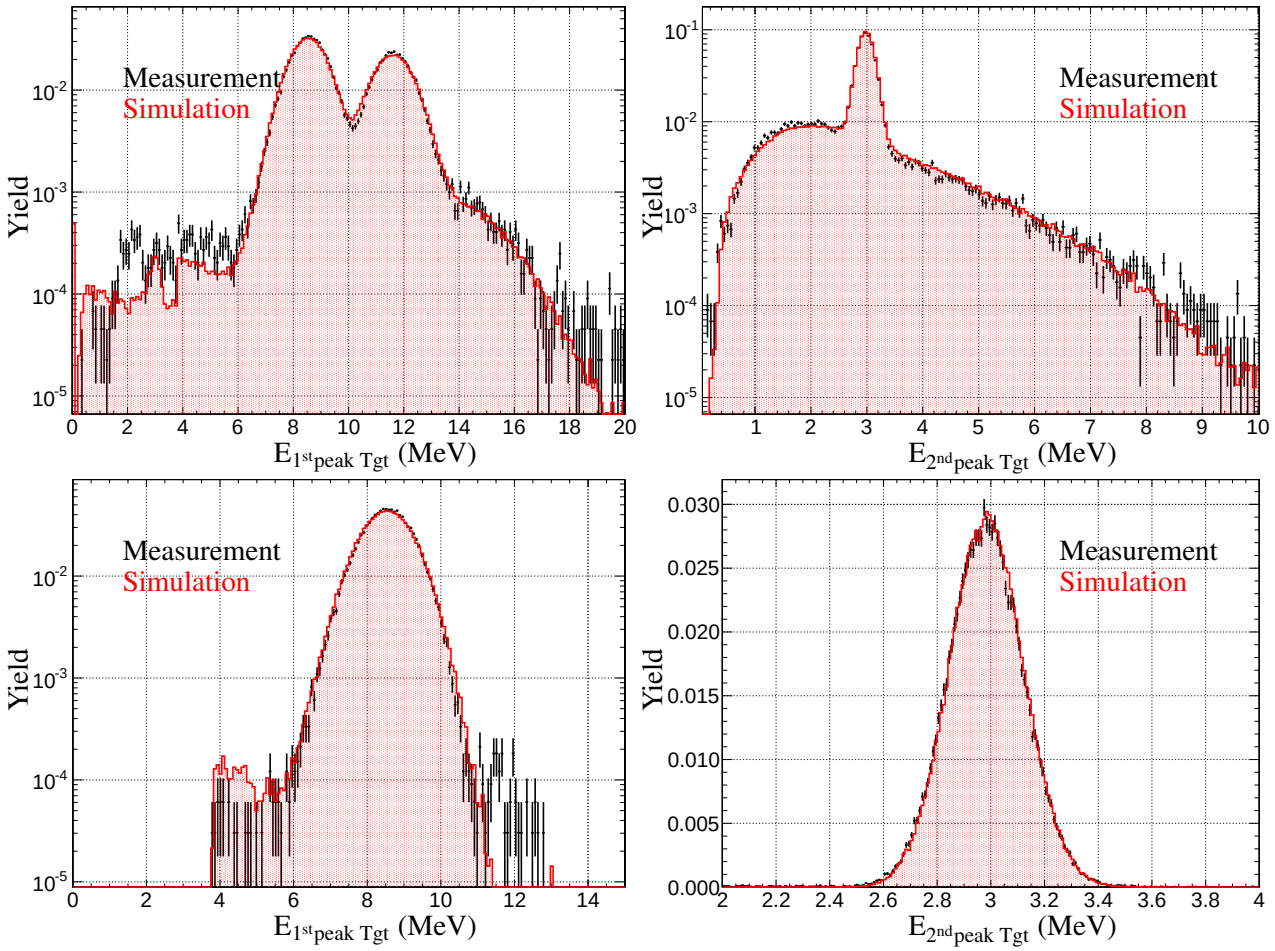

Figure 6.19: *Upper left: Signal in first peak of target waveform. Upper right: Signal in second peak of target waveform. Lower left: Signal in first peak of target waveform with a requirement that three peaks are well separated. Lower right: Signal in second peak of target waveform with a requirement that three peaks are well separated.*

Finally, if all is done correctly, the known time differences and energies in the simulation and the reconstructed time differences and energies based on waveform analysis should coincide with each other as shown in Fig 6.20.

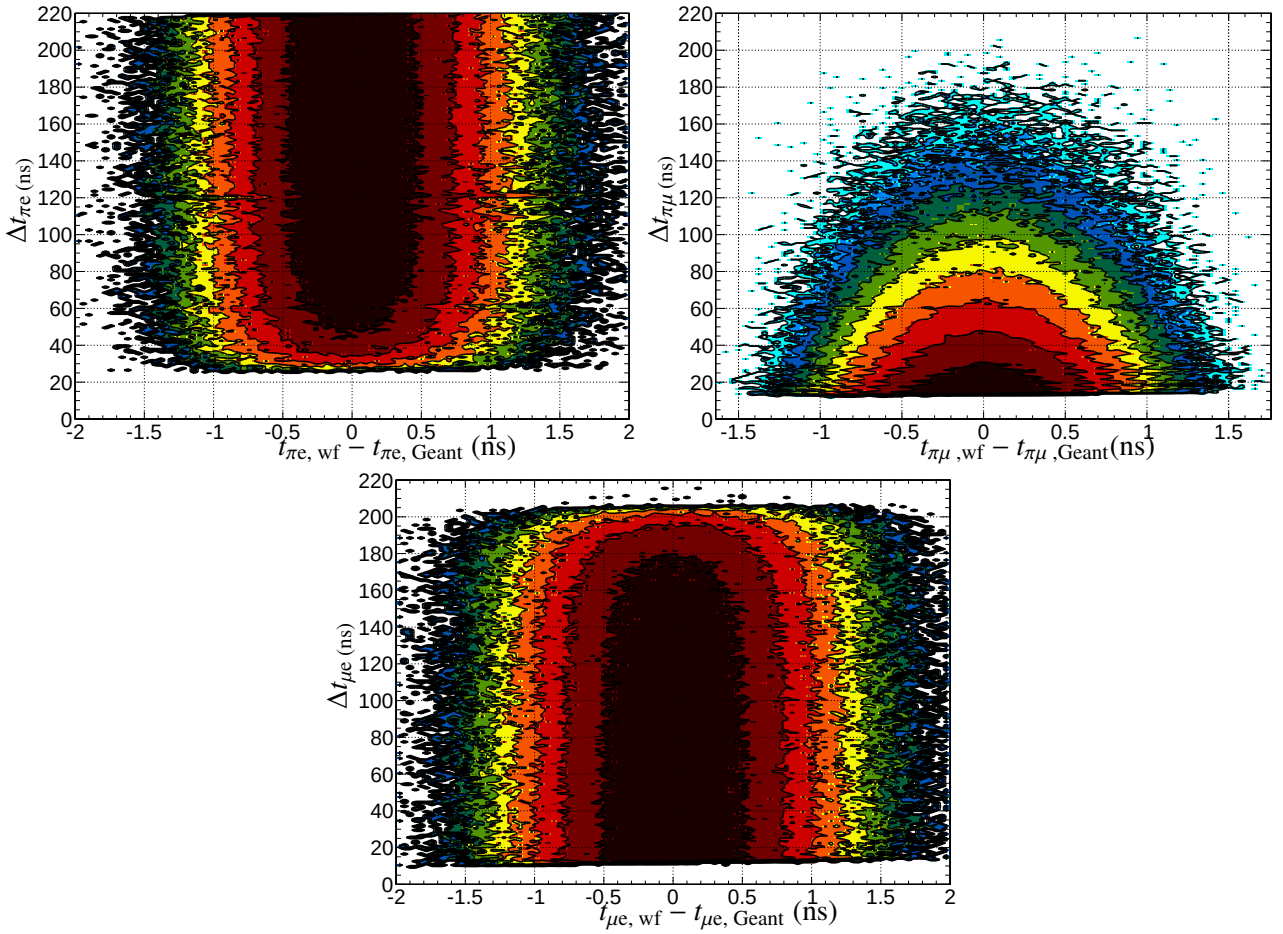

Figure 6.20: *Time differences between reconstructed (waveform) and Geant known time differences. Upper Left: Difference in time between pion and positron from maximum bin of waveform. Upper Right: Difference in time between pion and muon from maximum bin of waveform. Bottom: Difference in time between muon and positron from maximum bin.*

These fully reconstructed waveforms show the effect of the smearing and detector response. If the difference in time between the muon and positron or pion and positron were perfectly reconstructed, that is if the difference between reconstructed and known time intervals, were zero, then this would represent a perfect detector. The corresponding energy plots are seen in Fig 6.21.

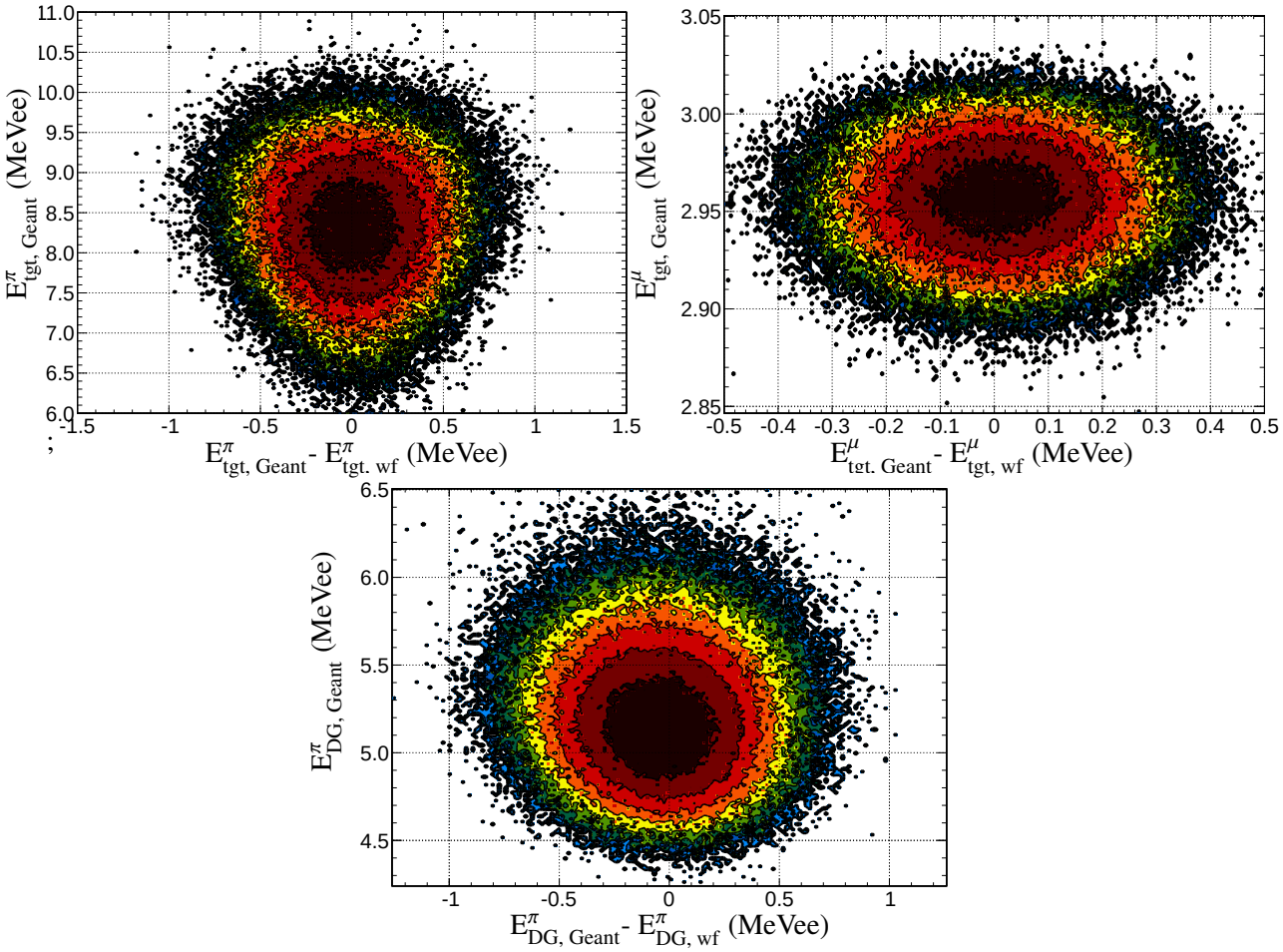

Figure 6.21: *Comparison of energy deposited against the energy reconstructed from simulated waveforms correcting for quenching. Upper Left: Pion energy deposition in target. Upper Right: Muon energy deposition in the target. Bottom: Pion energy deposition in the degrader. Energies are in electron equivalent energies (MeVee).*

6.6 WTPC Bank - mTPC Data

The task of beam tracking is assigned to the PEN mTPC. The apparatus consists of a 50 mm^3 cubic volume with four anode wires separated by 10 mm for the 2009 run period and 12.5 mm for the 2010 run period. The mTPC used a 250 MS/s waveform digitizer channel for the output signal. Left and right sides of each of the wires produce digitized signals which would result in eight waveform signals all together. In order to simulate the mTPC properly and produce synthetic events indistinguishable from real events, the output format of the simulation must be the same as that generated in the measurement, that is a digitized waveform. For this to be done correctly, a review of the workings of the mTPC is first in order. The time projection chamber is a combination of drift chamber and multiwire proportional chamber. As a particle passes through the detector, the gas in the detector ionizes. The resulting electrons and ions drift toward anode wires and cathode "pads" and the overall induced charge is proportional to the overall energy loss in the mTPC gas by ionization. In the MTPC, there are four wires with signals on the left and right. The relative amount of charge collected on the left and right wires gives the x position of the incoming pion. For instance, if the wires are completely symmetric with no offsets, and the left and right wires have equal charge collected, then the pion has gone through the center. If 99% of the charge is collected on the right side of the wire, the pion passed through a high negative x value. The other part of the mTPC is is the device which acts like a drift chamber. With a known drift velocity, the drift time is proportional to the y position and is indicated in the time bin (placement) of the MTPC waveforms. In the simulation, the simulators are privied to the energy deposited, x position, and y position of the pion beam. Using this "divine" knowledge, waveforms can be constructed further. If this is done correctly, the privied knowledge of the simulator, i.e., "god's" values could be reconstructed from the mTPC waveform analysis. In order to proceed, the first thing that must be done is to construct a response function from the mTPC data. Construction of the response function, was obtained by collecting a representative number of response waveforms, averaging, and interpolating them to make a response function, which is in turn be used to construct waveforms that are ultimately analyzed in the exact same manner as the digitized waveforms in the measured data as seen in Fig 6.22.

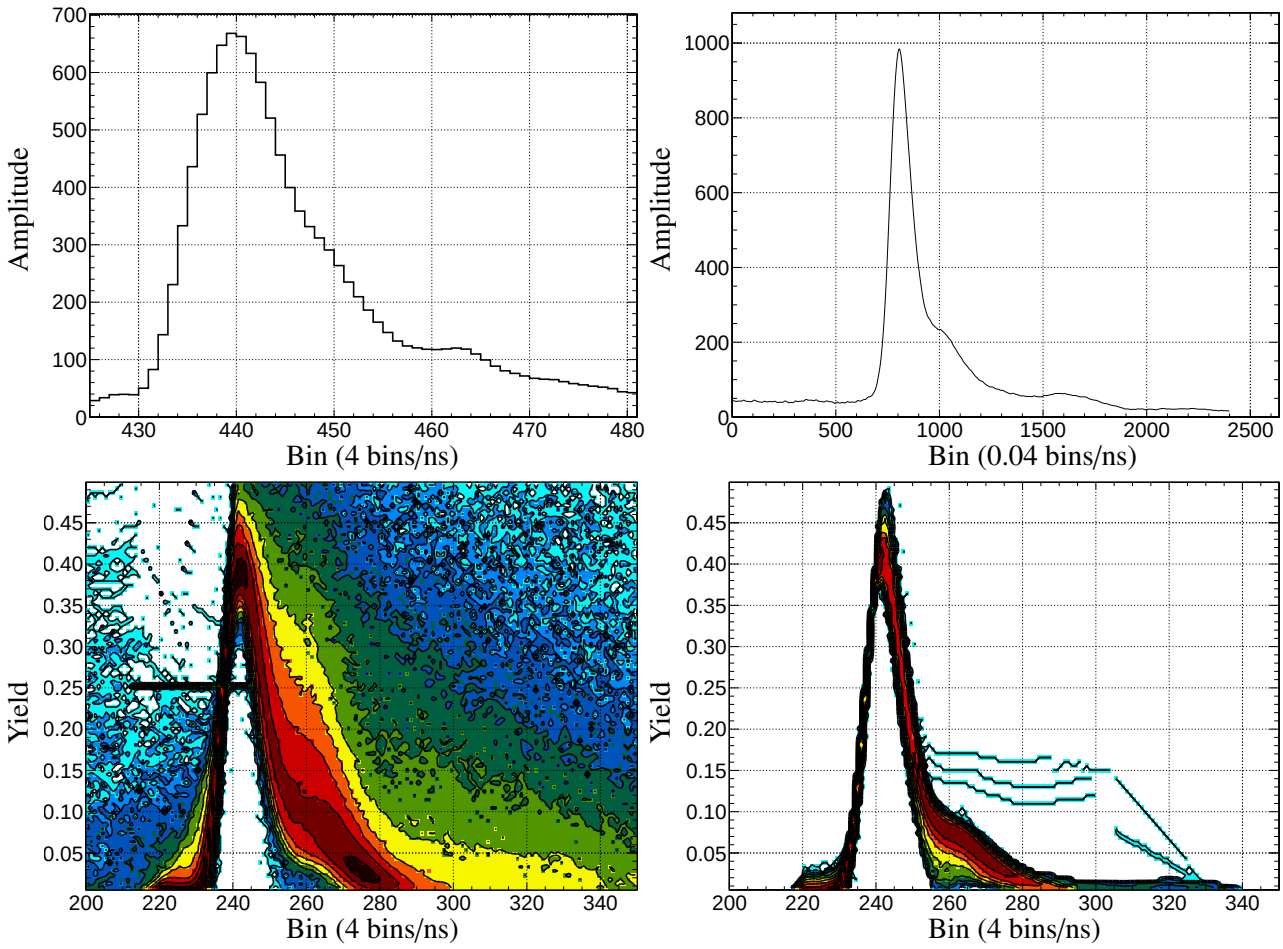

Figure 6.22: *Upper Left: Many measured signals averaged. Upper Right: Interpolated average. Lower Left: 2D measurement response. Lower Right: 2D reconstructed simulated responses.*

In order to appropriately simulate the mTPC waveforms, we start with the correct beam profile. As stated above, the amount of charge collected on the right and left sides of wires will determine the relative particle position. So the amplitudes of these signals are linear functions in x. Further, the amplitude should be proportional to the energy deposited in the gas in the vicinity of a given wires. The reason for this is because a higher energy particle will ionize more gas, which means more charge will be collected and therefore a higher signal amplitude is achieved. So by having the amplitudes in the form:

$$\text{Amplitude}_{\text{right}} = (1 + \text{offset} + \text{slope} \times x_{\text{Geant}}) \times \text{Gain} \times E_{\pi_{\text{loss}}}. \tag{58}$$

$$\text{Amplitude}_{\text{left}} = (1 - \text{offset} - \text{slope} \times x_{\text{Geant}}) \times \text{Gain} \times E_{\pi_{\text{loss}}}. \tag{59}$$

Here x_{Geant} is the known position of the GEANT4 simulation at the position of the wires and $E_{\pi_{\text{loss}}}$ is the energy the pion loses in the volume of the mTPC. When adding the two amplitudes, the energy loss of the pion is recovered, scaled by some gain. Given this construction, comparison of amplitudes to the simulation is shown in Fig 6.23

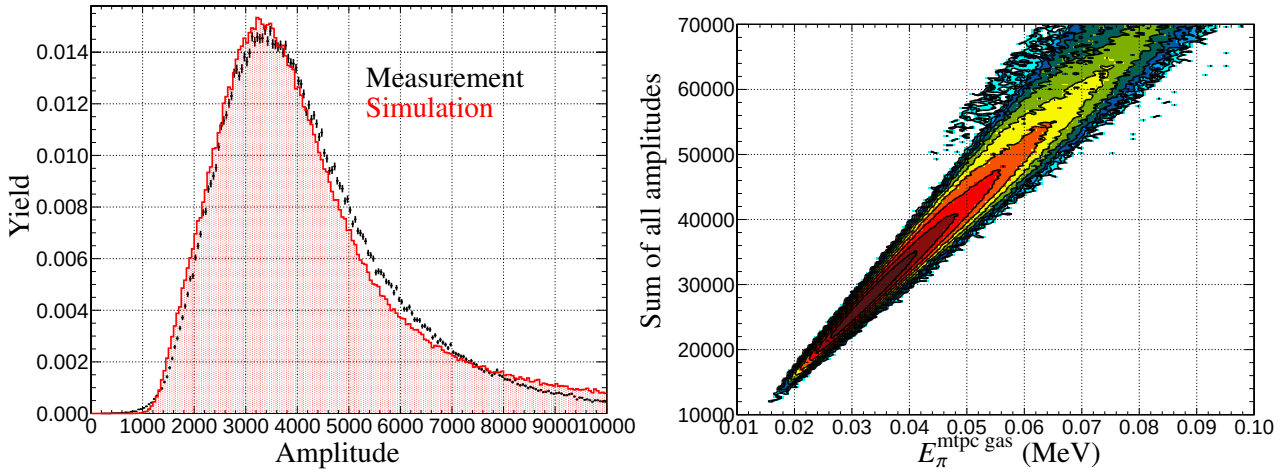

Figure 6.23: *Left: mTPC amplitude distribution - all wires added. Right: Correlation between energy deposited in the mTPC gas and the total amplitude.*

The distinguishing feature is the presence of the Landau tail, a shape indicative of a particle going through a thin detector, in this case a gas. It is also expected that the left and right wire amplitudes should be correlated and anti-correlated at the same time. They are correlated because higher energy pions will deposit less energy in the gas which means means both sides of the wire will have a smaller signal. They are anti-correlated because for a given pion, one side of the wire will receive less charge than the other. Nonetheless the correlation should is reproduced as seen in Fig 6.24.

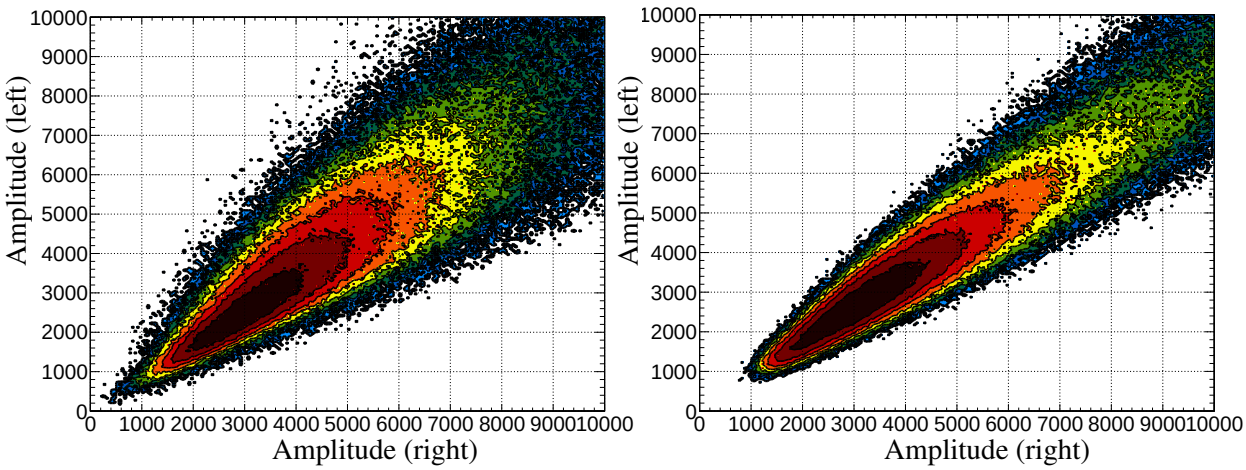

Figure 6.24: *Correlations of signals of mTPC amplitudes between left and right side of the wires. Left: Measurement. Right: Simulation.*

One of the caveats in the equations is that the offset is different for each of the four wires in that it represents a randomly chosen number to recreate the resolution of the detector. This produces a broader predicted stopping distribution for the beam profile. This seemingly small detail is actually quite important. There are two ways in which the stopping distribution, as determined by the mTPC, can be broadened. The first is by broadening the beam in the x and y direction (either in position or momentum), the effect of which is to broaden the energy in the degrader and target by the incoming pion, thus affecting predicted pion energies. The second is to worsen the resolution of the simulated mTPC. This doesn't affect the spread of the incoming pion's momentum distribution or tune and therefore doesn't affect the predicted pion energy. Both options will affect the predicted positron energy and thus should be done carefully. A way to check is to see the effect of simulated detector resolution on the colinearity that was discussed in the previous chapter. Using the known positions, the colinearity should be nearly a delta function. It is not quite a delta function because of nonzero step size in the simulation. If the known positions of the simulation are used to construct the waveform without smearing it, i.e., not putting in the resolution, then the position based on the waveform analysis alone produces a very slim distribution in colinearity. When adding the smearing factor that was measured by previous work [67], the effect of smearing is seen in Fig 6.25.

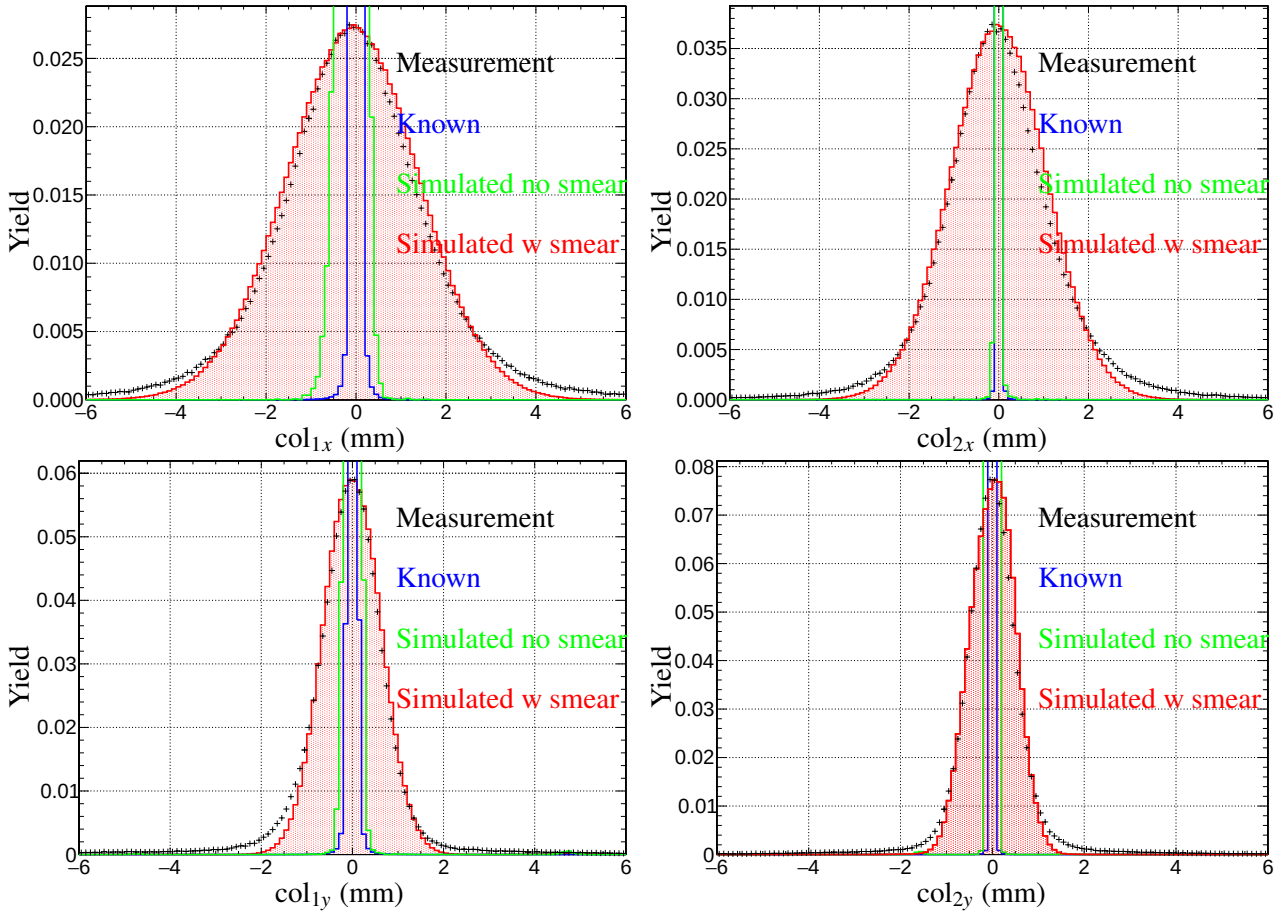

Figure 6.25: *Colinearity comparisons of the measurement (black), known GEANT values (blue), reconstructed waveform values with no smearing (green), and waveform values smeared with detector resolution (red). Upper left: col_{1x}. Upper Right: col_{2x}. Lower Left: col_{1y}. Lower Right: col_{2y}.*

Using the same algorithm as used in the analysis of the measured data, the simulated waveforms allow the prediction of the beam trajectory. This interpolated beam trajectory can be compared to the actual known values at particular upstream z values as shown in Fig 6.26 and Fig 6.27 for x and y respectively.

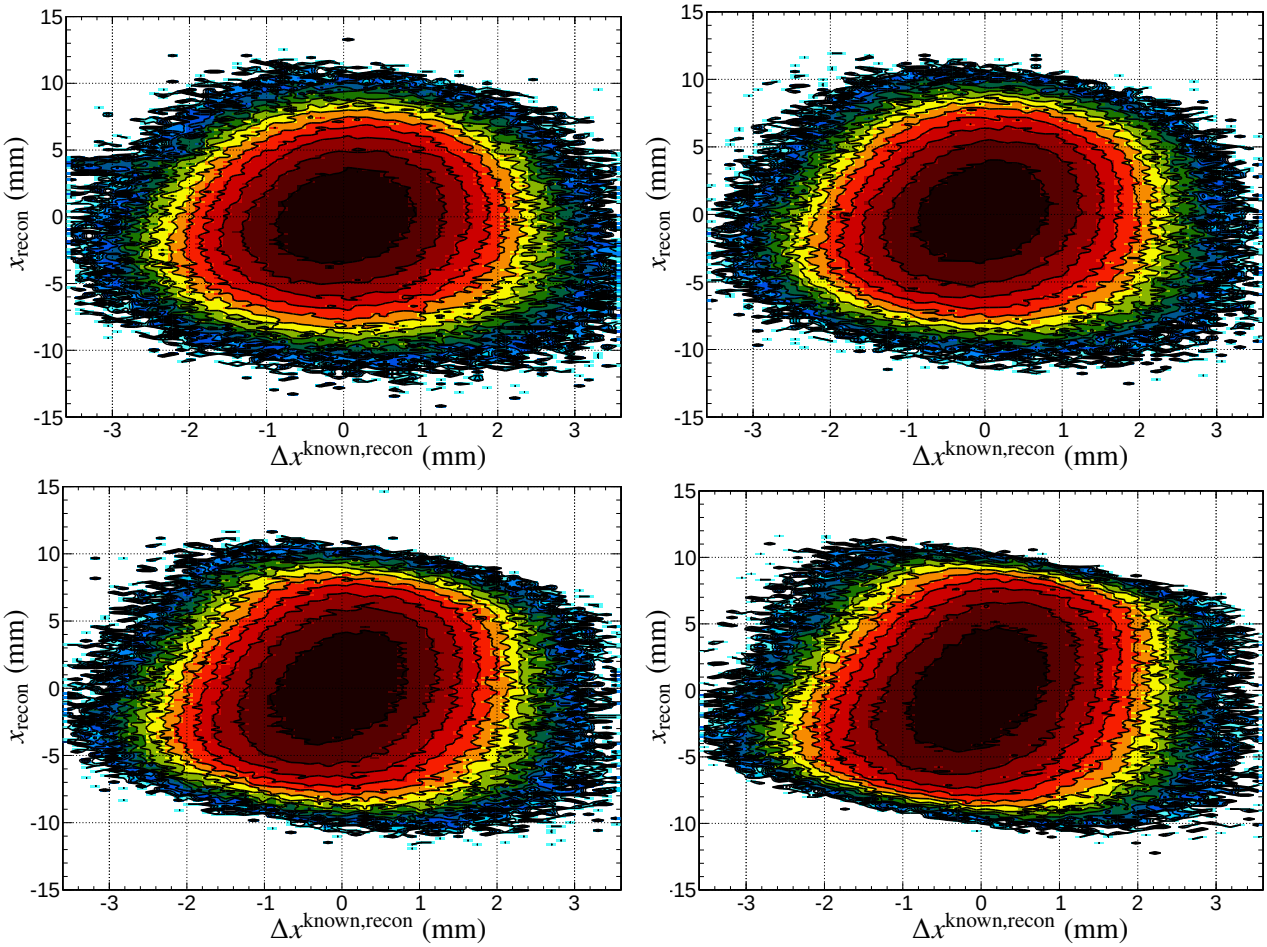

Figure 6.26: *Comparison of known and reconstructed x positions at mTPC wire 1 (upper left) wire 2(upper right), wire 3 (lower left) and wire 4 (lower right).*

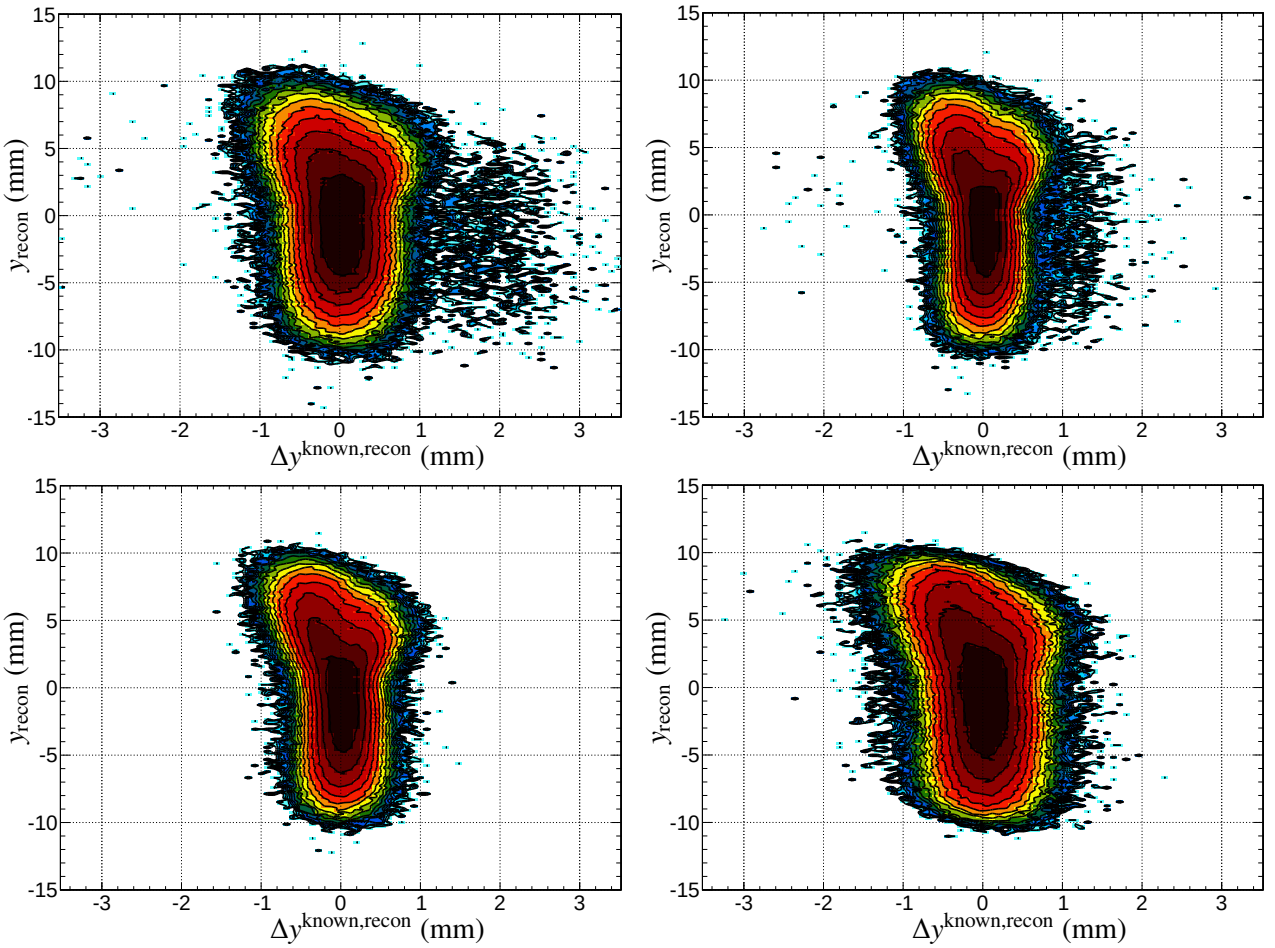

Figure 6.27: *Comparison of known and reconstructed y positions at mTPC wire 1 (upper left) wire 2(upper right), wire 3 (lower left) and wire 4 (lower right).*

Of course there are differences in how the simulation is treated for construction of the mTPC. First, in the measurement it is usual for delta electrons to distort mTPC signals. This feature is not used in the simulation, delta electrons are not used in constructing the synthetic waveforms for analysis. Further, the simulation always has one particle present in the beam and it is always the pion. In the measurement, there may be another beam particle traversing the mTPC volume such as a muon or positron. Protons may also be traversing through the mTPC gas, due to hadronic interactions of the pion with the degrader nuclei.

Once the simulated waveforms have been analyzed, the stopping positions x and y can be determined. These must be not only in agreement with measurement but also with the known GEANT4 values. The reconstructed stopping positions indeed agree well with the GEANT known values as shown in Fig 6.28.

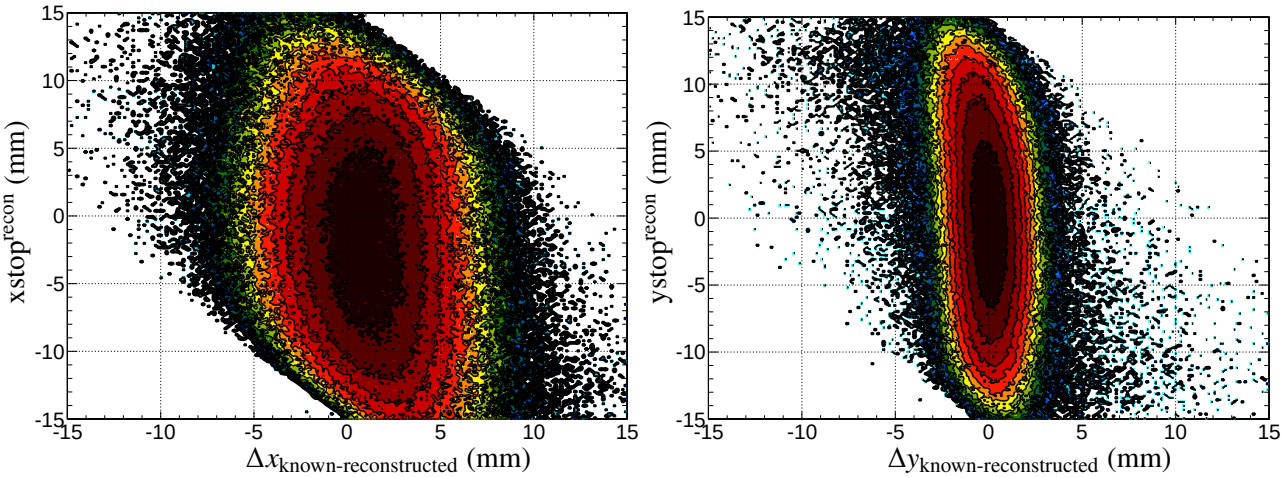

Figure 6.28: *Comparison of known values from GEANT4, and reconstructed from mTPC waveform analysis of the pion stopping positions in the target. Left: x stopping position. Right y stopping position.*

6.7 PCOS and ZCAT Bank - MWPC

As stated in the experimental description, the MWPC is used for charged particle tracking. Even though the simulation is privied to "god's values" in terms of position and tracking of secondary particles, proper simulation of MWPC is necessary for higher order observables such as positron predicted energy. The requirements that must be met are to ensure that the simulated MWPC is as realistic as the real MWPC. This entails ensuring the wires and cathode strips are placed in the proper position, the differences in the surfaces are represented, and that the full detector response (i.e., baseline, noise etc) is accounted for and the induced charge accumulated on the cathode strips is properly simulated. The first and arguably the easiest task is to ensure that the geometry of the MWPC is fully accounted for in the simulation. Since the cathode strips follow a helical pattern, and the wires are parallel the z-axis, there are only certain combinations for the wires and strips to concurrently produce a signal. By plotting the wire hit versus the strip hit for charged particles, both measurement and simulation should demonstrate the same structure representing the geometry associated with the MWPC. The allowed wire and strip combinations are shown in Fig 6.29.

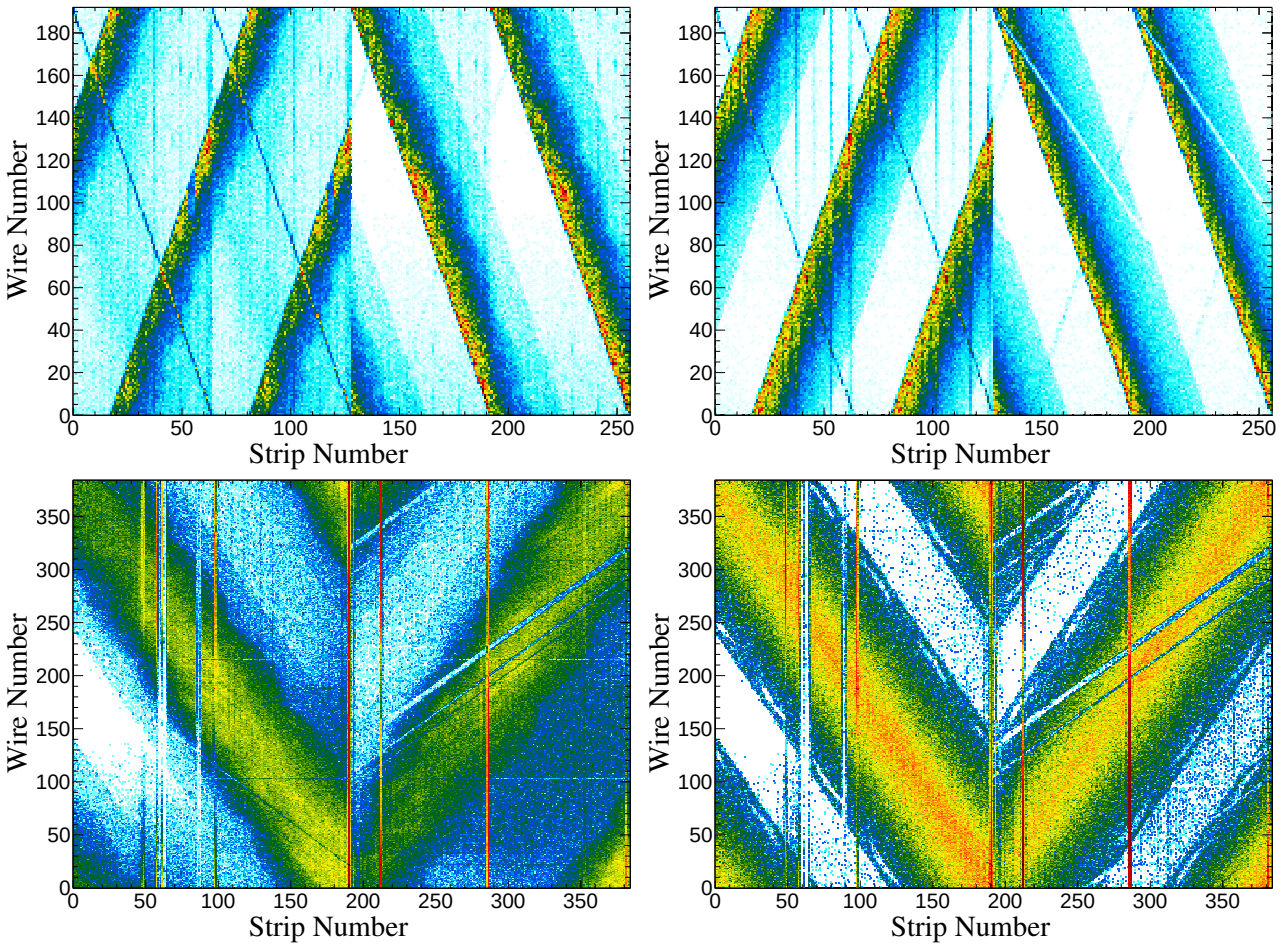

Figure 6.29: *A check on the geometry, strips corresponding to particular wires. Plots are of wire number vs strip number. Upper Left: Inner chamber measurement. Upper Right: Inner chamber simulation. Lower Left: Outer chamber measurement Lower Right: Outer chamber simulation.*

Notice the change in directions of the signals beyond strip 128. This occurs because the strips designated beyond 128 are in the outer surface of the inner chamber. Surface 1 is the inner surface of the inner chamber for $z < 0$ which comprises 64 cathode strips. Surface 2 is the inner surface of the inner chamber for $z > 0$ comprising also 64 strips. Surfaces 2 and 3 also are composed of 64 strips each for $z < 0$ and $z > 0$, but these are the outer surfaces of the inner chamber. This is precisely why the directions change. The structures for the combination of wires and strips are clearly matched. The outer chamber only comprises two surfaces, the inner and outer. Note there are blank (white) strips that appear in the different regions where combinations are allowed in particular in the outer chamber. In the outer chamber, there were various strips that had failed at various points and even three through the entire running period. No signal is seen in these strips. Simulation is constructed to also remove these strips by setting the gains of these particular strips to zero.

To determine the full detector response, other steps have to be introduced. The first and arguably the easiest thing to simulate with regards to the MWPC is the baseline. Since there are 640 cathode strips spanning six surfaces, for any given event or positron trajectory, the vast majority of strips will not be hit. Finding the baseline becomes trivial, all that is required to do to look at the raw cathode signals for the thousands of events and the peak for each cathode strip will represent the baseline. Baseline representation for different strips are shown below in Fig 6.30.

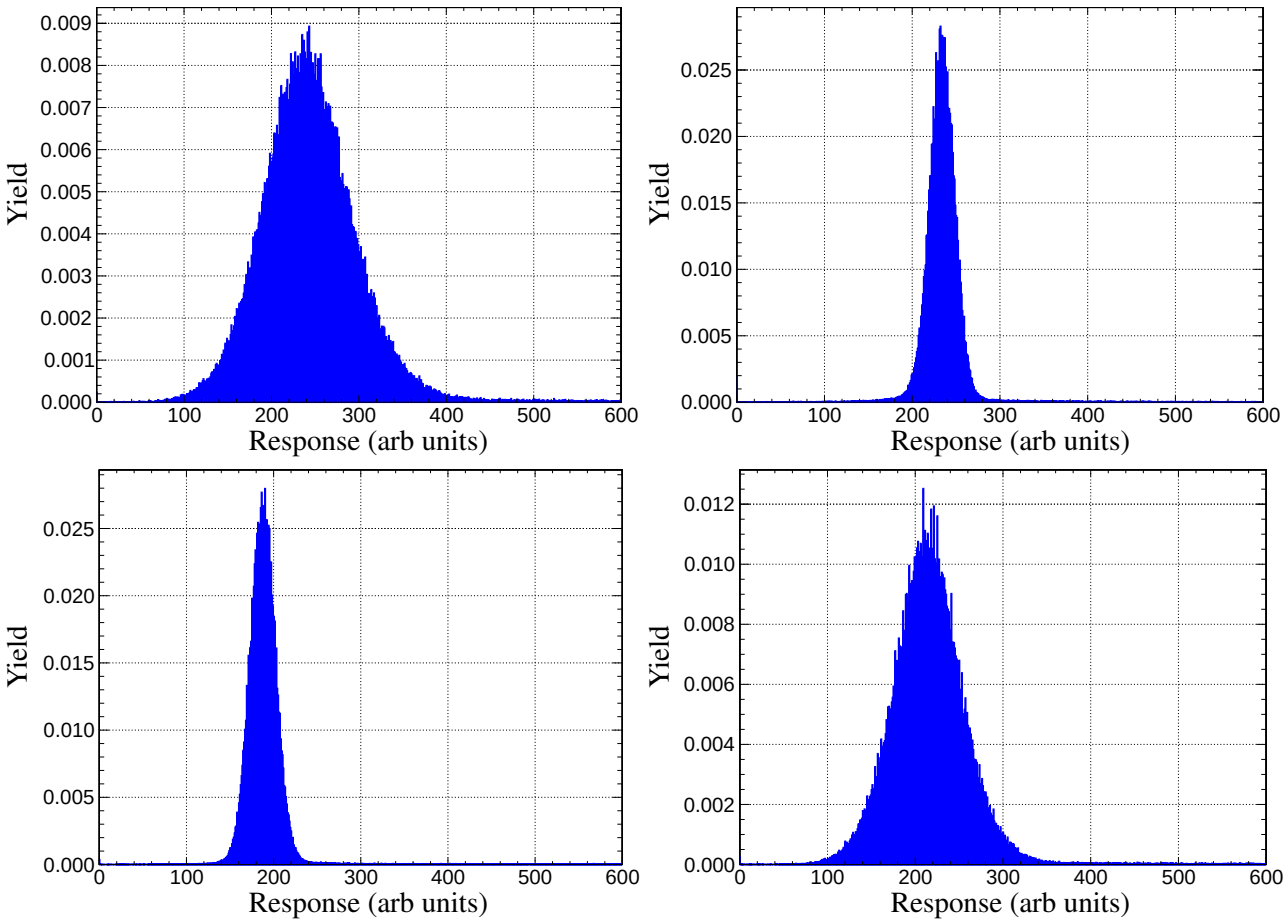

Figure 6.30: *Raw cathode signals for various strips in different surfaces. Upper Left: Strip 5. Upper Right: Strip 156. Lower Left: Strip 300. Lower Right: Strip 467.*

This ADC baseline is put into the simulation whether or not a strip was hit in the simulation. The baselines for strips not only have slightly different means, but also the rms values of these channels are different. The noise from the MWPC comes from two main sources. The first source is the common noise that comes from a common topology. There is a low-frequency oscillation, common to neighboring ADC channels, due

to being connected to common electronics. Of course, each channel will also have its own noise, associated with that particular channel and this is the second. So a common noise was put in each of the six surfaces and an individual noise was put on each channel in order to properly simulate the type of background that is used to determine positioning in the simulated MWPC chamber. Now the baseline that is used in analysis is the sum of three of the lowest lying strips in each of the surfaces, as stated already. Comparison of simulation and measurement of the baseline for all 640 channels is shown in Fig 6.31.

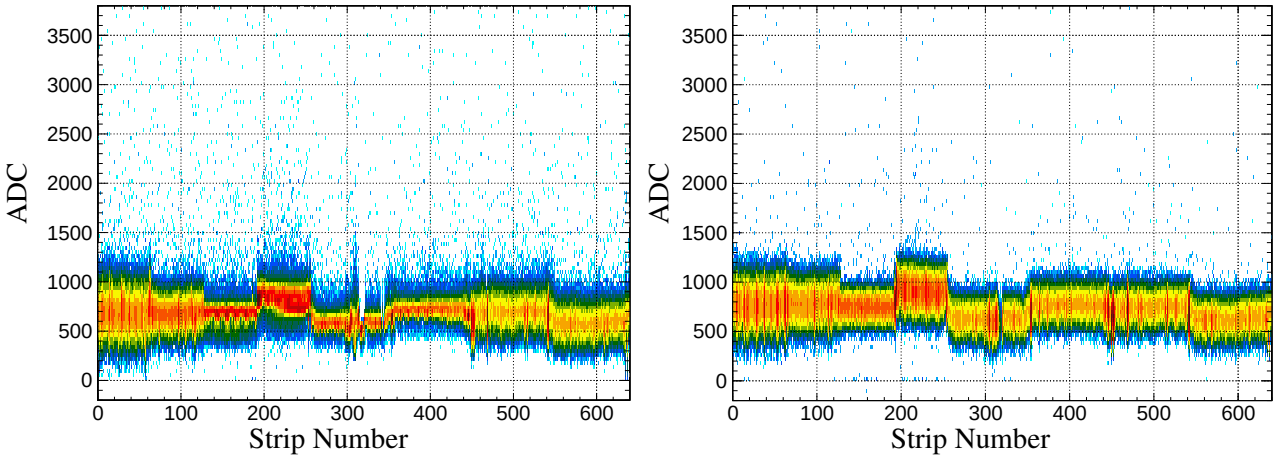

Figure 6.31: *Comparison of measurement (left) and simulation (right) for the MWPC baseline of all 640 cathode strips.*

Once the baseline is simulated, the signals must be properly simulated. Therefore a review of how a signal is constructed is described first.

A Multi-Wire Proportional Chamber, acts like a regular proportional chamber, but can be used to determine more than one coordinate of charged particles. Upon entering the gas in the proportional chamber, the charged particle creates ion pairs. The ions will be driven towards the anode wires, thus inducing a positive charge on the cathode strips. Since our detector has cylindrical geometry, the wire that lights up gives the ϕ direction (that is x and y) and the cathode strip that receives the most charge will give us the z direction. Thus the position that the charged particle traverses can be determined. Having two chambers, ensures that the charged particle projects back to the target.

In order to simulate the charge induced on the cathode strips, we use an empirical formula for symmetrical MWPCS. This formula uses a geometric function with only one parameter in order to determine the induced charge on the cathode strip. If we let $\rho(\lambda)$ be the cathode-induced charge distribution in a symmet-

rical chamber, with $\lambda = x/h$, with x being the distance from the anodes, then from Matheison[62]:

$$\frac{\rho(\lambda)}{q_a} = K_1 \frac{1 - \tanh^2(K_2\lambda)}{1 + K_3 \tanh^2(K_2\lambda)}. \tag{60}$$

where

$$K_1 = \frac{K_2\sqrt{K_3}}{4\tan^{-1}(\sqrt{K_3})} \qquad \text{and} \qquad K_2 = \frac{\pi}{2}\left(1 - \frac{\sqrt{K_3}}{2}\right). \tag{61}$$

Here q_a is the net anode charge. The values of the single parameter K_3 have been presented as a function of chamber parameters, typically either the ratio of the anode wires divided by the pitch or anode cathode separation divided by the pitch.

Before using this formula, it only makes sense to see whether this formula accurately describes the charge distribution induced on the cathode strips in the first place. The comparison is illustrated in Fig 6.32

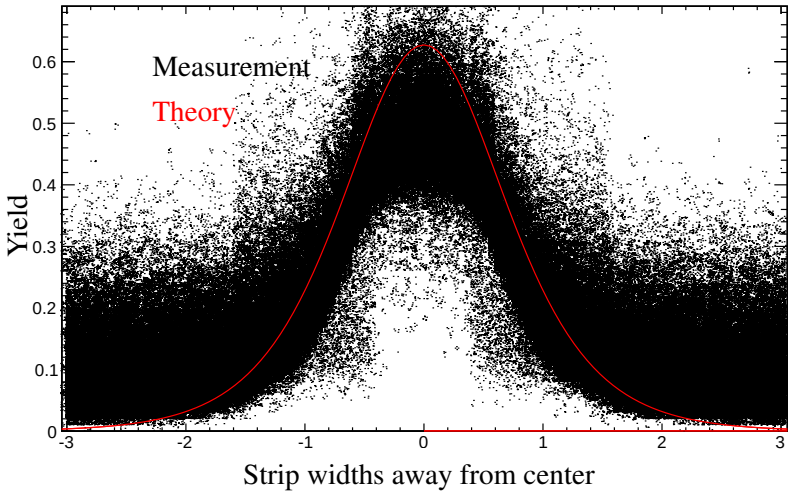

Figure 6.32: *Empirical induced charge fraction (red) and induced charge fraction from measured data (black) vs strip lengths away.*

By inspection, the empirically determined induced charge distribution agrees well with the measurement. Thus using the empirical formula to calculate charge induced on cathode strips is acceptable. The importance of the distribution cannot be overstated, in particular because the inner chamber has four surfaces rather than two (as pointed out in the experimental section). When looking at cathode signals, and determining charge collected on the strips, the measured data and the simulated data should be consistent.

This is observed in Fig 6.33

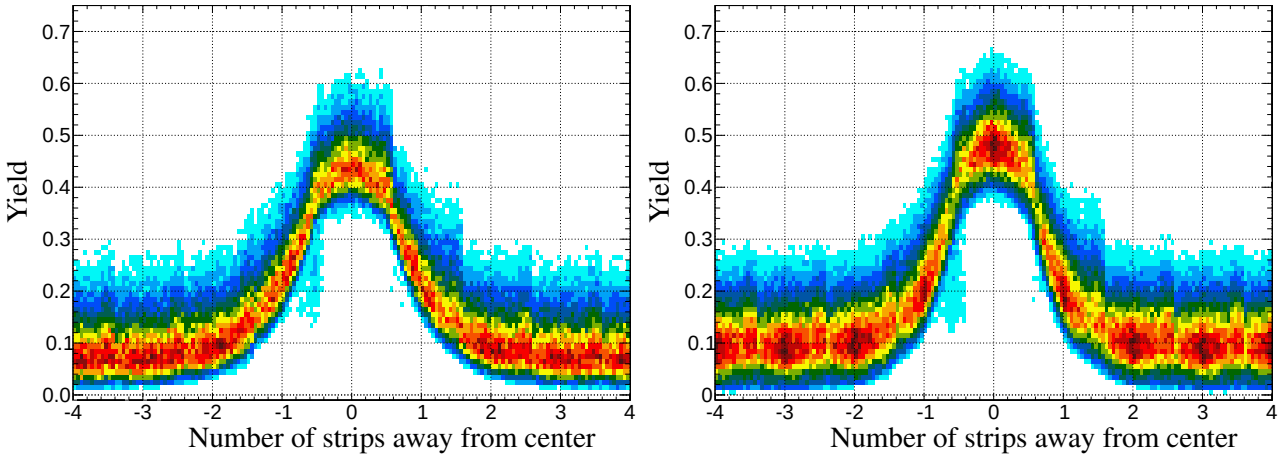

Figure 6.33: *Induced charge as a function of distance away from the main strip. Left: Measurement. Right: Simulation.*

Once the geometry and the simulated charge distributions are comparable to the measured data, the subtle intricacies of the detector are included to ensure that Monte Carlo properly simulates the measured data. In particular, it was noted that the inner chamber has four surfaces that are divided at the z=0 plane. It begs the question then how does the detector respond when a positron traverses near this plane. When positron crosses near the z=0 plane, the surface charge is shared by both the upstream and downstream surfaces for the inner chamber. The further downstream the positron is, the more induced charge will appear on the downstream strips and vice versa for upstream. This feature must be replicated in the simulation if the simulated MWPC is to be useful. By observing perpendicular tracks, (tracks where the polar angle of the main crystal is between 80 and 100 degrees) comparing the simulated cathode strips and measured strips upstream signal versus downstream signal, any correlation or pattern must be replicated. This is indeed the case as illustrated in Fig 6.34 and Fig 6.35.

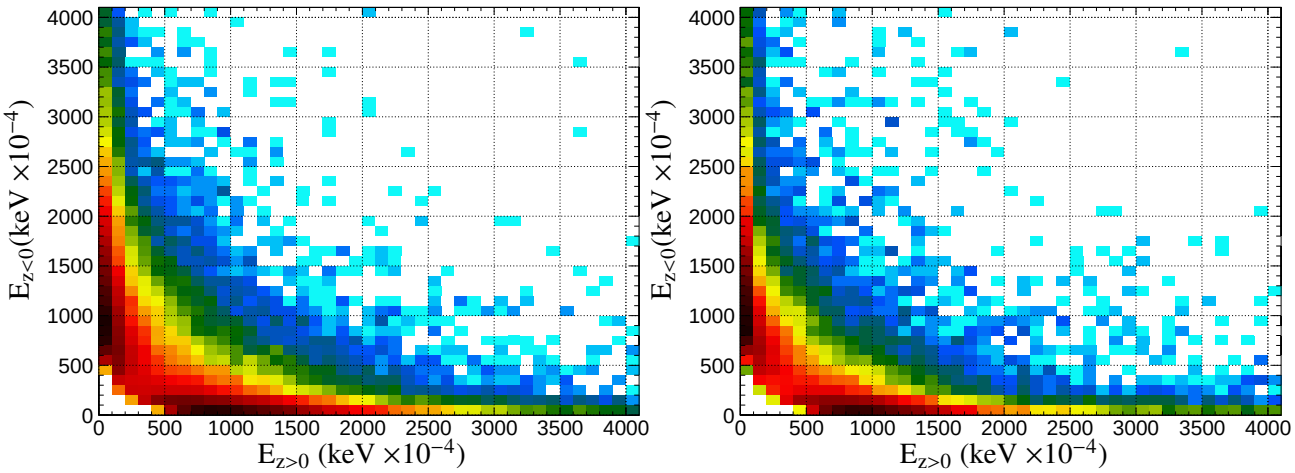

Figure 6.34: *Check on proper correlation between upstream and downstream for perpendicular tracks around z=0. Left: Measurement. Right: Simulation.*

This is also corroborated by viewing the z profile of the inner chamber and comparing measurement and simulation.

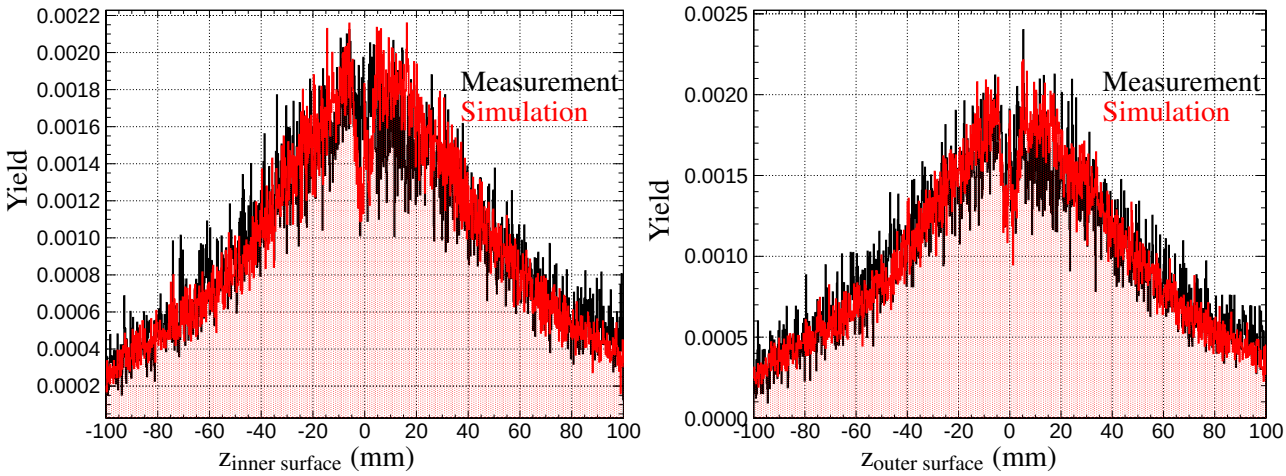

Figure 6.35: *Profile of z distribution in inner and outer surfaces of inner chamber.*

Finally, the charge distributions relations for inner and outer surfaces must be reconciled. That is ensuring that the charge differences between inner and outer surfaces and the correlations are correct. There is no reason to suspect that inner and outer surfaces should be different. If a decay particle induces a significant amount of charge in the inner surface, it should do the same with the outer surface. These correlations are, not unexpectedly, reproduced in the simulation as seen in Fig 6.36.

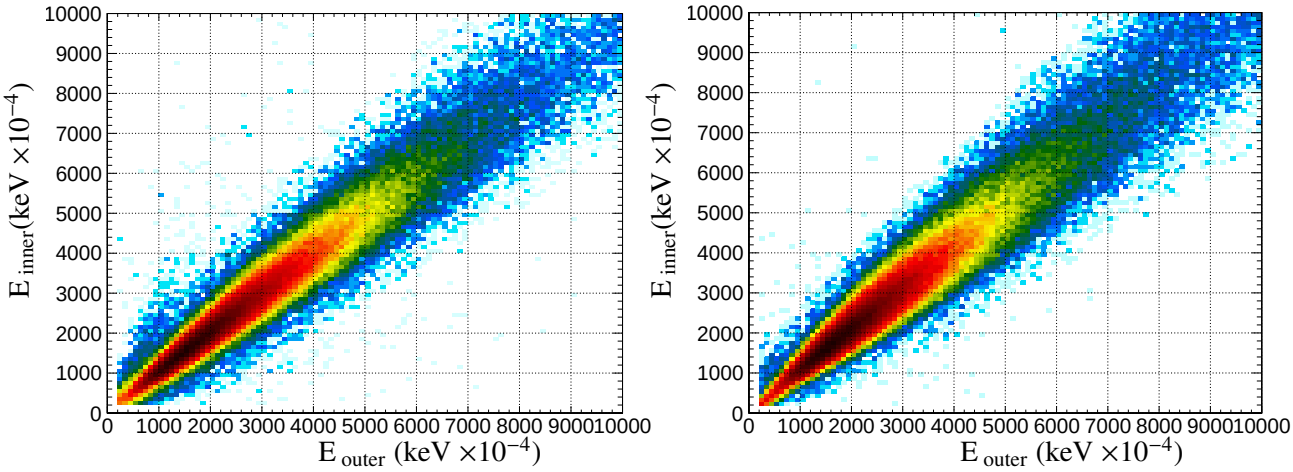

Figure 6.36: *Comparison of inner and outer charge for measurement (left) and simulation(right).*

Recall, there are two data banks for the MWPC. One bank records whether or not a wire was hit, the other records the ADC response of each of the 640 cathode strips. After the same algorithms on the MWPC from the data are performed on the simulated MWPC signals, the deduced z position of the positron in both z and ϕ are reproduced from the known values. Fig 6.37 shows these residuals.

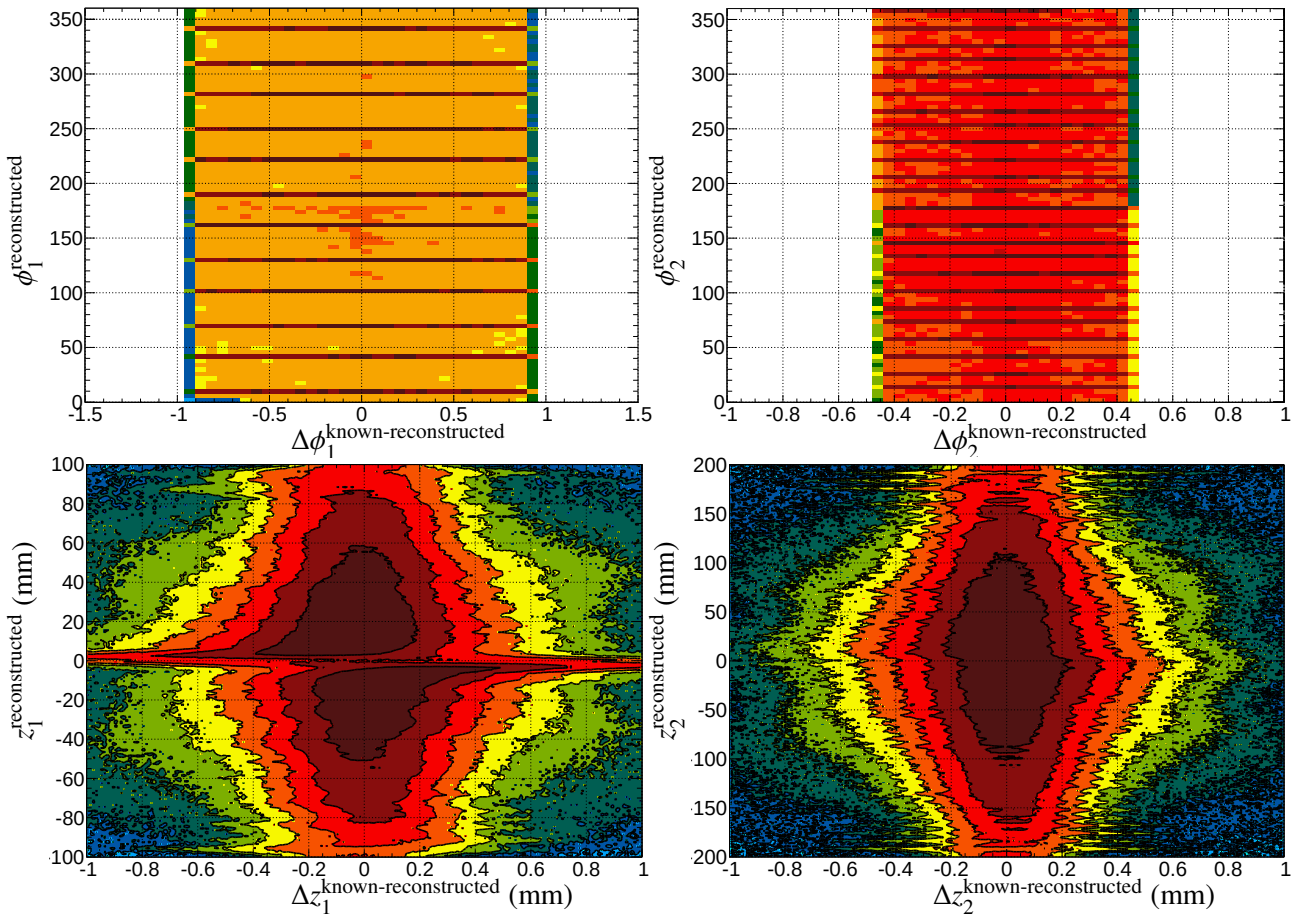

Figure 6.37: *Comparison of Residuals for z and ϕ values of the MWPC as a function of z and ϕ respectively. Upper Left: Wire 1 ϕ residuals. Upper Right: Wire 1 z residuals. Lower Left: Wire 1 z residuals. Lower Right: Wire 2 residuals.*

The plots of the residuals in Fig 6.37 highlight two important features. The first is that the inner chamber has a worse azimuthal reconstruction then that of the second wire. This is because there are two times more wires in chamber 2 than in chamber 1. The second is that the difference between known and reconstructed z values are consistent for the second chamber but not so much for chamber 1 around z=0. In the simulation, the analysis is privied to the exact information as to where the positron intersects the MWPC volume. However, because of the splitting of the chamber 1 down the middle, when the positron crosses this region, the charge is shared upstream and downstream and thus there is ambiguity as to where exactly the positron traversed the region when analyzing the signal charges, a feature of the inner chamber in the PEN experiment. When compared to the known energy deposited in the gas, it is expected that the amount of induced (and recovered) charge is proportional to the energy lost in the chamber. Fig 6.38 shows the MWPC gains on the order of 10^6.

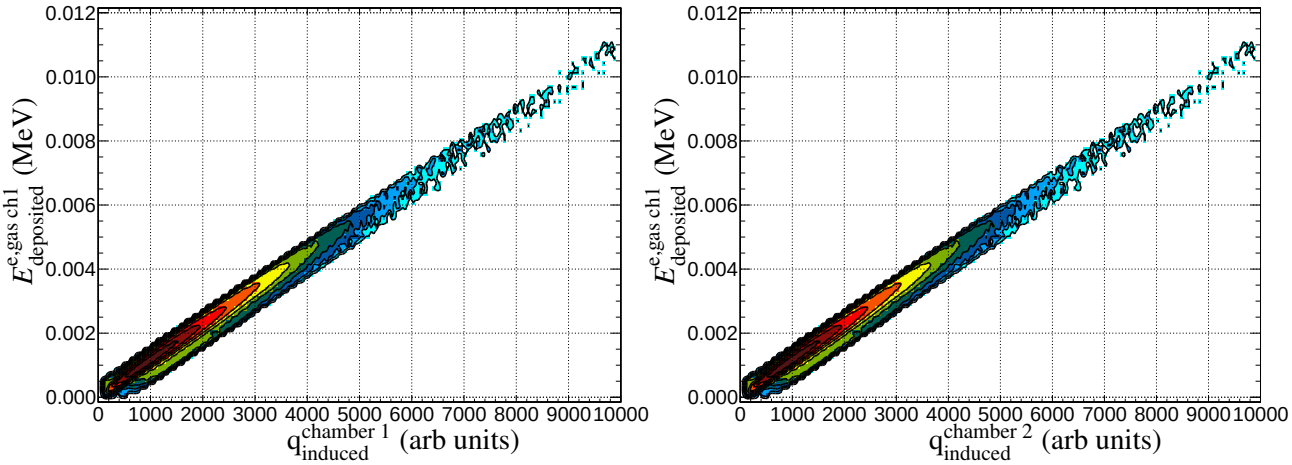

Figure 6.38: *Reconstructed induced charge as a function of energy deposited in the gas by the positron. Left: Inner chamber. Right: Outer chamber.*

In the measurement, there is a threshold of energy deposition that must achieved in order to record whether any charge accumulates on the wire. Similarly for the cathode strips, or at least there is an efficiency for recovering whether or not a cathodes strip produces a signal. In the simulation there is no threshold put on any of these two detectors for two reasons. The first is that since MWPC is not present in the triggering conditions, whether or not a strip/wire is fired does not affect recorded events. It may however, affect event selection, which brings us to the second reason. That is that in the simulation, it is known that the positron goes through the gas and that a wire and set of strips get fired. By accurately recreating the signals and full detector response in the simulation, we can understand the inefficiencies of cathode signals and wire signals in the measurement. In other words, efficiency of seeing a signal in the MWPC does depend on the particle energy so the simulation can help determine how well we reconstruct a signal at given energies knowing a positron was there. By doing this, the efficiencies of the MWPC as a function of positron energy can be constructed. One might inquire as to why the simulation is needed to do this. In the measurement, the energy that positron has going into the MWPC is not known for Michel events (because this is an energy spectrum). If an event is classified as a signal event, this means the birth energy of positron is 69.8 MeV and by subtracting the energy deposited in the target, one can obtain the energy of the positron as it goes into the MWPC. However, if it is a Michel event, the birth energy is unknown. An educated guess may be made based off of energy detected in the calorimeter, but this is not precise. So by having no threshold in the simulation, inefficiencies of the MWPC may be understood and reproduced. As will be shown, the MWPC efficiency will be necessary in order to calculate the branching ratio.

6.8 ZADC/LTDC bank - Plastic Hodoscope

The plastic hodoscope is a plastic scintillator array which serves multiple purposes. It is used to veto hadronic events, it is used for event timing, and for identifying charged particles. The apparatus contains twenty such staves which are approximately 40 cm long and each stave has an ADC and TDC attached to lightguides at each end. When a charged particle crosses the stave, the scintillated light will have to travel to the two ends in order for the light to be recorded for time or energy. When simulating the response of the hodoscope this propagation of light must be fully accounted for in order to fully recreate the PEN detector response. In the GEANT4 simulation, the time when the positron crosses the hodoscope can easily be obtained. However, this is not the time the TDCs will record. As stated, the light must travel to the ends of the hodoscope in order for the TDC times to be recorded. This time can be determined by taking the global time, otherwise known as the "Geant time" and adding to it the time it would take for light to propagate to the ends of the scintillator stave:

$$\mathrm{TDC_{time}} = \text{Global time} + \frac{|z - L/2|}{c/n} \tag{62}$$

where $|z - \frac{L}{2}|$ represents the distance from the positron position in the hodoscope to the one of the ends of the hodoscope and c/n is the velocity of light in the plastic, where n is the index of refraction, in this case, $n = 1.6$.

However, this is not the whole story, the light itself will undergo reflections within the material which makes the effective speed even lower. In order to determine the effective speed of light in the material one can look at the time differences between the upstream and downstream hodoscope signals as a function of where the positron crosses the hodoscope as determined by the MWPC. This was shown already in the previous chapter. When observing the time difference as a function of the position, one-half the slope gives the effective velocity. This is derived by considering a positron crossing at a position z. Then the times that it takes to reach the upstream and downstream ends respectively are

$$\mathrm{t_{up}} = \frac{z + L/2}{v_{\mathrm{effective}}} \qquad \text{and} \qquad \mathrm{t_{down}} = \frac{L/2 - z}{v_{\mathrm{effective}}}. \tag{63}$$

Hence, the difference in times $\Delta t = t_{up} - t_{down} = 2z/v_{effective}$. Plotting Δt against z gives the slope as $2/v_{effective} = 0.15$ this gives an effective light velocity of 133.3 mm/ns. Using this velocity in the simulation we see the time differences between the hodoscope ends are plotted in Fig 6.39.

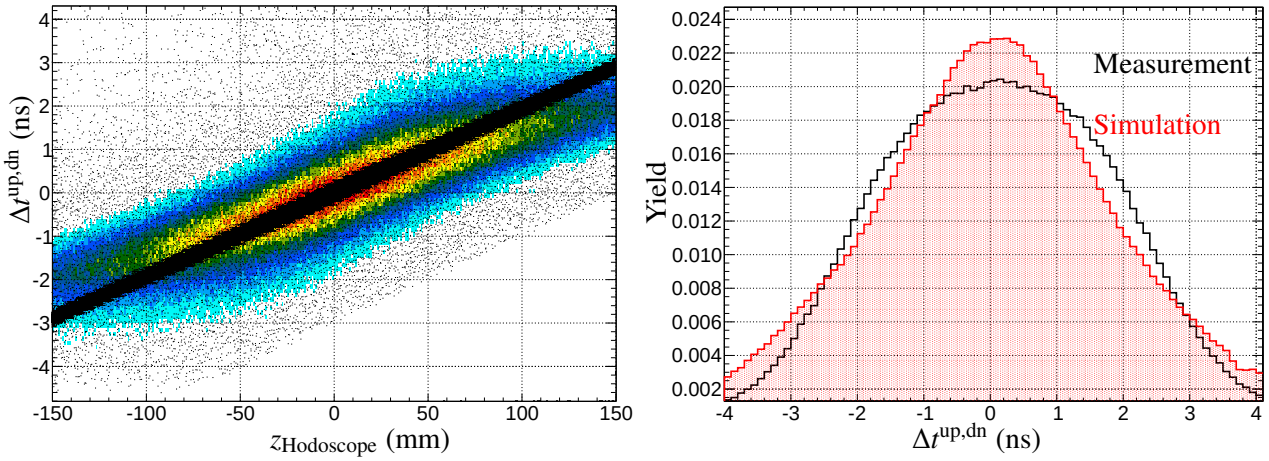

Figure 6.39: *Difference in time between upstream and downstream times in the hodoscopes. Left: As a function of the z position where the positron is hit. Right: Comparison of simulation and measurement.*

The broadened Gaussian distribution between the upstream and downstream times in the hodoscope is attributed to the internal reflections of light within the hodoscope. If positron passes near the end of one hodoscope, there will be little if any light reflections within the hodoscope on that side, and substantially more reflections when the light reaches the other side. In the middle, there is roughly equal amount of reflections so the delay in time is symmetric. The simulation only utilizes the time expected time of flight and the resolution of the TDC. It does not include position dependent time difference based on internal reflections. In addition, there are slightly different effective velocities within each of the hodoscopes because of non-uniformities. This is not included in the simulation, mainly because these are smaller effects that will have no bearing on the analysis itself. But it is seen that the speed in the simulation is properly utilized and could (arguably) be made even more realistic. In addition, the difference between the times in the target and the hodoscope or rather the average of the up and downstream TDC values should be consistent with measurement. Fig 6.40 shows that this is the case.

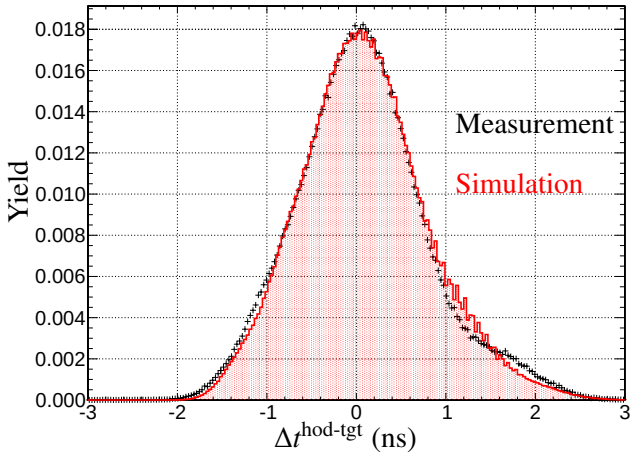

Figure 6.40: *Average timings in the hodoscopes relative to the target time.*

Since the light must travel a certain distance, the intensity of the light produced will be attenuated when it reaches the ends of the hodoscope. There are two methods which can account for this process. The first is to that the energy is attenuated according to a simple relationship:

$$\text{Energy Recorded} = \frac{1}{2}\text{Energy Deposited} \times e^{-\frac{|z-L/2|}{\lambda}} \tag{64}$$

where Energy Deposited is the amount of energy that the positron deposits in the hodoscope, and λ represents the attenuation length of the hodoscope. This method however, has one major drawback. This method assumes the attenuation length of a given hodoscope is the same throughout. In other words non-uniformities are not taken into account. This can be rectified by using the second method to fully account for the attenuation. This method relies on the data calibrations and analysis which allow us to parameterize the attenuation for each hodoscope as a function of position, which was briefly discussed in the previous chapter. To reiterate, if the positron crosses the hodoscope in the center, one would expect the ADC signals to be identical because the scintillated light must go the same distance in order to reach the ends of the hodoscope. However, if the positron crosses the hodoscope closer to one edge of the hodoscope, one would expect this ADC to have a higher value precisely because the light is not attenuated as much. Using this fact and the fact that since the positron is a minimum ionizing particle and dE/dx for this particle is well known for this scintillator, a position dependent parameterization of the attenuation can be achieved for each of the twenty hodoscopes. Fig 6.41 shows the different attenuation features of the twenty separate staves and the simulated responses of each of these scintillators.

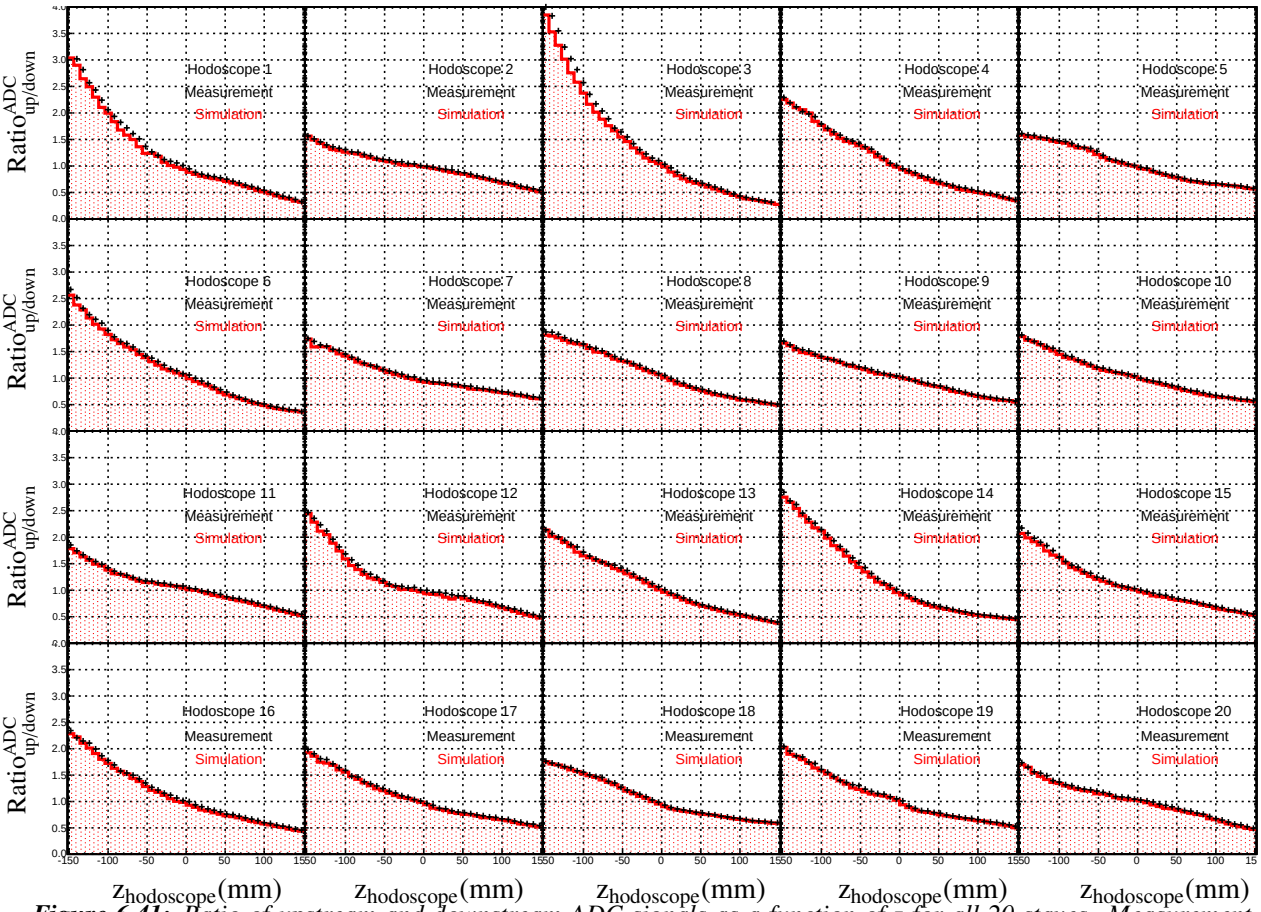

Figure 6.41: *Ratio of upstream and downstream ADC signals as a function of z for all 20 staves. Measurement in black and simulation in red.*

As was stated, the hodoscope TDC value represents the trigger time and is used to calculate the predicted positron time in the target. As was demonstrated, depending on which hodoscope was hit, the trigger is delayed by a certain amount. So this property must be reproduced in the predicted as well as the observed target times.

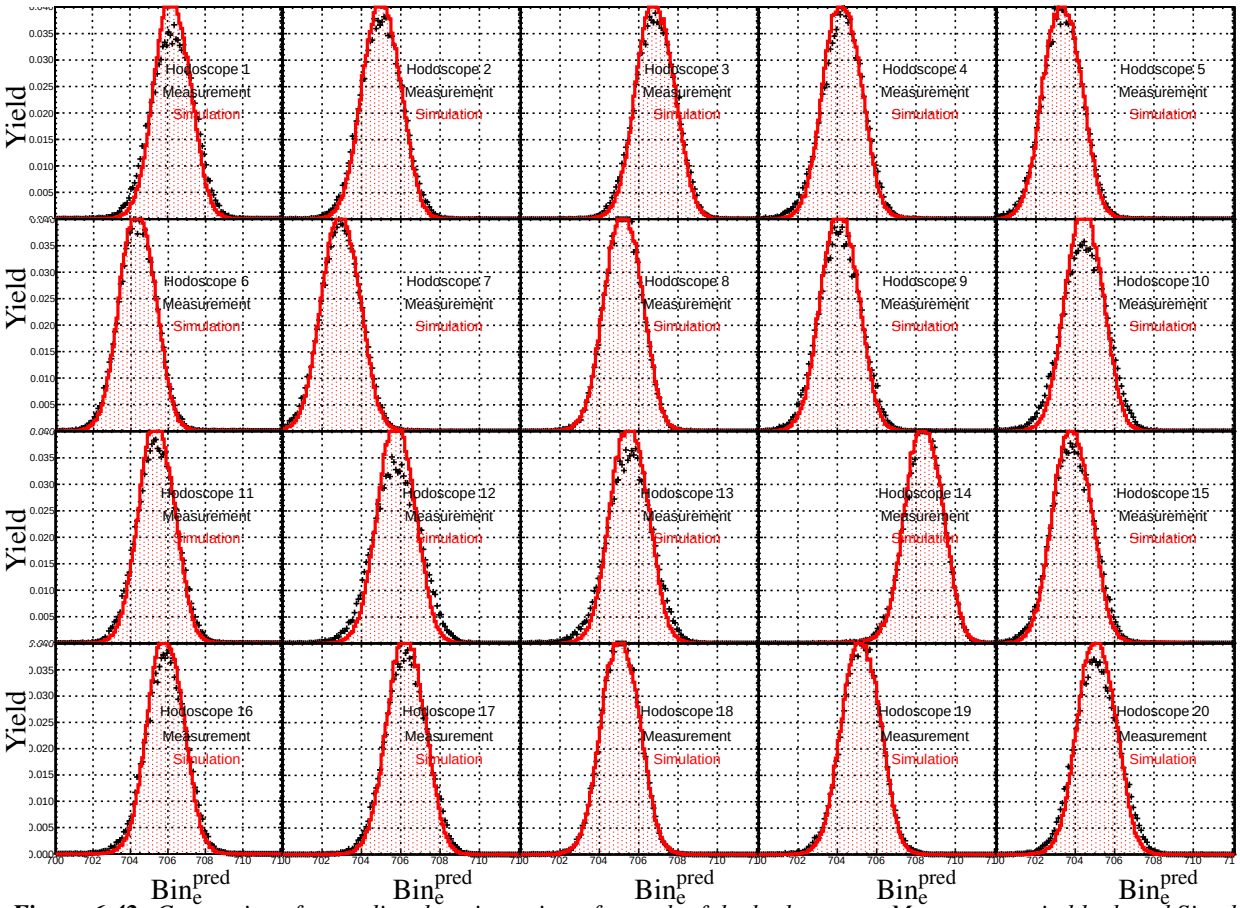

Figure 6.42: *Comparison for predicted positron times for each of the hodoscopes. Measurement in black and Simulation in red.*

There are two key things that must be addressed with regards to the predicted time of the positron, i.e., the hodoscope times. The first is that much like the waveform, the timing depends on which hodoscope was hit because of different delays in the hodoscope. However, all this does is shift the time in all the waveforms and TDCs because everything is relative to the trigger (hodoscope) time. In other words, all times are shifted by the same amount (the delay) in a given hodoscope, so that the difference in times will be the same. The second noticeable feature is that the hodoscope times in the simulation have a smaller rms than the measurement as seen in Fig 6.42. This is because time difference between upstream and downstream TDCs in the hodoscope add a level of complexity which is not simulated as seen in Fig 6.39. This does not become problematic because the analysis actually relies on the difference between the predicted and observed times which is more consistently matched between simulation and measurement as will be seen.

6.9 ZADC/LTDC bank - CsI Calorimeter

The CsI EM calorimeter is arguably the most important detector element. It is this detector element where most of the positron's energy is deposited and thus discrimination of the different decay channels is obtained. In addition, this detector contains the crucial knowledge of the response of the energy spectrum for the $\pi^+ \to e^+\nu_e$ channel which contains a low energy tail due to energy leakage as shown in Fig 6.1. The ratio of the events in the tail to those in the peak for this channel is a necessary quantity for the branching ratio calculation. The GEANT4 simulation determines the energy deposited in the CsI calorimeter for every simulated event. However, it does not reproduce the full detector response. As an example, suppose a mono-energetic particle of 69.5 MeV were thrown into the calorimeter and suppose there was a method to fully contain the electromagnetic shower. Then the energy deposited for each such event would be 69.5 MeV. Even if this type of detector were constructed, this would not be the measured reading. The shower produces photons which were are eventually guided to photomultiplier tubes. The light guide efficiency, the quantum efficiency of the PMTs and the fact that the total number of photoelectrons produced is a statistical process, prevents any monoenergetic peak in any "perfect" detector from ever occurring. So in order to reproduce the measurement data, these features must be included in the simulation. Further, the GEANT4 simulation would treat all crystals the same when this is not true due to non-uniformities. To see this, we can compare two crystals from the data and see that their energy spectra are different from each other seen in Fig 6.43 below.

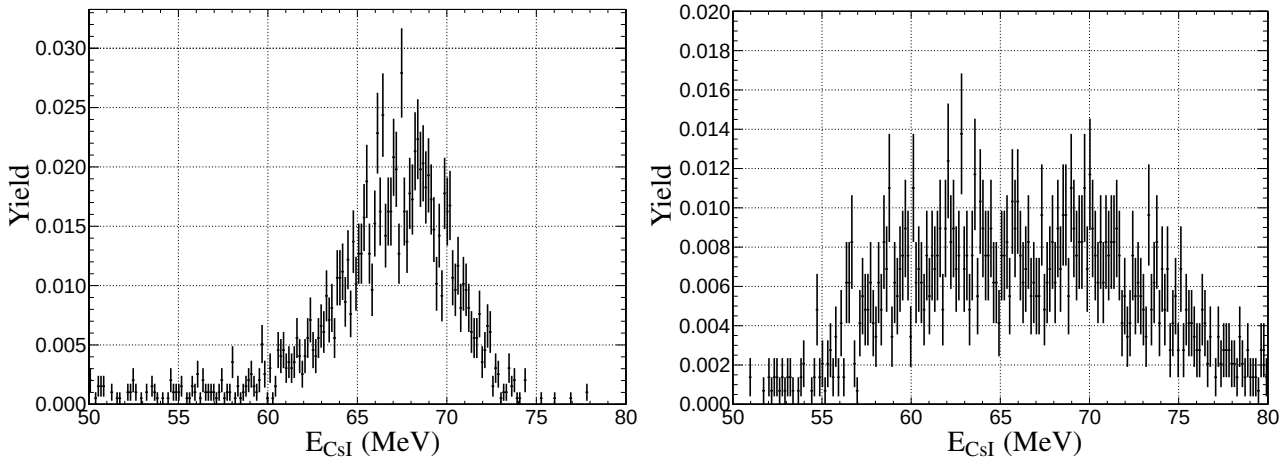

Figure 6.43: *Crystal responses and demonstration of non-uniformities. Left: Crystal 14. Right: Crystal 114.*

In order to ensure that measurement and simulation are consistent, each crystal must be properly calibrated both in rms and mean. The rms is accounted for by the overall photoelectron statistics. It has been shown [60] that the number of photoelectrons produced in CsI is a Poisson distribution where the parameter is proportional to the energy. This is provided that three assumptions be satisfied. The first is that the probability of producing a photoelectron in a time interval t to t+dt is proportional to the intensity of the incoming light $P(1, t, t + \mathrm{d}t) \propto \gamma I(t)$. The second is that the time interval can be chosen arbitrarily small so that only one or zero photoelectrons are produced. The final assumption is that the production of a photoelectron does not affect the probability of producing a photoelectron at a later time. The experiment (and simulation) is constructed and conditioned so that it is safe to make these assumptions. Therefore photoelectron statistics are accounted for in the simulation utilizing random number generators with Poisson statistics. For proper simulation, the energy deposited in a particular crystal is taken from the GEANT4 values. This is multiplied by a scaling factor, call it α. This α has units of MeV^{-1} and $\alpha \times E_{\mathrm{pure}}$ is the parameter that is put into a Poisson distribution. The returned value is divided by α once again in order to return to MeV. Each individual crystal resulting energy value is then scaled to ensure that the crystal peaks are aligned between simulation and measured data. This is necessary because each individual crystal can have had different gains during the course of the experiment. This MeV value is turned into ADC values by dividing MeV per ADC channel which is returned as an integer. Once all of these nuances are implemented, each individual crystal in the simulation displays consistent energy spectra with the measured data. Summarizing, the energy as determined by GEANT4 is smeared by photoelectron statistics, translated into ADC channels with the conversion of the appropriate value (depending on the year) using the ADC channel per MeV, which is then passed on as an integer for analysis. These ADC values are analyzed using the same algorithm that is used for the measured data in order to reconstruct the detected energy. The calibration of all 220 Crystals used (recall 20 crystals are veto crystals) are plotted in the Appendix, while a representative sample of 20 are shown in Fig 6.44 below.

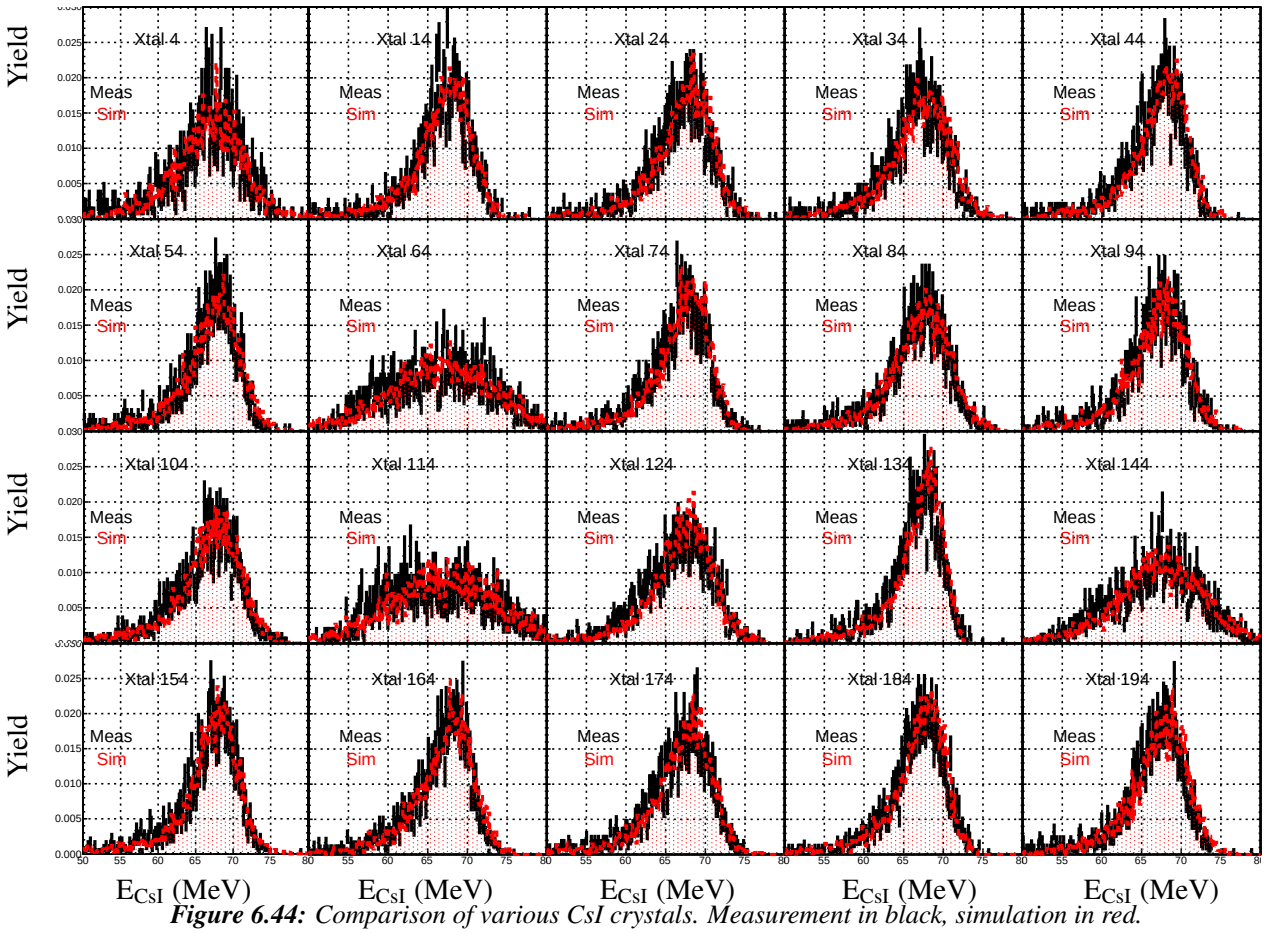

Figure 6.44: *Comparison of various CsI crystals. Measurement in black, simulation in red.*

Applying the proper photoelectron statistics and gains to the simulation was done so by choosing $\pi \rightarrow e\nu$ decays in the measured data. Both the simulated and measured energy of the main crystal was added to the nearest neighbors and was plotted. Events used in this exercise satisfied the condition that the main crystal had at least 80% of the total energy in that clump. The selection also required no energy in the veto crystals (crystals 220-239) unless they were crystals 110-119 or 200-219 as these crystals are right next to the veto crystals. For these particular crystals, 10 MeV was allowed to be in the veto crystals. The simulated veto crystals were calibrated using Michel decays where the veto crystal contained at least 50% of the total energy in the clump. Once each individual crystal is properly calibrated, it is expected that the sum of all crystal energy should be consistent with measurement no matter which method is used to calculate the energy in the crystal as shown in Fig 6.45.

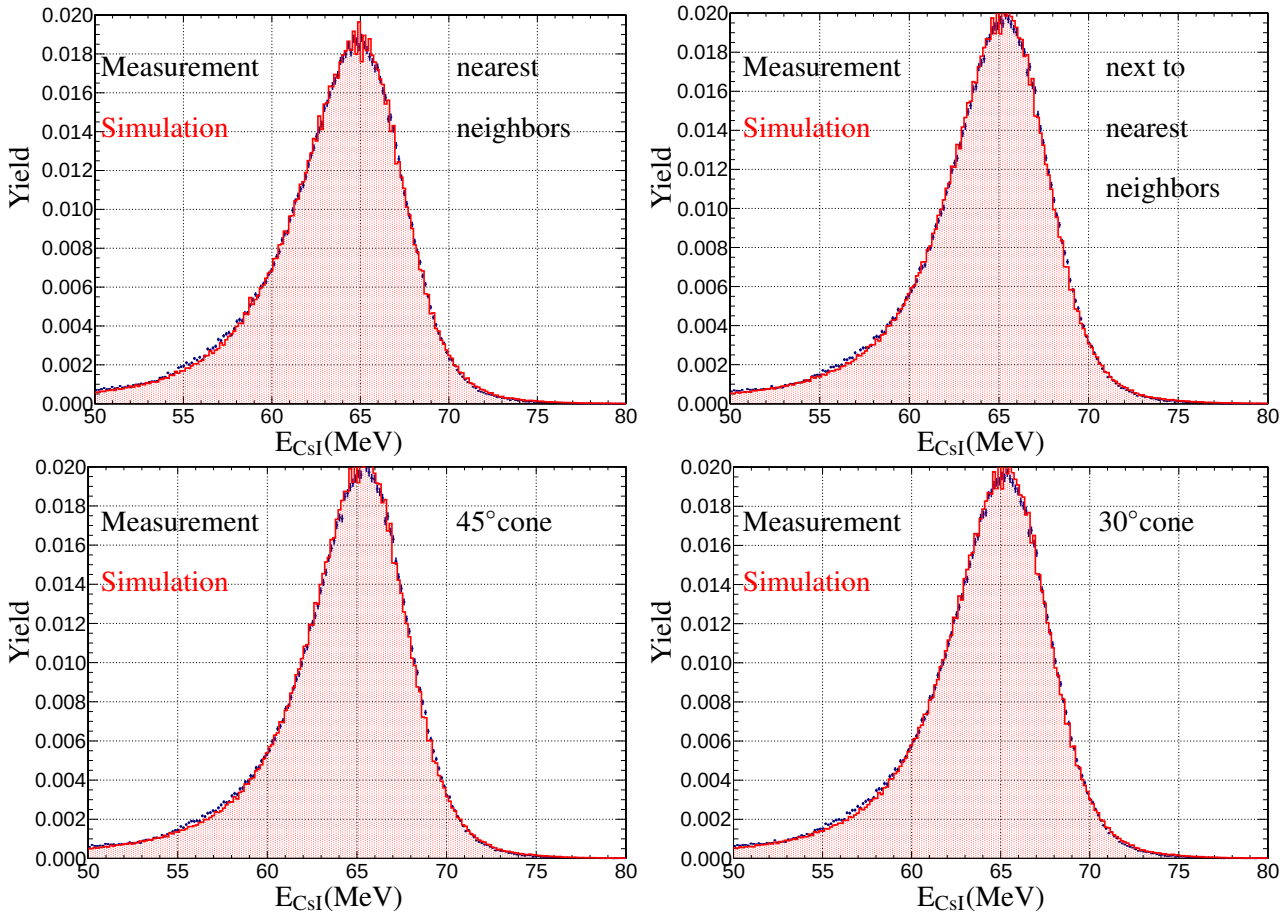

Figure 6.45: *Comparison between measurement (black) and fully detected simulated energy (red) of the CsI calorimeter for the positron shower. Upper Left: Main crystal plus nearest neighbors. Upper Right: Main crystal plus nearest neighbors plus next to nearest neighbors. Lower Left: 45 degree cone. Lower Right: Energy captured in a 30 degree cone.*

The calibration of each crystal was performed at energies above 50 MeV. In order to get the tail to peak fraction, which can only be obtained by simulation at the required level of precision, the simulation must be calibrated to measurement (to represent the detector response of our apparatus) but the measured data must be as clean as possible (free from Michel decays) in order to compare simulation (pure processes by design) and measurement (pure process above 50 MeV by physics). By calibrating the simulation above 50 MeV, the measurement has pure pion decay events, or at least pretty close to clean, and therefore can be used to calibrate the simulation which is pure. The tail itself of course cannot be calibrated and is expected to fall out from the physics of accounting for photoelectron statistics in the higher energy range. Reconstructed energies upon proper reconstruction recreate the energy deposited with proper smearing.

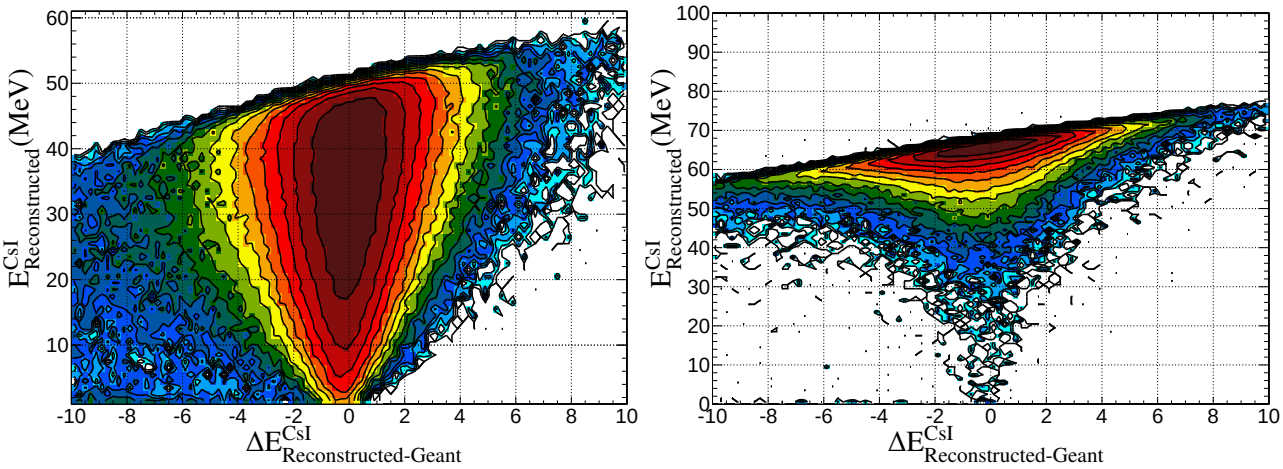

Figure 6.46: *Energy in the CsI as recorded by GEANT versus the difference between recorded and reconstructed. Left: Simulated Michel channel. Right: Simulated $\pi \rightarrow e\nu$ channel.*

Fig 6.46 shows that the difference between reconstructed and known energy is not centered at zero. This is due to a cut in the analysis performed by both measurement and simulation which requires at least 0.3 MeV in a given crystal. If this energy requirement is not met, the software sets the energy value in that crystal to 0. This is to ensure that no distorted signal occurs due to relatively high ADC pedestal noise. Energy reconstruction, while the most important aspect of the CsI, it is not the only purpose of the CsI calorimeter.

The CsI calorimeter also has timing aspects of the showers which can become of great importance in particular for non charged tracks associated with radiative decays. In the simulation, the instance a shower particle deposits energy in a particular crystal, the global time is recorded. The global time once again is the time relative to the start of the simulated event. Since all times are relative to the trigger time, that is the hodoscope time, the global time recorded for the individual crystals is subtracted from the global time of the hodoscope. This time is passed on, a smearing is applied to represent the timing resolution in the actual detector and the resultant time is converted to TDC bins which are then analyzed in the exact same manner as the measurement. The consistency between simulation and measurement is highlighted in Fig 6.47.

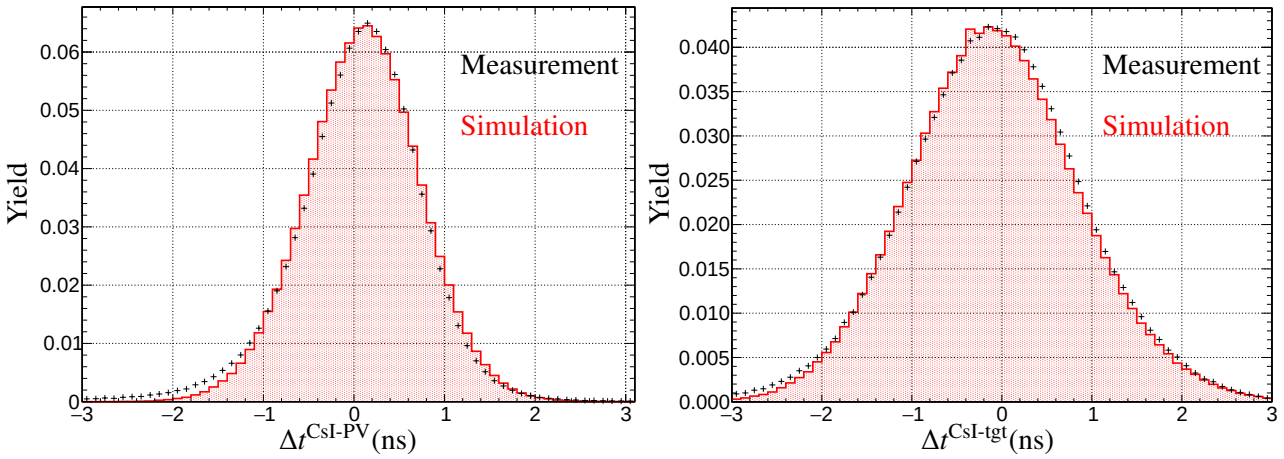

Figure 6.47: *Comparison between time differences of simulation and measurement. Left: Time difference between CsI and plastic veto hodoscope. Right: Time difference between CsI and target for well separated Michel events. Time of flight between the target and CsI was accounted for in the right plot.*

6.10 Validation

Up until now, this chapter has described how the simulation recreates the full detector response using the underling physics as a guideline and showing that measurement and simulation are consistent with each other for particular detector elements. This section demonstrates that for full detector response the data and measurement are virtually indistinguishable for higher order observables, those mentioned in the previous chapter. In other words, this is where everything is put together and any doubt about the accuracy and realism of the simulation is put to rest. By comparing higher order observables which incorporate many different detectors, the conclusion can only be that the unique response of all the detector is recreated accurately in the simulation. Any (small) discrepancies will be explained, but will mostly be due to unwanted contamination of the measured data that was not fully eliminated.

The first important quantity that must be accurate is the beam momentum. In the real experiment, the beam momentum is known only to a certain level of precision. The beam configuration also fluctuates from run to run. In the run period that was canonically simulated, the beam momentum was ascertained to be 72 MeV/c. This is the first place to start. To ensure the proper beam momentum in the simulation, a simple yet effective method is to check to see if the beam particles' time of flight, that is the time of flight between B0 and degrader is consistent for all thee types of beam particles: pions, muons and electrons. In the experiment, these particles have the same momentum, and due to their different masses, their times of flight are different. Further, one can check the ratio of energy deposited in the degrader by the three dif-

ferent particles. Because of the different masses of the muons and pions, the ratio of the quenched energy should be indicative of whether or not the particles have the correct beam momentum. This ideally could be done with the B0 as well, however, there was an energy threshold on the B0 and since this detector is only 3 mm thick and positrons are minimum ionizing, the positron beams won't always produce a signal in the B0. So only the degrader gives a fully reliable option. Since the times of flight for various beam particle simulations were already shown, the degrader energy for these beam particles are now shown in Fig 6.48.

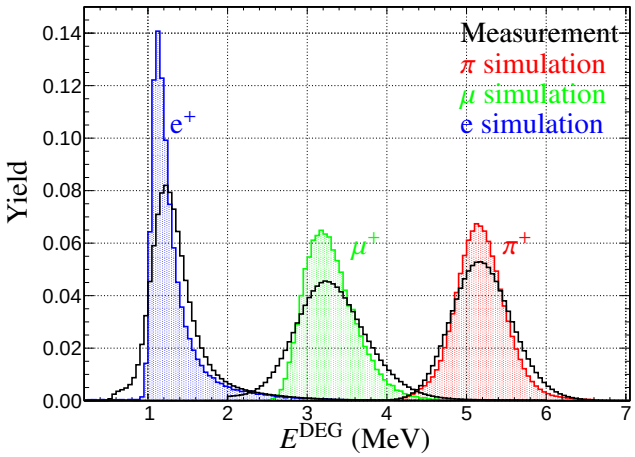

Figure 6.48: *Energy depositions in the degrader for different simulated beam particles compared to the measured counterparts. These are known energy depositions associated with GEANT and photo electron statistics and detector response are not applied here to show raw energy expectations of each particle.*

We can further check to see if the beam momentum is correct by observing the energy deposited in the target by the pion and comparing this to the energy deposited by the muon, as well as the decaying electron. We use ratios here because this will eliminate any ambiguity on target gains for the waveform digitizer. We can also check the time of flight between the degrader and first target signal.

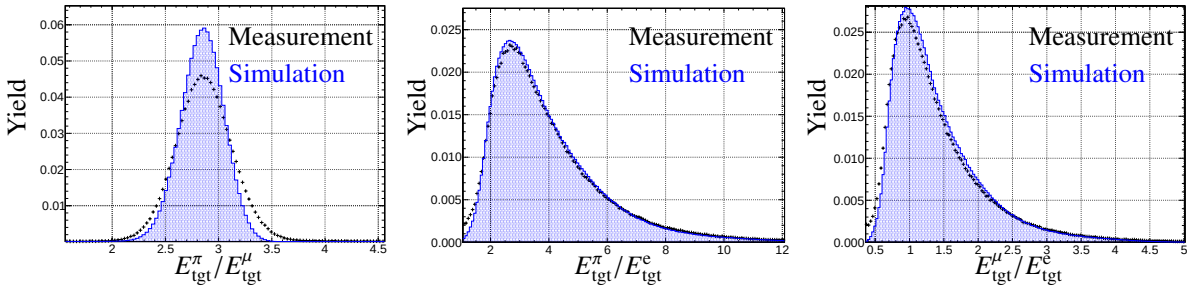

Figure 6.49: *Ratio of energy depositions in target for various events. Left: Target energy of pion divided by target energy of muon. Middle: Target energy of pion divided by target energy of positron. Right: Target energy of muon divided by target energy of positron. Measurement is in black and simulation (known) is in blue. Note these are quenched energies and since these energies are known, photoelectron statistics have not been accounted for nor detector response. The peak and shape are of importance here, not the spread.*

One more check on the beam momentum, is to observe the energy deposited in the target by outgoing positrons when they leave through the back or front of the cylindrical target. Choosing well separated Michel events is the best candidate for these because of the easily identified signals. This was already shown earlier in Fig 6.5. This with Fig 6.6 and Fig 6.48 indicate clearly that the z momentum of the simulation is being replicated in the simulation. This can also be seen by the stopping position in the z direction, designated zstop, as well as the time of flight between the degrader and target. The deduced stopping z position is based on the energy of the incoming pion as it enters the degrader. Knowing the time of flight, and the energy deposited in the degrader, the pion energy leaving the degrader (and thus right before it enters the target) can be deduced. Since there is an established relationship between the momentum and particle range through plastic, the stopping z position may then be calculated and compared with the known value as seen in Fig 6.50.

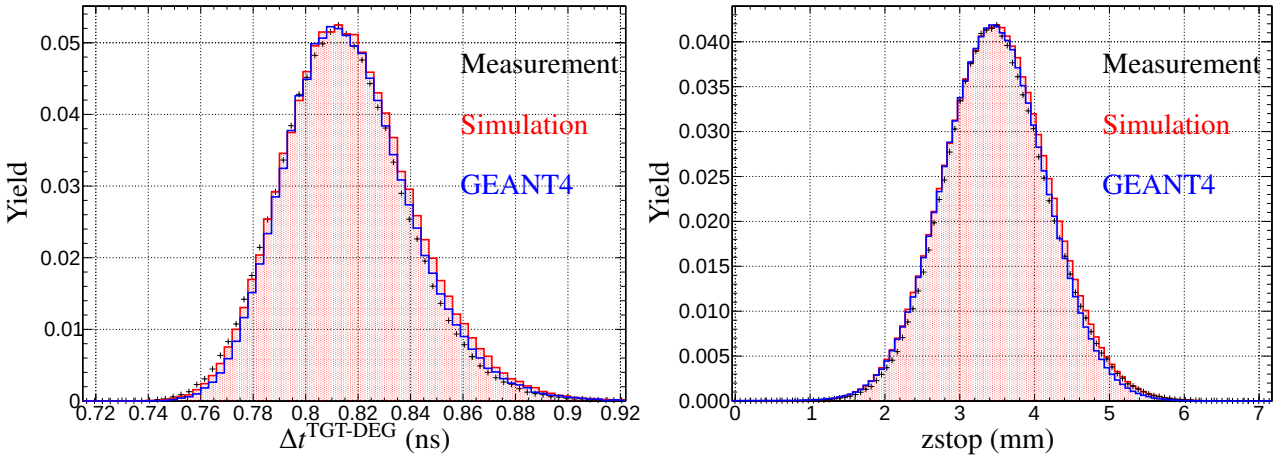

Figure 6.50: *Left: Comparison of time of flight from degrader to target Right: Comparison of z stopping distribution. Measurement in black, simulated (known) values in blue and simulated (reconstructed) values in red.*

But just as important is the profile of the momentum in the x and y directions. The lateral distribution of momentum is crucial because it will determine the stopping distribution of the pion in the x-y plane. This is necessary in order to recreate the experiment fully in the simulation. The beam profile is interpolated from mTPC digitized waveform signals. So not only must it be shown that analysis of the mTPC signals recreates the beam distribution of the experiment, but that the mTPC signals are properly constructed such that they show that the reconstructed beam profile and the known GEANT4 beam profile are a good match. The beam profile, already shown, was produced using the algorithm in the mTPC to determine the x and y positions at any given z based on the response of the traversing pion through the mTPC. Since the reconstructed profiles are consistent, the stopping positions in x and y should also be consistent. This is seen in Fig 6.51 below.

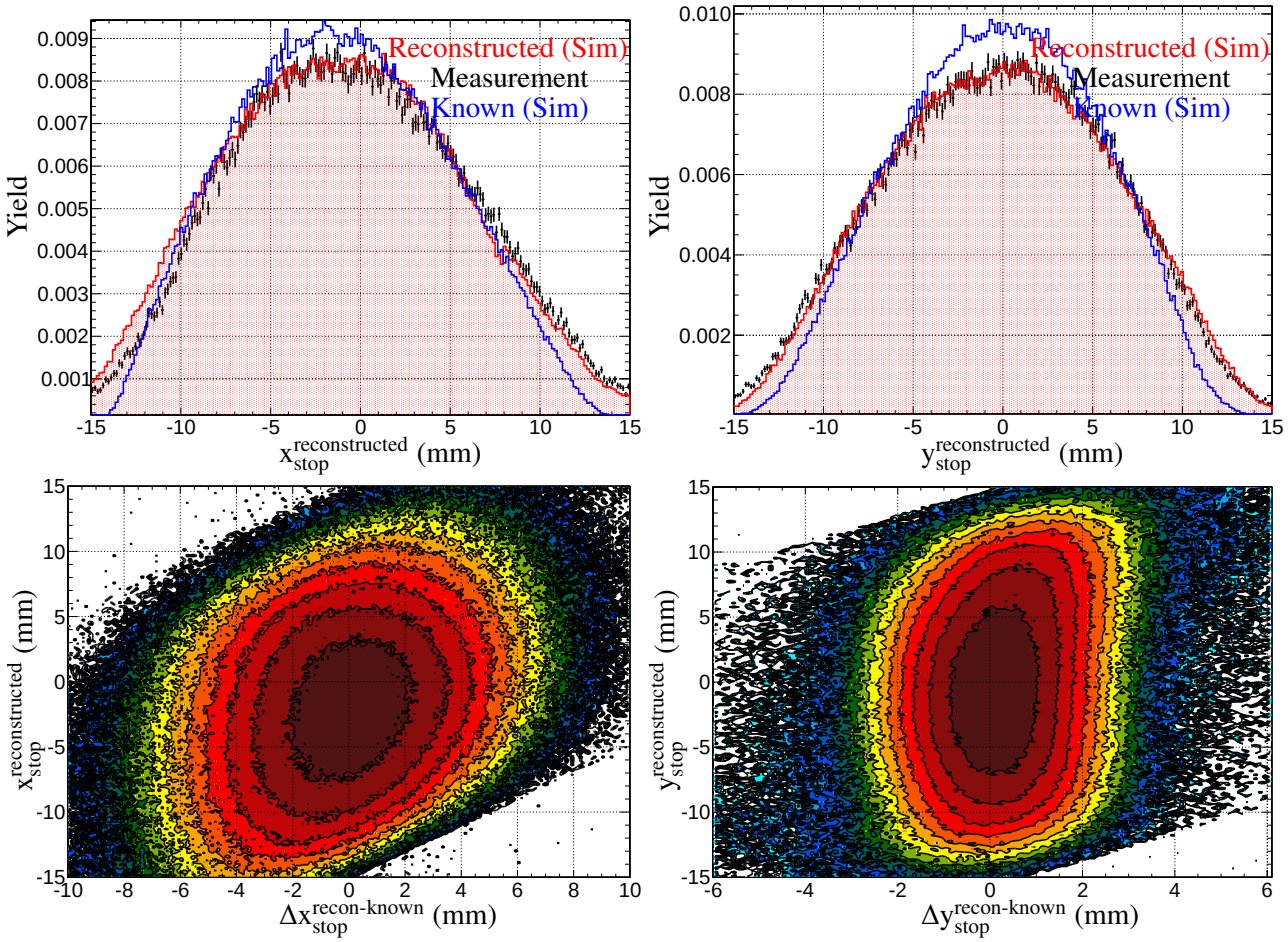

Figure 6.51: *Comparison of stopping distribution in x and y for simulation and measurement. Upper Left: Stopping distribution in x for measurement (black), simulated known (blue) and reconstructed (red). Upper Right: Stopping distribution in y for measurement (black), simulated known (blue) and reconstructed (red). Lower Left: Difference between known and reconstructed x as a function of reconstructed x. Lower Right: Difference between known and reconstructed y as a function of reconstructed x.*

The reconstructed stopping distribution as determined from the mTPC response is fully consistent with the measured data and consistent with the known stopping positions from the known GEANT4 values. The stopping distribution may also be checked by observing positron target energy when a particular crystal number in the CsI calorimeter is hit. For a given stopping distribution, or stopping volume, the pathway to a particular crystal is limited by the solid angle that subtends that crystal, which means there are certain pathways which that positron will traverse in order to hit the CsI crystal. By looking at observed energies in the target, we expect there to be distortions of a simple distribution of energies given the different trajectories that would enable a particular crystal to be hit. Consistency of the positron target energy between measurement and simulation would necessarily imply that the simulated stopping distribution is also consistent.

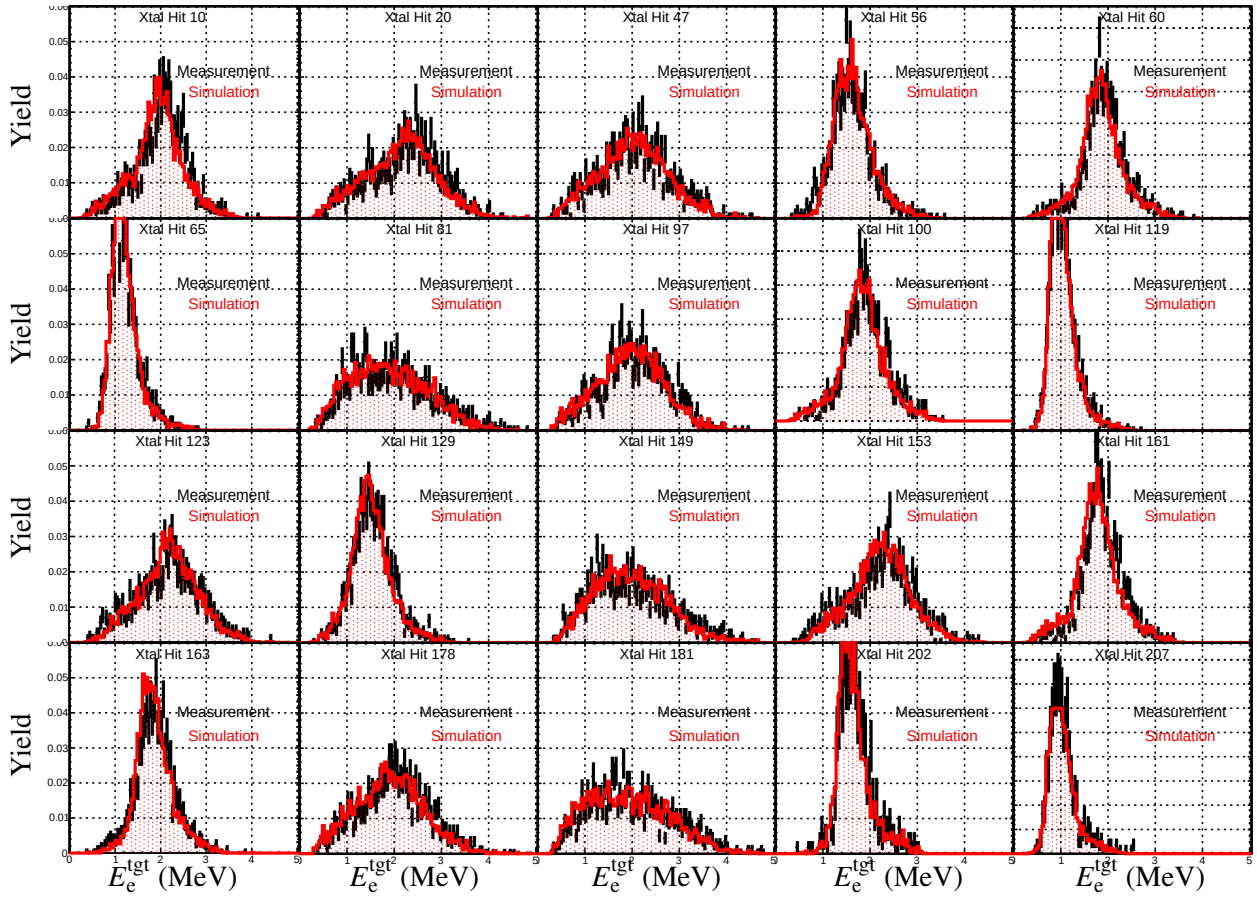

Figure 6.52: *Positron Target energy depositions for a particular crystal hit for various main crystals hit. Figures for all 220 crystals are available in the appendix. Note this is target energy observed (as in from the waveforms). There is also the predicted energy based on which crystal is hit also available in the appendix.*

The "odd" shaped spectra and the simulation matching of these shapes in Fig 6.52 displays how com-

plicated the stopping distribution can be. Once the positron leaves the target, whether it was a signal, $\pi \rightarrow e\nu(\gamma)$, event or Michel background, the positron traverses through the MWPC. If properly simulated the charge induced should be representative of the energy deposited in the MWPC volume (known in the simulation) and charge signals should be consistent with measurement.

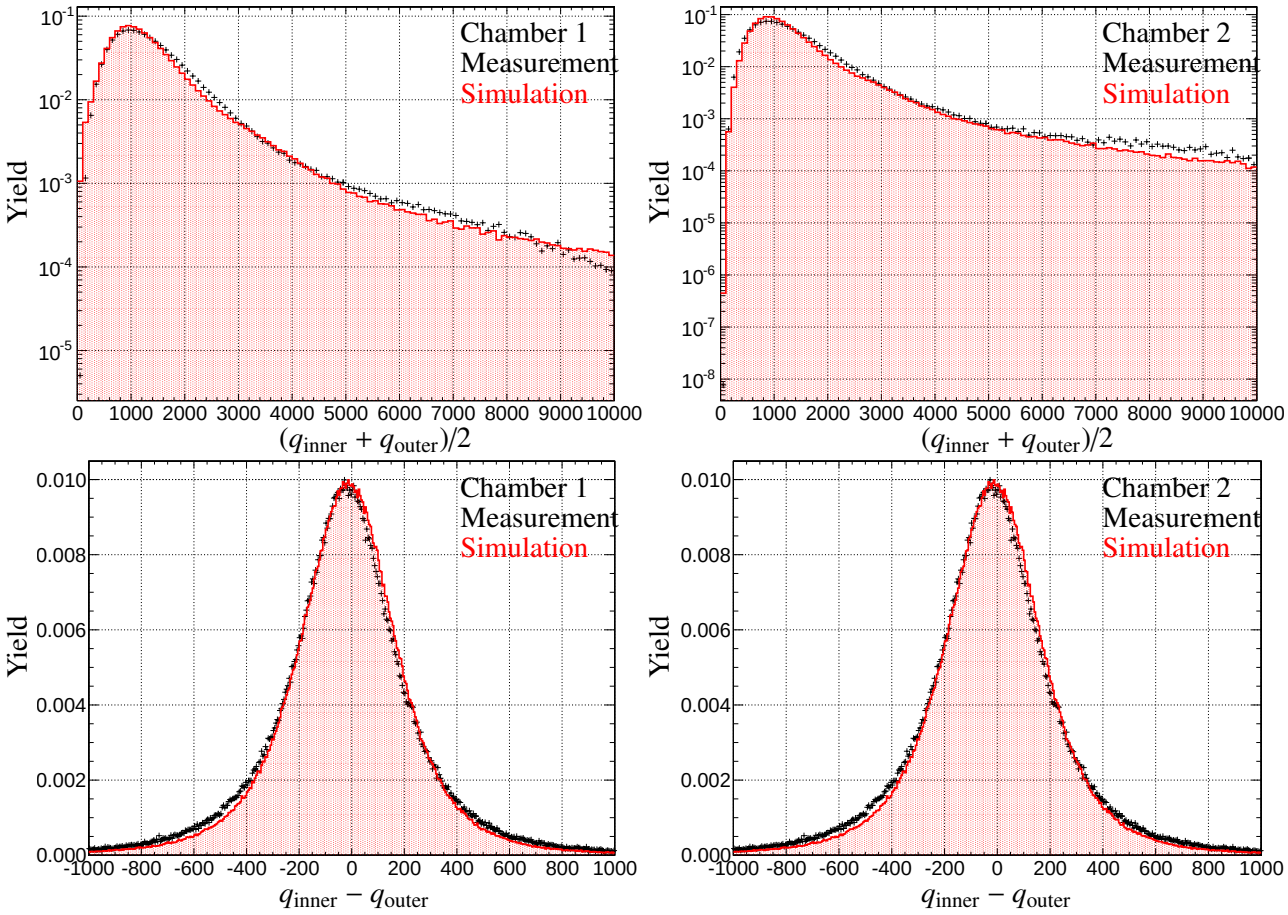

Figure 6.53: *Comparison of measurement (black) and simulation (red) for induced charge on the the cathodes in the MWPCs.*

The difference between the measurement and simulation in Fig 6.53 is due to the semi-empirical method used to determine the simulated induced charge on the cathode strips. Despite this small discrepancy, the overall shape is in very good agreement as are the observables constructed from the induced charge. The charge induced on the cathode strips is used to reconstruct the z positions and further variables involving tracking. This includes predicted positron energy and vertex quality (as explained in the previous chapter). The simulated induced charge should therefore accurately represent and recreate these distributions not only with the measured data but also the known values should be consistent with the reconstructed observed

values as seen in Fig 6.54.

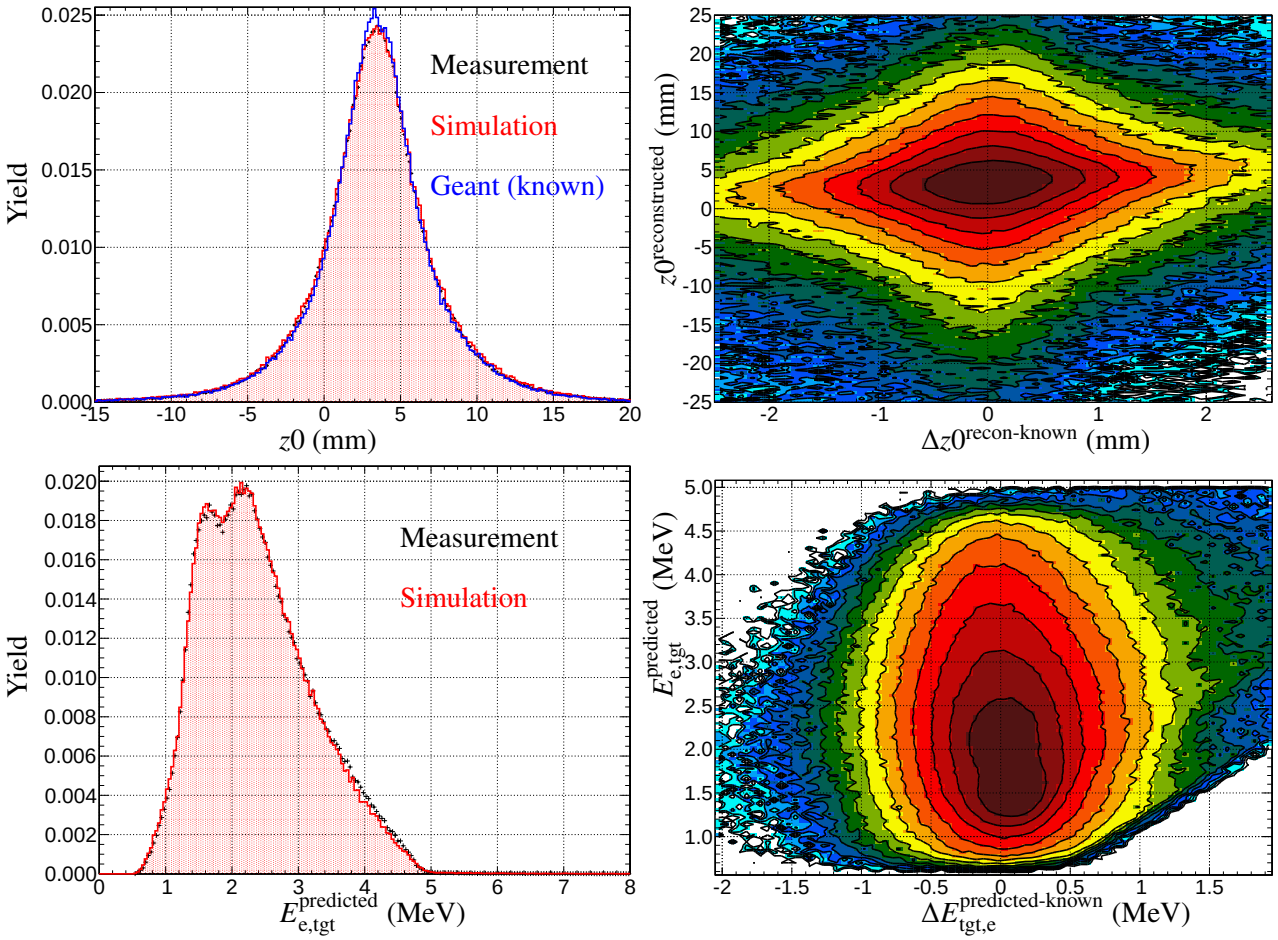

Figure 6.54: *Comparison of measurement and simulation for z0 (closest approach in the z position), predicted positron energy, and vertex quality. Upper Left: z0 comparison with measurement (black), known simulated (blue) and reconstructed simulated (red). Upper Right: Comparison of known and reconstructed z0 for simulation. Lower Left: Predicted positron energy comparison for measurement (black) and simulation (red). Lower Left: Difference between predicted positron energy and the known positron energy deposited. Note predicted positron energy requires knowledge of both the mTPC and MWPC.*

In addition, there are tracking variables that do not have known equivalents such as `vertex quality2`, `vertex quality3`, and `dz0` discussed earlier that are reconstructed in the same fashion as the measured data. The comparison is in Fig 6.55.

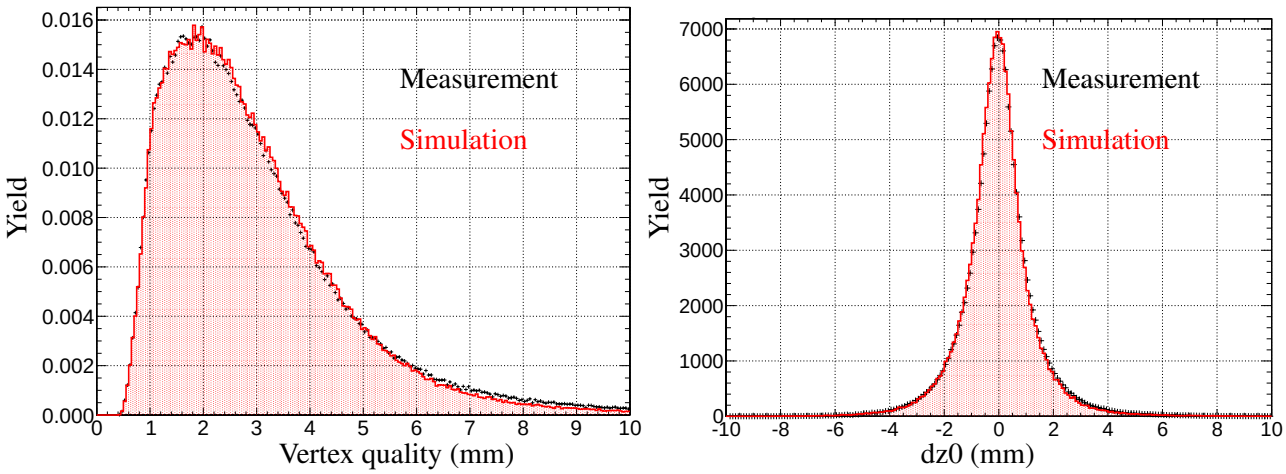

Figure 6.55: *Comparison of variables reconstructed by both the mTPC and MWPC of simulation (red) and measurement (black) Left: Vertex quality 2. Right: dz0.*

The observables deduced from the MWPC response are important due to the fact that the predicted positron energy (which requires both mTPC and MWPC) will be used in one of the most discriminating higher order observables for the PEN analysis. In order to accurately understand the cut efficiency of this observable, these detector elements which are used to deduce the higher order observable must be well understood. That is to say, accurately simulated.

After the MWPC, the positron will traverse the hodoscope. Each of the 20 staves will have an energy spectrum and a timing spectrum. In particular, the timing of the hodoscope is important because it is used in the predicted timing of the positron in the target. As stated, each hodoscope has its own time delay, and must be accounted for as each hodoscope triggers the end of the waveform digitizer for the target waveform. Timing in the hodoscope with respect to the target time and energy spectrum for all 20 staves must be checked individually. While the energy in the hodoscope is of less concern, as this was only used to distinguish between hadronic events and events in which a positron emerged. However, the energy in the hodoscope is used in the construction of the invariant mass spectrum, and the difference in the predicted times effects the higher order waveform variables. Predicted and observed target positron time comparisons for each of the hodoscopes are shown in Fig 6.56

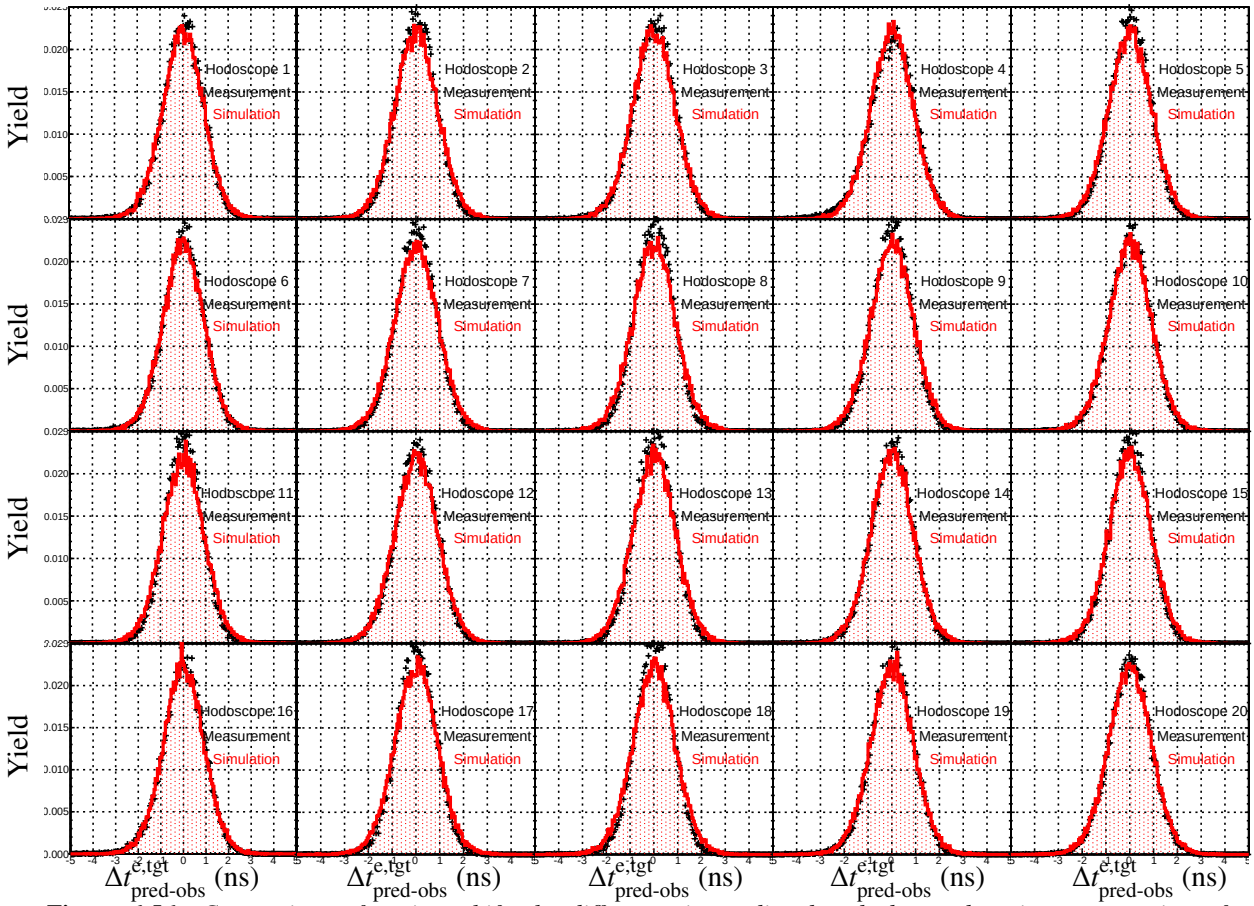

Figure 6.56: *Comparison of positronshift- the difference in predicted and observed positron target times for the measurement and simulation for all 20 hodoscopes being triggered.*

Earlier it was seen that the predicted positron target times and the observed positron target times were put at different bins for different hit hodoscopes. However, the difference in the predicted and observed is zero because any time offset that is effected in the hodoscope (trigger) offsets all times in all the other detectors. So every single trigger offset (all 20 of them) are applied in the simulation depending on what hodoscope is hit and all times prior to the hodoscope are offset by the same amount so that the difference is independent of which hodoscope is hit. The energy spectra of all twenty staves are shown in Fig 6.57.

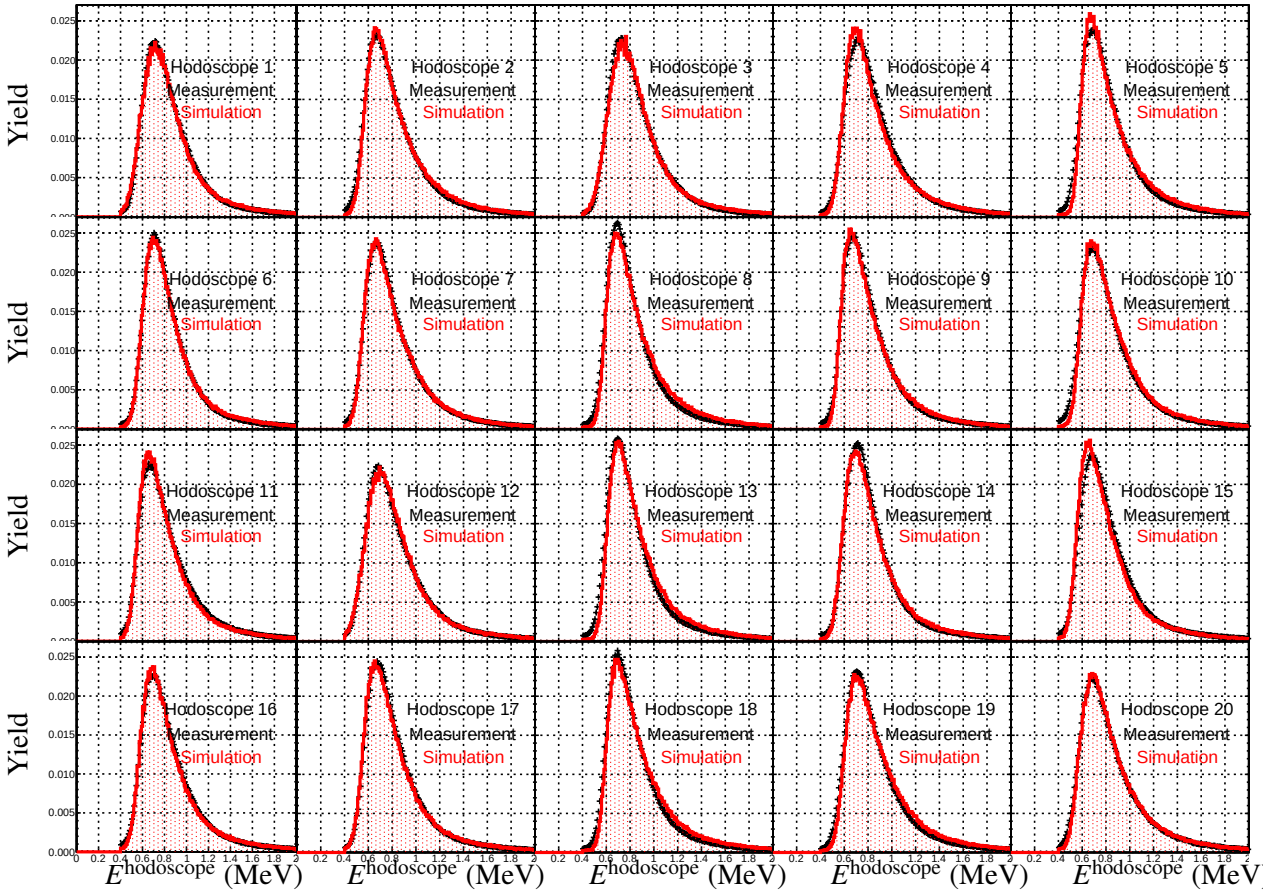

Figure 6.57: *Comparison of energy deposition in the individual hodoscopes. Measurement in black and Simulation in red.*

Using the combination of both the hodoscopes and the MWPC gas chamber, the total dE/dx in the hodoscope and gas, dEdx_total, may be constructed. An additional version of vertex quality, `vertex quality3` is shown in Fig 6.58.

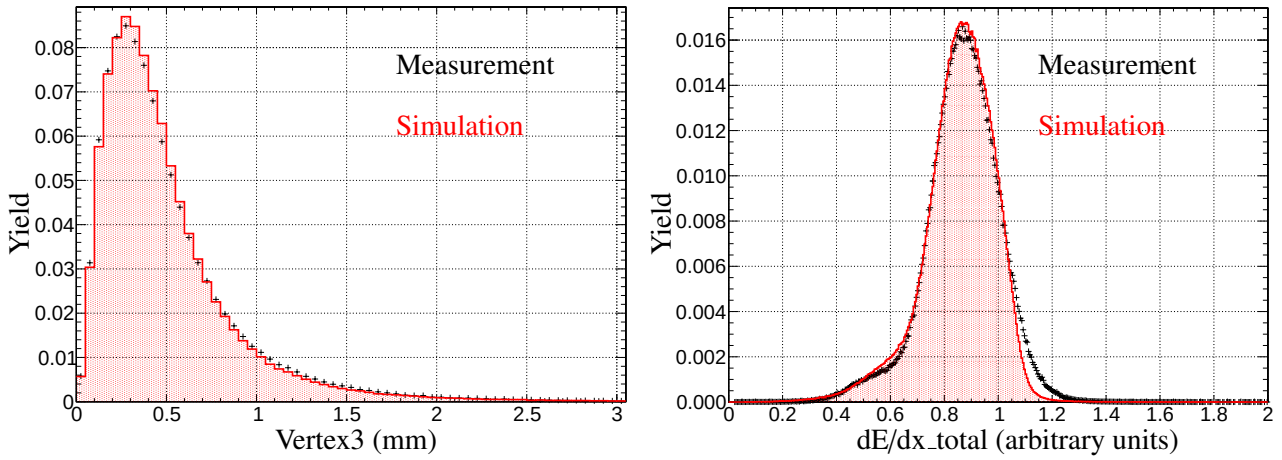

Figure 6.58: *Left: Comparison of vertex3, a measure of the distance of closest approach between the decaying pion position, and the outgoing positron. Right: Comparison for dE/dx_total, a calculation which uses both the MWPC knowledge of the induced charges on cathodes and the energy deposited in the plastic hodoscopes. Note discrepancy at the high end in part due to shortcomings of the empirical charge distribution and due in part to a combination of both Michel and $\pi \to e\nu$ in the measurement and other contamination in the measurement.*

Discrepancy between dE/dx_total is due to the semi-empirical nature of the cathode charge model deduced on the MWPC.

After traversing the hodoscope, the decay positron encounters the CsI calorimeter. The energy deposition in the CsI (which was already shown before) but also the timing in the CsI, can be checked by observing the difference in timing between CsI calorimeter and plastic hodoscope as well the calorimeter and target. This was already shown before in Fig 6.47. But what about time differences between two tracks? Or rather, what happens in the hard radiative decays. In this case, the simulation is needed to study both the time difference and the opening angle between the outgoing positron and photon. The opening angle between these two particles is determined by the response of MWPC for the charged track and the ability to reconstruct the shower for the non charged track (photon). When a photon emerges from the target, the only way to determine its momentum is to use the pion stopping position and a weighted average of the shower position weighted by the energy that is ignited by the photon. A more thorough discussion of the radiative decays is presented in the next chapter as well as a comparison to simulation and measured data for hard photons emerging from the target.

When all of the basic detector responses and low to medium level observables are consistent between the measurement and the simulation, then the highest order observables should be consistent with measurement and data. That is the `decaytime` spectra, `restwave`, $\Delta\chi^2$, ΔE_{2p}, and χ^2_{2peak}. `Decaytime` is determined from the time difference between the degrader and the hodoscope. A comparison on the reconstructed and known

decay time as well as measured decay time spectra is shown in Fig 6.59

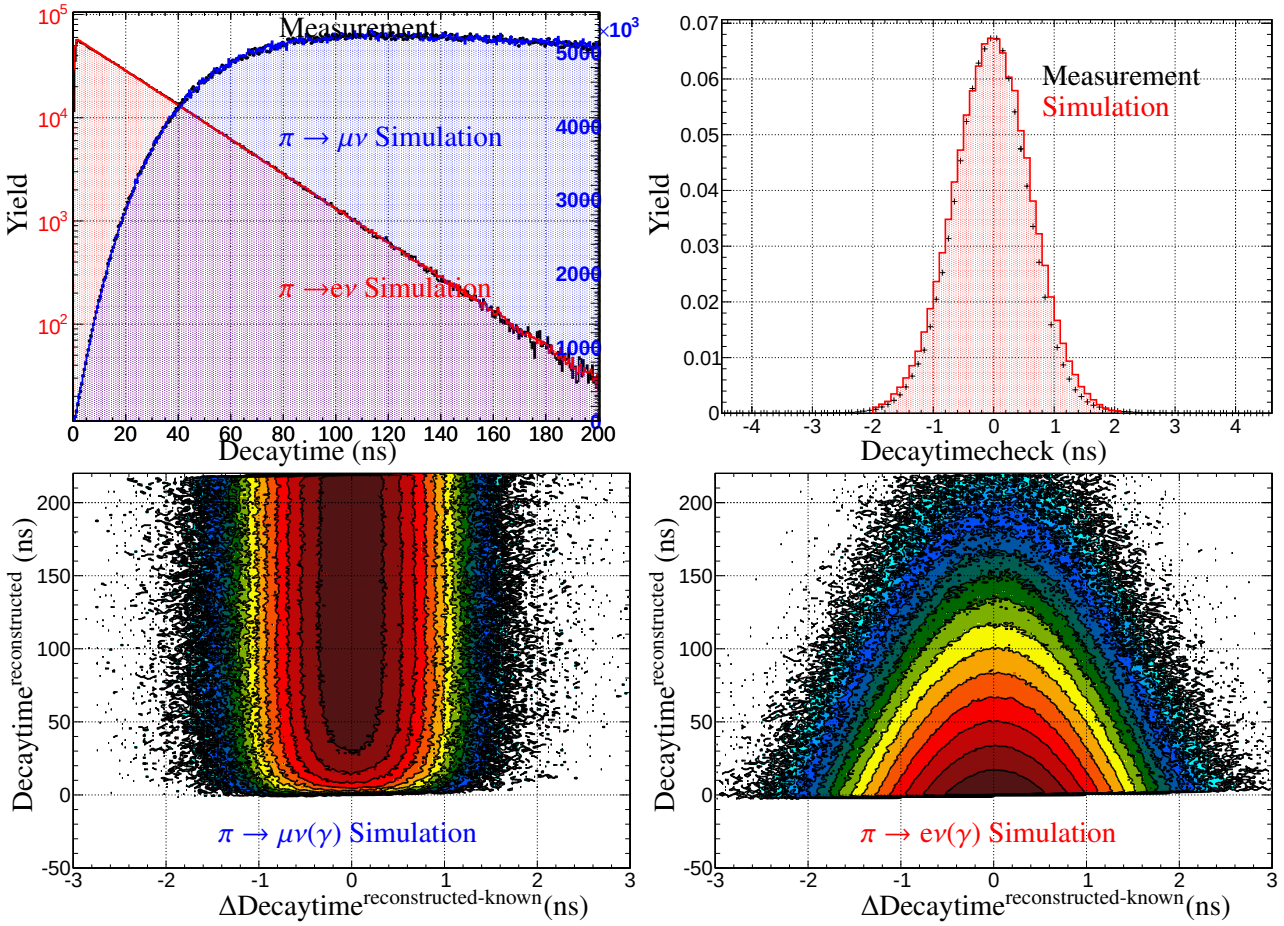

Figure 6.59: *Decay time checks. Left: Comparison of decay time spectra for measurement and simulation for the two decay channels using degrader and hodoscope time. Blue for Michel decay spectrum and red for $\pi \to e\nu(\gamma)$. Right: The observable* `decaytimecheck` *which is the difference between decay time as determined by the predicted times and that determined by observed target times for well separated Michel decays. Reconstructed decay time vs difference in known decay time and reconstructed decay time for simulation. Difference in decay time for measurement and simulation using timing in hodoscope and degrader subtracted by using waveform timing.*

Recall, `restwave` takes the difference between predicted pion and positron energies and subtracting them from the observed target waveform. This means that for $\pi \to e\nu(\gamma)$ decays, the target experiences energy deposition from the incoming pion and the outgoing positron. By subtracting the predicted energies of these two particles, the `restwave` energy is expected to center at zero. In the case of the $\pi \to \mu\nu \to e\nu\bar{\nu}(\gamma)$, the target receives energy depositions from three particles. By subtracting the predicted energies of the positron and pion, the remaining energy in the target is that of the muon, which is close to 4 MeV. These complex observables are compared with measured data for appropriately selected events in Fig 6.60.

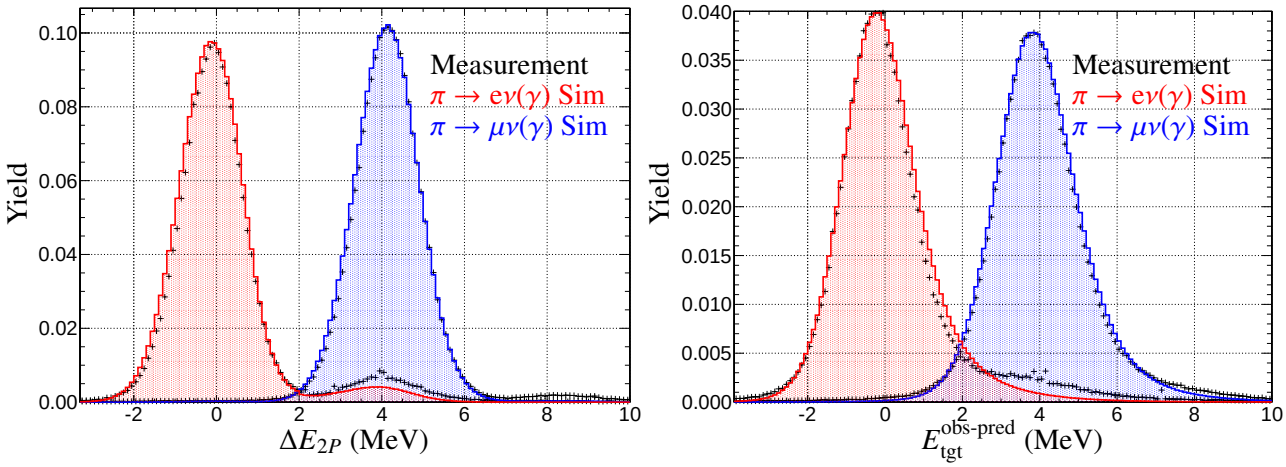

Figure 6.60: *Comparison of measurement (black) and Michel decay (blue) simulation and pion decay (red) simulation. Left:ΔE_{2p} Right: Restwave energy, observed energies of pion and positron subtracted from total target waveform.*

The ΔE_{2P} and `restwave` plots shows discrepancies for the pion decay selection. There are some events which have signals around 4 MeV. This occurs when the predicted energy of the positron fails to properly predict the energy. Recall that the predicted energy of the positron is determined by first determining the pathlength that the positron traverses and then multiplying it by 1.78 MeV/cm, the peak dE/dx. However, because the positron has a high energy tail for energy deposition, these events will result an abundance of target rest energy. This effect is seen in Fig 6.61. For the ΔE_{2P} observable, the structure of a local maximum is due to the fact that this observable uses waveform energy with predefined shapes. The measurement excess is due to positrons in the high energy deposition regime which can't be eliminated easily.

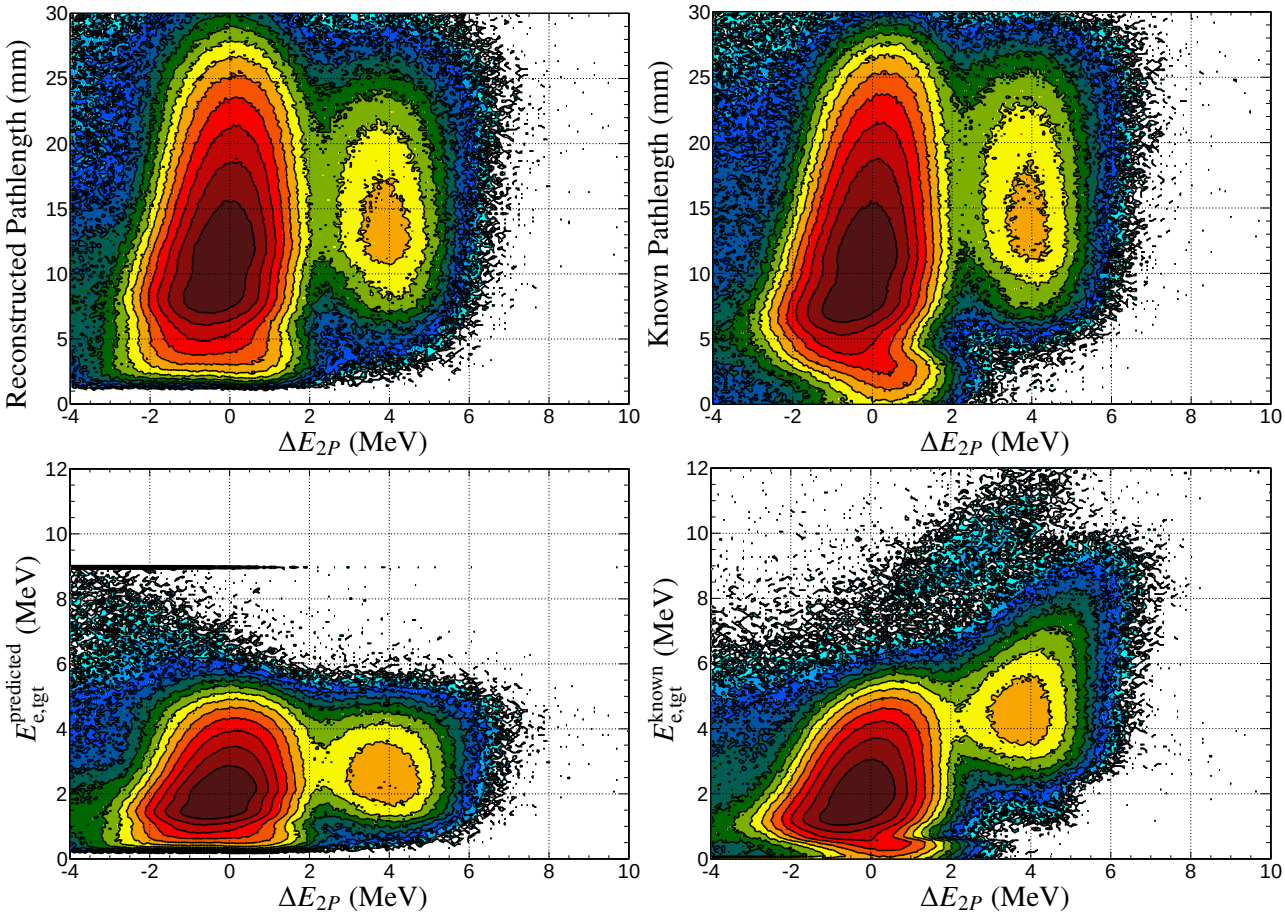

Figure 6.61: *Demonstration where the* `restwave` *and* ΔE_{2P} *give too high a values. Upper Right: Reconstructed pathlength versus* ΔE_{2P}*. Upper Right: Known pathlength versus* ΔE_{2P}*. Lower Left: Predicted energy (reconstructed pathlength times 1.8) versus* ΔE_{2P}*. Lower Left: Known energy deposition versus* ΔE_{2P}*.*

There is also the particularly powerful discriminating observable, $\Delta\chi^2$. Described in the previous chapter, this variable uses predicted pion and positron energies to form a predicted waveform, subtracts it from the observed waveform to find a muon, using a muon kernel and chi squared fit to determine where the best fit muon would be. This highly discriminating observable is the best method to separate background and signal in the PEN arsenal and to properly use this observable, it must be understood at the 10^{-4} level. The comparison for simulation and measurement for $\Delta\chi^2$ is shown in Fig 6.62.

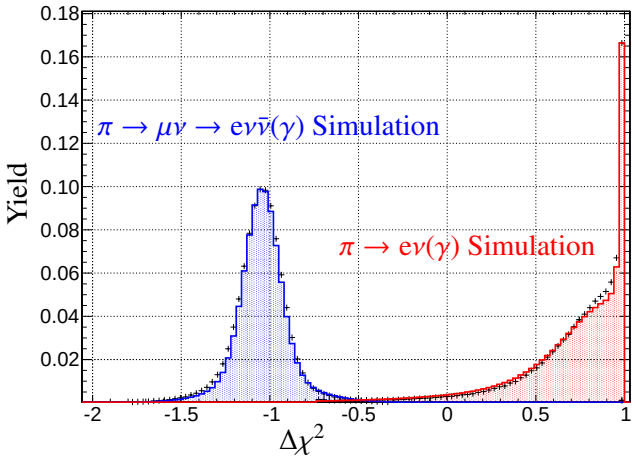

Figure 6.62: *Comparison of waveform observables for measurement (black) with simulated Michel decay chain (blue) and simulated $\pi \to e\nu(\gamma)$ (red). Right: $\Delta\chi^2$. Selection of Michel from data was done with energy between 20 MeV and 50 MeV in the CsI calorimeter. For pion decay selection energy was chosen above 62 MeV and below 75 MeV in the CsI calorimeter. Small discrepancies in the simulation may be attributed to lack of decays in flight from the Michel decay chain. In particular, no muon decays in flight that contribute to false positives in the measured data.*

Good discrimination using the observables `restwave`, ΔE_{2P}, χ^2_{2peak} and $\Delta\chi^2$ should not go undiscussed. The analysis aimed at branching ratio extraction requires event selection criteria that differ between the Michel selection and pion decay selection, so the efficiency of that cut must be understood to the 10^{-4} level or better. These highly discriminatory observables would be of such use. It is absolutely necessary to be able to understand the cut efficiency on these highly discriminatory observables. The only way that the efficiency could be determined to the level of precision desired is if the Monte Carlo reproduced these highly discriminatory observables. This in turn could only happen if the all facets of the detector were accurately and precisely represented by the Monte Carlo. Hopefully the reader has been convinced now that this is indeed the case.

6.11 To simulate or not to simulate (that is the question)

While the simulation permits the study of both pure signal and background events, not all background events are simulated. The different background events that are present in the data sample are four types of decays in flight, $\pi_{\text{DIF}} \to e\nu$, $\pi_{\text{DIF}} \to \mu\nu \to e\nu\bar{\nu}$, $\pi \to \mu_{\text{DIF}}\nu \to e\nu\bar{\nu}$, $\pi_{\text{DIF}} \to \mu_{\text{DIF}}\nu \to e\nu\bar{\nu}$, hadronic interactions, scattered beam interactions, pileup, decays with three daughter leptons, pion beta decay and radiative decays (above, "DIF" stands for decay in flight). As stated before, there is no real distinction between radiative and non-radiative decays for pions or muons. So all of the Michel simulations have the radiative component

present. The same goes for the pion decays. Pion beta decay and the three lepton channels are not simulated as they are very rare. In the case of $\pi \rightarrow eee\nu$ on the order of 10^{-9} and in the case of $\mu \rightarrow eee\nu\bar{\nu}$, easily identified in the data set. Hadronic interactions can be easily included in the simulated events, but are not. This stems from the fact that the hadronic interactions are efficiently suppressed in the data sample as will be shown. The double decays in flight are too rare to be a contributing factor to the data sample. They would occur on the order of 1 in every 10^9 pion stops. The pileup and the scattered beam particles are not simulated. The reason is two-fold. The first is that in the experiment, a magnetic quadrupole was used to guide the beam particles. In the simulation, no magnetic field is simulated, the beam is longitudinalized up to a certain point and then constructed so as to match the profile and emittance of the beam deduced from the mTPC data analysis. Without knowing the details of the magnetic field, the actual trajectories of the scattered beam particles would not be simulated satisfactorily. The second reason is that if these charged particles were to induce a shower in the calorimeter prior to the trigger, then only a fraction of the energy from the first particle would be recorded. Without knowing how well the energy is captured at a given time before the trigger, the electronics of this process could not be simulated to the desired precision. While this analysis is done in PiBeta, and could conceivably be used in the PEN simulation, it is not clear that this is needed. This is one of the main reasons that this analysis was a cut-based analysis and not a maximum likelihood analysis. If more details were known about these extraneous processes, a maximum likelihood analysis may be more appropriate.

6.12 Simulation key plots

While the Monte Carlo simulation is indeed complex, simulating every nuance of the experiment may not be feasible. There are however, some observables which are crucial and therefore should show very good agreement between the measured data and Monte Carlo simulation. For this reason, there are "diagnostic" plots that are used to compare the simulation and the measurement for each of the different simulation configurations. These histograms are chosen because they include information from tracking, timings, target energies, are used to construct the highest order observables. The following plots are from the simulation configuration 15330. The diagnostics from one of the 2010 configurations are shown because the previous figures in this chapter use the simulation 90000 configuration.

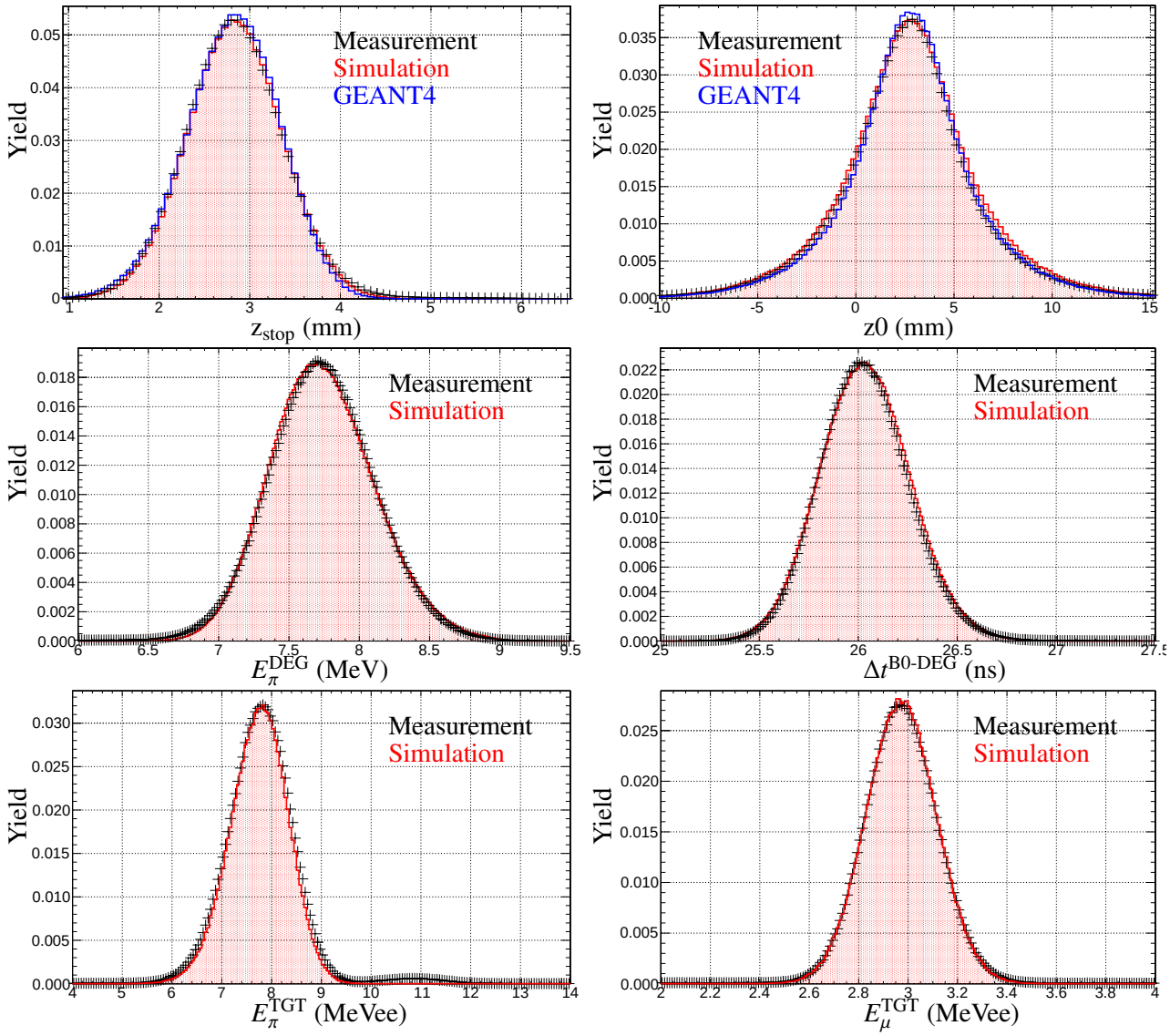

Figure 6.63: *Upper Left: Stopping position in z. Upper Right: z0. Middle Left: Pion energy deposition in the degrader. Middle Right: Time of flight between the B0 and the degrader. Lower Left: Pion target energy. Lower Right: Muon target energy.*

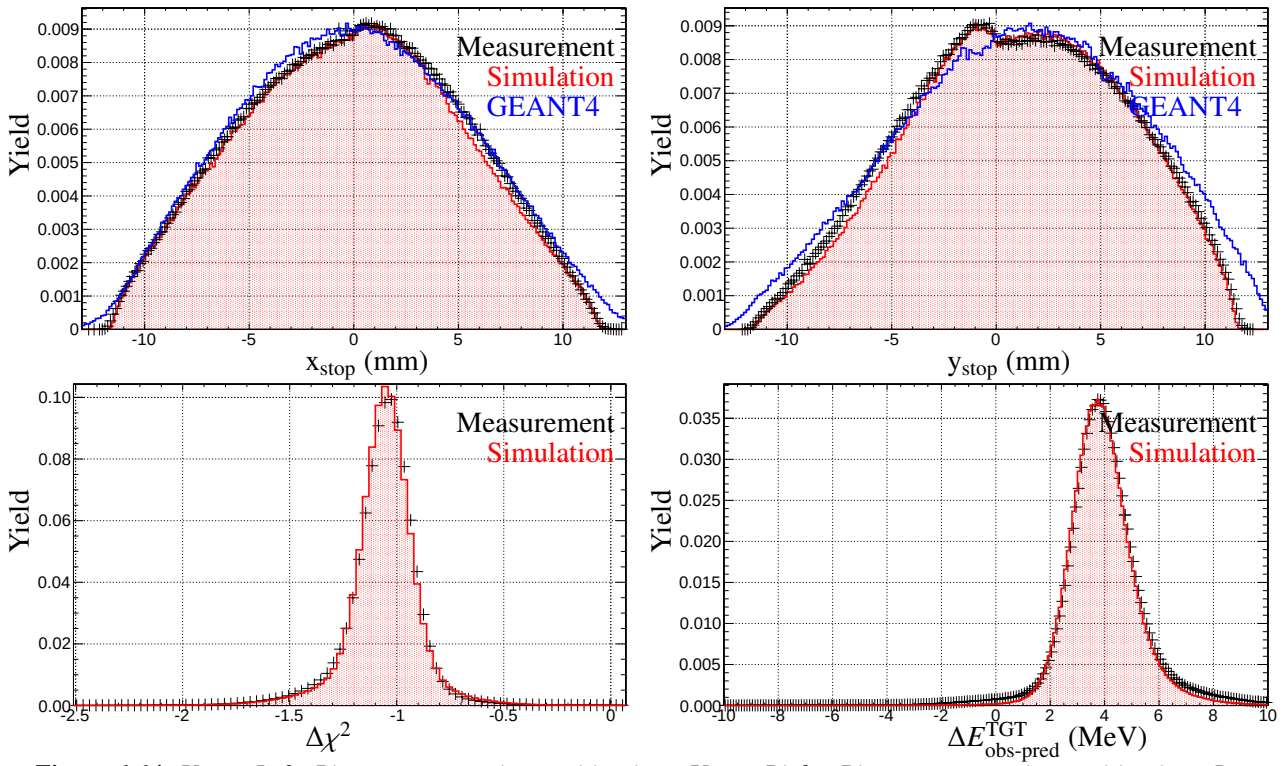

Figure 6.64: *Upper Left: Pion target stopping position in x. Upper Right: Pion target stopping position in y. Lower Left: $\Delta\chi^2$. Lower Right: Observed target energy minus predicted target energy.*

Fig 6.64 shows a significantly different pion stopping distribution than that shown in Fig 6.51. This is one of the key differences between the 2010 and 2009 beam profiles. The 2009 run period (and its simulation) had a beam collimator immediately downstream from the mTPC. The 2010 run period did not have the beam collimator but did have the mTPC closer to the target producing a more reliable description upstream from the target. In addition, Fig 6.63 shows a shorter time of flight than its 2009 counterpart yet also shows more energy deposited in the degrader. In the 2010 data run, the momentum was increased by about 5 MeV which required a thicker degrader to ensure that the pion would stop near the target. The thicker degrader therefore has more pion energy deposited despite having a faster pion.

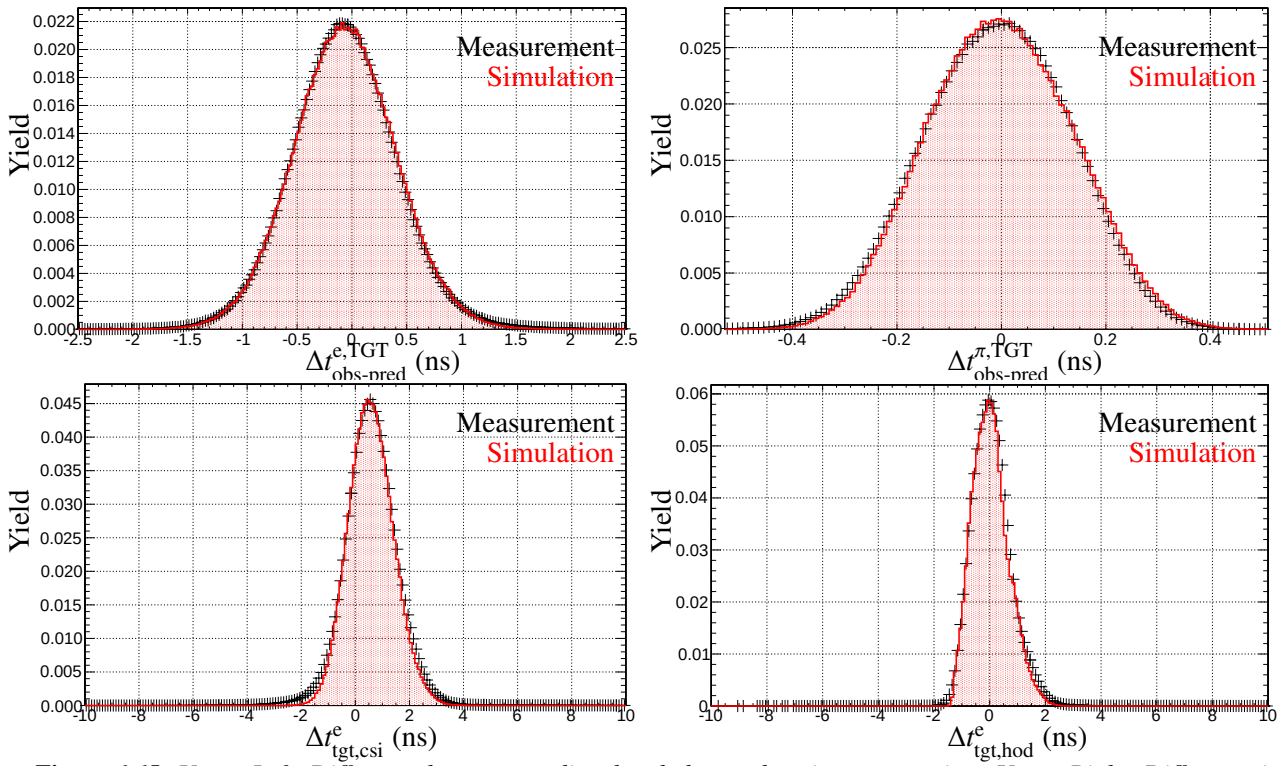

Figure 6.65: *Upper Left: Difference between predicted and observed positron target time. Upper Right: Difference in predicted and observed pion target time. Lower Left: Positron CsI time relative to the target. Lower Right: Positron plastic hodoscope time (average of up and downstream TDCs) relative to the target.*

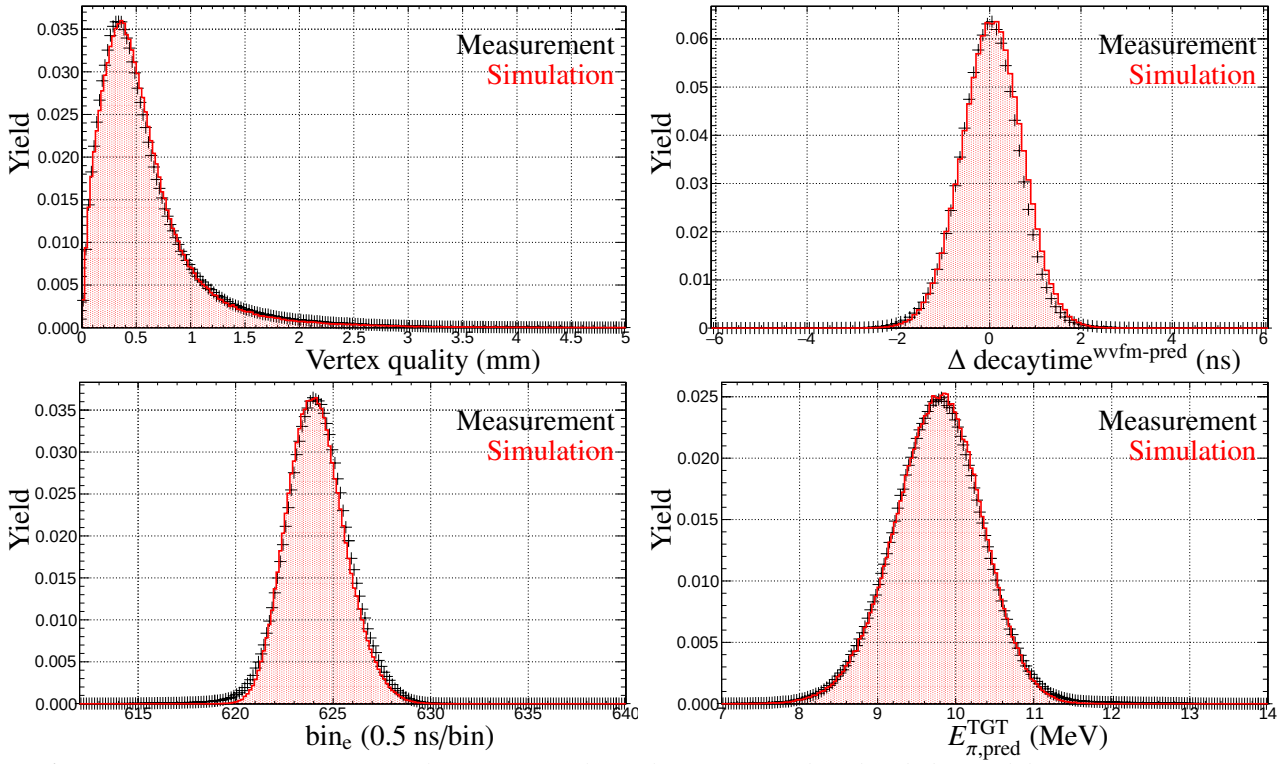

Figure 6.66: *Upper Left: Vertex quality. Upper Right: Difference in predicted and observed decay times. Lower Left: Positron target time. Lower Right: Pion predicted target energy.*

The 2010 run period also shows the position of the positron in the target around channel number 623 in Fig 6.66. This again is different than the 2009 counterpart where it is present around channel 704. Though these differences are minute, since the simulation is presented in a way that is indistinguishable to that of the measured data, the calibrations, and method by which higher order observables are constructed are done in the exact same manner for both the simulation and measurement because of these details.

7 Analysis

> Science cannot solve the ultimate mystery of nature. And that is because in the last analysis, we ourselves are a part of the mystery that we are trying to solve
>
> Max Planck

This chapter reviews the analysis intended to separate background from signal events. This is accomplished by first considering the different types of background events that occur in the PEN data, demonstrating how to eliminate them, and if needed, make corrections for them in the analysis. The second part of this chapter discusses the determination and characterizations of the acceptances, multiwire proportional chamber efficiencies, signal and background count, tail fraction, and eventually the branching ratio and the accompanying systematic uncertainties. The branching ratio, simply speaking is the number of signal events, $N_{\pi\to e\nu(\gamma)}$ that occur divided by the number of $\pi \to \mu\nu(\gamma)$ decays, $N_{\pi\to\mu\nu(\gamma)}$, that occur. However, there are instances in which any one of these decays occur but the event is not counted or not recorded. This occurs if the decay positron doesn't produce an event trigger or fails cuts that sanitize the data from background contamination. The elimination or lack of events must be accounted for and is done in the acceptances. The acceptance, A, is the probability of detecting the event given that the event actually occurred. The acceptances are obtained from the Monte Carlo simulation because only in the simulation is it known that an event absolutely occur and pass, or doesn't pass, the cuts. Instinctively then, the branching ratio, B, is given by

$$B = \frac{N_{\pi\to e\nu(\gamma)}}{N_{\pi\to\mu\nu(\gamma)}} \frac{A_{\pi\to\mu\nu(\gamma)}}{A_{\pi\to e\nu(\gamma)}} \tag{65}$$

This expression is naively true, but not sufficient in order to obtain an experimental branching in this experiment. As was seen in Fig 6.1, the number of $\pi \to e\nu(\gamma)$ events requires determining the number of events underneath a substantial Michel background. Counting these events accurately and precisely is very challenging. One possibility is to write the number of signal events,

$$N_{\pi\to e\nu(\gamma)} = N_{\text{tail}} + N_{\text{peak}} = N_{\text{peak}}(1 + N_{\text{tail}}/N_{\text{peak}}) = N_{\text{peak}}(1 + \epsilon_{\text{tail}}) \tag{66}$$

Using this expression, it is no longer desirable to obtain the total count of $\pi \to e\nu(\gamma)$ events, but rather those events that appear in the peak region followed by a characterization of the tail fraction, which as stated, can be done by the Monte Carlo simulation. Even after this caveat is handled, there are still more caveats to properly extracting the branching ratio. Since the experiment only took data for a particular time window following a pion stop, this means not all events are recorded to begin with. The probability function, f, of a particular decay occurring in a given time window is determined by theoretical decay times. The uncertainty of this value will depend on the uncertainty in timing and the window chosen. In addition, a positron in the MWPC will have a better chance of inducing a signal if the energy is higher. This means low energy positrons from Michel decays are less likely to induce a signal in the chamber, whereas the signal from the high energy positron from a pion decay should will have a higher chance. The experimental branching ratio that accounts for all these corrections is

$$B = \underbrace{\frac{\mathrm{N}^{\mathrm{peak}}_{\pi\to \mathrm{e}\nu}}{\mathrm{N}_{\pi\to\mu\nu}}}_{r_N}(1+\epsilon_{\mathrm{tail}})\,\underbrace{\frac{\epsilon(E_{\mu\to e\nu\bar{\nu}})_{\mathrm{MWPC}}}{\epsilon(E_{\pi\to \mathrm{e}\nu})_{\mathrm{MWPC}}}}_{r_\epsilon}\,\underbrace{\frac{f_{\pi\to\mu\to \mathrm{e}}(T_{\mathrm{e}})}{f_{\pi\to \mathrm{e}\nu}(T_{\mathrm{e}})}}_{r_f}\,\underbrace{\frac{A_{\pi\to\mu\to \mathrm{e}}}{A_{\pi\to \mathrm{e}\nu}}}_{r_A}, \tag{67}$$

where,

N= number of events for a particular process,

A = Ratio of the Acceptances of events, $(A_{\pi\to\mu}/A_{\pi\to \mathrm{e}})$,

ϵ_{tail} = Tail-to Peak ratio,

$\epsilon(E)_{\mathrm{MWPC}}$ =Efficiency of MWPC as function of energy, i.e, averaged over the decay energy spectrum,

$f_{\pi\to \mathrm{e}}(T_{\mathrm{e}})= 1 - e^{-T/t_\pi}$= decay probability between pion stop time t=0 and trigger gate t=T,

$f_{\pi\to\mu}(T_\mu)$= decay probability between pion stop time t=0 and trigger gate t=T for Michel events,

Using this expression for the branching ratio, the relative error (with a goal of 5×10^{-4} or better) is given as

$$\frac{\delta B}{B} = \sqrt{\left(\frac{\delta r_N}{r_N}\right)^2 + \left(\frac{\delta\epsilon_{\mathrm{tail}}}{1+\epsilon_{\mathrm{tail}}}\right)^2 + \left(\frac{\delta r_\epsilon}{r_\epsilon}\right)^2 + \left(\frac{\delta r_f}{r_f}\right)^2 + \left(\frac{\delta r_A}{r_A}\right)^2} \tag{68}$$

7.1 Blinding

The goal of the PEN experiment is to make a high precision measurement. This measurement will either confirm or contradict a precise, theoretically predicted value of the Standard Model. In either case, the

result of such a measurement may have far-reaching consequences. Thus it is important and necessary not to introduce any kind of bias in the analysis of the data. This is achieved by doing the analysis blind. This means that the final result will be unknown to the author of this work (and the collaboration) until the analysis is done to full completion. This is to ensure that between the preliminary and final analysis, the analysis team is not using the knowledge of the possible result to "guide" them to a specific final answer. If an unblinded analysis were to take place, and a result which emerged is one which agrees with Standard Model, the experimenter might be inclined to conclude the analysis is being performed correctly and that the analysis and experiment were proceeding in the correct direction. The problem is that if the analysis/experiment were done incorrectly and a result agreed with the Standard Model, then result that should have been obtained if the everything was done correctly would have been one which differs from Standard Model. Therefore the knowledge of the preliminary result before everything is complete may bias the experimenter and the method by which they wish to proceed. Thus blinding in these types of experiments is often a necessity. The question then remains as to how to blind the analysis. It is desired to give a "false" or incomplete result without actually affecting the analysis. The easiest way to blind is to take one of the values above and multiply (or add) a random number to one of the values or leaving it out of the calculation completely. Doing this to the number of Michel positrons may not be feasible since these numbers are fairly big, a small random number would not affect the perceived value and therefore not really hide the result. Blinding the number of positrons from pion decays would be extremely problematic, because the statistical uncertainty is dominated by the number of $\pi \to e\nu(\gamma)$ events. This value needs to be characterized regardless of which way the analysis is taken because if not, then it would not be known if a different path would be needed to obtain a more satisfactory result for lack of statistics. The tail fraction, apriori is the most difficult quantity to obtain and understand to a high level of precision. This was discussed in the history of pion experiments, thus it would be prudent to understand this tail fraction and its associated uncertainty. The time window probability is theoretical, it could be used to blind if the lifetime of the pion and muon were "changed". However, error in the time window chosen changes the number of events that are used in the statistics, therefore this is chosen to not be blinded. The best way of blinding then is to do something with the acceptances. Apriori it is not expected that the acceptances will be too different for different geometries. It is also known, apriori, that accounting for the efficiencies, will be on the order of a percent or so correction. By blinding the collaboration to the efficiencies, or rather the quantity $r_A \times r_\epsilon$, the analysis is not affected,

the statistical uncertainty will not be affected, and all but the correction due to the efficiencies/acceptances will be necessary for a preliminary analysis. To further blind, in case of inadvertent unblinding (because people do crazy things), a second blinding will be done by employing only one simulation for the 2009 data and one simulation for the 2010 data instead of the required number of simulations to properly obtain $r_A \times r_\epsilon$. This blinds the result by very slightly, altering the acceptances or cut efficiencies. The usage of only two simulations instead of the 12 necessary makes no significant deviation from the current blinding of the branching ratio nor the analytical process.

7.2 Background and Cuts

The PEN experiment, like any physics experiment, is charged with the task of analyzing the data to separate background and signal. As pointed out in the introduction to this work, the pion is a versatile particle and has several different decay modes. The spectra of the main/basic observables in the experiment before proper event selection (cuts) is shown in Fig 7.1.

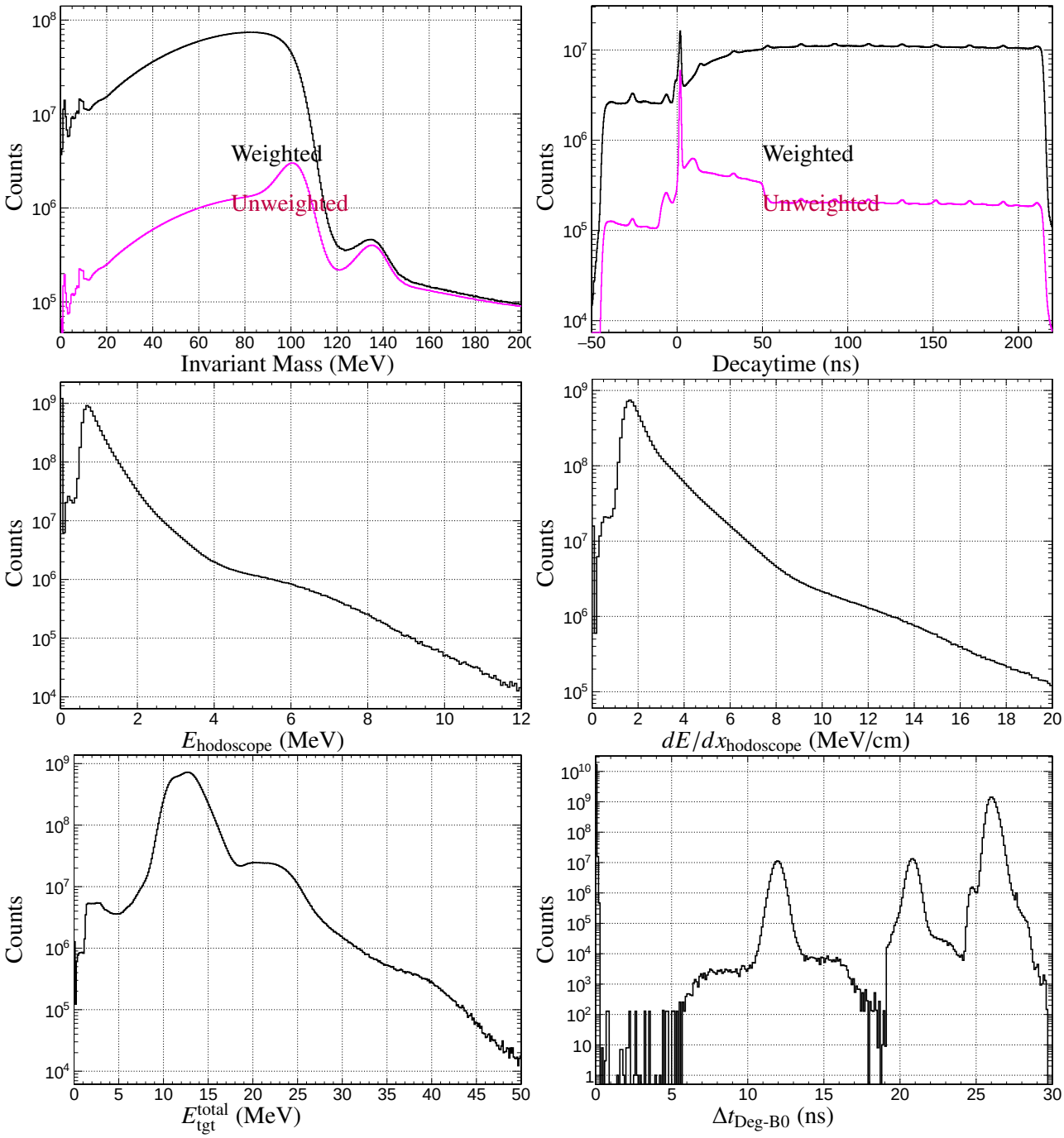

Figure 7.1: *Raw data before cuts and events selection. Upper Left: Invariant mass. Upper Right: Decay time Middle Left: Energy in the hodoscope. Middle Right: dE/dx in the hodoscope. Lower Left: Total target energy. Lower Right: Time of flight between in B0 and degrader.*

The first two plots showing weighted and unweighted events illustrate the effectiveness and need for prescaling. In the raw, there are a significant number of events with 140 MeV invariant mass and early decay times as compared to the properly weighted histograms. We recall that an event would be recorded

every time a high energy threshold was reached in the CsI calorimeter and once every 64 times (roughly) otherwise. This permits more signal events to be recorded for purposes of analysis. As stated prior, this chapter focuses on two main things. The first is to identify the unwanted background that is present in the plots above and demonstrate methods to eliminate them without bias to the two pion decay channels of interest. The second part of this chapter is to show the method by which the branching ratio is obtained.

7.2.1 Beam Contamination and Selection

In order to select the events that are used in the extraction of the branching ratio, a beam particle selection is made to ensure that the particle that enters the target is a pion. Aside from the pion, the beam particles that are expected to pass through the upstream detectors are muons and positrons. Fig 7.2 shows that cuts on time of flight and degrader energy veto any contamination from the non-pion particles.

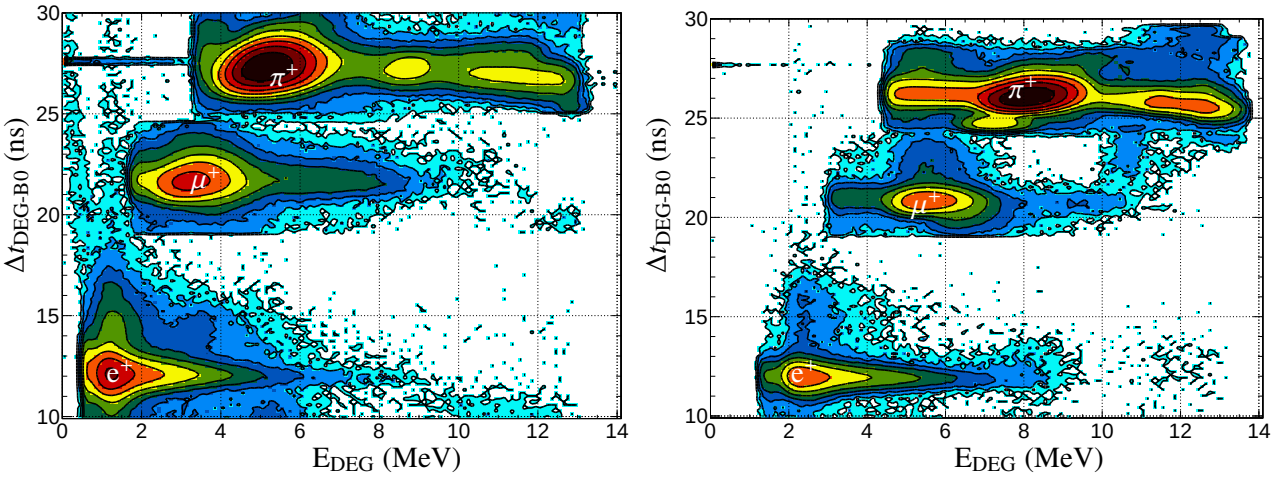

Figure 7.2: *Time of flight between B0 and Degrader for 2009 (left) and 2010 (right).*

Requiring the proper time of flights and degrader energies for the respective year also aids in eliminating multiple beam particles. For 2009, requiring a pion with time of flight between 25.5 ns and 29 ns and energy in the degrader less than 7.0 MeV and higher than 3.5 MeV will keep the sample of incoming beam particles to be relatively clean pions. For 2010, the time of flight is lower (higher beam momentum) so the time of flight is chosen to be between 25 ns and 27.0 ns with degrader energy between 6.5 and 10 MeV. Once this "mundane" requirement is made, events which result in positrons from the Michel decay or from pion decay are selected without favoring one process or the other unless the separation is for the purpose of counting

the number of events for the respective process. In other words, we want to eliminate as much unwanted background as possible by using cuts that will not favor the Michel positrons over positrons from pion decay. The main source of these background events are hadronic interactions, pileup and scattered beam events.

7.2.2 Scattered Beam Positrons

More often than not, when a pion decays into a muon, the muon will remain contained in the target during the 220 ns trigger window. However, during this time a positron from the beam within the same time window may reach the target or degrader and scatter into the the calorimeter. In this scenario, a stopped pion is present in the target and some time after the pion stops, a beam positron scatters, hits the hodoscope, triggering the event, and deposits energy in the CsI, hence, a false Michel or pion decay will be inferred. It is therefore desirable to veto these kinds of events. Not all beam positrons cross the B0 and the degrader as the degrader has a smaller cross section than the target. So it is possible that the beam positron miss the degrader and still enter and/or scatter off the target. The beam particle may also graze the degrader. The first detection of these events is a signal in the B0 at different times with the pion that did appear in the target. The energy and timing for positrons, muons and pions is seen in Fig 7.3.

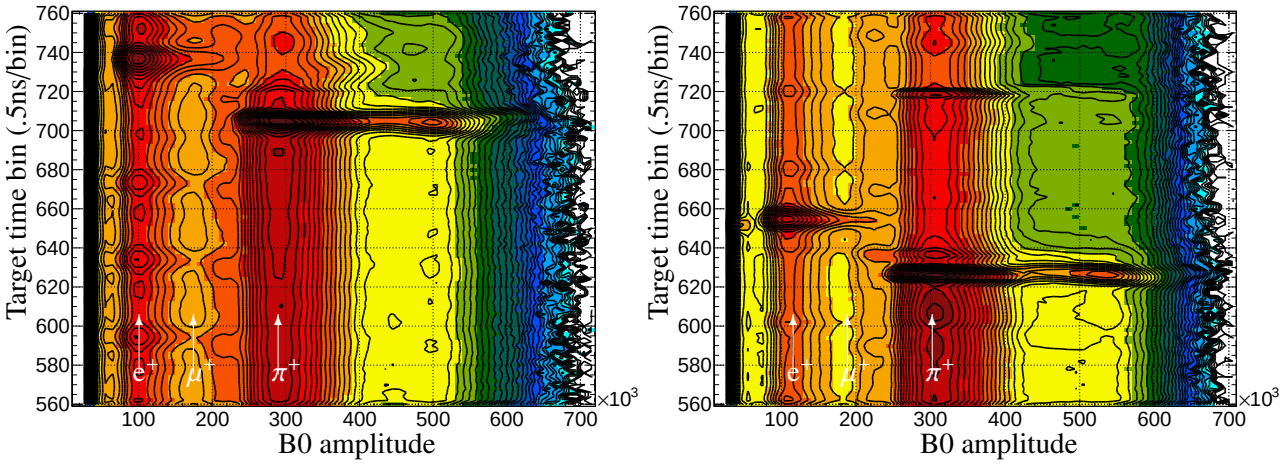

Figure 7.3: *Target time vs B0 amplitude. Left: 2009. Right: 2010.*

Fig 7.3 shows a time signature corresponding to roughly every 40 bins or 20 ns. This is also seen in the decay time spectrum at the beginning of this section in Fig 7.1. This feature originates from the ~ 50 MHz proton beam that produces the beam particles. The signature at 100 $\times 10^3$ amplitude possess less overlap than the signature the structure at nearly 180 $\times 10^3$ for nearby time bins. That is because the former is due

to scattered beam positrons which have a well defined time of flight, whereas the latter is due to muons which move slower and have more of a momentum spread. One should note that in 2009, the positron and pion are almost in phase with respect to the proton beam so the positron beam signal can't be found in early decays since it piles up with the pion. In 2010, the particles are optimally separated with respect to the 50 MHz signal and therefore the early positron signals cannot be masked by a pion. Fig 7.4 shows that in 2009 the beam positrons scatters are prevalent in the earlier part of 2009. This is due to a change in triggering conditions. In the beginning of the 2009 run period, there was only a very small minimal energy required in the target. Shortly after the 2009 run period began, there was an additional minimal energy requirement at the time of trigger (positron target energy in the target). While this condition lowered the number of beam positrons for 2009 slightly, this condition produces unwanted consequences that are discussed later on. The run year 2010 has fairly constant beam positron signals as seen in Fig 7.4.

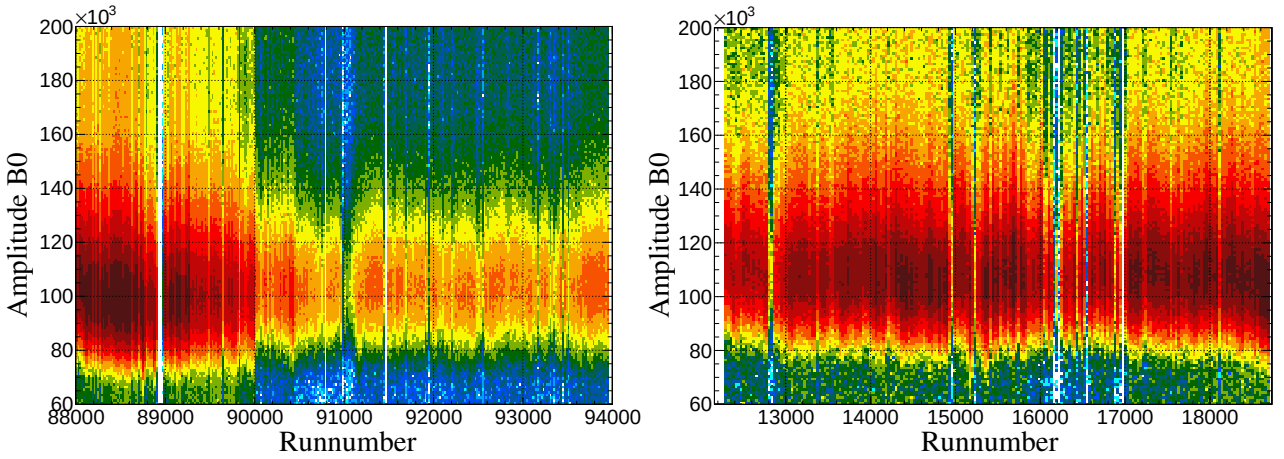

Figure 7.4: *B0 amplitudes as a function of runnumber in the scattered beam positron regime. Left: 2009 data run. Right: 2010 data run. The population of events diminishes around run 89000 for the 2009 data. The effect of implementation of minimum energy requirement at the positron decay signal (trigger time).*

There are two main ways in which these scattered beam positrons can contaminate the data set. The first is if the positron from the pion (or muon) does emerge from the target and in that same time window, the scattered beam positron also scatters into the fiducial volume. The second is if the pion or muon does not decay and the scattered beam positron will be attributed from a decay which doesn't occur. To eliminate these events, a requirement in the timing and energies in the upstream detector relative to the time in the target is implemented. In the case of no decay in the target, a requirement that the the positron tracking backtraces the positron trajectory to the target is imposed. The combination of these two requirements is built into a boolean observable called `scattered`. The effect and danger of the events can be seen by a

comparison of `decaytime` versus total track energy. The energy overlaps with both the tail and peak region of the $\pi \rightarrow e\nu(\gamma)$ decays. So not only do these events distort the decay time spectrum, but also contribute and distort the energy spectrum of the peak and tail in the CsI calorimeter. Depending on the length of the decay time window chosen for signal events, they can contribute a significant number of false signals as seen in Fig 7.5. Hence the necessity to eliminate them.

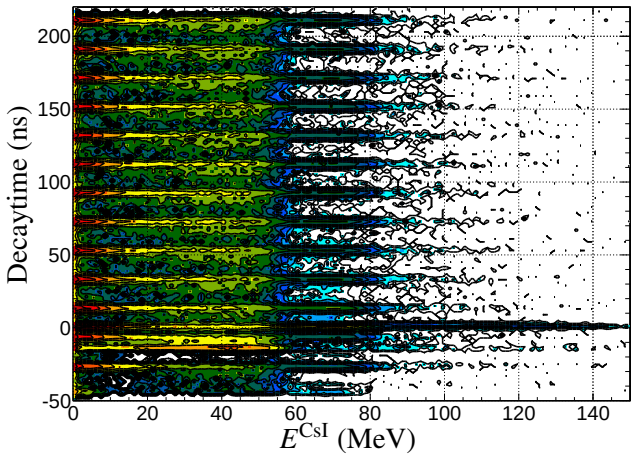

Figure 7.5: *CsI energy of a positron vs decay time when scattered==1.*

7.2.3 Hadronic Events

All stopped pion experiments must use the π^+ rather than the π^-. If the negative pions were used, then they would be captured by the plastic scintillator by virtue of attraction towards protons in nuclei, interacting hadronically, thus making a decay branching ratio measurement impossible. However, the π^+ is not immune to hadronic interactions either. The hadronic process that typically occurs is a pion being absorbed by Carbon (plastic scintillators) and a resulting proton (or deuteron) emerges with other decay produces, denoted, in the case of a proton, as $^{12}C(\pi^+, p)X$. There is also a single exchange reaction $^{12}C(\pi^+, \pi^0)^{12}N$ Separating the hadronic events from the signal events can be accomplished by observing the energy differences between these two processes. Because the hadronic process consists of protons and sometimes deuterons as the main by-products, they are easily identified These particles are heavy particles and non-minimum ionizing, a high amount of energy would be deposited in plastic scintillators. For these heavy particles, $dE/dx \sim 1/\beta^2$. The slower the particle, the higher the energy deposited. The plastic hodoscopes are used precisely for these types of occurrences and were constructed to veto protons that would result from hadronic interactions. In addition, the amount of induced charge in the MWPC gas will be higher because a proton will be traveling

at lower velocity. Once the proton interacts with the CsI, the amount of energy deposited could be as high as the pion mass itself. Since these hadronic events must originate from the pion, and the pion must at least pass the degrader (recall the decay time is determined from the degrader and hodoscope time), this means the hadronic event occurs before the predicted pion stop time, that is at around t=0. This is seen in the plots in Fig 7.1 and in Fig 7.6.

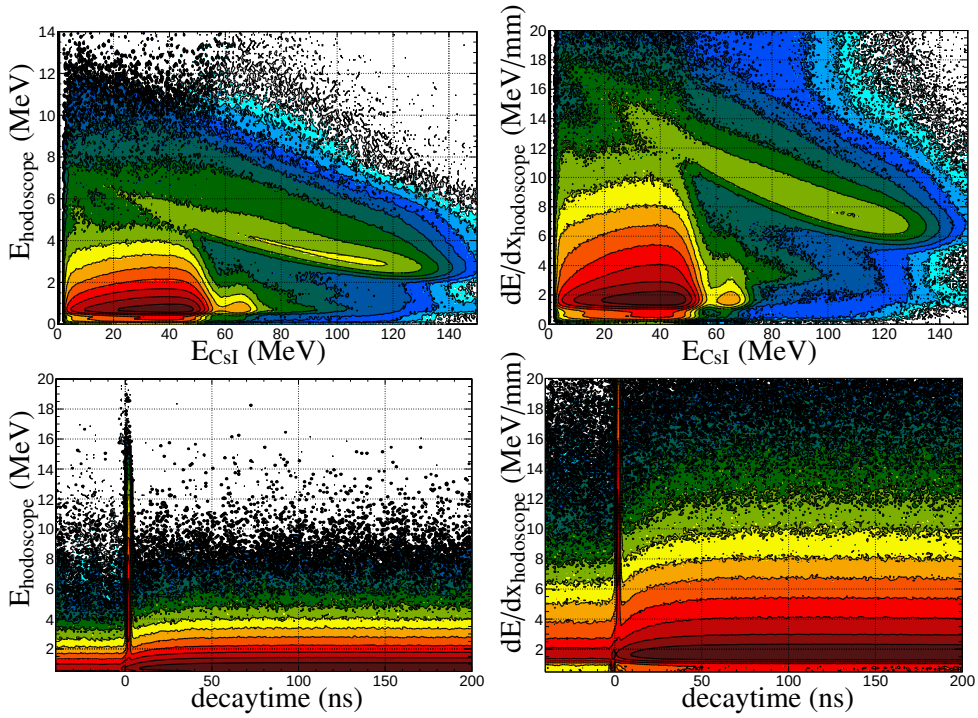

Figure 7.6: *Left: MWPC charge vs Energy in the hodoscope. Right: Energy in the hodoscope vs Energy in CsI. Hadronic events are identified by high energy deposition in the plastic hodoscope. CsI energy peak can occur as high as 140 MeV.*

While a cut on the early decay time does eliminate the hadronic events, this cut also eliminates a number of signal events. This inefficient cut would also contribute substantially to the error in the time window (as discussed later on). So a cut on the energy in the hodoscope or a cut on the dE/dx on the hodoscope is preferable to a decay time cut. There is no noticeable hodoscope energy dependence in the CsI in the regime that includes Michel and pion decays. This is because positrons are minimum ionizing particles, and their energy deposition in the plastic is virtually independent of the energy of the positron since the thickness is minimal. In reality the energy deposition is dependent on the natural logarithm of the energy, but is also related to number of protons in material in which the positron traverses. The upper right portion in Fig 7.6 shows dependence of the CsI energy and hodoscope energy for protons, which are not minimum ionizing

particles. A two dimensional cut in the energy spectrum between the CsI and hodoscope energy would seem appropriate. However, this cut may go cut away some of the hard radiative decays from pion decays while having no effect on the radiative muon or Michel decays. So a two dimensional cut on hodoscope energy and CsI energy may not affect the background and signal decays equally and is therefore not used, at least not at this stage. A signature with a high dE/dx around 10 MeV of energy is prominent at low CsI energy (roughly 10 MeV). This is indicative of a scattered beam pion. The pion deposits a relatively large amount of energy in the hodoscope because of the relatively slow moving particle. Since the pion has roughly 10 MeV of energy while entering the target, it will deposit roughly 4-6 MeV in the hodoscope and the remainder in the target. If the scattered pion decays into a muon in the CsI, the emergent muon has 4 MeV. The region where the Michel spectrum meets with the proton events around $dE/dx = 10$, is caused by more than one charged particle. The protrusion at $dE/dx = 3$ is caused by a scattered beam positrons with a decay positron. In short, a cut on the dE/dx of the plastic hodoscope is used to veto the protons and other contamination. This cut equally affects the number of $\pi \rightarrow e\nu(\gamma)$ and Michel events due to both processes possessing positrons with speeds near that of light and thus (roughly) the same energy signature in the hodoscope.

7.2.4 Pileup

When a pion decays in to a muon, the muon can stay "parked" in the target for a relatively long time. The lifetime of the muon is 2.2 μs compared to the lifetime of the pion, 26.03 ns. This means that the time that passes between the pion and stopping and the muon decaying is (in general) fairly long compared to the timing window for which the event would be recorded (220 ns). If a pion therefore decays into a muon which stays in the target, that muon may decay when a new pion makes its way to the target, or even after it hits the target. This muon decay would be counted as a Michel positron which is problematic because the emerging positron was not from the pion that is initially being studied. This is the essence of pileup and represents some of the background in the PEN experiment. In order to ensure that this background is fully removed, a cut on the ppileup (discussed earlier) is useful. Unfortunately, there is no magical selection to eliminate pileup completely and a subtraction is still necessary in the end. A bigger `ppileup` cut requires a smaller subtraction, but at the same time a bigger `ppileup` cut also decreases the number of events. Without a pileup cut, the possibility of having two particles in the target from different beam pulses is more likely which leads to a false branching ratio. The effect of pileup is best seen in the `decaytime` spectrum of the

Michel positron decay chain, chosen from the proper invariant mass as seen in Fig 7.7.

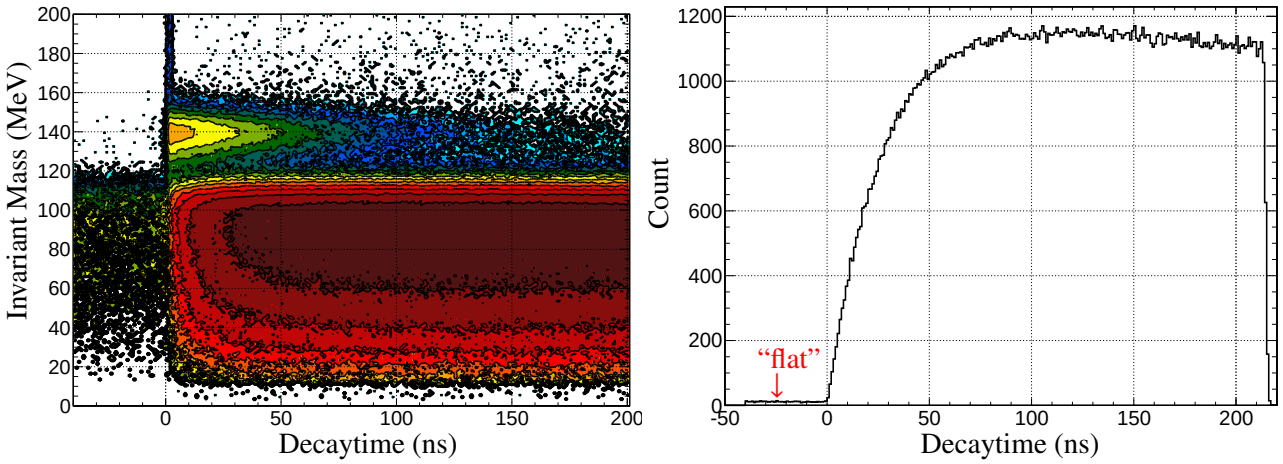

Figure 7.7: *Left: Invariant Mass plotted against decaytime. Right: Decay time for a slice of the invariant mass in the Michel region.*

One of the key features is that pileup manifests itself as a roughly flat background showing from -40 ns and going throughout the Michel decay time spectrum. This feature only occurs for the calorimeter energy regime in the Michel background because pileup events are positrons that are in fact Michel positrons but from previously stopped muons. Pileup is not present (or at least not statistically significant) in the pion signal decays. This in turn means that pileup cuts are not needed for the pion decay selection, but will be needed for muon decay selection. This brings up of a dilemma. Since a pileup cut is needed for Michel events, but not for $\pi \rightarrow e\nu(\gamma)$ events, then there would need to be a correction made to account for the two processes not being treated the same. This correction was not made by simulation because pileup is not simulated (as stated). If the same pileup cut is made for both event selections, then no correction is needed. In this analysis, the same pileup cut is used for both types of events.

7.2.5 Track and trajectory

Up until now, methods have been established to eliminate pileup, scattered beam events, and hadronic events. Aside from these cut selections that have already been discussed, it it advantageous to look at track conditions and how requirements on the track may eliminate unwanted background. The two observables of particular interest are *z0*, the z position that comes closest to the beam track using the MWPC from the trajectory, and the angular trajectory, specifically the polar angle, θ, which is also deduced from the MWPC

trajectories. This reveals knowledge as to where the decay particle originates and how the decay time and energy distribution behaves for certain trajectories. There is a spike in events that occur at `decaytime` of zero and throughout all `z0` values, and also a spike at `z0` = −70. The spike at decay time of 0 indicates that many of the events that originate at negative z values are either scattered pions or originate from hadronic events. A good number of these at `z0`= −70, the position of the degrader for 2009, the data used in Fig 7.8. This is where scattering of the pion or hadronic interaction (higher energy) would occur most prevalently, at least upstream. In addition, periodic signatures in decay time occur at this value as well, suggesting that some of the scattered beam events occur in the degrader, which was already explained. When studying the angular distribution as with the CsI energy, there are features at high and low angles with low energy. These features can be seen in Fig 7.8. This is mainly due to the energy leakage of the CsI calorimeter laterally near the detector holes. Losing energy in this fashion is problematic as events from peak signal in the CsI calorimeter would be forced into the low energy tail region making the tail fraction even more difficult to characterize.

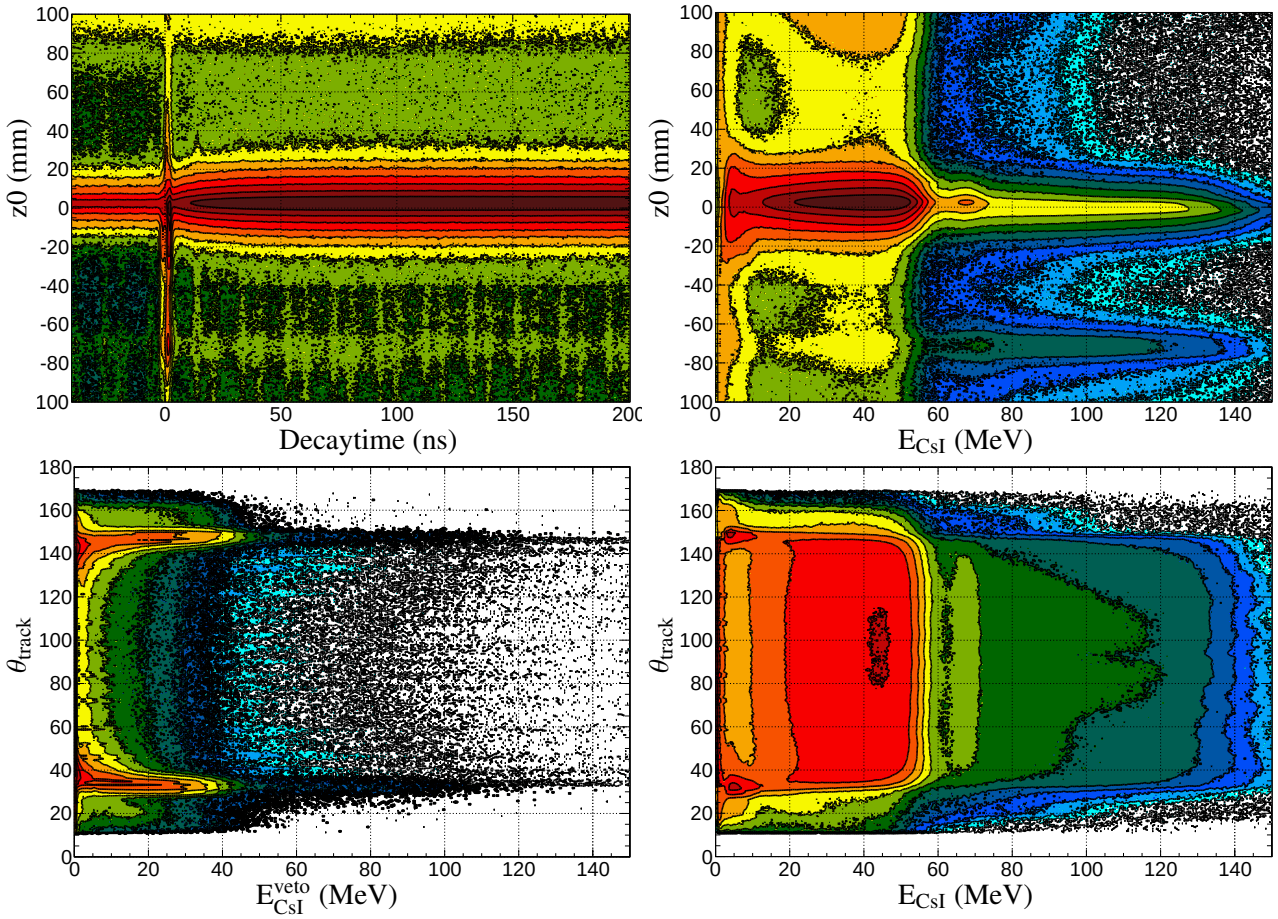

Figure 7.8: *Overview of positron selection with regards to energy in the CsI and decay time with information from the MWPC.*

A cut on both the θ distribution and z0 is thus desirable. A cut on θ will veto out many of these energy leakage problems without specifically putting an energy requirement on the CsI which prevents any of the signal and main background. A cut on the veto crystal energy, as was used in the PiBeta experiment, may be problematic because the amount of energy that would be collected in these crystals would be different for the $\pi \rightarrow e\nu(\gamma)$ and the Michel events. A requirement of zero energy in these crystals would be ideal, but does not treat the two processes equally as the fraction of the energy in the main crystal is different for the two different processes and thus the energy in the veto crystals are different in the two different processes as seen in Fig 7.9. By imposing a restriction on the energy in the veto crystals, the main signal channel and normalization background are affected differently and thus a further correction would be needed. This correction, however, would be accounted for by the acceptances. Since this analysis is performed without the acceptances, no cut on veto crystal energy is performed but rather a cut on track trajectory is used.

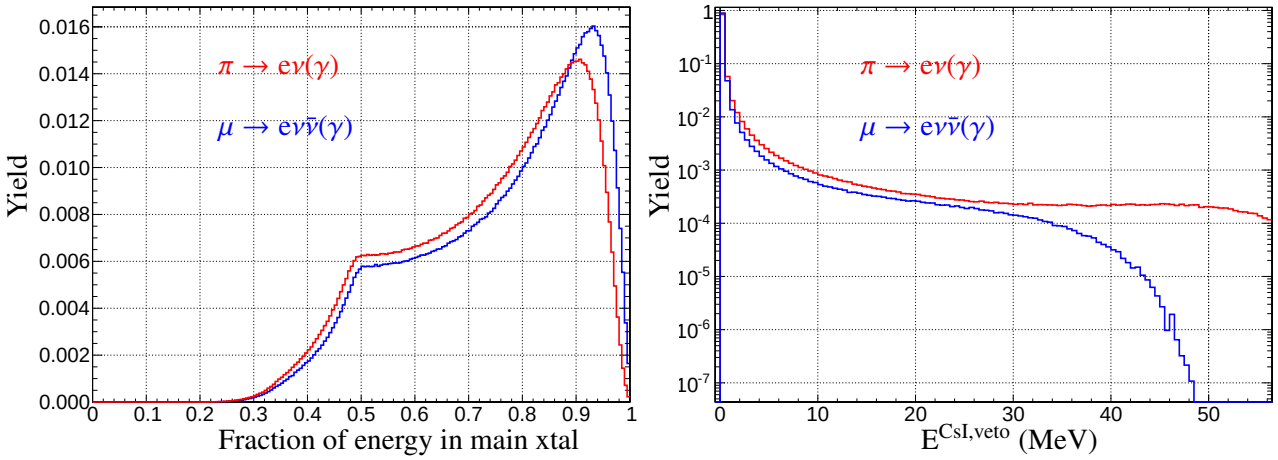

Figure 7.9: *Left: Fraction of energy in the main crystal for the two different main processes. Right: Energy spectrum in the veto crystals for the two main processes.*

7.2.6 Decays in Flight: General

Among the background events that may occur are the decays in flight. As pions travel through the beamline, a small amount of proper time passes in the particle's rest frame. For example, suppose the π takes 27 ns to travel from the B0 to the degrader as measured by the lab frame (This is the case with 2009). With this time of flight and the distance being slightly over 3.5 m, the velocity a pion is .44c. This in turn means that in the rest frame of the pion, 24.24 ns has passed. With a pion lifetime of 26.03 ns, a substantial amount of pions (roughly 60%) should have decayed in between these two detectors. While this is the case, if the pion doesn't reach the target, the event would not be triggered due to required minimum energy in the target. A degrader signal, and later on, a target signal is required in order for the event to be recorded. Therefore corrections needed for decays in flight are performed for those events in which the pion hit the degrader and result in some energy deposited in the target before decaying in flight, not the decays in flight that happen after the B0 and before the degrader. This subtlety is important because the branching ratio calculating in the experimental section assumes that the pion had actually stopped. Decays in flight are not always easy to separate from the decays at rest. Therefore we chose not to attempt to count them, but rather correct for them with the aid of the Monte Carlo and put them into the acceptance calculation.

There are four different types of decays in flight that the PEN experiment encounters. The first is when the pion decays in flight into a muon, π_{DIF}. The second is when the pion decays in flight into a positron, π_{DIF2}. The third is when the pion decays at rest, a muon emerges and the muon decays in flight, μ_{DIF}. Lastly,

is when there are two decays in flight that occur sequentially. That is a double decay in flight (DDIF) where the pion decays in flight and the muon that emerges also decays in flight, π_{DDIF}.

An overview of some signatures that these decays produce are given in Fig 7.10 along with the normal Michel and $\pi \rightarrow e\nu(\gamma)$ decay. One of the key features is that the muon decay in flight has similar target spectra to that of the main $\pi \rightarrow e\nu(\gamma)$ signal including rest target energy and identical decay time spectrum. This presents a problem for removing these particular events from the data set. To complicate matters further, the energy spectrum of the muon decay in flight dominates in the low energy tail regime to an extent that is greater than the yield of the tail for the $\pi \rightarrow e\nu(\gamma)$ decay main channel. This complicates the characterization of the low energy tail because of the necessary correction needed to subtract the muon decays in flight in order properly characterize the low energy tail in the measured data for proper comparison with the Monte Carlo.

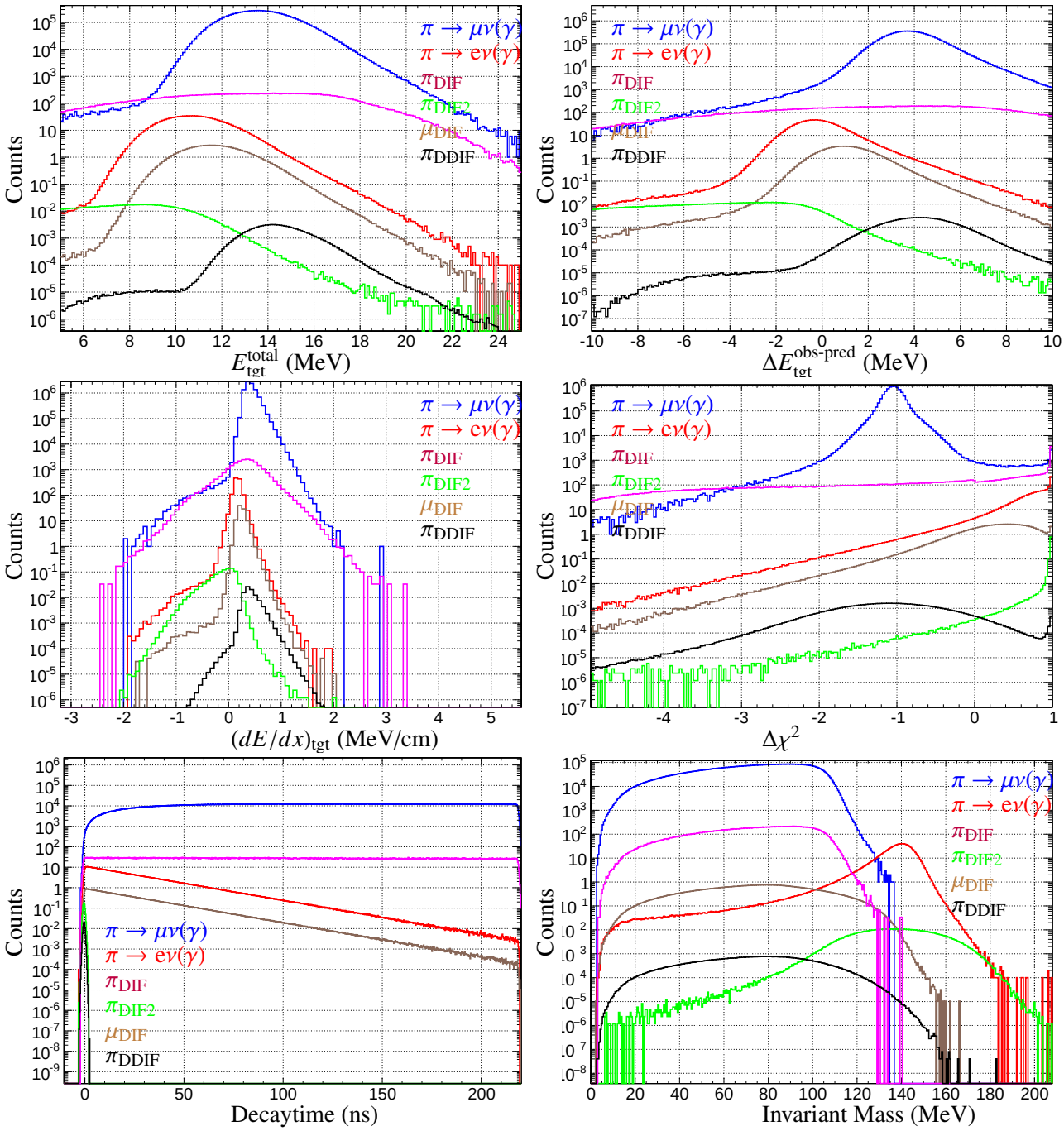

Figure 7.10: *Spectra for decays in flight for all decays in the PEN experiment compared to the main signal and background normalization. Upper Left: Total target energy. Upper Right: Restwave. Middle Left: Target dE/dx. Middle Right: $\Delta\chi^2$. Lower Left: Decay time. Lower Right: Invariant mass. Yields are normalized to the theoretical yields based off of particle lifetimes.*

Given the different types decays in flight, this section is broken up discussing each of these different decays individually. In particular, how to identify, to the degree possible, each of the decays in flight in the data, explain the above plots, and to the degree possible, remove a fraction of them from the data analysis

using cuts on various observables.

7.2.7 Decays in flight: $\pi_{\mathbf{DIF}}$

The probability of the pion decaying in flight while in the fiducial volume of the target is determined in a straightforward manner. A simple a back of the envelope calculation (or bar room napkin) to determine the probability, P, of the pion decaying in a certain time requires the time window and the pion lifetime. Using the time difference between the pion first entering the target and the time it takes for the pion to stop, which, the GEANT4 simulation determines to be roughly 0.07 ns as seen in Fig 7.11.

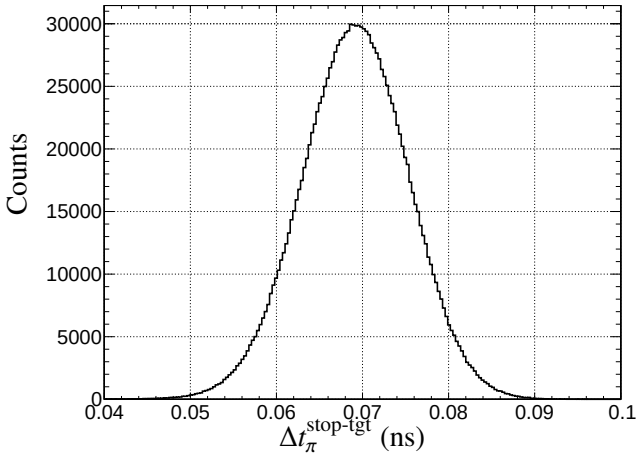

Figure 7.11: *Time it takes for the pion to stop after entering the target according to Monte Carlo simulation.*

Using this time, and the pion lifetime, which is well known, the probability of the pion decaying in this short time is

$$P_{\text{DIF}} = (1 - e^{-.07/26.03}) \simeq 0.0027 = 0.27\% \tag{69}$$

Thus decay in flight happens on average one for every 400 pion stop events recorded. This is not negligible but it also does not yet account for any trigger conditions and or cuts that would be used in the cleansing of the data. Since the pion decays into a muon (more often than not), this value will be taken as the probability of a pion decaying into a muon while the pion is in flight in the target. Since the muon would have appeared only fractions of nanoseconds after the pion appeared in the target, for all intended purposes, the time at which the muon appears in the target for pion decays in flight is still at time $t = 0$ or

at the predicted pion stop time. Now the muon itself will traverse the target and will take some time to stop. Once the muon stops which again GEANT4 determines takes, on average, 0.0223 ns as shown in Fig 7.12. So for all intended purposes, the time at which the muon stops is at still time equal to 0 ns.

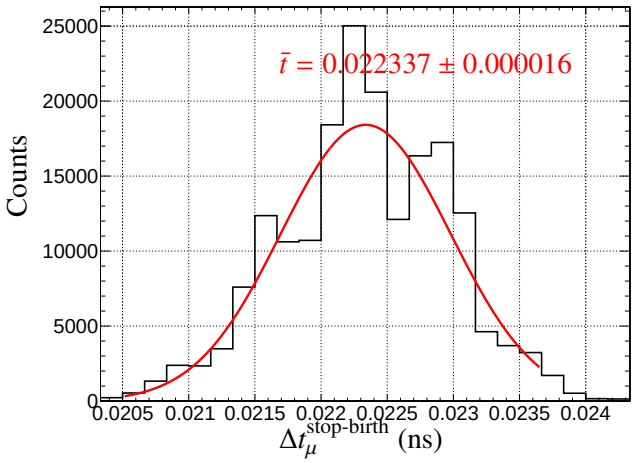

Figure 7.12: *Muon travel time before it stops, obtained from GEANT4 simulation. Coarseness of the figure is due to the discrete finite stepping in the small time window.*

This means when we normally expect a pion to be at rest, we have a muon at rest in the target as well. The decay time spectrum for these types of events will be indicative of a muon decay time curve instead of a pion decay time curve. This is precisely depicted in Fig 7.10. The predicted pion energy is based on time of flight between the B0 and the degrader and therefore will have no knowledge of decaying in flight. In other words, the predicted pion energy is the expected energy that the pion would deposit if it were to decay at rest. Subtracting from the observed pion energy will be informative because although the pion will deposit less energy than predicted because it decays in flight, the muon will also deposit energy. Therefore, the further the pion goes into the target, the more energy deposited into the target and the smaller discrepancy between predicted and observed pion target energy. There exists a caveat however, in that this is slightly dependent on the direction of the emerging muon when the pion decays in flight. If the muon emerges and stops in the direction of the pion, then the predicted stopping position of the pion is close to the predicted stopping position of the muon. This in turn means that the predicted energy of the decay positron will be well matched with what the emerging positron from said muon decay. However, if the muon emerges from the pion decay in a different trajectory, the emerging positron may deposit more or less energy than it is predicted. This is why the target rest energy may take a variety of values. However, it should be observable, that as the pion decays closer to the entrance to the target, there is expected to be more of an energy deficit

in the target. By comparing the difference in predicted and deposited energy in the target with the z position using the MWPC where the positron is born using the predicted stopping x,y positions, it becomes fairly apparent how to see decays in flight of this type compared to Michel events that originate from stopped pions from Fig 7.13.

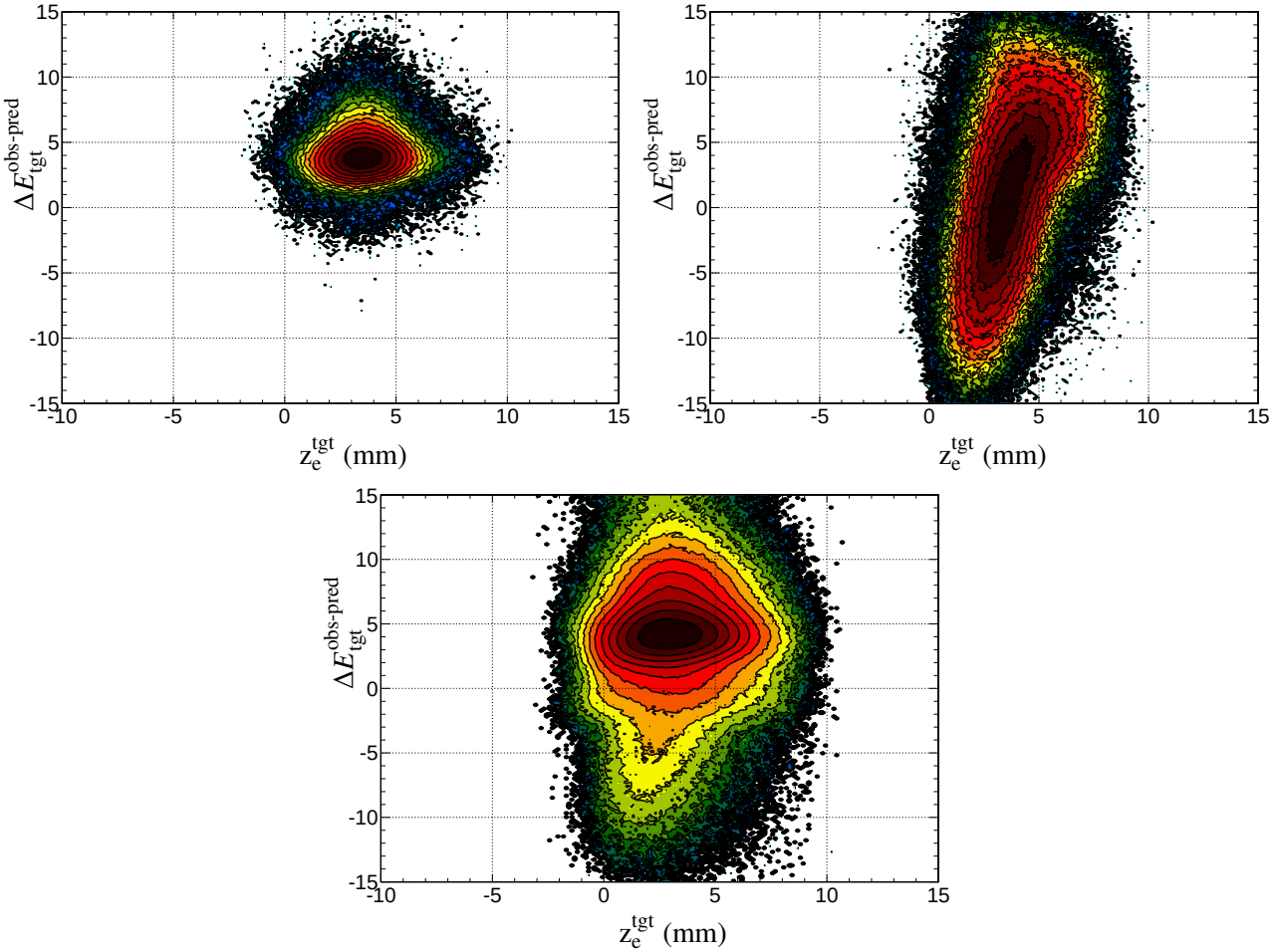

Figure 7.13: *Predicted energy subtracted from observed target energy plotted against the z birth of positron extrapolated using MWPC and predicted x,y stop positions. Left: Simulation $\pi \rightarrow \mu\nu$ events decaying at rest. Right: Simulation π_{DIF} Bottom: Measured data.*

It must also be mentioned that since the muon stops, the emerging energy of the positron is the same as if the pion stopped and produced a stopping muon. This means of course that the energy in the CsI should be no different from the Michel spectrum because the positron leaving the target comes from a muon that decays at rest in both cases. The side possibility, is the notion that the muon, since it has more than 4.1 MeV it will travel farther than 1.3 mm that the muons produced in stopped pion decay will traverse. If this muon leaves the target, then the decay time spectra will be indicative of a pion decay signal to positron. The

energy deposition in the CsI has a different spectra. While the pion decaying in flight will mostly decay into a muon, it is possible that it decays into a positron, which is considered next.

7.2.8 Decays in flight: π_{DIF2}

While the pion decaying in flight more often than not decays into a muon and neutrino, it is possible that it decays to a positron and neutrino. In these type of situations, the positron appears in the target very shortly after the pion appears in the target. This means there will be no more than one pulse in the target that shows up at around decay time of zero (recalling the pion stop time is predicted using the degrader time and time of flight of the pion from degrader to target). While this type of decay is rare, it happens $\sim 10^{-7}$ for every pion that enters the target. However, since the $\pi \rightarrow \mathrm{e}\nu(\gamma)$ branching ratio is on the order of 10^{-4}, then the number of times the decays in flight occur for this decay branch is on the order of 10^{-3} relative to the $\pi \rightarrow \mathrm{e}\nu(\gamma)$ at rest. This means that a small correction for these decays in flight is required to account for events that occur in the signal peak of the CsI calorimeter. Note these decays will not affect the Michel positron count, since this is determined using a long time window far away from time 0. From theory, we expect $1 - e^{-t_{\mathrm{stop}}/26.03\mathrm{ns}}$ decays in flight for the pion, regardless of daughter particle (positron or muon). According to simulation, the average stopping time for the pion is 0.07 ns. In order to account for these, the simulation must be employed. So first one must identify these events in the measured data, and show that the data and the simulation are consistent with each other as was done with π_{DIF}. Then using the simulation, the number of decays in flight can be counted to ensure that the branching ratio calculation is correct if the contamination exists in the $\pi \rightarrow \mathrm{e}\nu(\gamma)$ branching ratio selection.

Identifying these events in the data is fairly straightforward. Since these decays occur at early times (around or before the predicted pion predicted stopping time), these events are isolated by selecting early decay time events. Since the pion decays before depositing all of its energy, the predicted pion energy will be an over prediction. By selecting events with a target energy deficit, further isolation of these events occurs. Simply choosing the events in the spike of the decay time near zero is not sufficient because these contain the aforementioned hadronic events. From simple kinematics of a particle decaying in flight, a relationship

between the angular distribution of the positron with its energy given by

$$\cos\theta = \frac{E_\pi}{\sqrt{E_\pi^2 - m_\pi^2}} - \frac{m_\pi^2}{2E_e\sqrt{E_\pi^2 - m_\pi^2}} \tag{70}$$

where E_π is the energy of pion when it decays. Although the pion energy is not precisely known for decays in flight, the pion energy after the degrader is predicted (as stated earlier), so a range of values of pion decay energies may be used to predict the region of phase space where to look as seen in Fig 7.14.

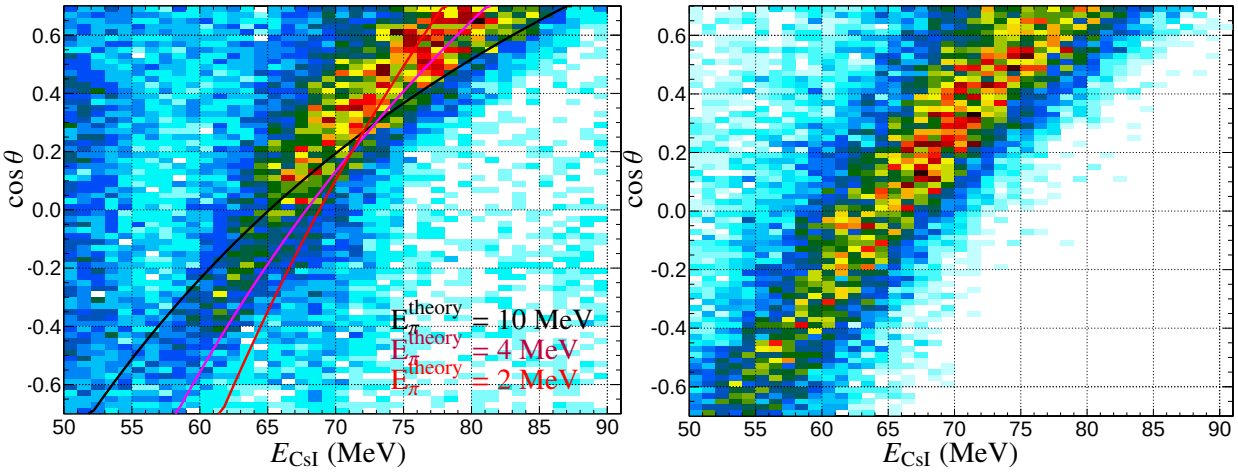

Figure 7.14: *Relationship between trajectory and positron energy for selection of pions decaying in flight to positron. Left Measurement. Right Simulation. The measured data is selected by choosing events with a large target energy deficit (4 MeV) and decay times less than or equal to zero.*

Since the number of pions is counted using the first few nanoseconds before the zero time, there will be a number of positrons that are assumed to be decays from pion stops when in fact they are decays in flight. While the two processes that involve solely the pion decaying in flight are identifiable in the measurement data, the events where muons decay in flight are not easily separable from the data sample and indeed cause for concern in the branching ratio calculation.

7.2.9 Decays in Flight: μ_{DIF}

Similar to the pion decay in flight, a back of the envelope calculation can be made as to how often a muon decays in flight. Using the average stop time of the muon,

$$P_{\mu_{\mathrm{DIF}}} = (1 - e^{-.0223/2197}) \simeq 1.0 \times 10^{-5} \tag{71}$$

While this is small compared to the number of pions stops, this is not small compared to the number of pions that stop and decay into a positron. The probability of a pion stopping and decaying into a positron is about 1.23×10^{-4}. The probability of a pion stopping and a muon decay in flight occurring is the same as the probability of a muon decaying in flight given that the pion stopped and decayed into a muon which is approximately the result given. This means that for every ten pion decays into a positron, we expect roughly one muon decay in flight. Thus this process is non-negligible compared to the signal event which may cause problems. Since the muon decays in flight, the positron is born, on average, only 0.0223 ns after the pion stops, which for all intended purposes is the pion stop time. This means that the positron detection time (decay time spectrum) will have the same decay time spectrum if a pion stopped and directly decayed into a positron (the signal event!). This is why the decay time spectrum for muon decays in flight is virtually identical to that of the $\pi \rightarrow \mathrm{e}\nu(\gamma)$ decay. As seen in Fig 7.10, the energy deposited in the target by the muon may be very small and as a result, the rest target energy possesses a similar spectrum to that of the $\pi \rightarrow \mathrm{e}\nu(\gamma)$ decay. This makes it difficult to eliminate or even identify the muon decays in flight in the experiment. The only separating characteristic is the energy that the emerging positron will deposit in the CsI calorimeter. This means depending on how the events are chosen, and where the tail/peak dividing line is chosen, corrections are needed; they can be performed reliably using the known values and response of the Monte Carlo.

7.2.10 Decays in Flight: π_{DDIF}

The frequency of the double decays in flight can be calculated by multiplying the probability of the pion decaying flight and the probability of the muon decaying flight. This is on the order of 2×10^{-8}. This means that the relative number between the double decay in flight is on the order of 10^{-4}. However, by choosing

a peak/tail separation, the relative number then becomes statistically insignificant. Hence this type of decay will not affect the branching ratio.

7.2.11 Other background processes

The remaining possible background processes from pion decays that could show up in the data sample are $\pi^+ \to \pi^0 e^+ \nu_e$, $\pi^+ \to e^+ e^+ e^- \nu_e$, or $\mu^+ \to e^+ e^+ e^- \nu_e \bar{\nu}_\mu$. The first process occurs approximately once for every 10^8 pion decays. It results in a positron with no more than 4 MeV, a neutrino, and a neutral pion. The neutral pion immediately decays with 99% probability into two gammas back to back, depositing roughly 135 MeV total in the calorimeter. The up to 4 MeV positron is very unlikely to register energy in the calorimeter as energy is lost in the target, the chamber, and the hodoscope. The very low energy positron is somewhat unlikely to register hits on the chamber. So if no charged track is reconstructed, by not igniting the chamber, then these events will be cut out. An additional requirement to to eliminate these events is to impose the restriction of two neutral showers from being back to back. These simple requirements will not affect the number of Michel events counted nor will it affect the number of positrons from pion decays but will suppress the pion beta decays from the data sample sufficiently so as to not affect the branching ratio. The decay into three leptons from a pion occurs once every 10^9 decays so is not in the range of the desired precision of the experiment. At any rate, requiring one charged track would eliminate them. The Dalitz decay $\pi^0 \to \gamma e^- e^+$ that follows from $\pi^+ \to \pi^0 e^+ \nu$ occurs at the 10^{-9} rate as well. The same goes for the $\mu \to eee\nu\bar{\nu}$ which occurs three times in every 100,000 decays. With the cuts discussed in this and the previous sections, the only types of pion decays that remain to any statistical significance are $\pi \to e\mu(\gamma), \pi \to \mu\nu(\gamma)$, the decays in flight, and pileup.

7.3 Radiative decays and invariant mass

Now that the data sanitation has been explained, some comments about radiative decays are noted in this section. Throughout this work it has been noted that there is no separation between radiative and non-radiative decays for the π and the μ. Therefore, the radiative decays must be included to obtain the correct branching ratio. In order to do that, two things must be established. The first is to identify the hard (high energy) photons and the second is to ensure that the simulation correctly models these decays. When study-

ing radiative decays, it will be seen that it is advantageous to use the reconstructed invariant mass in lieu of the positron energy primarily because by construction, the energy of the photon is included. To give a simple idea of why invariant mass, and therefore inclusion of radiative decays in the analysis is beneficial is to consider the tail fraction. For example, suppose a hard radiative decay occurred with photon energy of 120 MeV and positron energy 15 MeV. Though the probability of this is small, if one were to count the positron energy only in the CsI, then positron energy in this case would most definitely end up in the tail region but not due to energy leakage, but rather due to the fact that it only had 15 MeV to begin with. This complicates the tail analysis in that these hard radiative events would need to be accounted for. In addition, suppose a radiative muon event occurred with total energy of 60 MeV contained in one shower. This kind of event may easily end up in the peak region and falsely give perceived positron from a pion decay rather than muon decay. Without including the radiative decays automatically and only using the energy in CsI by the positron, additional corrections to the tail and peak count would be needed. The different tail fraction responses are shown in Fig 7.15 for different considerations.

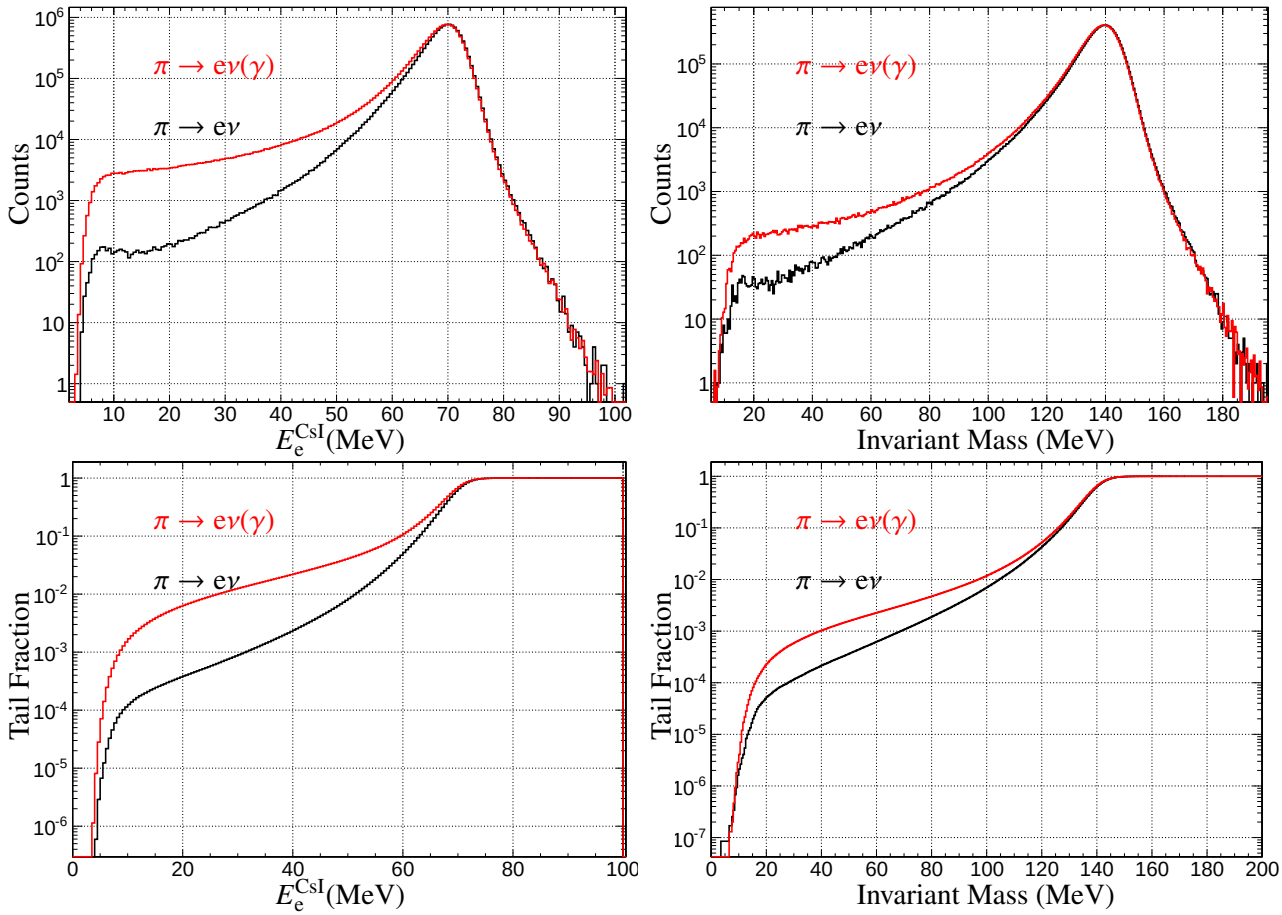

Figure 7.15: *Comparison of fictional $\pi \to e\nu$ non-radiative decay and real radiative decays $\pi \to e\nu(\gamma)$ Upper Left: Response of the CsI calorimeter for the charged track. Upper Right: Reconstructed Invariant mass. Lower Left: Tail fraction as a function of energy in the CsI for the charged track. Lower Right: Tail fraction as a function of reconstructed invariant mass.*

These features originate from the geometry and setup of the PEN detector. Since the PEN detector is capable of measuring the momenta of the photon and positron, it indirectly measures the momentum of the neutrino,

$$\vec{p}_\nu + \underbrace{\vec{p}_e + \vec{p}_\gamma}_{p_{\text{observed}}} = 0 \qquad \underbrace{E_\gamma + E_e}_{E_{\text{observed}}} + E_\nu = m_\pi c^2 \tag{72}$$

By measuring sum of the two momentum vectors of the photon and positron, the neutrino momentum vector is reconstructed. Since the neutrino is taken to be massless, the magnitude of the neutrino's momentum, which is the magnitude of the observed momentum, equals its energy. Rearranging the energy conservation formula gives

$$E_{\text{obs}} + p_{\text{observed}} c = m_\pi c^2 \tag{73}$$

The features of this scheme can be seen most easily when plotting CsI momentum (the magnitude of the vector sum) vs the energy. These plots are sometimes referred to in the group as "florida" plots in the PEN collaboration seen in Fig 7.16 and shows not only how the reconstructed invariant mass is formed but also shows that there is no such thing as "non-radiative" decays.

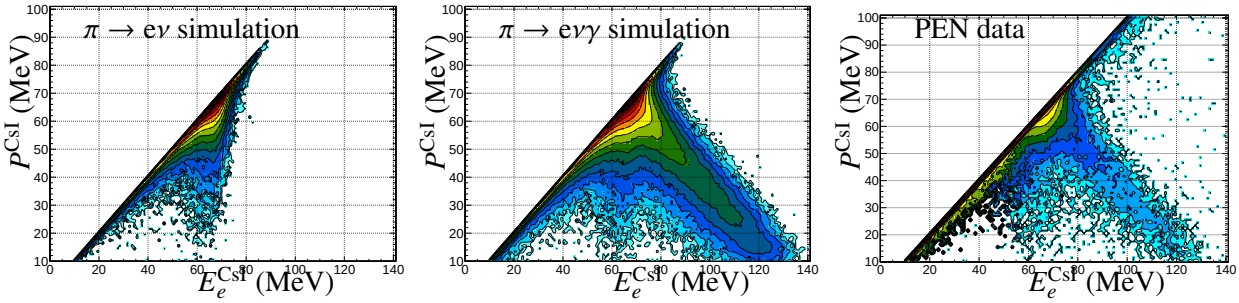

Figure 7.16: *"Florida" plots. Upper Left: $\pi \rightarrow e\nu$ simulation. Upper Right: $\pi \rightarrow e\nu(\gamma)$ simulation. Lower: Selection of 2010 Data.*

Fig 7.16 shows for simulated $\pi \rightarrow e\nu$ decays that the reconstructed momentum lies on the E=pc line (c=1 in the plots above). This is also true for the three body $\pi \rightarrow e\nu(\gamma)$ decay where the energy of the photon is very small (and hence collinear with the positron). This follows from the kinematics of a two-body decay with two massless particles. In such a two body decay, the positron and neutrino must have the same momentum (in opposite directions) and thus for massless particles same energy. The reconstructed momentum of the neutrino then is the same as the momentum of the positron, which is the energy of the positron measured by the CsI calorimeter. In hard decays (upper left) the the total E+pc= m_π (for minimal energy leakage) and this is what is seen in the data. The small tail in the "non-radiative" decays is attributed to split clumps. This is where a photon in an a electromagnetic shower splits off the main clump and ignites a shower in a different region of the calorimeter. The comparison and agreement between simulated and observed radiative decays is crucial in order to include them in the branching ratio. The comparison can be accomplished by taking a similar approach used similar the PiBeta analysis. Firstly, the phase space is broken up into regions A, B, C, and D. It should be noted because of triggering conditions, PiBeta could only observe regions A, B, C [27].

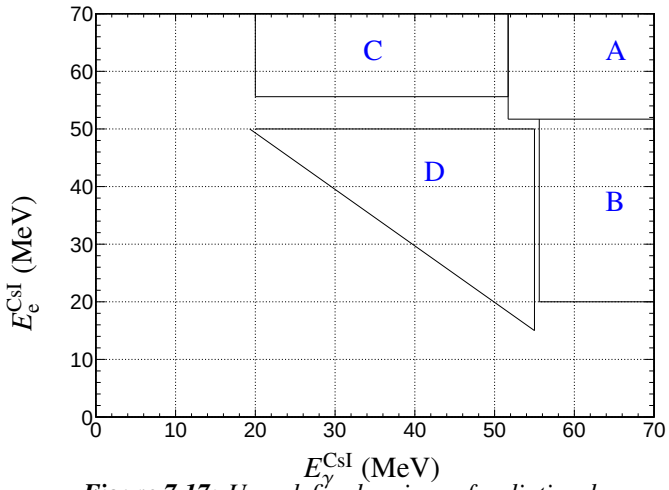

Figure 7.17: *User defined regions of radiative decay*

It should be noted that region D is in the region of the lowest opening angle between the photon and the positron, spanning and opening angle, $\theta_{e\gamma}$ between zero and eighty. Whereas the majority of other regions have opening between 120 and 180. Constructing the parameter, λ,

$$\lambda = 2E_e/m_\pi \sin^2(\theta_{e\gamma}) \tag{74}$$

simulation and data can be compared in the four regions as seen in Fig 7.18. A friendly reminder to the reader that because of kinematic constraints, the energy of the photon and positron combined must be greater than half the pion mass. In other words, nothing appears below the diagonal that connects the upper left and lower right.

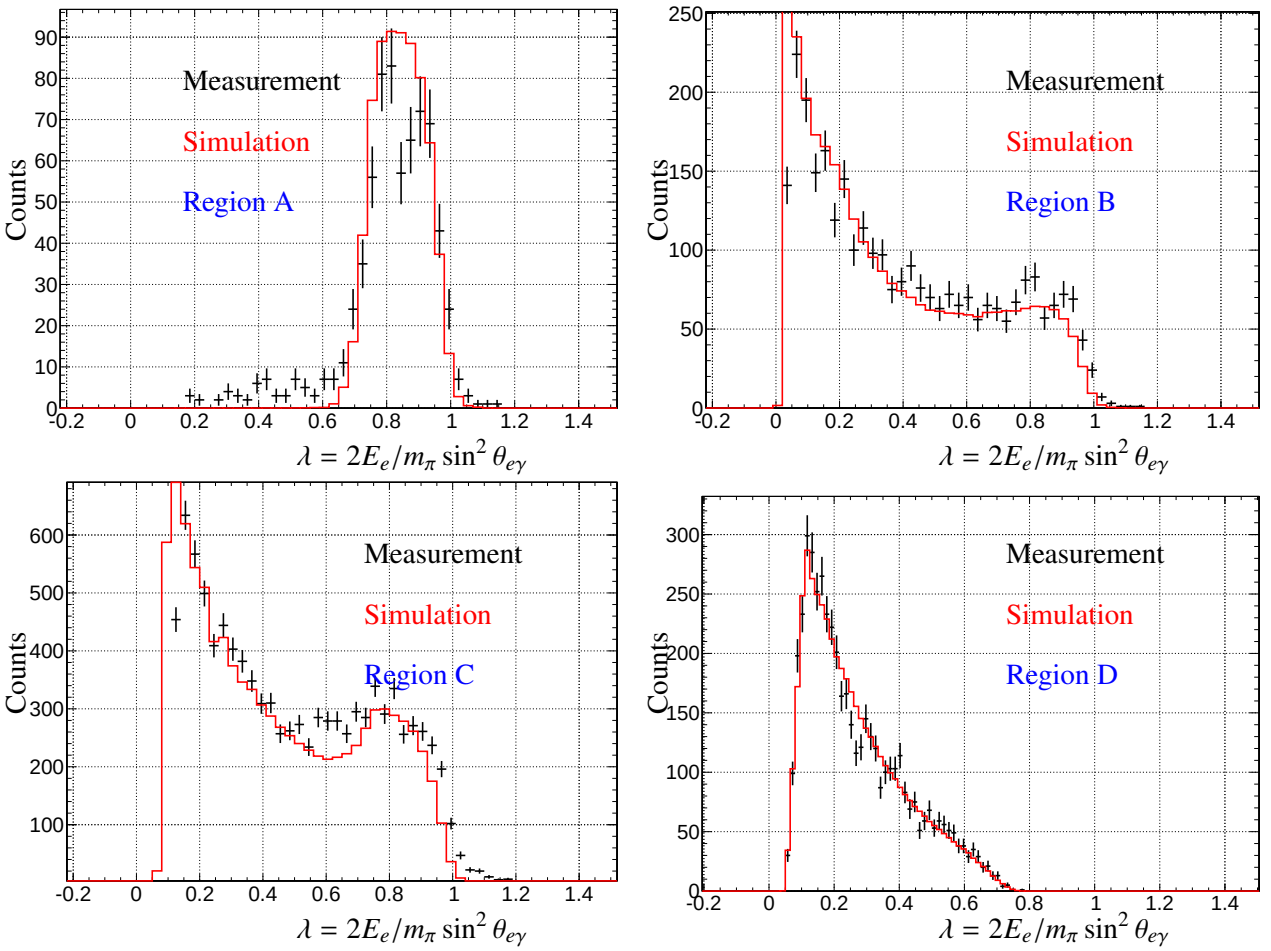

Figure 7.18: *Selection of 2010 data in the four regions of λ with simulation comparison. Upper Left: A. Upper Right B. Lower Left C. Lower Right:D.*

Comparing with PiBeta analysis and focusing on regions A, B, and C, the decay time spectra and the coincident times between the positron and the gamma in the CsI show consistency with the simulation and show the same decay time signature of pion “non-radiative” decays.

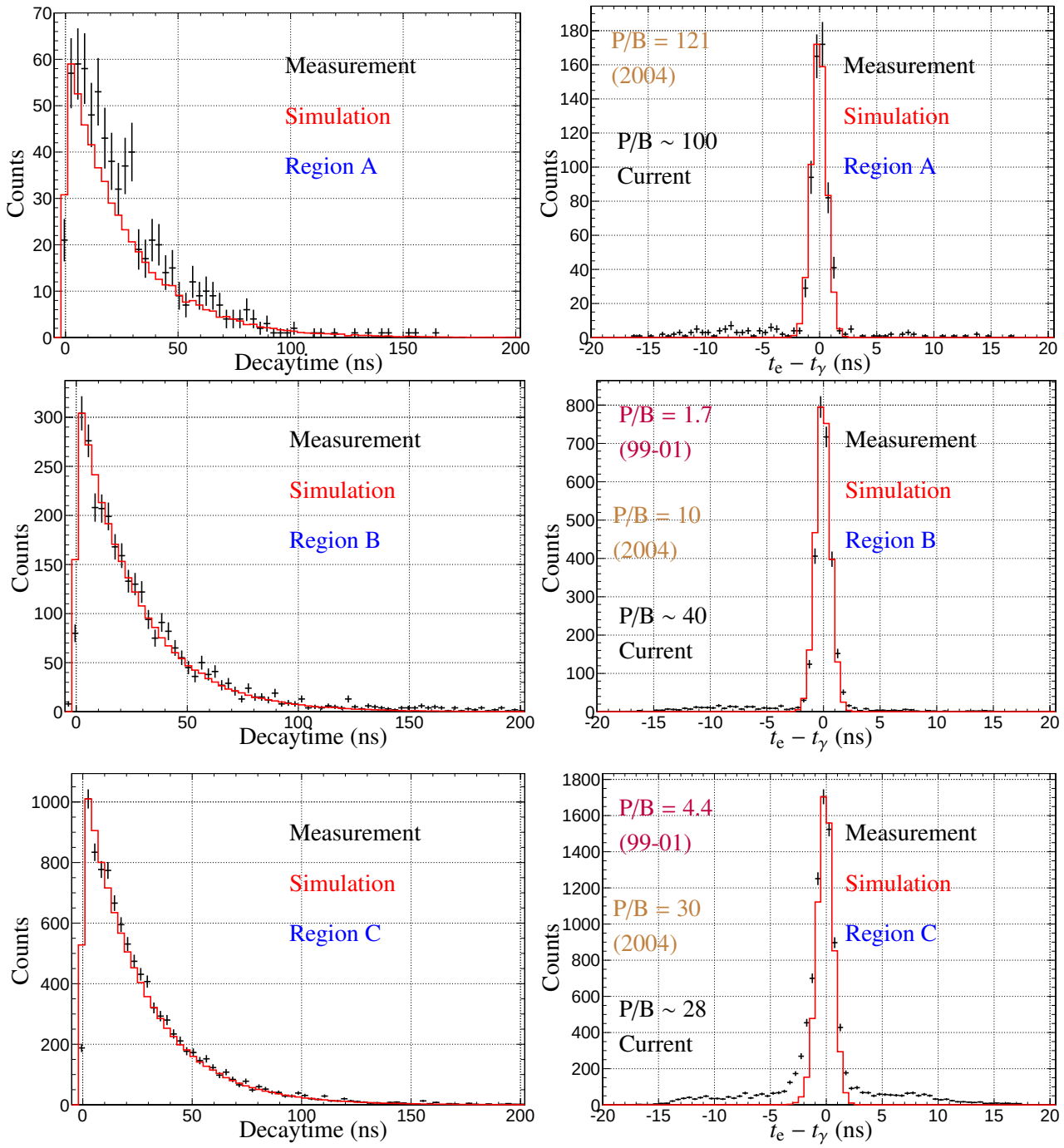

Figure 7.19: *Timing profiles for radiative pion decays in regions A, B, C. The Peak to background ratio for PEN (black), the 2004 PiBeta decay (brown) and 1999-2001 Pibeta decay (purple).*

The above plots in Fig 7.19 show that the radiative pion decays are in good agreement between the expected signatures (simulation) and comparable to the quality of data achieved in the PiBeta experiment. As

stated. the PEN experiment has access to Region D and its spectra are shown here in Fig 7.20.

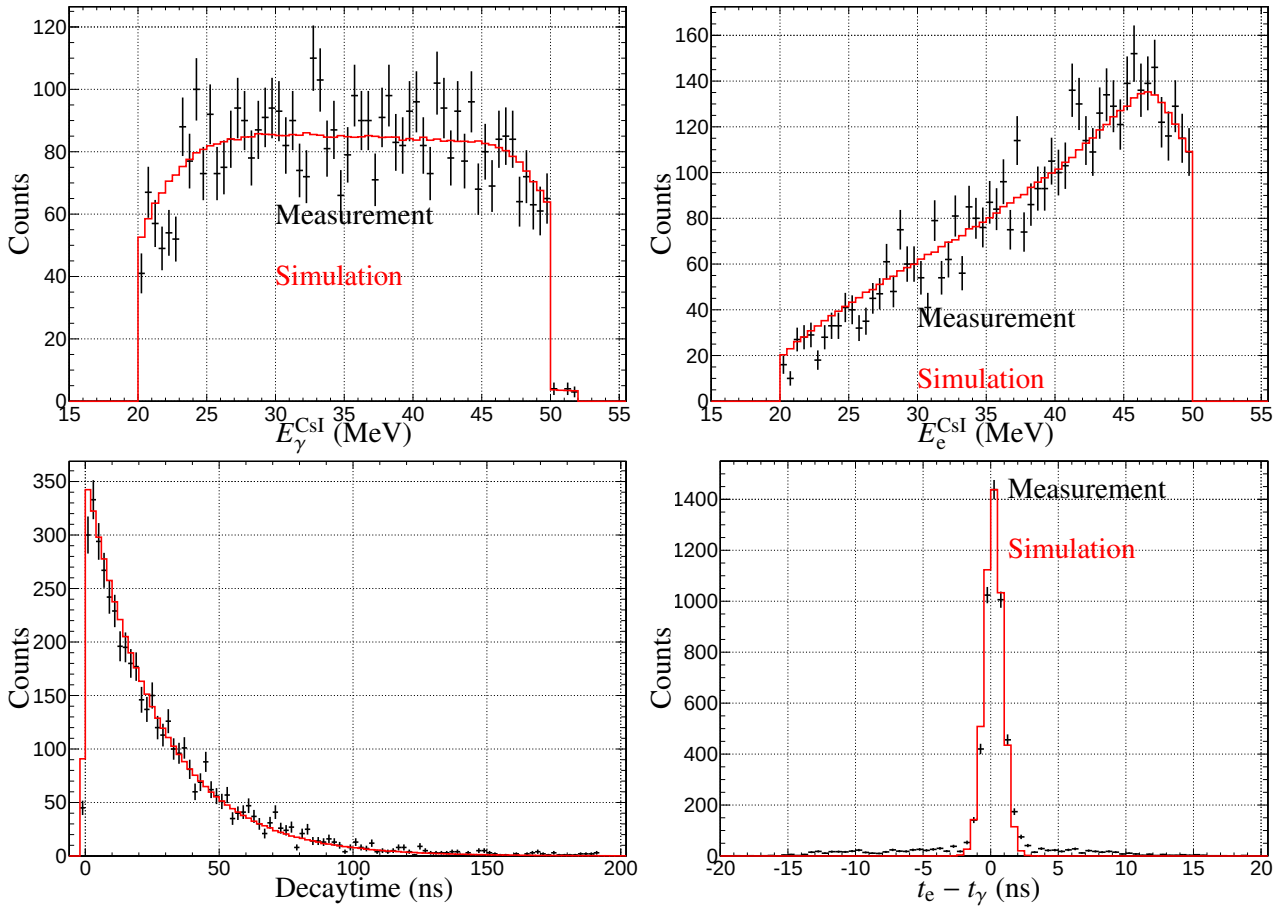

Figure 7.20: *Spectrum in Region D radiative pion events. Upper Left: Photon energy. Upper Middle: Positron energy. Upper Right: Time difference between the photon and positron in the CsI. Lower Left: Decay time spectrum. Lower Right: Lambda.*

Similar observations are seen with radiative muon decay.

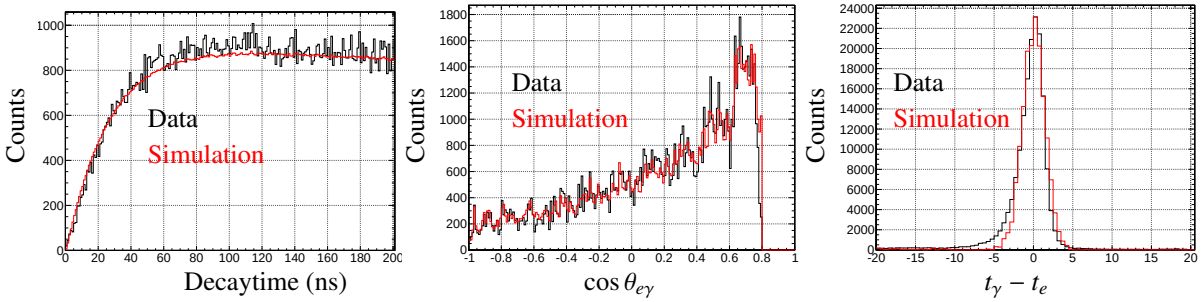

Figure 7.21: *Plots comparing simulation and measurement for radiative muon decays. 1 charged, 1 neutral track selected. Target cuts only were made.*

Since the observed radiative decay spectra are consistent with the radiative decay spectra simulated, not only is there confidence that the radiative decays are properly identified in the measurement, but with the construction of invariant mass, can be used in the branching ratio calculation. In particular the number of $\pi \to e\nu(\gamma)$ events and its associated tail fraction should not be determined using the energy in the CsI but rather using the reconstructed invariant mass. Now that the inclusion of radiative decays has been discussed, the first portion of this chapter is completed and a quick inventory is in order before determining branching ratio parameters.

7.4 Gather, cut, and go

As stated, this chapter is broken into two parts. The first is dedicated to understanding the background and developing methods to eliminate unwanted background. Elimination of background is not always possible and either a subtraction (in the case of pileup) or correction (in the case of decays in flight) is necessary. The second part of this chapter focuses on obtaining the necessary quantities to evaluate the branching ratio. Before proceeding with this, a chapter review section and what lies ahead is appropriate here. It was first established that the analysis would be blinded. Meaning the acceptances and the chamber efficiencies, $r_A r_\epsilon$ would be left out of the result of this work for the branching ratio. An inventory of the different types of processes in the PEN data sample includes beam contamination, hadronic events, pileup, decays in flight, and three-lepton events. It has been shown how to include radiative events in the analysis and in the end decided that the number of signal events and its characteristic tail fraction is determined from the reconstructed invariant mass spectrum. Here it seems appropriate to tabulate the cuts used to arrive at this stage. The cuts listed to achieve a clean data set are listed.

Table 11: *List of cuts currently used to eliminate unwanted background. None of these cuts preferentially favors the pion decay mode over the Michel decay mode as seen by the plots in the background section.*

Observable	2009	Purpose
Time of flight (`tof`)	25.5 <`tof` < 29 (2009) 25 <`tof` < 27 (2010)	Beam Contamination
Degrader Energy (`edeg`)	3.75 <`edeg`< 7 (2009) 6.5 <`edeg`< 10 (2010)	Beam Contamination
Theta of the track θ_{track}	$45 < \theta < 145$	Limit Energy Leakage
Energy Hodoscope (`epv`)	.4 <`epv`< 2	Veto Hadronic
Hodoscope dE/dx (`totaldedxpv`)	`totaldedxpv` < 2.75	Veto Hadronic
Vertex quality (`vtx_qual2`)	0 <`vtx_qual2`< 10	Ensure positron from decaying particle
z of closest approach (`z0`)	$\lvert$`z0` $- 5\rvert < 26$	Ensure π^+ from target.
Number beam particles (`nbeam`)	`nbeam` = 1	Beam Pileup
Scattered beam positrons (`scattered`)	`scattered` = 1	Veto scattered beam positron
Number charged particle (`ncharged`)	`ncharged` = 1	Veto Three charged leptons

At this point, cuts have only been executed that show no bias to the main signal decay channel , $\pi \rightarrow e\nu(\gamma)$ or the normalization background, $\pi \rightarrow \mu\nu(\gamma)$. However, there are still events in the high energy regime that may overlap in the signal events. In addition there are seemingly unwanted events with high and low target rest energy in the Michel energy range. Understanding and eliminating these events is crucial. If this can be done by a method that equally affects the two channels then all the better. Once this is accomplished, then the number of Michels and positrons from pion decays can be counted and the branching ratio determined. To understand what remains in the data, it is advantageous to observe some of the easily understood, yet still powerfully discriminating observables plotted against the invariant mass reconstruction. Information on the energy deposition (`dEdx_total`) in the actual chambers aids in the elimination of some of the higher energy events as is seen in Fig 7.22.

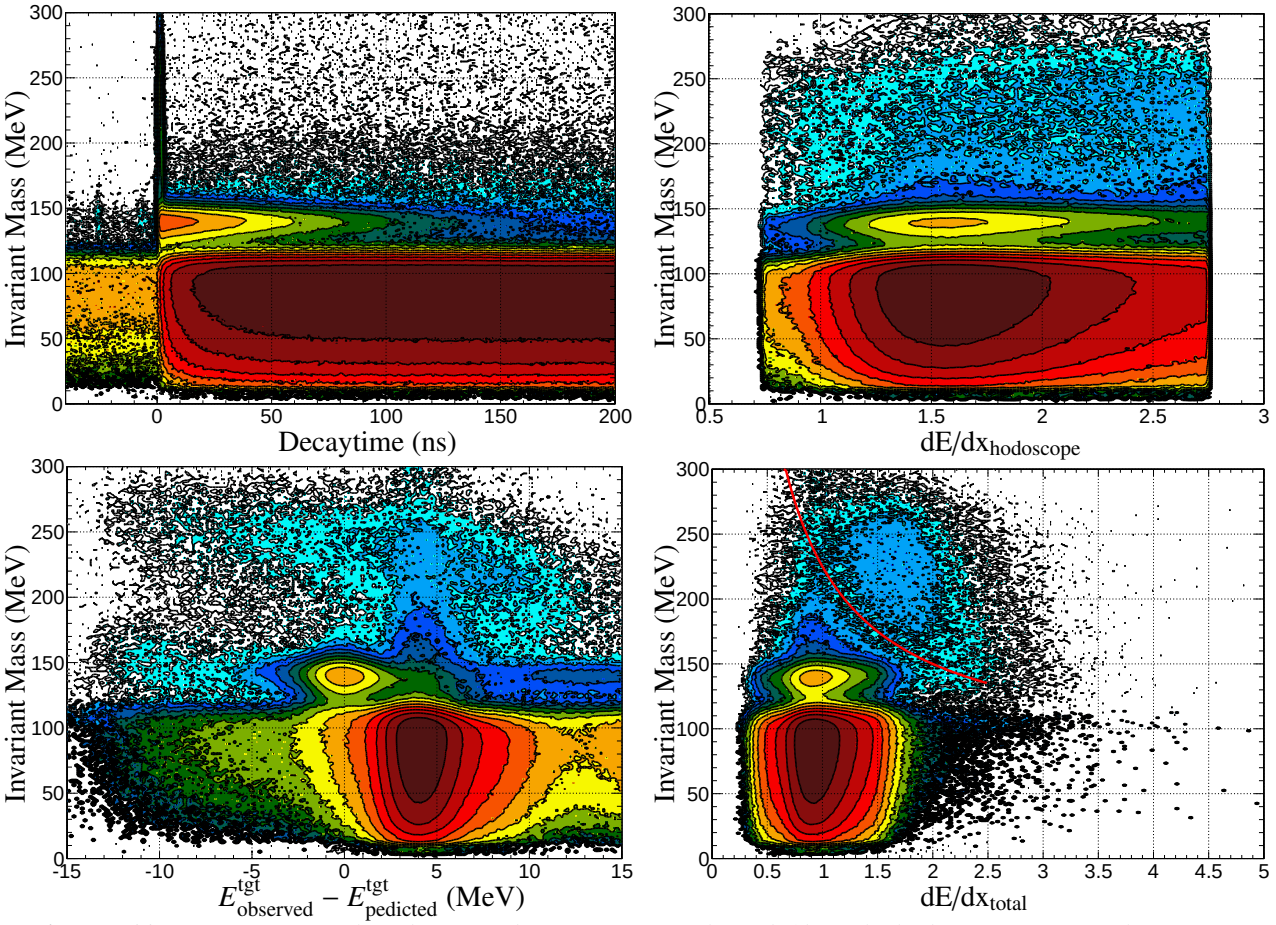

Figure 7.22: *Invariant mass plotted against decay time (upper left), dE/dx in the hodoscope (upper right),* `restwave` *(lower left) and dEdx total (lower right).*

Fig 7.22 shows that there are still some prompt contamination events in the decay time spectrum that go to high values of invariant mass. This suggest that there may be some hadronic events lurking in the peak region of the invariant mass spectrum. These prompts are not easily identified with the energy in the hodoscope alone. These events also have `restwave` energy in both the Michel region and signal region. When observing the `dE/dx_total` response however, these prompt events bundle up making it easier to eliminate. The decay time spectrum above the red line in Fig 7.22 is solely composed of events at decay time near one nanosecond. These are hadronic prompt events that can be eliminated with a 2-D cut in the high energy regime. An additional cut is `dE/dx_total` being less than 1.8 is made to eliminate the extraneous events.

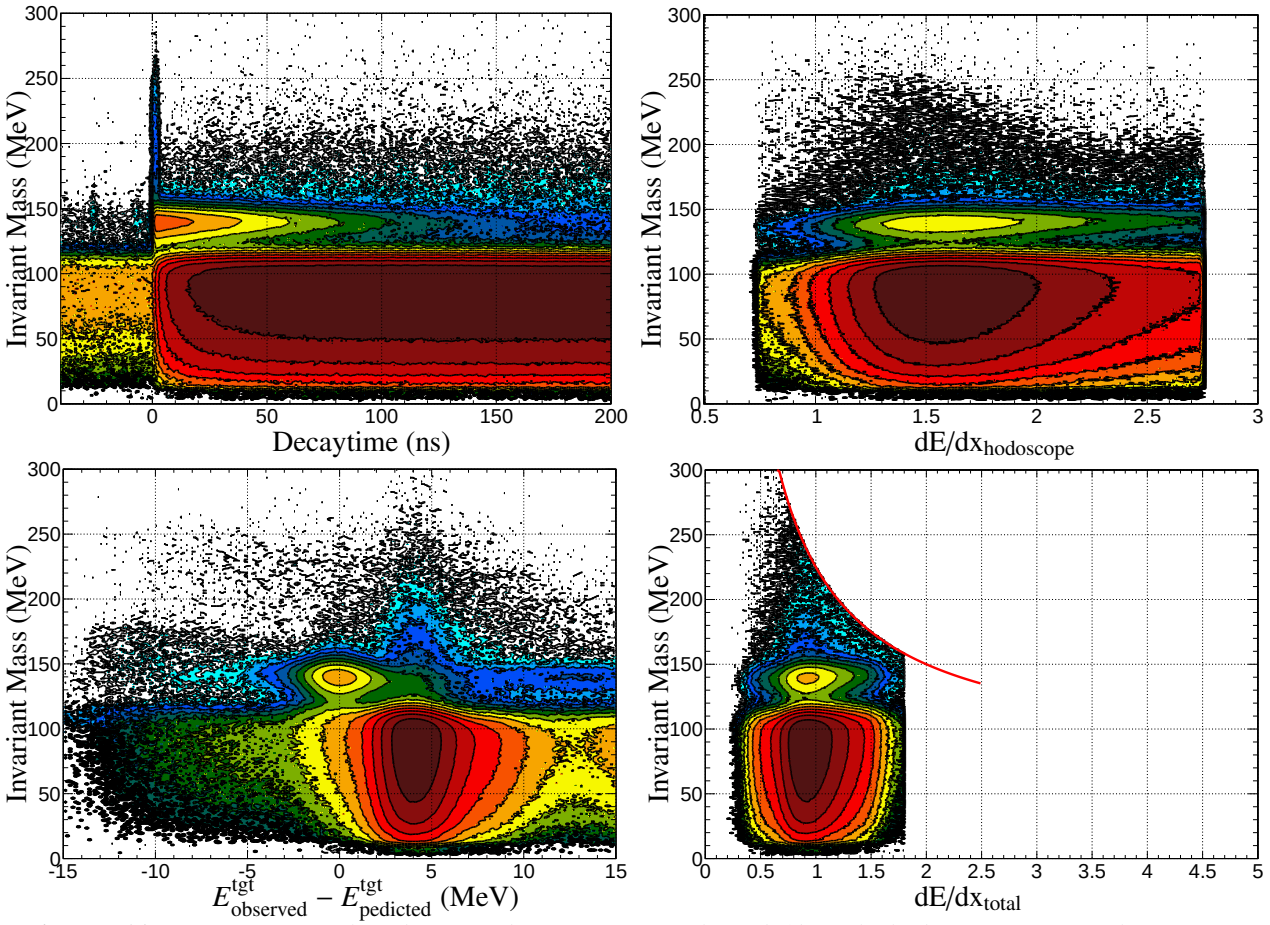

Figure 7.23: *Invariant mass plotted against decay time (upper left), dE/dx in the hodoscope (upper right),* `restwave` *(lower left) and dE/dx total (lower right). The additional dE/dx total cut has been put into the data sample.*

With this cut, the amount of high invariant mass events with acceptable dE/dx in the hodoscope is cleaned up. A cut on the hodoscope would never have been feasible, as there was almost no way to isolate those high energy events with information from the hodoscope alone. With the additional cuts, the spectra still show some contamination. In particular, there are still some events with high invariant mass. Some will be due to detector resolution, but there are far fewer that will be due to hadronic interactions. The lower left plot in Fig 7.23 shows events in the Michel energy regime with both energy deficits and energy surpluses with `restwave` energy well below 0 MeV and well above 12 MeV. The Michel positrons with high levels of negative `restwave` are the decays in flight that were spoken of earlier. A simple cut of `restwave`>-5 will eliminate a good number of the decays in flight. This will not (statistically) affect the number of $\pi \rightarrow e\nu(\gamma)$ decays as the `restwave` spectra comparison for Monte Carlo and measurement were seen in the previous chapter. If there were an effect, the Monte Carlo simulation will absorb this effect (since it will be very

small) into the acceptances. With this cut, the spectra now appears clean in the Fig 7.24.

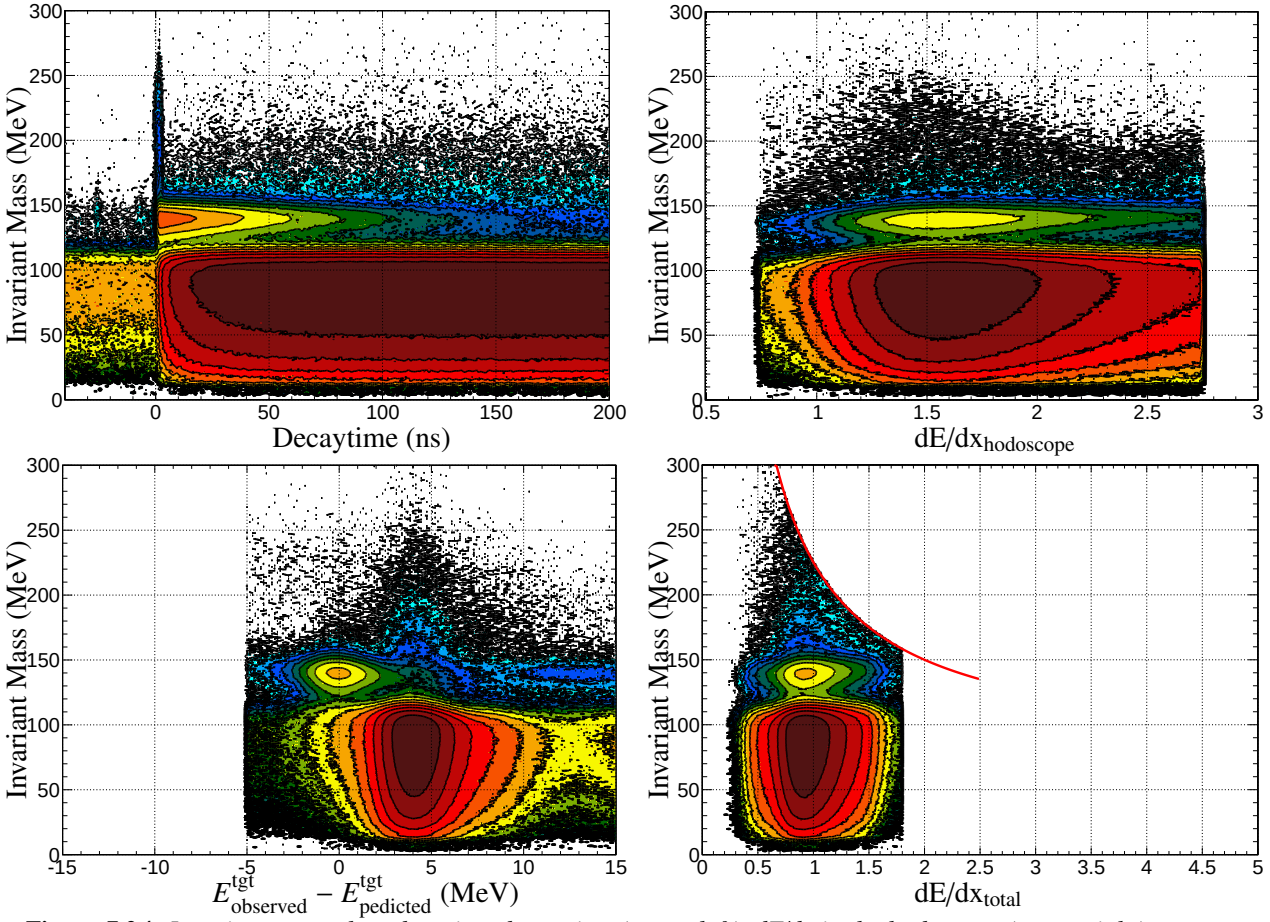

Figure 7.24: *Invariant mass plotted against decay time (upper left), dE/dx in the hodoscope (upper right),* `restwave` *(lower right) and dEdx total (lower right). The additional* `restwave` *cut has been put into the data sample.*

The events with target energy surplus are the pileup events. As a reminder, this is where there is a pion in the target along with a muon or positron not originating from the incoming pion (so from a previous pion). There is no "magical" cut that will eliminate these events however, there are cuts that can diminish them. The remainder will be subtracted off. Now that all of the cuts that can be used to provide relatively clean Michel and $\pi \to e\nu(\gamma)$ decays have been made, branching ratio extraction can begin. As a reminder, the expression for the branching ratio is

$$B = \underbrace{\frac{N^{peak}_{\pi\to e\nu}}{N_{\pi\to\mu\nu}}}_{r_N}(1+\epsilon_{tail})\underbrace{\frac{\epsilon(E_{\mu\to e\nu\bar{\nu}})_{MWPC}}{\epsilon(E_{\pi\to e\nu})_{MWPC}}}_{r_\epsilon}\underbrace{\frac{f_{\pi\to\mu\to e}(T_e)}{f_{\pi\to e\nu}(T_e)}}_{r_f}\underbrace{\frac{A_{\pi\to\mu\to e}}{A_{\pi\to e\nu}}}_{r_A} \tag{75}$$

The relative uncertainty in the branching ratio, (with a goal of 5×10^{-4}) is repeated here.

$$\frac{\delta B}{B} = \sqrt{\left(\frac{\delta r_N}{r_N}\right)^2 + \left(\frac{\delta \epsilon_{\text{tail}}}{1+\epsilon_{\text{tail}}}\right)^2 + \left(\frac{\delta r_\epsilon}{r_\epsilon}\right)^2 + \left(\frac{\delta r_f}{r_f}\right)^2 + \left(\frac{\delta r_A}{r_A}\right)^2} \tag{76}$$

Apriori, it is easily imaginable that the relative errors can be correlated or anti-correlated between some of these values. Choosing a higher peak/tail dividing line produces a higher tail fraction with a higher relative uncertainty while producing a smaller count in the peak which may have smaller or bigger relative uncertainty. A longer time window provides more events with a smaller relative uncertainty on the time window. This means looking ahead, the tail fraction and number of counts in the peak is chosen such that the overall uncertainty in the branching ratio is minimized. The decay time window must also be chosen which may or may not have a significant impact on these aforementioned values. The same goes for the number of Michel events. Each of these values are addressed in the preceding sections specifically demonstrating the impact on the branching ratio and how to choose the proper windows, dividing lines, etc. The final section of this chapter puts all the contributions together to minimize the relative uncertainty while obtaining the branching ratio.

7.5 Time window selection, r_f, for $\pi \to e\nu$ and $\pi \to \mu\nu$ decays

In determining the branching ratio, a count in the number of decays observed is necessary. Since decays are probabilistic, the only way to count all of the decay events that occur is to let the experiment run indefinitely. Since this is obviously not an option, a count on a fraction of the number of total decays that occur is what is done. The fraction of the events counted depend on the well-known theoretical decay time distributions of the decay processes of interest. Because this fraction originates from theoretically well-known quantities and phenomena, this parameter and its associated uncertainty is arguably the easiest to quantify in the expression for the branching ratio. Despite being the easiest, it must still be done with great care. In particular the probability of positron appearing at a particular time for the Michel decay chain, is shown in Fig 7.25.

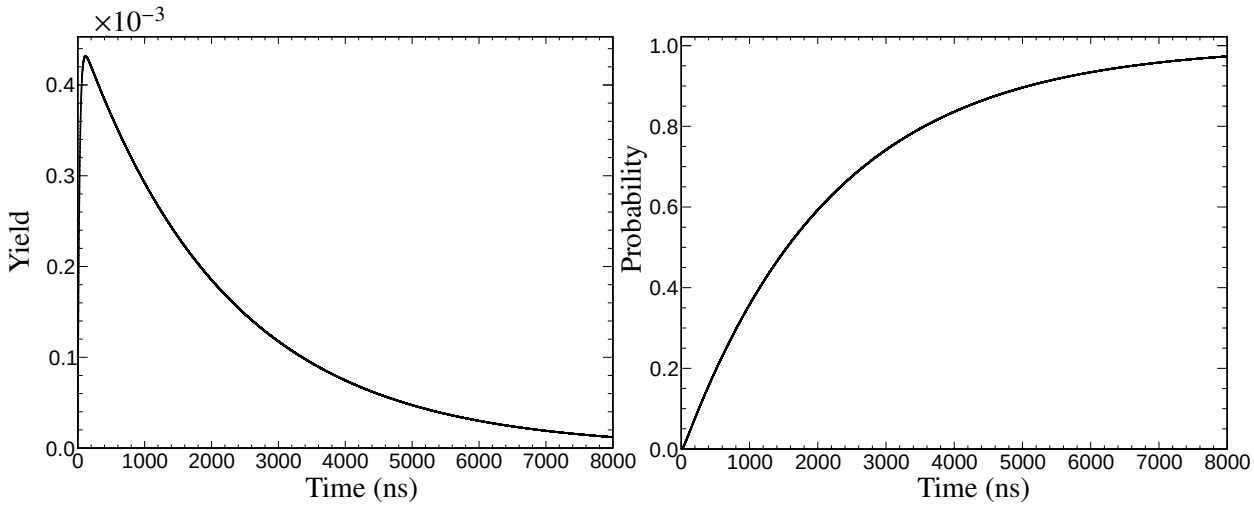

Figure 7.25: *Left: Decay time spectrum for the Michel decay. Right: Probability of observing a decay from time equal to 0 up to time t.*

Fig 7.25 shows that the experiment would have to take data for 8000 ns (nearly 4 muon lifetimes) to record 90% of the Michel positrons. A time window is chosen to record the events and the percentage of missed events, that is the number of total Michel decays, can be determined using the theoretical decay time spectrum and its integral. The percentage of all event types recorded depends on the time window used. Subsequently, the error in this fraction depends on how well the time is known. This section is where a method to determine the fraction of the events recorded and associated error is performed. The probability distribution function of a pion decaying between t_1 and t_2 is

$$f_{\pi\to e\nu}(t_1, t_2) = 1/\tau_\pi \int_{t_1}^{t_2} e^{-t/\tau_\pi} = e^{-t_1/\tau_\pi} - e^{-t_2/\tau_\pi} \tag{77}$$

Notice if $t_1 = 0$ and $t_2 = \infty$ the probability will be 1. A simple calculation shows for the pion decay time window the uncertainty in the fraction is

$$\delta f = \delta t/\tau_\pi \sqrt{e^{-2t_1/\tau_\pi} + e^{-2t_2/\tau_\pi}} \tag{78}$$

By choosing $t_1 = 0$ the second term under the square root is negligible compared to the first. This however, determines an uncertainty in the time window correction with $\delta t = .06$ ns, $\delta f = 0.0023$. This in turn means $\delta r_f/f = 0.0023$ which means the uncertainty in the branching ratio would be on the order of 2×10^{-3}! Even if the uncertainty in the time were to go down by a factor of 10, δr_f would still be too high being $\delta r_f/f = 2 \times 10^{-4}$. There are two options to proceed then. The first is to use a time window with higher t_1

which would lower δr_f, but this means that the number of events in the pion decay channel would decrease substantially which is unacceptable. The second option is to actually take t_1 to be a negative number. By taking events sufficiently earlier than the $t = 0$, then there is no uncertainty contribution in the fraction of events recorded at zero time because all events in a time window $t = 0 \pm \delta t$ are counted. In this case, the only uncertainty from the time window will be attributed to the later time chosen in the time window with uncertainty

$$\delta f = \delta t/\tau_\pi e^{-t_2/\tau_\pi} \tag{79}$$

The probability of a pion decaying into a muon which subsequently decays into a positron can be determined either by setting up a system of differential equations in the chain decay of $A \to B \to C$ where the lifetimes of $A,\ \pi$, and $B,\ \mu$, are known. A simple convolution of the decay times will also suffice. So

$$f_{\pi\to\mu\to e}(t) = \int_0^t f_{\mu\to e}(t-t')f_{\pi\to e}(t')dt' = \frac{1}{\tau_\mu - \tau_\pi}\left[\tau_\mu(1-e^{-t/\tau_\mu}) - \tau_\pi(1-e^{-t/\tau_\pi})\right]. \tag{80}$$

This in turn means that the probability of a Michel positron being born from the $\pi \to \mu\nu \to e\nu\bar{\nu}$ between time t_1 and t_2 is

$$f_{\pi\to\mu\to e}(t_1,t_2) = \frac{1}{\tau_\mu - \tau_\pi}\left[\tau_\mu(e^{-t_1/\tau_\mu} - e^{-t_2/\tau_\mu}) - \tau_\pi(e^{-t_1/\tau_\pi} - e^{-t_2/\tau_\pi})\right]. \tag{81}$$

As for the uncertainty in the decay time spectra for the Michel decay chain, a symmetric window is used. Calling the central time, t and the length of the window w, the uncertainty associated with the decay time spectra is negligible for this channel provided the window and the central times are appropriately chosen. Using this approach the substitution $t_1 = t - w$ and $t_2 = t + w$ the expression for the probability of a decay occurring in this time window is given here.

$$f_{\pi\to\mu\to e}(t-w,t+w) = \frac{1}{\tau_\mu - \tau_\pi}\left[\tau_\mu(e^{-(t-w)/\tau_\mu} - e^{-(t+w)/\tau_\mu}) - \tau_\pi(e^{-(t-w)/\tau_\pi} - e^{-(t+w)/\tau_\pi})\right]. \tag{82}$$

With a little algebra, this becomes

$$f_{\pi\to\mu\to e}(t-w,t+w) = \frac{2}{\tau_\mu - \tau_\pi}\left[\tau_\mu e^{-t/\tau_\mu}\sinh(w/\tau_\mu) - \tau_\pi e^{-t/\tau_\pi}\sinh(w/\tau_\pi)\right] \tag{83}$$

The uncertainty in f, δf, is easily calculated

$$\delta f = \frac{2\delta t}{\tau_\mu - \tau_\pi} \left| e^{-t/\tau_\mu} \sinh(w/\tau_\mu) - e^{-t/\tau_\pi} \sinh(w/\tau_\pi) \right| \tag{84}$$

Since the lifetimes, τ, of both the muon and pion are known very well, the only uncertainty that these fractions contain will be from the uncertainty of the timings and the length of the window. A little more algebra permits the calculation of the central time that minimizes the error. By taking the derivative of f with respect to time and setting the resultant derivative equal to zero, the central time t, for a given time window w which minimizes error.

$$t = \frac{\left[\ln\left(\frac{\sinh(w/\tau_\pi)}{\sinh(w/\tau_\mu)} \right) \right]}{1/\tau_\pi - 1/\tau_\mu} \tag{85}$$

In order to calculate these uncertainties and use later on, the uncertainty in the decay time must be determined as these are the times used in these time window correction fractions.

The decay time spectrum is the difference between the plastic hodoscope time and degrader time, with a small correction due to the time after passing the degrader until the pion stops and emerging positron passing through the hodoscope. Writing the decay time as

$$\text{Decay time} = t_{\text{e,birth}} - t_{\pi\text{stop}} = (t_{\text{hodoscope}} - t_{\text{deg}}) - (t_{\text{tgt}} - t_{\text{deg}}) - (t_{\text{stop}} - t_{\text{tgt}}) - (t_{\text{hodoscope}} - t_{\text{e,birth}}) \tag{86}$$

The uncertainty in the decay time is then determined by adding in quadrature the uncertainties of all four of these quantities. The first of which can be obtained by using the fact that the RF frequency of the accelerator is well known and that beam pulses with this frequency are expected to appear in the TDCs and waveforms. Since this time is well known (to about 8 significant digits!), this is the clock that is best used to determine the uncertainty in timing, more specifically the difference in times between the trigger (hodoscope) and degrader. The different beam pulses are seen in the waveform digitizer by choosing appropriate particles, in this case positrons, selecting them by requiring the appropriate time of flight and energy deposition in the degrader. Beam positrons are chosen because they have the same time of flight regardless of the momentum as seen in Fig 5.15.

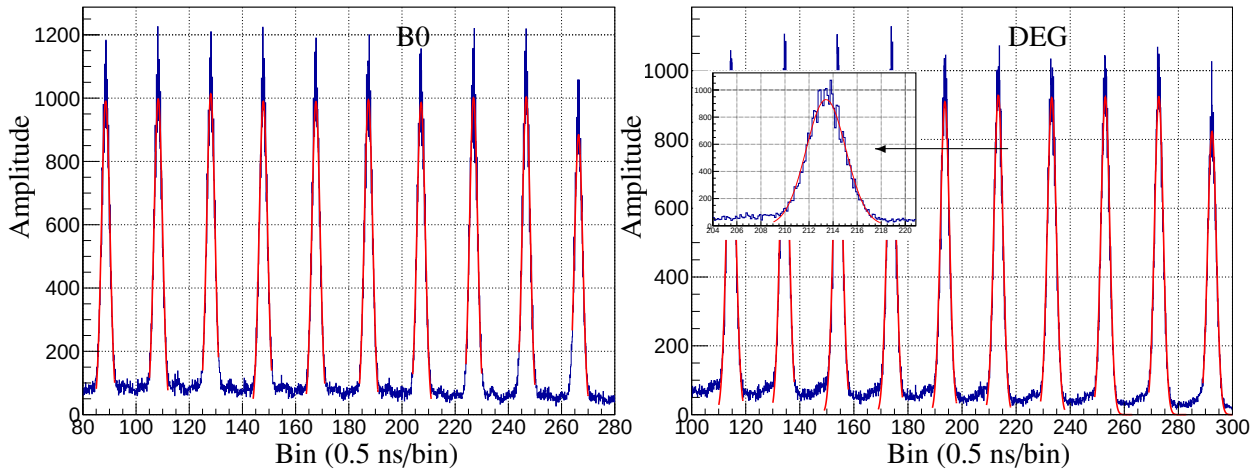

Figure 7.26: *Left: B0 signals the digitizer waveform for beam positron. Right: Degrader signals in the digitizer waveform for beam positrons.*

Fitting each of the individual peaks with a Gaussian fit, to obtain the time in which these beam particles appear in the beam and plotted as a function of the peak number, a slope of 19.75 ns is expected (1/RF frequency of the beam).

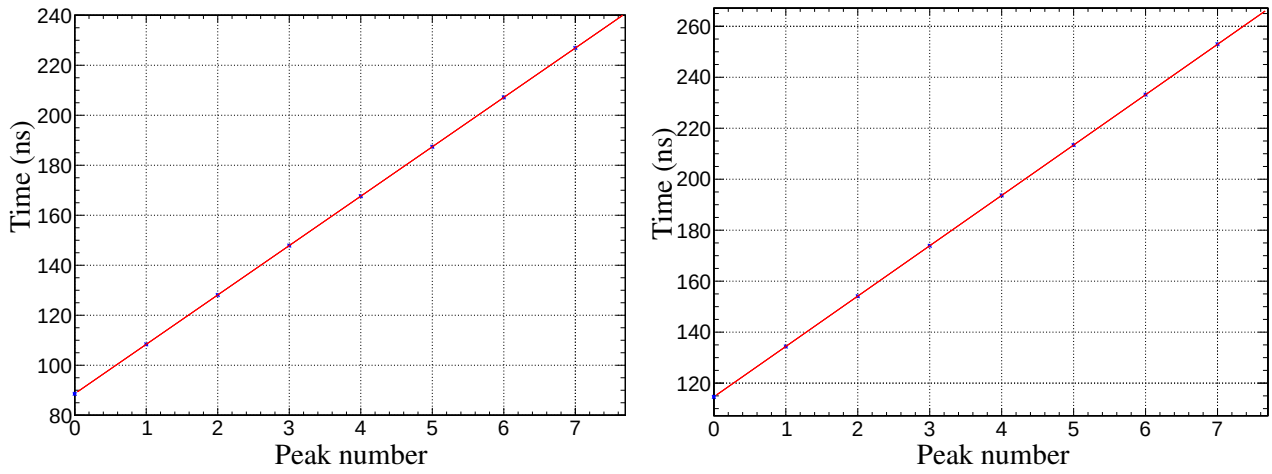

Figure 7.27: *Left: Linear fit for peaks in B0. Right: Linear fit for peaks in DEG.*

A linear fit was performed using MINUIT keeping the y-intercept and slope as a free parameter. The fit was then done again by fixing the slope to the known PSI accelerator frequency of 50.63280(4) MHz which translates to a time interval between pulses of 19.750 ns. The difference in the time of the y-intercept provides the uncertainty in timing, whereas the difference in slopes provides the information on systematic shifts of "t=0" for beam positrons. The best fit for the degrader was $y = 19.76x + 114.591$, and for the B0 was $y = 19.76x + 88.578$. When keeping the slope constant at 19.75, the the y-intercepts given were

88.6278, 114.649 for the B0 and degrader, respectively. This gives an uncertainty in the time between the hodoscope and degrader to be $\delta t_{\text{PV-DEG}} = 0.058$ ns, consistent as to what was found in the PiBeta experiment [56]. The B0 time signature, while not needed in the uncertainty in the decay time, was shown to ensure that the particle passed through both upstream detectors and that similar signatures are observed, the time of flight of about 12 ns for example. All that remains is to find the uncertainty in the timing for the path of pion from degrader to the time it takes to stop and from the time between the positron birth to the time it takes to reach the hodoscope. The total uncertainty is the uncertainty in the decay time δt.

The second term in the decay time equation can be determined by comparison of measurement and simulation. Since the difference in time between the target and degrader is available for both simulation and measurement, the simulation times can be varied to minimize the χ^2 to determine the uncertainty when $\chi^2 + 1$ is reached. The uncertainty in the third term, the time it takes to enter the target and stop is performed with the aid of the Monte Carlo. By varying the momentum of the pion beam, or time of flight, the variation of the pion stop time can be determined in the simulation. The last term can be done similarly to the second term. While the uncertainties in these times are expected to be small, because the times themselves are small, they are characterized for completeness.

The time difference between the degrader and the target is readily available as both detectors produce signals in the form of digitized waveforms. Even if there is pileup of signal in the target waveform, the first signal in the target is indicative of the pion entering the target. Taking the difference between these two times and observing the variation of the time using simulation, the uncertainty of this time difference is quantified. The error in the timing between the between the degrader and the target is thus on the order of 0.001 ns (or 1 ps).

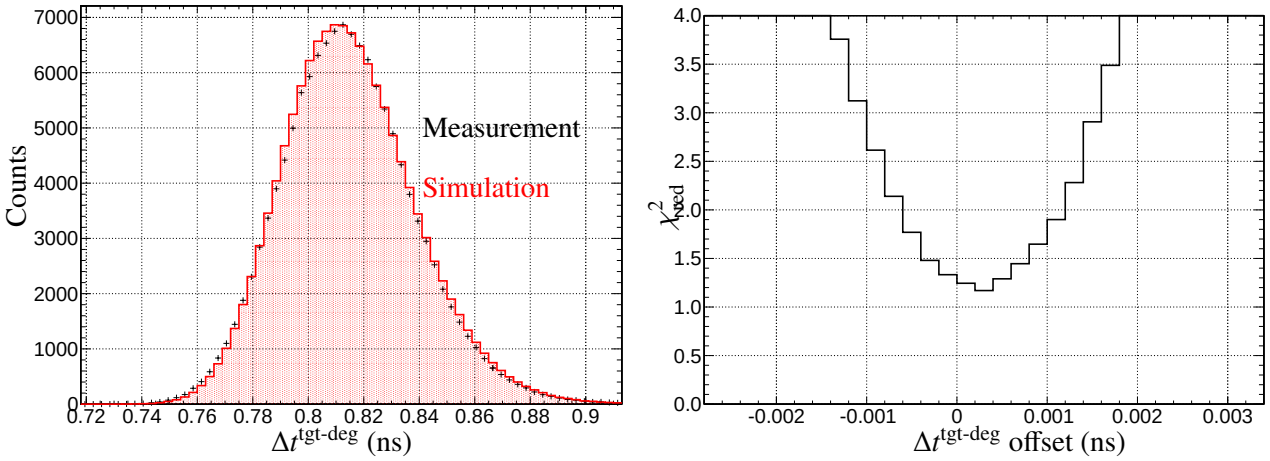

Figure 7.28: *Left: Minimum χ^2_{red} for time of flight between degrader and target. Right: χ^2_{red} as a function of an time offset*

The best method for determining how much the momentum should vary and thus how how much the pion stop time varies is to study the time of flight. A higher beam momentum not only means more initial pion energy, but also that less energy is lost in the upstream detectors, which in turn result in a longer time between reaching the target to the time it stops. Studying variation in the time of flight by putting an artificial offset provides the uncertainty in the time of flight simulated and thus the beam momentum which in turn is used as an indicator of how long the pion stop time varies. The χ^2 deviation shows an uncertainty in the time of flight of $\sigma_{\text{tof}} = 0.012$ ns. Using the relationship between beam momentum and time of flight and fitting a fourth order polynomial, the uncertainty in the beam momentum is $\sigma_{\text{p}} = 0.052$ MeV/c. With this beam momentum spread, the spread in the time from entrance to the target until stopping is $\sigma_{t_{\text{stop}}} = 4 \times 10^{-4}$ ns, or 0.4 ps. Not surprisingly very small and negligible.

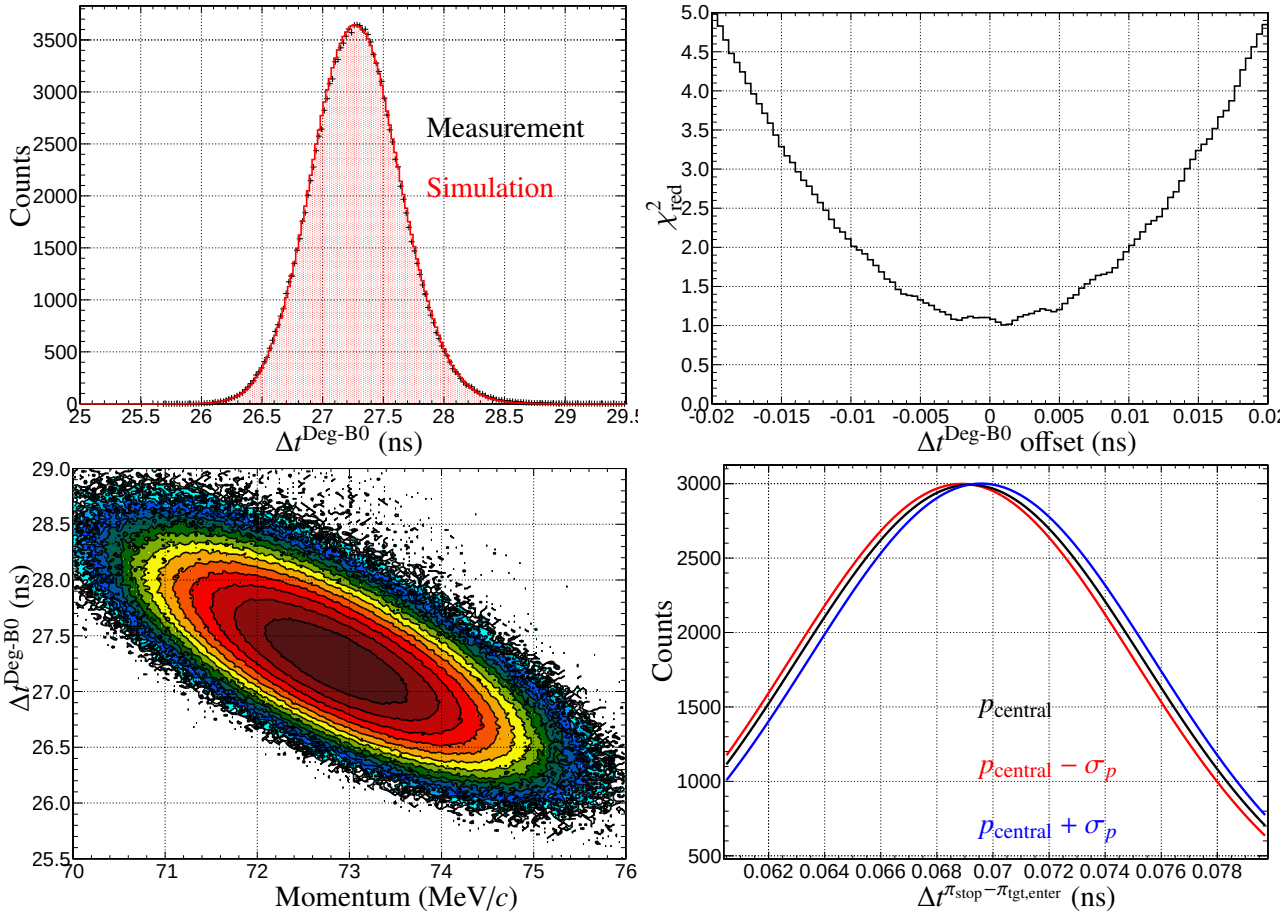

Figure 7.29: *Upper Right; Time of flight best χ^2 fit. Upper Right: Time of flight offset as a function of χ^2_{red} Lower Left: Time of flight versus beam momentum. Lower Right: Pion stop time with different momentum.*

Lastly, the time difference between the positron and the hodoscope (known in the PEN analysis as `positronshift`) is the last piece of this timing. The individual timing uncertainties will be used because this quantity is needed later on.

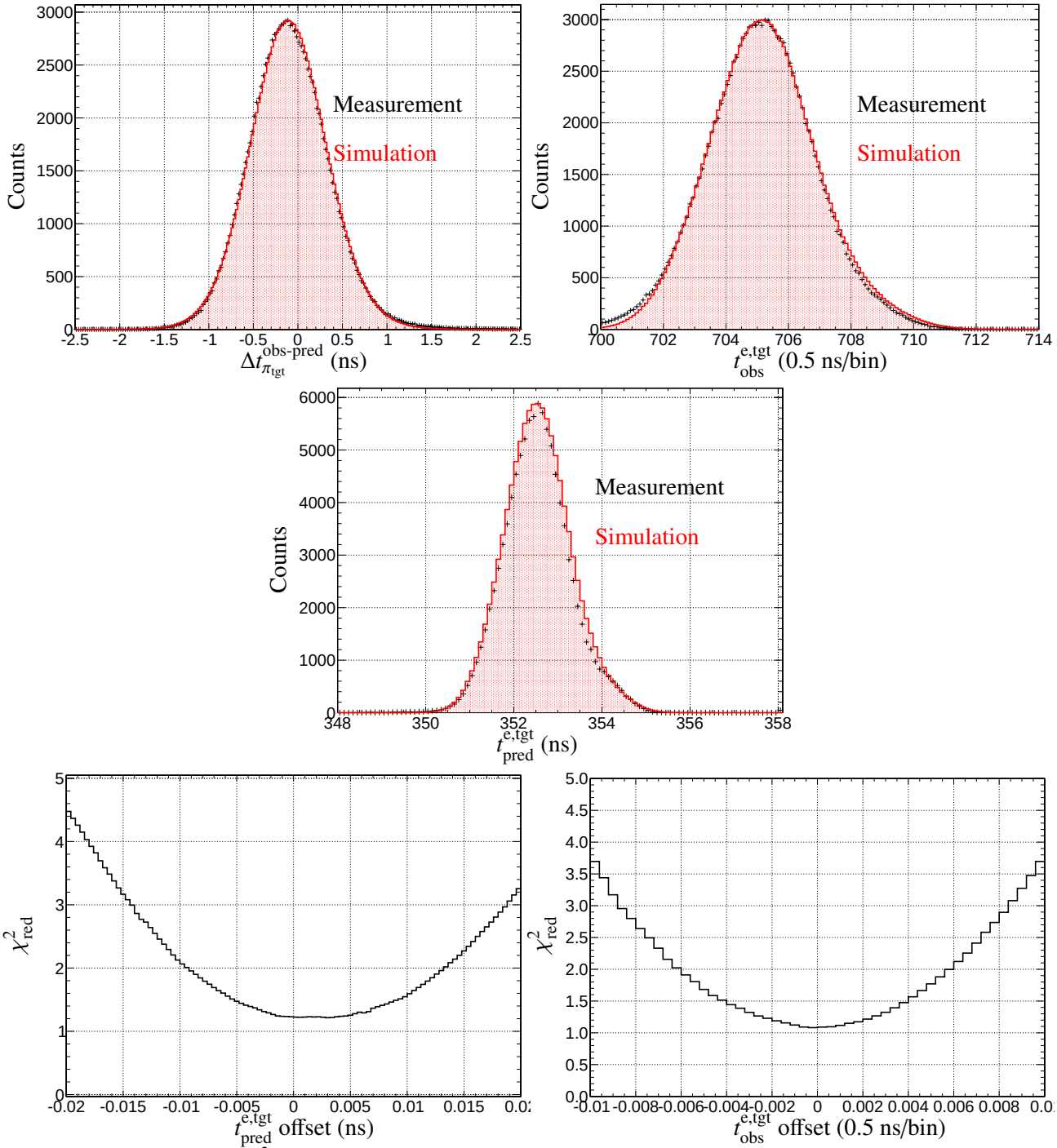

Figure 7.30: *Minimum χ^2 comparisons for pionshift (Top Left), positron target time (Top Right), and positron predicted time (Middle). χ^2_{red} as a function of offsets for the predicted positron time (Lower Left), and observed positron time (Lower Right).*

Putting all of the uncertainties in the timing together, the uncertainties in the decay time in picoseconds

$$\sigma^2_{\text{decaytime}} = 58^2 + 0.4^2 + 1^2 + 10^2 + 6^2$$

This gives an uncertainty in decay $\sigma_{\text{decay time}} = 59.17 \sim 60$ ps. Recall, the true decay time is the time between which the positron is born in the target and pion stop time in the target, the uncertainty in the decay time is not the uncertainty between these two times. The decay time experimentally is determined using both the degrader and the plastic hodoscope and this is why the uncertainty in decay time is determined in this seemingly round about way. In the previous experiment, the PiBeta experiment, the decay time spectrum, as they defined it, is the difference between the hodoscope (technically CsI) and the degrader. Thus the uncertainty in the PiBeta experiment only required studying the difference between the hodoscope and the degrader. Now that the uncertainty in the timing is determined, the proper time window can be chosen for each of the individual processes. The different time windows produce a different number of counts and subsequently a different time correction. Counting the number of events and choosing the appropriate time window then is not an independent process and thus we move to counting the number of events for each of the processes.

7.6 Michel, $\pi \to \mu\nu \to e\nu\bar{\nu}(\gamma)$, yield

As was pointed out previously, the number of Michel positrons detected depends on the time window that is used. We saw that an analytical expression can be formed by using a symmetric time window, $t \pm w$. Using this approach, the question naturally arises as to what time window, w, should be used and what should be the central time, t. One would like a window where the number of signal events is small so as not to produce a significant number of false Michel events due to the $\pi \to e\nu(\gamma)$ low energy tail, so a later time window is appropriate. It is also desirable to minimize the uncertainties, both systematic and statistical. Since the number of Michel events are orders of magnitude more numerous than the number of signal events, the branching ratio statistical uncertainty will come from primarily from the $\pi \to e\nu(\gamma)$ decays, not from the number of Michel events, provided the time window is sufficiently large. Therefore the time window and central value must be chosen such as to minimize the systematic uncertainty associated with the uncertainty in the time window while keeping the statistical uncertainty in the number of Michel positrons insignificant. By observing various time windows, each individual time window possesses an optimal central time that should be chosen. This central time, will have little change in f as the time is varied around the optimal time as demonstrated in Fig 7.31.

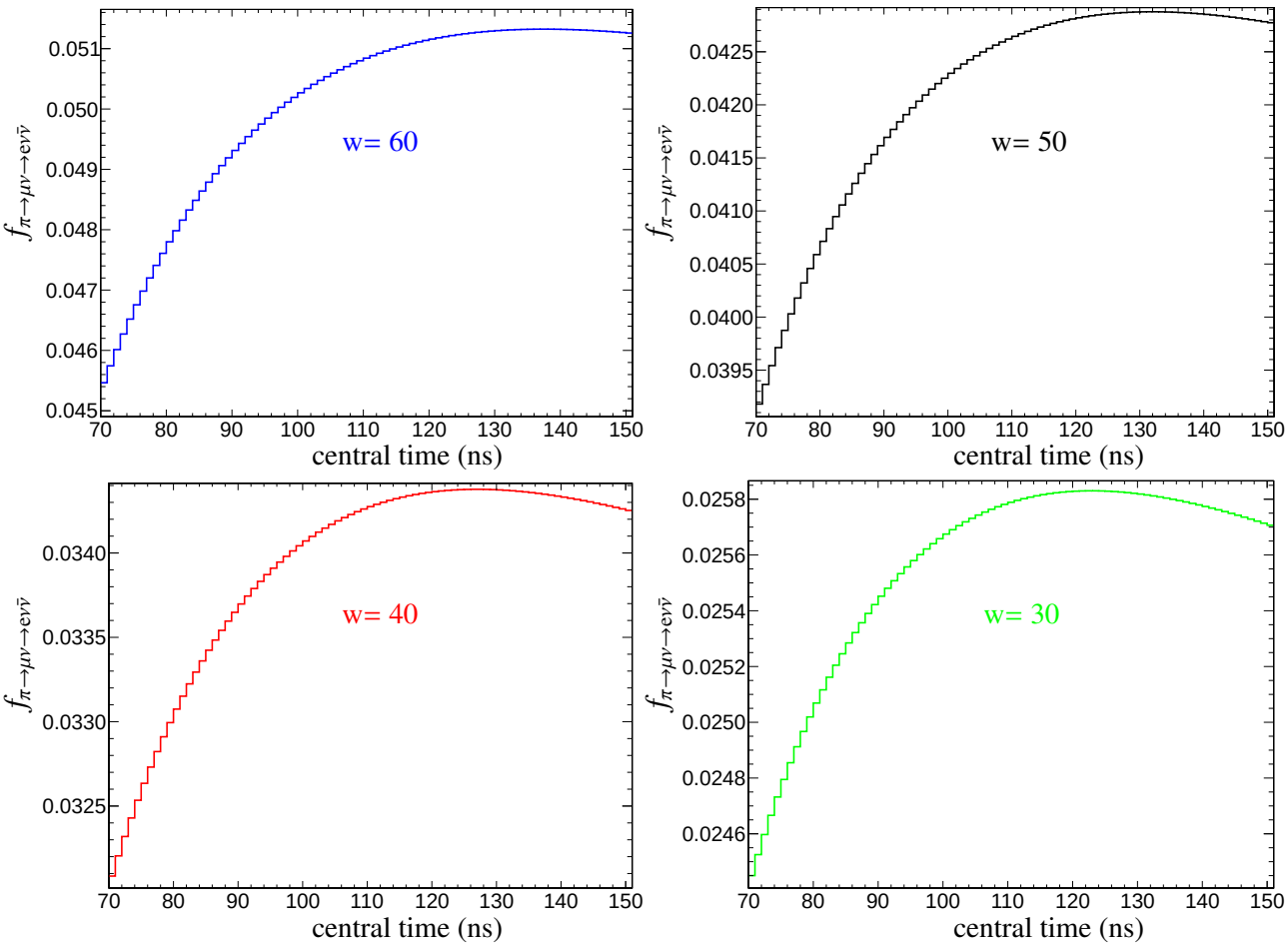

Figure 7.31: *The correction factor for four different time windows as a function for the central time chosen. Upper Left: Time window = 60 ns Upper Right: Time window = 50 ns. Lower Left: Time window = 40 ns. Lower Right: Time window = 30 ns. Note there is a maximum, where small deviations result in little change in $f_{\pi\to\mu\nu\to e\nu\bar{\nu}}$. These are the ideal central times for a given time window.*

The time window chosen determines the correction factor, $f_{\pi\to\mu\nu\to e\nu\bar{\nu}}$ and the time correction factor for multiple symmetric time windows as well as their ranges facilitates the choice to determine the best time window in order to count the total number of Michel positrons. Using the above notation in the derivation of the time window calculation, the central time, t, is shown in Fig 7.32 for all windows possible as well as the higher and lower time ranges that would be encompassed.

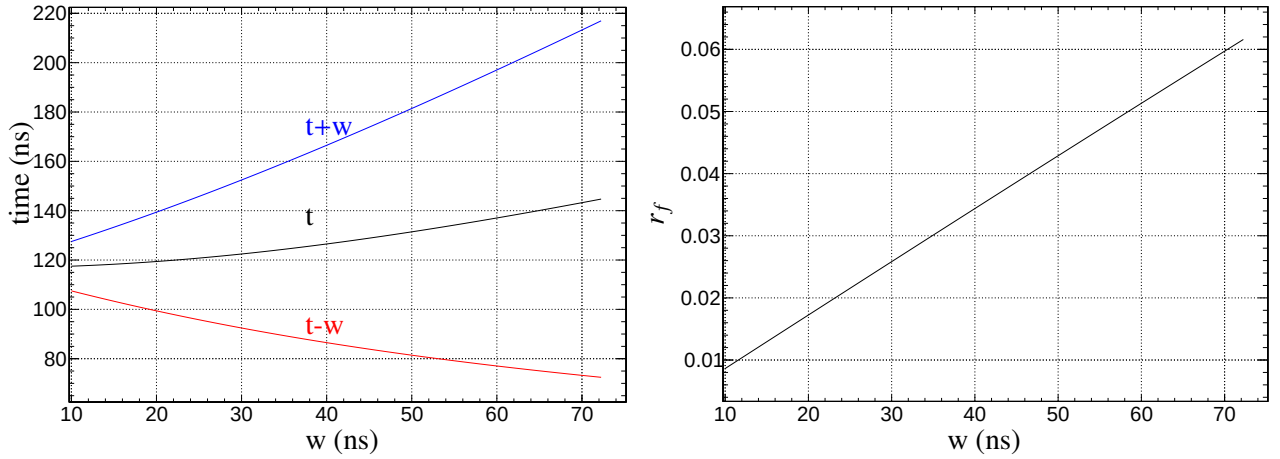

Figure 7.32: *Left: Central (black), upper time (blue), and lower time (red) that the decay time would include for a given time window for minimum error (or maximum $f_{\pi\to\mu\nu\to e\nu\bar{\nu}}$ Right: The correction factor needed as a function of the time window, given the minimized error is used.*

While there are lots of options available for choosing the length of the window, as always, there are caveats. Going near 60 ns for the time window is not desirable since the time gate lasted for nearly 200 ns after the pionstop, the closer to the 200 ns mark, the more likely trigger and gate efficiencies will come into play. However, a wider time window is desired because this will produce a greater number of counted events and thus a smaller statistical uncertainty. The correction to the counts is $1/r_f$ for the number of Michels which means a higher r_f is desired. But the above plot shows that the bigger the time window, the closer to the end of the timing gate. Taking a sample for the 2009 and 2010 data set, the effect of the relative error of the Michel count is shown as a function of the length of the time window.

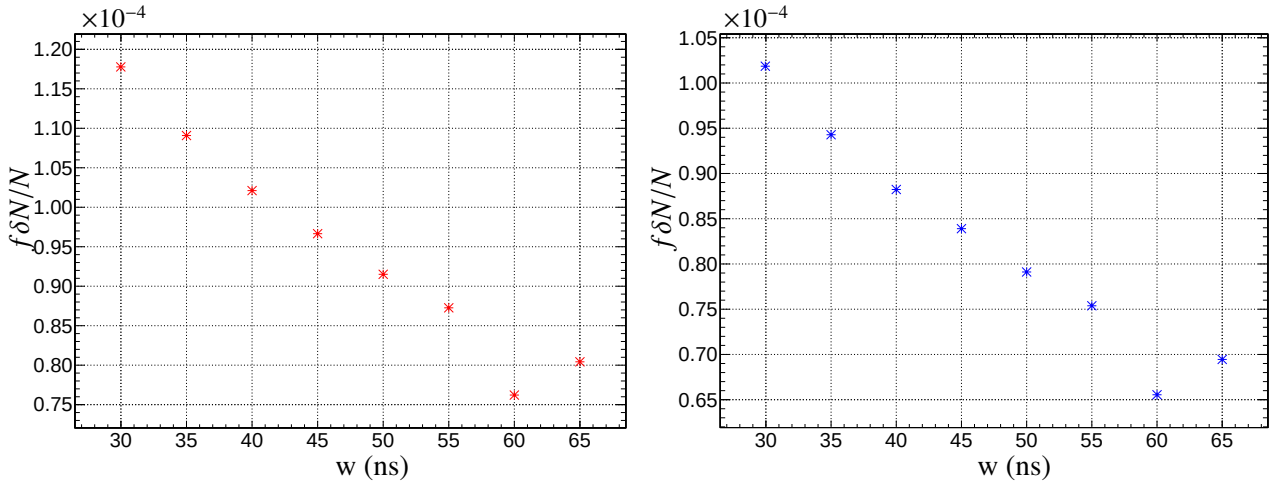

Figure 7.33: *Left: Relative Statistical uncertainty for Michel count as a function of the length of the time window. Left 2009. Right 2010.*

Fig 7.33 shows that there is some abnormal behavior between 55 and 65 ns that is observed. As the size of the time window increases, the number of Michels is expected to increase proportionally, which makes the relative error decrease. However, if the events are missing due to gate inefficiencies, discrepancies occur. Since a small time window diminishes the overall number of Michel events causing statistical uncertainty to be a concern for this channel, the decay time window of 50 ns was chosen for the analysis. Using the the 50 ns time window, the uncertainty in the timing can be obtained analytically for various central times. The central time used was that which minimizes uncertainty. The relative uncertainty in $f_{\pi\to\mu\nu\to e\nu\bar{\nu}}$ is plotted as a function of the central time for w = 50. The minimum time is 131.423 ns.

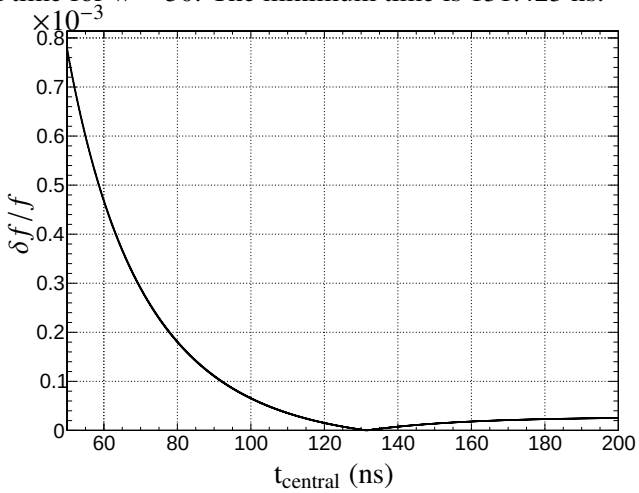

Figure 7.34: *Relative uncertainty in the Michel time spectra using a window of ± 50.*

Fig 7.34 shows that this time window has a relative uncertainty that will not be a significant contributing factor in the relative uncertainty of the branching ratio. Since time window has been chosen, the range of invariant mass for the Michel selection should be discussed and in doing so, we must ensure that the decay time spectrum is the same for the 2009 and 2010 run periods.

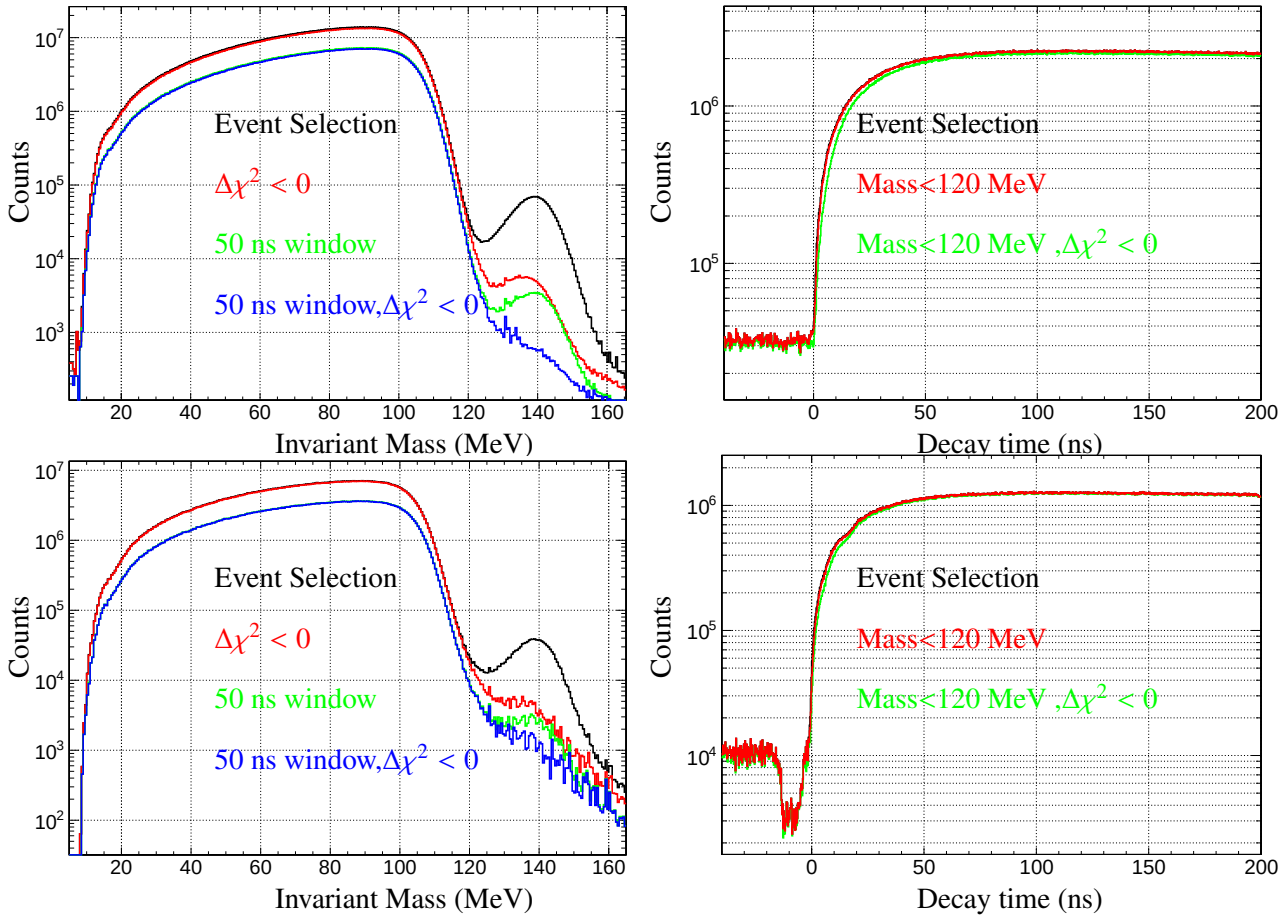

Figure 7.35: *Event selection and decay time for the Michel count. Left column: Invariant Mass spectrum for various possible selections of events. Black is obtained by applying the cuts listed in the previous section. The variation is observed by applying the time window with or without a $\Delta\chi^2$ cut. Right column: Decay time spectrum for selection of events. Top Row: 2010. Bottom Row: 2009.*

There are two noticeable features in the 2009 decay time spectrum in Fig 7.35. The first is the dip prior to time zero in the so-called "porch" region. The second is the small dimple around 15 ns. These features are due to the aforementioned trigger added early in the 2009 data. The requirement of minimum energy by the target decay signal had the unwanted effect such that if a particle were to trigger the event by hitting the hodoscope, say from pileup or scattered beam instance, while simultaneously a pion was decaying in the target, the event may not trigger, due to the dead time in the electronics. Put another way, an isolated pileup spectra with no electronic defects would appear to be a horizontal line. So when obtaining the decay time spectra for Michel decays, one obtains the spectrum of Michel plus a flat background. But when this trigger was implemented, the pileup spectrum gets a dip in and around 15 ns due to failure of trigger recognizing a legitimate pion stop due to dead time. This means that the observed combined Michel+pileup spectrum

possesses a dip around 15 ns. This may be cause for concern. If the Michel spectrum is electronically distorted, then the Michel count may not produce the correct number of events for a given time window. Comparing the Michel decay time spectra of data in early 2009 and late 2009, the feature does not exist prior to the trigger modification and the ratio of the two spectra are consistent within statistics in the time window that will be used, i.e., the number of events are properly accounted for in the later decay time window which is used in the analysis as demonstrated in Fig 7.36.

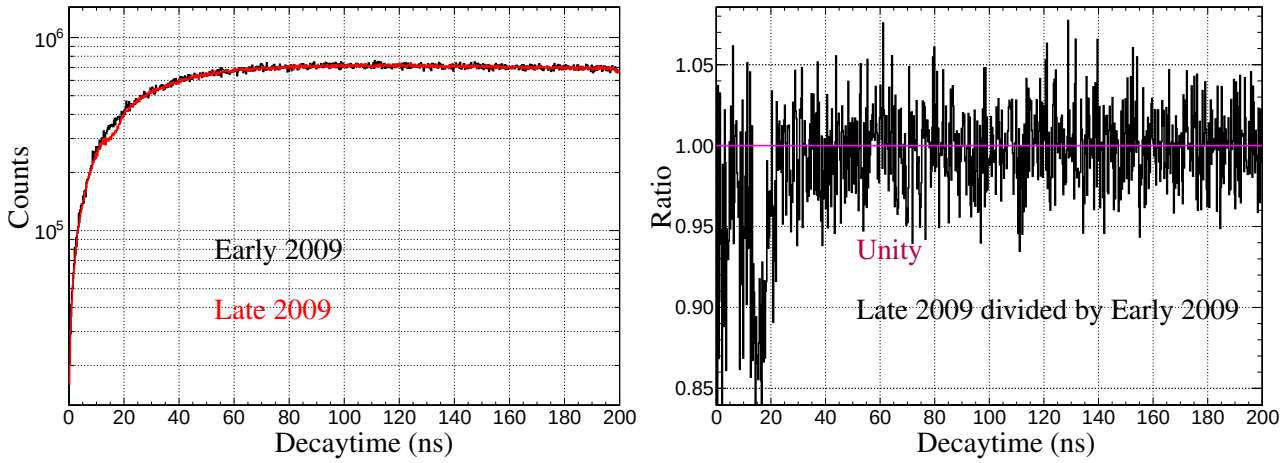

Figure 7.36: *Comparison of early and late 2009 data runs. Left: Decay time spectrum highlighting the distortion in early decaytimes. Right: Ratio of early and late data. Distortion is noticeable in the ratio, but not not in the later times.*

Note since this distortion is caused by pileup, the decay time spectra of positrons originating from pion decays will not be affected. This is shown in the next section. With the window chosen and the invariant mass selection being chosen to be below 125 MeV (where the local minima occurs) the number of Michel positrons is then determined for the entire year run by choosing the the window and then subtracting the pileup background. This method is demonstrated in Fig 7.37

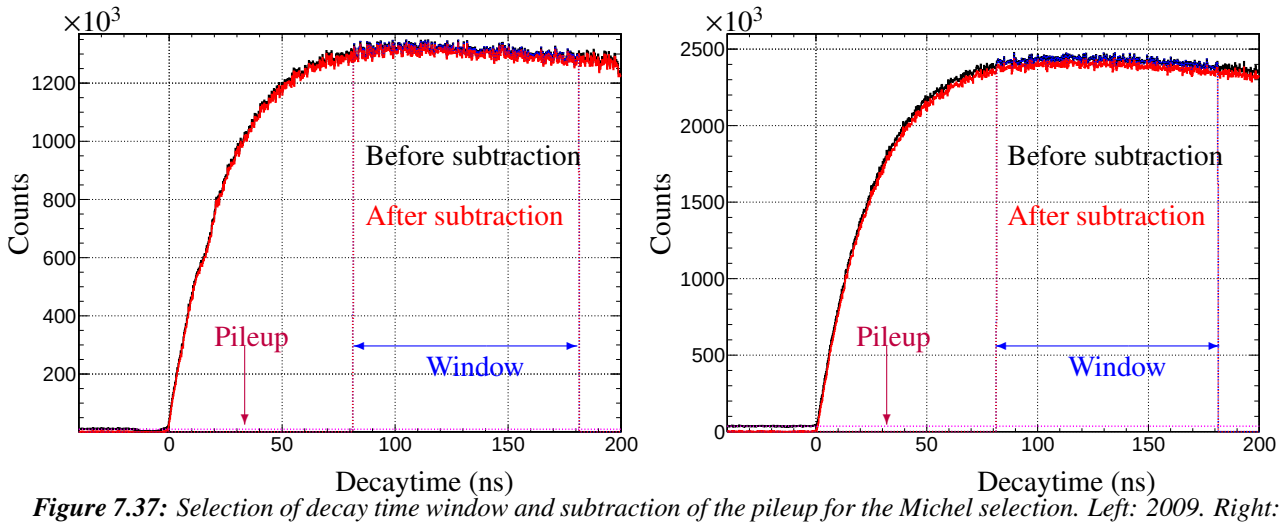

Figure 7.37: *Selection of decay time window and subtraction of the pileup for the Michel selection. Left: 2009. Right: 2010.*

After the subtraction of the pileup the number of Michel events were determined to be

$$N_{\text{michel,2009}} = (5225.68 \pm 0.23) \times 10^5 \text{ and } N_{\text{michel,2010}} = (954550 \pm 43.9) \times 10^3$$

However, this is not the total number of Michel events in this time window. There are still tail events under the Michel spectrum and there are some Michel events from the high energy Michel edge that are not counted (as seen from simulation). The fraction in the tail can be accounted for by using simulation. Normalizing the response of the signal decay to the peak region in the Michel dominated spectrum the number of tail events can be obtained. Knowing the integral of the Michel spectrum relative to the rest of the spectrum using simulation provides the fraction of the Michels that are missing from the count. In this case, the fraction of the Michel events which occurs beyond 125 MeV is roughly 2×10^{-5}. The number of Michel events that would not be counted is statistically insignificant. Further, the number of over counting events below the Michel spectrum that belong to the tail events for the pion decay spectrum is also statistically insignificantly in that is less than the $2{\times}10^{-5}$ value.

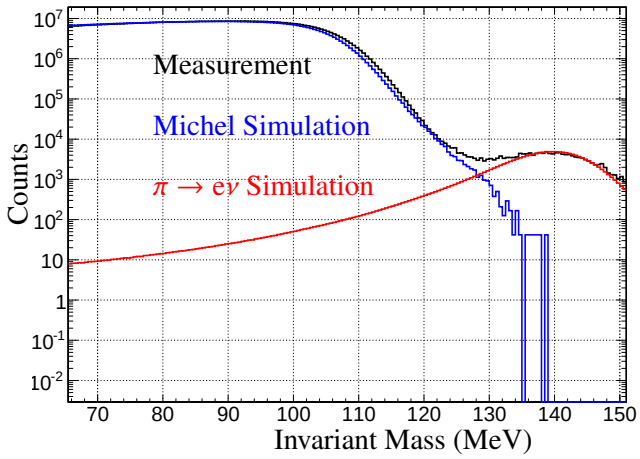

Figure 7.38: *Illustration of including over/under counting or high invariant mass Michel edge and tail events from pion decays.*

Time window correction of 0.0428777 applies for a time window of `decaytime` = 131.423 ± 50 ns, and gives a number of Michel decays as $N^{\text{corrected}}_{\text{michel,2009}} = 1.21358 \times 10^{10} \pm 753839$ and $N^{\text{corrected}}_{\text{michel,2010}} = 2.22622 \times 10^{10} \pm 1.02283 \times 10^{6}$. This is, roughly, the number of Michel decays which occurred in fiducial volume during the experiment that passed the cuts. Now that the number of Michel events (and its uncertainty) have been determined, the number of signal events in the peak portion of the $\pi \to e\nu(\gamma)$ invariant mass spectrum needs to be determined.

7.7 $\pi \to e\nu(\gamma)$ yield

One of the advantages of having a time window for taking data for 200 ns, is that most of the $\pi \to e\nu(\gamma)$ decays that occur in nature are recorded.

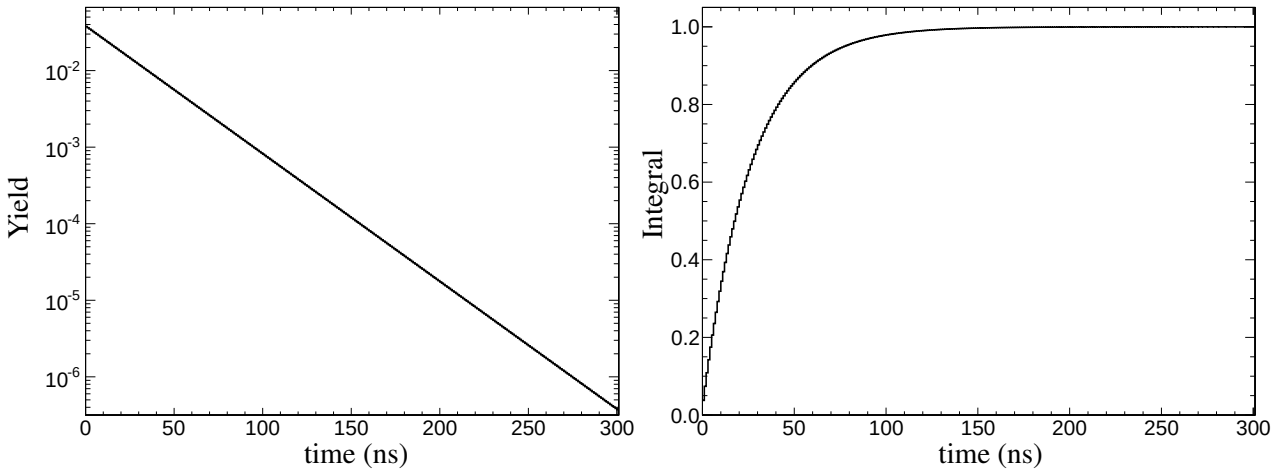

Figure 7.39: *Left: Decay time spectra of $\pi \rightarrow e\nu$. Right: Integrated up to time t*

This means that only a small time correction is required in order to calculate the number of positrons emerging from pion decays. If only the events in the first 70 ns were recorded, this comprise 93.46% of all the $\pi \rightarrow e\nu$ decays that occur. By choosing the first 200 ns 99.95% of the events are recorded. The amount of uncertainty associated with the time correction is dominated by the time window selected for pion decays. As demonstrated above, the time window uncertainty is negligible for the Michel time window. As explained prior, the best approach to minimize the uncertainty in the time window correction factor for pion decays is choose decay times sufficiently earlier than the time zero. This will prevent a substantial uncertainty in the attributed to early decay times and the uncertainty thus will be attributed to the later time alone with

$$\delta f = \delta t / \tau_\pi e^{-t_2/\tau_\pi} \tag{87}$$

With this expression, the uncertainty and relative uncertainty in the pion decay window is characterized in Fig 7.40 for various time uncertainties.

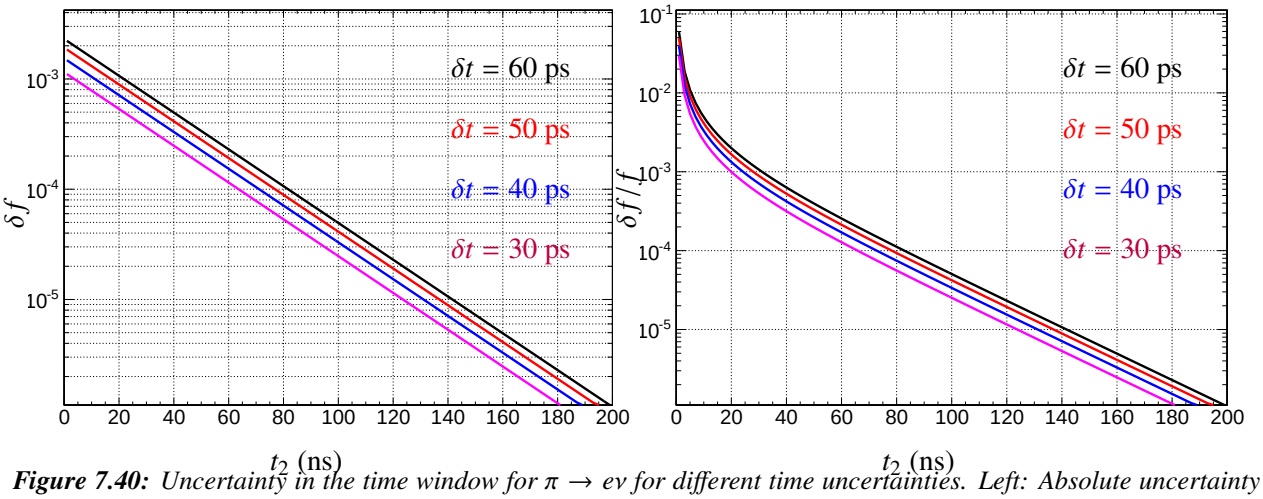

Figure 7.40: *Uncertainty in the time window for $\pi \to e\nu$ for different time uncertainties. Left: Absolute uncertainty in the fraction. Right: Relative uncertainty in the fraction.*

The determination of the time window for the pion decay channel is a delicate process. By choosing a smaller decay time window, it becomes easier to obtain a cleaner peak isolation and therefore easier to take the cutoff for peak/tail events at a lower energy, which reduces the uncertainty of the tail (a smaller energy cut off for tail/peak will reduce the error in the tail fraction). However, a smaller decay time will also diminish the number of events in the peak, increasing the statistical uncertainty, as well as increasing the uncertainty of the time window. There are still more complications that occur.

Thus far, the Michel positron selection and the pion decay selection have been treated the same. From the previous section, the invariant mass spectrum shows there is a relatively high amount of background on top of the pion decay peak at 140 MeV. Even when choosing a relatively short time window, the number of background Michel decays may not be suppressed as greatly as desired. In fact, from the above plot, a time window at least greater than 80 ns must be chosen in order for the decay time for the pion selection to produce no significant source of error. Even the shortest of time windows will not diminish the amount of Michel background a substantial amount.

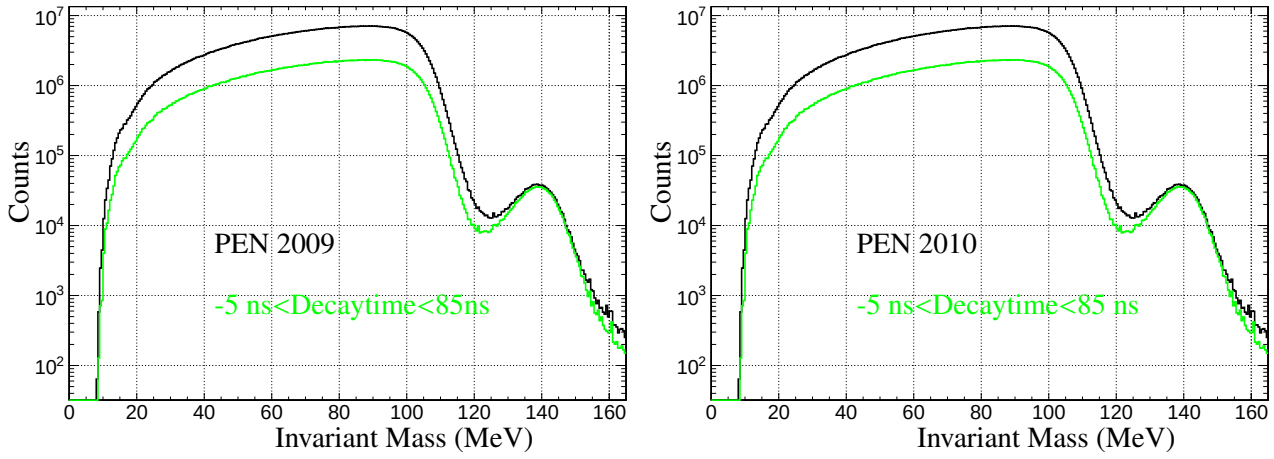

Figure 7.41: *PEN data clean invariant mass. Left: 2009 run. Right: 2010 run.*

Fig 7.41 shows a cut is needed that favors the pion decay over the Michel decay channel. Ideally, a cut for this kind of analysis is one that produces a large signal to background ratio and introduces small systematic error. The Monte Carlo once again comes to the rescue. Using the Monte Carlo to study the amount of signal, S, to number of background events, B, for a particular cut on a variable. Comparing the quantity of $S/\sqrt{S+B}$ as a function of cuts from above and below for the most discriminating waveform variables, a cut window can be chosen. This expression is often referred to as signal significance which is often used in particle physics. While the implementation of this particular quantity may not be the usual method for this observable [80], this nonetheless provides information as to which observable is most discriminatory and where the cut roughly optimizes the amount of signal.

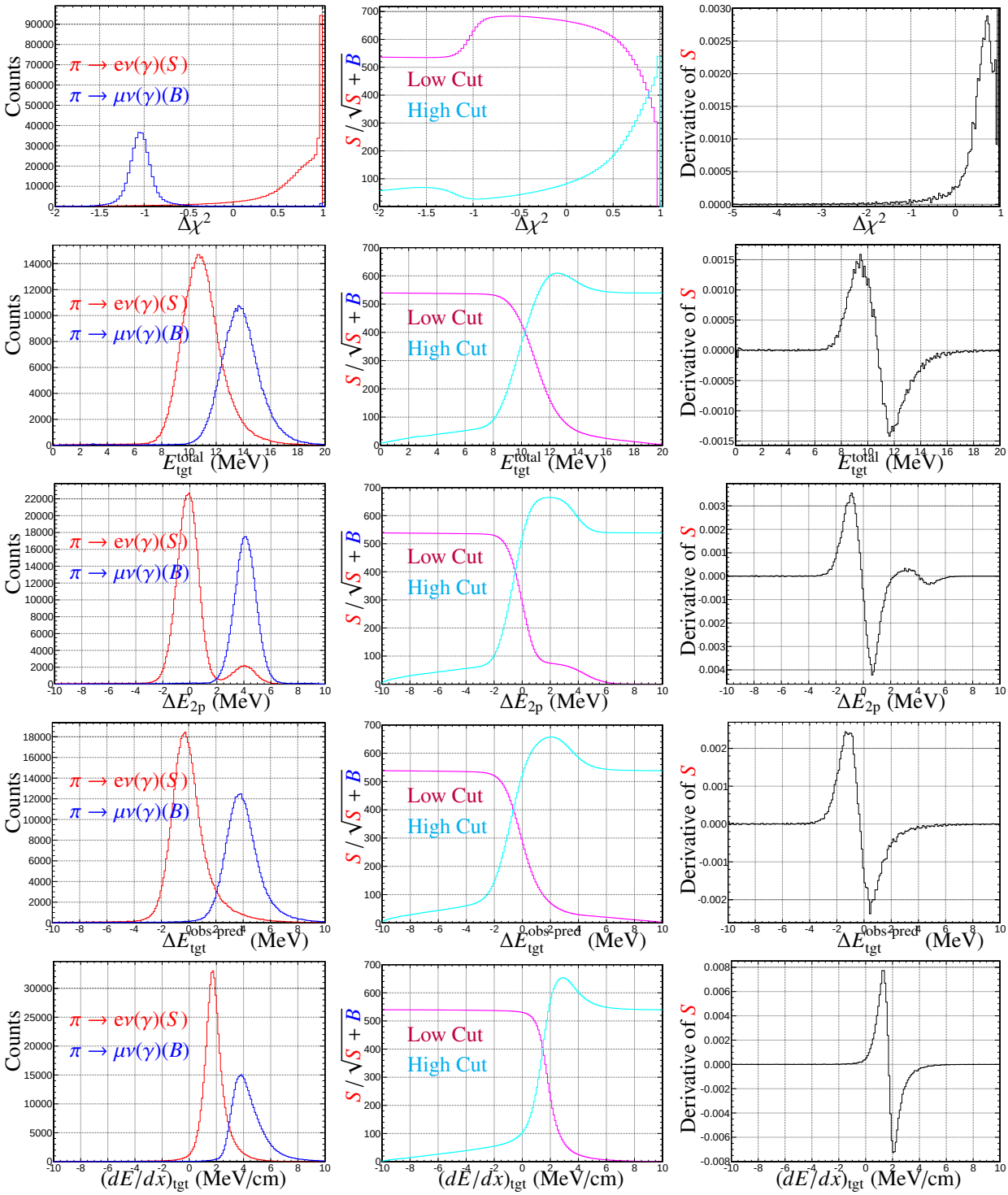

Figure 7.42: *Comparison of signal (red) and background (blue) as a function of cuts for the most discriminating waveform variables. Top Row: $\Delta\chi^2$. Second Row: Total target energy. Third Row: ΔE_{2p}. Fourth Row: Restwave. Fifth Row: Target dE/dx. First Column: Plotted observable for the two modes from Monte Carlo. Middle Row: Signal to Background ratio as a function of cutting above (purple) and below (cyan). Third Column: Derivative of the signal normalized to the yield.*

Selecting one or more of these observable to produce a more pure pion decay spectrum, a cut efficiency and associated uncertainty quantification becomes necessary. The efficiency and uncertainty can only be characterized by observing the systematics of the observable and studying them using the Monte Carlo simulation. The systematic uncertainty arises from not having a perfect simulation and therefore deviations from ideal simulations result in changes in the observables. While an in depth characterization of the uncertainties in these cuts is done in the last section of this chapter, the sensitivity and expected error is seen by observing the first and second derivatives of the signal spectrum for each of the individual observables. The first derivative of the signal provides an insight into how much the value changes in that region. In particular, a region in which the derivative is fairly constant signals a region that is not too sensitive to changes in that particular value. This most likely results in a smaller systematic uncertainty associated with characterizing that cut in the Monte Carlo. So while the derivative is zero for a maximum in the the four bottom plots, the change in the derivative is quite drastic in that region and would thus be an unfavorable position to make a cut. The flatter the derivative, the more appealing it is to cut in that region because the less likely systematic uncertainties will play a role. The best position without taking into account the error is one in which the signal to background value is maximized. Standout value occurs in the $\Delta\chi^2$ observable for two reasons. The first is that the signal to background maxes out at a very high value for the low cut between -1 and -0.5. The second is that the high cut value maximizes at the saturation value which means that only a one sided cut is needed for a $\Delta\chi^2$ selection as opposed to two cuts. A single cut is preferable to two cuts because error propagation is determined then only once (on one side). Further, the derivative of the $\Delta\chi^2$ in the aforementioned region shows high levels of stability and thus apriori is not expected to produce a relatively high error. Therefore a $\Delta\chi^2$ cut is used to reduce the Michel background for branching ratio extraction.

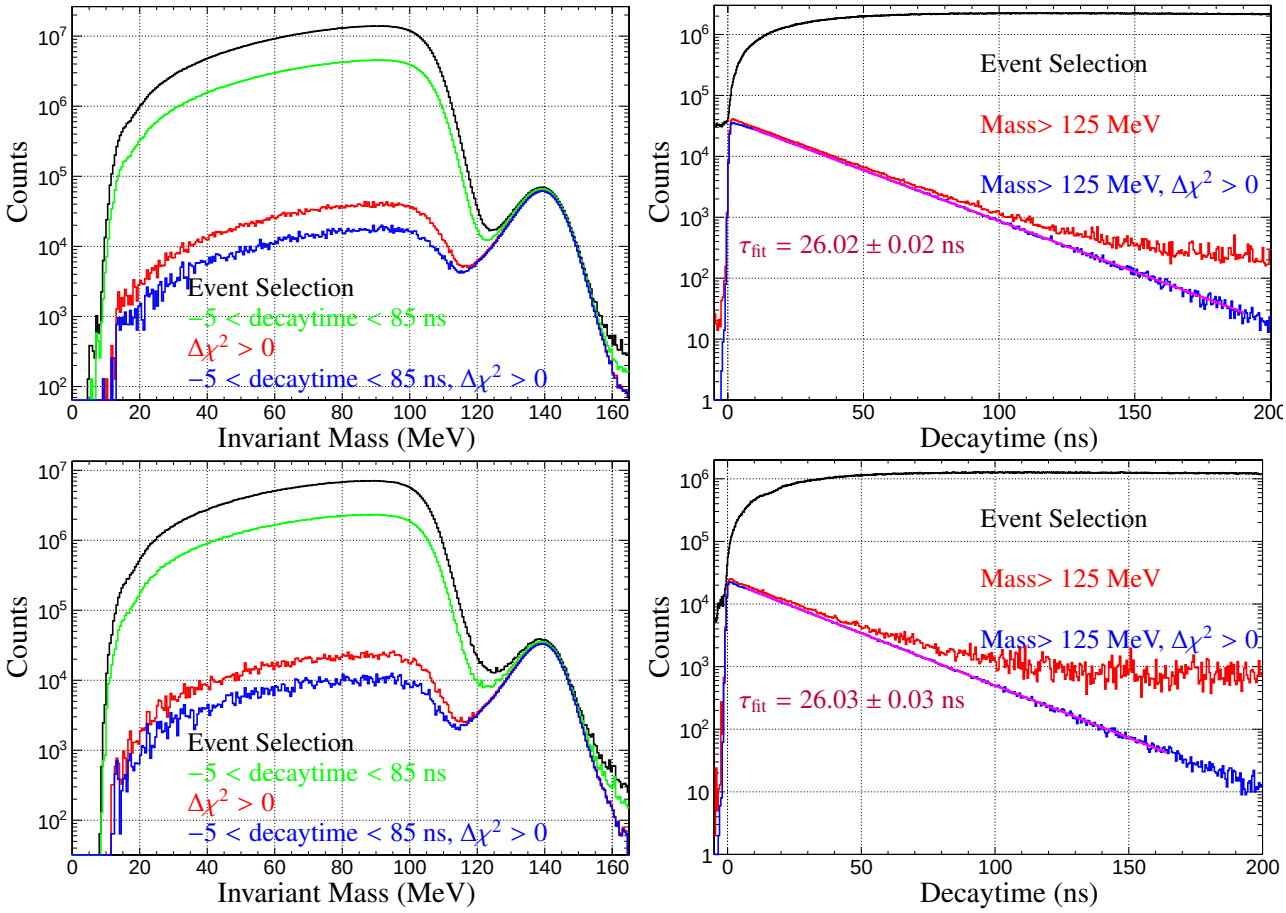

Figure 7.43: *Event selections for the pion decay channel with various cuts. Upper Left: Invariant mass for 2010. Upper Right: Decay time for 2010. Lower Left: Invariant mass for 2009. Lower Right: Decay time for 2009.*

Fig 7.43 shows the substantial elimination of the background with a non-restrictive, efficient, cut on the $\Delta\chi^2$ variable. With this cut, the number of $\pi \rightarrow e\nu(\gamma)$ events can be determined.

In order to obtain the number of events, the tail/peak dividing line needs to be chosen. The best line to use is to take minimum of the dip in the above plots to obtain the number of positrons emerging from pion decays. The further away from the peak the better the uncertainty that will emerge for the tail. There are notably a remaining amount of Michel decays in the invariant mass spectrum and some of these will seep into the peak region. This is accounted for by subtraction. To minimize the number of events being subtracted from the tail it desirable to get a smaller number of Michels in the signal dominated histogram and subtract off a Michel spectrum that has few if any positrons from pion decays. Therefore from the perspective of subtraction, a higher threshold line is preferable. By using a pure Michel spectrum with the $\Delta\chi^2$ cut and proper admixture of muon decays in flight both accomplished with the simulation, a subtraction

can be performed. It should be noted, that even early decay times still have a substantial Michel background without the $\Delta\chi^2$ cut. If $\Delta\chi^2$ cut is not used, then there will be a substantial subtraction, and the number of peak events would need to be taken higher to minimize the error from the subtraction. If the peak/tail dividing line is taken lower, the statistical uncertainty from the high subtraction would be undesirably high. In the subtraction, aside from the statistical uncertainty properly propagated, there are also two sources of systematic uncertainties in the subtraction. The first is the normalization, specifically where to normalize the simulated Michel spectrum, and the second is gain variation that is seen in the tail fraction section. Since the Monte Carlo simulation results are being used to subtract, there is an uncertainty in the gain (peak position) of the invariant mass. With different gains, there is a different number subtracted from the number of peak events for different gains. Without using the $\Delta\chi^2$ cut, different decay time windows and invariant mass tail/peak dividing lines are taken and the relative statistical uncertainty alone in the peak region shows that the cuts are required.

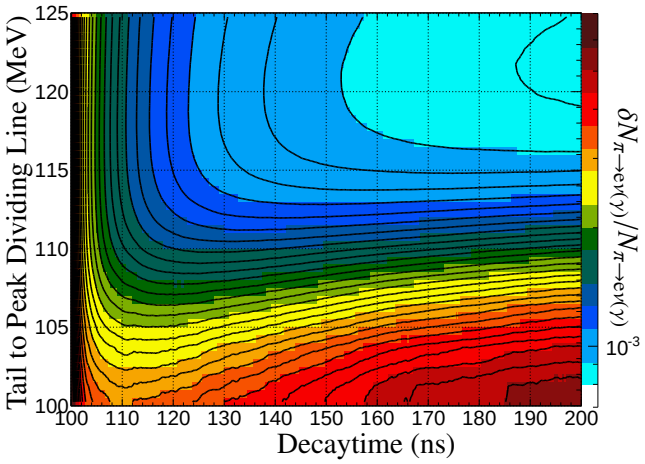

Figure 7.44: *Relative statistical uncertainty for the 2009 data set when subtracting the Michel background (using simulation) for different decay time windows where the highest decay time value is shown. The lower threshold for the decay time used here is −5 ns. Different peak-tail dividing lines are used.*

Fig 7.44 shows that the lowest relative statistical uncertainty in a subtraction with no further reduction of the Michel background occurs by taking the decay time window between −5 ns and 200 ns with a dividing line at 121.5 MeV which produces a relative (statistical) uncertainty of 8.4×10^{-4}. Even if this statistical relative uncertainty was acceptable, such a high dividing line with the addition of the tail fraction uncertainty would most certainly produce a relative error well above 10^{-3}. In addition to the statistical uncertainty, the systematics associated with the gains and normalization must be accounted for by employing the Monte Carlo simulations. Since the uncertainty in the gain has already been established in the study of the tail

fraction, this gain is then put in to the simulation and compared with the optimal gain input. The difference in the number of events is divided by the number of events in the simulation to obtain the fractional difference in the Michel spectrum as a function of invariant mass as seen in Fig 7.45.

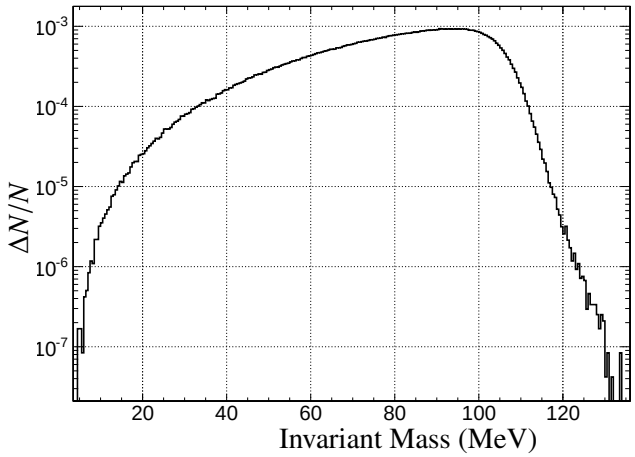

Figure 7.45: *Fractional difference in the number of Michel positrons as function of invariant mass due to variations in the gains.*

In the region of interest between 100-120 MeV, the fractional difference decreases as a function of energy which is not unexpected. Even though the fractional difference is small, the amount subtracted is the fractional difference multiplied by the Michel yield. For the case where of 115 MeV, for example, the fractional difference is nearly 10^{-5}. However, the Michel yield with no cuts is between 10^8 and 10^9, which means the number subtracted in the peak region would be optimistically $\sim 10^3$ events. With a yield of $\sim 10^6$ peak events, this produces an unacceptably high relative error in the peak of nearly 10^{-3}!. Further, there is a systematic uncertainty in how the normalization of the Monte Carlo affects the subtraction which is seen in Fig 7.46.

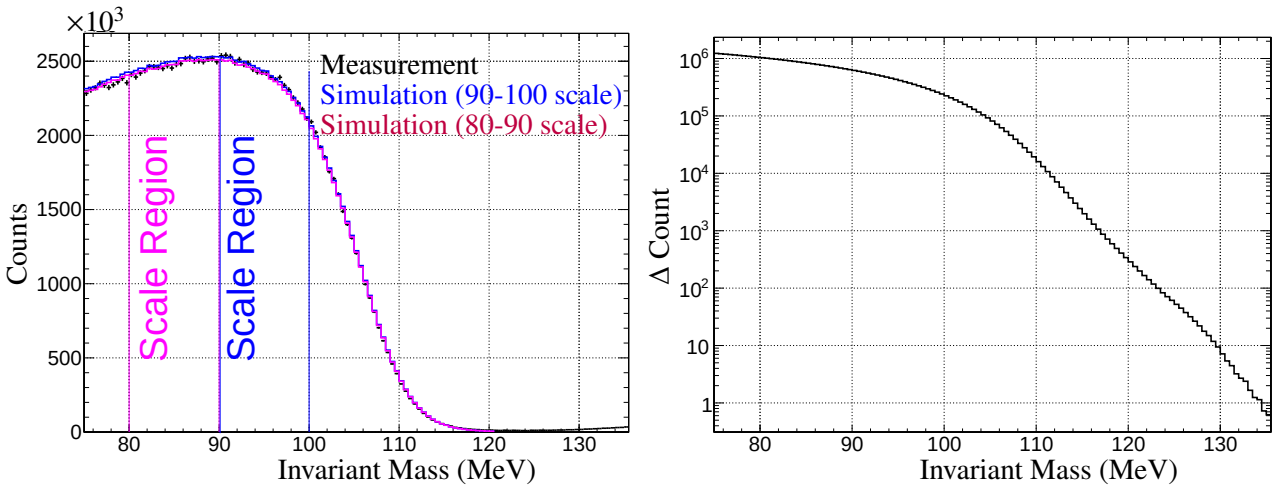

Figure 7.46: *Left: Comparison of measurement and simulation in the high energy regimes for different simulation normalizations. Right: Difference in the normalizations in the peak region as a function of the invariant mass (where the peak is defined).*

Normalization with such a vast number of events is done at the high values of the Michel spectrum in order to ensure that the number of tail events in the background are statistically insignificant so as to not distort the spectrum overall. In addition, the invariant mass window chosen was such that there is little (if any) distortion in the Michel spectrum due to MWPC efficiencies which slightly diminish the relative number of events reconstructed at lower energies. Around 115 MeV, the difference in the peak region due to the different normalizations is roughly 10^3 events, again slightly lower than a relative error in the peak of 10^{-3}. These plots show that if the number of Michel background events can be diminished by a factor of about 100 with little loss to the peak events, then the gain, normalization, and subtraction will contribute very little to the relative error in the peak.

At this point, it should be obvious that a cut is needed, in particular, $\Delta\chi^2$, in order to eliminate the high level of Michel background and minimize the subtraction and the relative statistical uncertainty which results. Furthermore, including the proper admixture of muon decays in flight ensures for a more realistic subtraction in the peak region. This procedure was done for multiple decay time windows all starting at -5 ns and ending anywhere between 65 ns and 200 ns, the window which provided the minimum error was the one that was chosen to obtain the branching ratio. The relative error of this process was

$$\sigma_{\text{relative}} = \sqrt{\sigma^2_{N\text{peak}}/N^2_{\text{peak}} + \sigma^2_{\epsilon_{\text{tail}}}/\epsilon^2_{\text{tail}}} \tag{88}$$

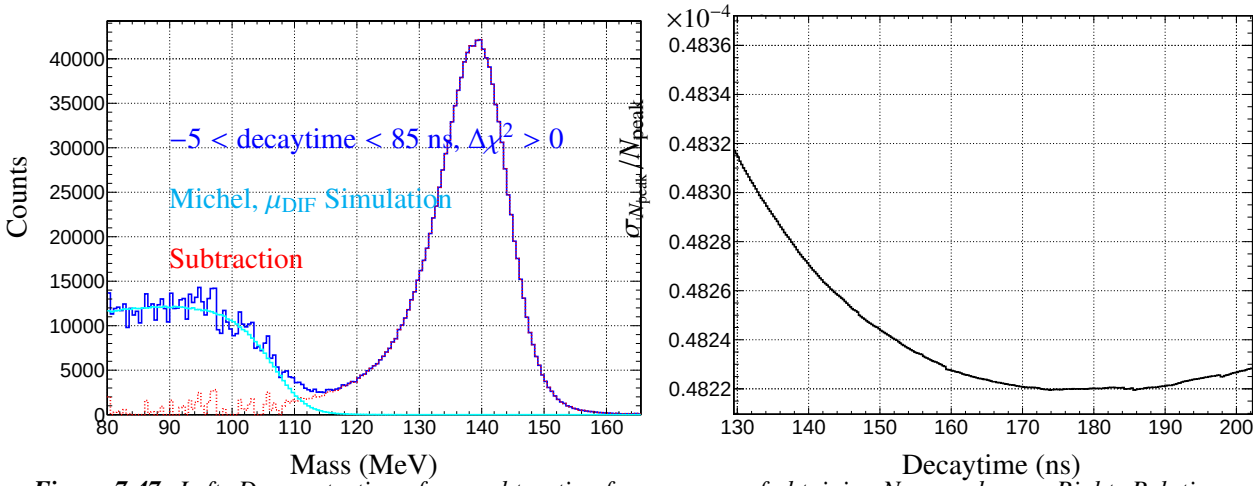

Figure 7.47: *Left: Demonstration of one subtraction for purposes of obtaining N_{peak} and $\sigma_{N_{peak}}$ Right: Relative error of the subtraction in the peak region as a function of the decay time window chosen, starting from* `decaytime` $= -5$.

Fig 7.47 contains two important features. The first is that the change in the peak region is small due to the inclusion or lack of muon decays in flight. In the above plot, for example, the number of the peak events decreases by 0.16% and the difference stemming from including muon decays in flight is a difference of 0.00078%; i.e., the inclusion of decays in flight entails a small correction. This is not the case for the tail fraction because the vast majority of muon decays in flight will have energy in the low energy tail regime. The second noticeable feature of the above plot is the continuity of the peak into the tail region below the local minimum before the subtraction. If this were not the case, then the subtraction would not be reliable. After scanning through different decay times, the minimum bin in the peak selection does not change significantly which means the tail fraction error will be the same regardless of the decay time window. Accounting for the error in the counts after subtraction, a chosen decay time window of -5 to 179.7 ns was chosen by fitting a quadratic function and finding the minimum in the above plot. Fig 7.47 also shows that even with one year (2010), the relative uncertainty is (barely) below the PEN goal. However, it should be noted that this does not have a pileup cut. Once this cut is implemented the statistics will fall and the uncertainty will be (slightly) above the PEN goal.

Since the decay time window for $\pi \to e\nu(\gamma)$ events includes the early decay times, there may be some concern among the readers because it was shown earlier that the Michel decay time spectrum is problematic around 15 ns for the late data in 2009. That problem again arises due to pileup which are only relevant for muon decays. The decay time spectrum for late and early 2009 data is consistent for the pion decay channel as illustrated in Fig 7.48.

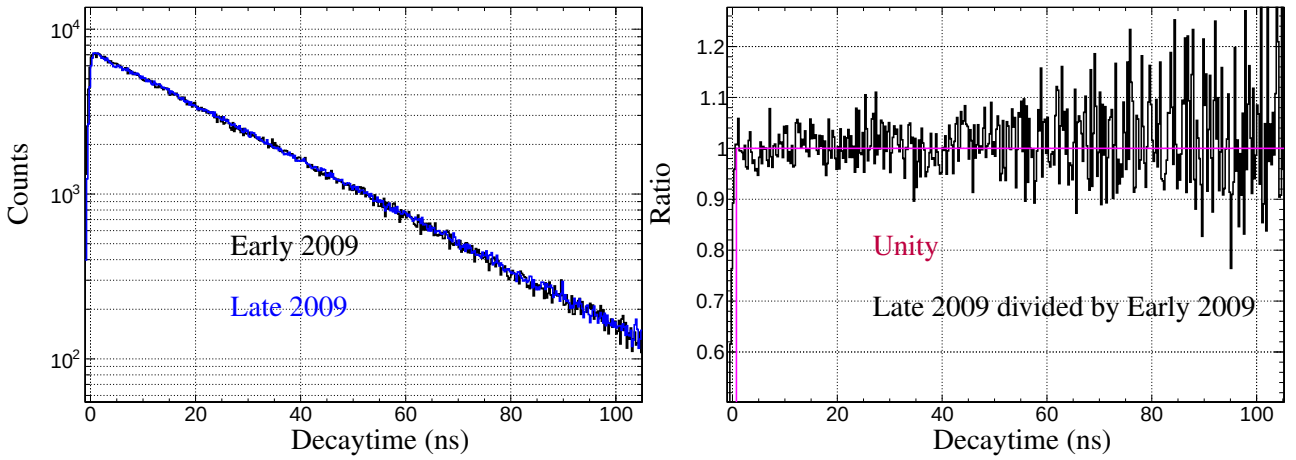

Figure 7.48: *Comparison of early and late decay time spectrum for $\pi \to e\nu$ decay. Left: Plot of decay time spectrum for late and early 2009 data. Right: Ratio of the decay time spectrum for late and early 2009 data.*

Using these cuts and events selection of $\Delta\chi^2 > 0$ the same four plots above are shown for the pion decay selection.

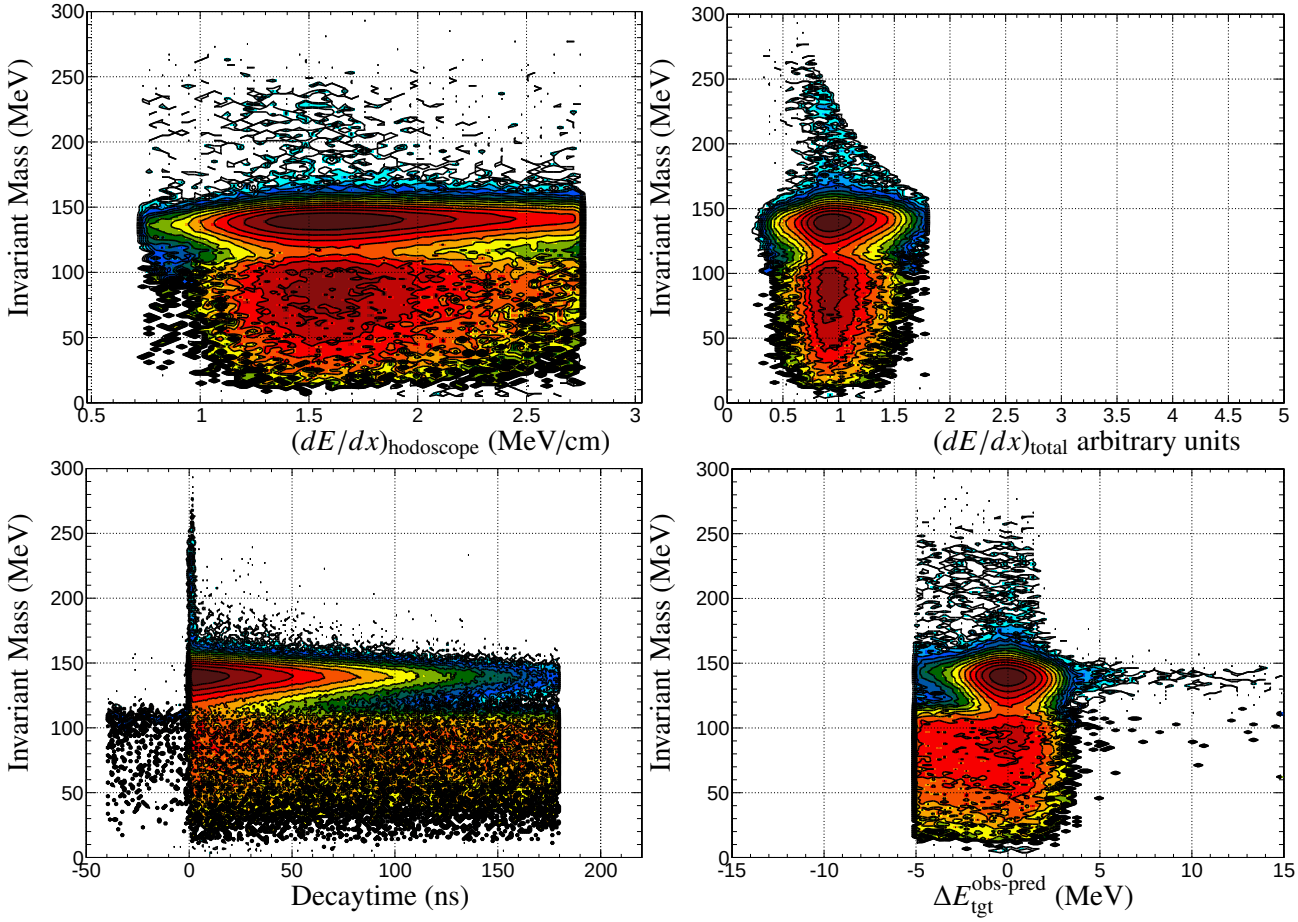

Figure 7.49: *Various spectra compared with the pion decay selection. Upper Left: Hodoscope dE/dx. Upper Right: dE/dx total. Lower Left: Decay time. Lower Right: Restwave.*

With the $\Delta\chi^2$ cut, one can see how subtraction from the pion peak diminishes not only in the Michel background but also from systematic effects of gains and scaling.

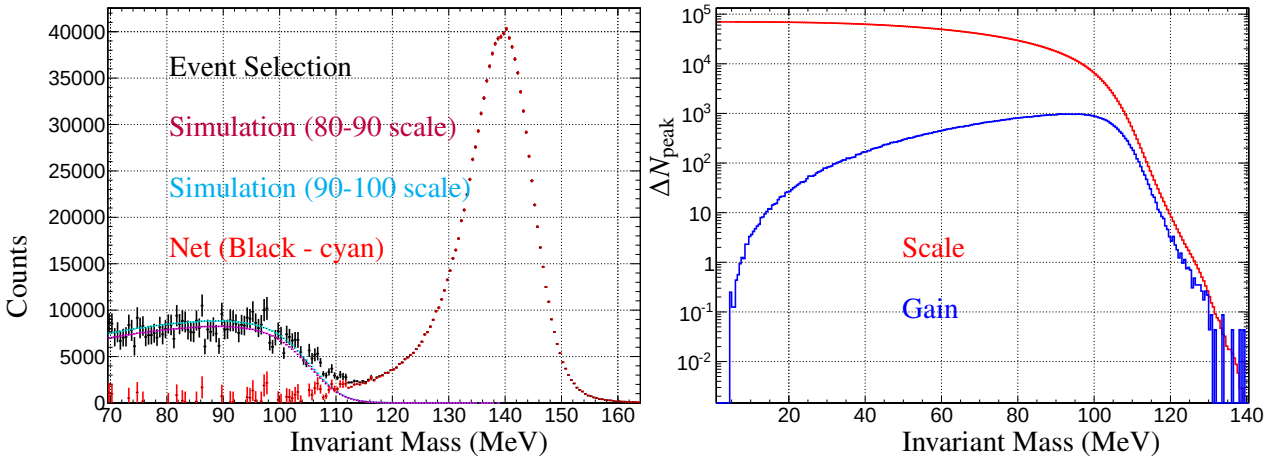

Figure 7.50: *Left: Comparison of different scalings with $\Delta\chi^2$ cut. Right: Systematic uncertainties associated with subtraction from gains and scaling.*

It is clear that due to gain variations, the dividing line between the tail and the peak with the $\Delta\chi^2 = 0$ should be above 110 Below this value produces a systematic uncertainty of greater than 10^{-3} assuming roughly one million events. The question, then arises as what is the best $\Delta\chi^2$ cut to be used. Using decay time of 180 ns, this process is repeated for various $\Delta\chi^2$ from -1 to 0 and the relative uncertainty in the number of peak events is shown in Fig 7.51.

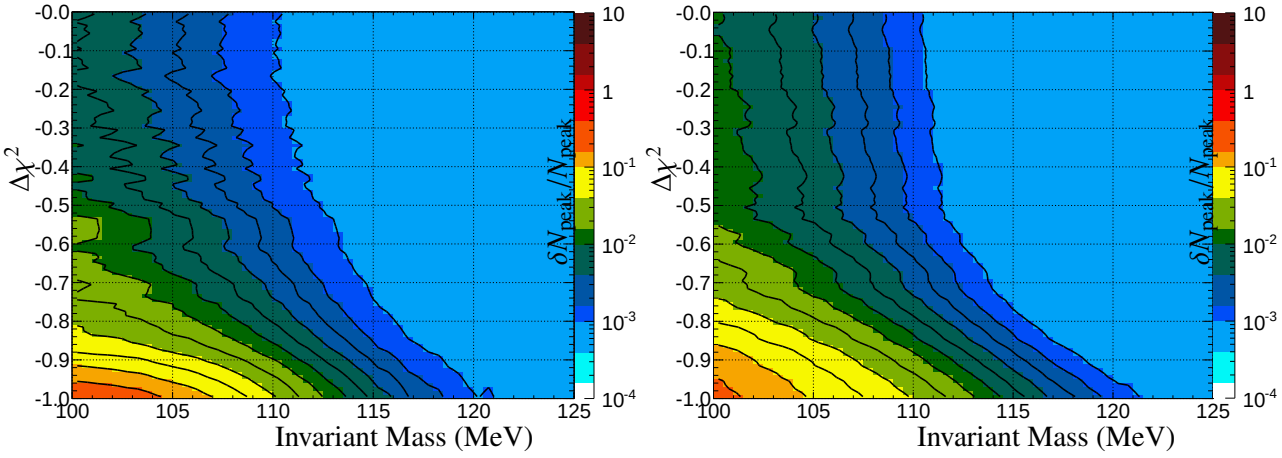

Figure 7.51: *Total relative uncertainty (statistical and systematic) for 2009 (left) and 2010 (right) data for the peak number as a function of invariant mass and $\Delta\chi^2$ cut at decay time between -5 and 180 ns.*

Without the $\Delta\chi^2$ cut, there is no method by which the subtraction would lead to a relative uncertainty in the number of peak events below 10^{-3} at any decay time. At 180 ns, it is possible with this cut. For

the 2010 data at decay time window from −5 ns to 180 ns the lowest relative uncertainty occurs at 117.5 MeV and $\Delta\chi^2 = -0.51$ with $\delta N_{\text{peak}}/N_{\text{peak}} = 6.76 \times 10^{-4}$. For 2009, the lowest uncertainty is $\delta N_{\text{peak}}/N_{\text{peak}} = 8.36{\times}10^{-4}$. Around these regions, however, there is little variation (they are all in the same color) This in turn means that changing the dividing line between the tail and the peak doesn't change the relative uncertainty in the number of counts but can change dramatically the tail fraction uncertainty. To fully account for all variations that can minimize the error, the decay time, tail/peak and $\Delta\chi^2$ are all scanned using the process that has been demonstrated; the lowest relative uncertainty provides the optimum values for the decay time window, peak/tail cutoff and $\Delta\chi^2$ cut value. The final $\Delta\chi^2$ and window selection is obtained by choosing selections which depend on not just the uncertainty in this selection but also the tail, $\Delta\chi^2$ efficiency, and decay time window. Since the tail fraction is not discussed yet, the proper $\Delta\chi^2$ and relative uncertainty discussion is saved for the last section of the chapter. Before the tail fraction is discussed however, stabilities regarding the ratio of the counts (which are now determined) are discussed.

7.8 Stability of B when applying cuts

The ratio of the counts have been discussed and how the counts are obtained. Everything else in the branching ratio calculation consists, for the most part, of applying corrections. However, cuts that are somewhat unorthodox have been made and we demonstrate that there is no bias in the count arising from these cuts. In particular, the three that are most critical are the radial stopping distribution, $\Delta\chi^2$, and the pileup cut.

As was stated before, the radial stopping distribution selection is made such that the muon is ensured to stop well within the target after the pion decays into a muon. If the muon leaves the target prematurely, then the signal is falsely perceived to be an early decay time, when it that would not be the case. This means in a late time window that was chosen, the number of Michel decay events would be under counted at high radial stopping distribution, which suggests that the ratio of the signal to background events would tend to increase as the radial stopping distribution increases. At lower enough radial distance, the branching ratio should be stable.

In the case of pileup, since a subtraction is performed after the pileup cut is instigated, it must be shown that after the subtraction, the ratio is consistent regardless of the cut on pileup. $\Delta\chi^2$ is a little more complex, but since it uses information regarding predicted energies of the pion, the branching ratio should then be stable with observables used to predict pion energy. The predicted pion energy, as discussed earlier, is

determined from the the time of flight of the pion and the energy in the degrader. There were cuts that were made to eliminate unwanted background (hadronic events, beam contamination,etc). Beyond certain limits in the cuts, branching ratio is expected to be independent within the event selections after these cuts. For these stability checks, the tail fraction and time correction factor is not used. The only thing that ultimately matters here is the ratio in the count. However, a multiplicative factor was put in roughly equal to the correction factor needed for taking only a fraction of the Michel positrons in a given time window. The deviation of the ratio should remain within statistic uncertainty limits. The selection for stability check is the exact same as that for determining the actual branching ratio. The method by which this was done is very similar to obtaining the counts of Michel and $\pi \to e\nu(\gamma)$. Applying the appropriate cuts produces a two dimensional histogram with decay time on one axis and the observable on the other. Slices of these histograms in various regions of the observable of interest are taken for both Michel and signal events. A subtraction of the pileup is performed and the ratio of events in the appropriate time window for Michel are divided into the number of signal events in the appropriate time window demonstrated below in Fig 7.52.

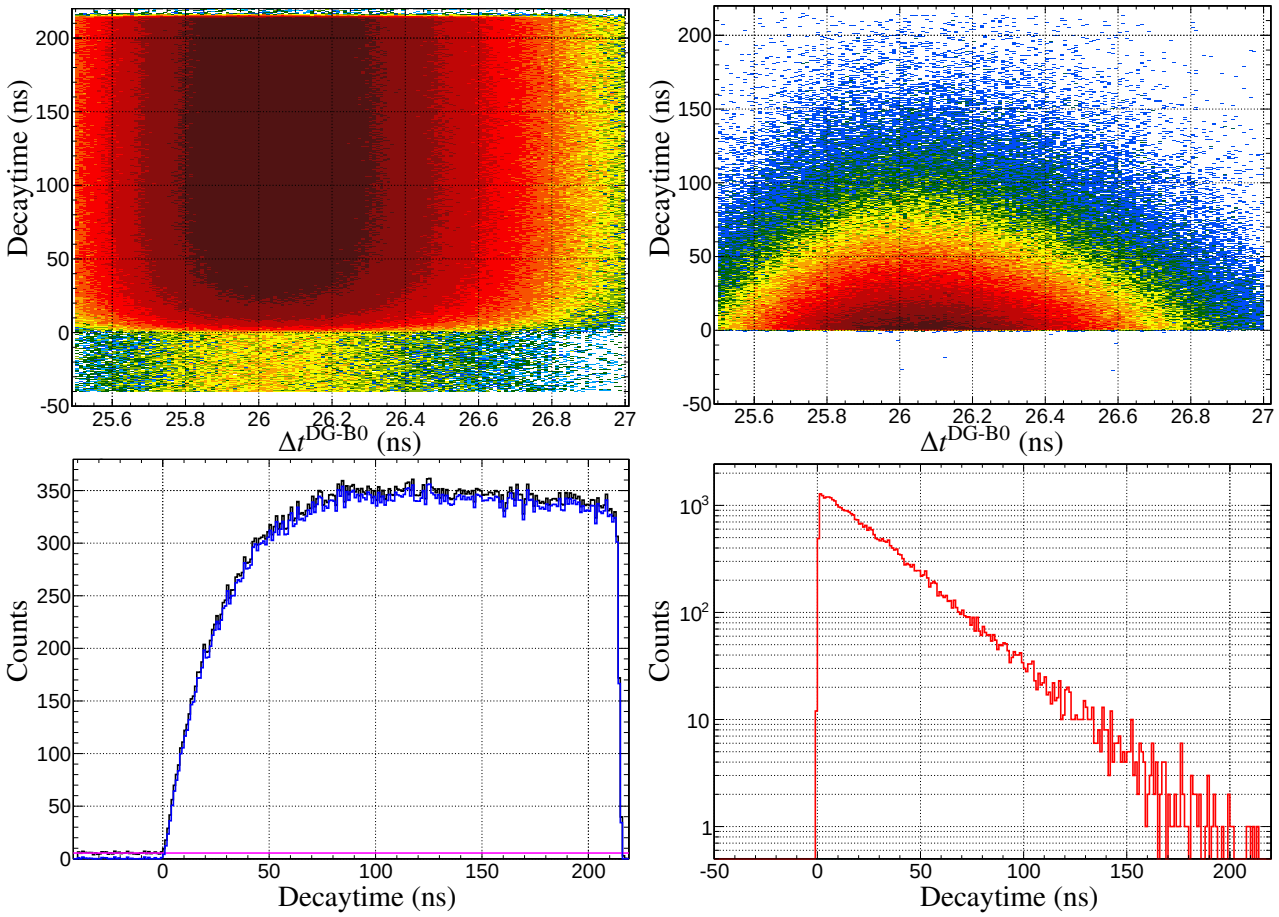

Figure 7.52: *Demonstration of how ratios for stabilities are determined. Upper Left: Decay time as a function of time of flight for Michel selection. Upper Right: Decay time as a function of time of flight for pion decay selection. Lower Left: Slice of the Michel time of flight. Lower Right: Slice of pion decay time of flight. Slices were obtained for* $\Delta t^{DG\text{-}B0}$ *between 26 and 26.1 ns.*

By performing this procedure through many smaller selections of a given observable of interest, the stability of the ratio as a function of the cut windows is tested and shown in Fig 7.53, Fig 7.55, and Fig 7.56.

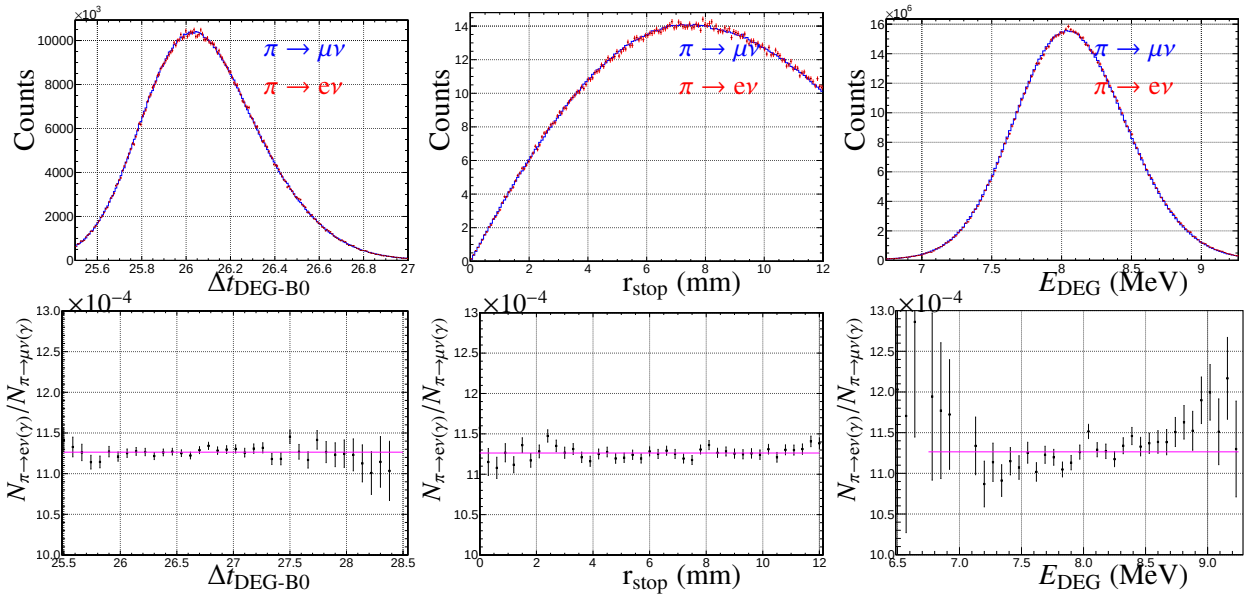

Figure 7.53: *2010 Stability of Branching Ratio with respect to time of flight (left) rstop (middle) and degrader energy (right). Profiles are shown on the top row for Michel positron selection (blue) and positrons from pion decays (red). Bottom shows stability of branching ratio as a function of variable of interest. Note corrections due to timing gate and tail are not in place.*

An example of a "bad" region is illustrated in a less restrictive cut on the radial stopping distribution in Fig 7.54.

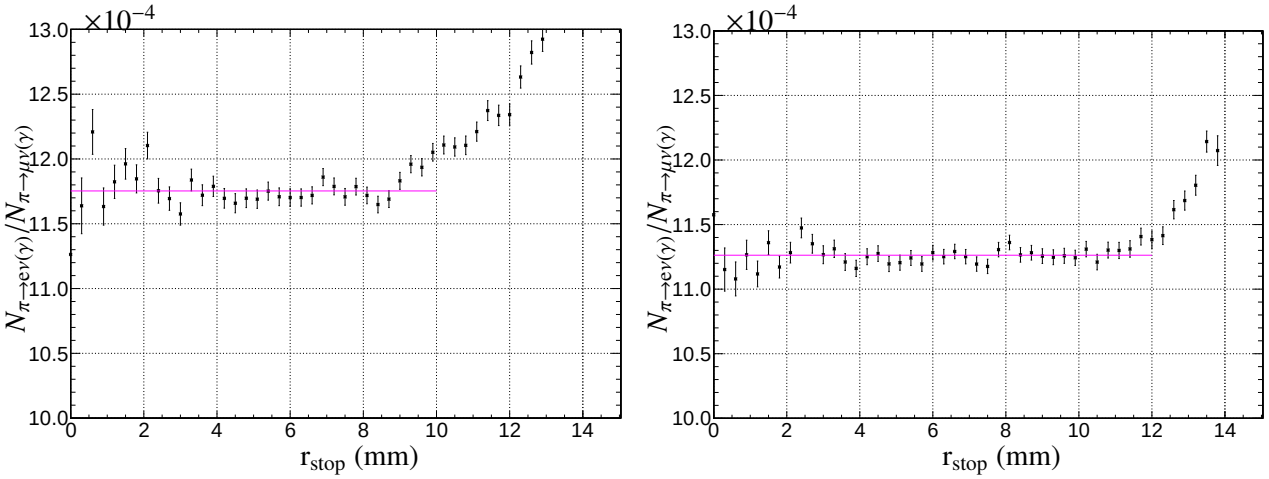

Figure 7.54: *Ratio of the counts as a function of radial stopping distribution. Left: 2009. Right: 2010.*

A deviation from the consistency of the branching ratio is not unexpected. When the muon stops too close to the skin of the target, it can leave the target before decaying, triggering the event and producing a decay time that occurs earlier than the actual Michel decay time that should occur. This means the later time window, which is used in the Michel count, has a deficit in the count which results in a larger branching

ratio as seem in Fig 7.54.

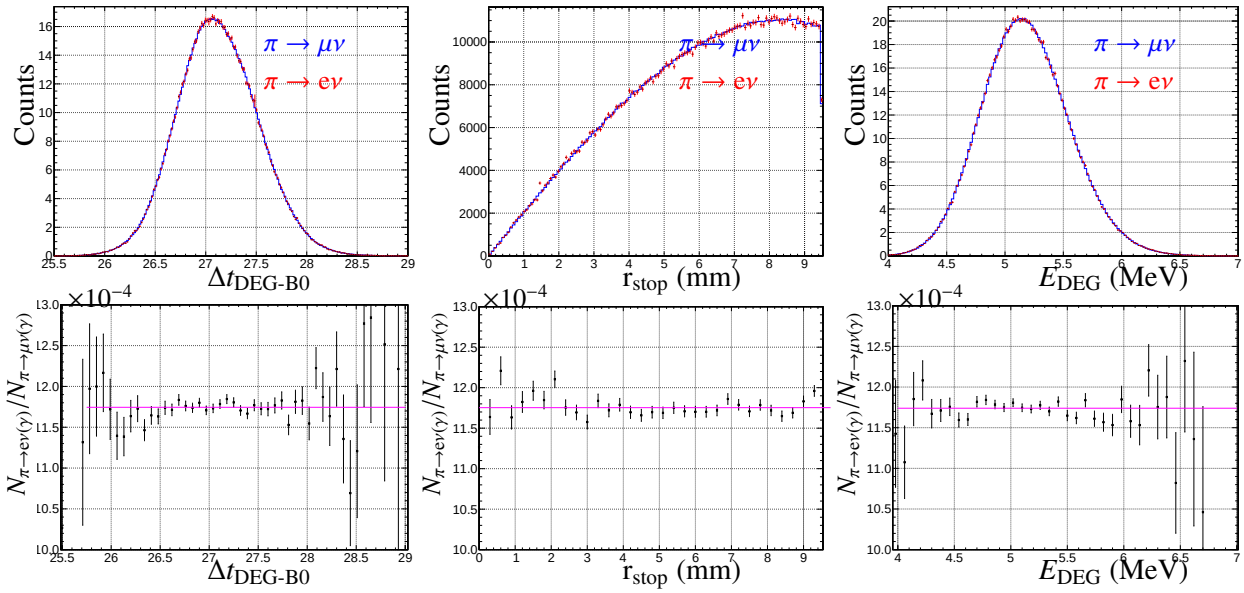

Figure 7.55: *2009 Stability of Branching Ratio with respect to time of flight (left) rstop (middle) and degrader energy (right). Profiles are shown on the top row for Michel positron selection (blue) and positrons from pion decays (red). Bottom shows stability of branching ratio as a function of variable of interest. Note corrections due to timing gate and tail are not in place.*

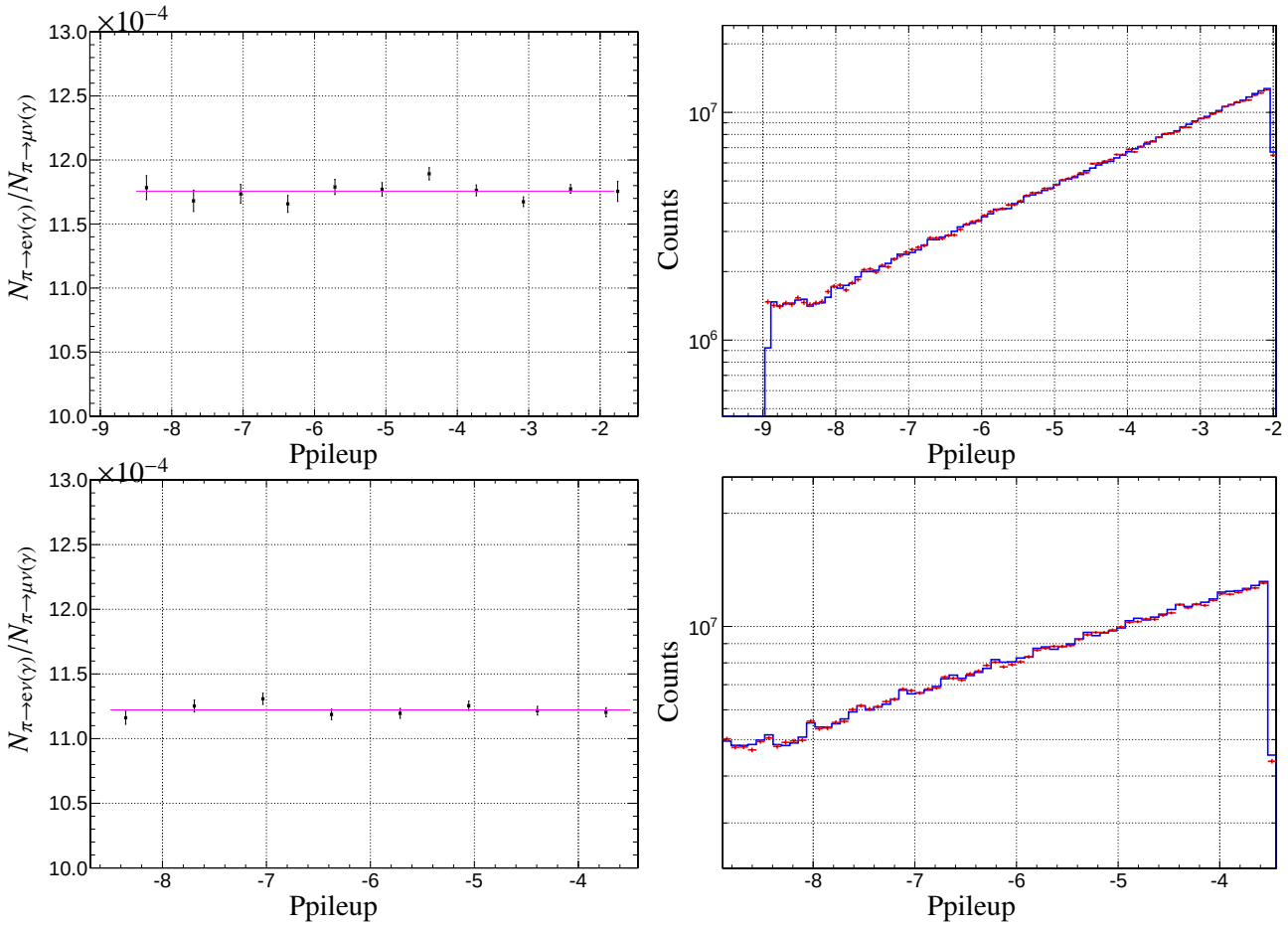

Figure 7.56: *Effect of branching ratio with Ppileup cuts. Left Column: Consistency as a function of cutoff. Right Column: Ppileup spectrum. Top Row: 2009 data. Bottom Row: 2010 data.*

With the demonstration of stability of the branching ratio for the radial stopping distribution, the pileup cuts, and the variable which form the predicted pion energy for purpose of $\Delta\chi^2$ cut, the tail fraction is now ready to be determined.

7.9 Tail Fraction, ϵ_{tail}

The positron low energy tail in the CsI calorimeter is a result of the energy leakage from electromagnetic showers in the calorimeter. The calorimeter is 22 centimeters thick, or 12 radiation lengths, so all of the induced electromagnetic shower energy will not always be detected. The tail fraction presents the most difficult systematic uncertainty in the experiment to evaluate. One has to rely on simulation for the the tail fraction. This however assumes that the simulated tail is correct and this will bias the measured tail result to

the simulation. This is not desirable. The simulation should provide the level of precision necessary to obtain the PEN goal. Not solely relying on simulation but rather ensuring the tail fraction relative uncertainty for measurement is consistent with simulation to the level possible which is on the order 10^{-3}, in which case, the simulation should be able to provide that extra level of certainty. In other words, it desirable to evaluate a tail fraction from the measured data (with less certainty) first, ascertain that it agrees with the simulation results and then the simulation can be used to reach the desired level of uncertainty. To obtain a tail fraction to the desired precision, the physics describing the creation of the tail must be well understood. The processes, aside from the energy leakage that contribute to the low energy tail need to be studied. A difficulty arises because pure CsI has relatively poor energy resolution. In order to see if there is physics affecting that low energy tail is to look for energy responses in detectors with better resolution. The PiENu experiment will suffice[24].

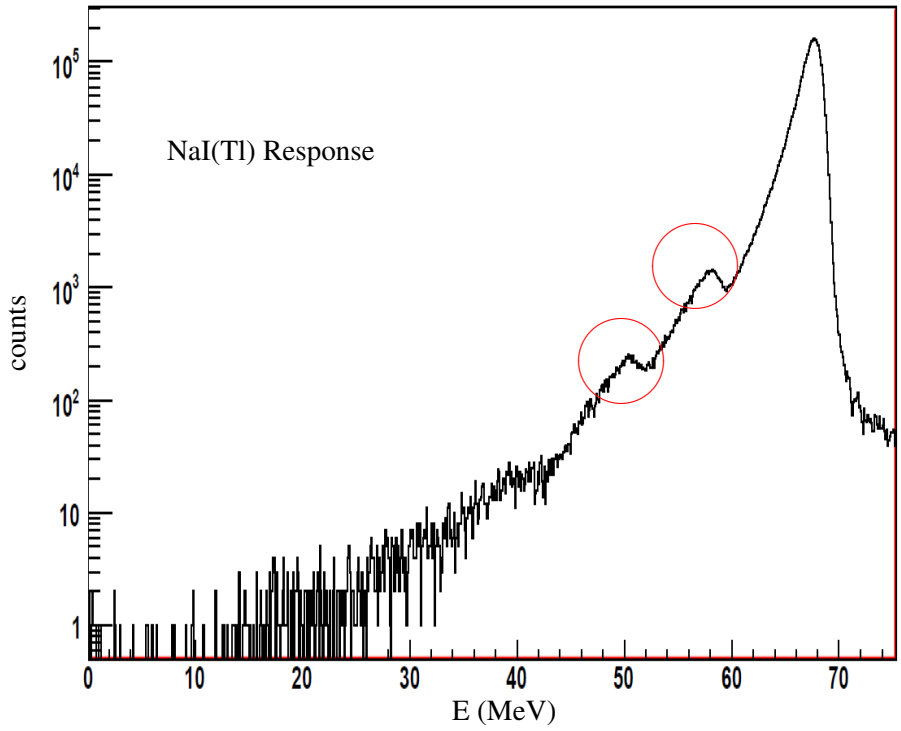

Figure 7.57: *Effect of Photonuclear absorption On NaI(Tl) on PieNU from Triumf. [24]*

Fig 7.57 shows lower energy peaklets from the main positron peak. This results from a nucleon being expelled from a nucleus after the absorption of a photon, a process called photonuclear absorption. Loosely

speaking, the nucleus absorbs a photon from the electromagnetic shower, this causes the emission of nucleon, which may or may not (in the case of a neutron) lose all of its energy electromagnetically leaving the detector taking any energy excess with it. One can see that the main peak is roughly 8 MeV from the first peaklet which in turn is 8 MeV from the second. This energy corresponds roughly to the binding energy of the nucleon, that is the energy required to knock loose one of the two nucleons. This section therefore, is broken into three parts. The first gives a little background and theory behind this process, the second demonstrates how the simulation incorporates this process into the low energy tail, the third shows the process of obtaining a low energy tail from the measurement and comparing it to the Monte Carlo simulation in order to obtain the tail fraction and uncertainty contribution to the branching ratio.

7.9.1 Photonuclear absorption and giant dipole resonances

The emission of a nucleon from a nucleus due to an incoming photon is a contributor to the uncertainty in the low energy tail. There is a (relatively) high cross section for the emission of a nucleon due to an incoming photon in the 10-25 MeV energy regime which increases in energy with mass of the nucleus. The measurements for this resonance phenomenon, known as the giant dipole resonance, was first performed by Baldwin and Klaiber in 1948 [13]. In the most general case,

$$\sigma_{\text{absorption}} = \sigma(\gamma, n) + \sigma(\gamma, p) + \sigma(\gamma, d) + \sigma(\gamma, 2n) + ... \tag{89}$$

While both a proton and a neutron are subject to emission from the nucleus, the cross section where a proton is expelled from the nucleus is highly suppressed for higher atomic numbers due to coulombic forces; it is more advantageous to emit a neutron than a proton for higher Z nuclei. In addition, protons lose energy due to electromagnetic interactions in the calorimeter and are therefore detected when they are ejected. Thus when discussing and implementing the photonuclear absorption, only the neutron cross sections are of importance for the PEN analysis. The high cross section is indicative of a collective phenomenon and is due to the collective relative motion of the neutrons and protons to opposite sides of the nucleus upon absorption of a photon. For spherical nuclei, the cross sections for these events produce a prominent Lorentz peak. For less symmetric nuclei, the peak broadens and for “cigar-shaped” nuclei, two peaks appear one from each the semi-major and semi-minor axis. The relatively high cross sections compared to other incoming photon

energies is shown in Fig 7.58 taken from Findlay [43].

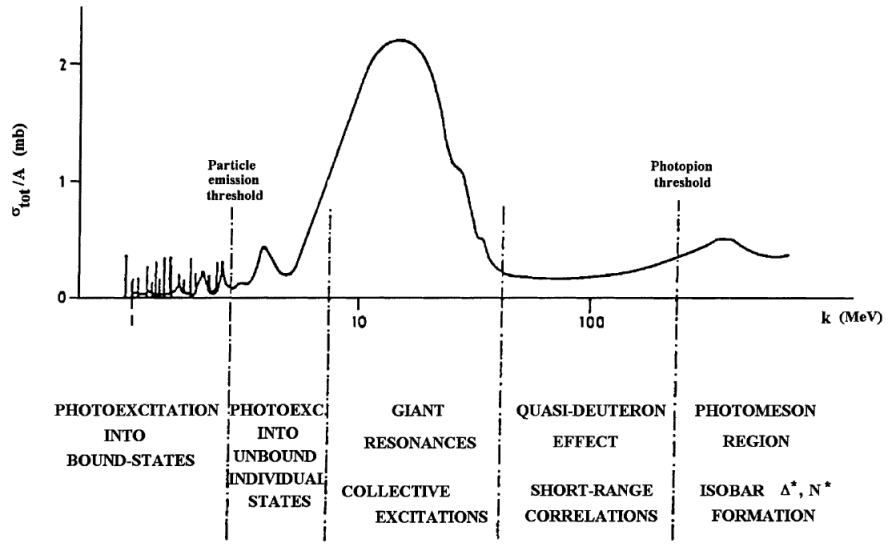

Figure 7.58: *Nuclear responses as a function of incoming photon energy.[43]*

Moving forward, the cross sections of this process must be properly simulated in order to properly characterize the low energy tail and its uncertainties.

7.9.2 Simulation Implementation

In order to fully recreate the low energy tail of the PEN CsI calorimeter, all of the aspects and caveats of the underlying physics are needed to reproduce the full detector response of the CsI calorimeter. Not only the digitization of energies, and implementation of the photoelectron statistics, but also fundamental physics which affects the tail. The photonuclear absorption of a photon and the ejection of a neutron affects the shape of an EM calorimeter's response as seen in the experiment performed by TRIUMF. In order to fully ensure that the tail is being properly simulated, the physics underlying photonuclear absorption must be coded in the simulation. The GEANT4 package has these physics processes built in, and the photonuclear cross sections are calculated using different models. As long as these cross sections are consistent with the experimentally determined values, if it exists, then there is no underlying problem Measurements on the photonuclear cross sections have been performed on iodine by Bramblet [17] and Bergere [14], and on Cs, by Berman[15], and Lepretre[55]. GEANT4 package producing cross sections which are not consistent with

the experimental data, and the experimental data conflict with each other, most notable in the cross sections of ^{127}I(γ,n). The issue becomes a two-fold problem. The first is to put in photonuclear cross sections such that they are consistent with data and the second is to put bounds on the tail fraction using the conflicting data set. Because of conflicting data and the data age, an updated evaluation was performed by Varlamov [92] which was used in this analysis. These evaluations were used preferentially over the other values because they are more recent and their group has done such evaluations for many different nuclei. A user defined function was created using Minuit [20] to fit the data to a 13th order polynomial to these evaluations. Cross sections from the stated works are in the Fig 7.59.

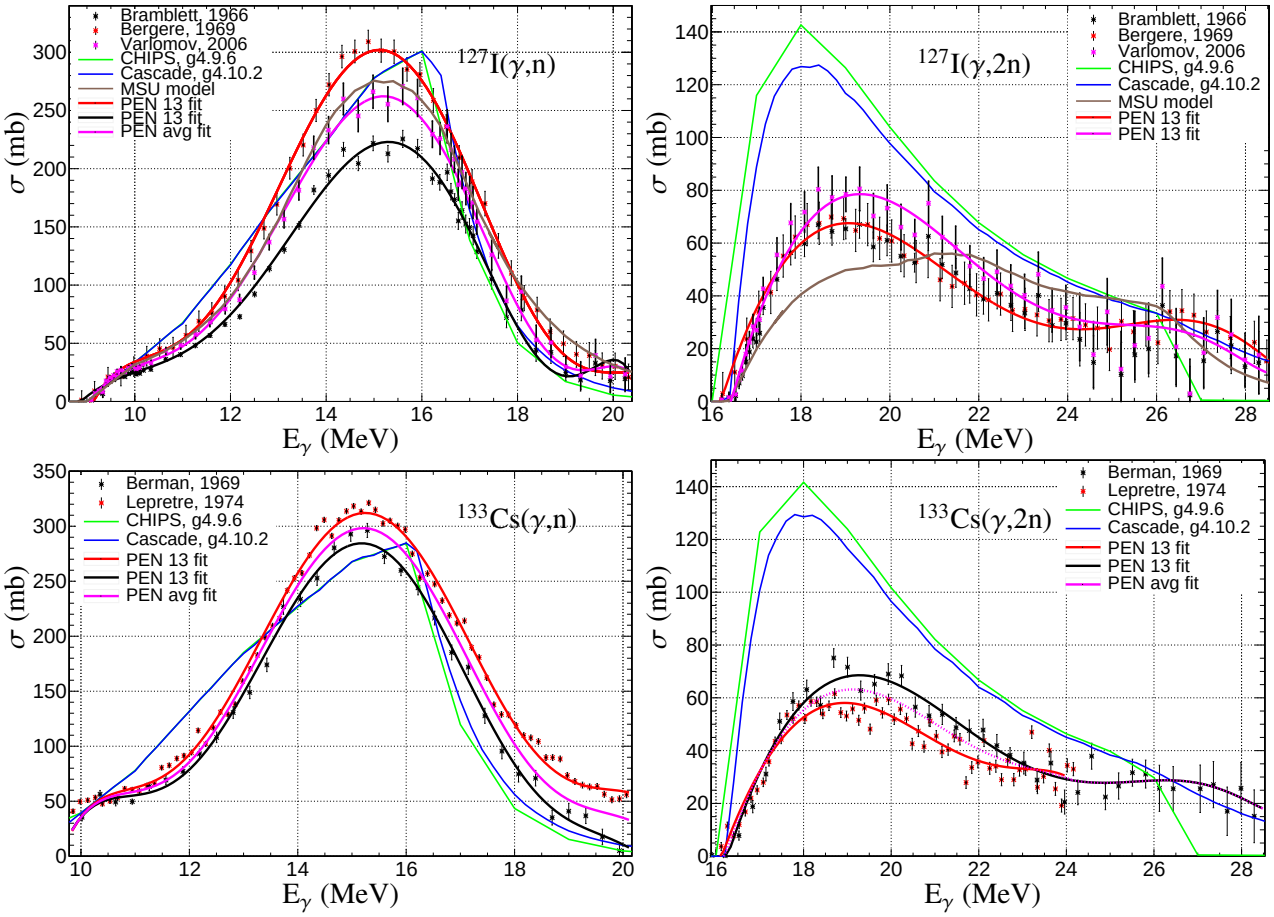

Figure 7.59: *Measurements of the photonuclear cross sections for neutron escape from different experiments. Comparison with two different GEANT4 models, CHIPS and Bertini Cascade are presented along with a 13th order polynomial function fit.[14] [17] [15] [55] [92].*

Since the emission of neutrons contributes to the low energy tail fraction and the probability of the this occurring is related to the photonuclear cross sections, a lower limit on the uncertainty of the tail is

established by studying the tail fraction as a function of the different cross sections put into the simulation. By studying the tail fraction with the full detector response as a function of the different cross sections, limits on the uncertainties of the tail fraction may be established.

7.9.3 Tail fraction and uncertainties

As previously discussed, the simulation is only reliable enough to provide the value and uncertainty for the low energy tail if proven consistent with the measured low energy tail. While it is not possible to obtain the low energy tail experimentally at the relative precision of 10^{-4}, it is possible to obtain it to the level of 10^{-3}. Moving forward then requires an experimental low energy tail and a comparison with the simulation. In order to obtain a tail fraction from the measured data, a subtraction must take place between two event sets separated by different discriminating cuts. One set has an abundance of the signal events, and the other has abundance of Michel background events. The energy spectrum of the high abundance of background is subtracted from high signal set and the resulting energy spectrum results in a response that has a clean low energy tail. The PEN tail trigger was designed specifically to study the low energy tail. The PEN hardware performed a real time search for a muon peak in the target in the first 80 ns of the pion stop for 2009 and 50 ns for 2010. If no muon signal was found, then this event was labeled as tail event. No energy requirements in the CsI were necessary for these events, only a search in the target to prevent any CsI bias in studying the tail. These are the events that are used for the analysis.

Quantitatively, the set of events with a high number of signal events which will be called “good” events will have a lot of signal events and few background Michel events.

$$N_{\text{good}} = C_1 \times N_{\text{signal}} + C_2 \times N_{\text{background}} \tag{90}$$

Then “bad” events that are chosen will have lots of background and few signal events.

$$N_{\text{bad}} = C_3 \times N_{\text{signal}} + C_4 \times N_{\text{background}} \tag{91}$$

A subtraction factor α is defined as

$$N_{\text{good}} - \alpha \times N_{\text{bad}} = C_1 N_{\text{signal}} + C_2 N_{\text{background}} - \alpha C_3 N_{\text{signal}} - \alpha C_4 N_{\text{background}} = (C_1 - \alpha C_3) N_{\text{signal}} \tag{92}$$

i.e., $\alpha = C_2/C_4$ eliminates background and gives a pure signal. The relative error may be studied to give an idea on what we want our distributions to look like. Since the number of good events is $C_1 + C_2$ and the number of bad events is $C_3 + C_4$. This means the relative error in the subtraction, assuming the background cancels is

$$\frac{\sqrt{C_1 + C_2 + \alpha^2(C_3 + C_4)}}{C_1 - \alpha C_3} \tag{93}$$

Since $C_2 = \alpha C_4$ this can be replaced, and reordered to give a relative error of

$$\frac{\sqrt{C_1 + C_4(\alpha^2 + \alpha) + \alpha^2 C_3}}{C_1 - \alpha C_3} \tag{94}$$

So to minimize the uncertainty in the tail, it would be desirable to have α be very small. (Notice if $\alpha = 0$, we would have no background events in the "good" events, everything would be signal, and the relative error would be the expected $1/\sqrt{C_1}$). Having α be a small value, eliminates the α^2 terms in the numerator, reducing the relative uncertainty. However, the linear terms can be big if C_3 or C_4 are sufficiently big. In addition to a small value for α, it is desirable to have the bad events set have as few events as possible for a relatively small subtraction error. This also means that a high value of C_1 is also preferable. So for the "good" events we want a high number of peak events with as little Michel spectra as possible. For "bad events" it is not desirable to have too many events in the peak or the tail region. The tail region for both the good and bad events should have close to comparable events to ensure these conditions. The big challenges presented in the process are finding the subtraction factor and the selection criteria for signal and background events.

Since the two spectra that are being subtracted are at the energies of the two main channels, the selection cuts cannot be positron energy dependent, otherwise the energy spectra will be distorted and the subtraction will not provide a representative low energy tail. Hence, in order to make these selections, observables constructed from target signals, MWPCs and hodoscopes are allowed. The best method to proceed is to make highly discriminating cuts to eliminate as much Michel background as possible and then make one final cut that will separate the sample into two sets, one Michel dominated, and the other signal dominated. A procedure is also needed to ensure that the proper subtraction factor is achieved. There are two philosophies to accomplish this. The first is that the subtraction should result in a smooth curve i.e., continuous derivatives. The problem with this philosophy lies in some of the intricate nature of the low energy tail. In particular the photonuclear absorption complicates this scheme. Small peaklets, when differentiated, es-

pecially with relatively small statistics are most likely not going to result in a smooth derivative in binned data. The second available approach is to ensure that the subtraction resultant decay time spectra be energy independent and give the same slope for all ranges of energies. This is the philosophy that will be followed. With this approach, the event selection can not affect the decay time spectra, i.e., cuts on decay time may not be made. The observables needed to achieve a proper subtraction would be one in which the the $\pi \rightarrow e\nu$ peak would have a noticeable separation from the Michel dominated background. The possible candidates are `tgt dedx`, `dz0`, `vertex quality`, `restwave`, $\Delta_E 2p$, $\Delta\chi^2$, $\chi_{\texttt{2peak}}$, and `totalwave`.

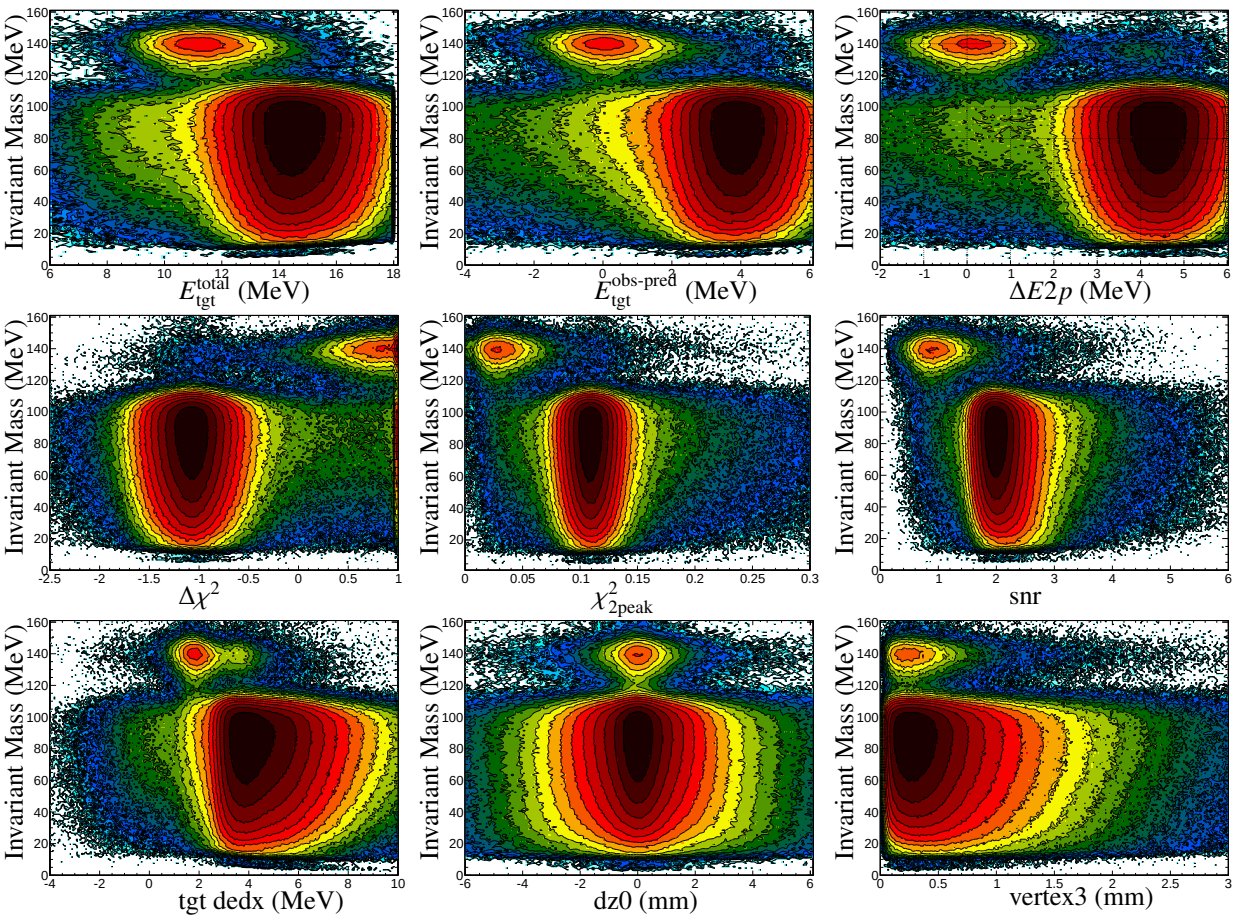

Figure 7.60: *Invariant Mass plots versus various target and tracking observables used to discriminate the two different processes. Data is taken from the tail trigger events.*

Fig 7.60 shows different higher order observables that can be used to diminish the number of events in the tail region due to the Michel decays. By taking regions where the peak to tail ratio is flat for all these observables, an optimal set of cuts may be achieved. However, this may sacrifice too many peak events so a compromise must be reached. The tail trigger events used in this analysis contain invariant mass spectrum

in which the peak in the Michel portion is more than an order of magnitude greater than the $\pi \rightarrow e\nu$ peak. After applying said cuts, the spectrum gets to a shape where $\pi \rightarrow e\nu$ peak is almost two orders of magnitude greater than the peak in the Michel region as seen in Fig 7.61. In the end, once a set of cuts has been chosen, one more cut is used to separate the remaining data into signal dominated, or "good" events and background dominated or "bad" events.

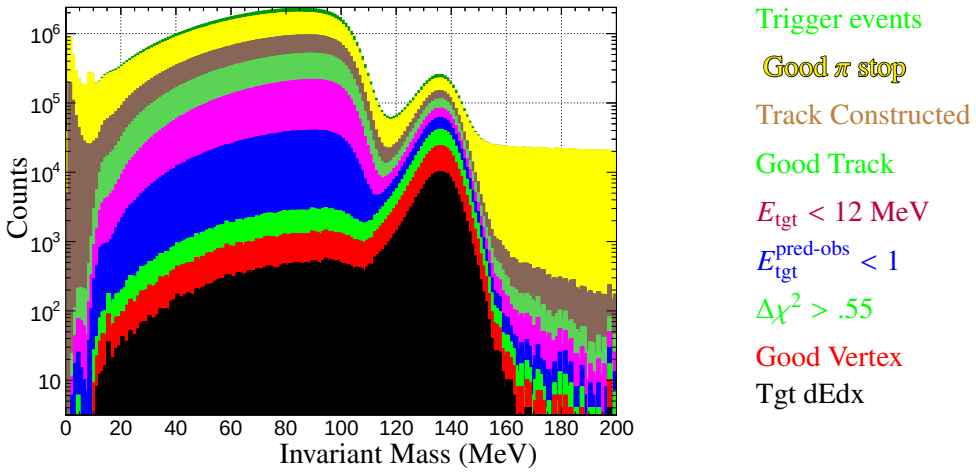

Figure 7.61: *Diminishing of background events with subsequent cuts. 2010 shown.*

After applying various cuts to get a good separation between signal and background dominated events, a subtraction must be done. This is done by taking the `decaytime` spectra in the tail region (20-100 MeV) of the signal dominated events and the background dominated events. A subtraction factor is chosen such that the decay time spectrum resulting from the subtraction of these two groups is consistent with the decay time spectrum with that of the peak events (120-160 MeV) in the signal dominated region. Even after this subtraction is completed, there are caveats.

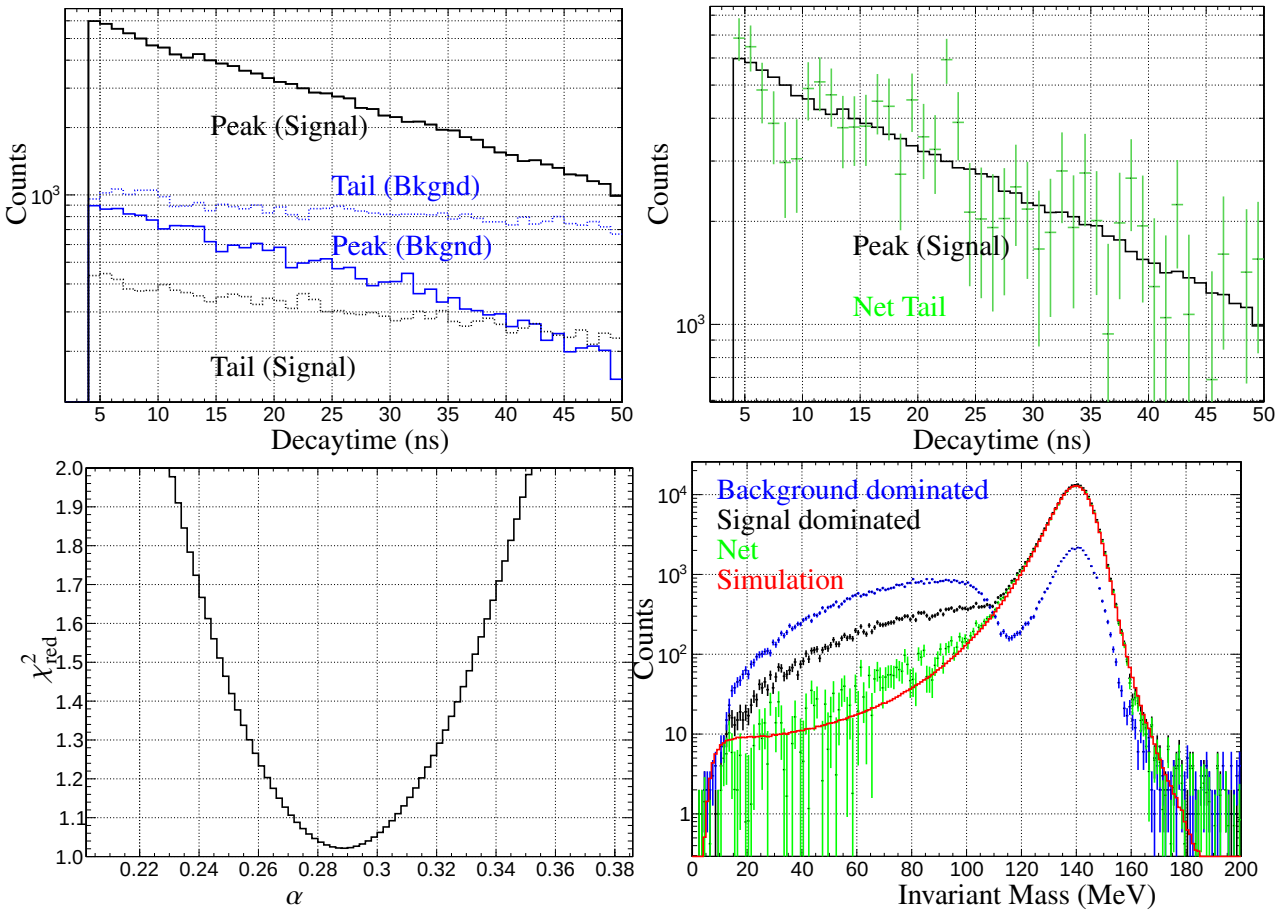

Figure 7.62: *Subtraction process of background dominated data set from the signal dominated set. Two disjoint sets of data are separated into signal dominated (black) and background dominated (blue). The decay time spectra are subtracted from the decaytimes for events with invariant mass between 20 and 100 MeV such that the resulting spectra (green) is best matched (lowest χ^2_{red}). This same subtraction factor is applied to the entire invariant mass spectra so as to obtain the net response of the detector. Upper Left: The decay time spectra for tail regions. Upper Right: Comparison of net decay time in the net tail with the peak region for signal dominated events. Lower Left: The $\chi^2_{reduced}$ as a function of the subtraction factor α. Lower Right: Invariant Mass spectra.*

Fig 7.62 shows that there is a little discrepancy in the low energy tail region around 80 MeV. This can be understood and corrected. The cuts used were to take on events with fast decay times and two peak energy signatures in the target. Before the cuts, both the signal and background dominated events have a combination of Michel positrons, positrons from pion decays, but also positrons arising from muon decays in flight. Rewriting with this inclusion,

$$N_{\text{good}} = \kappa_1 N_{\mu_{\text{DIF}}} + \kappa_2 N_{\text{Michel}} + \kappa_3 N_{\pi\to e\nu} \text{and } N_{\text{bad}} = \beta_1 N_{\mu_{\text{DIF}}} + \beta_2 N_{\text{Michel}} + \beta_3 N_{\pi\to e\nu} \tag{95}$$

Where each of the types of events has its representative decay time structure. Since the subtraction relies

on having the subtracted spectrum have a pion decay time this poses problems because the muon decays in flight has the same decay time spectrum as the pion decay time spectrum as seen in Fig 7.10. So upon finding the proper subtraction factor, α to obtain the decay time spectrum of the pion, there are still some remaining muon decays in flight.

$$N_{\text{signal}} - \alpha N_{\text{background}} = (\kappa_1 - \alpha\beta_1)N_{\mu_{\text{DIF}}} + (\kappa_3 - \alpha\beta_3)N_{\pi\to e\nu} \tag{96}$$

This additional spectrum has to be subtracted using the simulation. Since the total number of events are known for the signal and background dominated events (which contain the three decay modes), the ratio of the $\pi \to e\nu(\gamma)$ in the two samples is known from the ratio of peak regions. A system of equations is set up with the subtraction factor and the ratios of muon decays in flight to both Michel and pion decays using simulation. Using these systems of equations, the number of muon decays in flight is determined and subtracted off producing an invariant mass spectrum from the measured data and compared with the Monte Carlo simulation seen in Fig 7.63.

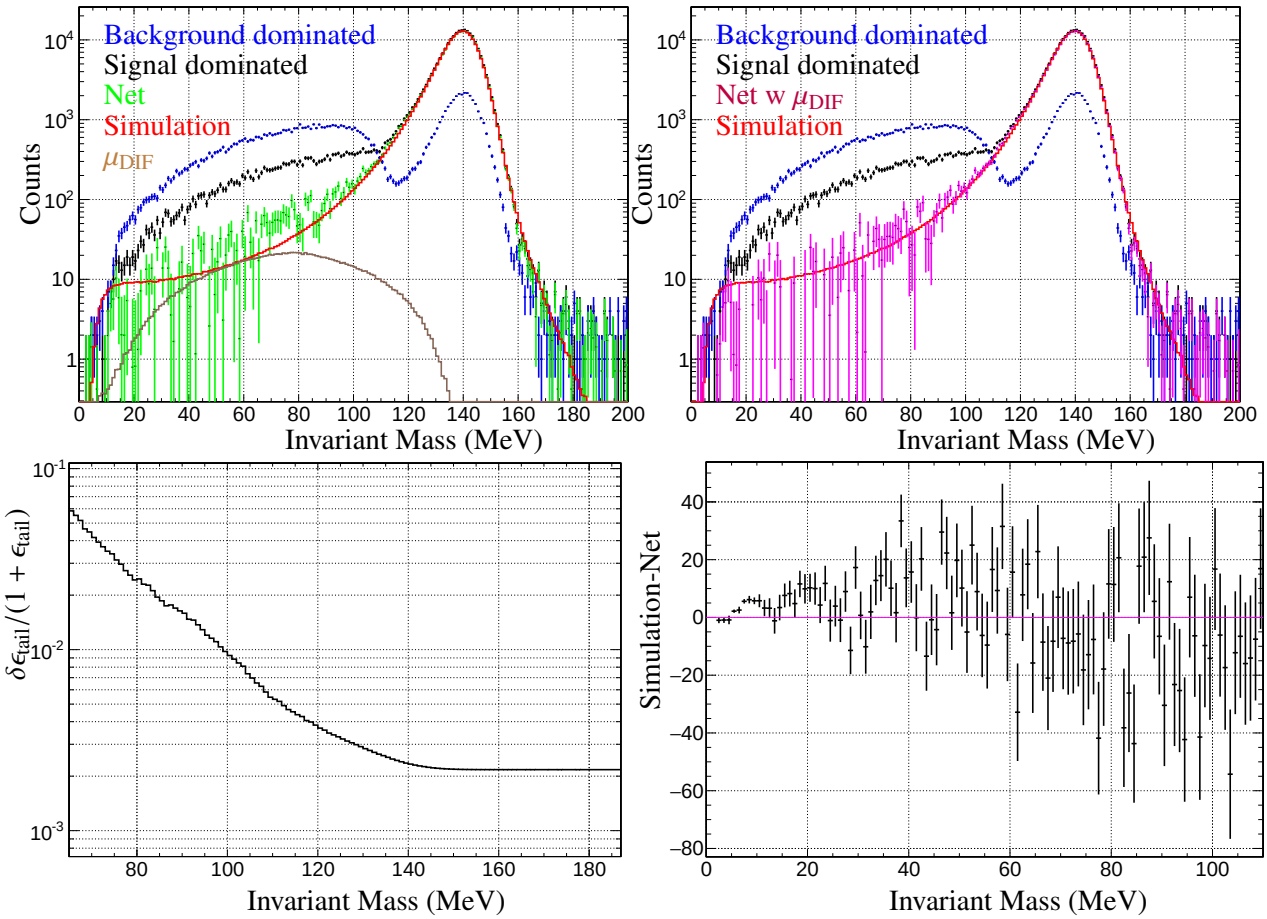

Figure 7.63: *The tail fraction compared with simulation including the effect of subtracting off the muon decays in flight present in the net response. Upper Left: Demonstration of muon decays in flight invariant mass relative to net invariant mass from above. Upper Right: Additionally subtracting the muon decays in flight invariant mass to get a net tail response. Lower Left: Relative error in the tail as a function of the invariant mass for tail trigger data. Lower Right: Difference in simulation and net tail from subtraction in the tail region as a function of invariant mass.*

This additional subtraction to obtain a proper tail should not be a surprise. In the discussion regarding decays in flight, the decay time spectrum and invariant mass spectrum of (among others) both the muon decay in flight and $\pi \rightarrow e\nu(\gamma)$. The decay time structure was shown to be identical and the invariant mass spectrum of the muon decays in flight are more abundant in the region where the tail occurs than the $\pi \rightarrow e\nu(\gamma)$ decay. The correction shows that the muon decay in flights now lie under the tail response. The cuts applied to obtain the tail ultimately do favor less target energy and a high $\Delta\chi^2$ cut. This provides the setting for which the signal channel is (slightly) more abundant than the muon decays in flight in the tail region.

Before proceeding to the uncertainties in the tail fraction it is useful to discuss the prospect of a fit function to the tail response in the calorimeter. What has been suggested within the PEN collaboration [72]

is to use a fit function, specifically, the crystal ball function to characterize the CsI response. A crystal ball function is function for which characteristics of a Gaussian combine with a low end power law. The function is characterized by five parameters: the mean of the Gaussian, $\bar{x}$, the standard deviation of the Gaussian, σ, the height of the peak, N, the power law, n, and a parameter α which aids in determining where the power law starts and Gaussian portion ends. Three of these parameters may easily be chosen by fitting a gaussian around the peak of the invariant mass spectrum. Doing so, suggest that the values $N = 13301, \bar{x}_{\text{mass}} = 139.71\text{MeV}, \sigma = 5.708$ MeV provide the best fit. The other two parameters are then obtained by minimizing the chi squared value in the tail region (< 115 MeV). This is illustrated in Fig 7.64

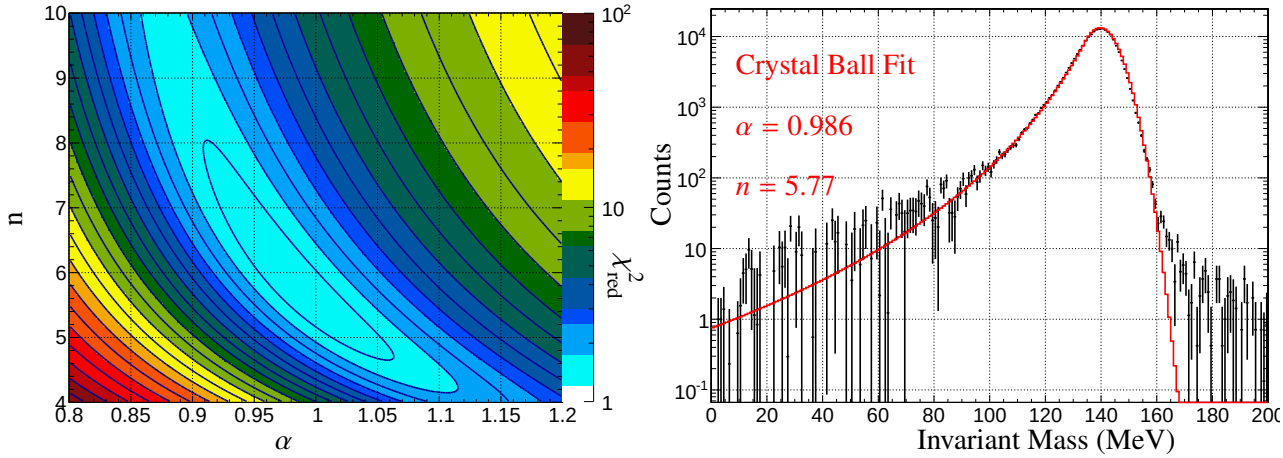

Figure 7.64: *Left: χ_{red} as a function of the two fit parameters, α and n. Right: Crystal ball function using best fit parameters.*

While the fit of the crystal ball function is in good agreement in the tail and peak region, it does not fit well for the high energy tail which emerges because of hard radiative decays along with CsI non-uniformities and detector response. An additional issue is the treatment of the photonuclear physics. There is no easy way to account for the emission of the neutron because of the giant dipole resonances and study the systematics thereof. If these two not so small details were not an issue, then the crystal ball function would probably be a good way forward to study the low energy tail and its uncertainty.

Once the tail has been shown to be in agreement with the measured data, the uncertainty in the tail then has to be estimated. The uncertainty arises from two different quantities. The first is the uncertainty associated with the photonuclear absorption models used in the simulation. Bigger photonuclear cross sections means more events will be pushed “downstream” by 8 MeV which suggests that a bigger tail fraction would result. The second source of the uncertainty in the tail is due to the uncertainty in the

invariant mass spectrum peak position. An incorrect gain would push more events out of the tail or back in depending on the value of that gain thus increasing or decreasing the tail fraction. To minimize the error, a quick check to make sure that the invariant mass peak location is consistent over the entire run period. If the invariant mass peak varies significantly, this will increase the spread in the invariant mass peak and increase tail error because of gain variations. By plotting the peak of the invariant mass over time for given years, the variation in the peak can be quantified, calibrated as best as possible and thus the variation in tail fraction (by use of Monte Carlo) may be obtained.

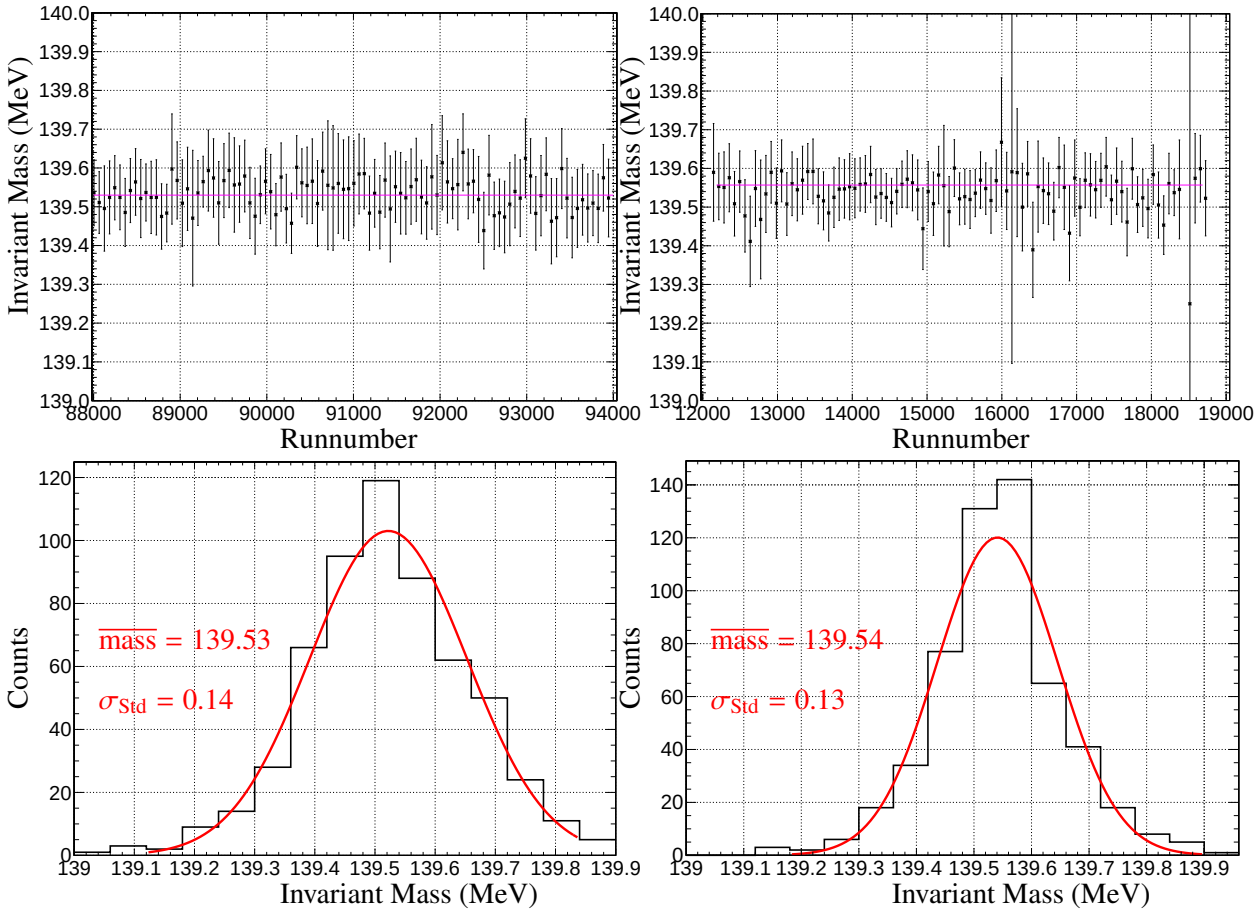

Figure 7.65: *Top Row: Invariant mass peak as a function of runnumber. Bottom Row: Invariant mass for groups of sixty runs. Left Column: 2009 data. Right Column: 2010 data.*

Fig 7.65 shows that the measured data have few variations in the peak. The variations in the peak position of the invariant mass then provides a method by which the simulation may be adjusted to adjust the peak position by multiplying the invariant mass by a gain, a deviation from the minimum χ^2_{red} maybe observed. Taking the gains for $\chi^2_{\text{red,minimum}} + 1$ and comparing the tail fraction with that of the minimum provides a

value for the uncertainty of the tail fraction associated with the peak of the invariant mass spectrum.

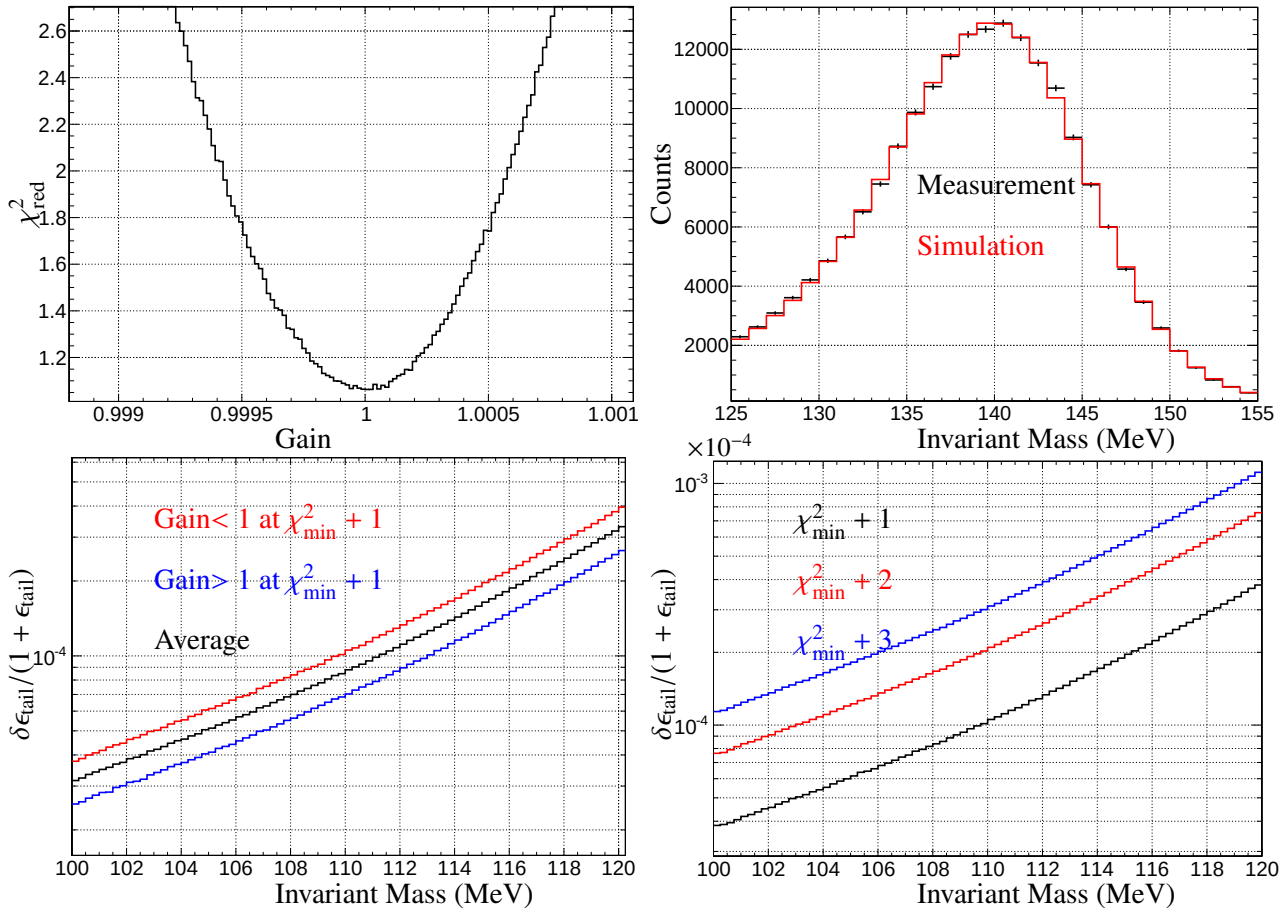

Figure 7.66: *Demonstration of the error of the tail fraction with position of the invariant mass peak by comparing simulation and measurement between 125 MeV and 155 MeV. Upper Left: Reduced χ^2. Upper Right: Comparison of simulation and measurement for best χ^2 fit. Lower left: Tail fraction (fraction/whole) of the simulation with different χ^2 values plotted as a function of where the tail is determined. Lower Right: Relative error as a function of the energy cutoff for the tail*

Notice Fig. 7.66 shows the "relative error" as $\delta\epsilon/(1+\epsilon)$. In the branching ratio, the lowest relative uncertainty due to variations in the gain alone occurs around the value of 50 MeV (not shown) for the invariant mass, which produces a huge statistical uncertainty due to a substantial subtraction. This demonstrates the balancing act between the statistical and systematic uncertainties that needs to be carefully balanced in order to minimize the error in the branching ratio. In addition to the systematic uncertainties associated with various gains, the uncertainty due to the different photonuclear cross sections must also be included. For this experiment, there are two different nuclei that have to be taken into account. In the case of iodine, ^{127}I, the cross sections due to Varlamov are chosen as these are the most recent evaluations and the author has studied many the systematics of all published photoneutron measurements on iodine as well as many other

different nuclei. Apriori, the high relative error in the Iodine cross sections produces concern as it seems this may result in too high a relative error in the tail fraction. Indeed, this is the case.

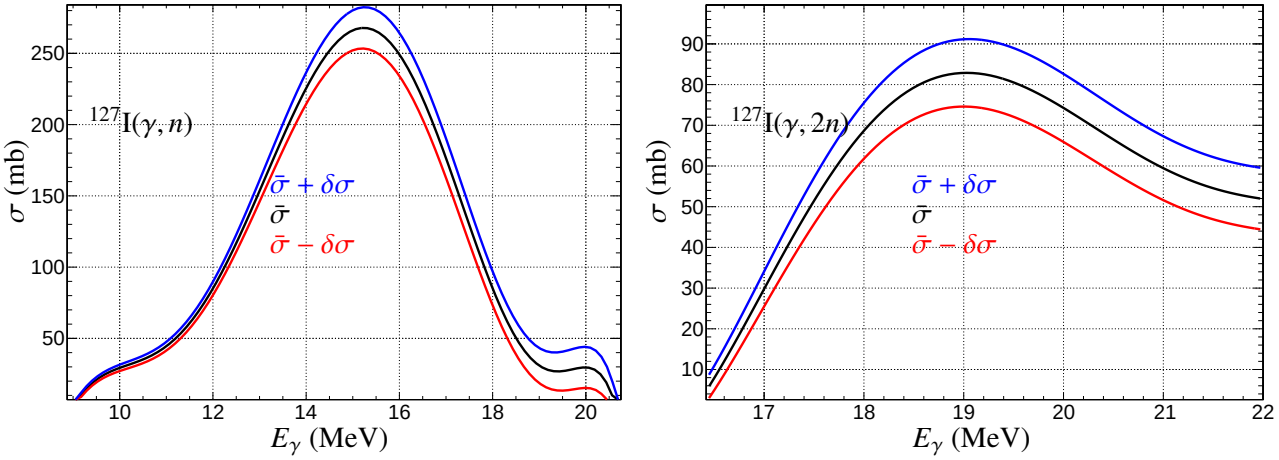

Figure 7.67: *Different cross sections simulated for ^{127}I using Varlamov's evaluations . Left: 1n cross sections. Right: 2n cross sections.*

Using the three different evaluations from Varlamov: the mean, the mean+σ and the mean−σ and observing the difference in the tail fraction and subsequently relative difference, the relative error is obtained. The region beyond 22 MeV $\sigma(\gamma, 2n)$ is exponentially decayed rapidly to zero and therefore is not shown.

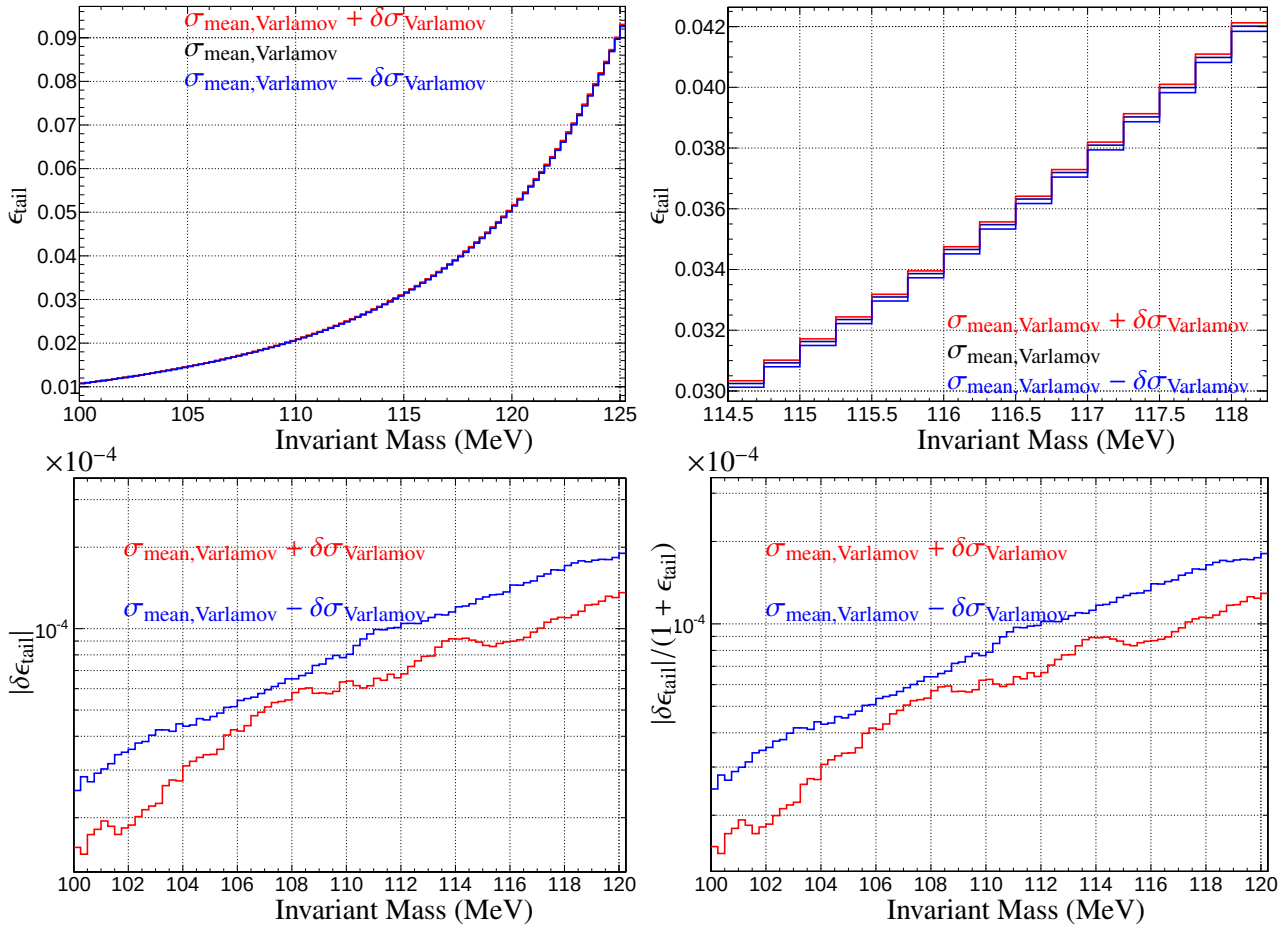

Figure 7.68: *Upper left: Tail fraction due to variations in Iodine cross sections using Varlamov's evaluations. Upper Right: Tail fraction due to variations in Iodine cross section using Varlamov's evaluations zoomed in the region between 114 and 121 invariant mass. Lower Left: Difference in the tail fraction for the Iodine cross sections as a function of invariant mass. Lower Right: Relative error in the branching ratio due to the different cross sections for Varlamov's evaluations.*

Fig 7.68 shows the intuitive result that as higher photonuclear cross sections are used, the tail fraction becomes larger (upper right plot). There is also a smaller difference between the mean fit for the cross sections and the higher error value than there is for the mean fit and the lower error value. The higher error value is taken for this analysis. Since the mean values in the cross sections associated with Cesium-133 (From Lepetre and Berman) compared with Iodine-127 (from Varlamov) are similar, the same features are expected when using the mean between Lepetre and Bergere and using their cross sections as upper and lower limits. It is worthy however to note, the cross sections due to Bergere, have a relatively smaller uncertainty in the cross sections. The peak values for Varlamov have a relative uncertainty at nearly 10%. The relative uncertainty due to Bergere are less than 3%. However, since there is no reason one evaluation is "better" or more correct than the other, an independent experiment may be needed in order to properly

obtain the correct cross sections at least to high enough precision.

For the Cesium cross sections, both Berman and Lepetre have relatively small errors, however, their mean values are separate from each other. Taking the (weighted) average between the two evaluations and using the Lepetre and Berman as the extreme values, the difference in the tail fractions with these various evaluations are shown in Fig 7.69.

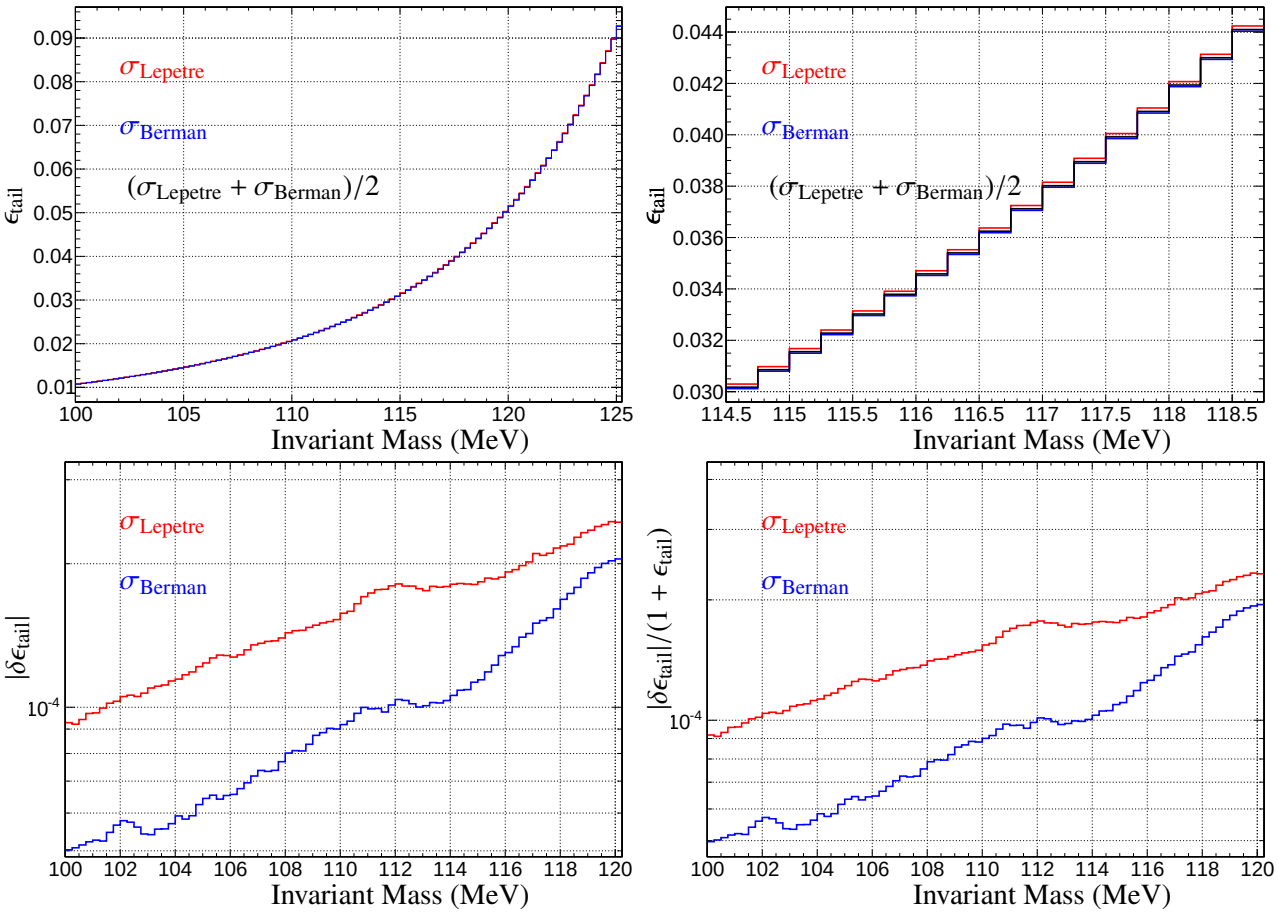

Figure 7.69: *Upper left: Tail fraction due to variations in Cesium cross sections using Lepetre's and Berman's evaluations. Upper Right: Tail fraction due to variations in Cesium cross section using Lepetre's and Berman's evaluations zoomed in the region between 114 and 121 invariant mass. Lower Left: Difference in the tail fraction for the Cesium cross sections as a function of invariant mass. Lower Right: Relative error in the branching ratio due to the different cross sections for ^{133}Cs cross sections.*

The error in Fig 7.69 has similar characteristics with the Varlamov cross section evaluations, though it is smaller. Putting the major sources of error together for the tail fraction, adding in quadrature the error in the branching ratio associated with the tail fraction as a function of invariant mass cutoff is shown

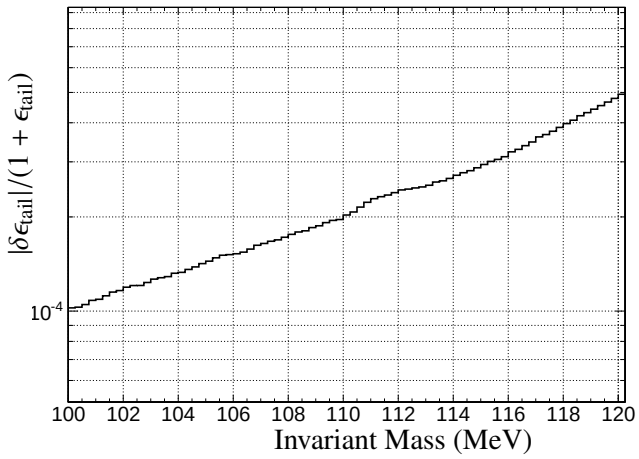

Figure 7.70: *Error in the branching ratio associated with the tail fraction as function of the cutoff of the invariant mass. The error is obtained by adding in quadrature the errors from the cross section models for ^{133}Cs and ^{127}I as well as the error in the tail fraction due to peak position.*

Fig 7.70 shows that with a tail/peak cutoff at 115 MeV, the relative error in the branching ratio is 3×10^{-4}. Apriori, the tail was expected to be the biggest systematic error associated with this experiment. A higher cutoff between tail and peak events produces a higher error in the tail fraction but a smaller error due to subtraction of Michel background. There is something to be said on the comparison between the PEN calorimeter and the PiENu calorimeter The PiENu calorimeter, comprised of NaI(Tl), is a calorimeter of 18 radiation lengths thick. The advantage of a thicker detector is that more energy is collected before energy leaks out the back of the detector. The more energy that is collected, produces an energy spectrum that has better separation from the tail and peak, which results a smaller systematic uncertainty in the tail fraction. In addition to higher light output, the PiENu detector is made up of a single crystal which inherently is more uniform in response at the expense of a lower solid angle coverage. However, a bigger thickness also results in more photonuclear reactions, which in turn increases the systematic uncertainty due to these cross sections. The low atomic number of Sodium (Z=11) provides an extra difficulty. In low atomic numbers the photonuclear absorption of a photon which results in an emission of a proton, two protons, or a neutron and proton are non-negligible. Whereas in the higher atomic number nuclei such as Iodine (Z=53) and Cesium (Z=55), the ejection of charged particles is more than an order of magnitude smaller and is not a significant contribution to the low energy tail.

Now that the tail fraction has been obtained, the only factors remaining for branching ratio extraction are the MWPC efficiencies and the acceptances which as stated are blinded to this analysis. However, a demonstration of how these are obtained, and in particular the cut efficiencies which are normally absorbed

into the acceptances are shown for the benefit of the reader since it is a part of the final analysis that is to be done.

7.10 MWPC efficiency

In order to properly count the events, whether they be Michel or signal, the possibility of a failed track reconstruction must be included. The primary cause of reconstruction failure given that there is a legitimate pion stopped in the target is the failure to properly produce a signal in one or both of the MWPC chambers. In general, a well reconstructed track comprises of a single hit in each of the chambers that coincide geometrically with the azimuthal direction in the hodoscope and the polar direction with the calorimeter. In other words, a straight line from the target to the calorimeter hitting all detectors on the way is a well constructed track. A signal in the MWPC depends on many different externalities such as gas gains, voltages, and even the geometry/effective detector volume. Even with all these features contributing to the effectiveness of the chamber, the ability to construct a signal depends on the energy deposited in the chamber volume. We might naively turn to the (in)famous Bethe Bloche formula to understand how much energy loss occurs in the MWPC volume.

$$-\langle dE/dx\rangle = \frac{4\pi n z^2}{m_e c^2 \beta^2}\left(\frac{e^2}{4\pi\epsilon_0}\right)^2\left[\ln\left(\frac{2m_e c^2\beta^2}{I(1-\beta^2)}\right)-\beta^2\right] \sim 1/\beta^2 \tag{97}$$

This expression shows that a higher amount of energy deposition occurs if the velocity is smaller. This is seen in the event selection for eliminating protons using the plastic hodoscope. The protons with smaller energy deposit more energy in the plastic. This is also seen in the chamber gas for protons. However, this expression is not the entire story. The Bethe Bloche formula applies to "heavy" charged particles and not so much for electrons and positrons because of larger deflections of smaller mass electrons/positrons. In addition, for these low mass particles, the energy loss due to Bremsstrahlung is non-negligible and indeed dominates over collision energy at high enough ($\sim$ 10's MeV) energy. For positrons and electrons traversing a given material [49],

$$(dE/dx)_{\text{total}} = (dE/dx)_{\text{Bremsstrahlung}} + (dE/dx)_{\text{collision}} \tag{98}$$

With

$$(dE/dx)_{\text{Bremsstrahlung}} \sim E \qquad (dE/dx)_{\text{collsion}} \sim \ln E \tag{99}$$

Since the energy loss due to collisions (ionization) produces the signal in the MWPC, the ability to produce a signal rises roughly logarithmically with the energy the positron has as it traverses the MWPC. In the case of a positron from a pion decay, nearly all positrons traverse the MWPC with similar energy. Therefore positron from pion decay has nearly equal probability to produce a signal in the MWPC. However, a Michel positron will not have equal probability in producing a signal in the MWPC because of the energy spectrum that a Michel positron possess. The ability to reconstruct a track depends on the process occurring (Michel or pion decay) as well as the energy the positron has in the case of the Michel decay. This systematic has to be included in order to fully account for track reconstruction failures. In the case of an outgoing positron, an ideal track would have both chambers, the hodoscope, and the calorimeter all possess coincident signals. Since events are not recorded unless there is an energy deposition in the hodoscope this being part of the trigger, and if there is no energy in the calorimeter then the event would not be considered, the failure of track reconstruction occurs in the wire chambers. If reconstruction fails with equal probability for both Michel and signal events, then in calculating the branching ratios these corrections would cancel and not need to be included. This is not the case and the efficiency of track reconstruction must be included.

The efficiency is defined by the number of times something happened divided by the number of times it should have happened. In this case the something happening is that one of the chambers produces a valid signal. That is at least one anode wire fired, and both the inner and outer cathode surfaces fires as well. But how is it known if it should have fired?. One might surmise that if there is a signal in the other chamber, then there should have been one in the chamber under study. This is not sufficient because of backsplash of charged particles from the shower in the electromagnetic calorimeter. In order to ensure that a valid event occurred, there must first be a valid signal in the target. That is a pion with a well defined amount of energy, a positron with a well defined energy, and if applicable, i.e., for Michel decays, a muon signal in the target. A valid event should have a hodoscope signal coincident in time with target positron signal. In addition to a requirement that the other chamber has a spatial coincidence, in phi, with the plastic hodoscope and theta coincidence with the calorimeter. Further restrictions can be made by the chamber not under study. The cathode surfaces (inner and outer) must be spatially related with each other and the anode. Since the surfaces are shaped as helices, knowing the strip numbers that are hit provides information on both the z

position of the two cathodes, the angular position (in the form of predicted wire hit) of the track which should be consistent with the anode that was fired. The sum of the strip numbers gives information on z and the difference provides information on phi. With these features, we can include requirements on how coincidences between differences in cathode hits and wire hits for example. The inner chamber efficiency can be defined as follows: Find the number of events in which the outer chamber fired (two cathode surfaces and anode wire coincident with each other) where the polar angle, theta, between the CsI and strips coincide, the azimuthal angle, ϕ, of the anode wires coincide with the azimuthal angle of the hodoscope that fired and the inner and outer surfaces coincide geometrically with other and anode (to make sure there are no random wires/strips firing) and that the combination of strip numbers that fire give coincidence in z and phi of the anode. If these conditions are met, this is most definitely have a valid hit for the outer chamber from a charged particle. The number of events which satisfy these criteria are N. The subsample of these events where the inner chamber fired and where the ϕ of the anode is consistent with the ϕ of the anode from the other chamber as well as inner chambers strips, is the number of events where a legitimate hit occurred in the inner chamber. Call this number of events M. The efficiency is therefore M/N. The geometric requirements for a legitimate hit can be changed to minimize the uncertainty and the range of requirements is seen in the simulation as seen in Fig 7.71.

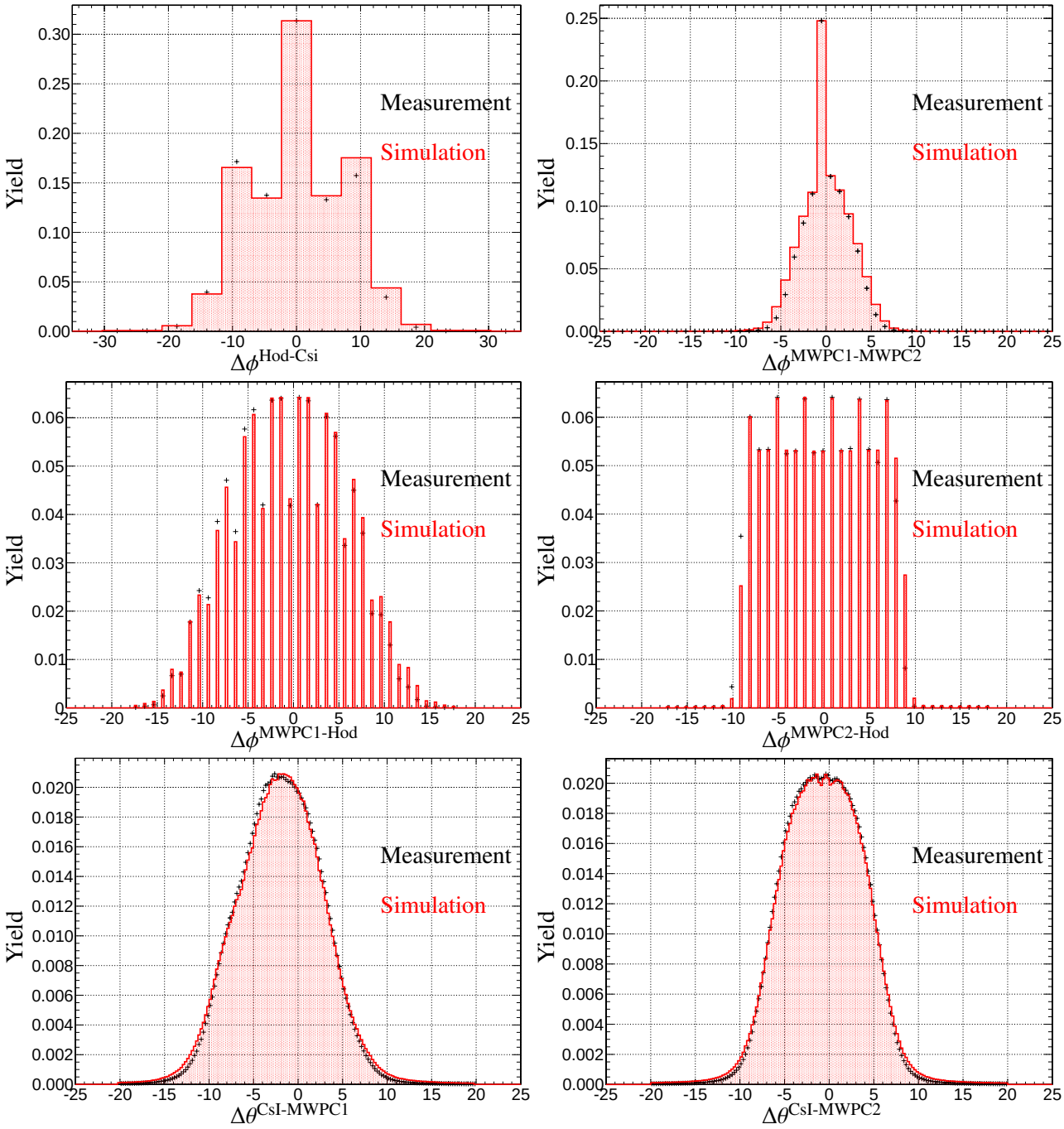

Figure 7.71: *Various coincidences between different detectors in theta and phi which can be used to define a legitimate track or detector hit. Upper Left: $\Delta\phi$ between the Hodocope and CsI. Upper Right: $\Delta\phi$ between the two chambers. Center Left: $\Delta\phi$ between the inner chamber (MWPC-1) and the hodoscope. Center Right: $\Delta\phi$ between the outer chamber (MWPC-2) and the hodoscope. Lower Left: $\Delta\theta$ between CsI and MWPC-1. Lower Right: $\Delta\theta$ between CsI and MWPC-2.*

In addition, there is the question of coincidence within an individual detector. If a requirement of all three planes producing a signal is imposed, then coincidence in the planes may be used. In the case of the

inner and outer surface of the cathode planes, where the z position is determined, the difference in the z positions can have stringent requirements. Since the combination of the strip numbers also can be used to determine the wire numbers, a coincidence between wire numbers and predicted wire numbers from the strip numbers may also be suggested as seen in Fig 7.72.

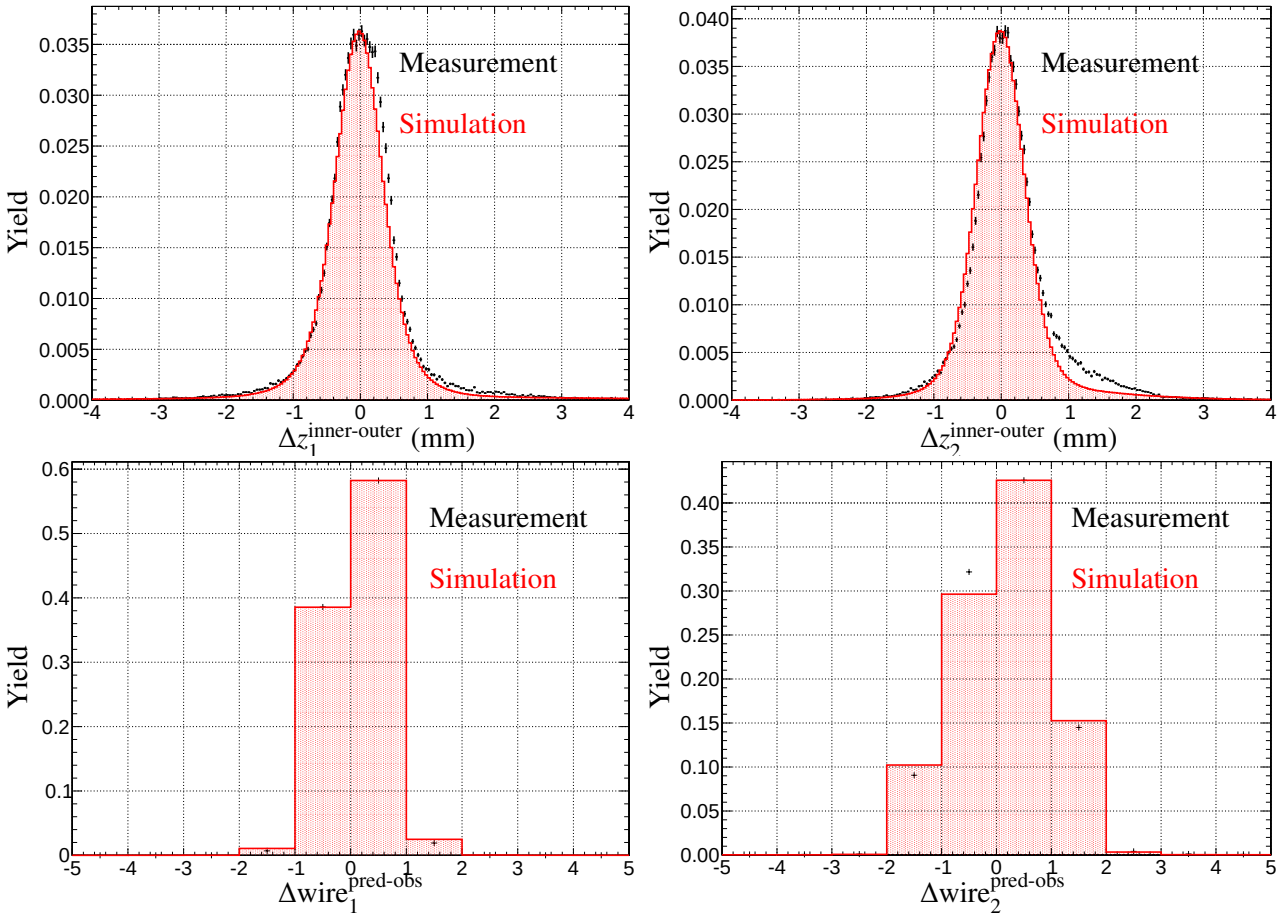

Figure 7.72: *Geometric coincidences between individual detectors. Upper Left: Difference in z in chamber 1 for the inner and outer surface. Upper Right: Difference in z in chamber 2 for the inner and outer surface.*

In determining the efficiency, it is assumed that both an inner and outer cathode strip fire. However, one can easily be misled by pedestal noise. The ability to determine whether or not there is a cathode peak is dependent on how well the pedestals are contained.

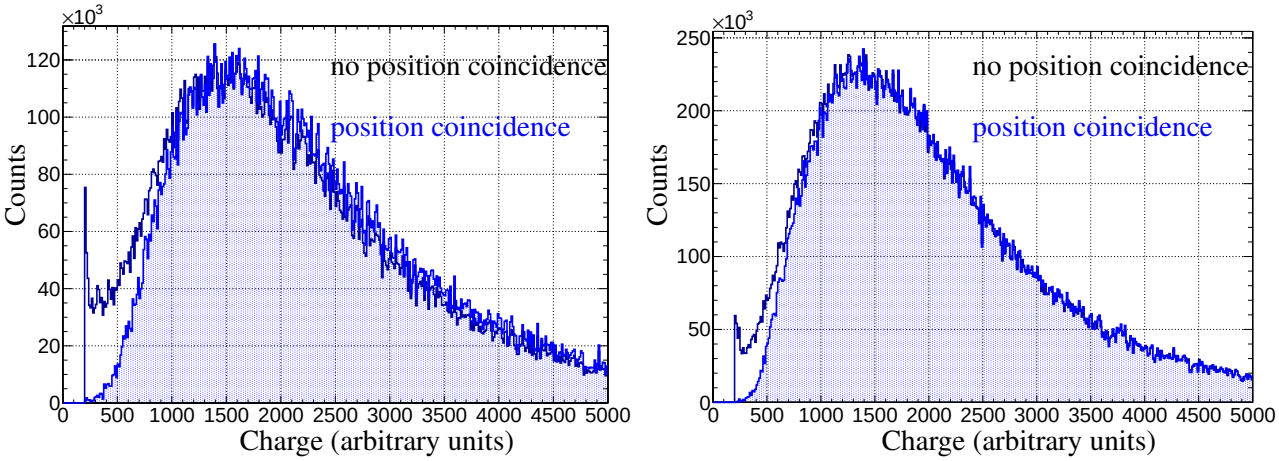

Figure 7.73: *Charge distributions with (blue) and without (black) coincidences in position. Left: Inner surface of inner chamber. Right: Inner surface of outer chamber.*

Even though the pedestals may be subtracted well, there is still some remaining "background" from the pedestal noise in the cathodes even for the highest signal cathode. Once geometric coincidence is required for charged tracks, false positives due to pedestal noise become statistically insignificant, if present at all as seen in Fig 7.73. In addition to the energy dependence, which was already discussed, there is a polar angle, θ dependency of the efficiency. A larger theta trajectory, produces and effectively greater volume for the gas, which means there is more likely to be a signal for larger theta. So the efficiency not only depends on energy of the positron, but also the polar angle.

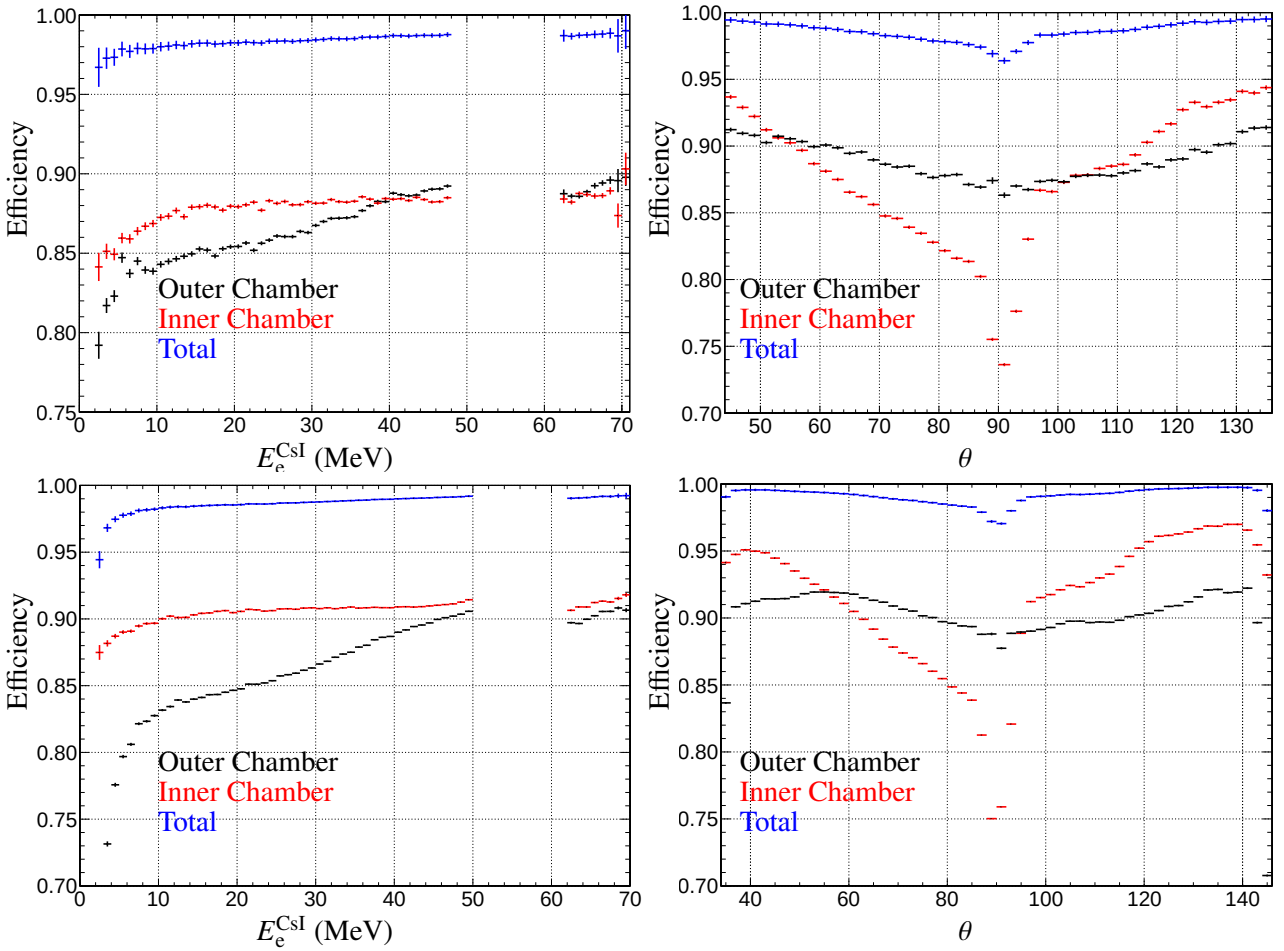

Figure 7.74: *Efficiencies as a function of trajectory (θ) of the positron and of the positron measured energy. Upper Row: 2009. Lower Row: 2010.*

Fig 7.74 shows several important noticeable features. The first is that indeed the efficiency rises with energy in both chambers for both years. The second is that the efficiency increases with larger deviation away from 90 degrees. This is also expected from the discussion earlier. However, the efficiency as a function of the polar angle is symmetric for 2009 in the outer chamber but not for 2010 and not for the inner chamber for either years. As described previously, the inner chamber was separated at $z = 0$ into effectively two separate detectors to produce upstream and downstream surfaces in order to achieve a higher data rate capability. It is therefore not unsurprising that the upstream $\theta < 90^\circ$ and downstream, $\theta > 90^\circ$ have different efficiencies for the inner chamber. The asymmetry in the individual outer chamber for 2010 is attributed to sporadic failures in the outer chamber cathode strips readout throughout the 2010 period. For completeness one may also look at the efficiency as a function of the azimuthal angle, ϕ.

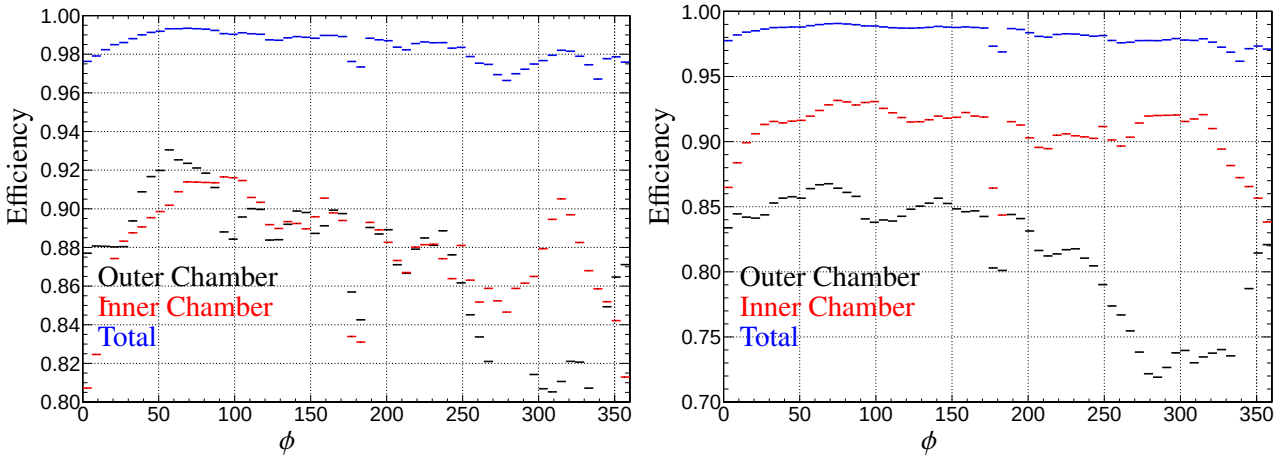

Figure 7.75: *Efficiencies as a function of ϕ. Left: 2009. Right: 2010.*

The fluctuation in the azimuthal angle in Fig 7.75 is somewhat peculiar and one may come to the conclusion that since the anodes are in distributed in the phi direction, there may have been some anode wires which varied being between hot and cold, this is not the case. It is in fact the strips that cause the efficiency to vary in phi direction. Because of the geometry of the cathode strips, a helix, the efficiency in phi is not solely dependent on the anodes, but also on the cathodes. Strips that varied between hot and cold would easily cause this feature. One can clearly see this from a two dimensional efficiency map in θ and ϕ.

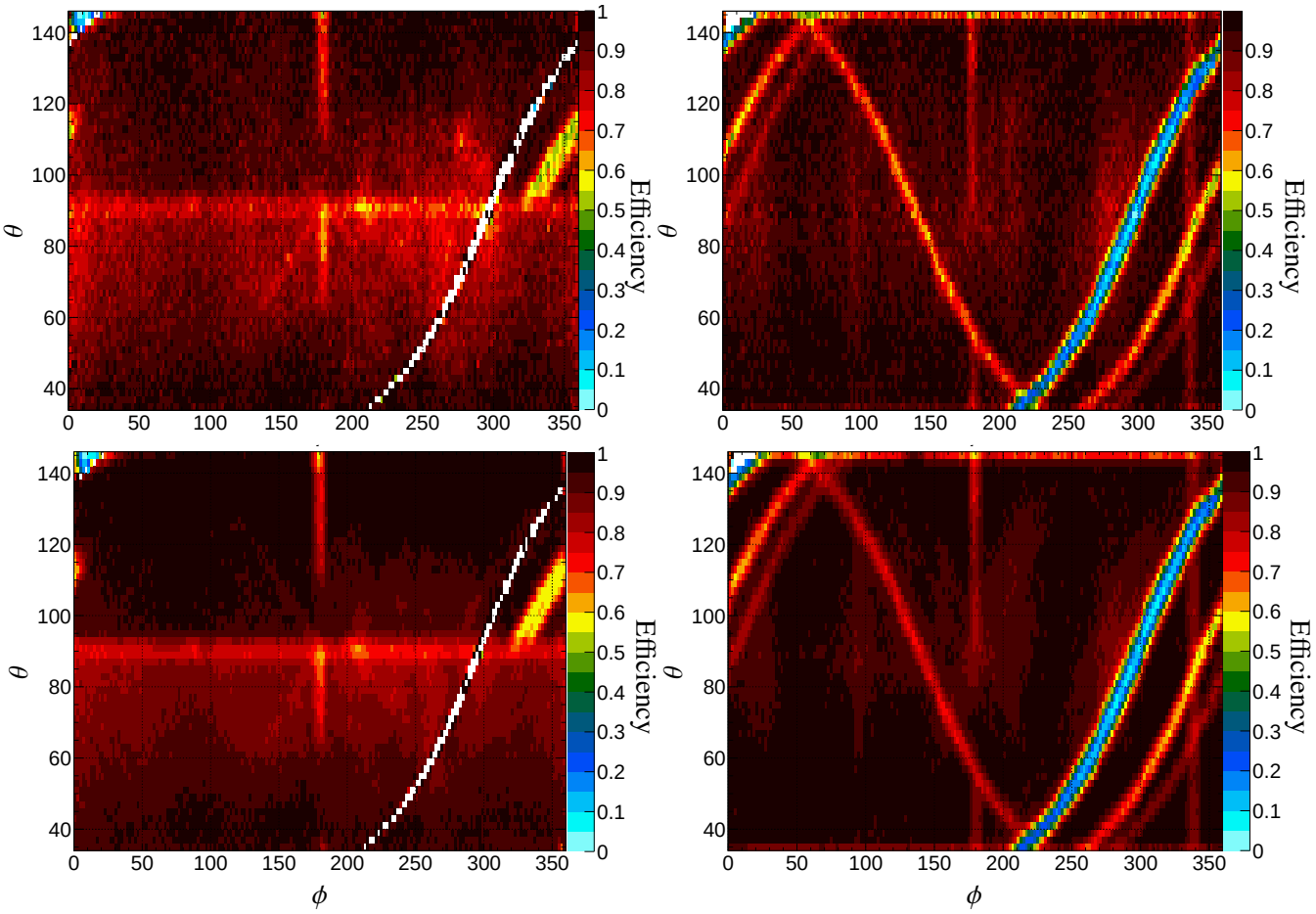

Figure 7.76: *2-Dimensional map of MWPC efficiency. Left: Inner MWPC. Right Outer MWPC. Top Row 2009. Bottom Row 2010.*

Fig 7.76 shows regions where the efficiency is equal to zero. This originates from cathode strips which were inoperable during the entire year of 2009 and 2010. A comparison of response for live strips and dead strips by runnumber is given in Fig 7.77. In both years, the same strips were dead, however in 2010, additional strips failed for extended periods of time in the second (outer) chamber. This is why the chamber efficiency as a function of the angles is noticeably smaller than in the 2009 data run.

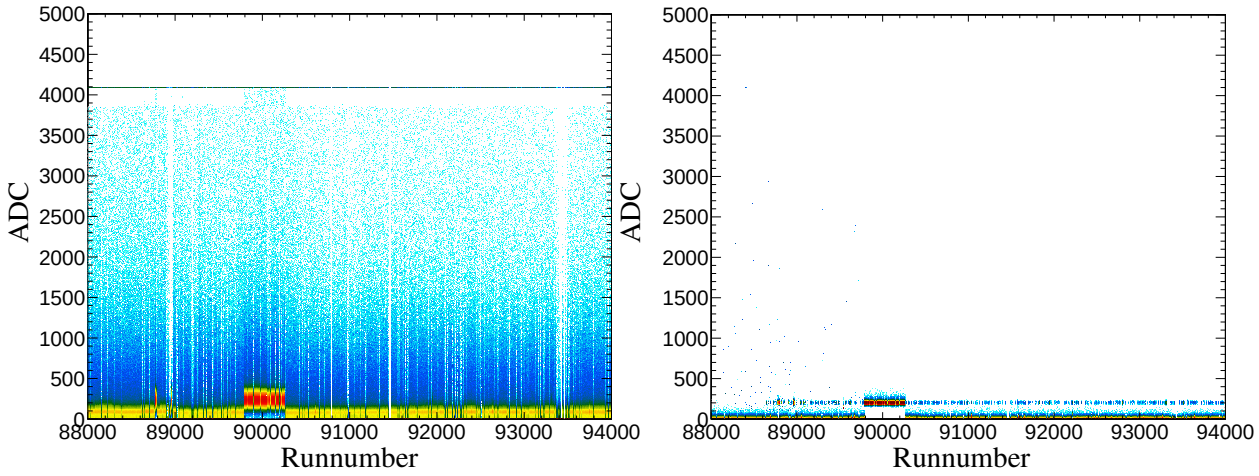

Figure 7.77: *Demonstration of a working strip's response (strip 5 on the left) and a non-working strip's response (strip 319 on the right).*

Because of the different efficiencies in each of the chambers, the efficiency of track reconstruction must be accounted for in the branching ratio calculation. This of course depends on the definition of a well constructed track. The purpose of having two chambers is to increase the ability to reconstruct a track, and in particular the MWPC is structured such that a particular cathode plane can fail to fire and yet a track can be reconstructed. As already discussed, the efficiencies ultimately depend on how a track is defined and because of the design of the two chambers, there is some flexibility in determining these efficiencies. Since this is one of the two components that are blinded, the next section discusses as to how the efficiencies are incorporated into the simulation so that they are absorbed into the acceptances.

7.11 Acceptances and cut efficiencies

The acceptances and the cut efficiencies are the last pieces of the $\pi \rightarrow e\nu(\gamma)$ puzzle. The acceptances are an important piece because it aids in the understanding of what the experimenter does not know. Events which do not get recorded or do not pass the cuts are not known apriori by the experimenter. For example, suppose that 1 million pions decayed into muons and 123 pions decayed into positrons. This would give a branching ratio of 1.23×10^{-4} branching ratio, consistent with the Standard Model value. But, suppose only 80% of the muon channel decays were detected and reconstructed after cuts and 87% of the positron channel decays were reconstructed and detected. This means the observer would naively say that 800,000 pions decayed into a muon and 107 pions decayed into a positron. The naive observer would claim the

branching ratio is then 1.34×10^{-4}, which would be wrong. So not only does the observer have to understand what was detected, but also what was not detected. This understanding is manifested in the acceptances. The acceptance, for the most part, is the probability of detecting an event given that the particular event actually occurred. Apriori, this is not known to the experimenter, after all how can someone know that the event occurred given they haven't detected it (yet). In order to obtain the acceptances, the Monte Carlo simulation is once again needed. The Monte Carlo simulation allows the experimenter to determine the probability of analyzing an event given the event occurred, provided the Monte Carlo simulation accurately represents the physics embedded in the experiment. As was seen (and heavily emphasized) the PEN Monte Carlo performs this task extraordinarily well. Using the Monte Carlo, the experimenter can generate N_{gen} events where the pion stops in the target. After the full detector response has been achieved, and identical cuts are made to the simulation, the number of detected events, N_{det}, can be determined. With that in mind, the acceptance for a given process is nothing else than conditional probability of an event being detected given it was thrown (generate).

$$A = \frac{N_{\text{det}}}{N_{\text{gen}}} \tag{100}$$

The error in the acceptance is the utmost importance. The acceptance uncertainty might be calculated in the same fashion as the uncertainty in x/y. This is not quite correct because the two values in the acceptance are correlated. The fraction of events detected is a subset of the number of events generated. This correlation complicates the uncertainty calculation. The acceptance is not much different than an efficiency. The number that pass the geometric requirements is akin to a geometric efficiency. It can be shown using Bayes' theorem [29] that if there are N events before selection and K events after the selection, then the efficiency is K/N and the uncertainty in this ratio is given by

$$\sigma_{K/N} = \sqrt{\frac{(K+1)(K+2)}{(N+2)(N+3)} - \frac{(K+1)^2}{(N+2)^2}} \tag{101}$$

The geometric efficiency should be about 75% (the solid angle coverage), and the relative uncertainty is desired to be on the order of 1×10^{-4}. The thrown events that would trigger events would need to be $\sim 1.5 \times 10^{8}$. This gives an idea of how many events apriori would need to be simulated for each of the processes to get the acceptances to the desired precision. There are two aspects to the acceptances. The first is the geometric acceptance. The relative position between the target and the detectors may favor the

detection of one process over another. To first order, the ratio of the acceptances between the two process will be unity. However, in a more thorough description including accounting for radiative decays, it is not the case that the acceptances cancel in the branching ratio. The second aspect is of course the cuts. If cuts are made on the pion, that is to say, before the pion has stopped, then this will not affect the ratio of the acceptances because no particular decay channel is assumed. This is why in the simulation, a requirement of the pion stopping is the first cut made. This also accounts for all the upstream cuts, i.e., time of flight, one beam particle, etc. So the only cuts that can be made that would affect the ratio of acceptances are those that would preferentially favor one process over the other, such as cuts on `restwave` or $\Delta\chi^2$. It was stated earlier that the efficiencies would be introduced into the simulation by means of weighting. This process is demonstrated in Fig 7.78. However, in the end, the track reconstruction efficiency, that incorporates the detector efficiencies, and effects of cuts, should also be reproduced as seen in Fig 7.79.

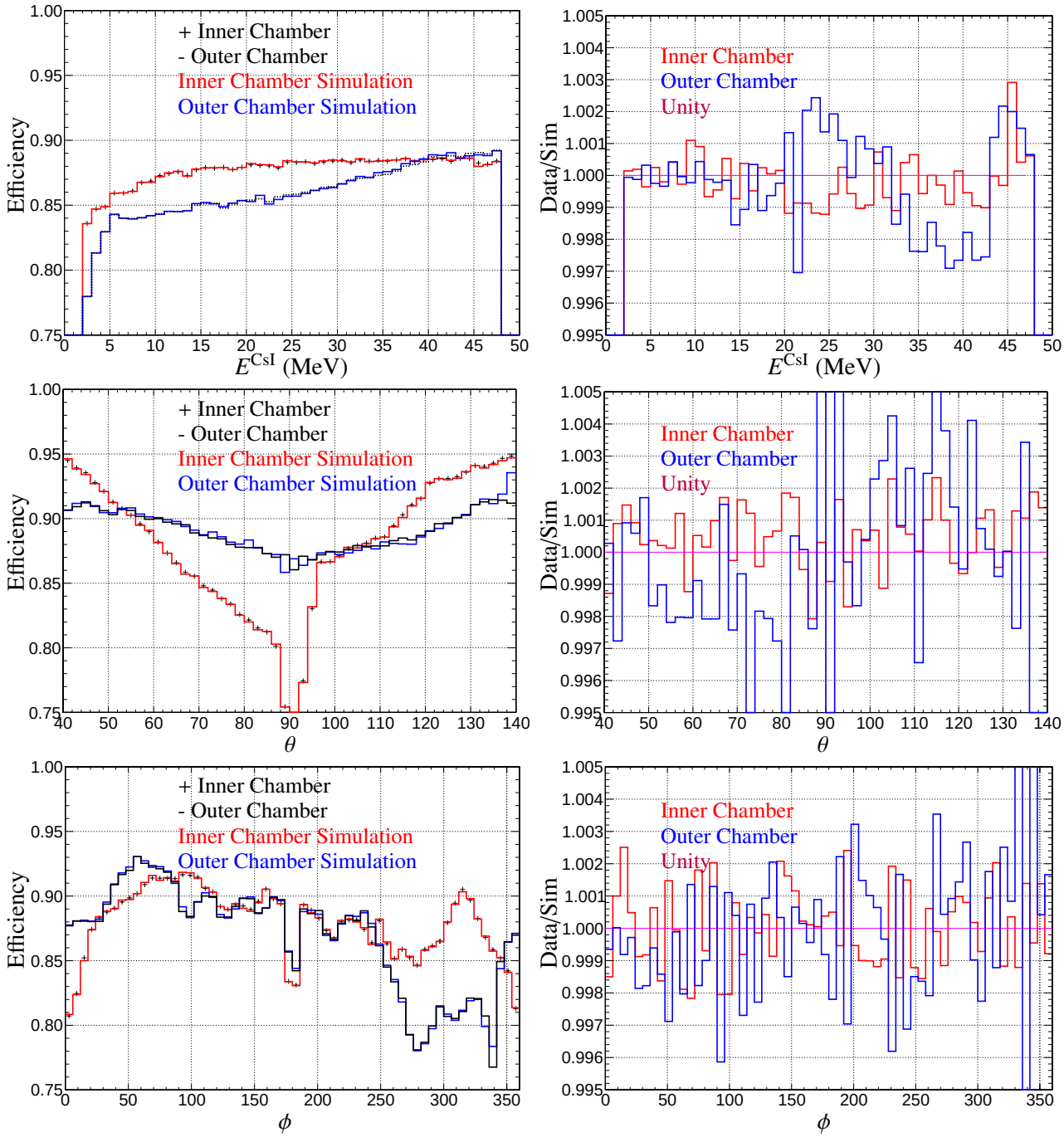

Figure 7.78: *Comparison of chamber efficiencies of simulation and measurement by implementing weights in the simulation. Top represents efficiency as a function of clump energy (right) theta (center) and phi (right). Bottom represents ratio of efficiencies of data and simulation as a function of energy (left) theta (center) and phi (right).*

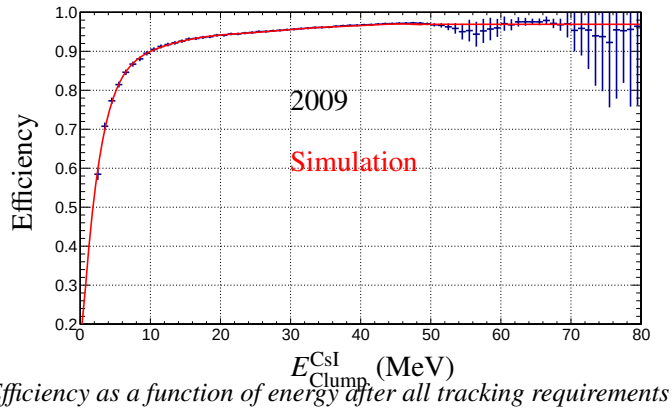

Figure 7.79: *Efficiency as a function of energy after all tracking requirements are implemented.*

The cut efficiencies are values that must be included in order understand what percentage of events are not counted in the raw numbers. If the cuts for both the Michel and pion decays were identical, then there would be no need to include the cut efficiencies, and only the acceptances would be required. In this analysis, there are two cuts which favor one decay channel over the other. The most important is the $\Delta\chi^2$ cut for the pion decay selection and and while it does remove a substantial amount of Michel background, the number of pion decays removed has to be understood at the 10^{-4} level. There are smaller corrections on cut efficiencies due to the energy in the hodoscope, for example.

It should also be noted that because of the different versions of the detectors used and different configurations within run years, certain cut efficiencies may well vary between years and even run period because of these detector changes. For instance, vertex quality which is a measure of how close the positron track approaches the pion stopping position varies for different run periods. In 2009, the mTPC, the device used to predict where the pion stops, was further away from the target and had a collimator afterwards. This means the mTPC is not as precise as it would be if it were close up. The collimator also can produce scattering effects as well. Contrast that to the 2010 mTPC which was closer to the target and had no such collimator. The vertex quality of the 2010 data set is expected to be better than 2009. However, even in 2010, there are variations. In the middle of the 2010 run period, one of the wires of the mTPC apparatus ceased to function. This decreased the ability of the mTPC to function properly. Later in 2010, a second wire ceased to work, which produced even worse reconstruction as seen in Fig 7.80.

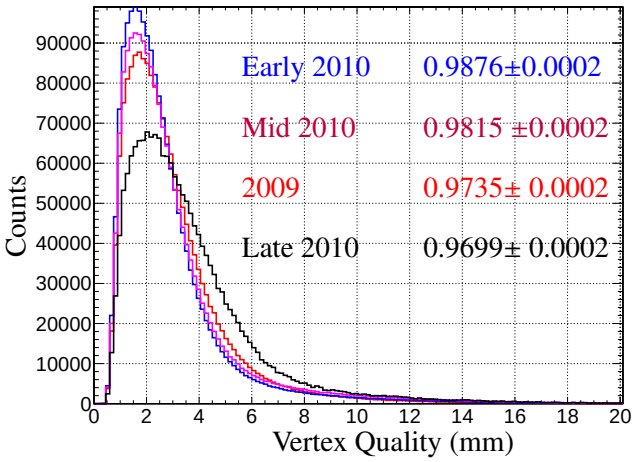

Figure 7.80: *Vertex quality through different run periods for the Michel selection. Values listed are the fractions that pass the cut vertex quality*< 10 *mm.*

While the ratio of the acceptances (and therefore number that pass the cut) are what is of interest, apriori, it is not obvious that these differences can be ignored since the fractions differ at the sub-percent level, hence the reason for the multiple number of configurations of the simulation. While the cut efficiencies, along with the MWPC efficiencies, can be absorbed into the acceptances, the discriminating cut, $\Delta\chi^2$, is discussed and quantified here.

The efficiency of the cut is simply the fraction of events that survive when the cut is made. In order to get the efficiency to the desired precision, the simulation is once again needed as there are not enough events in the data set to provide information on the efficiency of the cut. The uncertainty in the cut has two aspects. The first is the statistical uncertainty. This does not become a problem provided enough simulated events are thrown. The second is the systematics. $\Delta\chi^2$ is a complicated observable and thus in order to understand the systematic uncertainty associated with this observable, the uncertainty in values which form it must be understood. $\Delta\chi^2$ uses both predicted and observed energies and timings in the target in order to perform a χ^2 comparison of the observed and predicted target waveforms. Thus to understand the systematics, a study of how $\Delta\chi^2$ changes when the predicted values of the energy and timing change. Since the predicted pion energy is calculated, this calculation can be varied to see how $\Delta\chi^2$ changes. The predicted pion energy is changed is determined by varying the two observables, time of flight and degrader energy, which predict the pion energy. The amount that the predicted pion timing adjustment is hard to quantify since all times are relative to the trigger (target time). A method forward then is to quantify the amount by noting the effect on the difference between pion observed and predicted times.

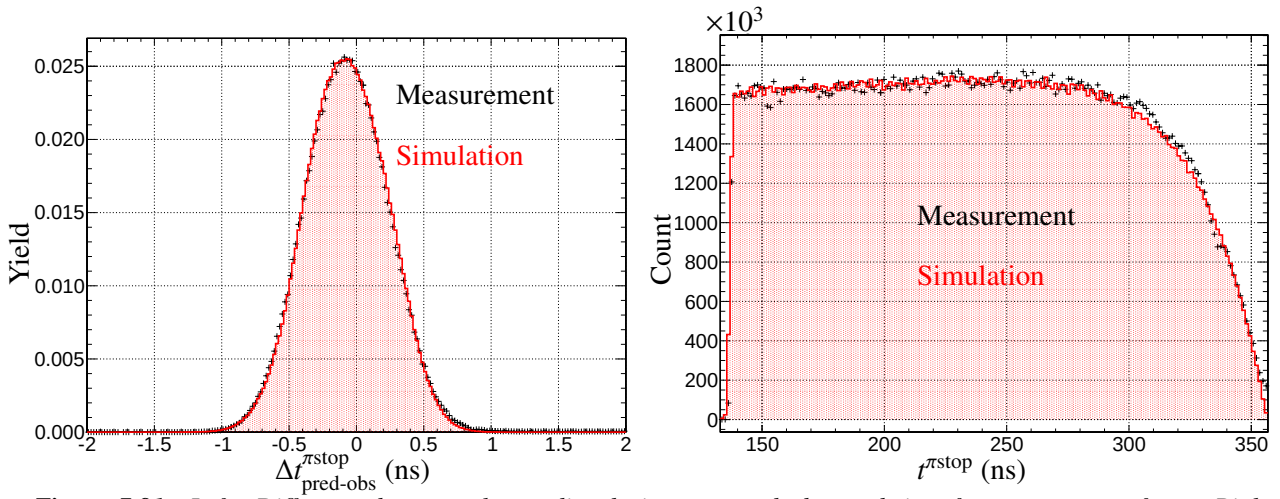

Figure 7.81: *Left: Difference between the predicted pion stop and observed time from target waveform. Right: Predicted pion stop time.*

The predicted times of the positron come from the hodoscope, which can easily be adjusted, whereas the predicted energy of the positron is derived from the path through which it traverses in the target. The predicted values are only half the battle. The second part is the observed energies and timings of the target waveform. The observed energies may be off relative to the simulation due to gain variations or incorrect quenching factor. The observed timings in the simulation are relative to the positron. Varying the positron target time in the simulation will take care of these. The amount of variation of these observables is determined by observing the χ^2 fit between simulation and measurement and at $\chi^2_{\text{min}} + 1$, the uncertainty is determined. Putting in these limits determines the uncertainty in the cut. It also is important to understand how correlated these observables are to $\Delta\chi^2$ and how false positives and negative occur. For this reason, the $\Delta\chi^2$ observable is plotted against various other variables for the Michel decay to identify instances where Michel decays would appear to be a pion decay.

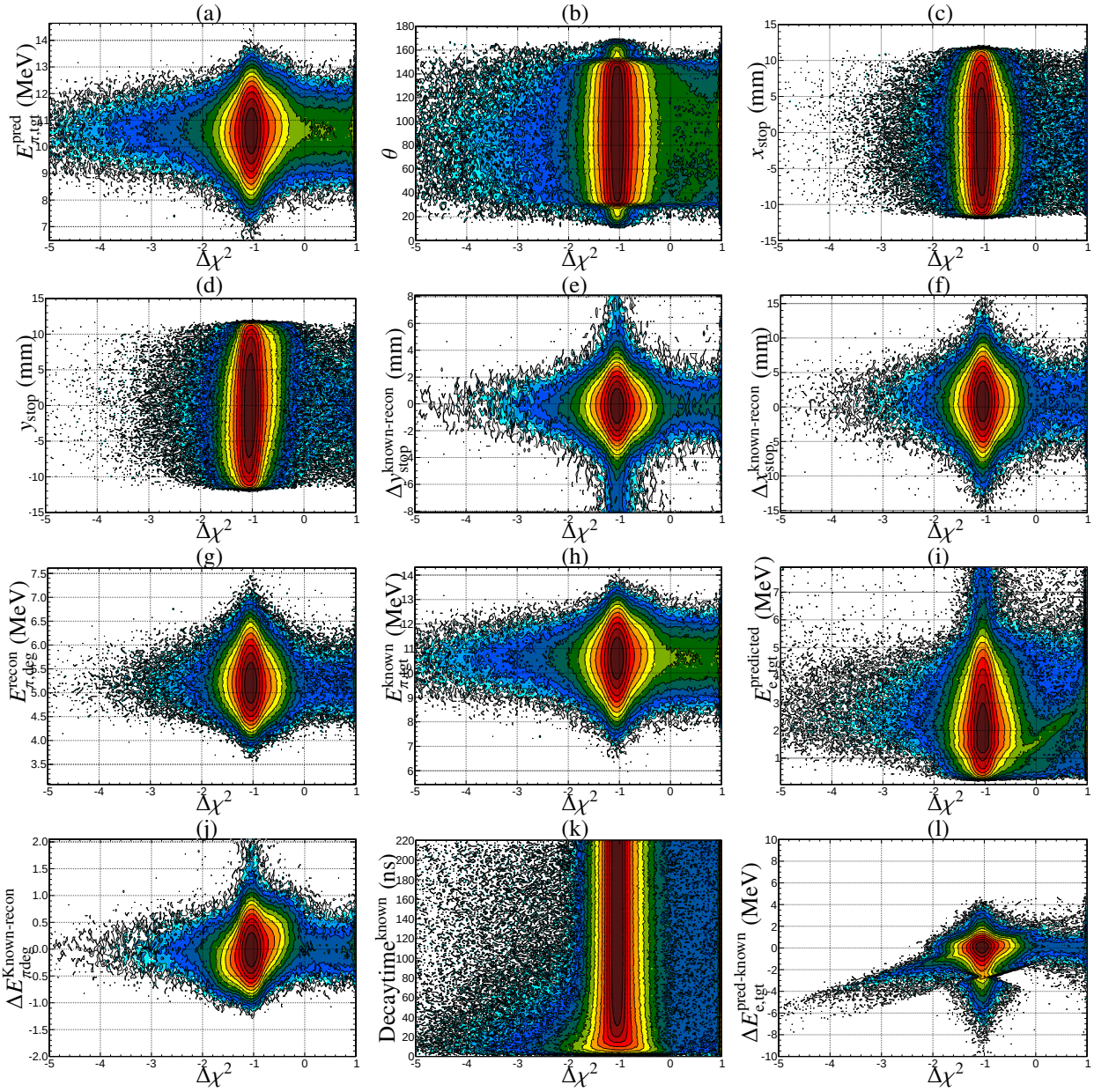

Figure 7.82: *Various observables plotted against $\Delta\chi^2$ for Michel simulation. (a) Predicted pion target energy. (b) Polar angle from tracking analysis. (c) x stopping position. (d) y stopping position. (e) Difference between known and reconstructed stopping position in y. (f) Difference between known and reconstructed stopping position in x. (g) Reconstructed degrader energy. (h) Known pion energy deposited in the target. (i) Predicted positron energy. (j) Difference in known and reconstructed degrader energy. (k) . (l) Difference between predicted and known positron energy in the target.*

Some noticeable features that in Fig 7.82 are that the cut does have efficiency based on the decay time. For faster decay times, the observables are not as cleanly reconstructed. This is not a big surprise because the identifying three peaks on top of each other (which occurs in a fast decay time) is a very difficult endeavor, even with the predicted times and energies. Falsely identified pion decays are not due to poor

beam reconstruction, i.e., when x and y stop value are not cleanly reconstructed, there is no $\Delta\chi^2$ dependence. There is however, a push to lower $\Delta\chi^2$ value when the predicted energy is not sufficiently high. This occurs when there is more energy deposited in the target, but the prediction lacks this. In such cases, the $\Delta\chi^2$ observables is pushed downward in value. For clean pion decay selections, the same features are seen in Fig 7.83.

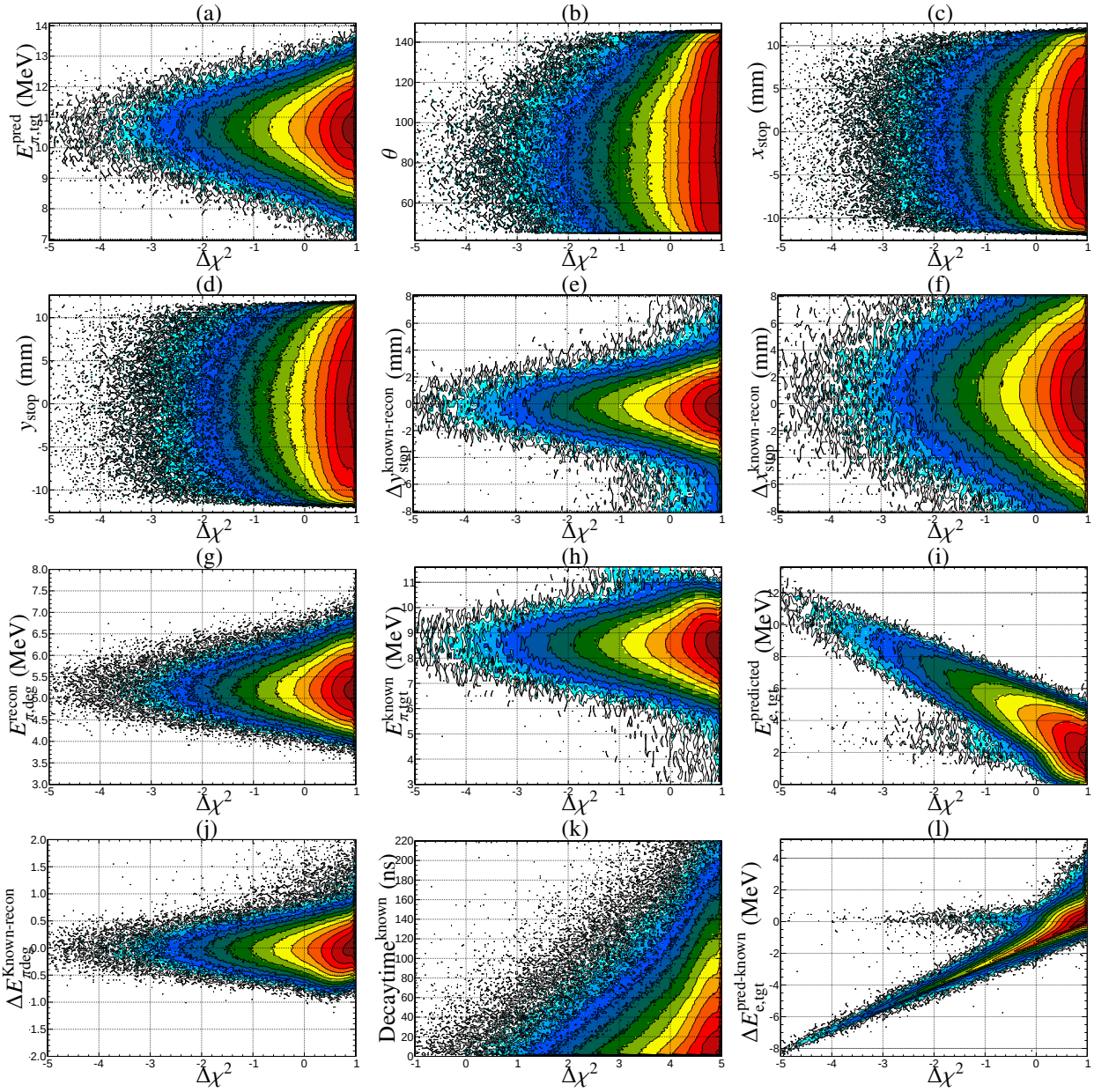

Figure 7.83: *Various observables plotted against $\Delta\chi^2$ for $\pi \to e\nu(\gamma)$ simulation. (a) Predicted pion target energy. (b) Polar angle from tracking analysis. (c) x stopping position. (d) y stopping position. (e) Difference between known and reconstructed stopping position in y. (f) Difference between known and reconstructed stopping position in x. (g) Reconstructed degrader energy. (h) Known pion energy deposited in the target. (i) Predicted positron energy. (j) Difference in known and reconstructed degrader energy. (k) Decay time. (l) Difference between predicted and known positron energy in the target.*

The reconstruction of the positron energy due to the high energy tail from the Landau energy deposition distribution results in a higher deposited energy than predicted and thus the appearance of an extra particle from excess energy, which then lowers the $\Delta\chi^2$ cut observables. The efficiency, therefore is lowered, but even with this effect, the $\Delta\chi^2$ cut remains very effective.

Care is needed in the understanding of the $\Delta\chi^2$ cut as the responses of the $\Delta\chi^2$ with two years is different because of the different upstream detectors and effectiveness of downstream detectors.

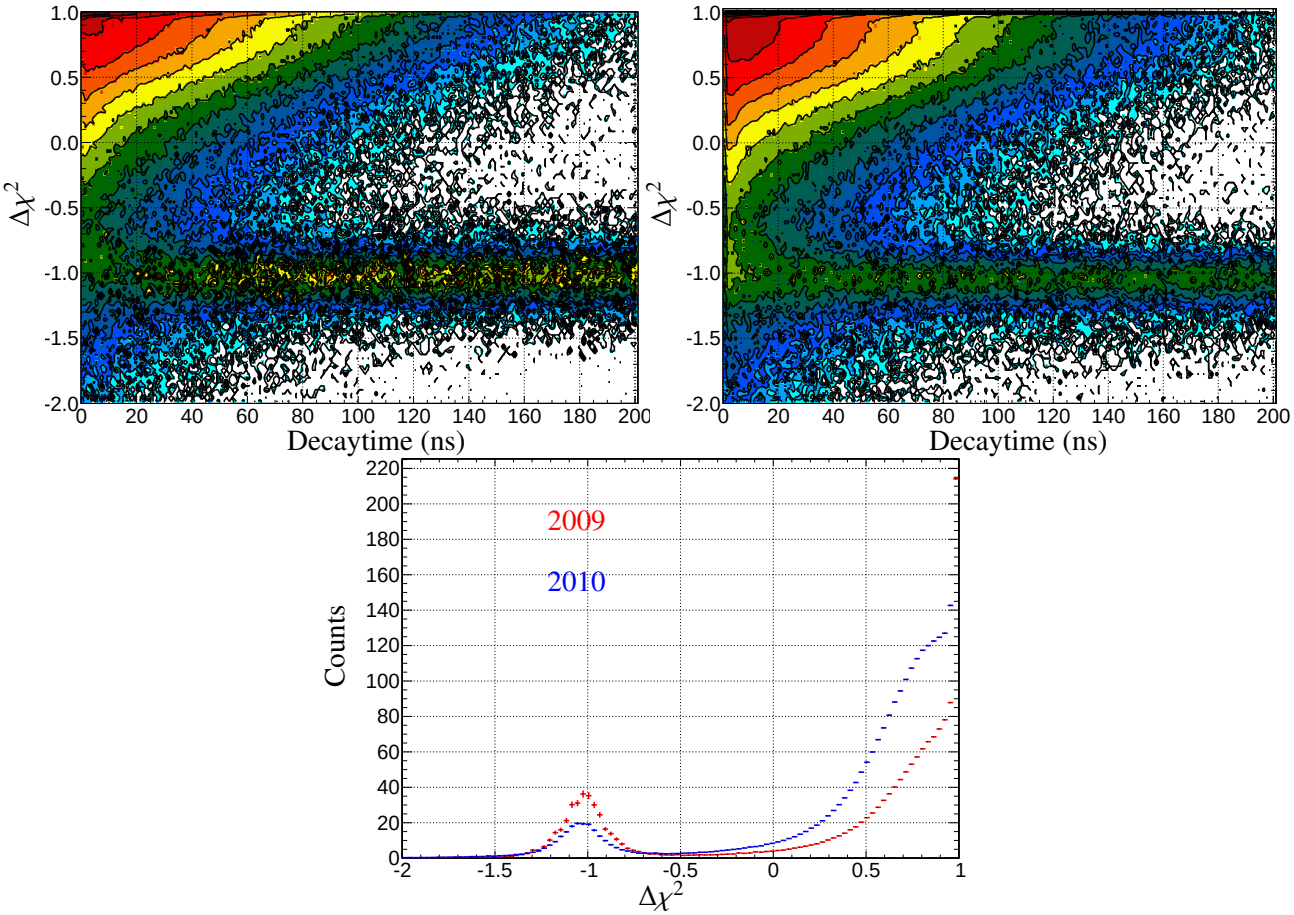

Figure 7.84: *Upper Left: $\Delta\chi^2$ versus Decay time for 2009. Upper Right: $\Delta\chi^2$ versus Decay time for 2010. Bottom: $\Delta\chi^2$ one dimensional plots for 2009 and 2010 separately.*

Fig 7.84 shows that the two years possess different responses in the $\Delta\chi^2$ observable. This is not surprising because the 2010 run used a thicker degrader, a closer and lighter mTPC, wires that failed in the mTPC as well as cathodes that failed in the MWPC. The efficiency in the 2010 run therefore is expected to be different.

The efficiency of the $\Delta\chi^2$ cut is simply the determining the number of events that survive the cut from the Monte Carlo simulation. By simulating events, the statistical uncertainty in this cut becomes negligible

and only the systematic uncertainty is non-negligible.

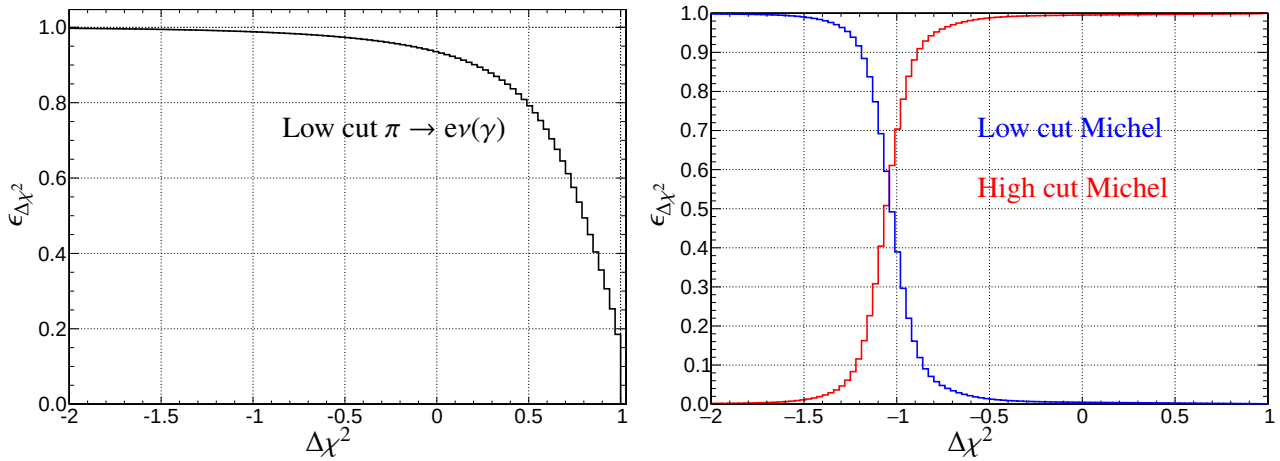

Figure 7.85: *Efficiency of $\Delta\chi^2$ as a function of the value on the cut. Left: $\pi \rightarrow e\nu(\gamma)$ efficiency for lower cut. Right: Michel efficiency for lower (blue) and higher (red) cut.*

The efficiency of the $\Delta\chi^2$ cut, shown in Fig 7.85, depends on the value of the cut that is used as does the uncertainty. Different regions of the response are more sensitive to changes in the observables that construct the value. To determine the uncertainty, the calculation of the $\Delta\chi^2$ cut is repeated for different values of the variables which construct $\Delta\chi^2$. The amount of which these observables are varied is determined by varying the simulated values and quantifying the deviation from the χ^2_{min} values. The variables which construct $\Delta\chi^2$ and comparison of the simulation are listed. Variations from energies are done by applying a gain and variations in timing by applying an offset. These results of these are shown in Fig 7.86

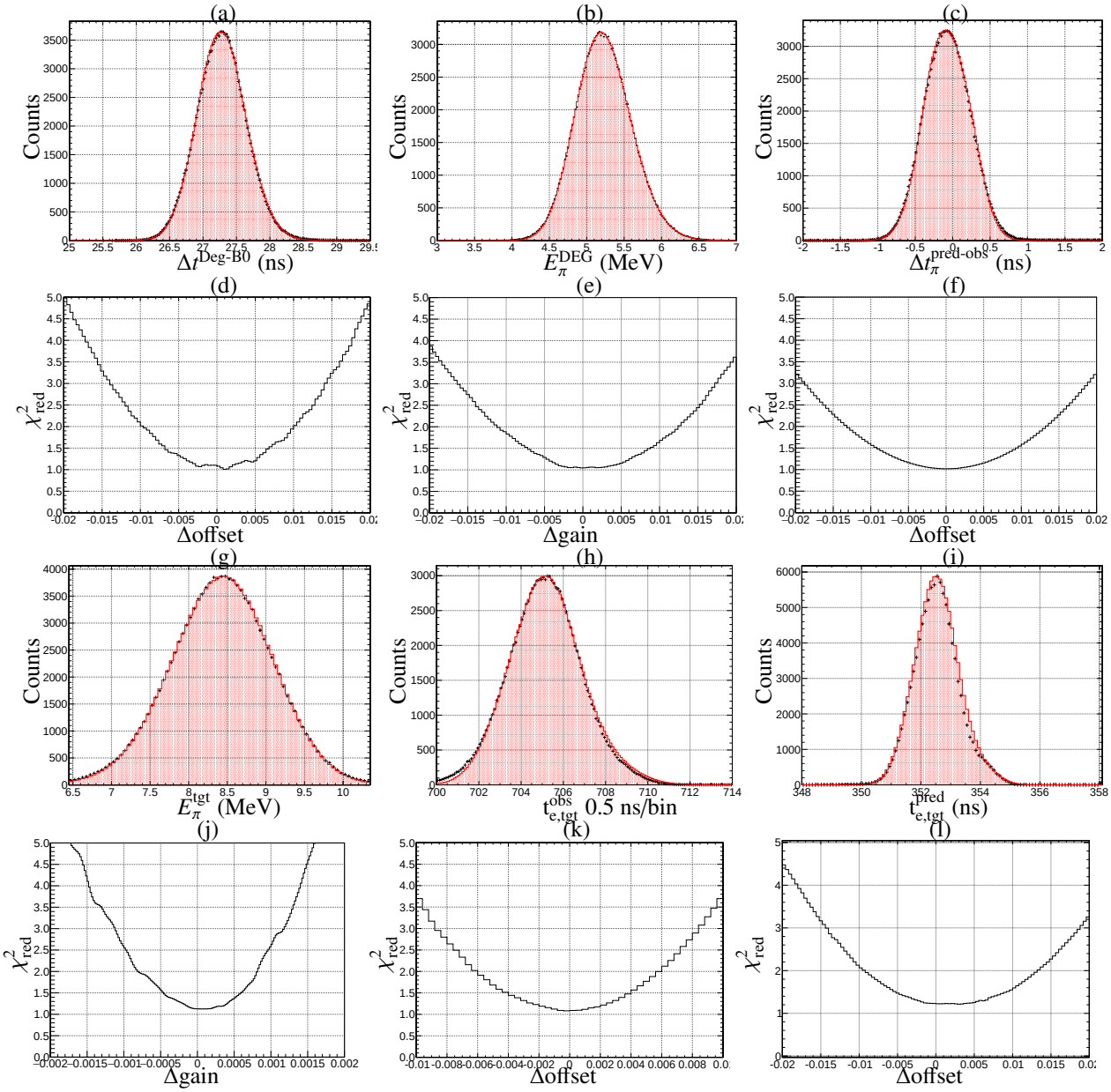

Figure 7.86: *Variations in timing and energy that contribute to the $\Delta\chi^2$ observable. Best fit of observables for (a) Time of flight, (b) Degrader energy, (c) Difference between pion predicted and observed time, (g) Pion target energy, (h) Positron target time, (i) Predicted positron target time. Reduced chi squared values on these observables for (d) Time of flight, (e) Degrader energy, (f) Difference between pion predicted and observed time. (j) Pion target energy, (k) Positron target time, (l) Predicted positron target time.*

The gain variation in the target for the pion may also be used for the positron since the gain is the same for all particles in the target. There is one more observable that is used in the calculation of the $\Delta\chi^2$ variable. The predicted positron energy uses the calculated pathlength that the particle traverses and multiplies it by the dE/dx of the target. Since the pathlength is not a simple Gaussian it is not so easy to determine the

uncertainty. However, the pathlength is determined by the x, y, and z stopping positions and the target surface through which the positron traverses:

$$\text{pathlength} = \sqrt{(x_{\text{surface}} - x_{\text{stop}})^2 + (y_{\text{surface}} - y_{\text{stop}})^2 + (z_{\text{surface}} - z_{\text{stop}})^2}. \tag{102}$$

Using simple error propagation,

$$\sigma_{\text{pathlength}} = \frac{\sqrt{2(x_{\text{surface}} - x_{\text{stop}})(\sigma^2_{x_{\text{surface}}} + \sigma^2_{x_{\text{stop}}}) + 2(y_{\text{surface}} - y_{\text{stop}})(\sigma^2_{y_{\text{surface}}} + \sigma^2_{y_{\text{stop}}}) + 2(z_{\text{surface}} - z_{\text{stop}})(\sigma^2_{z_{\text{surface}}} + \sigma^2_{z_{\text{stop}}})}}{\text{pathlength}} \tag{103}$$

The uncertainty in the pathlength therefore depends on the uncertainties in the x, y, and z positions of the pion stop position and the position at which the positron crosses the target. Some of these are known already. The uncertainty in the x and y stopping position using the results of mTPC analysis has been completed [67], yielding: $\sigma_{x_{\text{stop}}} = 1$ mm, $\sigma_{y_{\text{stop}}} = 0.4$ mm. The uncertainty in the z stop uncertainty can be achieved by varying times of flight, as discussed earlier. Using these two different momenta, difference in the stopping z position is $\sigma_{z_{\text{stop}}} = 0.025$ mm.

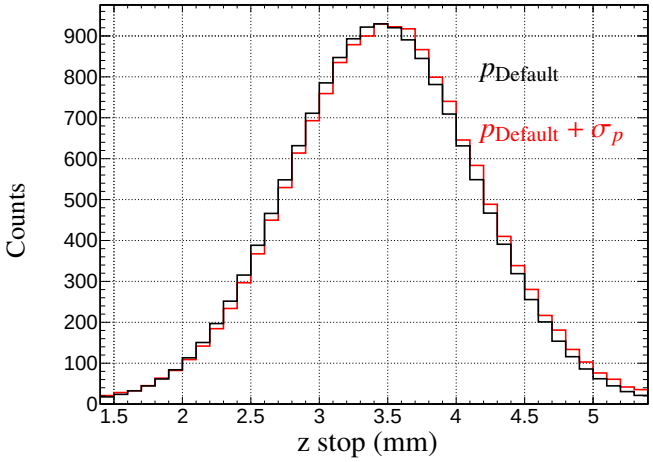

Figure 7.87: *Stopping z position with momentum change*

The position at which the positron crosses the surface depends on the x, y, and z of the MWPC trajectories and subsequently its uncertainty depends on the uncertainty in the MWPC positions. Since $x_{\text{surface}} = r_{\text{target}} \cos\phi$ and $x_{\text{surface}} = r_{\text{target}} \sin\phi$ and the radius is pretty well known, the uncertainty in these positions depend on the uncertainty in ϕ. $\sigma_{x_{\text{surface}}} = r|\sin\phi|\sigma_\phi$ $\sigma_{y_{\text{surface}}} = r|\cos\phi|\sigma_\phi$. Taking the maximum values, $\sigma_{(x,y)_{\text{surface}}} = r\sigma_\phi$. Since 192 anodes (used to find ϕ) surround the target in the azimuthal plane, the uncertainty in the ϕ from the inner MWPC is $2\pi/192 = 0.033$ rad. The uncertainty in ϕ for the outer chamber

is half of this since there are twice as many wires. $\sigma_{\phi_1} = 0.033$ rad and $\sigma_{\phi_2} = 0.0165$ rad allows for the determination of the uncertainty in the ϕ_{surface}. Since lines require two coordinates, the coordinates r, ϕ, and using the uncertainties in the studies characterized by previous detector characterizations, [52], [67], the $\sigma_{\phi_{\text{surface}}} = 0.0448$ rad which gives an uncertainty in $(x, y)_{\text{suface}} = 0.67$ mm. The same procedure can be done the z position. Using the known distances and the uncertainties in z and r as characterized in Karpuhkin,[52], $\sigma_{z_{1,2}} = 0.4$ mm. This in turn provides an uncertainty, $\sigma_{z_{\text{surface}}} = 0.583$ mm. It should be pointed out that the pathlength uncertainty using above formula is an upper bound. The simple chain formula calculation of the pathlength is technically not correct because the x and y position of the surface are anti-correlated. As x goes up in value, y must go down in value because $x^2_{\text{surface}} + y^2_{\text{surface}} = 15^2$. Therefore a more correct calculation of the uncertainty in the pathlength would require calculating the covariance between x and y. Since these observables are anti-correlated, the covariance is negative and would thus result in a slightly smaller value for the uncertainty in the pathlength. The higher value is chosen for simplicity. The pathlength used to construct the $\Delta\chi^2$ cut is is adjusted by the uncertainty for each event and the new $\Delta\chi^2$ is constructed. With these uncertainties, the variations in different calculated paths can be determined, a needed values for the uncertainty in the predicted energy of the positron.

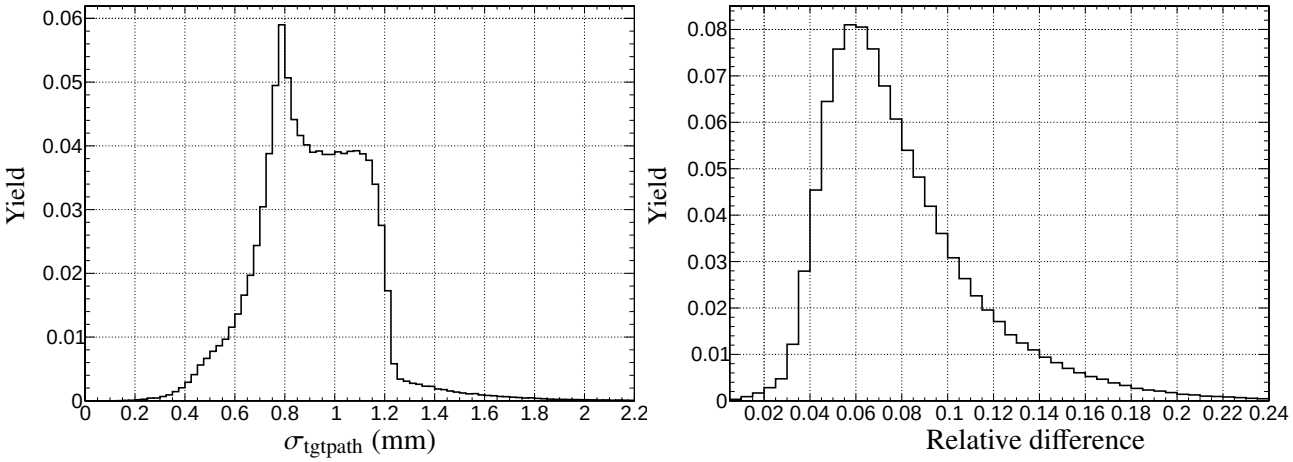

Figure 7.88: *Left:The extreme values in which the actual path differs from the predicted based on the uncertainties. Right: Relative difference*

Since the predicted energy is determined from the pathlength and the $dE/dx \sim 1.8$ MeV/cm, and the pathlength will typically have 2 mm uncertainty, the uncertainty in the predicted energy of the positron is at most 0.36 MeV.

By reconstructing the $\Delta\chi^2$ cut with the deviations of each of these discussed observables separately,

quantifying its deviation from the best fit, and adding the deviations in quadrature, a systematic uncertainty in the $\Delta\chi^2$ cut is obtained. From the observations above, the variations for the key observables tabulated

Table 12: *Table of uncertainties on observables that are used to construct $\Delta\chi^2$.*

Observable	σ
Time of flight	σ = 0.01 ns
Degrader Gain	σ = 0.013
Target Gain	σ = 0.001
Positron Predicted time	σ = 0.013 ns
Positron Observed time	σ = 0.007 ns
Pion predicted time	σ = 0.013 ns
Positron predicted energy	$\sigma \leq$ 0.36 MeV

An easy way to see the effects in the $\Delta\chi^2$ observable is to change one of these observables drastically. In this case, the 2010 data set has been analyzed in the exact same fashion except that the gain in the degrader is decreased by 3%. The difference is seen below in Fig 7.89.

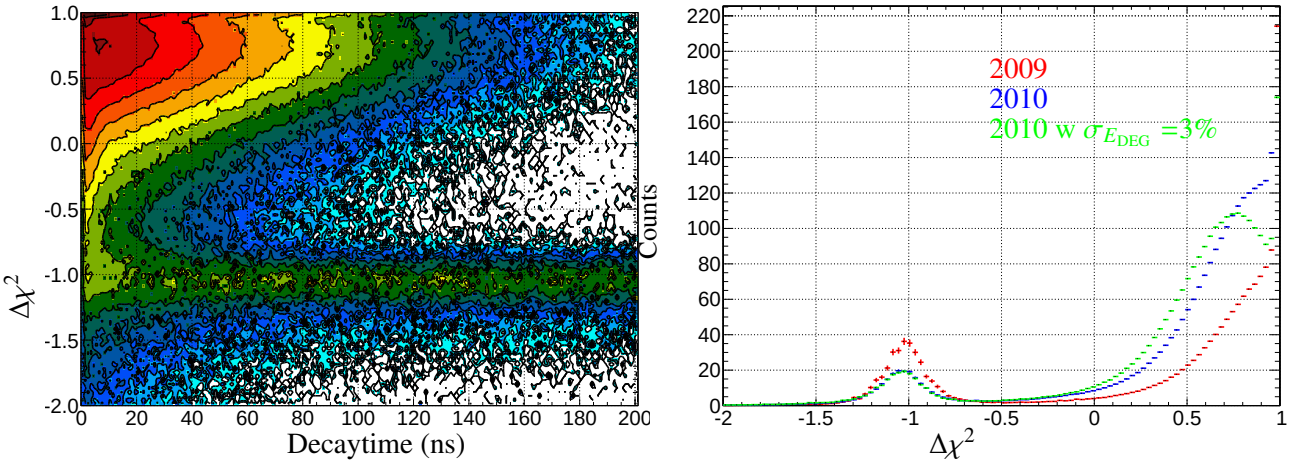

Figure 7.89: *Response of $\Delta\chi^2$ with a 3% decrease in the degrader gain. Left $\Delta\chi^2$ versus decay time. Right: $\Delta\chi^2$ compared with the the 2009 and normal 2010.*

While 3% is more than the actual uncertainty in the gain, this shows the effect. By decreasing the degrader energy, the predicted energy decreases. This means there is more target rest energy which makes the event look more like a Michel event, hence the clear movement to the left in the higher regime. However, the difference in the region around $\Delta\chi^2 = 0$ is on the order of 10^{-3} and around $\Delta\chi^2 = -0.5$ the difference is on the order of 10^{-4}. The sensitivity at higher $\Delta\chi^2$ values is not surprising as this was discussed earlier. The origin of these changes and how they affect the variable all relies on the predicted waveforms and how they compare to filtered target waveforms. As a reminder, the observable is formed by first filtering

target waveforms and and comparing the predicted waveforms to the filtered waveforms. This algorithm is demonstrated in Fig 7.90

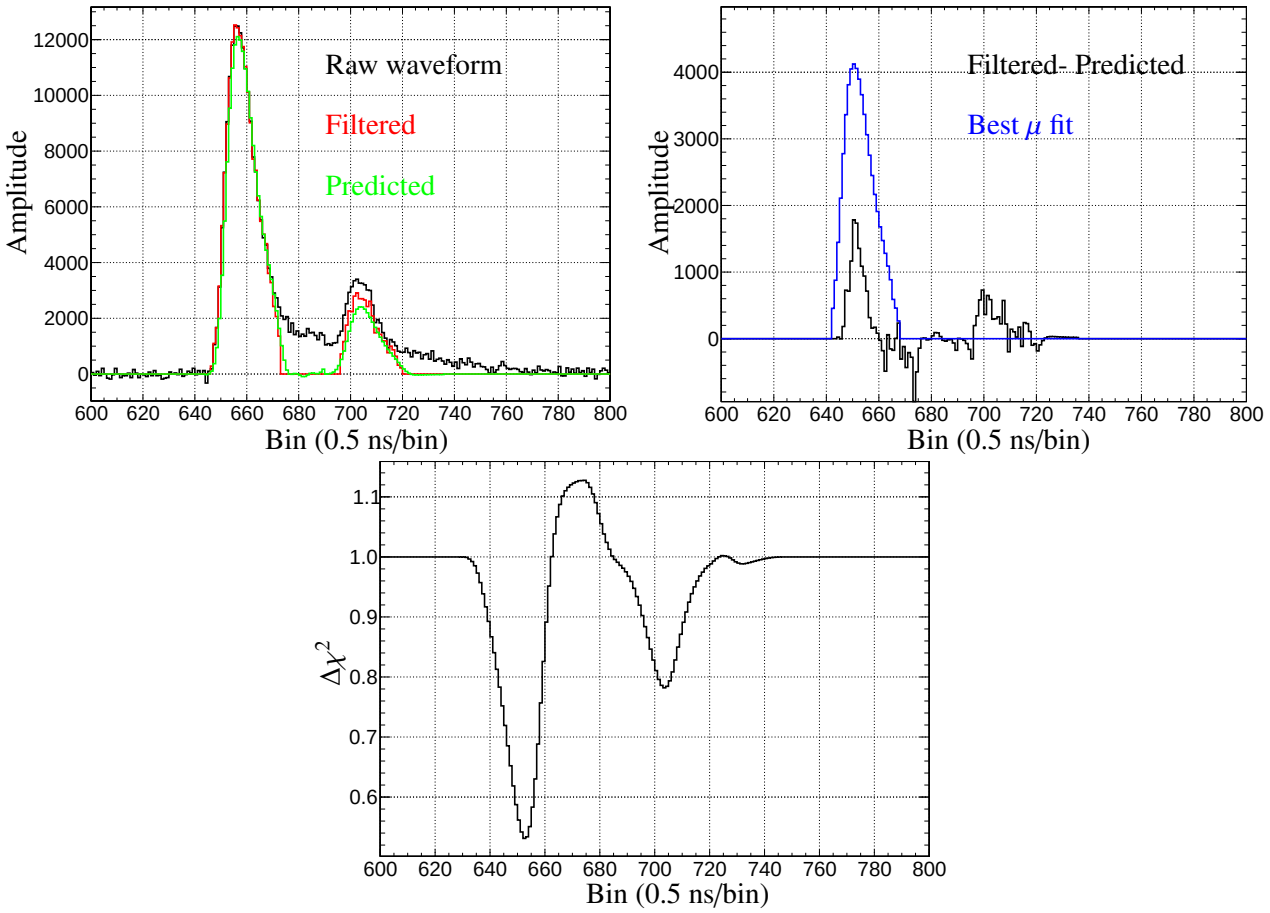

Figure 7.90: *Demonstration of $\Delta\chi^2$ determination. Upper Left: Raw, filtered and predicted target waveforms. Upper Right: Subtraction (black) of predicted and filtered with the muon best fit put in as determined from minimum χ^2. Bottom. $\Delta\chi^2$ as a function of muon position.*

The minimum $\Delta\chi^2$ value is the $\Delta\chi^2$ value taken. The inverted net histogram from predicted and filtered is also used if there is a case in which the energy is over subtracted. This over subtraction is more relevant for the positron energy because of the Landau tail, whereas the pion is more deterministic due to the well defined times and energies of the pion going into the target. The exception of course occurs in decays in flight. When comparing the effects of the different systematics, the calculation is done in the case for higher and lower values of the predicted and observed energies and times of the positron and pion. The observed times, showed no significant change in the value because of the construction of binning. Thus the predicted times, energies, and observed energies are the most important in the determination of the uncertainty in the $\Delta\chi^2$ values. The different subtractions as seen in Fig 7.91 are subjected to the same algorithm to obtain the

different minimum $\Delta\chi^2$ values as seen in Fig 7.93.

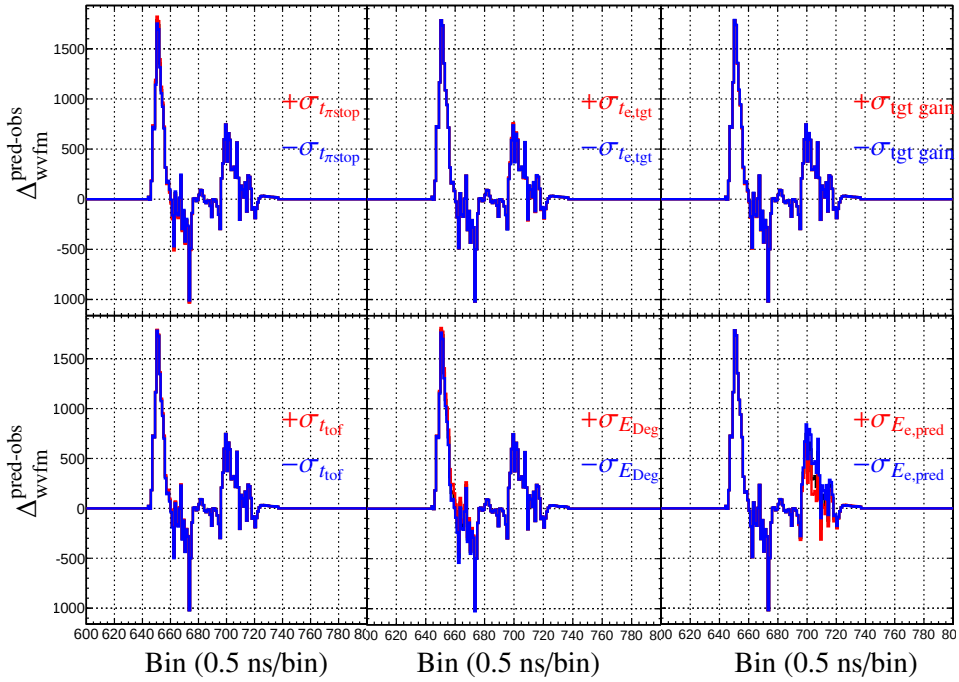

Figure 7.91: *Different subtractions from predicted and observed energies with different changes in systematics.*

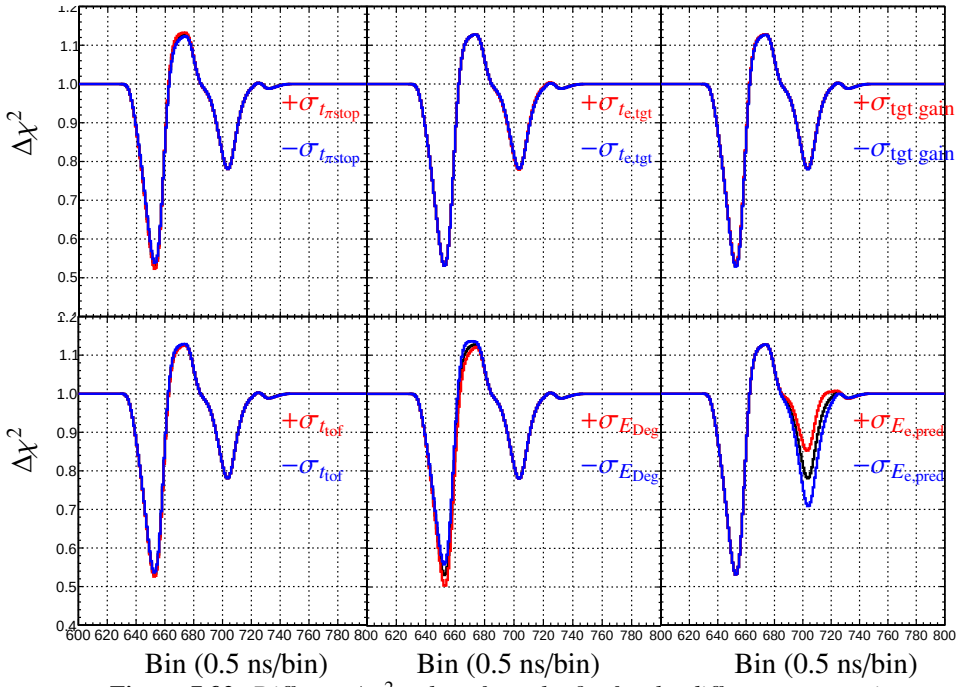

Figure 7.92: *Different $\Delta\chi^2$ values from the fits for the different systematics.*

The smallest value of $\Delta\chi^2$ is the one that is chosen for the event. This also demonstrates why the highest value of $\Delta\chi^2$ is one. If the prediction and the filtered observed target waveform are a perfect match in both

time and energy, then the the difference is zero. The χ^2 of a two peak is performed first by comparing the difference between the predicted and filtered target waveform. The difference, called the netto target waveform is determined as seen in the above figure. The netto squared is the $\chi^2_{2\text{peak}}$.

$$\chi^2_{2\text{peak}} = \Sigma_{i=0}^{1000}(\text{obs}_i - \text{pred}_i)^2 = \Sigma_{i=0}^{1000}\text{netto}_i^2 \tag{104}$$

The muon response, which is well defined in energy, is subtracted from the netto waveform from different positions originating before the pion stop bin and going beyond the positron time. The result is squared. This value is the $\chi^2_{3\text{peak}}$.

$$\chi^2_{3\text{peak}} = \Sigma_{i=0}^{1000}(\text{netto}_i - \text{muon}_i)^2 \tag{105}$$

The value of $-\text{netto}^2 + (\text{netto} - \text{muon})^2$ is performed and the result is divided the square of the integral of the muon response function.

$$\underbrace{\left(-\text{netto}^2 + (\text{netto} - \text{muon})^2\right)}_{\chi^2_{3\text{peak}} - \chi^2_{2\text{peak}}} / \text{muon}^2 = 1 - 2\text{netto}/\text{muon} = \Delta\chi^2 \tag{106}$$

In this light, if the netto waveform is zero indicating a perfect match between predicted and observed energies and times, then the value is one. If the netto is a perfect match for a muon, then the value goes to negative one. Notice the netto can be greater than than the muon waveform due to failures of predicted energies to properly predict the target waveform. Thus values less than negative one are possible. With these systematic limits, the different $\Delta\chi^2$ values are constructed for these shown in Fig 7.93.

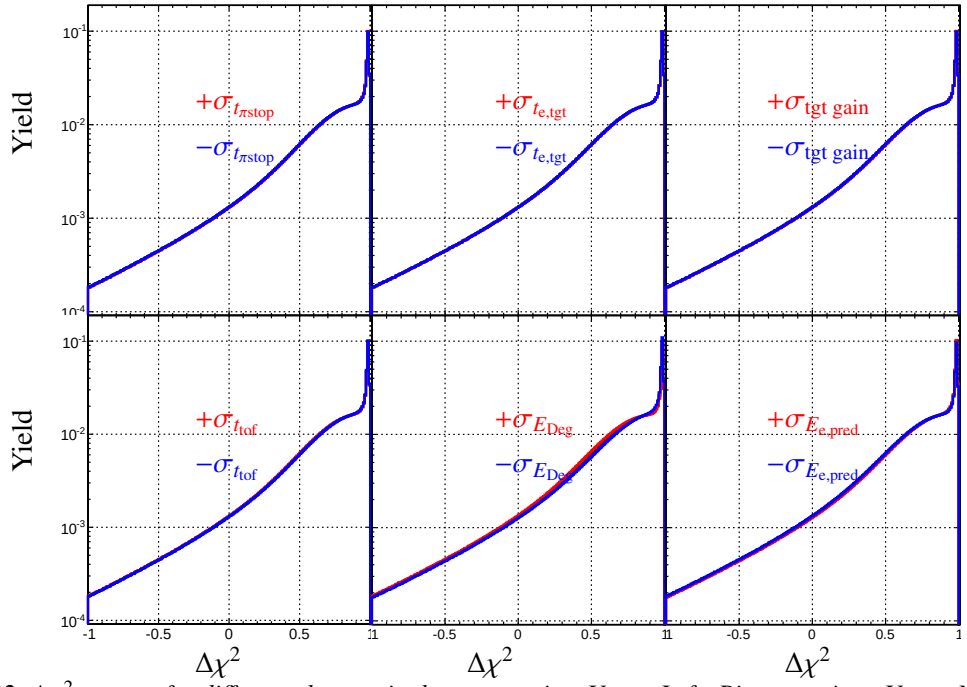

Figure 7.93: *$\Delta\chi^2$ spectra for different changes in the systematics. Upper Left: Pion stop time. Upper Middle: Positron predicted time. Upper Right: Target gain (observed target energies). Lower Left: Pion time of flight. Lower Middle: Degrader energy. Lower Right: Predicted positron energy.*

With variation of the different observables used in the construction of the $\Delta\chi^2$ variable, The cut efficiencies for various offsets and gains for the $\Delta\chi^2$ can then be determined as seen in Fig 7.94.

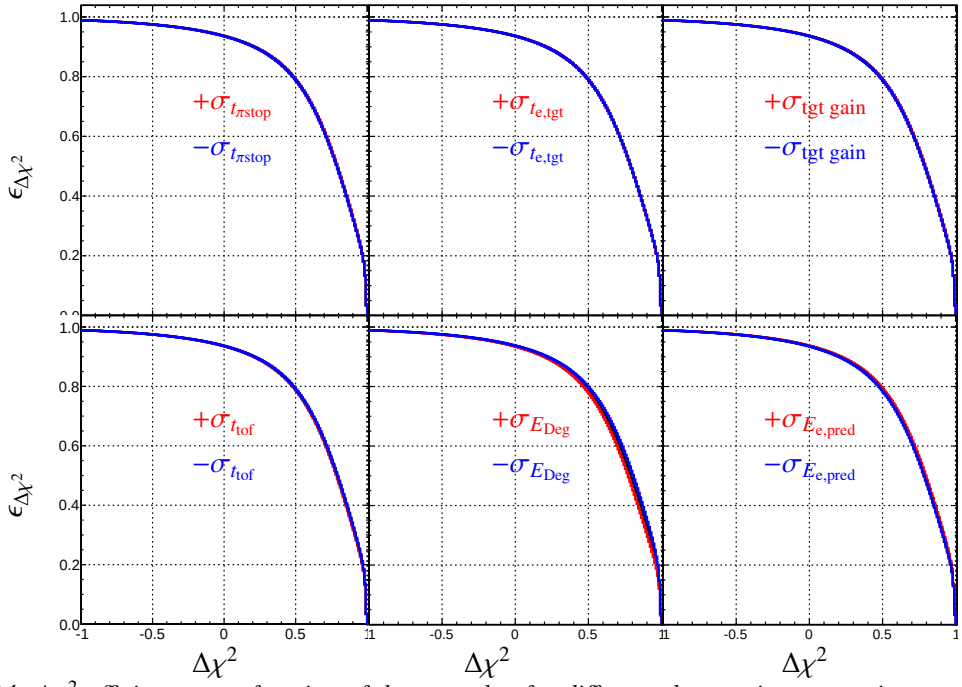

Figure 7.94: *$\Delta\chi^2$ efficiency as a function of the cut value for different changes in systematic contributions. Upper Left: Pion stop time. Upper Middle: Positron predicted time. Upper Right: Target gain (observed target energies). Lower Left: Pion time of flight. Lower Middle: Degrader energy. Lower Right: Predicted positron energy.*

.

With these efficiencies, differences from the extremes are quantified to determine the relative uncertainty in the cut value based on which observables are being varied as depicted in Fig 7.95.

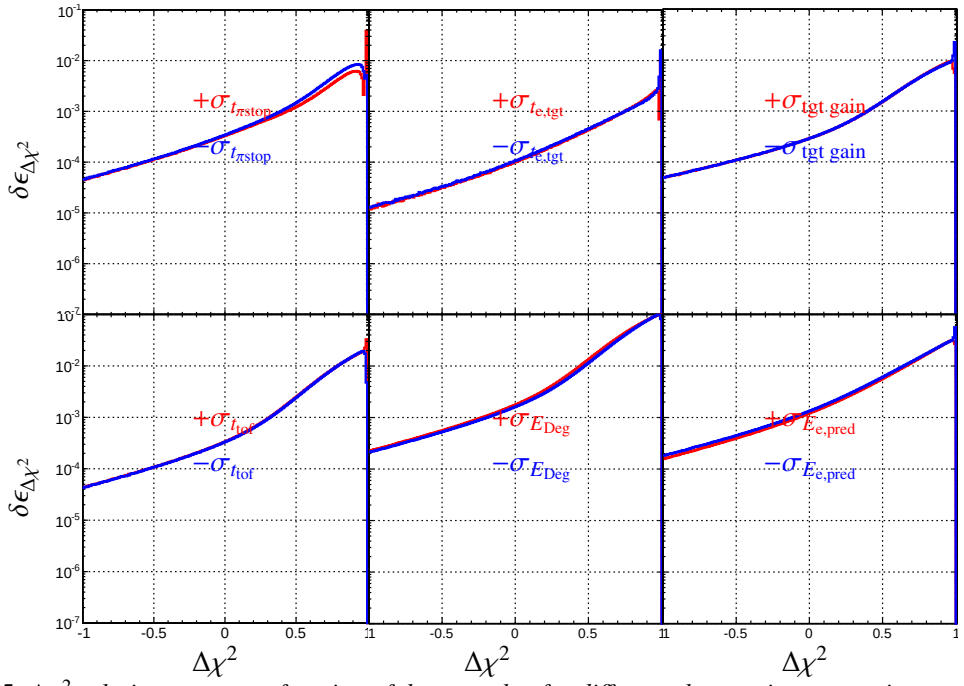

Figure 7.95: *$\Delta\chi^2$ relative error as a function of the cut value for different changes in systematic contributions. Upper Left: Pion stop time. Upper Middle: Positron predicted time. Upper Right: Target gain (observed target energies). Lower Left: Pion time of flight. Lower Middle: Degrader energy. Lower Right: Predicted positron energy.*

.

Taking the higher error in each of these systematics, adding in quadrature and normalizing to the actual efficiency, the cut relative error is determined as function of the $\Delta\chi^2$ observable seen in Fig 7.96.

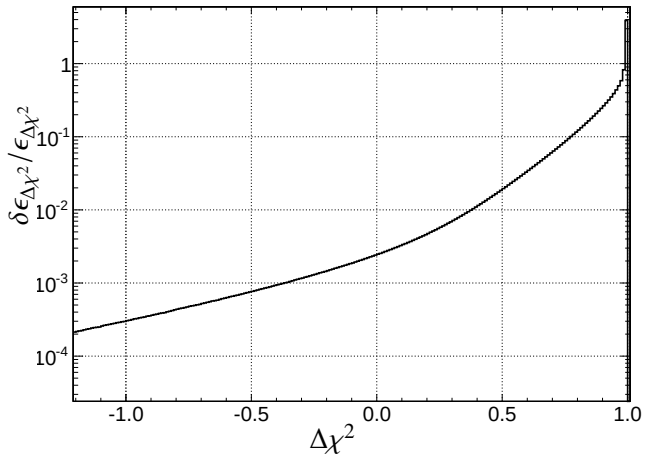

Figure 7.96: *Total relative error of the $\Delta\chi^2$ cut as a function of the cut value.*

The total relative error in the $\Delta\chi^2$ is higher than desirable but manageable nonetheless as long as it is above -1 and less than -0.75. In this region the error in the cut is sufficiently low enough to stay beneath the PEN goal (at least for the cut efficiency, not so much for the statistics).

7.12 Acceptances and DIF

In the determination of the number of events for both Michel decays and $\pi \rightarrow e\nu(\gamma)$ decays, there has been no mention of the corrections needed to account for the decays in flight, until now. Events in which the pions decay in flight to a positron, π_{DIF2} contribute nothing to the Michel count. These events have a characteristic decay time centered close to decay time equal to zero, while the Michel window was taken between 81 and 181 ns. Therefore these decays in flight contribute only to a (small) correction in the count of $\pi \rightarrow e\nu(\gamma)$. Repeating the same event selection cuts that is performed in the analysis of the data while simulating 1.5 billion events, the ratio of π_{DIF2} to the number of decays at rest is obtained. This number of simulated events prevents statistical uncertainty from being a problem for this correction and thus only systematic uncertainties contribute to this correction. Not surprisingly the biggest systematic for these events (and the ratio) is the $\Delta\chi^2$ cut.

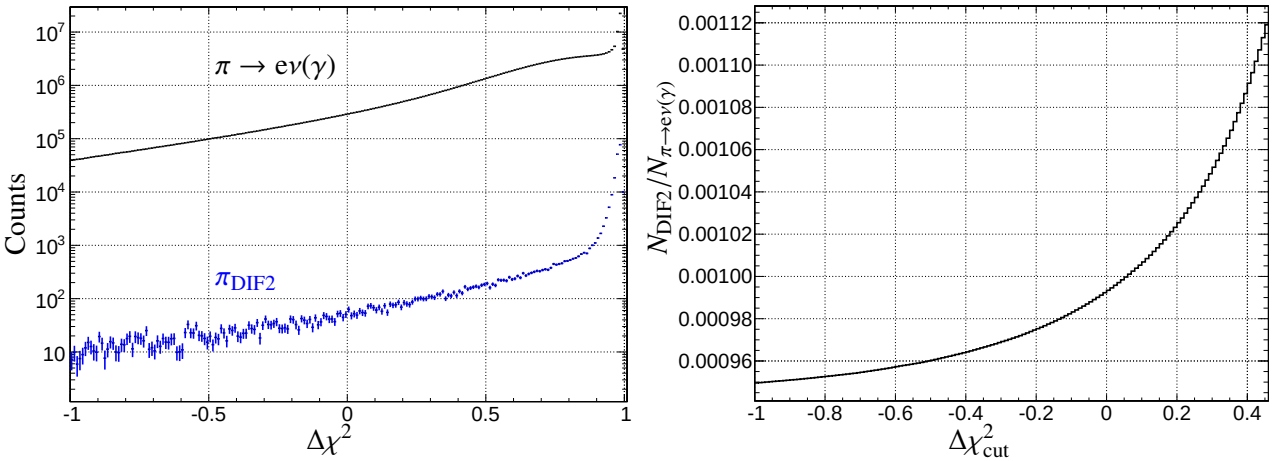

Figure 7.97: *Left: Number of events for pion decays and pion decays in flight as a function of $\Delta\chi^2$. Right: Ratio of π_{DIF2} to pion decays as a function of the $\Delta\chi^2$ cut.*

Fig 7.97 shows the ratio of the decays in flight to that at rest as a function of where the $\Delta\chi^2$ cut occurs. It is important to note that even though it was shown earlier that the ratio of decays in flight to that at rest is roughly 2.7×10^{-3}, the ratio in Fig 7.97 is smaller. This is attributed to the cuts. The `restwave` cut of greater than -5 eliminates a substantial amount of events from the decays in flight. In addition, tracking requirements will also diminish the number. It is also seen that the as the $\Delta\chi^2$ cut increases, the correction factor increases. This is not unexpected as a lower value of the $\Delta\chi^2$ has target signatures more akin to muon decays, i.e., excess target energy. This will not be the case for the pion decays and thus higher $\Delta\chi^2$ cuts

favor decays in flight of the pion directly to a positron. While this correction is not needed until the final analysis is performed, it is instructive to have the plot show what is expected. The systematic uncertainties are below 10^{-4} for this factor.

In addition to correcting for the number of signal events due to decays in flight, the number of Michel events need a correction due to decays in flight. As stated, π_{DIF2} do not contribute to these events. The muon decays in flight, happen on the order of 10^{-5} to begin with, and since the muon decay in flight have a decay time spectrum of pion decay and Michel time window is chosen between 81 and 181, then only a fraction (4%) of these are in the time window, meaning the muon decays in flight occur once in every 1 million Michel events. Therefore μ_{DIF} does not contribute to the Michel count with any statistical significance, and therefore only π_{DIF} events are present to correct the number of Michel events. Since there is no $\Delta\chi^2$ cut in determining the Michel count, the biggest contributors to the systematics is then the invariant mass used to determine the Michel count.

The invariant mass relies on the predicted pion stopping along with the positron measured trajectory to properly reconstruct. Since the pion decays in flight have a weaker correlation between the predicted and observed positions for the pion, cuts on the predicted pion positions introduces a systematic effect. Since there are no cuts on the pion stopping other than the radial position (which is determined far upstream), there is no discernible systematic uncertainty introduced from pion stopping. However, the invariant mass uses both predicted pion stopping and reconstructed positron trajectory for proper calculation. Thus a small systematic is introduced when cutting on the invariant mass. The correction for the decays in flight as a function of invariant mass is shown in Fig 7.98

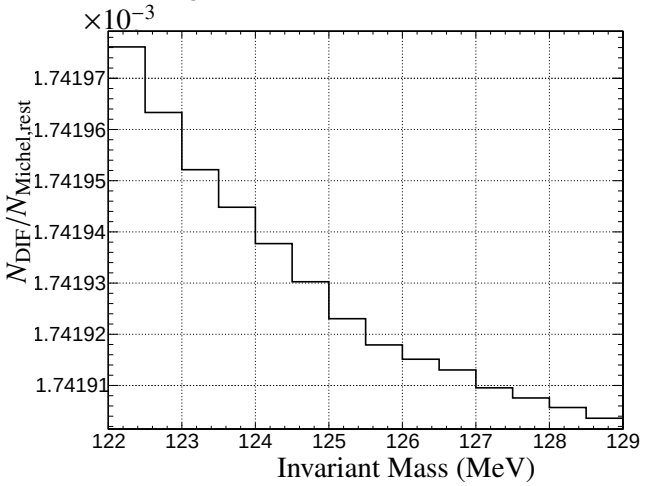

Figure 7.98: *Ratio of pion decays in flight to that of the number of pion stops decaying into a muon as a function of invariant mass. Ratio uses the same cuts used in the analysis for the branching ratio.*

7.13 Acceptances and trigger efficiency

During the measurements, every event with total energy in the CsI calorimeter above a high threshold would be recorded, while events below this threshold would be prescaled, recorded once every 64, 128, or 256 times they occur depending on the run period. A natural question arises as to what happens if the high energy trigger does not fire for the high energy event from a $\pi \rightarrow e\nu(\gamma)$ decay. This event would not be recorded for this decay and the prescale counter for lower energy events would increment. The more inefficient the trigger, the fewer number of pion decays will be recorded. This leads to a deficit in the pion decay count. These trigger efficiencies are placed into the acceptances by reproducing the efficiencies in the simulation. The correction for this count is determined by observing events that should have fired the high energy trigger event and ultimately resulted only in the medium energy trigger. This is needed for both the 2009 and 2010 data set. In order to account for trigger efficiencies, it is advantageous to check individual crystals as high voltage/gains varied somewhat during the runs thus affecting the trigger efficiency.

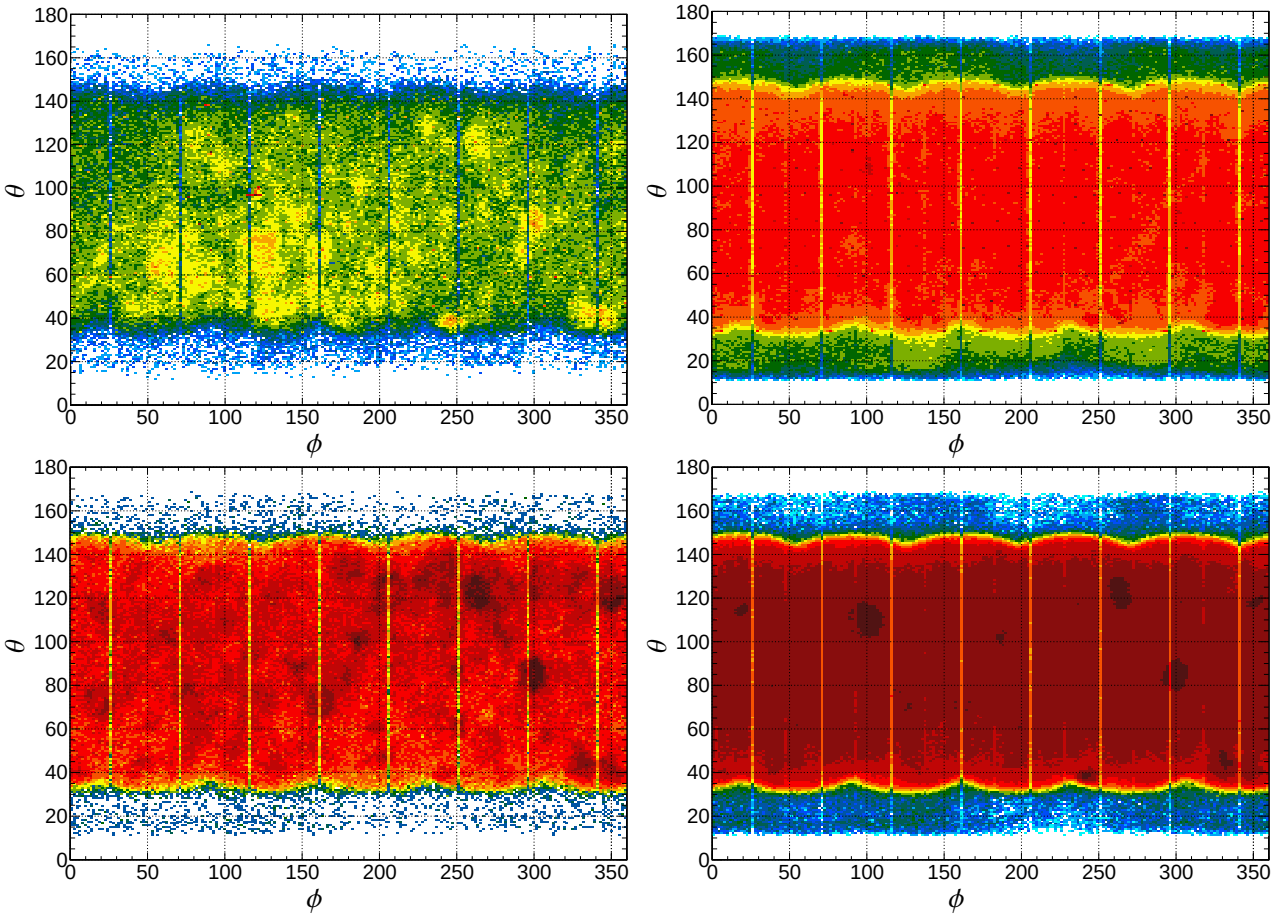

Figure 7.99: *Left Column: Failed hi trigger events with CsI energy above trigger threshold as a function of ϕ and θ. Right Column: Hi trigger events with energy above the threshold as a function of ϕ and θ. 2009 on the top row and 2010 on the bottom row.*

The effect of the failures of the hi energy threshold trigger can be seen by observing the energy in the CsI for events in which the hi trigger did fire. Efficiency mapping as a function of crystal hit (or θ, ϕ) may be performed. Differences in crystal size as well as non-uniformities can account for the differences in the trigger performance crystal by crystal which is accounted for in the Monte Carlo simulation.

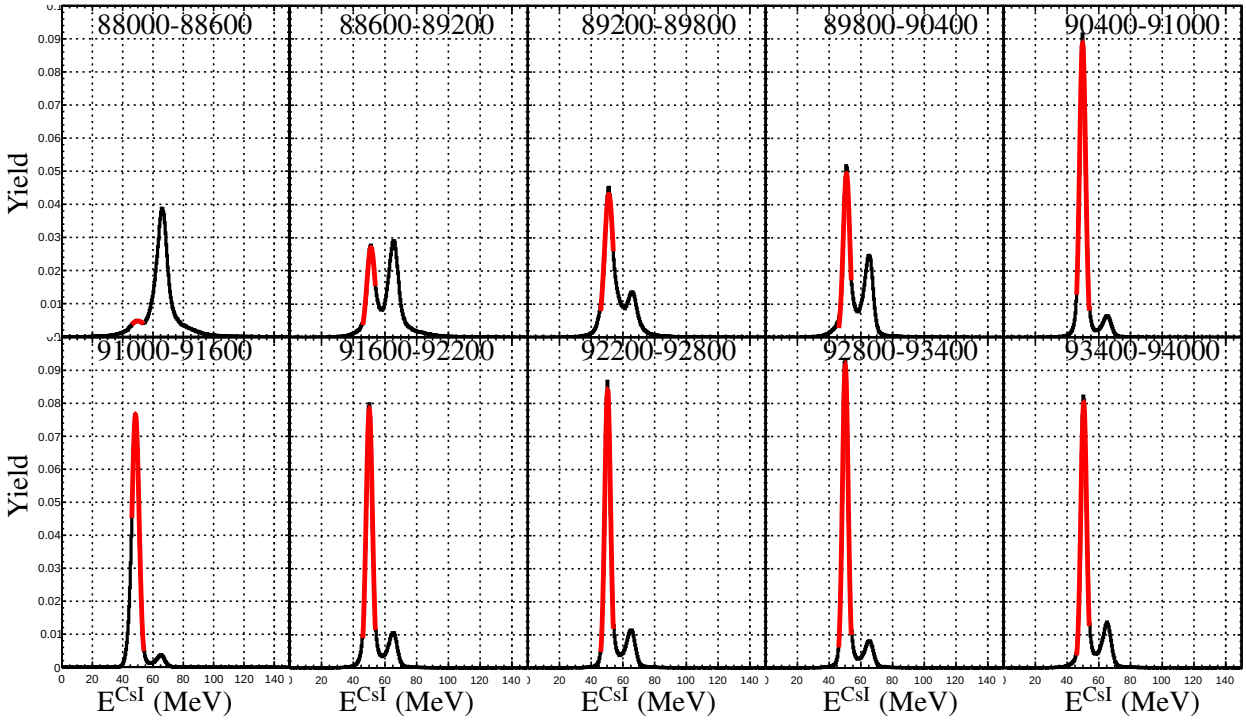

Figure 7.100: *CsI total energy for hi trigger events for the 2009 data run broken into 600 run periods. A Gaussian fit in red.*

The 2009 data in Fig 7.100 shows peaklets around 50 MeV for the different run periods, The standard deviation and mean are important as they represent how far away from the trigger cutoff we have to be in order to record the correct number of events in the high energy regime. If the peak energy cut-off for the $\pi \rightarrow e\nu$ branching ratio analysis is too close to the trigger threshold, there is a deficit in the number of events, and thus fewer $\pi \rightarrow e\nu$ events are recorded. The first two panels in Fig 7.100 show a high concentration in the high energy regime as compared to the panels that follow. This is due once again to the high concentration of scattered beam positrons. The trigger only depends on the total energy in the CsI so when positrons scatter into the calorimeter from the beam, these events were recorded. The minimum energy requirement for the target positron at the time of the trigger aids in diminishing these numbers, but as discussed, produces less desirable consequences. For the 2009 data combined, the Gaussian fit yields a mean fit at 49.88 MeV with a standard deviation of 2.06 MeV.

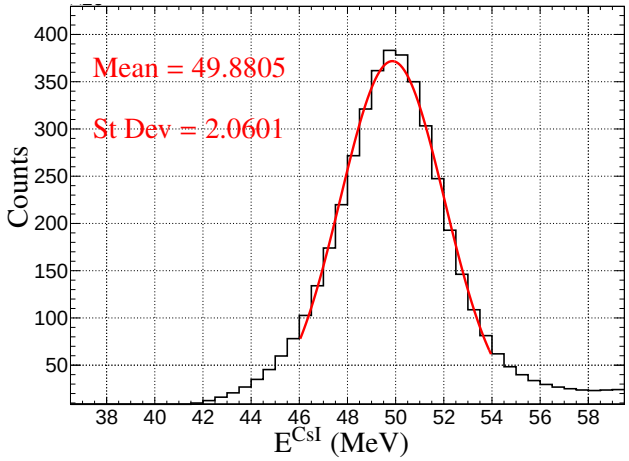

Figure 7.101: *2009 full data hi trigger response of the CsI calorimeter*

For the 2010 because of higher software gains needed, the peak is present at a higher energy.

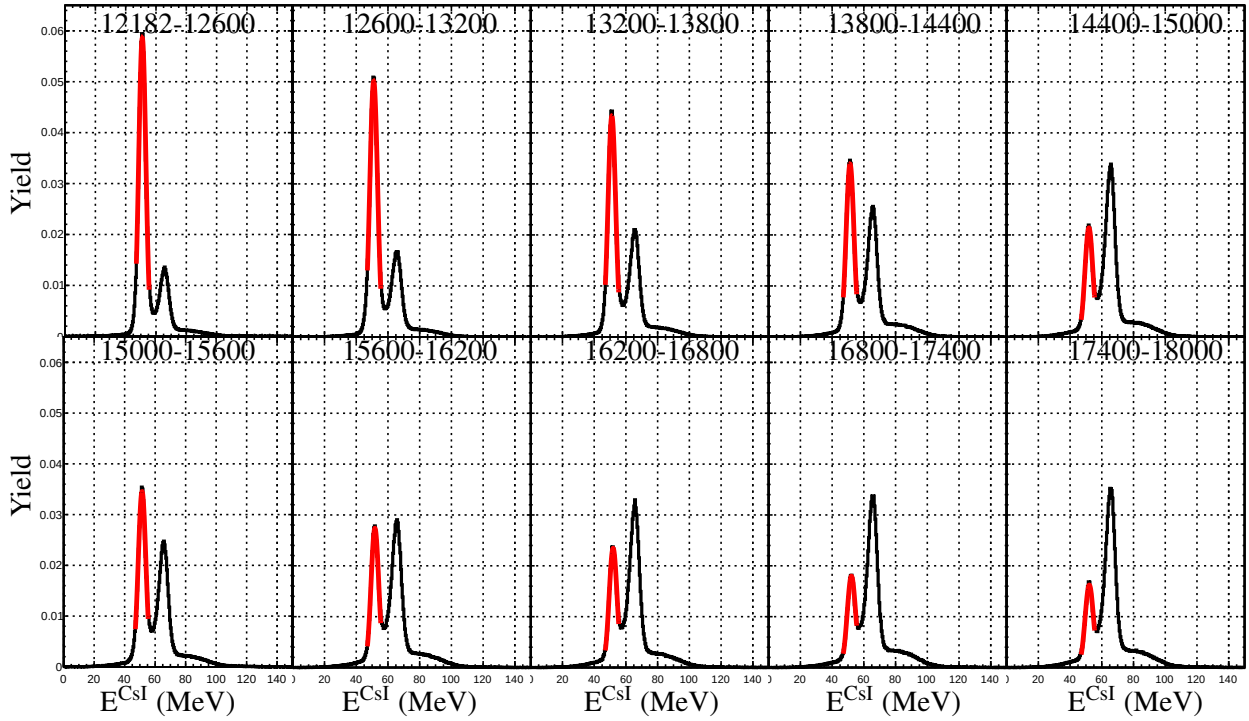

Figure 7.102: *CsI total energy for hi trigger events for the 2009 data run broken into 600 run periods. A Gaussian fit in red.*

The combined 2010 data set is shown in Fig 7.103 below.

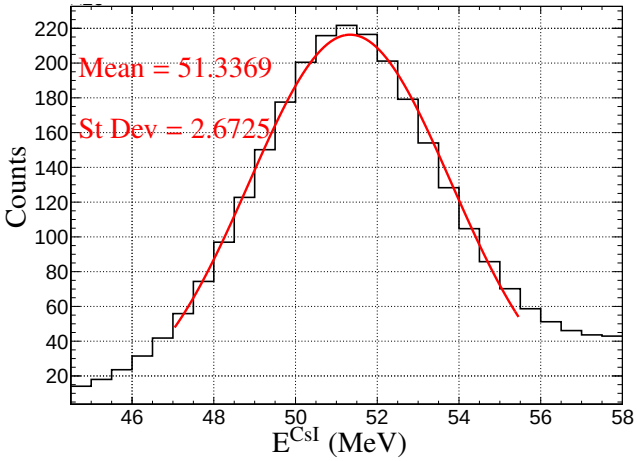

Figure 7.103: *2010 full data hi trigger response of the CsI calorimeter.*

The difference in the peak and rms of the of the CsI response between the 2009 and 2010 run periods indicate that different trigger efficiencies are needed for the acceptance calculations for the 2009 and 2010 data sets. While a more in depth analysis is forthcoming in the final analysis, the scope of the correction is quantified here.

The correction to the trigger depends on how the trigger is implemented. If the trigger is an all or nothing trigger, then determining the number of missing (non-recorded) events is straightforward. Since the number of counts in the pion decay is determined above a particular invariant mass threshold (117.5 MeV), there are events which would should have been recorded but did not due to trigger inefficiencies. A plot of invariant mass versus the total CsI energy (the signal used in the trigger) is necessary in order to quantify how efficient the trigger is at that particular invariant mass. These observables are well correlated as seen in Fig 7.104 below.

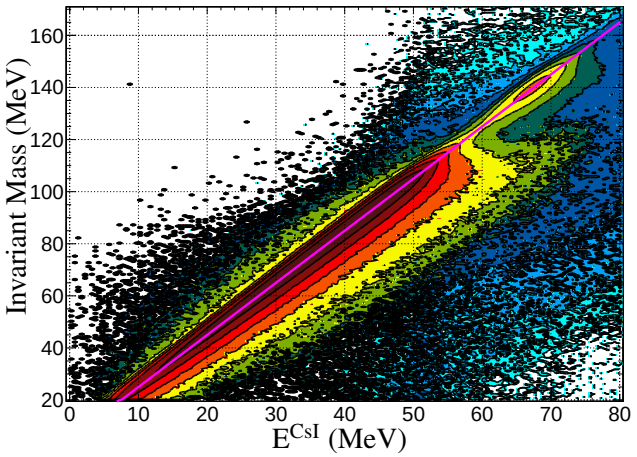

Figure 7.104: *Invariant mass as a function of total CsI energy. A linear fit is in purple.*

Using a linear fit function, the invariant mass of 117.5 MeV corresponds to the total CsI energy of 55.5 MeV according to the linear fit. In order to account for the trigger efficiencies, the number of failures of the hi trigger to record an event above the appropriate energy levels must be quantified. For the 2009 data, the threshold being 48.88 MeV, and using the standard deviation of 2.06 from above, this means that the invariant mass cutoff is 3.2 σ away from the trigger threshold. This requires a small (on the order of 10^{-4}) correction for the 2009 data run period for the number of pion decay counts for that run period when the acceptances are put into the simulation for the final analysis. However, the 2010 data shows a 1.55 σ separation from this cutoff threshold. This requires a bigger correction, on the order of nearly 5%. Apriori then, an expected raw branching ratio, number of pion decays divided by the number of Michel decays, is expected to be about 5% lower for the 2010 data then that of the 2009. The exact value and its uncertainties are quantified in the Monte Carlo simulation by reproducing the hi trigger Michel Gaussian like edge in these events. This is accomplished by using the cumulative distribution function of the Gaussian distribution where the mean and sigma are determined by the above fit. This effectively convolves the Gaussian distribution with the high energy regime of the Michel spectrum, reproducing the features of Fig 7.101. Once this is done, the number of pion decay events that fail this trigger threshold is determined through invariant mass requirements and the total CsI energy. A small correction due to a similar feature in the Michel positron count is not necessary from the hi trigger because the Michel cutoff in invariant mass is at 125 MeV which is sufficiently far away from the trigger thresholds.

These corrections assume that the triggers themselves suffer from no inefficiencies due to electronics dead time, signal pileup or other unavoidable circumstances. This may be checked by observing the number of events where a particular trigger fired divided by the number of events where any of the triggers fired. In the PEN experiment, there are three main triggers. The first is TR0, which represents the lowest positron energy trigger is dependent only on a signal in the hodoscope and is prescaled by a factor of 64, 128 or 256 depending on the run period. The medium calorimeter energy trigger, TR1, is prescaled by a factor of 8, with threshold near 45 MeV in the CsI energy alone. The high energy trigger, TR2, is not prescaled and fires when the energy in the CsI is higher. In order for an event to be recorded, one or more of these triggers must have fired. As the energy in the CsI increases, the efficiency of the triggers should increase.

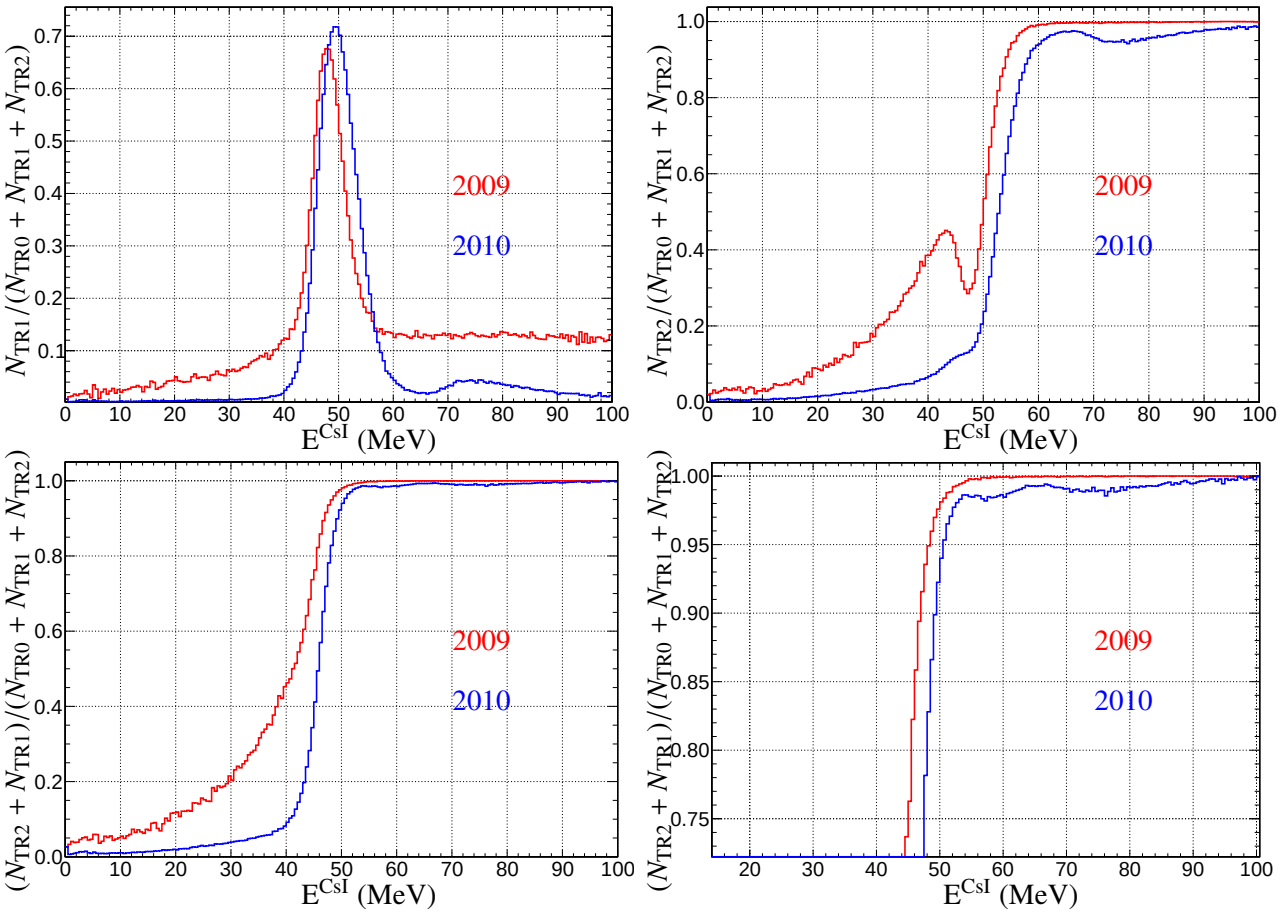

Figure 7.105: *Upper Left: Medium trigger efficiency. Upper Right: High trigger efficiency. Lower Left: Combined medium and high trigger efficiency. Lower Right: Combined medium and high trigger efficiency zoomed.*

In Fig 7.105 shown above, the high energy trigger shows a clean response as practically all the events beyond 55 MeV signals a high energy trigger recording properly for the 2009 data run. However, the 2010 run shows not only an inefficient trigger, but also some electronic distortion in the high energy regime. This complicates the analysis, of the acceptances as these distortions must either be included in the Monte Carlo simulation or a correction for this distortion has to be made in the final analysis.

As in most experiments, the physical implementation of the PEN trigger brings about certain distortions that must be examined in a 10^{-4} level analysis. It should be noted that since the low energy trigger is energy independent, if this were the only trigger available, the number of pion decays to muon decays recorded would be comparable to Standard Model value (accounting for acceptances) there would just be fewer recorded. As pointed out, higher-threshold triggers implemented to count more higher energy events relative to the lower energy events, so in the PEN experiment, more than one trigger is allowed to fire, For

example, a 70 MeV positron, would pass through the hodoscope, firing the low energy trigger, and initiates an electromagnetic shower with energy eventually added up in the form of ADC channels. Once it passes a particular value, roughly 45 MeV, the medium energy trigger fires, and after passing roughly 50 MeV, the high energy trigger fires. The weighting, or prescaling, for the event depends on which trigger fires, using the highest energy threshold exceeded to determine the weight. So in the PEN experiment, it is not a problem for the analysis to account for all or nothing triggers, but rather one does have to consider consequences of this particular scheme, the biggest of which is corrections to weighting.

Improper weighting can arise from two main sources. The first is that the trigger number is recorded incorrectly (which would be a little more problematic) and the second is due to inefficient triggering that over-or under counts background or signal. A simple example would be to consider a branching ratio of one and a prescale factor of 2 occurring at anything below a certain energy. As seen in Fig 7.105, the efficiency in the high energy regime for 2010 is about 97%. Imagine the high trigger failing to fire and the low energy trigger being the trigger taken to determine the weight. One of two things will happen in this case. Either, the low energy will increment once, i.e., not met the prescale conditions and the event will not be counted, or the event will be counted and given a weight of two. If given a weight of two, the number of signal events is over counted. If not counted, then the very next event to trigger the lo energy is the Michel background (due to the energy regime in which it falls) and this will produce a weight of two in the Michel background event where it should not have been the case. This back and forth over/under counting occurs throughout the experiment. Statistically, in the end, the weights should wash out at least to the desired precision. While true, the effect depends on the efficiencies, the prescaling factor, and the number of events. This procedure can easily be modeled using the 2010 as an example.

To account for this phenomenon, the CsI responses are needed for both decay channels, which is obtained from the Monte Carlo simulation, the efficiencies, obtained from the data, and the prescale factors for each of the triggers. The responses are trivially turned into a probability distribution which is then transformed into a cumulative distribution function shown in Fig 7.106.

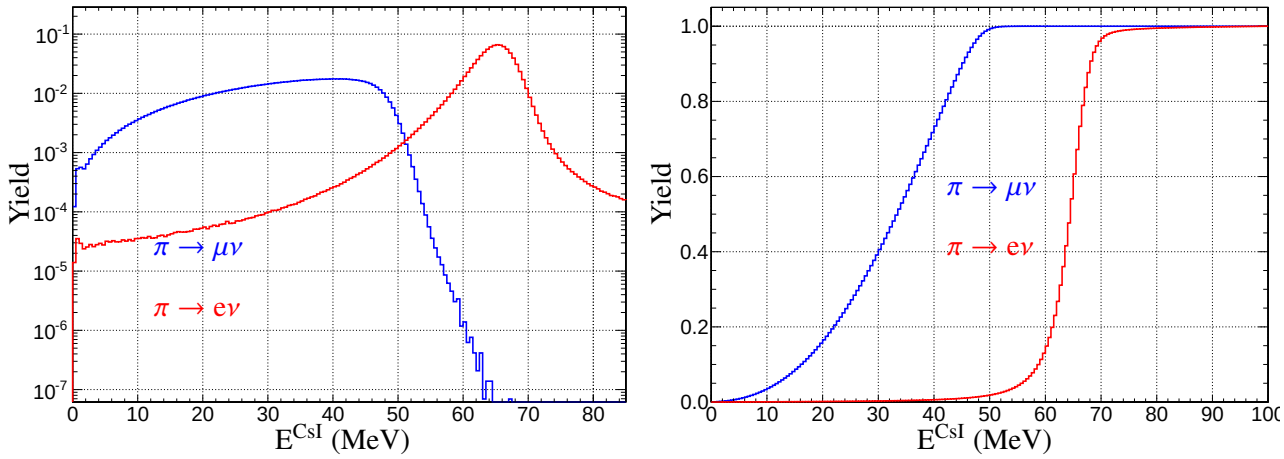

Figure 7.106: *Left: Probability distribution function for the CsI responses from the two processes. Right: Cumulative distribution function of CsI response from the two processes.*

Using the Standard Model branching ratio, accounting for the appropriate time window, the response functions are recreated by throwing a random number between zero and one. Once the energy in the CsI is simulated for a given event, the simulated trigger which fires is determined using the trigger efficiencies above. If the low energy trigger is fired, a counter is incremented by one and the event is not recorded until it reaches the appropriate prescale factor, 128 and 8 for low or medium energy triggers for 2010. By construction, the Monte Carlo reproduces the efficiencies of the measured data as indicated in Fig 7.107.

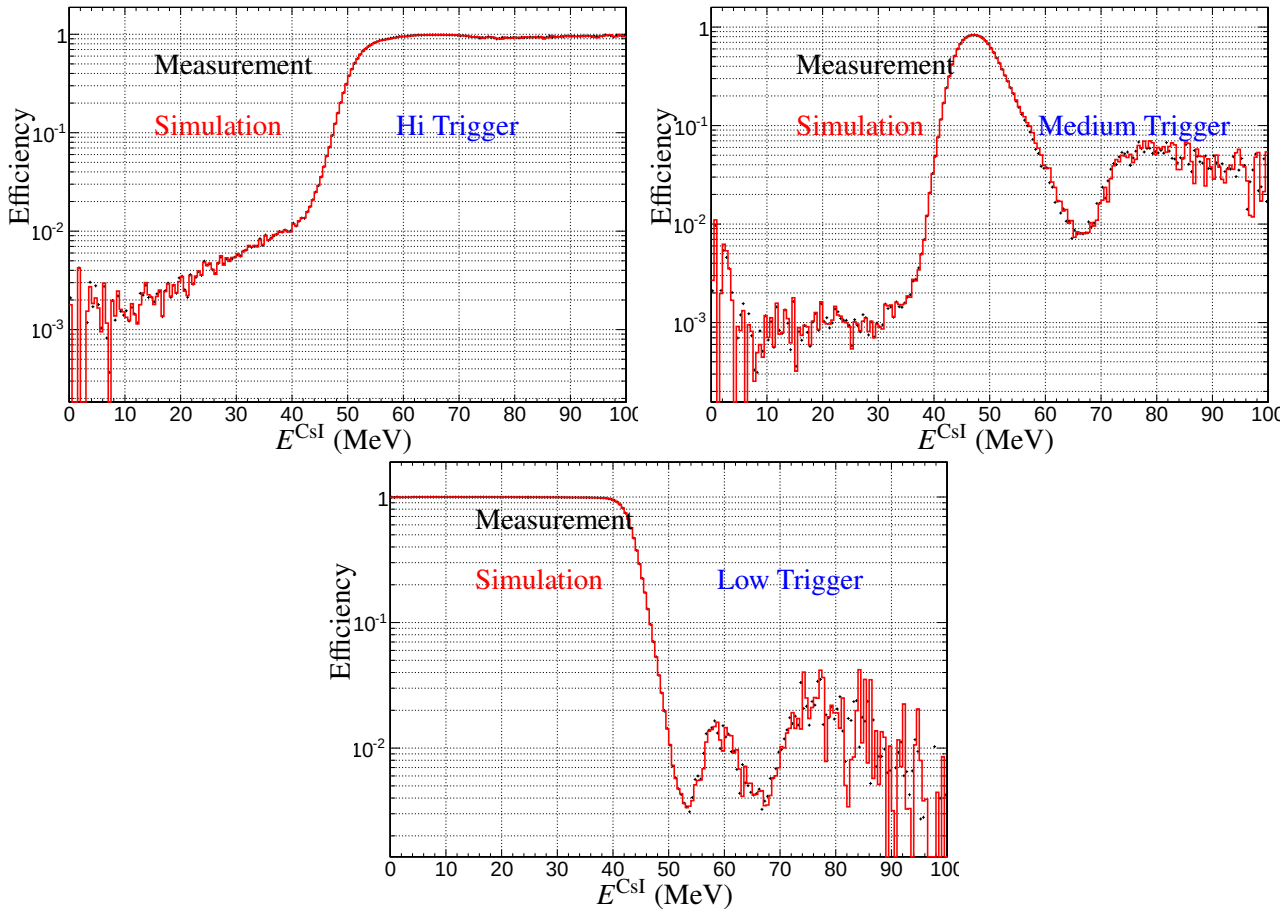

Figure 7.107: *Comparison of simulated trigger efficiency (red) and trigger efficiency from measurement (black) for 2010. Upper Left: Hi trigger. Upper Right: Medium trigger. Bottom: Low trigger.*

With these efficiencies put into the Monte Carlo, a comparison between the thrown branching ratio and the recovered branching ratio can be done by performing integration on the spectra when they are filled by the thrown values and when they satisfying the prescaling requirements.

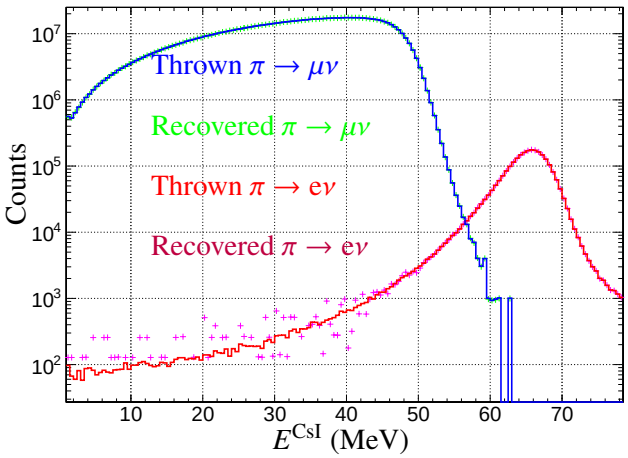

Figure 7.108: *Energy spectrum of thrown and recorded energies using Monte Carlo simulation to recreate the effect of prescaling and trigger inefficiencies that lead to "incorrect" prescaling.*

The prescaling effect is easy to see in the lower energy of the $\pi \to e\nu$ spectrum in Fig 7.108. Relatively fewer events end up producing an incorrect reconstructed number of events that actually occurred because of prescaling. As more events are more prevalent with a lower prescaling value, the total number of events recovered converges to the total number of events thrown. The integral of the Michel events with the prescale factor should be compared to the number of Michel events counted in the experiment and any correction resulting in difference from thrown and reconstructed be accounted for. While a preliminary check for the 2010 data run shows a correction on the order of 10^{-4} needed, the final analysis should include a slight difference in the prescaling factor for the low energy trigger for the first 800 runs in the 2010 data set to properly account for this deviation. The 2009 data set can be done in a similar manner, however, the exclusivity of 2010 doesn't apply, so more than one trigger can fire and be recorded. However, when multiple triggers fire, the higher energy, lower prescale factor should be analyzed. Since the 2009 hi energy trigger is very efficient, the 2009 data set will require a minimal correction, if any, based on trigger inefficiencies.

The second cause of improper weighting would be due to the incorrect weights or trigger values being recorded. Since the weights were determined during the running time, it is possible that some of the events may have the wrong weight recorded due to the complex nature of the triggers, in particular the exclusivity setup for 2010. The possibility should be carefully examined and either eliminated or corrected prior to the final branching ratio analysis. Without unblinding, expectation of the branching ratio deviation can be deduced by normalizing the 2009 and 2010 events to the $\pi \to e\nu$ peak, which will only have weighting of one to each other and see if any discrepancies are seen between the two data sets.

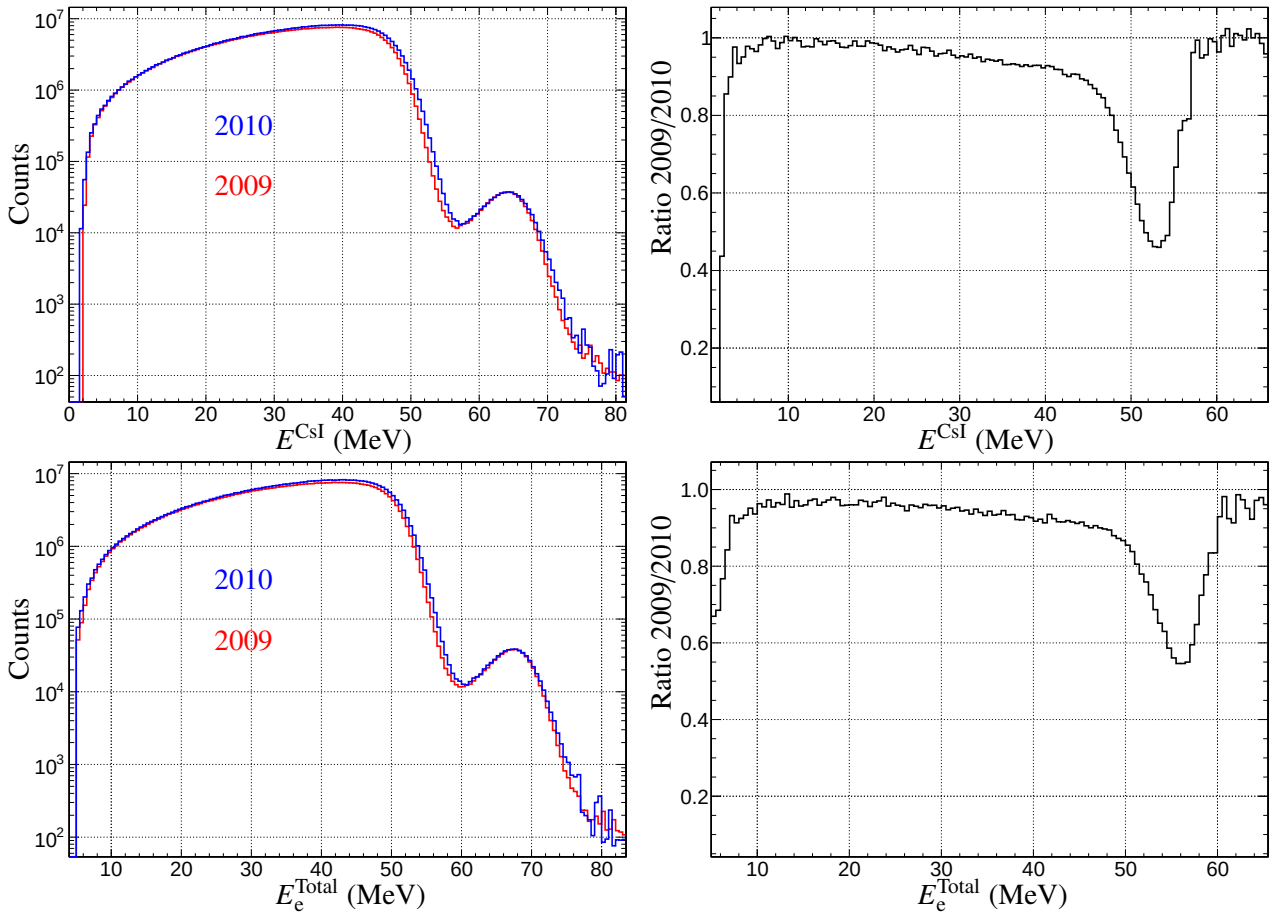

Figure 7.109: *Left: Comparison of 2009 and 2010 CsI energies. Right: Ratio of the two years. Bottom: Same figures but with total positron energy to show that this effect is not due to energy smearing in the target.*

Fig 7.109 shows that indeed there is a discrepancy between the 2009 and 2010 data sets. Given that there appears to be an over abundance of Michel decays most prominent at the high and medium energy trigger thresholds, this could be due to incorrect weighting in real time. This may be remedied using the TDCs values of the triggers and/or quantifying incorrect weighting and implementing them in the Monte Carlo. This procedure should be folded in with the evaluation of the acceptances and thus saved for the final analysis. Because of this feature, the preliminary uncorrected value for the 2010 branching ratio is expected to be smaller than the 2009 value.

7.14 Branching Ratio Extraction

Now that all of the values have been determined, it is time to put them all together. With the two different cuts that are used to identify Michel positrons and positrons originating from pions, pileup and $\Delta\chi^2$, the branching ratio determination is given by

$$B = \underbrace{\frac{N^{peak}_{\pi\to e\nu}}{N_{\pi\to\mu\nu}}}_{r_N}(1+\epsilon_{tail})\underbrace{\frac{\epsilon(E_{\mu\to e\nu\bar{\nu}})_{MWPC}}{\epsilon(E_{\pi\to e\nu})_{MWPC}}}_{r_\epsilon}\underbrace{\frac{f_{\pi\to\mu\to e}(T_e)}{f_{\pi\to e\nu}(T_e)}}_{r_f}\underbrace{\frac{A_{\pi\to\mu\to e}}{A_{\pi\to e\nu}}}_{r_A}\underbrace{\frac{\epsilon_{pileup}}{\epsilon_{\delta\chi^2}}}_{r_{cut}} \tag{107}$$

With the associated error

$$\frac{\delta B}{B} = \sqrt{\left(\frac{\delta r_N}{r_N}\right)^2+\left(\frac{\delta\epsilon_{tail}}{1+\epsilon_{tail}}\right)^2+\left(\frac{\delta r_\epsilon}{r_\epsilon}\right)^2+\left(\frac{\delta r_f}{r_f}\right)^2+\left(\frac{\delta r_A}{r_A}\right)^2+\left(\frac{\delta r_{cut}}{r_{cut}}\right)^2} \tag{108}$$

As seen in the previous sections, the minimal error in the branching ratio is not trivial. The error in the tail depends on where the cutoff energy is chosen which in turn affects the error in the number of events because of subtraction of the Michel background. A particular decay time window is used to diminish the number of Michel events. A smaller decay time window diminishes the number of Michel events but also diminishes the number of signal events. A cut on $\Delta\chi^2$ is used to mitigate the effect of the subtraction. The more stringent the cut, the greater the uncertainty from the cut but the smaller the subtraction needed. The minimized error is achieved by determining which selection in this case the decay time, $\Delta\chi^2$, and tail/peak cutoff results in the smallest error. By adding in quadrature the error in the number of events after subtraction, the tail, and the $\Delta\chi^2$, the minimum was selected for the result of this analysis. The end point of the decay time was incremented by 0.25 ns starting from 90 ns and ending at 90 ns. The $\Delta\chi^2$ varied from -1.2 by 0.01 to -0.2. The peak/tail cutoff value scanned between 110 MeV to 120 MeV in increments of 0.5 MeV. This is demonstrated in Fig 7.110 below.

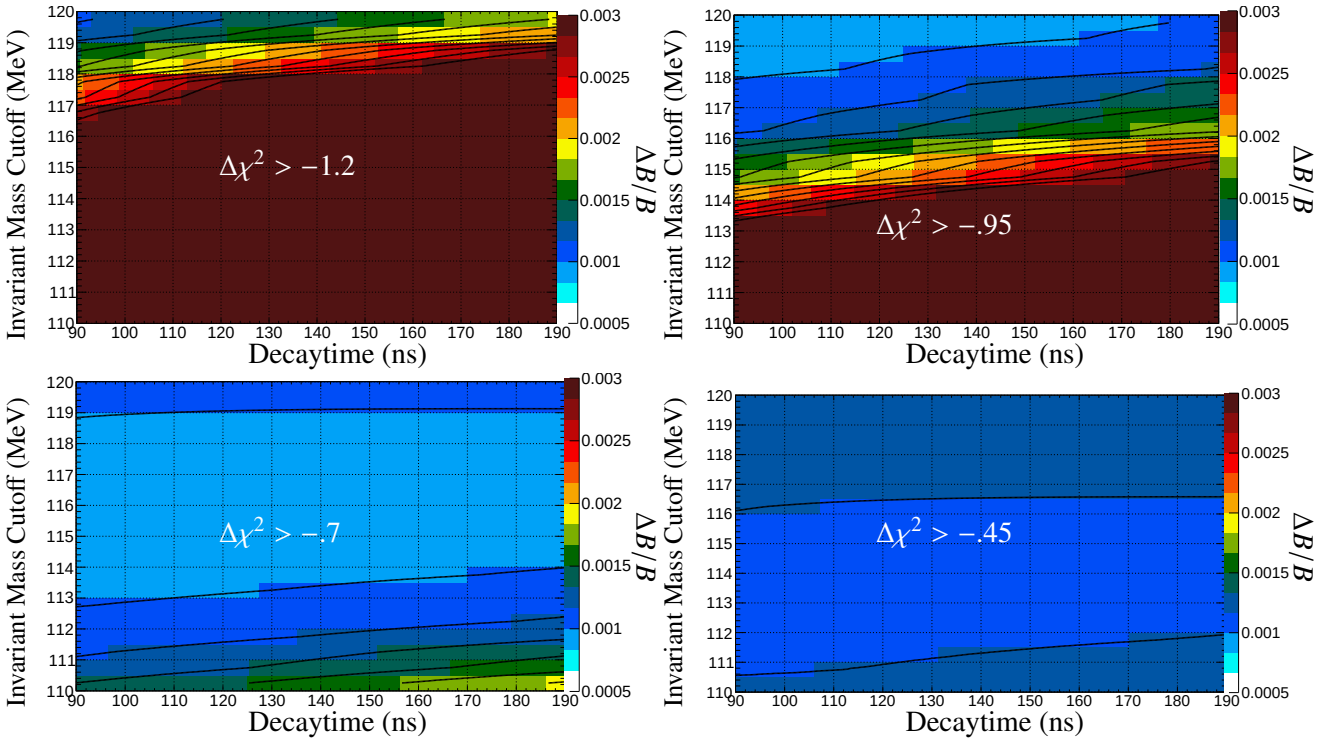

Figure 7.110: *Uncertainties in the branching ratio as a function of decay time and cutoff selection with various* $\Delta\chi^2$ *cuts for 2010. Upper Left;* $\Delta\chi^2 > -1.2$. *Upper Right:* $\Delta\chi^2 > -.95$. *Lower Left:* $\Delta\chi^2 > -.7$. *Lower Right:* $\Delta\chi^2 > -.45$.

The minimized relative uncertainty for the 2009 data set occurs with $\Delta\chi^2 > -.83$, `decaytime` <95.5 ns, and cutoff at 117.5 MeV. The minimized relative uncertainty for the 2010 data set occurs with $\Delta\chi^2 > -.80$, `decaytime` <93.5 ns, and at cutoff of 117.5 MeV. Not unsurprising, the $\Delta\chi^2$ cut is roughly the same for the two years as this cut is fairly insensitive to the decay channel near -1. In combining the data, we use the same cuts for all data. Since there is little change in going from -0.83 to -0.80 in the $\Delta\chi^2$ cut for a given year in terms of overall relative uncertainty, we choose the 2010 configuration providing -0.80 for $\Delta\chi^2$, cutoff of 117.5 MeV, and a `decaytime` between -5 ns and 93.5 ns for the combined data.

8 Results and discussion

> Success is the result of perfection,
> hard work, learning from failure,
> loyalty, and persistence
>
> Colin Powell

This section reviews the analysis, the cuts, and the results. The goal is to obtain the branching ratio $\Gamma(\pi \to e\nu(\gamma))/\Gamma(\pi \to \mu\nu \to e\nu\bar{\nu}(\gamma))$. This proceeded by ensuring that the data set contains only the two processes of interest, or at least no statistically significant background. In the data set, these are hadronic events, scattered beam positrons, scattered beam pions, $\pi \to eee\nu$ and $\mu \to eee\nu$, and decays in flight. Beam contamination was eliminated through cuts on time of flight between B0 and degrader and energy deposition in the degrader. Scattered beam positrons and pions were eliminated through the requirement of positron originating from the target (vertex quality) using the MWPCs information. Hadronic events were eliminated by cuts on the energy and dE/dx in the hodoscope. The three lepton decays were eliminated requiring that only one charged track exists as determined with the MWPCs. Since decays in flight may not be cut easily, they must be accounted for in the simulation acceptances provided the simulation accurately portrays the features of decays in flight. This was shown to be the case. The remaining events were the two channels of interest. In order to obtain the number of $\pi \to \mu\nu \to e\nu\bar{\nu}(\gamma)$, $N_{\pi\to\mu\nu}$, a time window was chosen so as to eliminate $\pi \to e\nu$ contamination beyond statistical significance while ensuring that the time window added no new systematic uncertainties due to the time window chosen while still maintaining a sufficiently high number of events such that the uncertainty in the number of Michel decays is negligible. The events with invariant mass less than 125 MeV were counted after a pileup cut and subtraction and this provided the value and uncertainty for $N_{\pi\to\mu\nu}$. The number of $\pi \to e\nu(\gamma), N_{\pi\to e\nu}$, is obtained with the same pileup cut. A $\Delta\chi^2$ selection is used and the efficiency of the cut is accounted for by both simulation and measurement. A time window is obtained so that the relative error in the branching ratio is minimized accounting for the statistical error of the peak events, the subtraction of Michel events leaking into the peak region, the tail fraction uncertainty, and the $\Delta\chi^2$ efficiency and associated error. The events in the peak region are those that are above 117.5 MeV in the invariant mass. The decay time window is taken from -5 ns to 93.5 ns. Table 13 below lists the aforementioned cuts along with all the other cuts used in the analysis of the two

years of PEN data.

Table 13: *Summary of all cuts used in the analysis.*

Observable	2009	2010
Time of flight `tof`	25.5 <`tof` < 29	25 <`tof` < 27.5
Degrader Energy `edeg`	3.75 <`edeg`< 7	6.5 <`edeg`< 10
θ_{track}	$45 < \theta < 135$	$45 < \theta < 135$
Radial stopping `rstop`	`rstop`< 9.5	`rstop`< 12
Energy Hodoscope `epv`	.4 <`epv`< 2	.4 <`epv`< 2
Hodoscope dE/dx `totaldedxpv`	`totaldedxpv` < 2.75	`totaldedxpv` < 2.75
Vertex quality `vtx qual2`	0 <`vtx_qual2`< 10	0 <`vtx_qual2`< 10
Number beam particles	`nbeam` = 1	`nbeam` = 1
Number charged particle	`ncharged` = 1	`ncharged` = 1
Target rest energy	`Restwave`> −5	`Restwave`> −5
Pileup	`ppileup` < −2	`ppileup`< −3.5
$\Delta\chi^2$ $\pi \to e\nu(\gamma)$ $\pi \to \mu\nu(\gamma) \to e\nu\bar{\nu}(\gamma)$	 $\Delta\chi^2 > -.8$ no cut	 $\Delta\chi^2 > -.8$ no cut
Invariant mass $\pi \to e\nu(\gamma)$ $\pi \to \mu\nu(\gamma) \to e\nu\bar{\nu}(\gamma)$	 117.5 <Mass< 180 0 <Mass< 125	 117.5 <Mass< 180 0 <Mass< 125
Decay time $\pi \to e\nu(\gamma)$ $\pi \to \mu\nu(\gamma) \to e\nu\bar{\nu}(\gamma)$	 −5 <`decaytime`< 93.5 |`decaytime` − 131.423| < 50	 −5 <`decaytime`< 93.5 |`decaytime` − 131.423| < 50

Subsequent to applying the cuts, the tail fraction was determined through the Monte Carlo simulation. This was achieved by simulating each of the crystals (all 240) individually consistent with the simulation by applying photoelectron statistics and digitizing the energy in the form of ADC values. The simulation was compared to the measured data for the tail region obtained from tail trigger events. The uncertainty in the tail was determined by varying the gains of the invariant mass peak effectively characterizing the uncertainty in the peak and its effect on the tail fraction as a function of the energy cutoff. In addition, the different models of the photonuclear physics were implemented at the highest deviations from the mean and its effect on the tail fraction was observed.

The uncertainty in the time window was calculated from theory and depended only on the uncertainty in the experimental timing. The uncertainty in time was determined using the known RF frequency of the cyclotron at PSI as well as the pion flight time from the degrader to stop, and the positron flight time from the target to the hodoscope. The acceptances will be determined using the ultra-realistic Monte Carlo

simulation that was constructed for this experiment. Finally the efficiencies for the detector were determined and were put into the Monte Carlo, but not used so as to maintain blindness. Specifically the product of the acceptances and the efficiencies were kept secret. However, the efficiency and uncertainty of the $\Delta\chi^2$ cut was determined in order to "semi-unblind" the result. The results are tabulated below.

Table 14: *Summary of results. Note f, r_f have no uncertainties listed because the relative uncertainties are lower than* 10^{-4}.

Value	2009	2010
r_A	*	
r_ϵ	*	
$f_{\pi\to\mu\nu\to e\nu\bar{\nu}}$	0.0428777	
$f_{\pi\to e\nu}$	0.972446	
r_f	0.0440926	
ϵ_{cut}	0.984936 ± 0.00043	
r_{cut}	1.01529 ± .00040309	
$\epsilon_{\text{tail}}(117.5\text{MeV})$	0.038037 ± 0.000396	
$N_{\pi\to\mu\nu}$	$(5225.68 \pm 0.23) \times 10^5$	$(9545.50 \pm 0.33) \times 10^5$
$N_{\pi\to e\nu}$	$(1409.43 \pm 1.18) \times 10^3$	$(2413.81 \pm 1.63) \times 10^3$
r_N	$(26.9712 \pm 0.0226) \times 10^{-4}$	$(25.2874 \pm 0.0171) \times 10^{-4}$
B	$(1.2534 \pm 0.001282) \times 10^{-4}$	$(1.17509 \pm 0.0010247) \times 10^{-4}$
$\Delta B/B$ (combined)	7.6×10^{-4}	

At first glance, the branching ratio produces a value which is fairly high for the 2009 data set at least compared to the Standard Model predictions. However, the MWPC chamber efficiencies have yet to be included. Already discussed, we know that the Michel positron is less likely to produce a signal in the multi-wire proportional chambers which compromises the ability to reconstruct a charged track. Low energy positrons from Michel decay are more susceptible to track reconstruction failure. Therefore requiring a charged track disproportionately eliminates Michel positrons over positrons from pion decays. Correcting for this will produce an effectively higher count for the Michel positrons which subsequently results in a lower branching ratio. Preliminary work on the chamber efficiencies produce an expected increase in the number of Michel events by a few percent. In addition, the 2010 data set produces a value which is about 6% lower than the 2009 data. This was described in the section 7.13 as an inefficient high energy trigger which produces a correction on the order of 6% which is to be applied in the final analysis to the PEN experiment.

9 Conclusions and reflections

> We're always, by the way, in fundamental physics, always trying to investigate those things in which we don't understand the conclusions. After we've checked them enough, we're okay
>
> Richard Feynman

> The truth is, time marches on and you have two choices: You move forward, come what may, and you experience all the sour and sweet things that fly at you from around corners, or you sit still. Don't sit still.
>
> Suzanne Palmieri

Now that the data, simulation, and analysis have been explained, it seems appropriate to take a step back and reflect upon the work done and to look forward as to what could be done better for future analysis and experiments. This short chapter briefly reviews the results and offers an insight into what should and could be done with the data and simulation. The boundaries set forth on new physics as the uncertainties stand are discussed and the uncertainties as they stand now are compared to the most recent works performed by graduate PhD students in the PiENu experiment performed at TRIUMF [79]. A comparison of systematics between this experiment and the PiENu experiment is discussed. Finally, a reflection on what could have been done better with regards to the current experiment given what is now known and how future experiments investigating the pion electronic decay branching ratio could proceed using the knowledge that the PEN experiment has learned. It should be noted, in comparison to the more recent thesis work released by PiENu, their expected relative uncertainty is on the order of 1×10^{-3}. Currently the PEN experiment should be able to get to a relative uncertainty several times 10^{-4} slightly more precise than the PiENu experiment.

9.1 To be improved-Why Preliminary-Why Blinded?

All of the results, plots and analyses were done on the data comprising specific runs through the years 2009 and 2010. Specifically, runs 12192-18788 for 2010 and runs 88000-94000 for 2009. There are however more runs in these years (roughly 1000 for each) which maybe used depending on the quality of the data. This would require quite a bit of work, but would lower the statistical uncertainty in the branching ratio. Data were also taken in the 2008 run period. Some details were mentioned in this work but no analysis of the 2008 data was done here. It was previously explored by Anthony Palladino and Pete Alonzi [8][72] but more needs to be done to properly calibrate these runs due to significantly different triggering conditions and geometry. The data however, are perfectly usable and should be included in the final analysis. The inclusion of this data set is expected to increase the statistics for the signal $\pi \rightarrow e\nu$ channel by nearly one million events which will correspondingly decrease the statistical uncertainty by adding an estimated one million signal peak events.

In addition, work is currently under way on increasing the number of events using the simulation to account for the instability of the branching ratio as a function of higher radial stopping shown in Fig 7.54. While this will introduce new systematics, the improvement of the statistical uncertainties may very well exceed a possible increase of systematic uncertainty, specifically regarding the acceptances of the simulated detector. In the case of 2009, this is more apparent, as more than one million events are lost simply due to energy conditions on a trigger. A possible failure may arise due to the difficulty in reproducing the beam profile at higher radial stopping position due to upstream degraders in the beamline prior to reaching the PEN area. The difficulty in correcting 2009 is exacerbated by the numerous geometric and beam changes that occurred throughout the year. However, this if this systematic can be corrected, this will add another one million peak events. This alone will bring the statistical uncertainty to below 5×10^{-4} when combined with the 2010 data. In addition, if 2008 data is also included then the statistical uncertainty can be brought down further to nearly six million peak events total producing a relative statistical uncertainty $\sim 4.1 \times 10^{-4}$

Finally, a more satisfactory result may be achieved with better evaluations of the cross sections of the photonuclear processes. A future option for the PEN experiment is to characterize the photonuclear cross sections for the detector experimentally in lieu of using the individual nuclear cross sections. If this can be done effectively, then the PEN apparatus may be used to obtain the tail fraction to the desired precision. Alternatively, if one of the two dominant measurements of the photonuclear cross sections for each of the

given nuclei is discredited or supported by a newer measurement, then the uncertainty from the different cross sections may be diminished to a more satisfactory value. In addition to the branching ratio, there are other processes that may be studied that occurred in the PEN experiment, since it is sensitive to other physical processes including the ultra-rare $\pi^+ \to e^+e^+e^-\nu$, and the physics of radiative muon decay.

9.2 For the future experiments

The PEN experiment is an experiment in a long line of experiments that has studied rare pion decays, in particular the electronic decay. Since the 1960's the approach has always been to use electromagnetic calorimeters in order to obtain an increasingly more precise value of the branching ratio. In all of these experiments, the low-energy tail seems to be the most difficult and typically limiting factor in obtaining a precise branching ratio that is competitive with the theoretical predictions. This characterization is not immune to the photonuclear process as has been shown in this work as well as the work done most recently at TRIUMF. Photonuclear physics, however, is very niche and hasn't been truly in the mainstream of nuclear physics for nearly forty years. Future experiments that use CsI, BGO, or NaI scintillators will have to carefully approach the way in which they perform the analysis. In particular, proper characterization of the photonuclear cross sections is an absolute must in order to obtain a branching ratio that will ever be as precise as the theoretical predictions ($< 1 \times 10^{-4}$ relative error). An alternative route is to study the tail using a beam of monoenergetic positrons by spraying the EM calorimeter with beam positrons with varying energy levels from the near 70 MeV (the rough energy produced from pion decays) to 62 MeV. A small correction may be necessary for incorporation of the actual radiative decay in this method. It may also mean that the electromagnetic calorimeters are getting to the limits of their ability to characterize the responses to the desired precision of these experiments.An alternative method of detection may be required by future experiments and new techniques may be required. Whichever route is preferred, only time will tell.

9.3 Reflection-Woulda Shoulda Coulda What If

Hindsight is 20-20, but foresight is indispensable. Unfortunately, more could have been exercised in the execution of this experiment (and any experiment for that matter). The biggest systematic in this experiment

follows from energy resolution of the CsI calorimeter which systematically affects the tail fraction and the peak count in the response toward pion decays in the CsI calorimeter. The full width half max of the decay positron from a pion is roughly 11% for the CsI calorimeter, whereas it is roughly 2% in the PiENu experiment conducted at Triumf[79]. Part of this resolution difference is due to pure CsI lacking good energy resolution whereas doped inorganic scintillators produce more photoelectrons per MeV deposited. It is also due in part to various crystals underperforming because of non-uniformities, as well as aged crystals and PMTs. The total CsI response for all events adds the different responses for all of the individual crystals. This is most easily seen in Fig 6.43 and in the comparisons of 200 crystals for measurement and simulation in the appendix. It should be pointed out that CsI was used in the PiBeta experiment because of the fast response needed for a very rare decay which required a higher beam rate. In PiBeta experiment, energy resolution was less of an issue as the signal was two well separate photons with roughly 65 MeV. In the PiENu experiment, the Michel edge is around 55 MeV with few discriminating cuts used in the analysis. This energy spectrum, would lead to an invariant mass Michel edge, if they had the PEN setup, of roughly 110 MeV with very few cuts to eliminate unwanted Michel events. The best PEN could do, at least for the main analysis, is 117.5 MeV with very complicated cuts drawn from the target response. If PEN were to achieve a 110 MeV with less restrictive cuts, then using the more complex cuts, most notably $\Delta\chi^2$, arguably a Michel edge close to 105-110 MeV could be achieved which would substantially reduce the error associated with the tail fraction. Or the requirement of the $\Delta\chi^2$ cut would not be needed, as this cut has a fairly high systematic built in and perhaps a different discriminating observable could be used. In addition, if PEN had calibrated the calorimeter with monoenergetic positrons with various energies, the gains, photoelectron statistics, and even the cross sections could arguably be accounted for and the only remaining necessary task in the simulation would be to match the stopping distribution which is achievable. However, due to the design, spacing and other technical aspects this was not feasible in the PEN experiment. Looking forward to future experiments, this would be a necessity in order to push the experimental branching ratio below the theoretical value to the $\sim 10^{-5}$ relative uncertainty.

The second biggest systematic in the experiment are from trigger effects either from the pion radial stopping position in the 2009 data set or the 2010 hi energy trigger. The elimination of a good portion of the data because of broad beam profile diminished the number of usable events in the 2009 data set which could be recovered using a bigger target. Originally, the PEN trigger was going to involve solely

the CsI energy response and therefore a bigger target would not be advantageous due to energy smearing in the target which would add an extra layer of systematics. Thus a smaller target was decided upon. The problem with this systematic was of course exacerbated by the trigger condition to eliminate scattered beam positrons, requiring a minimum energy deposition at the positron target time. In addition, there were also grouping of run periods where the mTPC failed to produce a signal completely which forfeits their usability in the branching ratio analysis because of this radial stopping systematic. The 2010 data set has its own complications due to high energy triggering conditions. The electronic distortion most likely resulting from the exclusivity of the trigger conditions can be overcome by inputting it into the Monte Carlo simulation, however, to get this effect to the level of 10^{-4} requires yet much work.

Time marches on, or as I like to say, "Physics doesn't physics itself." There is yet still much to do in the grand scheme of things pertaining to not only this experiment but also experiments which probe the very fabric of our universe. Those that would test the Standard Model to a level of precision never done before are always on the horizon. Newer more precise experiments or higher energy colliders are always in the minds of particle and nuclear physicists alike. The very reason scientists, and in particular this author, endeavors to study science is not only the enjoyment that comes when curiosity is satisfied, but also because that the field is still somewhat uncharted. Very much like Magellan, scientists are explorers. Though not exploring the uncharted seas of the Earth, but rather exploring the uncharted possibilities of existence. And that is the great exploration.

References

[1] R. Aaiji et al. Phys Review Lett **115** 111803 (2015).

[2] R. Abela et al., Phys.Lett. **105B**, 263 (1981).

[3] Acqiris (now Agilent Technologies). Acqiris High-Speed compact PCL Digitizers, Model DC282. Technical report.

[4] B. Aharmin et al. Phys. Rev. C, **72** (5): 055502 (2005).

[5] S. Agostinelli et al. Nuclear Instruments and Methods in Physics Research Section A. **506**, 3 250 (2003).

[6] H.L. Anderson and C.M.G Lattes, Nuovo cimento **6**, 1356 (1957).

[7] H.L. Anderson, T. Fujii, and R.H. Miller. Phys.Rev. **119**:2050, 1960.

[8] L. Alonzi Thesis. *Measuring the Pion Substructre with Radiative Positronic Pion Decays* (2011).

[9] Y. Ashie et al. Phys. Rev. Lett., **93** (10):101801 (2004).

[10] Atlas Collaboration. Physics Letters B. **716**, 1 (2012).

[11] G. Azuelos et al., Phys. Rev. Lett. **56**, 2241 (1986).

[12] J.A. Bailey et al. Phys. Rev. Lett **109**, 071802 (2012).

[13] G. C. Baldwin and G. S. Klaiber, Phy. Rev. **73**:1156 (1948).

[14] R. Bergere, et al. Nuclear Physics **A133** 417-437 (1969).

[15] B.L. Berman, et al. Physical Review **162** 4 (1967).

[16] F. Bloch and A. Nordsieck, Phys. Rev. **52** 54 (1937).

[17] R.L. Bramblett, et al. Physical Review **148** 3 (1966).

[18] D.I. Britton, et al. Physical Review D, **46**:3, 885-887 (1992).

[19] D.I. Britton, et al., Phys. Rev.D **49**, 28 (1994).

[20] R. Brun and F. Rademakers, Nucl. Inst. an Meth. in Phys. Res. A **389** 81-86 (1996).

[21] D. A. Bryman, P. Depommier, and C. Leroy. Review Section of Physics Letters **88** 3 151-205 (1982).

[22] D.A. Bryman, R. Dubois, T. Numao, B. Olaniyi, A. Olin, et al. Phys.Rev D., **33**:5,1211-1221 (1986).

[23] D. A. Bryman, D.I. Britton, et al. Phys. Rev. Lett **68**:3000-3003 (1992).

[24] D. A. Bryman et al. Nucl Inst. and Methods Phys Res A **621** 188-191 (2010).

[25] D.A Bryman et al. Phys. Rev. Lett. **115**, 071801 (2015).

[26] M. Bychkov, Thesis *A Study of the Structure of the Pi Meson via the Radiative Pion Decay* $\pi^+ \to e^+\nu\gamma$ (2005).

[27] M. Bychkov, Phys. Rev. Lett. **103** 5 (2009).

[28] CAEN Technical Information Manual: MOD. V1720 8 Channel 12 Bit 250 MS/S Digitizer Manual Rev. 26

[29] D Casadei, arXiv: 0908.0130v2 (2009).

[30] Vincenzo Cirigliano and Ignasi Rosell Phys. Rev. Lett., **99**:231801, (2007).

[31] Commins, E.D and Bucksbaum, P.H. *Weak Interactions of leptons and quarks* (1983).

[32] B. Campbell and A. Ismail. *Leptonic Pion Decay and Physics Beyond the Electroweak Standard Model* arXiv:0810.4918.

[33] G. Czapek, A. Federspiel, A. Fluckiger, D. Frei, B. Hahn, et al. Phys.Rev.Lett., **70**:1720, (1993).

[34] M. Daum et al., Phys.Rev.D **36**, 2624 (1987).

[35] S. Davidson, D. Bailey, B. Campbell. Zeitschrift fr Physik C Particles and Fields, **61**:613643, (1994). 10.1007/BF01552629.

[36] E. Di Capua, R. Garland, L. Pondrom, and A. Strelzoff. Phys. Rev.,**133**:B1333B1340, (1964).

[37] J. Donoghue and L. Li. Phyical Review D **19** 3 945 (1979).

[38] K. Eguchi et al., Phys. Rev. Lett **90** 021802 (2003).

[39] J. Evans and N. Nagata. Physical Review D **92**, 015022 (2015).

[40] S. Fajifer, J.F. Kamenik, and I. Nisandzic, Phys. Rev. D **85**, 094025 (2012).

[41] T. Fazzini, et al., Phys. Rev. Letters **1**, 247 (1958)

[42] R. P Feynmann and M. Gell-Mann, Phys. Rev. **109**, 193 (1958)

[43] D.J.S Findlay, Nucl. Instr. and Meth. B **50** 314 (1990)

[44] Markus Finkemeier, Phys. Lett., B**387**:391394, (1996).

[45] Frlez, E. Pocanic, D. Ritt, S. Nuclear Instruments and Methods in Physics Research Sec A. **463** 341-349 (2001).

[46] Gammow, G. and E.Teller Phys. Rev. **49** 895 (1936).

[47] D. Griffiths, *Introduction to Elementary Particles* (2008).

[48] J Grange et al. arxiv:1501.06858v1 (2015).

[49] D.E Groom, S.R. Klein, The European Physical Journal C-Particles and Fields. **15** 1-4 163 (2004).

[50] R.S. Hayano et al., Phys. Rev. Lett **49**, 1305 (1982).

[51] G. Impeduglia et al., Phys. Rev. Letters **1**, 295 (1958).

[52] Karphkhin et al. Instruments and Experimental Techniques **42** 3 335-341 (1999).

[53] Langacker, P. *The Standard Model and Beyond* (2009).

[54] C.M.G. Lattes, H. Muirhead, G.P.S. Occhialini, and C.F. Powell. Nature, **159**:694697 (1947).

[55] A. Leptretre. Nuclear Physics **A219** 39-60 (1974).

[56] W. Li Thesis *A Precise Measurement of the* $\pi^+ \to \pi^0 e^+ \nu$ *Branching Ratio* (2004).

[57] L. Littenberg and R. Shrock. Phys. Rev Lett., **68** (4):443-446, (1992).

[58] T.D Lee and C.N Yang Phys Rev **104**, 254 (1956).

[59] W. Loinaz, N. Okamura, S. Rayyan, T. Takeuchi, and L.C.R Wijewardhana. Phys.Rev.D **70**, 113004 (2004).

[60] L. Mandel. Proc. Phys. Soc. **74** 233 (1959).

[61] William J. Marciano and A. Sirlin. Phys. Rev. Lett.,**71**(22):36293632, (1993).

[62] E. Mathieson Nuclear Instruments and Methods in Physics Research A **270** 602-603 (1988)

[63] S. Mele. The Measurement of the Number of Light Neutrino Species. 60 Years of Cern Experiments and Discoveries 89. (2015).

[64] L. Michel Proc Phys. Soc A**63** 415 (1950)

[65] E. Munyangabe Thesis. *Measurement of the Radiative Muon Decay as a Test of the V − A Structure of the Weak Interactions* (2006).

[66] M. Musolf, Phys. Rev. D**76** 095017 (2007)

[67] R/ Mudegger Thesis. *Optimizing the charge division Algorithm for the mini-TPC used in the tracking of the PEN experiment* (2012).

[68] S. H. Neddermeyer and C. D. Anderson. Phys. Rev. **51**(10):884886, (1937).

[69] K Nakamura and Particle Data Group. Journal of Physics G; Nuclear and Particle Physics, **37**(7A):075021 (2010).

[70] G.P.S. Occhialini and C.F. Powell. Nature, **159**:186190, (1947).

[71] N.De Leener-Roser et al., Phys. LettB **177**, 228 (1986).

[72] A. Palladino Thesis. *Investigating Lepton Unverisality via a Measurement of the Positronic Pion Decay Branching Ratio* (2012).

[73] J. Pati and A. Salam, Physical Review Letters **31** 10 661 (1973).

[74] J. Pati and A. Salam, Phy Rev D **10** 1 275 (1974).

[75] D Pocanic et al. Phys Rev Let **93** 181803 (2004).

[76] Schroeder, P. *Introduction to Quantum Field Theory* (1995).

[77] M. Schwartz, Quantum Theory of Fields and Particles.

[78] E. C. G Sudarshan and R. Marshak. Phys.Rev. **109**, 1860, (1958).

[79] T. Sullivan Thesis. *A high-precision measurement of the $\pi \to ev$ branching ratio.* (2017).

[80] M. Tanabashi et al. Phys Rev. D **98** 030001 (2018).

[81] C.S Wu et al Phys Rev **105**, 1413, (1957).

[82] H. Yukawa, I. Proc. Physico-Math. Soc. Japan, **17**:4857, (1935).

[83] H. L. Riedman and J. Ranwater, Phys.Rev. **84**, 684 (1949)

[84] R. Smith. Thesis. *Radiative Muon Decay Measurements of the Branching Ratio* (2020).

[85] J.Steinberger and S. Lokanathan Suppl. Nuovo cimento 1, **151** (1955)

[86] J.Steinberger, Phys.Rep. **203**,345 (1991)

[87] J. D. Ullman, H. Farauenfelder, H.J. Lipkin, and A. Rossi. Phys Rev. **122** 2 (1961)

[88] B. VanDevender, Thesis. *An Experimental Study of Radiative Muon Decay* (2006).

[89] M. Vitz. Thesis. *Numerical Considerations in the Analysis and Simulation of Radiative Pion Decay* (2019).

[90] S Weinberg, *Quantum Field Theory* vol1 (2005).

[91] G.T. Wright. Phys. Rev.**91** 1282 (1953).

[92] V. Varlamov et al. Eur. Phys. J. A. **50**:114 (2014).

A Appendix A - Derivation of Decay Rates

There are no great limits to growth
because there are no limits of
human intelligence, imagination,
and wonder

Ronald Reagan

The writer of this work wanted to include this particular section because more often than not a reader may want to see where the theory originates from first principles. Often textbooks outline these types of calculations but seeing it in its entirety should useful. Starting out with deriving the decay rate from Fermi's golden rule and then reviewing some tricks involving gamma matrices, this will enable the reader to follow along the calculation of the 2-Body Decay as well as (hopefully) the pion radiative decay.
Here it will be shown how the full decay rate is derived. However, the Feynman rules for the Matrix element calculation will not be derived. This is something to be done in a quantum field theory class, and is found by looking at the Standard Model Lagrangian. Starting from Fermi's golden rule:

$$\Gamma_{i\to f} = 2\pi|\langle f|H_{int}|i\rangle|^2\rho(\Sigma E_i - \Sigma_f E_f) \tag{A.1}$$

In this equation, ρ is the density of states which enforces conservation of energy and momentum. Upon working with this term, one obtains the kinematics of a particular interaction. Whereas, the H_{int} term is dependent on the type of interaction that is being observed. (Which makes sense since it is the interaction term in the Hamiltonian).

A.1 Michel/Electronic (2-Body Decay)

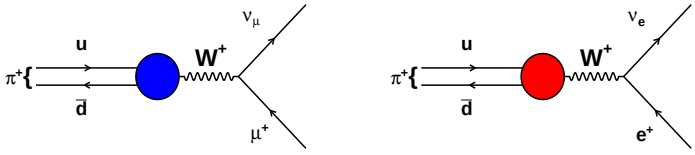

Figure A.1: *Pion 2 Body Decay*

The kinematics of a 2-body decay is well understood and here it will be reviewed for the benefit of the reader. This will enable full understanding of the calculation of the decay rates of the pion into a muon or positron. The small difficulty in worrying about this particular type of decay is the interaction of the pion with the W^+ boson. The pion is a composite particle, so simple Feynman rules are not so simple or at least not that obvious. We can make headway based on Lorentz invariance. The lepton current is pretty straightforward:

$$j_l^\gamma = \bar{u}(\nu_e)\gamma^\mu(1-\gamma^5)\bar{v}(l^+)\frac{g_w}{2\sqrt{2}} \tag{A.2}$$

The term on the far right is the coupling of the interactions, the $\gamma^\mu(1\text{-}\gamma^5)$ is the $V-A$ interaction that spoken of in chapter two, and the $\bar{u}$ and $\bar{v}$ are the dirac spinors of the ν and lepton respectively. But what about the interaction of the W^+ boson with the quarks? One would expect something of the effect of $\frac{g_w}{2\sqrt{2}}O$, where O is some kind of operator that would act similarly to to the gamma matrices of the leptonic current. This operator is the second half of the matrix element for this process and since the lepton current is a vector, in order for $\mathcal{M}$ to be Lorentz invariant, this operator must also be a vector. So this could be a vector, axial vector, or a combination. But given the fact that the pion is a pseudoscalar particle, we should expect a vector. The only vector available to us is the four-momentum of the incoming pion. So we expect $O = f_\pi p^\mu$, where f_π is some scaling factor called the pion decay constant. In principle this constant could depend on p^2, but since the pion is on mass-shell, we can say $f_\pi = f_\pi(m_\pi)$= constant. So this will be taken as a constant. So the matrix element is then

$$\mathcal{M} = \frac{g_w^2}{8M_w}f_\pi p_\mu \bar{u}(\nu_e)\gamma^\mu(1-\gamma^5)\bar{v}(l^+) \Rightarrow |\mathcal{M}|^2 = \left(\frac{g_w^2}{8M_w}f_\pi\right)^2\left[p_\mu\bar{u}(\nu_e)\gamma^\mu(1-\gamma^5)\bar{v}(l^+)\right]\times\left[p_\nu\bar{u}(\nu_e)\gamma^\mu(1-\gamma^5)\bar{v}(l^+)\right]^* \tag{A.3}$$

Using Casmir's trick, reviewed in [47], we end up with

$$< |\mathcal{M}|^2 >= \left(\frac{g_w^2}{8M_w}f_\pi\right)^2 p_\mu p_\nu Tr\left[\gamma^\mu(1-\gamma^5)(\not{p}_l - m_l)\gamma^\nu(1-\gamma^5)\not{p}_{\nu_l}\right] \tag{A.4}$$

Working out the traces alone by expanding and letting $\not{p}_l = \gamma^\alpha p_\alpha$ and $\not{p}_{\mu_l} = \gamma^\beta p_\beta$, the trace becomes:

$$Tr(\underbrace{\gamma^\mu\gamma^\alpha\gamma^\nu\gamma^\beta p_\alpha p_\beta}_{1} - \underbrace{\gamma^\mu\gamma^\alpha\gamma^\nu\gamma^5\gamma^\beta p_\alpha p_\beta}_{2} - \underbrace{m_l\gamma^\mu\gamma^\nu\gamma^\beta p_\beta}_{3} + \underbrace{m_l\gamma^\mu\gamma^\nu\gamma^5\gamma^\beta p_\beta}_{4} -$$
$$\underbrace{\gamma^\mu\gamma^5\gamma^\alpha\gamma^\nu\gamma^\beta p_\alpha p_\beta}_{5} + \underbrace{\gamma^\mu\gamma^5\gamma^\alpha\gamma^\nu\gamma^5\gamma^\beta p_\alpha p_\beta}_{6} + \underbrace{m_l\gamma^\mu\gamma^5\gamma^\nu\gamma^\beta p_\beta}_{7} - \underbrace{m_l\gamma^\mu\gamma^5\gamma^\nu\gamma^5\gamma^\beta p_\beta}_{8})$$

Doing this term by term:

Term1: $Tr(\gamma^\mu\gamma^\alpha\gamma^\nu\gamma^\beta p_\alpha p_\beta)$

Term2: $Tr(\gamma^\mu\gamma^\alpha\gamma^\nu\gamma^5\gamma^\beta p_\alpha p_\beta) = Tr(\gamma^\mu\gamma^5\gamma^\alpha\gamma^\nu\gamma^\beta p_\alpha p_\beta)$

Term3: $Tr(m_l\gamma^\mu\gamma^\nu\gamma^\beta p_\beta) = 0$ (Because Tr(odd# of gamma matrices)=0)

Term4: $Tr(m_l\gamma^\mu\gamma^\nu\gamma^5\gamma^\beta p_\beta) = 0$ (Because Tr($\gamma^5\times$ odd# of gamma matrices)=0)

Term5: $Tr(\gamma^\mu\gamma^5\gamma^\alpha\gamma^\nu\gamma^\beta p_\alpha p_\beta)$

Term6: $Tr(\gamma^\mu\gamma^5\gamma^\alpha\gamma^\nu\gamma^5\gamma^\beta p_\alpha p_\beta) = Tr(\gamma^\mu\gamma^\alpha\gamma^\nu\gamma^5\gamma^5\gamma^\beta p_\alpha p_\beta) = Tr(\gamma^\mu\gamma^\alpha\gamma^\nu\gamma^\beta p_\alpha p_\beta)$

Term7: $Tr(m_l\gamma^\mu\gamma^5\gamma^\nu\gamma^\beta p_\beta) = 0$(Because Tr(odd# of gamma matrices)=0)

Term8: $Tr(m_l\gamma^\mu\gamma^5\gamma^\nu\gamma^5\gamma^\beta p_\beta) = -Tr(m_l\gamma^\mu\gamma^\nu\underbrace{\gamma^5\gamma^5}_{1}\gamma^\beta p_\beta) = 0$ (Because Tr(odd# of gamma matrices)=0)

So terms 1 and 6 are the same and 2 and 5 are the same and everything else is 0. Collecting the nonzero terms:

$$2\times Tr(\gamma^\mu\gamma^\alpha\gamma^\nu\gamma^\beta p_\alpha p_\beta) + 2\times Tr(\gamma^5\gamma^\mu\gamma^\alpha\gamma^\nu\gamma^\beta p_\alpha p_\beta) = 2(4g^{\mu\alpha}g^{\nu\beta} - 4g^{\mu\nu}g^{\alpha\beta} + 4g^{\mu\beta}g^{\alpha\nu}) + 2(4i\epsilon^{\mu\alpha\nu\beta})p_\alpha p_\beta$$

So the expression for the matrix element goes from

$$< |\mathcal{M}|^2 >= \left(\frac{g_w^2}{8M_w} f_\pi\right)^2 p_\mu p_\nu Tr\left[\gamma^\mu(1-\gamma^5)(\not{p}_l - m_l)\gamma^\nu(1-\gamma^5)\not{p}_{\nu_l}\right]$$

to

$$< |\mathcal{M}|^2 >= \left(\frac{g_w^2}{8M_w} f_\pi\right)^2 p_\mu p_\nu \times \left[2(4g^{\mu\alpha}g^{\nu\beta} - 4g^{\mu\nu}g^{\alpha\beta} + 4g^{\mu\beta}g^{\alpha\nu}) + 2(4i\epsilon^{\mu\alpha\nu\beta})p_{\alpha,l}p_{\beta,\nu_l}\right] \tag{A.5}$$

Recall that p_ν and p_μ both are momenta vectors for the pion so there product is symmetric with exchange of indices, but μ and ν are antisymmetric with exchange of μ and ν in the Levi-Civita symbol. If two tensors are being contracted with each other and one is symmetric with exchange of indices and the other is antisymmetric, then their contraction must yield 0. Therefore, $p_\mu p_\nu \times 2(4i\epsilon^{\mu\alpha\nu\beta})p_{\alpha,l}p_{\beta,\nu_l}) = 0$ Thus,

$$|\mathcal{M}|^2 >= \left(\frac{g_w^2}{8M_w} f_\pi\right)^2 p_\mu p_\nu \times \left[2(4g^{\mu\alpha}g^{\nu\beta} - 4g^{\mu\nu}g^{\alpha\beta} + 4g^{\mu\beta}g^{\alpha\nu})\right] \tag{A.6}$$

Isolating the tensor products:

$$8p_\mu p_\nu \times \left[(g^{\mu\alpha}g^{\nu\beta} - g^{\mu\nu}g^{\alpha\beta} + g^{\mu\beta}g^{\alpha\nu})\right] = 8(p^\mu p_{\alpha,l} g^\mu_\alpha p^\nu p_{\beta,\nu_l} g^\nu_\beta - p^\mu p_\nu g^\nu_\mu p^\alpha_l p_{\beta,\nu_l} g^\alpha_\beta + p^\mu p_{\beta,\nu_l} g^\mu_\beta p^\nu p_{\alpha,l} g^\nu_\alpha)$$

Recalling, $g^\alpha_\beta = \delta^\alpha_\beta$ and $\delta^\alpha_\beta p^\alpha k_\beta = p \cdot k$. Where $p \cdot k$ is the 4 vector dot product,

$$< |\mathcal{M}|^2 >= \left(\frac{g_w^2}{8M_w} f_\pi\right)^2 \times 8\left(2(p_\pi \cdot p_l)(p_\pi \cdot p_{\nu_l}) - p_\pi^2(p_l \cdot p_{\nu_l})\right)$$

Doing the dot products, notice $p_\pi = p_l + p_{\nu_l}$ and that squaring both sides, gives:

$$p_\pi^2 = p_l^2 + p_{\nu_l}^2 + 2p_l \cdot p_{\nu_l} \Rightarrow m_\pi^2 = m_l^2 + 2p_l \cdot p_{\nu_l} \Rightarrow (p_l \cdot p_{\nu_l}) = \frac{m_\pi^2 - m_l^2}{2} \tag{A.7}$$

Taking $p_\pi = p_l + p_{\nu_l}$ and doing the dot product with p_{ν_l}, we get

$$p_{\nu_l} \cdot p_\pi = p_l \cdot p_{\nu_l} + p_{\nu_l}^2 \Rightarrow p_{\nu_l} \cdot p_\pi = p_l \cdot p_{\nu_l} = \frac{m_\pi^2 - m_l^2}{2} \tag{A.8}$$

Doing the dot product with p_l we find $p_l \cdot p_\pi = \frac{m_\pi^2+m_l^2}{2}$

So from $< |\mathcal{M}|^2 >= \left(\frac{g_w^2}{8M_w} f_\pi\right)^2 \times 8\left(2(p_\pi \cdot p_l)(p_\pi \cdot p_{\nu_l}) - p_\pi^2(p_l \cdot p_{\nu_l})\right)$, we get

$$< |\mathcal{M}|^2 >= \left(\frac{g_w^2}{8M_w} f_\pi\right)^2 \times 8\left(2\frac{m_\pi^2 + m_l^2}{2}\frac{m_\pi^2 - m_l^2}{2} - m_\pi^2\frac{m_\pi^2 - m_l^2}{2}\right) \tag{A.9}$$

This produces the result,

$$< |\mathcal{M}|^2 >= \left(\frac{g_w}{2M_w}\right)^4 f_\pi^2 m_l^2 (m_\pi^2 - m_l^2) \tag{A.10}$$

To get the full decay rate recall

$\Gamma = \frac{|\vec{p}_l|}{8\pi m_\pi^2} < |\mathcal{M}|^2 >$, where from similar arguments from the above $|\vec{p}_l| = (m_\pi^2 - m_l^2)/(2m_\pi)$

So

$$\Gamma = \frac{f_\pi^2}{\pi m_\pi^3}\left(\frac{g_w}{4M_W}\right)^4 m_l^2 (m_\pi^2 - m_l^2)^2 \tag{A.11}$$

Now of course, it has been assumed up until this point that the coupling of the W boson is lepton flavor neutral, ie that the couplings are the same. The assumption may be relaxed by replacing g_W with g_l where g_l is the coupling of a particular lepton flavor, l with the W boson. So looking at the ratio of rates i.e., the branching ratio, we get:

$$\frac{\Gamma(\pi^+ \to e^+ + \nu_e)}{\Gamma(\pi^+ \to \mu^+ + \nu_\mu)} = \frac{g_e^2 m_e^2 (m_\pi^2 - m_e^2)^2}{g_\mu^2 m_\mu^2 (m_\pi^2 - m_\mu^2)^2} \tag{A.12}$$

This is to first order $\delta = 0$ for the theoretical result of the pion electronic decay branching ratio.

A.2 Muon Decay

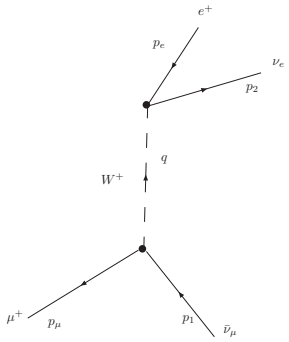

Figure A.2: *Muon decay Feynman Diagram*

The derivation of the muon lifetime/decay rate will follow closely to Weak Interactions [31]. The differential decay rate is given by :

$$d\Gamma = |\mathcal{M}|^2 \frac{1}{2m_\mu}\left[\frac{d^3\vec{p}_e}{(2\pi)^3 2E_e}\frac{d^3\vec{p}_1}{(2\pi)^3 2E_{\nu_e}}\frac{d^3\vec{p}_2}{(2\pi)^3 2E_{\bar{\nu}_e}}\right]\times(2\pi)^4\delta^4(p_\mu - p_e - p_1 - p_2) \tag{A.13}$$

Here :

$$\mathcal{M} = \bar{v}(\mu^+)\frac{g_w}{2\sqrt{2}}\gamma^\mu(1-\gamma^5)u(\bar{\nu}_\mu)\frac{g_{\mu\nu}}{M_w}\bar{u}(\nu_e)\gamma^\nu(1-\gamma^5)\frac{g_w}{2\sqrt{2}}v(e^+) \tag{A.14}$$

which means

$$\mathcal{M} = \left(\frac{g_w}{m_w 2\sqrt{2}}\right)^2 \bar{v}(\mu^+)\gamma^\mu(1-\gamma^5)u(\bar{\nu}_\mu)\bar{u}(\nu_e)\gamma_\mu(1-\gamma^5)v(e^+) \tag{A.15}$$

Using Casmir's trick once again to get the square of the matrix element:

$$\langle|\mathcal{M}|^2\rangle = \underbrace{\frac{1}{2}}_{\text{Average}}\left(\frac{g_w^2}{8m_w^2}\right)^2 \times \underbrace{Tr[\gamma^\mu(1-\gamma^5)\not{p}_{\nu_\mu}\gamma^\nu(1-\gamma^5)(\not{p}_{\mu^+} - m_{\mu^+})]}_{\text{First Part}} \times \underbrace{Tr[\gamma_\mu(1-\gamma^5)(\not{p}_e - m_e)\gamma_\nu(1-\gamma^5)\not{p}_{\nu_e}]}_{\text{Second Part}} \tag{A.16}$$

Looking at the First Part:

$$Tr[\gamma^{\mu}(1-\gamma^5)\not{p}_{\nu_\mu}\gamma^{\nu}(1-\gamma^5)(\not{p}_{\mu^+}-m_{\mu^+})] = Tr[\gamma^{\mu}\not{p}_{\nu_\mu}\gamma^{\nu}(1-\gamma^5)(1-\gamma^5)(\not{p}_{\mu^+}-m_{\mu^+})]$$

Because $\gamma^5\gamma^{\alpha} = -\gamma^{\alpha}\gamma^5$ so anticommuting twice gives us this result

$$Tr[\gamma^{\mu}\not{p}_{\nu_\mu}\gamma^{\nu}(1-\gamma^5)(1-\gamma^5)(\not{p}_{\mu^+}-m_{\mu^+})] = 2\times Tr[\gamma^{\mu}\not{p}_{\nu_\mu}\gamma^{\nu}(1-\gamma^5)(\not{p}_{\mu^+}-m_{\mu^+})]$$

Because$(1-\gamma^5)^2 = 2(1-\gamma^5)$

$$2\times Tr[\gamma^{\mu}\not{p}_{\nu_\mu}\gamma^{\nu}(1-\gamma^5)(\not{p}_{\mu^+}-m_{\mu^+}) = 2Tr(\gamma^{\mu}\gamma^{\alpha}\gamma^{\nu}p_{\alpha}(1-\gamma^5)(p_{\beta}\gamma^{\beta}-m_{\mu}))$$

Where $\not{p}_{\nu_\mu} = \gamma^{\alpha}p_{\alpha}$ and $\not{p}_{\mu} = \gamma^{\beta}p_{\beta}$

$$= 2Tr(\underbrace{\gamma^{\mu}p_{\alpha}\gamma^{\alpha}\gamma^{\nu}\gamma^{\beta}p_{\beta}}_{\text{First term}} - \underbrace{m\gamma^{\mu}p_{\alpha}\gamma^{\alpha}\gamma^{\nu}}_{\text{Second Term}} - \underbrace{\gamma^{\mu}p_{\alpha}\gamma^{\alpha}\gamma^{n}u\gamma^5 p_{\beta}\gamma^{\beta}}_{\text{Third Term}} + \underbrace{mp_{\alpha}\gamma^{\mu}\gamma^{\alpha}\gamma^{\nu}\gamma^5}_{\text{Fourth Term}})$$

First Term: $2Tr(\gamma^{\mu}p_{\alpha}\gamma^{\alpha}\gamma^{\nu}\gamma^{\beta}p_{\beta}) = 2p_{\alpha}p_{\beta}\times 4(g^{\mu\alpha}g^{\nu\beta} - g^{\mu\nu}g^{\alpha\beta} + g^{\mu\beta}g^{\alpha\nu})$

Second Term: $2Tr(m\gamma^{\mu}p_{\alpha}\gamma^{\alpha}\gamma^{\nu}) = 0$ because Tr(odd # of gamma matrices)=0

Third Term: $-2Tr(\gamma^{\mu}p_{\alpha}\gamma^{\alpha}\gamma^{n}u\gamma^5 p_{\beta}\gamma^{\beta}) = 2Tr(\gamma^5\gamma^{\mu}p_{\alpha}\gamma^{\alpha}\gamma^{\nu}p_{\beta}\gamma^{\beta}) = 8i\epsilon^{\mu\alpha\nu\beta}$

Fourth Term: $2Tr(m_{\mu}p_{\alpha}\gamma^{\mu}\gamma^{\alpha}\gamma^{\nu}\gamma^5) = 0$ because Tr(odd # of gamma $\times\gamma^5$)=0

So the first part of the matrix element $8p_{\alpha}p_{\beta}\times(g^{\mu\alpha}g^{\nu\beta} - g^{\mu\nu}g^{\alpha\beta} + g^{\mu\beta}g^{\alpha\nu} + i\epsilon^{\mu\alpha\nu\beta})$,

Now the second part of the matrix element. Using $\not{p}_e = p^{\sigma}\gamma_{\sigma}$ and $\not{p}_{\nu_e} = p^{\kappa}\gamma_{\kappa}$

We get:

$$Tr(\gamma_\mu(1-\gamma^5)(p^\sigma\gamma_\sigma - m_e)\gamma_\nu(1-\gamma^5)p^\kappa\gamma_\kappa)$$

$$= Tr(\gamma_\mu(p^\sigma\gamma_\sigma(1+\gamma^5) - m_e(1-\gamma^5))(1+\gamma^5)\gamma_\nu p^\kappa\gamma_\kappa)$$

Notice the m_e term has $(1-\gamma^5)(1+\gamma^5) = 0$ so m_e terms will vanish, so can rewrite:

$$= Tr(\gamma_\mu p^\sigma\gamma_\sigma(1+\gamma^5)(1+\gamma^5)\gamma_\nu p^\kappa\gamma_\kappa)$$

$$= 2Tr(\gamma_\mu p^\sigma\gamma_\sigma\gamma_\nu p^\kappa\gamma_\kappa + \gamma_\mu p^\sigma\gamma_\sigma\gamma^5\gamma_\nu p^\kappa\gamma_\kappa)$$

$$= 2Tr(\gamma_\mu p^\sigma\gamma_\sigma\gamma_\nu p^\kappa\gamma_\kappa) + 2Tr(\gamma_\mu p^\sigma\gamma_\sigma\gamma^5\gamma_\nu p^\kappa\gamma_\kappa)$$

$$= 2\times 4(g_{\mu\sigma}g_{\nu\kappa} - g_{\mu\nu}g_{\sigma\kappa} + g_{\mu\kappa}g_{\sigma\nu} + i\epsilon\mu\sigma\nu\kappa)p^\kappa p^\sigma$$

So the products of the traces are:

$$\underbrace{8p_\alpha p_\beta \times (g^{\mu\alpha}g^{\nu\beta} - g^{\mu\nu}g^{\alpha\beta} + g^{\mu\beta}g^{\alpha\nu} + i\epsilon^{\mu\alpha\nu\beta})}_{\text{First part}} \times \underbrace{8(g_{\mu\sigma}g_{\nu\kappa} - g_{\mu\nu}g_{\sigma\kappa} + g_{\mu\kappa}g_{\sigma\nu} + i\epsilon\mu\sigma\nu\kappa)p^\kappa p^\sigma}_{\text{Second part}}$$

$$\begin{aligned}= 64p_\alpha p_\beta p^\kappa p^\sigma[&g^{\mu\alpha}g^{\nu\beta}(g_{\mu\sigma}g_{\nu\kappa} - g_{\mu\nu}g_{\sigma\kappa} + g_{\mu\kappa}g_{\sigma\nu} + i\epsilon_{\mu\sigma\nu\kappa})\\ &-g^{\mu\nu}g^{\alpha\beta}(g_{\mu\sigma}g_{\nu\kappa} - g_{\mu\nu}g_{\sigma\kappa} + g_{\mu\kappa}g_{\sigma\nu} + i\epsilon_{\mu\sigma\nu\kappa})\\ &+g^{\mu\beta}g^{\alpha\nu}(g_{\mu\sigma}g_{\nu\kappa} - g_{\mu\nu}g_{\sigma\kappa} + g_{\mu\kappa}g_{\sigma\nu} + i\epsilon_{\mu\sigma\nu\kappa})\\ &+i\epsilon^{\mu\alpha\nu\beta}(g_{\mu\sigma}g_{\nu\kappa} - g_{\mu\nu}g_{\sigma\kappa} + g_{\mu\kappa}g_{\sigma\nu} + i\epsilon_{\mu\sigma\nu\kappa})]\end{aligned}$$

$$\begin{aligned}= 64p_\alpha p_\beta p^\kappa p^\sigma[&\delta^\alpha_\sigma\delta^\beta_\kappa - \delta^\alpha_\nu g_{\sigma\kappa}g^{\nu\beta} + \delta^\alpha_\kappa\delta^\beta_\sigma + i\epsilon^{\alpha}{}_{\sigma}{}^{\beta}{}_{\kappa}\\ &-\delta^\nu_\sigma g_{\nu\kappa}g^{\alpha\beta} + g^{\mu\nu}g_{\mu\nu}g^{\alpha\beta}g_{\sigma\kappa} - \delta^\nu_\kappa g_{\sigma\nu}g^{\alpha\beta} - i\underbrace{\epsilon^{\nu}{}_{\sigma\nu\kappa}g^{\alpha\beta}}_{0}\\ &+\delta^\beta_\sigma\delta^\alpha_\kappa - \delta^\nu_\beta g_{\sigma\kappa}g^{\alpha\nu} + \delta^\beta_\kappa\delta^\alpha_\sigma + i\epsilon^{\beta}{}_{\sigma}{}^{\alpha}{}_{\kappa}\\ &+i\epsilon_\sigma{}^\alpha{}_\kappa{}^\beta - i\underbrace{\epsilon_\nu{}^{\alpha\nu\beta}}_{0}g_{\sigma\kappa} + i\epsilon_\kappa{}^\alpha{}_\sigma{}^\beta - \epsilon^{\mu\alpha\nu\beta}\epsilon_{\mu\sigma\nu\kappa}]\end{aligned}$$

$$
\begin{aligned}
= 64 p_\alpha p_\beta p^\kappa p^\sigma [&\delta^\alpha_\sigma \delta^\beta_\kappa - g_{\sigma\kappa} g^{\alpha\beta} + \delta^\alpha_\kappa \delta^\beta_\sigma + i\epsilon^\alpha{}_\sigma{}^\beta{}_\kappa \\
&- g_{\sigma\kappa} g^{\alpha\beta} + \underbrace{g^{\mu\nu} g_{\mu\nu}}_{4} g^{\alpha\beta} g_{\sigma\kappa} - g_{\sigma\kappa} g^{\alpha\beta} \\
&+ \delta^\beta_\sigma \delta^\alpha_\kappa - g_{\sigma\kappa} g^{\alpha\beta} + \delta^\beta_\kappa \delta^\alpha_\sigma + \underbrace{i\epsilon^\beta{}_\sigma{}^\alpha{}_\kappa}_{-i\epsilon^\alpha{}_\sigma{}^\beta{}_\kappa} \\
&+ \underbrace{i\epsilon_\sigma{}^\alpha{}_\kappa{}^\beta + i\epsilon_\kappa{}^\alpha{}_\sigma{}^\beta}_{i\epsilon_\sigma{}^\alpha{}_\kappa{}^\beta - i\epsilon_\sigma{}^\alpha{}_\kappa{}^\beta = 0} - \epsilon^{\mu\alpha\nu\beta}\epsilon_{\mu\sigma\nu\kappa}]
\end{aligned}
$$

Notice the terms on the very right in line 1 and line 3 cancel and we have $4g^{\alpha\beta}g_{\sigma\kappa} - 4g^{\alpha\beta}g_{\sigma\kappa} = 0$. Also the last term

$$
-\epsilon^{\mu\alpha\nu\beta}\epsilon_{\mu\sigma\nu\kappa} = -\epsilon^{\mu\nu\alpha\beta}\epsilon_{\mu\nu\sigma\kappa} = -(-2(\delta^\beta_\kappa\delta^\alpha_\sigma - \delta^\alpha_\kappa\delta^\beta_\sigma))
$$

$$
= 64 p_\alpha p_\beta p^\kappa p^\sigma [2\delta^\sigma_\alpha \delta^\beta_\kappa + 2\delta^\beta_\sigma \delta^\alpha_\kappa + 2(\delta^\beta_\kappa \delta^\alpha_\sigma - \delta^\alpha_\kappa \delta^\beta_\sigma)] = 256 p_\alpha p_\beta p^\kappa p^\sigma \delta^\sigma_\alpha \delta^\beta_\kappa
$$

So finally the multiplication of the traces gives $256(p_{\nu_\mu} \cdot p_e)(p_\mu \cdot p_{\nu_e})$

$$
\Rightarrow < |\mathcal{M}| >^2 = \frac{1}{2}\left(\frac{g_w}{m_w 2\sqrt{2}}\right)^4 \times 256(p_{\nu_\mu} \cdot p_e)(p_\mu \cdot p_{\nu_e})
$$

$$
\langle |M| \rangle^2 = 2\left(\frac{g_w}{M_w}\right)^4 (p_{\nu_\mu} \cdot p_e)(p_\mu \cdot p_{\nu_e}) \tag{A.17}
$$

In the muon rest frame, $p_\mu = (m_\mu, \vec{0})$, which means $p_\mu \cdot p_{\nu_e} = m_\mu E_{\nu_e}$, and using $(p_\mu - p_{\nu_e})^2 = (p_{\nu_\mu} + p_e)^2$, this gives,

$$
p_{\nu_\mu} \cdot p_e = m_\mu^2/2 - m_\mu E_{\nu_e} \tag{A.18}
$$

This leads to

$$
\langle |M| \rangle^2 = \left(\frac{g_w}{M_W}\right)^4 m_\mu^2 E_{\nu_e}(m_\mu - 2E_{\nu_e}) = \left(\frac{g_w^2 m_\mu^2}{M_W^2}\right)^2 |\vec{p_{\nu_e}}|(m_\mu - 2|\vec{p_{\nu_e}}|) \tag{A.19}
$$

From Eq A.13 and performing the $\vec{p_{\nu_\mu}}$ integral, and using

$$
\delta^4(p_\mu - p_e - p_{\nu_\mu} - p_{\nu_e}) = \delta(m_\mu - |\vec{p_{\nu_\mu}}| - |\vec{p_{\nu_e}}| - |\vec{p_e}|)\delta^3(|\vec{p_{\nu_\mu}}| + |\vec{p_{\nu_e}}| + |\vec{p_e}|)
$$

$$
d\Gamma = \frac{\langle |M| \rangle^2}{16(2\pi)^5 m_\mu} \frac{d^3\vec{p_{\nu_e}} d^3\vec{p_e}}{|\vec{p_{\nu_e}}||\vec{p_{\nu_e}} + \vec{p_e}||\vec{p_e}|} \delta(m_\mu - |\vec{p_{\nu_e}}| - |\vec{p_{\nu_e}} + \vec{p_e}| - |\vec{p_e}|) \tag{A.20}
$$

Doing this integral in spherical coordinates where the $|\vec{p_{\nu_e}}|$ is integrated over the values between $m_\mu/2$ (maximum value) and $m_\mu/2 - |\vec{p_e}|$ (minimum value). This integral gives

$$d\Gamma = \left(\frac{g_w}{4\pi M_W}\right)^4 m_\mu \left(\frac{m_\mu}{2} - \frac{2}{3}|\vec{p_e}|\right) d^3\vec{p_e} \tag{A.21}$$

Again doing this integration in spherical coordinates where $|\vec{p_e}| = E_e$, the decay rate is realized

$$\Gamma = \left(\frac{m_\mu g_w}{M_W}\right)^4 \frac{m_\mu}{12(8\pi)^3} \tag{A.22}$$

The inverse of the decay rate produces the muon lifetime of $\sim 2.2\ \mu$s.

B Appendix B - Miscellaneous Plots

Listed below are individual CsI crystal comparisons with black as the measurement and red is the simulation. As stated already, event selection for both was such that the main crystal (highest energy) and its nearest neighbors are added all while the main crystal contains at least 80% of the total energy.

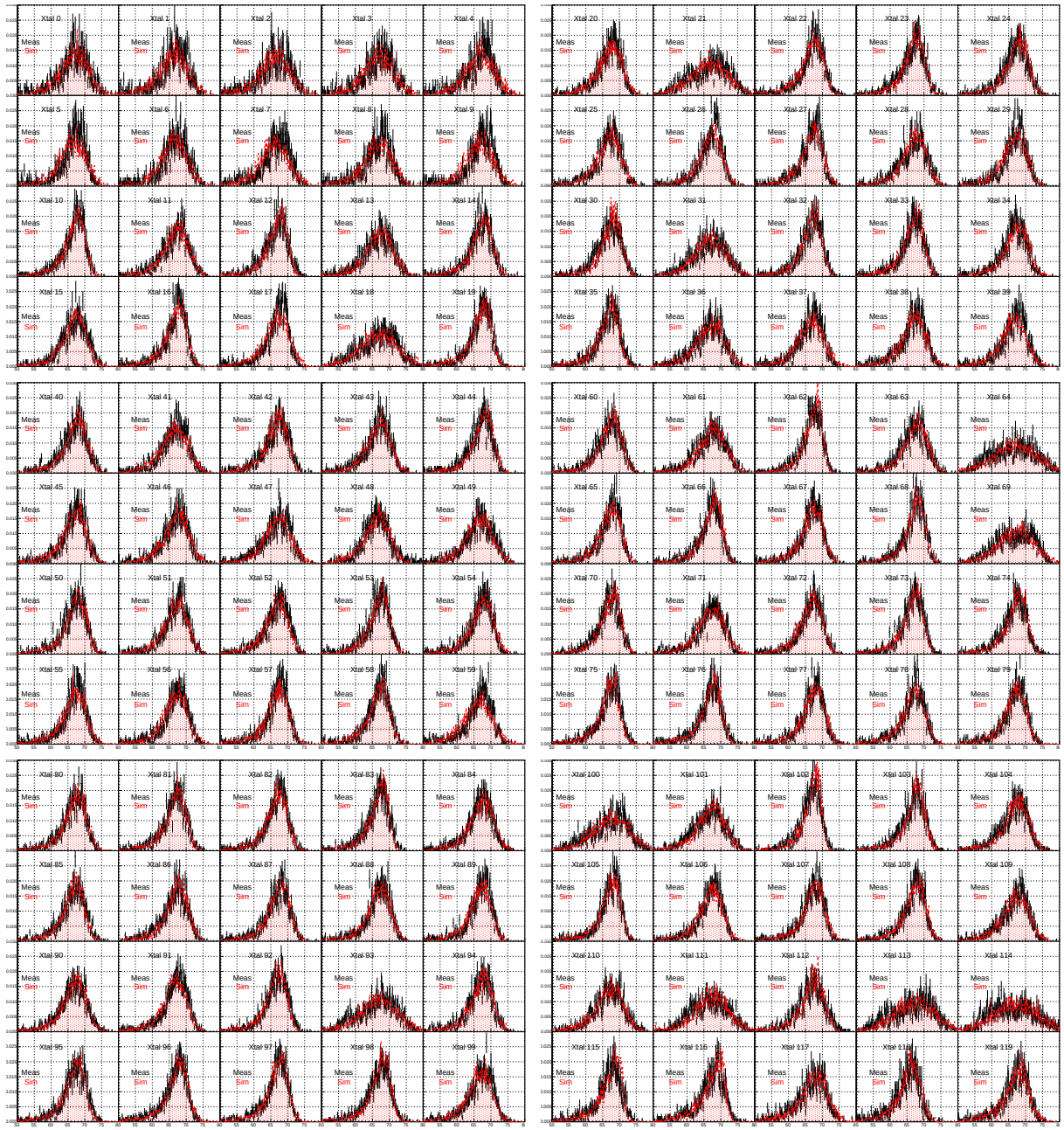
Xtal 0
Xtal 1
Xtal 2
Xtal 3
Xtal 4
Xtal 5
Xtal 6
Xtal 7
Xtal 8
Xtal 9
Xtal 10
Xtal 11
Xtal 12
Xtal 13
Xtal 14
Xtal 15
Xtal 16
Xtal 17
Xtal 18
Xtal 19
Xtal 20
Xtal 21
Xtal 22
Xtal 23
Xtal 24
Xtal 25
Xtal 26
Xtal 27
Xtal 28
Xtal 29
Xtal 30
Xtal 31
Xtal 32
Xtal 33
Xtal 34
Xtal 35
Xtal 36
Xtal 37
Xtal 38
Xtal 39
Xtal 40
Xtal 41
Xtal 42
Xtal 43
Xtal 44
Xtal 45
Xtal 46
Xtal 47
Xtal 48
Xtal 49
Xtal 50
Xtal 51
Xtal 52
Xtal 53
Xtal 54
Xtal 55
Xtal 56
Xtal 57
Xtal 58
Xtal 59
Xtal 60
Xtal 61
Xtal 62
Xtal 63
Xtal 64
Xtal 65
Xtal 66
Xtal 67
Xtal 68
Xtal 69
Xtal 70
Xtal 71
Xtal 72
Xtal 73
Xtal 74
Xtal 75
Xtal 76
Xtal 77
Xtal 78
Xtal 79
Xtal 80
Xtal 81
Xtal 82
Xtal 83
Xtal 84
Xtal 85
Xtal 86
Xtal 87
Xtal 88
Xtal 89
Xtal 90
Xtal 91
Xtal 92
Xtal 93
Xtal 94
Xtal 95
Xtal 96
Xtal 97
Xtal 98
Xtal 99
Xtal 100
Xtal 101
Xtal 102
Xtal 103
Xtal 104
Xtal 105
Xtal 106
Xtal 107
Xtal 108
Xtal 109
Xtal 110
Xtal 111
Xtal 112
Xtal 113
Xtal 114
Xtal 115
Xtal 116
Xtal 117
Xtal 118
Xtal 119
Meas
Sim

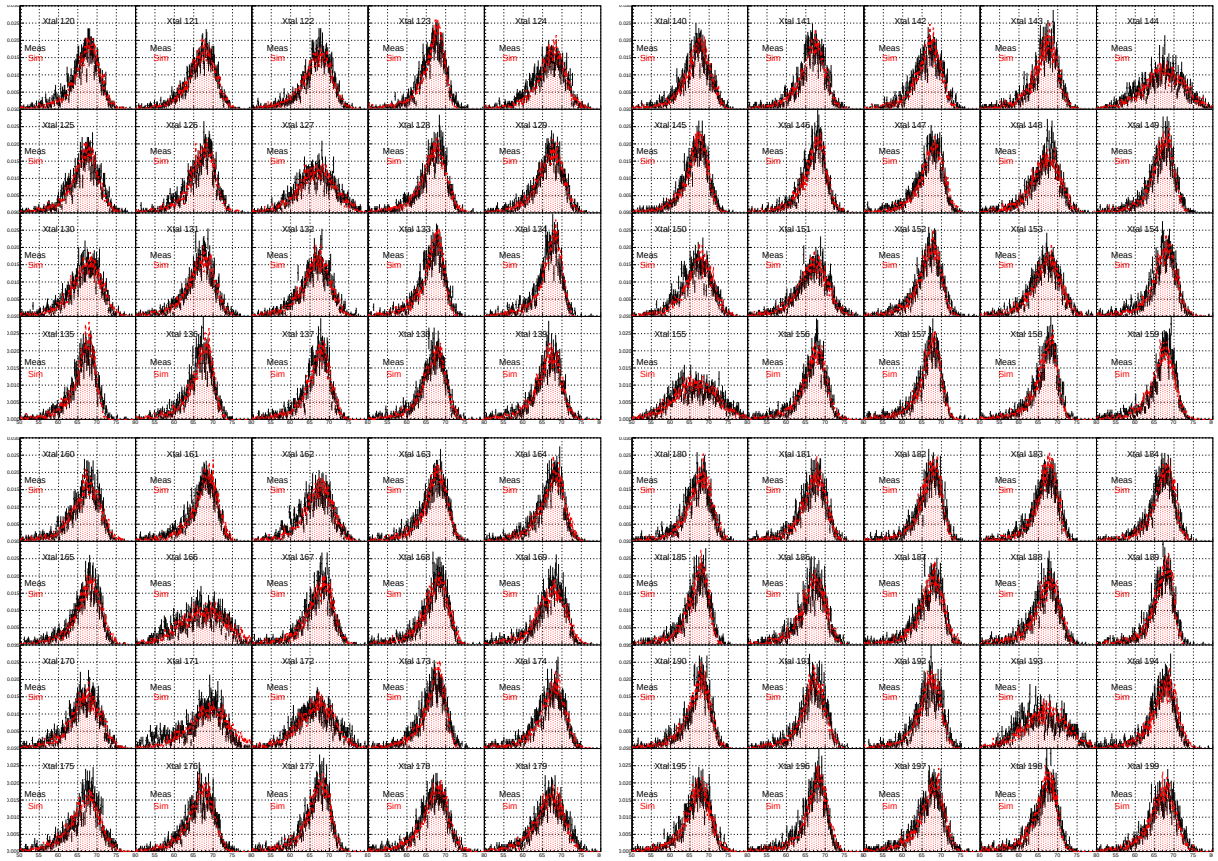

Figure B.1: *Comparison of measured data (black) against simulation (red) for $\pi \rightarrow e\nu$ selection 80% or more of the shower energy is contained in the main crystal.*

Predicted positron energies as a function of the main crystal hit. These plots show the agreement between the pathlength calculation for different trajectories through the target into the proper fiducial volume of an individual crystal.

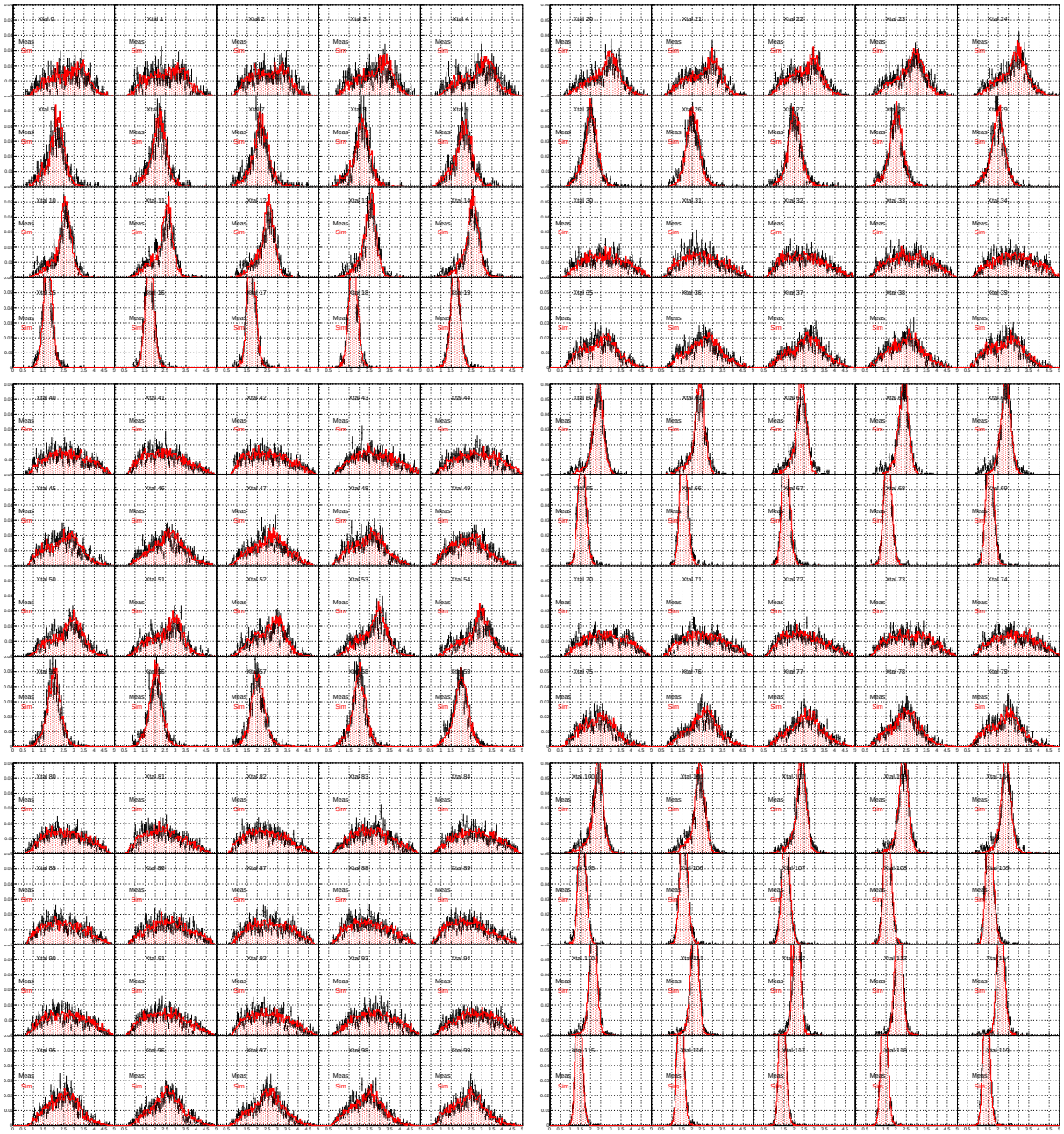

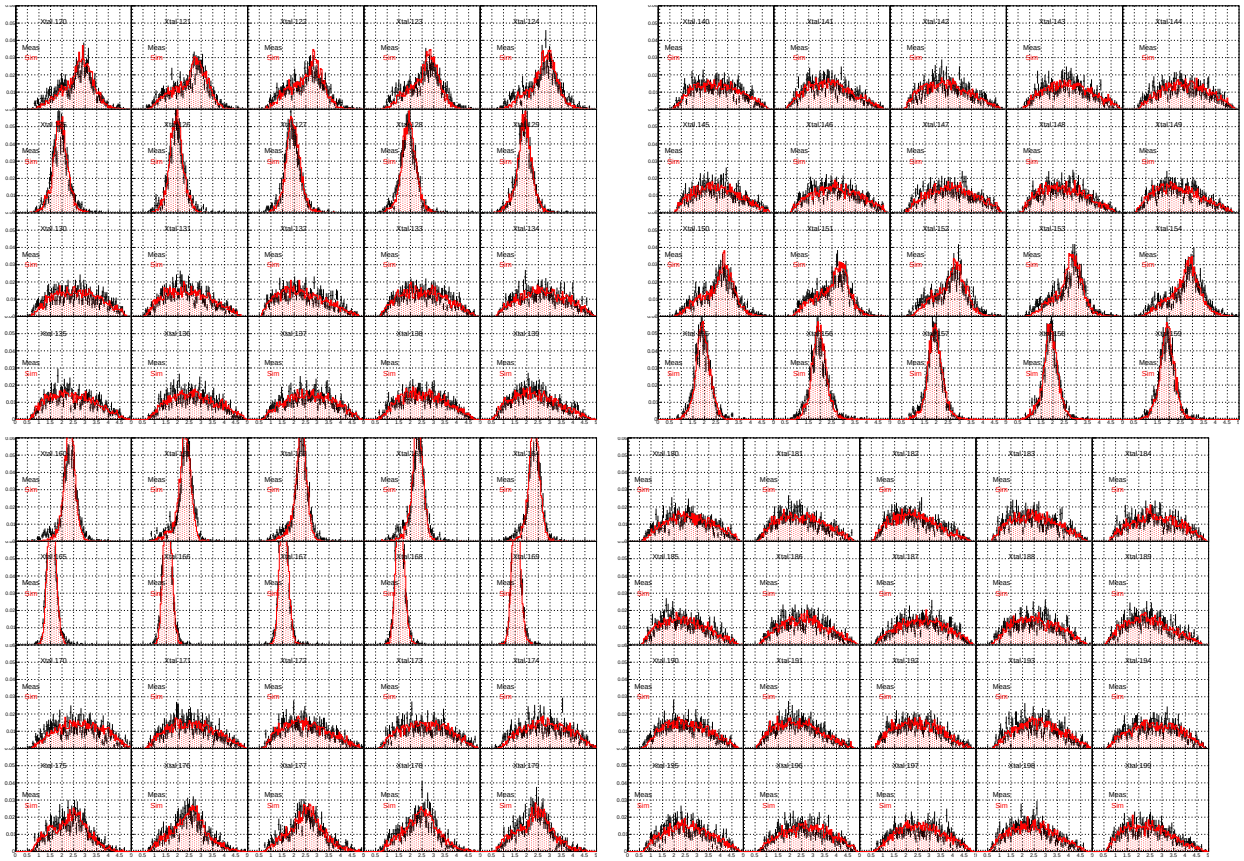

Figure B.2: *Predicted positron target energies based on crystal hit.*

These next plots show the energy deposited in the target as a function of crystal hit. It represents another independent method by which to show the stopping position is consistent between measured data and Monte Carlo simulation

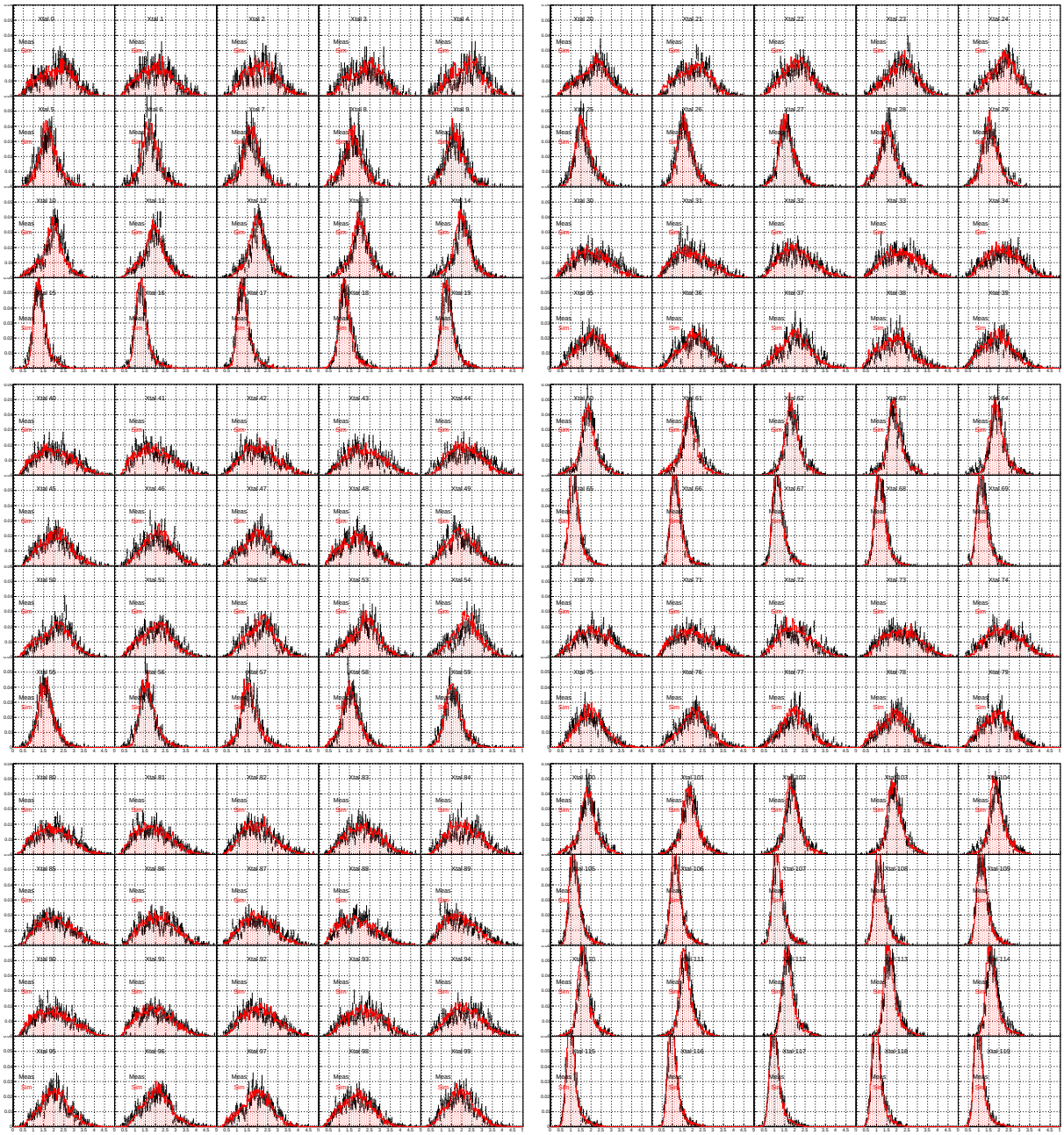

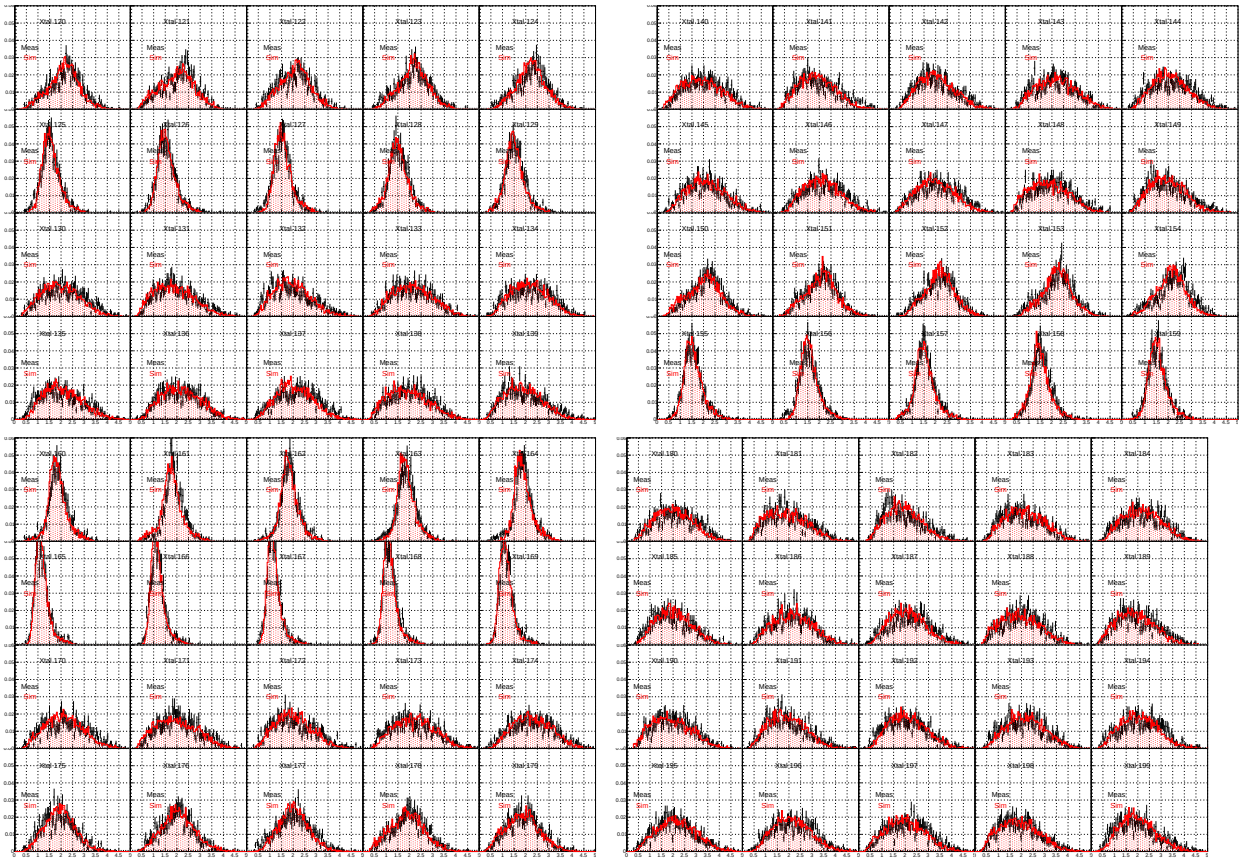

Figure B.3: *Observed positron target energies based on crystal hit.*